Springer Proceedings in Physics 179

Gongtian Shen
Zhanwen Wu
Junjiao Zhang *Editors*

Advances in Acoustic Emission Technology

Proceedings of the World Conference on Acoustic Emission–2015

Springer

Springer Proceedings in Physics

Volume 179

More information about this series at http://www.springer.com/series/361

The series Springer Proceedings in Physics, founded in 1984, is devoted to timely reports of state-of-the-art developments in physics and related sciences. Typically based on material presented at conferences, workshops and similar scientific meetings, volumes published in this series will constitute a comprehensive up-to-date source of reference on a field or subfield of relevance in contemporary physics. Proposals must include the following:—name, place and date of the scientific meeting—a link to the committees (local organization, international advisors etc.)—scientific description of the meeting—list of invited/plenary speakers—an estimate of the planned proceedings book parameters (number of pages/articles, requested number of bulk copies, submission deadline).

Gongtian Shen • Zhanwen Wu • Junjiao Zhang
Editors

Advances in Acoustic Emission Technology

Proceedings of the World Conference on Acoustic Emission–2015

Springer

Editors
Gongtian Shen
China Special Equipment Inspection and Research Institute
Beijing, China

Zhanwen Wu
China Special Equipment Inspection and Research Institute
Beijing, China

Junjiao Zhang
China Special Equipment Inspection and Research Institute
Beijing, China

ISSN 0930-8989 ISSN 1867-4941 (electronic)
Springer Proceedings in Physics
ISBN 978-3-319-29050-8 ISBN 978-3-319-29052-2 (eBook)
DOI 10.1007/978-3-319-29052-2

Library of Congress Control Number: 2017937014

Printed on acid-free paper

This Springer imprint is published by Springer Nature
The registered company is Springer International Publishing AG
The registered company address is: Gewerbestrasse 11, 6330 Cham, Switzerland

Preface

This volume includes the papers selected from the World Conference on Acoustic Emission—2015 (WCAE-2015) that was held on November 10 to November 13 in Hawaii, USA. WCAE was the formal conference of the International Society on Acoustic Emission (ISAE). WCAE-2015 was jointly organized by Acoustic Emission Technology Consulting (Mr. Allen Green) and the University of Memphis (Prof. Gary Qi). This was the third of such event of ISAE followed by its inaugural one in 2011 in Beijing and second in 2013 in Shanghai, China. WCAE is aimed at providing a platform to scientists and practitioners in both academia and industry in the field of acoustic emission and exchanging research and application information, with particular emphasis on scientific and technical development and cooperation worldwide.

The WCAE-2015 consisted of three invited keynote lectures, nine oral and one poster sessions. It covered all major areas of acoustic emission applications, including Instrumentation, Signal Processing and Analysis, Material Characteristics, Structure, Condition Monitoring and Diagnosis, and Miscellaneous.

WCAE-2015 received 38 submissions, which were documented in the extended abstracts of WCAE-2013. Thirty-seven full papers were submitted for the consideration of achieved formal proceeding. After peer reviews, 34 were included in this volume.

We are grateful to all the members of the committees who contributed their efforts to review the manuscripts. We would also like to express our sincere gratitude to Acoustic Emission Technology Consulting (Mr. Allen Green) and the University of Memphis (Prof. Gary Qi) for their enormous supports. Last, but not the least, we thank the contributions of all the delegates who participated in WCAE-2015.

Beijing, China

Gongtian Shen
Zhanwen Wu
Junjiao Zhang

Committees

Organization Committee

Chair	Allen Green, Acoustic Emission Technology Consulting
Co-chair	Gary Qi, University of Memphis
Member	Gongtian Shen, China Special Equipment Inspection and Research Institute
	Yongchang Xu, Chinese Society for Non-destructive Testing
	Bangxian Li, China Special Equipment Inspection and Research Institute
	Zhanwen Wu, China Special Equipment Inspection and Research Institute

Paper and Program Committee

Chair	Gongtian Shen, China Special Equipment Inspection and Research Institute
Co-chair	Gary Qi, University of Memphis
Members	Allen Green, Acoustic Emission Technology Consulting
	Manabu Enoki, University of Tokyo
	Oswaldo Santos Filho, Technology Center, Eletronorte
	Karen Holford, Cardiff University
	Andy C. C. Tan, Queensland University of Technology
	Peter Tscheliesnig, TÜV Austria Services GmbH
	Bangxian Li, China Special Equipment Inspection and Research Institute
	Cherdpong Jomdecha, King Mongkut's University of Technology
	Boris Muravin, Association of Engineers and Architects in Israel

Secretary Committee

Chair Bangxian Li, China Special Equipment Inspection and Research Institute

Members Zhanwen Wu, China Special Equipment Inspection and Research Institute
Yaqing Zhu, Chinese Society for Non-destructive Testing
Yingyun Wang, Chinese Society for Non-destructive Testing
Jingyuan Ji, Chinese Society for Non-destructive Testing
Xuerong Tao, China Special Equipment Inspection and Research Institute
Guanghai Li, China Special Equipment Inspection and Research Institute
Junjiao Zhang, China Special Equipment Inspection and Research Institute

Advisory Committee

Allen Green, Acoustic Emission Technology Consulting, United States of America
Gary Qi, University of Memphis, United States of America
Gongtian Shen, China Special Equipment Inspection and Research Institute, China
Manabu Enoki, University of Tokyo, Japan
Karen Holford, Cardiff University, United Kingdom
Oswaldo Santos Filho, Electrobras Eletronorte, Brazil
Bangxian Li, China Special Equipment Inspection and Research Institute, China
Cherdpong Jomdecha, King Mongkut's University of Technology, Thonburi, Thailand
Andy Tan, Queensland University of Technology, Australia
Boris Muravin, Association of Engineers and Architects in Israel, Israel
Rongsheng Geng, Beijing Aeronautical Technology Research Center, China
Shuichi Wakayama, Tokyo Metropolitan University, Japan
Martin Browne, University of Southampton, United Kingdom
Hartmut Vallen, Vallen Systeme GmbH, Icking, Germany
Didem Ozevin, University of Illinois, Chicago, United States of America
Joseph Labuz, University of Minnesota, United States of America
Christian Grosse, Technical University, Munich, Germany
Suherin, PT. Dimensi Barumas Perdana, Indonesia
Maochen Ge, Missouri University of Science and Technology, United States of America
Tomoki Shiotani, Kyoto University, Japan
Gerd Manthei, Technische Hochschule Mittelhessen, Germany
Antolino Gallego Molina, University of Granada, Spain
Peter Tscheliesnig, AT Consulting, Austria
Hajime Hatano, Tokyo University of Science, Japan
Shifeng Liu, Soundwel Technology Company, LTD., China

Zhen Huo, WuHan Boiler Pressure Vessel Inspection Institute, China
Guang Dai, Northeast Petroleum University, China
Luming Li, Tsinghua University, China
Yanting Xu, Zhejiang Provincial Special Equipment Inspection Institution, China
Wei Li, Northeast Petroleum University, China
Zhejun Liu, Aerospace Research Institute of Materials & Processing Technology, China
Guanghai Li, China Special Equipment Inspection and Research Institute, China
Yukuan Ma, Jilin University, China
Jun Jiang, Nanjing Boiler & Pressure Vessel Supervision and Inspection Institute, China
Zhanwen Wu, China Special Equipment Inspection and Research Institute, China
Qiang Wang, China Jiliang University, China
Chunguang Xu, Beijing Institute of Technology, China
Yaqing Zhu, Chinese Society for Non-destructive Testing, China
Xiling Liu, Central South University, China
Jason Weiss, Purdue University, USA

Contents

Part I
Keynote Lecture

Progress of Acoustic Emission Technology on Pressure Equipment in China

Gongtian Shen

Abstract Acoustic emission (AE) techniques were introduced into China in the end of the 1960s. AE was applied to pressure vessel testing in the early 1980s. Now six AE testing and evaluation standards for pressure vessel have been published. More than 120 inspection organizations and 670 level II and III personnel are engaged in AE testing services for pressure equipment. More than 1500 large size pressure vessels are tested by AE per year. This chapter introduces the progress of AE testing for pressure vessels in China. In addition, the main AE instruments made in China are introduced. A newly developed pipeline leakage location instrument based on acoustic methods and correlation of the locations of continuous signals is also introduced. The results of a new study of cast iron paper dryers are reported.

1 Introduction

Acoustic emission (AE) techniques were introduced into China in 1969. From 1972 to 1974, the Metals Institute of the Academy of Sciences of China performed research on AE characteristics of metallic deformation and fracture. Many researchers used AE to monitor and measure cracking and growth of cracks in steel in the latter half of the 1970s [1].

In the 1980s AE research and applications developed rapidly with the main objective of in-service testing for metallic pressure vessels [2–6]. Since then more than 3000 large pressure vessels have been tested by the China Special Equipment Inspection Institute (CSEI) [7–9], the Hefei General Machine Institute, the Wuhan Safety and Environmental Protection Institute, and the Daqing Petroleum Institute [10].

The first single-channel AE instrument was developed by the Shenyang Computer Research Institute in China in 1976. Two-channel and four-channel AE instruments were manufactured and sold in the 1980s. A 36-channel AE instrument was developed in 1986. The first multi-channel AE instrument based on a PC/AT bus and Windows software was developed by CSEI in 1996. The first digital

G. Shen (✉)
China Special Equipment Inspection and Research Institute, Beijing 100029, China
e-mail: shengongtian@csei.org.cn

G. Shen et al. (eds.), *Advances in Acoustic Emission Technology*, Springer Proceedings in Physics 179, DOI 10.1007/978-3-319-29052-2_1

multi-channel AE instrument based on AE signal wave acquisition was developed in 2000 by Soundwel Technology Co., Ltd [11]. The first digital multi-channel AE instrument based on USB techniques and wireless AE systems based on GPS techniques were developed in 2008 by Soundwel Technology Co., Ltd [12, 13].

The present chapter reviews the status of AE organizations, personnel, standards, application areas and recent research results related to pressure equipment in China.

2 Organizations and AE Personnel

The Chinese Committee on Acoustic Emission (CCAE) was formed in 1978 as one technical committee of the Chinese Society for NDT. The committee chairman and members are changed every 4 years. The committee chairman can hold the position for a maximum of two 4-year terms. In 2013, Prof. Shifeng Liu from Soundwel Technology Co., Ltd became Chairman, a position he still holds. There are 47 members on the CCAE. Meetings are held every summer.

The First National Acoustic Emission Conference was held in 1979. To date, 14 National Acoustic Emission Conferences have been held. Starting with the fifth conference, the conferences have been held once every 2 years. The number of delegates is usually between 80 and 120 and the proceedings usually collect 40–60 papers. Delegates from USA, Germany and Japan attended the 7th, 10th, 11th and 12th Conferences in China.

There are now more than 60 universities, colleges and institutes engaged in AE research and applications in China. There are more than 120 inspection organizations engaged in AE testing services for pressure equipment, atmospheric tanks, aircraft and steel structures.

Two NDT personnel certification bodies began to qualify and certify AE personnel in 1998 in China. One belongs to the General Administration of Quality Supervision, Inspection and Quarantine (AQSIQ). Twenty-three level III and 860 level II AE personnel have been qualified and certified by AQSIQ. The testing objects of these AE personnel are various types of special equipment including boilers, pressure vessels, pressure piping, cranes, passenger ropeways and amusement rides. The second certification body belongs to the Committee of Scientific and Technical Industry for National Defense (CSTIND). Four level III and 120 level II AE personnel have been qualified and certified by CSTIND. The testing objects of these AE personnel are aeronautical facilities, space equipment, weapons and nuclear industrial equipment.

The most important activities in AE testing in China have been in the field of pressure equipment testing and safety evaluation since 1980. More than 100 special equipment inspection agencies or NDT agencies are engaged in AE testing of pressure equipment. Almost 80% of the multi-channel AE instruments are used for pressure vessel testing. More than 1000 large size pressure vessels are tested every year. CSEI is the largest AE inspection agency for pressure vessels in China.

3 AE Instrument

A total of about 1500 channels-worth of AE instruments have been sold in China recent years. Sixty percent of AE instruments are imported from PAC of USA and Vallen Corporation of Germany. There are two domestic companies manufacturing AE instruments and systems in China. One is Soundwel Technology Co., Ltd, which produces and sells multi-channel digital AE instruments and wireless AE systems. The other is Softland Times Corporation, which produces and sells multi-channel digital AE instruments. Next, we describe the two main AE instruments made in China.

3.1 SAEU2S Multi-channel Integrated Acoustic Emission System

Figure 1 shows the SAEU2S Multi-channel Integrated Acoustic Emission System. Multiple acquisition cards are integrated into the acquisition unit, with two independent channels per acquisition card. Four types of acquisition card are available from which to choose. Their maximum sample rates and sample accuracies are, respectively, 40 MHz/18 bit, 10 MHz/16 bit, 5 MHz/16 bit and 3 MHz/16 bit.

USB 2.0 or 3.0 connections are used for data transmission between the computer and the data acquisition unit. The USB connection can operate with an extended cable of up to 100 m. There are four kinds of boxes for the data acquisition unit, which capcities of, respectively, 2 channels, 10 channels, 20 channels and 30 channels. Two or more boxes can be combined as a super-system for up to 200 AE channels.

Fig. 1 Picture of SAEU2S AE system

The main performance features of SAEU2S are:

- Real-time continuous AE hit data transferring rate over 400,000 hits/s
- Real-time continuous AE waveform data transfer rate over 30 MB/s
- Hardware real-time digital filter: any value can be set to straight, high pass, low pass, band pass or band stop within the frequency range from 0 kHz to 3 MHz
- Hardware real-time FFT analysis: Time domain waveforms and power spectral parameters output
- Waveform Sampling Length: Maximum length of a single waveform sampling up to 128k sampling points
- Before/after waveform sample length up to 128 kB
- Auto sensor testing: Built-in AST function, transmit AE for testing
- Noise: <10 dB (no load)
- Maximum signal amplitude: 100 dB
- Dynamic Range: 90 dB
- AE hit data: Time of First Threshold Crossing, Time of Peak, Peak Amplitude, Counts, Duration, Energy, Counts to Peak, Rise Time, RMS, ASL, Parametric 1–12, Power Spectrum Parametric 1–5

3.2 SAEW2 Multi-channel Wireless Distributed Acoustic Emission System [12]

The SAEW2 multi-channel wireless distributed AE system is built with multiple wireless single-channel acquisition units and a computer. The connections between multiple independent AE signal acquisition units and the computer are established by using wireless network switches and remote Wi-Fi or LAN. Every unit acquires data according to the PC software settings, and acquired data is uploaded back to the PC. Time synchronization between units is maintained by GPS time. Figure 2 shows a photograph of the wireless AE signal acquisition unit. Figure 3 shows the switch and long distance wireless model. The SAEW2 system is suitable for AE real time testing or monitoring situations in wiring presents an obstacle, such as large rotating equipment, high and steep slopes, viaducts and large hydropower reservoirs.

The main performance features of SAEW2 are:

- Wireless transmission distance is up to 100 m, 10 km when using a long-distance Wi-Fi unit and 100 km when using an optical Ethernet connection
- Time synchronization between units is maintained by GPS time, synchronous accuracy is better than 30 μs, time difference locate error is less than 0.1 m
- Waveform transmission rate is up to 2 MBps, 20,000 hits/s. This can satisfy the requirements of 64-channel positioning
- Multiple units transmit data in real-time. The unit can identify time differences among source locations in real time

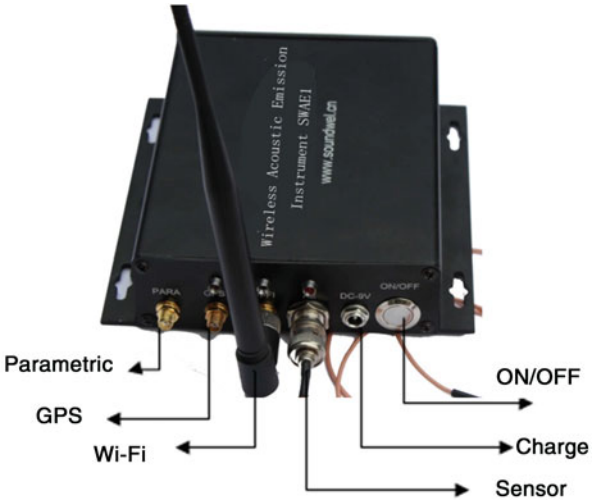

Fig. 2 The wireless AE signal acquisition unit

Fig. 3 The switch and long distance wireless model

- The acquisition card performs the functions of real time digital filter, wave reconstruction and parameter extraction after filter
- The system can be directly connected into other networks to establish a larger AE network system
- Signal Frequency: 1 kHz to 1.6 MHz
- Sample Rate/Resolution: 10M/16 bit, 5M/16 bit, 3M/16 bit are optional
- Dynamic Range: $\geq$70 dB. Noise: $\leq$30 dB
- Built-in pre-amplifier: 40 dB
- Hardware digital filter: Ignore, High-pass (20, 100, 400 kHz), Low-Pass (100, 400, 1200 kHz), Band-pass and Reject filter can be set to arbitrary frequency numerical values from 0 to 3 MHz
- Unit size: 170 $\times$ 120 $\times$ 40 mm
- Unit weight: 0.6 kg
- Operating Temperature: -10 °C to $+45$ °C
- Power supply: 9–12 V DC power supply, battery life is about 8 h

4 AE Standards

At this time, 11 AE standards relevant to pressure equipment have been published in China. These standards are:

GB/T 12604.4-2004 Non-destructive testing—Terminology—Terms used in acoustic emission testing
GB/T 19800-2005 Non-destructive testing—Acoustic emission—Primary calibration of transducers
GB/T 19801-2005 Non-destructive testing—Acoustic emission—Secondary calibration of acoustic emission sensors
JB/T 11603.1-2013 Non-destructive testing—Acoustic emission—Equipment characterization—Part 1: Equipment description
JB/T 11603.2-2013 Non-destructive testing—Acoustic emission—Equipment characterization—Part 2: Verification of operating characteristics
GB/T 18182-2012 Acoustic emission testing and evaluation of metallic pressure vessels
GJB 2044-1994 Acoustic emission testing of titanium alloy pressure vessels
JB/T7667-1995 Acoustic emission testing and evaluation of in-service pressure vessels
JB/T6916-1993 Acoustic emission testing and evaluation of in-service high pressure cylinders
JB/T 10764-2007 Non-destructive testing - Acoustic emission testing and evaluation of atmospheric pressure metal storage tanks
NB/T 47013.9-2012 Nondestructive testing of pressure equipment—Part 9: Acoustic emission testing

NB/T 47013.9 is the most-used. The unique point of this standard is that it gives a detailed evaluation method for AE test results of pressure equipment. The evaluation of AE sources is based on activity and intensity of AE source location. AE source activities (SA) are divided into four levels: weak, medium, strong and super. AE source intensities (SI) are divided into three levels: low, medium and high. The final evaluation classes of AE sources are given in Table 1 by colligating activity level and intensity level of AE sources. In addition, this standard stipulates that Class III and IV AE sources should be retested by other NDT methods such as UT, MT or PT. For class II AE sources, an inspector decides whether to retest or not. Class I does not need to be retested.

Table 1 Evaluation classes of AE sources

	Activity			
Intensity	Super	Strong	Medium	Weak
Low	IV	IV	III	II
Medium	IV	III	II	I
High	III	III	II	I

5 Main Research and Applications

5.1 Steel Pressure Vessel Testing

The most important activities in AE testing in China since 1980 have been in the field of pressure vessel testing and safety evaluation. At the present time more than 120 inspection agencies are engaged in pressure vessel testing using AE. Almost 70% of multi-channel AE instruments are used for pressure vessel testing. More than 1500 large pressure vessels are tested every year. CSEI is the largest inspection organization for pressure vessels. AE testing of steel pressure vessels falls into four classifications:

1. *AE testing of new metallic pressure vessels (MPVs)during proof hydrostatic pressure tests*
   This testing includes monitoring leakage to prevent catastrophic failure of the pressure vessel, evaluating its structural integrity and finding unknown flaws to prevent them from cracking and growing.
2. *AE testing and defect assessment of in-service MPVs*
   There are many welding defects such as porosity, slag inclusion, non-fusion, lack of penetration, particularly in the pressure vessels manufactured in the 1970s in China, when there were no strict quality control systems. How to handle these welding defects is a difficult challenge for inspection of in-service pressure vessels. Repair of all the welding defects is expensive and takes a long time. The conventional non-destructive testing methods such as ultrasonic tests and radiographic tests take a long time and have difficulties distinguishing the degree of activity of defects. Fracture mechanics assessment depends on knowing the exact size of the defect. Over time, AE testing has been found to be the most effective method for assessing welding defects of in-service pressure vessels. Cracking and growth of defects, slag inclusion fracture, residual stress releasing, oxide scales peeling off, structural friction and leakage can be distinguished through using time difference AE source location, modern spectrum analysis, pattern recognition analysis, artificial neural network pattern recognition and grey correlation analysis [14–17].
3. *AE on-line monitoring and safety evaluation of MPVs*
   According to relevant administration and supervision regulations of pressure vessels in China, in-service pressure vessels should be taken off line to perform inspections and tests every 6 years. But sometimes production can't be stopped. In such cases, AE on-line monitoring is used to evaluate the safety situation and extend the operating period of pressure vessels. In addition, AE on-line monitoring is frequently used to monitor the active situation of known welding defects for in-service pressure vessels.
4. *AE testing and safety evaluation of wrapped multi-layer pressure vessels (WMPVs)*

The wrapped multi-layer thick wall cylindrical pressure vessel is one of the designs most used for high pressure vessels in China. Because they offer many advantages, including high ductility, high safety, and low fabrication costs, a large number of WMPVs have been fabricated and used in China since 1958. One of the most used WMPV designs in China is the hydrogen and nitrogen gas cylindrical pressure vessel. However, due to the structural character of WMPVs, their in-service inspection and testing is very difficult for ultrasonic and radiographic tests. Because WMPVs, produce a lot of AE signals by friction between layers during load, obscuring signals from flaws, it was originally held that AE tests might not be applicable to WMPVs. However, after performing AE tests for 14 wrapped multilayer cylindrical nitrogen gas tanks, through two load sequences and many load-hold periods, it was found that there are many more AE signals in WMPVs than in single layer pressure vessels in the first loading, but the AE character of WMPVs is the same as single layer pressure vessels in the second loading. Now the AE testing technique of WMPV has been developed. At this time more than 500 WMPVs have been tested and evaluated.

5.2 Pressure Pipeline Leakage Testing [13]

Locating leakage points in underground gas pipelines is a difficult problem. In order to solve this problem, a new pipeline leakage location instrument based on acoustic methods and correlation of the locations of continuous signals was jointly developed by CSEI and Soundwel Technology Co., Ltd. This instrument uses advanced electronic techniques such as low frequency AE sensors, high speed acquisition of waveforms of leakage signals, wireless data communications based on the internet, high speed USB-based data communication, and time control based on GPS positioning. Real-time leakage location tests and remote wireless leakage location tests have been realized for different kinds of pipeline with different medium leaks. The testing results prove that this instrument can detect the leakage of a 1 mm hole from a distance of 50 m and a 2 mm hole from a distance of 100 m for a steel pipeline under 0.4 MPa compressed air.

Figure 4 shows one set of the newly-developed gas pipeline leakage testing instrument. There are two acquisition modules of acoustic waves and one computer in this picture. There are one sensor, one GPS antenna and one transmitter antenna for each acquisition module. The main functions of the instrument are as follows:

- Viewing of the original waveforms
- Analysis of the frequency spectrum of the waveforms by use of Fourier transforms
- Correlation analysis between waveforms from two acquisition modules
- Calculating and showing the location of the leakage point
- Giving the intensity of leakage with RMS

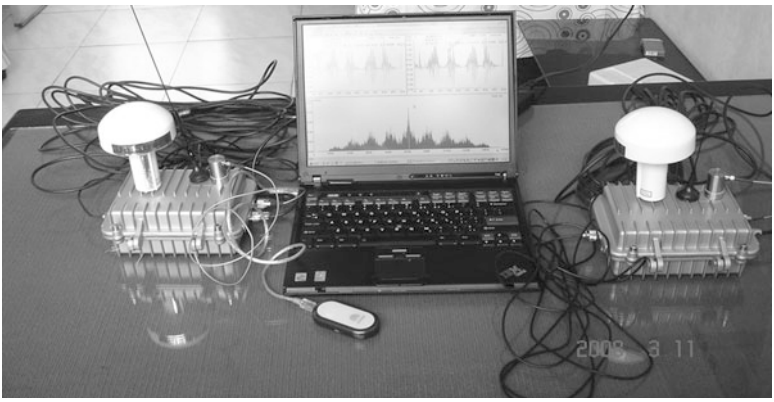

Fig. 4 The developed gas leakage testing instrument

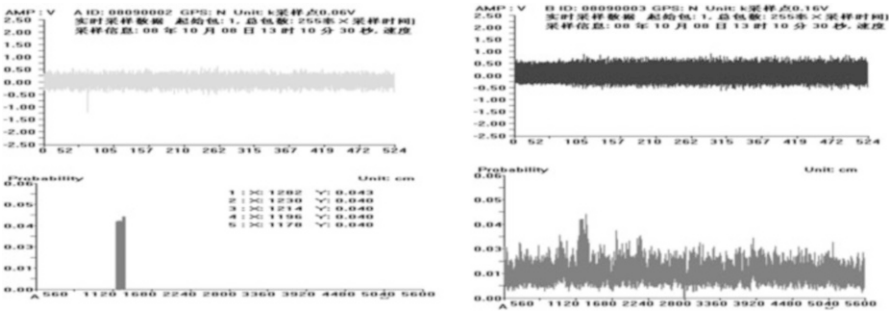

Fig. 5 The correlation located result for Φ 1 mm hole leakage

Figure 5 shows the waveforms from two sensors and the location results for a 1 mm diameter hole leakage for an underground steel pipeline of size Φ 159 × 6 × 65 mm with buried depth 0.5 m and air pressure 0.4 MPa. The distance between the leakage point and the sensor is 50 m. The location error was smaller than 0.5 m.

5.3 Cast Iron Paper Dryer Testing [18]

In order to evaluate AE's ability to detect signals from cracks in cast iron paper dryers, an AE test was carried out for one scrapped paper dryer. The paper dryer, made of HT250, with a maximum operating pressure of 0.3 MPa, had been out of service for some time. The details of the dryer shell are illustrated in Fig. 6. In order to decrease noise in the AE test, the dryer was subjected to an initial hydrostatic pressurization, which started at 0.1 MPa and increased incrementally to 0.4 MPa.

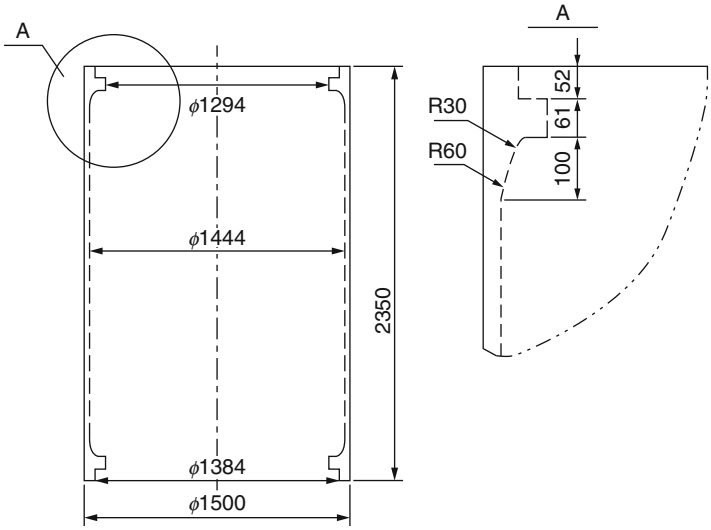

Fig. 6 Details of dryer shell

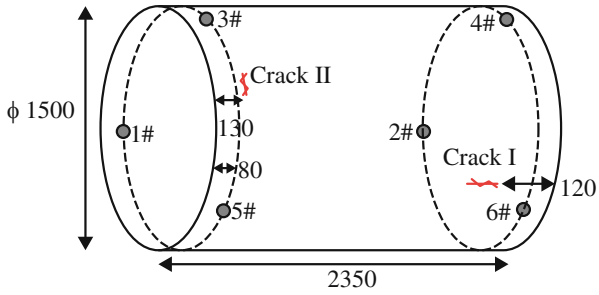

Fig. 7 Crack location and AE sensor array (unit, mm)

Then the first simulation crack was made. A grinder was used to make a slot on the shell, then a metal electrode with a copper wire was dropped into the slot to produce cracks in the dryer. The location of the cracks are shown in Fig. 7. Thereafter, the AE test was performed during hydrostatic pressurization. The loading program is illustrated in Fig. 8. A total of six AE sensors, type VS150, were used to cover the shell of the dryer. In the AE system, a cylinder location analysis program was used to determine any area of activity located in the shell region.

The AE parameter distribution for Crack I of the dryer is illustrated in Fig. 9, the only location in which AE events were analyzed. The range of these AE parameters and the number of locations in each load-hold Stage are detailed in Table 2. Figure 9a is the location diagram of the dryer shell during the entire pressurization program. The *X*-axis is along the circumference direction, and the *Y*-axis stands for the axial direction. It can be seen that the location area is in good agreement with the position of crack I. Figure 9b correlates the counts (line) and amplitude (points)

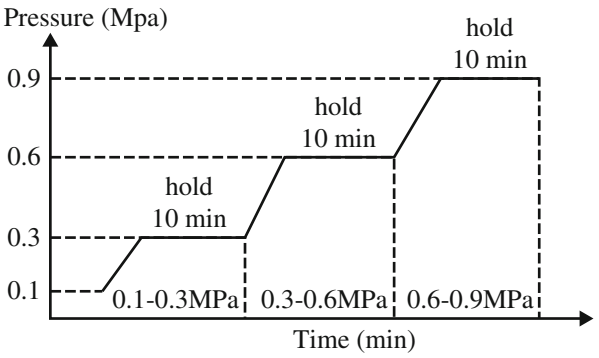

Fig. 8 Pressurization program

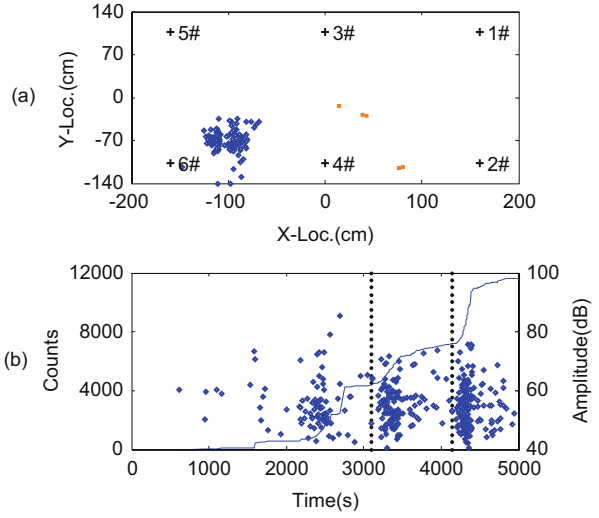

Fig. 9 AE parameter distribution for crack I

Table 2 Parameters for AE test I of dryer

Pressurization (MPa)	Amplitude (dB)	Rise time (μs)	Counts	Locations around Crack I
Load 0.1–0.3	43–73.5	2.6–145.6	1–296	63
Hold 0.3	42.6–85.5	2.4–146.8	1–1740	12
Load 0.3–0.6	40.4–71.6	0.2–205.6	1–86	81
Hold 0.6	44.9–73.8	2.8–172.4	3–96	30
Load 0.6–0.9	40.4–75.7	2.4–171.6	2–436	146
Hold 0.9	44.9–68.6	6.6–165.8	2–80	15

over time. Three areas bounded by two dotted lines are the three load-hold periods (0.1–0.3 MPa, 0.3–0.6 MPa, 0.6–0.9 MPa, respectively). The AE activity of crack I is shown to be very active for all three periods, and the numbers of locations in three loading stages are all larger than their corresponding holding periods (Table 2).

The testing results illustrate that the cast iron material of the paper dryer is an excellent emitter of AE when under stress. The propagation of cracks in the shell of the paper dryer can produce many AE source locations. AE testing is very suitable for cast iron paper dryers.

6 Conclusion

1. At present, there are 670 qualified AE personnel and more than 120 AE testing organizations engaged in AE testing services for pressure equipment in China. Due to a large number of in-service pressure vessels, China not only has a large requirement for AE instruments, but also for advanced techniques and AE testing services.
2. AE testing can find cracks, weld defects cracking, serious corrosion and leakage for pressure equipment.
3. The planar location of AE signals is the most important and direct method for locating AE sources. Planar location analysis can roughly distinguish the characteristics of AE signals. The distribution and value area of AE parameters are similar for almost all AE location sources. The correlation figures between parameters can obviously discriminate the AE signals produced by leakage from other AE sources.
4. Evaluation methods for AE sources have been introduced by AE testing standards for pressure equipment in China.
5. Two kinds of advanced AE instruments have been developed in China. They are multi-channel wireless distributed AE systems based on wi-fi and pipeline leakage location instruments based on acoustic methods and correlation of locations of continuous signals.

Acknowledgment This study was financially supported by Chinese National Nature Science Foundation Project 51377137.

References

1. *The Proceedings of the 1st National AE Conference*, Huangshan, China, July 1979
2. *The Proceedings of the 2nd National AE Conference*, Guilin, China, Apr 1983
3. *The Proceedings of the 3rd National AE Conference*, Changchun, China, Nov 1986
4. *The Proceedings of the 4th National AE Conference*, Qingdao, China, Aug 1989
5. R.G. Geng, Recent development of acoustic emission: twenty-year review of Chinese society for nondestructive testing. Nondestruct. Test. **20**(6), 151–154 (1998)
6. G.T. Shen et al., Acoustic emission progress in China: celebration for the 25th anniversary of Chinese Society for NDT. Nondestruct. Test. **25**(6), 302–307 (2003)
7. G.T. Shen, S.F. Liu, et al., in *Progress in Acoustic Emission IV, 9th International Acoustic Emission Symposium*. The correlation between active defects and source location in acoustic emission test of metal pressure vessels (JSNDI, Kobe, Japan, 1988)

8. S.F. Liu, Y.G. Wan, G.T. Shen, AE inspection and defect assessment for metal pressure vessels. Int. J. Press. Vessel. Pip. **38**, 57–67 (1989)
9. G.T. Shen et al., Acoustic emission test and safety evaluation of wrapped multilayer pressure vessel. China Boiler Pressure Vessel Saf. (English Edition) **2**, 68–73 (1995)
10. G. Dai et al., AE monitoring and data analysis for large spherical tanks. NDT&E Int. **26**(6), 287–290 (1993)
11. G. T. Shen, G. Dai S. F. Liu Review of acoustic emission in China, in *Proceeding for 6th International Conference on Acoustic Emission*, South Lake Tahoe, NV, USA, 28 Oct to 2 Nov 2007
12. G. Shen et al., The development of high speed Wi-Fi wireless acoustic emission system, in Advances in Acoustic Emission Technology, ed. by G. Shen, Z. Wu, J. Zhang (Springer, New York/Heidelberg/Dordrecht/London, 2014), pp. 3–13
13. G. Shen et al., Development of a pipeline leakage location instrument based on acoustic waves, in Advances in Acoustic Emission Technology, ed. by G. Shen, Z. Wu, J. Zhang (Springer, New York/Heidelberg/Dordrecht/London, 2014), pp. 47–54
14. S. F. Liu, G.T. Shen, et al. Spectral analysis of waveform acoustic emission data, in *Proceedings of 14th WCNDT*, New Delhi, 8–13, 1996
15. G. Dai, The acoustic emission characteristics and fuzzy comprehensive analysis of active defects for the pressure vessel in service, Dissertation of Ph.D., Zhejiang University, (1996)
16. S. F. Liu, Spectral analysis and artificial neural network pattern recognition of weld defect acoustic emission data, Dissertation of Ph.D., Tsinghua University, (1996)
17. G.T. Shen, The characteristics and discriminating methods of acoustic emission sources for metallic pressure vessel, Dissertation of Ph.D., Tsinghua University, (1998)
18. L. Li, G. Shen, Z. Zheng, Z. Wu, Investigation on acoustic emission characteristics of a paper dryer. Insight **56**(5), 269–275 (2014)

Part II
Instrumentation

Advanced Usage of the Software-Controlled Sensor Coupling Test

H. Vallen

Abstract By pulsing an acoustic emission (AE) sensor, AE of reproducible energy is artificially generated and used for the sensor coupling test. AE waves may travel from any AE source to a receiving AE sensor over multiple wave paths, e.g., over the shell or the liquid content of a pressure vessel. Waveform data may reveal different wave arrivals by so-called sub-events. Each wave arrival appears in waveform data by sub-events of different properties like arrival time, amplitude, frequency spectrum, and appearance of its envelope. Intelligent data processing software could automatically consider different wave propagation paths of an individual test object. This may answer questions like "did the wave of an individual sub-event propagate over the shell or over the liquid content of a pressure vessel?" and consider the right travel path and wave velocity for location calculation. By this, AE testing results could become in general more reliable. This chapter describes some basic work towards that objective. Development of such software would need feedback of waveform data from the sensor coupling check from real test objects.

1 Basics of the Software-Controlled Sensor Coupling Test

The original purpose of the software-controlled sensor coupling test was to offer the possibility that any channel can be selected by software to emit stimulated AE into a test object and to receive the resulting AE wave at the position of neighbored sensors. Each receiving sensor converts the wave to an electrical AE signal which is converted to digital AE data by an AE signal processor as usual (Fig. 1).

H. Vallen (✉)
Vallen Systeme GmbH, 82057 Icking, Germany
e-mail: hartmut@vallen.de

G. Shen et al. (eds.), *Advances in Acoustic Emission Technology*, Springer Proceedings in Physics 179, DOI 10.1007/978-3-319-29052-2_2

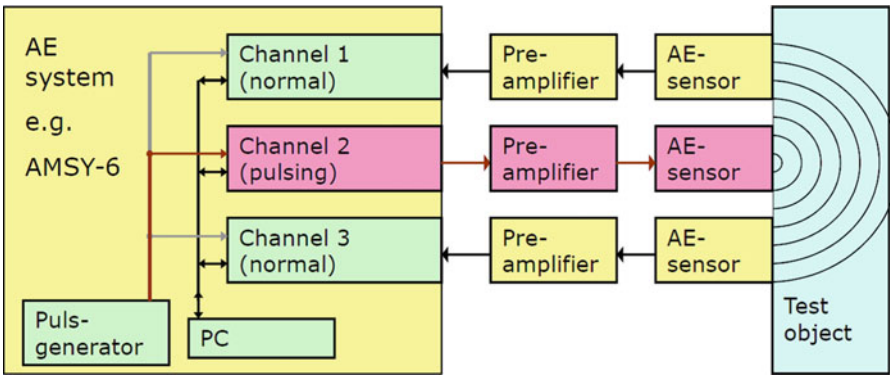

Fig. 1 Block diagram of the "pulse-through" mechanism for the software-controlled sensor coupling test

1.1 Pulse-Through Principle

In a so-called pulsing sequence, one channel is set to pulsing mode. That means, a few electrical pulses from a central pulse generator are passed through the channel up to the piezoelectric element. This causes one artificial AE event per pulse. Then the next channel is selected for pulsing until the last channel completes the pulsing sequence.

In "pulse-through mode" a programmable pulse amplitude in range 1 V–450 V_{PP} can be used. The high amplitude maximum allows to receive pulses even over a very attenuating wave propagating path, e.g., through a polymer-layered riser tube. In pulsing mode, the preamplifier is switched off and the pulse is passed through up to the piezoelectric element over relay contacts. Each pulse is also fed into the signal processor in order to generate a hit data set with accurate time of the pulse. All data shown in this chapter are created by the pulse-through principle. Chapters 2 and 3 are included for completeness only.

1.2 Auto Sensor Test in Self-Test Mode

This mode is defined by [1]: An electrical pulse is generated inside of a preamplifier in response to a control pulse on the 28 V power/signal line from the signal processor. The pulse is passed on to the piezoelectric element. The pulse amplitude can be modified in a small range by modifying the width of the control pulse. The preamplifier stays in operation and is driven into saturation by the pulse. After some settling time the preamplifier becomes able to receive an acoustic response from the test object. Under favorable circumstances, a change of coupling quality can be evaluated from the response on the emitted AE wave.

1.3 Auto Sensor Test in Near-Neighbor Mode

This mode is defined by [2]. A pulsing sequence is generated similar to the pulse-through principle described in Sect. 1.1 above, but the pulse is generated inside the preamplifier as with self-test mode described in Sect. 1.2. The pulse drives the preamplifier of the pulsing channel into saturation.

1.4 Pulsing Table

The amplitudes received during a pulsing sequence are shown in a pulsing table; see example of a six-channel configuration in Fig. 2. Lines are headed by the pulsing channel number, and columns by receiving channel numbers. Each cell shows the average of the few amplitudes (pulses) measured by a receiving channel. Non-plausible sensor responses can easily be identified. One of multiple pulsing sequences can be addressed by its tab on top of the table.

In addition, a variant of the pulsing table shows differences in amplitudes of two pulsing sequences, e.g., one before and the other after a test. This variant helps to quickly see whether acoustic coupling was constant before and after a test or has changed between any sensor pair.

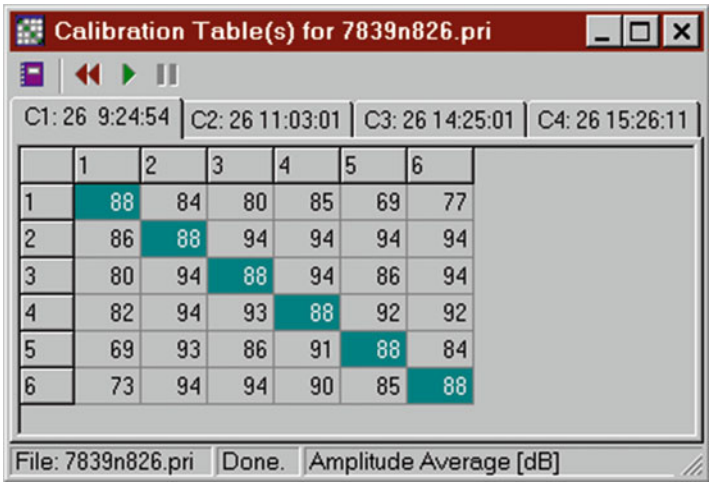

	1	2	3	4	5	6
1	88	84	80	85	69	77
2	86	88	94	94	94	94
3	80	94	88	94	86	94
4	82	94	93	88	92	92
5	69	93	86	91	88	84
6	73	94	94	90	85	88

Fig. 2 Pulsing table for a six-channel configuration. Channel 1 received 82 dB_{AE} from pulsing channel 4

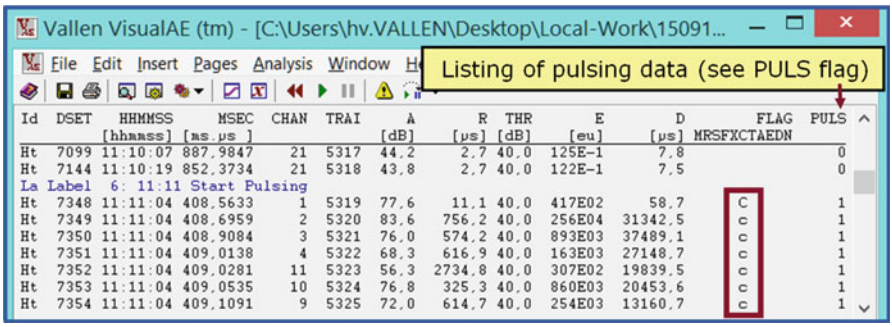

Id	DSET	HHMMSS [hhmmss]	MSEC [ms.µs]	CHAN	TRAI	A [dB]	R [µs]	THR [dB]	E [eu]	D [µs]	FLAG MRSFXCTAEDN	PULS
Ht	7099	11:10:07	887,9847	21	5317	44,2	2,7	40,0	125E-1	7,8		0
Ht	7144	11:10:19	852,3734	21	5318	43,8	2,7	40,0	122E-1	7,5		0
La Label 6: 11:11 Start Pulsing												
Ht	7348	11:11:04	408,5633	1	5319	77,6	11,1	40,0	417E02	58,7	C	1
Ht	7349	11:11:04	408,6959	2	5320	83,6	756,2	40,0	256E04	31342,5	c	1
Ht	7350	11:11:04	408,9084	3	5321	76,0	574,2	40,0	893E03	37489,1	c	1
Ht	7351	11:11:04	409,0138	4	5322	68,3	616,9	40,0	163E03	27148,7	c	1
Ht	7352	11:11:04	409,0281	11	5323	56,3	2734,8	40,0	307E02	19839,5	c	1
Ht	7353	11:11:04	409,0535	10	5324	76,8	325,3	40,0	860E03	20453,6	c	1
Ht	7354	11:11:04	409,1091	9	5325	72,0	614,7	40,0	254E03	13160,7	c	1

Fig. 3 Example of a listing showing normal hit data ("PULS = 0"in last column) and the beginning of stimulated data ("PULS = 1"). The upper-case "C"-Flag in the listing identifies the pulse-emitting channel, the lower-case "c"-flag identifies pulse-receiving channels

2 Further Usage of Stimulated Pulsing Data

Stimulated AE data from pulsing sequences can be analyzed and graphically and numerically presented like normal AE data, e.g., for checking location calculation, clustering, attenuation profiles, and more (see Fig. 3).

Stimulated AE data from pulsing sequences can be separated from normal AE data by a filter condition: "PULS > 0." The "PULS" flag is selectable from the "Parametric results" dialog. The PULS Flag is set to 1 before the first channel is set to pulsing mode and back to 0 after the last channel is set from pulsing mode to normal mode.

3 Advanced Usage of the Software-Controlled Sensor Coupling Test

After looking at sensor coupling test data obtained from a few test objects, we discovered potential for an advanced, beneficial usage of those kind of data. Figure 4 shows an example with different wave arrivals in one data set.

The software-controlled sensor coupling test always generates AE at a well-defined position, namely the position of the pulsing sensor and at an accurate source time, which is measured as arrival time by the pulsing channel. From the position of each sensor, the distances of different propagation paths between each pair of sensors can be calculated. With a cylindric structure, most important propagation paths are the shortest and the next longer distance over the surface of the test object, and the shortest distance over the pressurization fluid in the test object. See the three paths from S1 to S2 in Fig. 5.

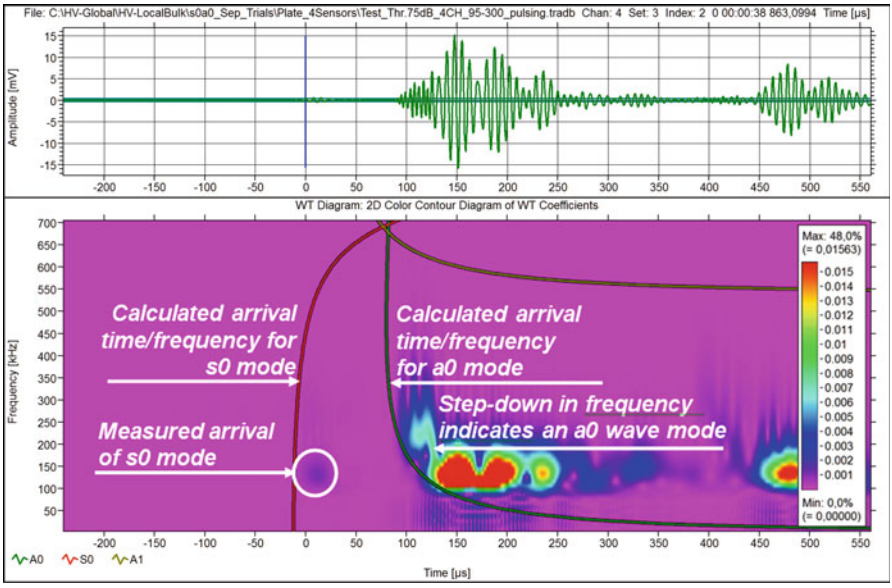

Fig. 4 Data of a pulse-stimulated event from a plate. Since the sensor positions and the distance between pulse-transmitting and -receiving sensors are known, curves for the arrival time of each wave mode can be calculated from dispersion curves and shown in a time-scaled diagram relative to the first threshold crossing time

Fig. 5 Shorter and longer paths between two sensors around a cylinder and over the liquid

3.1 Example 1: Thin-Walled Water-Filled Cylinder

Outer diameter of cylinder: 125 cm, height of cylinder (without end caps): 120 cm, wall thickness of cylinder: 0.63 cm,

A program has been written to calculate the three distances (see Fig. 5) between any two positions on a cylinder and the resulting arrival times using a defined velocity of sound for each path (Fig. 6). The following abbreviations were used for the entered velocities, distances, and arrival times; the numbers are results for one example of positions S1 and S2:

Entered velocities and positions S1(X1, Y1) and S2(X2, Y2):		
svel=	0.50 cm/μs	s0-velocity
avel=	0.32 cm/μs	a0-velocity
waterv=	0.15 cm/μs	Water velocity
X1=	148 cm	Circumferential position of the source (range −196.35 . . . +196.35)
Y1=	−25 cm	Height position of source (vertical cylinder)
X2=	−130 cm	Circumferential position of sensor 8
Y2=	−130 cm	Height position of sensor 8

Calculated distances:		
Degree=	105.15°	Angle between S1 and S2 (for water distance calculation)
surfDists=	115 cm	Shortest surface distance
surfDistl=	278 cm	Longer surface distance
volDist=	99.6 cm	Water path distance

Calculated arrival times:		
s0_short=	230 μs	Delta-t of source to s0 arrival, refers to $T = 0$
d_a0_short=	129 μs	Short path a0-arrival from $T = 0$
d_s0_long=	326 μs	Long path s0-arrival from $T = 0$
d_a0_long=	639 μs	Long path a0-arrival from $T = 0$
d_water=	434 μs	Water path arrival from $T = 0$

3.2 *Example 2: Thick-Walled Water-Filled Cylinder*

Dimensions		No. of channels used: 50
Length	42.61 m	40 at shell
Diameter	5.48 m,	3 at top head
Thickness (shell)	14.5 cm	7 at bottom head

We received only a part of the test data (see Figs. 7, 8, and 9). Only stimulated data from sensors 1 to 4 are available, with 2048 samples at 5 Mega samples per second (MSPS) record length and 200 samples pre-trigger, that gives a visible length of 40 μs pre-trigger and 370 μs post-trigger. See Fig. 10.

Figure 10 shows a waveform picked up by sensor 42, emitted by pulse-stimulated sensor 3. The large-amplitude burst beginning at about 275 μs fits very well to the velocity of the Rayleigh wave.

Figure 11 shows same waveform as Fig. 10 but zoomed around the time of the first threshold crossing (FTC) (also called arrival time). Obviously, first components of the wave arrived about 25 μs before the measured arrival time. That means at such a thick-walled structure, the arrival time measurement bears some uncertainties. The question comes up, whether the peak time gives a more reliable time criterion for distance evaluation and location calculation than the arrival time.

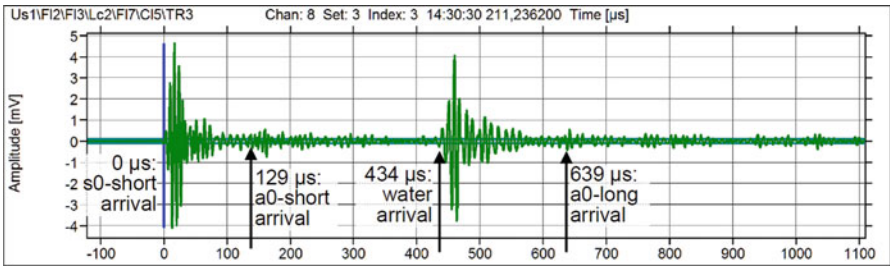

Fig. 6 AE event generated by a pencil lead break (PLB) at position S1. Waveform received by sensor 8 at position S2. *Arrows* point to calculated arrival times. The water path arrival is very accurate; the s0-long arrival (at 326 µs) can't be identified in the waveform

Fig. 7 Thick-walled cylinder

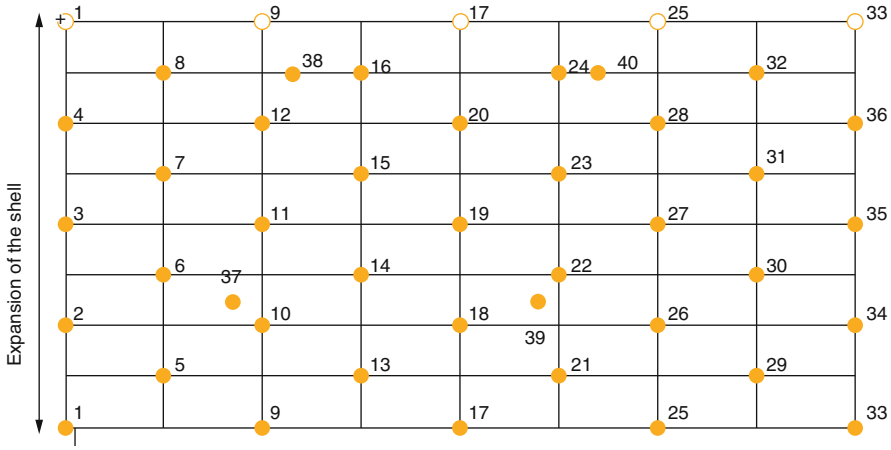

Fig. 8 Sensor positions at (unwrapped) cylindrical part of pressure vessel

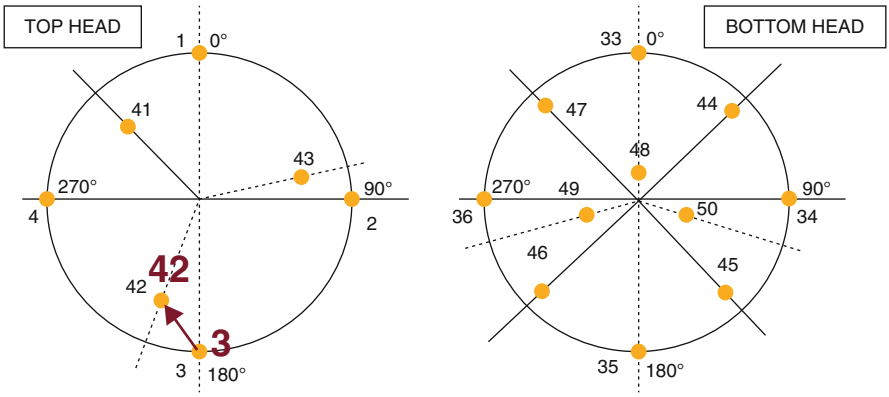

Fig. 9 Sensor positions at top head (*left side*) and bottom head (*right side*). Four sensors belong to cylindrical part. Only distance between channels 3 and 42 (and 2 and 43) is short enough to see the Rayleigh wave arrival in the waveform data

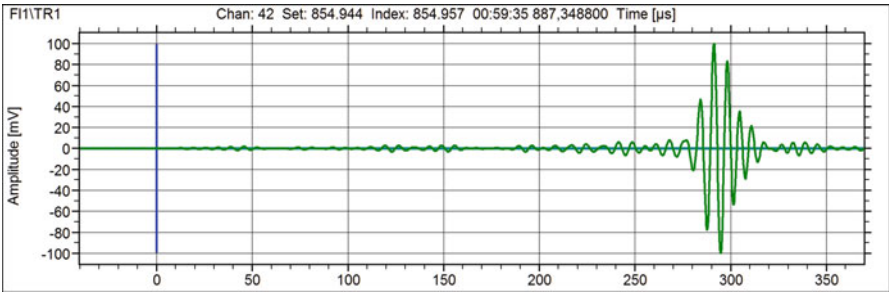

Fig. 10 AE stimulated by sensor 3 and recorded by sensor 42

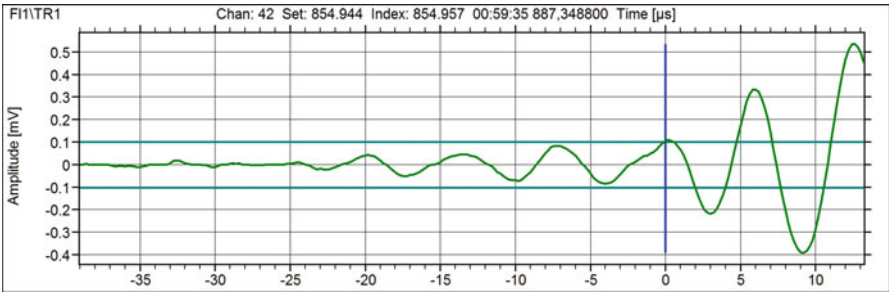

Fig. 11 Waveform shown in Fig. 10 zoomed around first threshold crossing

The first four columns of the following table are taken from the listing of the channel 3-stimulated event. It shows:

CHAN	Sensor number
DT1X	The difference between the measured arrival time of each subsequently hit channel to that of the FHC (channel 3)
A	The highest amplitude (peak amplitude) detected during the hit in dB_{AE}
R	The rise time, defined as time of A minus arrival time (FTC time)

The next columns show following calculated results:

PkT	Peak time or time of *A*, the time at which the highest amplitude is measured, =DT1X + *R*
Dist_DT	Distance derived from arrival time, =DT1X × arrival time velocity (AV, 5.58 m/ms)
Dist_PKT	Distance derived from peak time, =PkT × peak time velocity (PV, 2.95 m/ms)
Deviation_in_%	The deviation of both distances in percent, =(Dist_DT/Dist_PKT) − 1) × 100

A positive deviation usually means that the delta-t (DT1X) is too large. The plausible effect can be derived from Fig. 11. Fast wave components are attenuated below threshold, so the arrival time later, when more energetic wave components arrive. This explains the occurrence of larger positive deviations at distances above 4.7 m (Table 1).

A negative deviation usually means that the peak time is detected too late. This can be seen with channels 6 and 7. There the rise time is a bit larger than at channels

Table 1 Listing of subsequent hits of a stimulated event

CHAN	DT1X (µs)	*A* (dB)	*R* (µs)	PkT (µs)	Dist_DT (m)	Dist_PkT (m)	Dist_DT/ Dist_PkT − 1 (%)
3		81.0	10.6				
42	331.1	99.9	291.2	622.3	1.848	1.836	0.64
6	743.6	99.9	717.6	1461.2	4.149	4.311	−3.74
7	759.2	99.4	726.4	1485.6	4.236	4.383	−3.34
2	770.9	99.9	680.8	1451.7	4.302	4.283	0.45
4	771.3	99.9	674.2	1445.5	4.304	4.264	0.93
43	906.7	99.8	692.0	1598.7	5.059	4.716	7.28
41	1.139.8	99.9	854.4	1994.2	6.360	5.883	8.11
37	1.215.1	97.2	1.100.4	2315.5	6.780	6.831	−0.74
11	1.339.6	96.0	1.203.6	2543.2	7.475	7.502	−0.37
8	1.374.6	99.4	1.130.8	2505.4	7.670	7.391	3.78
5	1.391.1	98.7	1.145.6	2536.7	7.762	7.483	3.73
12	1.554.5	94.5	1.357.2	2911.7	8.674	8.590	0.98
10	1.570.6	93.8	1.367.6	2938.2	8.764	8.668	1.11
1	1.642.5	99.9	1.210.0	2852.5	9.165	8.415	8.92
38	1.921.6	92.3	1.576.8	3498.4	10.723	10.320	3.90
14	2.106.5	86.6	1.788.8	3895.3	11.754	11.491	2.29
9	2.139.2	92.7	1.711.2	3850.4	11.937	11.359	5.09

2 and 4. We could not look deeper into this phenomenon since the peak time is behind the recorded waveform length.

Since there are only very few occurrences of small negative deviations, we believe a peak-time-derived delta-t will lead to better location results than the arrival time delta-t, if the wall thickness is large and the AE source is at the outer surface of the object.

4 Conclusion

With two examples, a thin-walled and a thick-walled test object, this chapter shows that waveform data from the software-controlled sensor coupling test bear valuable information about details of wave propagation at the test object which might be helpful for the understanding of the involved wave propagation effects.

We would like to perform more studies on stimulated data from real test objects in order to define goals for the development of software that extracts most helpful information from such stimulated data. Substantial efforts are needed to equip a large structure with AE sensors for a properly performed AE test. It is very easy and needs almost no extra efforts to gather waveform data in addition to hit data during the automated sensor coupling test.

We herewith ask AE service providers to switch on waveform recording (TR recording) during the automatic sensor coupling test, use several ms long waveform length and about 1 ms pre-trigger setting, and pass on to us such data for further analysis. We will treat such data confidentially and eliminate any hint to the test object.

References

1. ASTM E2374-10 "*Standard Guide for Acoustic Emission System Performance Verification*," Section 5.1.3.2. ASTM International, West Conshocken, PA, service@astm.org, www.astm.org
2. ASTM E2374-10 "*Standard Guide for Acoustic Emission System Performance Verification*," Section 5.1.3.1. ASTM International, West Conshocken, PA, service@astm.org, www.astm.org

A New Generation of AE System Based on PCI Express Bus

E. Lowenhar, M. Carlos, and J. Dong

Abstract This chapter is to introduce a new generation of acoustic emission (AE) system based on the latest industrial PCI Express bus standard. Since an AE system based on standard computer bus has advantages in speed, compactness, scalability, customizability, connectivity, chassis selectivity, data storage capacity, and integrity with computer operating system and hard disk within one chassis, it is the most popular type of acoustic emission system used in worldwide AE field now. As the latest PCI Express bus has become de facto standard configuration of industrial PC supplied to customers, there is a great demand for an AE system that can take the advantages of the PCI Express bus and be compatible to latest industrial computers in the market. As such Mistras Group Inc. has developed a new generation AE system, named Express8, based on PCI Express bus to accommodate the technology evolution and application needs. This chapter describes design architecture and advanced features associated with the newly developed system.

1 Purpose

This chapter is to introduce a new generation of acoustic emission (AE) system based on the latest industrial PCI Express bus standard. Just like the evolvement of many other electronic equipment that are launched to the market along with the development of digital computer, acoustic emission system also follows the pace of personal computer evolution from one bus architecture to another new bus architecture. Since the AE system based on standard computer bus has advantages in speed, compactness, scalability, customizability, connectivity, chassis selectivity, data storage capacity, and integrity with computer operating system and hard disk within one chassis, it is the most popular type of acoustic emission system used in worldwide AE field now. As the latest PCI Express bus has become de facto standard configuration of industrial PC supplied to customers [1], there is a great demand for an AE system that can take the advantages of the PCI Express bus and be compatible to latest industrial computers in the market. As such MISTRAS

E. Lowenhar • M. Carlos • J. Dong (✉)
Mistras Group Inc., 195 Clarksville Road, Princeton Junction, NJ 08550, USA
e-mail: jason.dong@mistrasgroup.com

G. Shen et al. (eds.), *Advances in Acoustic Emission Technology*, Springer Proceedings in Physics 179, DOI 10.1007/978-3-319-29052-2_3

Group, Inc. has developed a new generation AE system, named Express8, based on PCI Express bus to accommodate the technology evolution and application needs. This chapter describes computer bus structure and compares a few generation of AE systems that were built based on different bus structures. It also shows design architecture of the Express8 system. Dimension of the system has been greatly reduced to increase the board robustness to meet the RoHS manufacturing requirement. Advanced features of the new system are particularly addressed in this chapter.

2 History of AE Systems Based on Standard Industrial Computer Bus Architecture

The first generation of personal industrial computer bus is the Industrial Standard Architecture (ISA) bus which firstly appeared in early 1980s along with the IBM PC/AT and compatible computers [2]. The first-generation AE system built on top of standard computer bus architecture or ISA bus was a two-channel AE system, AEDSP-32/16, made by Physical Acoustic Corporation in early 1990s. The ISA bus is a 16-bit data structure with speed 16 MB/s. As the Peripheral Component Interconnect (PCI) bus [3] gradually became the main bus architecture in later 1990s, various AE systems, e.g., DiSP-4, PCI-2, and PCI-8, based on the PCI bus have been developed by Physical Acoustics Corporation in the end of 1990s and early 2000s. Nowadays, PCI Express [4] bus has become the standard configuration of personal computers; AE system has also been evolved to PCI Express bus architecture to accommodate this change; and an 8-channel AE system, named Express8, based on the PCI Express bus has been developed by MISTRAS Group, Inc. recently. Since an occurrence of each new generation of bus architecture means technology revolution, the speed of PCI Express bus has been greatly improved in comparison with its predecessors; the performance of AE system has also been improved accordingly. Table 1 summarizes the history of internal computer bus architecture and associated AE systems. It is clear that the speed of internal computer bus has been improved significantly in the last two decades.

Actually, there is a major difference between the PCI Express bus and its predecessors, ISA and PCI buses, when multiple boards are installed in a computer. The architecture of ISA and PCI bus makes multiple boards share the same bus speed as listed in Table 1. However, each lane of PCI Express Bus is independent, and each added board enjoys its own full PCI Express bus speed. So, when multiple PCI Express boards are used in one system, the signal processing speed is multiplied instead of shared in the ISA bus and PCI bus system.

3 Architecture of AE System Built on PCI Express Bus

The new system developed is an 8-channel board based on PCI Express or PCIe bus. Different from AE system design based on ISA bus and PCI bus which builds all electronic components in one circuit board, modular design has been adopted in

Table 1 History of internal computer bus architecture and associated AE systems

Bus name	Year launched	Bus speed (MB/s)	AE system	Year launched	Dimension ($L \times W \times H$)
ISA	1981	16	2-channel AEDSP-32/16	1994	$13.0'' \times 4.0'' \times 0.7''$
PCI	1993	132	4-channel PCI/DiSP-4	1999	$12.28'' \times 4.2'' \times 0.8''$
			8-channel PCI-8	2002	$13.4'' \times 4.8'' \times 0.7''$
			2-channel PCI-2	2003	$13.4'' \times 4.8'' \times 0.7''$
PCI Express 1.0	2004	250/Lane	8-channel Express8	2013	$6.5'' \times 4.2'' \times 0.7''$

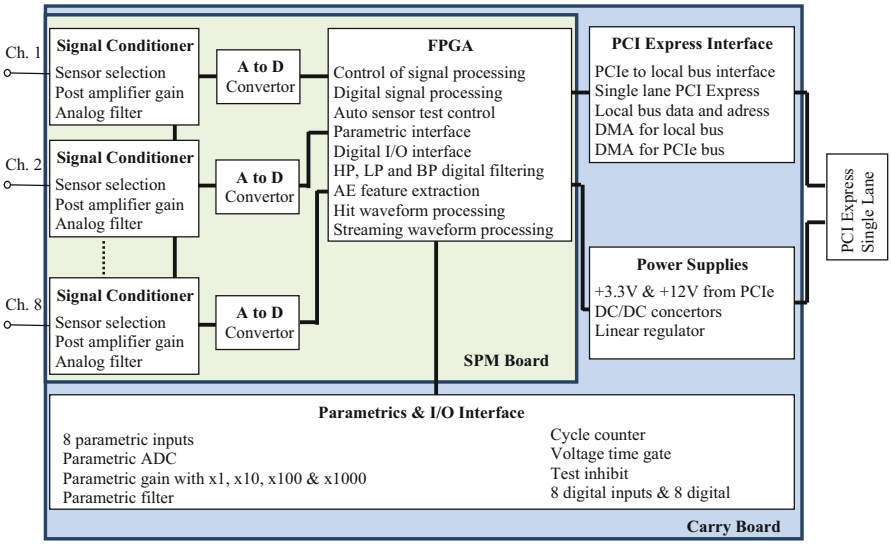

Fig. 1 Block diagram of Express8 system architecture

the development of PCI Express bus AE system. This modular design is aimed to improve the reliability, compactness, and reusability of the AE system. It is designed to have two separated circuit board modules: one (signal processing module or SPM) is plugged on top of another (carry board module). The carry board module of the Express8 is the base board that is standard PCIe card size; it has the PLX PCIe interface chip, power supplies, and other interface connectors such as parametrics, digital I/O, and PCI Express interface. The SPM module is the plug-in board which is integrated with all functions of 8-channel signal conditioning, data acquisition, and FPGA signal processing. Figure 1 shows a block diagram of the architecture of the modular design. A high-speed field program gate array or FPGA is the heart of the SPM module; it controls the signal processing, extracts AE features, and deals with waveform issues. With this modular design and thanks to

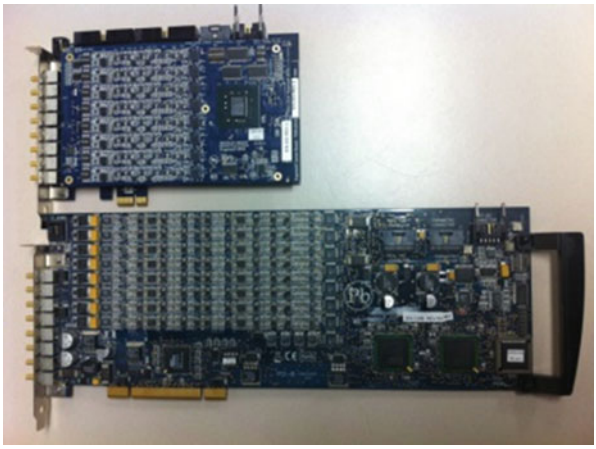

Fig. 2 Express8 (*top*) and PCI-8 (*bottom*)

the technological advancement of the PCI Express bus, the 8-channel PCI Express bus-based AE system has achieved the most dense circuit integration and the most compact size in $6.5'' \times 4.2'' \times 0.7''$ ($L \times W \times H$) which is about 50% smaller than previous ISA and PCI bus AE systems.

Figure 2 shows a photo of Express8 system with a comparison of a previous PCI-8 system. Not only the PCI Express bus-based system is more compact, but also an obvious advantage of this small dimension is increased rigidity of the board so that it avoids electronic component damage due to flexure bending of long board. This becomes more critical when RoHS requirement is enforced in manufacturing environment. Another advantage of this modular design is reusability of future product development; the same SPM board can be used in other type of carry board with different bus architecture or the same carry board can be used with a new SPM designed with advanced features or components.

4 Advanced and Enhanced Features

Compared with the most popularly used AE system, PCI-8, in worldwide region, not only the dimension of the Express8 has been greatly reduced, but also its functionality and performance have also been greatly improved. Some of these improvements and advanced features are summarized as below.

- Increased A/D rate and expanded bandwidth: The A/D conversion rate has been changed from 3 MSPS to 10 MSPS per each channel; the bandwidth is also expanded from 1–400 kHz to 1–1200 kHz as compared with the PCI bus-based system PCI-8. The A/D resolution is still kept as 16 bits, and the data acquisition rate can be set as low as 10 KSamples/s or as high as 10 MSamples/s. With the updated bandwidth and data acquisition rate, it can cover over 95% research and industrial application needs.

- Added hundreds of digital filters: While the Express8 still keeps software-selectable analog high-pass (1, 10, 20, and 100 kHz) and analog low-pass (100, 400, and 1000 MHz) filters on each channel, hundreds of digital filters have been added to Express8. Each channel is implemented with 256 tap digital FIR filters so that over 500 high-pass, low-pass, and band-pass filters can be selected on each channel independently. A combination of analog filter and digital filter gives the Express8 lower noise and higher dynamic range up to 80 dB. Specifically, the narrow band-pass digital filter consisting of high-pass and low-pass filters is particularly useful to focus the bandwidth to sensor's resonant frequency so that it eliminates noises outside the resonant frequency of the sensor drastically.
- Provided selection for different sensor input: From a historical point of view, an AE system usually provides phantom power or +28 VDC power to preamplifier or integral preamplifier sensor through a coaxial cable connecting the sensor/preamplifier to the system. However, +28 VDC is not an optimum configuration from a power consumption and noise suppression point of view; it consumes a lot power, i.e., about 0.7–0.8 W per each channel. Not only it generates a lot of heat, but also it induces higher noises. As there is an increasing demand for online monitoring and outdoor long-term monitoring applications, the drawback of using +28 VDC power for preamplifier has been noticed. There is an increasing demand for an AE system to be able to support low-power or +5 VDC pre-amplifiers or integral preamplifier sensors. Such a low-power preamplifier only consumes 0.03 W per each channel which is over 20 times lower than the power consumption of a +28 VDC preamplifier. The Express8 is now the first AE system that supports selection of different powers with a dip switch on the board, the phantom power on the board can be set as either +5 VDC or +28 VDC on the Express8 board. Additionally, the Express8 can also be set to ICP power mode so that accelerometers can also be connected to the system. If a customer just wants to use the Express8 other voltage inputs, the phantom power and ICP power on each individual channel can be disabled to allow voltage sensor input. This makes Express8 very flexible and to be able to connect to various types of sensors in a sensor fusion system for structure health monitoring or other applications.
- Integrated eight parametric channels in a single board: Besides eight AE channels in a single Express8 board, the parametric channels have also been expanded from two to eight in comparison with PCI-8 system; among them two can be differential inputs and the rest are single-ended inputs. In addition to time-driven parametric acquisition, hit-driven parametric acquisition is now available for all eight parametric channels; this extends the capability to correlate AE events to parametric inputs.
- Increased speed with adding multiple boards: Unlike AE systems with PCI bus and other external peripheral bus, e.g., USB bus, an increase of number of AE boards or AE channels would result in sharing the speed; the architecture of PCI Express bus allows to add on speed when more lanes or bus slots are used. In other words, when one more Express8 board is added to an AE system with one

Express8 board installed, the overall data throughput rate is doubled instead of keeping the same or each shares half of the throughput rate.

- Added waveform streaming function: One major difference of acoustic emission data acquisition with respect to general data acquisition in other applications is that not only AE features are extracted, but also AE waveforms are recorded simultaneously. Traditionally, in the meantime of AE feature extraction, hit-based waveforms can be recorded as well. With the technological development of AE hardware and computer, three types of AE waveforms can be recorded now, i.e., hit-based waveform, streaming waveform, and concurrently triggered transient waveform. The streaming waveform can be acquired with the hit-based waveform simultaneously. It does not use onboard memory to buffer the waveform, but it uses direct memory access (DMA) technology to save streaming data to hard disk directly. It eliminates the requirement for big onboard memory to temporarily store waveforms and enables non-interrupted streaming waveform to be stored in hard disk directly with very high rate. In the previous PCI bus-based AE system, PCI-2, the highest streaming waveform rate is 10 MSPS/s per system. This rate is shared if two channels are used in a system which made 5 MSPS/s per channel. If more than one PCI-2 boards are used in a system, the maximum streaming waveform rate per each channel would be 10 MSPS/s divided by the number of channels used. Thanks to the PCI Express bus architecture, the Express8 has made great improvement on streaming waveform rate when multiple channels or multiple boards are used. The maximum streaming waveform rate per each Express8 board is 80 Mbytes/s or 40 MSPS/s. As the data acquisition rate of the Express8 is 10 MSPS/s, a single-channel waveform streaming rate is 10 MSPS/s as well, but when more than one channel (up to four) is selected, each channel can keep 10 MSPS/s rate. In other words if four channels are selected in one Express8 board, the maximum streaming waveform rate of the system can reach 40 MSPS/s. If all waveform streaming of all eight channels in one Express8 board is selected, then each channel can keep 5 MSPS/s rate while the total waveform streaming rate is still kept as 40 SMPS/s. Due to the nature of independence of PCI Express bus lanes, when two or three Express8 boards are included in an AE system, the overall streaming waveform rate of the system would be doubled or tripled. For example, when three Express8 boards are installed in one system, the overall waveform streaming rate is 240 Mbytes/s or 120 MSPS/s. It is important to mention that there is no conflict to record both hit-based waveform and streaming waveform concurrently. The maximum hit-based waveform length of the Express8 is 15 KSamples, while the maximum length of streaming waveform is the limit of hard disk. The streaming waveform record can be triggered by different ways, e.g., hit-based trigger, external I/O trigger, manual trigger, and time-based trigger etc.
- System chassis: The Express8 is the densest AE system in terms of the number of channels versus the board dimension. The length of the Express8 board is just about half of previous PCI-2 and PCI-8 boards, and the rigidity of the Express8 board is greatly improved. This is particularly important for boards manufactured under RoHS requirement; it is very beneficial in increasing the

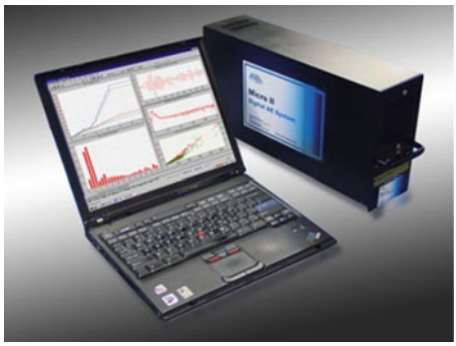

Fig. 3 A 32-channel micro chassis with a laptop

Fig. 4 A 96-channel industrial rack mount chassis

reliability of the system because it reduces tendency of damage and potential problems caused due to flexure of the board during installation and system transportation. With the small size of the Express8 board, the system chassis can be made even more compact than ever before. Figure 3 shows a 32-channel micro chassis with a laptop controller; the dimension of this chassis is just 110 × 220 × 450 mm (W × H × D), but up-to-dated high-performance CPU with Windows 7/8, 8 GB RAM, and 1 TB hard disk are included in the chassis; network connection is also with the chassis so that it can be remotely and smartly controlled. Additionally, the micro chassis can be either AC or DC powered; it is very convenient to be used in either labs or fields. Besides the micro chassis, 12 Express8 boards or 96 channels can be installed in a standard industrial rack mount chassis. Figure 4 shows a photo of such a 96-channel chassis; it maximized the capability to perform AE test with a big number of channels in a small system chassis.

- Digital I/O and strain gauge excitation: Besides eight parametric inputs, the Express8 also has eight digital input and eight digital output ports. These digital I/O ports can be used for external trigger coordination, test start, streaming start, test inhibit, alarm warning output, and alarm trip output. These ports are essential in many online monitoring applications. Additionally, a program-controllable output voltage port is also available for use as an excitation source of strain gauge bridge; it eliminates the requirement for a specific power source for excitation if strain gauges are used in the test.

5 Conclusions

The standard personal computer bus architecture has been evolved along with other computer and electronic technologies; now the PCI Express bus is becoming a common configuration in PC computer; a PCI Express bus-based system, Express8, has been developed to follow up the technological pace and to adapt to the change of the dominant standard bus architecture. The Express8 AE system fully utilized the advantages of the PCI Express bus so that it achieved the highest data transfer rate, the smallest dimension, and the highest number of channels in an industrial rack mount chassis. The Express8 also comes with some other advanced and enhanced functions as compared with previous AE system; the functionality, performance, and compactness have made it an ideal product for research, field testing, and online monitoring.

References

1. Understanding PCI Bus, *PCI-Express and InfiniBand Architecture* (White Paper of Mellanox Technologies Inc., 2006)
2. Industrial Standard Architecture, https://en.wikipedia.org/wiki/Industry_Standard_Architecture
3. Conventional PCI, https://en.wikipedia.org/wiki/Conventional_PCI
4. PCI Express, https://en.wikipedia.org/wiki/PCI_Express

Part III
Signal Processing and Analysis

Localization of Acoustic Emissions in a Numerical T-Shaped Concrete Beam Using Multi-segment Path Analysis

Stephan Gollob, Georg K. Kocur, and Thomas Vogel

Abstract Common source localization algorithms assume a straight-wave propagation path. If the straight connection between source and sensor passes air, this straight connection surely does not represent the wave propagation path. A crack can be such an air barrier between source and sensor. However, in case of complex specimens (e.g., T-shaped or C-shaped cross section) the straight connection between source and sensor can also pass the air surrounding the specimen. *FastWay* is a novel source localization method, based on multi-segmented path analysis and a heterogeneous velocity model. In order to determine the source location, the fastest wave travel path between the sensor and an estimated source location is determined. This wave travel path is multi-linear, bypasses air, and is based on a heterogeneous velocity model. In this chapter, the estimated source location of acoustic emissions within a numerically simulated T-shaped concrete beam, determined with *FastWay*, is compared with the results provided by a homogeneous and a heterogeneous Geiger method.

1 Introduction

Assessment of health conditions of existing structures is becoming more and more important. Acoustic emission (AE) analysis, a nondestructive testing and monitoring method, can be used for that specific purpose. Common source localization algorithms assume a straight-wave propagation path. This prerequisite limits the area of application of AE analysis. If the arrival time of the detected AE is used for the estimation of the source location, the fastest wave propagation path is of particular interest. The straight connection between the source and a sensor is only the fastest wave travel path if the wave propagates through a homogeneous specimen. Whenever the specimen consists of a heterogeneous material (e.g.,

S. Gollob (✉) • T. Vogel
Institute of Structural Engineering, ETH Zurich, 8093 Zurich, Switzerland
e-mail: gollob@ibk.baug.ethz.ch

G.K. Kocur
Research-Development-Engineering, Halfen GmbH, 40746 Langenfeld, Germany

G. Shen et al. (eds.), *Advances in Acoustic Emission Technology*, Springer Proceedings in Physics 179, DOI 10.1007/978-3-319-29052-2_4

concrete) or a combination of different materials (e.g., reinforced concrete), the fastest wave propagation path is usually not a straight path. In addition, the wave will have to bypass obstacles on its way between source and sensors. These obstacles can develop over time (e.g., cracks) or can be the surface of the specimen (e.g., T-shaped girder). *FastWay* is able to consider such obstacles. Moreover, it is possible that the monitored specimen/area is not surrounded by sensors. In some cases, not all of the specimen's surfaces are accessible. In case of a T-shaped girder, the bearing element is often loaded at the top, and/or an additional structure is placed on top of it. The flanges and/or the web may still be covered by permanent formwork. Therefore, sensors can sometimes only be applied to a part of the monitored specimen.

Numerical simulations of elastic wave propagation in a T-shaped beam are used to investigate the influence of a complex specimen shape and different sensor layouts on the wave propagation behavior and on the accuracy of estimated source location. The source location is estimated using three arrival-time-based source localization methods: homogeneous Geiger method, heterogeneous Geiger method, and *FastWay*.

2 Simulations

2.1 Numerical Specimen

For the simulations of elastic wave propagation, a numerical model of a T-shaped beam is used. The beam has a length of $l_x = 500$ mm, a flange of 280 mm $\times$ 80 mm, and an 80 mm $\times$ 180 mm web, as displayed in Fig. 1. The numerical specimen consists of a numerical concrete model (NCM) [1]. The NCM is composed of three phases: cement matrix, aggregates, and air voids. The material properties are listed in Table 1. The aggregate particles are simplified by ellipsoids and the air voids by spheres. The aggregate particles and the air voids are randomly distributed in space

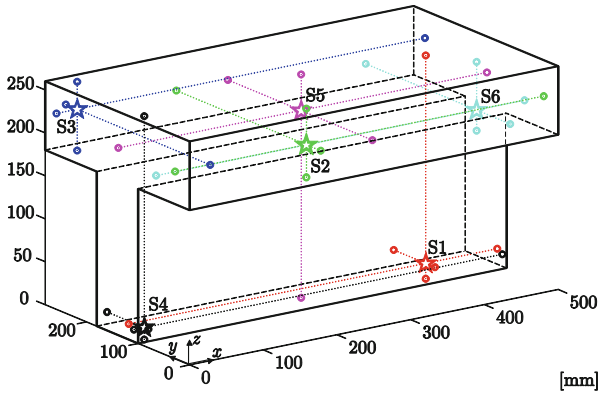

Fig. 1 Numerical specimen with source locations and their projection on the specimens surface

Table 1 Material properties taken from [1]

	c_p (m/s)	c_s (m/s)	ρ (kg/m^3)
Concrete EEP	3912.15	2271.91	2200
Reinforcement steel	5900	3200	7820
Cement	3950	2250	2050
Aggregate	4180 ± 210	2475 ± 125	2610 ± 130
Air	0	0	0.0001

as suggested in [2]. The aggregate has a maximum grain size of 16 mm. The material properties of aggregates usually vary within a defined range. This variation is also implemented in the NCM. Reinforcements and cracks have a significant influence on the wave propagation behavior [3]. The specimen is modeled as uncracked and without reinforcement in order to study the influence of a complex layout of the specimen (T-shaped cross section) on the wave propagation behavior only.

The specimen was numerically discretized on a three-dimensional layout with a grid size of 1 mm. The T-shaped beam consists of a total number of 1.84×10^7 voxels. The edge length of a voxel is referred to as 1 grid point (gp). The information of the numerical model is stored in a three-dimensional cell array. Each cell represents one voxel. A certain material is assigned to each voxel. The material properties of each voxel are stored in the corresponding cells. If the information stored in the cell is reduced to only one entry, namely the p-wave velocity c_p, the cell is simplified to a three-dimensional matrix referred to as C_{mo} [3]. The matrix C_{mo} is the basis for the heterogeneous Geiger method as well as for *FastWay*.

2.2 Sources

The numerical source was defined as an explosion source and applied as a displacement in all directions of space. Two sources (S1 and S4) were located inside the web. Three sources (S2, S3, and S6) were located inside the flange and the sixth source (S5) was located at the intersection of web and flange. The coordinates of the sources were selected randomly and are listed in Table 2. The source locations are displayed in Fig. 1.

2.3 Wave Propagation Simulation

An algorithm developed by Saenger [4], based on the finite-difference method, was used to numerically simulate the elastic wave propagation for a duration time of 200 µs. Figure 2 visualizes the wave field 50 µs after the excitation in three cross

Table 2 Source coordinates

	S1	S2	S3	S4	S5	S6
x (mm)	403	178	28	14	248	435
y (mm)	118	28	258	108	138	65
z (mm)	18	208	228	14	218	204

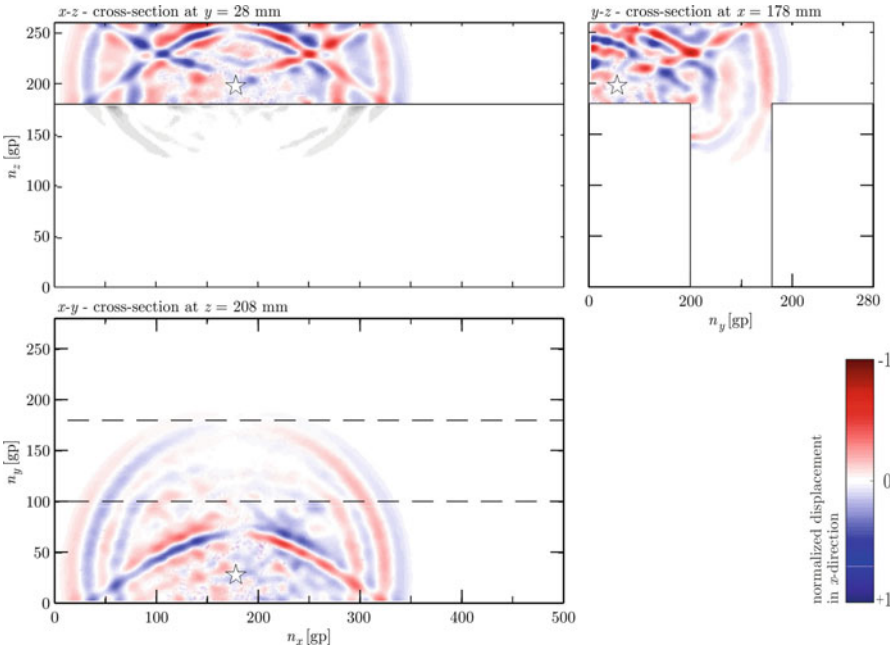

Fig. 2 Snapshot of the elastic wave-field propagation due to a Ricker wavelet (source marked with *white star*) displayed in three cross sections of a three-dimensional numerical specimen at time step $T = 50$ µs

sections. The cross sections were positioned at the location of the source, which is marked with ☆. The wave field propagating in the specimen is clearly visible in all three cross sections as well as the reflection of the wave front at the specimen's surface. In the *y*–*z* cross section, displayed in Fig. 2, it is clearly visible that the wave cannot reach the lower part of the web by propagating along a straight line. It has to bypass the air surrounding the specimen. If the specimen is homogeneous, the fastest wave propagation path from the marked source to the lower part of the web is bilinear. The wave front within the web is circular. The epicenter is not the origin of the source, but it is the inner edge between web and flange. Moreover, it becomes visible that the AE-induced displacements within the web are smaller than those within the flange (geometrical dispersion).

Table 3 Sensor coordinates and sensor layouts

sensor layout			sensor	x [mm]	y [mm]	z [mm]
E	D	C	SE1	50	100	50
			SE2	130	100	130
			SE3	210	100	60
			SE4	290	100	115
			SE5	370	100	55
			SE6	450	100	125
			SE7	55	180	150
			SE8	135	180	35
			SE9	215	180	155
			SE10	295	180	35
			SE11	375	180	160
			SE12	455	180	35
		B	SE13	80	80	180
			SE14	250	20	180
			SE15	420	70	180
			SE16	90	260	180
			SE17	240	210	180
			SE18	400	230	180
		A	SE19	150	140	260
			SE20	350	150	260
			SE21	90	20	260
			SE22	255	80	260
			SE23	425	30	260
			SE24	70	205	260
			SE25	230	270	260
			SE26	410	240	260

2.4 Sensors

A total number of 26 virtual sensors were installed on the numerical specimen. Displacements perpendicular to the surface at the sensor's positions were calculated analogously to physical measurements with piezo-electrical sensors. Twelve sensors (S1–S12) were located on the lateral surfaces of the web; six sensors on each side. Three sensors (S13–S15 and S16–S18) were located on the bottom side of the flange, three on each side of the web. The remaining eight sensors (S19–S26) were located on the top surface of the flange. There were no sensors on the end faces of the specimen or the bottom surface of the web. The coordinates of the sensor positions are listed in Table 3.

3 Source Localization

The arrival time of the wave was determined threshold based. There was no white noise since the waveforms were obtained from a numerical simulation. Therefore, a very small threshold could be used. A sensor was excluded from the source

localization estimation process if the maximum absolute amplitude of the signal calculated at the sensor positions was smaller than ten times the threshold. In addition, AIC-based picking [5] was used to verify the accuracy of the threshold-based picking. If the threshold-determined and the energy-based-determined (AIC picker) onset times differ significantly (+10/−30 µs) the sensor was also excluded. The onset time determined using the threshold picking was the input for all source localization methods. The heterogeneous Geiger method as well as *FastWay* rely also on a velocity model of the specimen C_{mo}.

3.1 Homogeneous Geiger Method

The Geiger method is a stable, efficient, and fast way to calculate the source location of an AE in three-dimensional homogeneous space [6]. In the case of a heterogeneous or cracked specimen however, the estimated source location can differ clearly from the actual source location. The governing equation of the homogeneous Geiger method is formulated as

$$t_{\mathrm{a}}(s) = \frac{\sqrt{(x_{\mathrm{s}} - x_{\mathrm{c}})^2 + (y_{\mathrm{s}} - y_{\mathrm{c}})^2 + (z_{\mathrm{s}} - z_{\mathrm{c}})^2}}{c_{\mathrm{p}}} + t_{\mathrm{c}}, \tag{1}$$

where the observed onset time $t_{\mathrm{a}}(s)$ at sensor s correlates with the source time t_{c} by assuming a straight-wave propagation path between source and sensors. The source coordinates x_{c}, y_{c}, and z_{c} and the source time t_{c} are unknowns. The known input values are the sensor coordinates, x_{s}, y_{s}, and z_{s}; the picked arrival time of the p-wave at each sensor $t_{\mathrm{a}}(s)$; and the global p-wave velocity c_{p}.

The data of at least four sensors are needed to determine the four unknown values. The system of equations is overdetermined if the data of more than four sensors is available. In that case, minimizing the residuals between calculated and observed arrival times at each sensor is the goal. A linear least-squares algorithm can be used to determine the source location iteratively [7]. A covariance matrix C based on the partial deviations of (1) can also be calculated. The eigenvalues of C (excluding the values considering the source time) represent the axis ratio, and the eigenvectors represent the orientation of an error ellipsoid. Schechinger recommended the use of 68% error ellipsoids [5]. Therefore, with a probability of 68%, the source is located within the error ellipsoid. A small error ellipsoid indicates an accurate estimation of the source location.

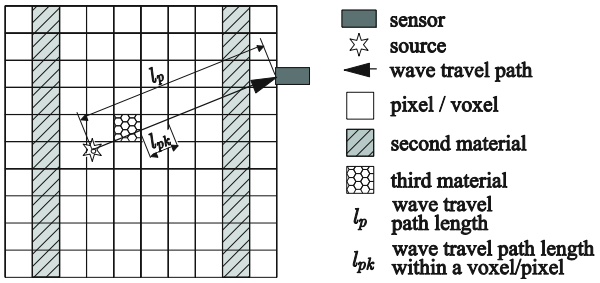

Fig. 3 Two-dimensional scheme for determination of the average wave travel velocity between source and sensor, based on a heterogeneous velocity model and straight-wave travel path (from [3])

3.2 Heterogeneous Geiger Method

If the Geiger method is applied to a heterogeneous specimen, a small modification in (1) can improve the accuracy of the determined source location significantly [8]. Substituting c_p by the average p-wave velocity $\bar{c}_{p\_het}(s,c)$, which can be determined for the straight connection of the estimated source c and sensor s (Fig. 3).

The determination of the average p-wave velocity $\bar{c}_{p\_het}(s,c)$ requires that the coordinates of the sensor, the coordinates of the estimated source location, and a numerical velocity model C_{mo} have to be known a priori. The p-wave velocity $c_p(k)$ is assigned to each of the k voxels. The length of the wave travel path within a voxel $l_{pk}(k)$ needs to be determined for each voxel [9]. Subsequently,

$$\bar{c}_{p\_het}(s,c) = \sum_k \frac{l_{pk}(k) \cdot c_p(k)}{l_p} \tag{2}$$

can be calculated.

In order to incorporate a heterogeneous velocity model, the average wave velocity between the estimated source location and each sensor has to be determined for each iteration step. Hence, the computational effort increases considerably. Moreover, the method relies on straight-wave propagation paths and is not able to consider the influences of cracks or air inclusions [3]. In case of complex specimens (e.g., T-shaped beams) the straight connection between source and sensor leads through the surrounding air.

3.3 **FastWay**

FastWay is a novel approach to estimate the location of AE sources based on a heterogeneous velocity model and multi-segment wave propagation paths. The major difference between *FastWay*and common arrival time-based source localization methods is that the fastest, rather than the direct (shortest), wave travel path between the source and a sensor is used to estimate the source location. This new

localization method can adapt to geometry and material properties of the investigated specimen.

In order to identify the fastest wave travel path, a modified Dijkstra's algorithm [10] is applied. A heterogeneous velocity model and the sensor coordinates are the input for the Dijkstra's algorithm. The output is one matrix $A_{\mathrm{tot}}(s)$ for each sensor s. The matrix entries are the earliest arrival time of a wave, starting from sensor s (source time $t_{\mathrm{c}} = 0$ µs) at the center of a voxel. The position of the voxel corresponds to the position of the value within $A_{\mathrm{tot}}(s)$ [3]. It is assumed that the fastest wave travel path and wave travel duration between two points (i and j) do not depend on which of the points is the emitting one (source) and which of the points is the receiving one (sensor). Hence, a potential source time $s_{\mathrm{pot};xyz}$, based on the value $a_{\mathrm{tot};xyz}(s)$ of the matrix $A_{\mathrm{tot}}(s)$ and the arrival time $t_{\mathrm{a}}(s)$ picked for sensor s, can be determined for each voxel with the coordinates [x y z]. The resulting source-time matrix $S_{\mathrm{pot}}(s)$ can be calculated for each sensor. One entry of all source-time matrixes should be (approximately) identical. The corresponding voxel, fulfilling

$$t_{\mathrm{a}}(s_1) - a_{\mathrm{tot};xyz}(\mathrm{s}_1) \approx t_{\mathrm{a}}(s_2) - a_{\mathrm{tot};xyz}(s_2) \approx \cdots \approx t_{\mathrm{a}}(s_n) - a_{\mathrm{tot};xyz}(s_n) \qquad (3)$$

contains the source location [3].

It has to be mentioned that the size of the voxels used for *FastWay* is larger than that used for the wave propagation simulation as well as for the heterogeneous velocity model that is applied in the heterogeneous Geiger method. The grid size of the numerical specimen implemented in *FastWay* is 5 mm. One *FastWay* voxel is equivalent to 125 wave propagation simulation voxels. *FastWay* determines the voxel which most probably contains the source. However, it is not possible to determine the exact location of the source within this voxel. The source localization output represents the coordinates of the voxel center. This results in a systematical inaccuracy of (half an edge length) 2.5 mm in each spatial direction or 2.5 mm $\times \sqrt{3} = 4.33$ mm in total [3].

4 Outcome of the Simulations and Source Localizations

4.1 Localization Setups

Six simulations with different source locations were performed. A total of 26 virtual sensors recorded the calculated, time-dependent displacements induced by the artificial sources (see Sect. 2). The recorded discrete wave forms were used for the determination of the onset time. The onset times were the input for the estimation of the source location applying a homogeneous Geiger method, a heterogeneous Geiger method, and *FastWay*. Five different sensor layouts were used to estimate the source location. The layouts consisted of:

- Sensor layout A: All sensors applied to the upper surface of the flange, SE19–SE26
- Sensor layout B: All sensors applied to the lower surface of the flange, SE13–SE18
- Sensor layout C: All sensors applied to the web, SE1–SE12
- Sensor layout D: All sensors applied to the web and the lower surface of the flange, SE1–SE18
- Sensor layout E: All sensors, SE1–SE26

The layouts are schematically visualized in Fig. 6. The sensor layouts consisted of 6–26 sensors. For the estimation of the source location using all three methods, the data of the six sensors with the largest absolute amplitudes within the first 20 µs after the picked arrival time of the wave at the respective sensor were used.

4.2 Localization Results

The results of the Geiger source localization algorithms are the coordinates of an estimated source location and an error ellipsoid to visualize the estimated accuracy of the determined solution (see Sect. 3). The result of *FastWay* is a normalized error matrix. The values of this matrix represent the normalized deviations from the condition formulated in (3) and range from 0 to 1. The lowest value corresponds to the voxel, which most likely contains the source [3]. Hence, the results do not represent straightforwardly the coordinates of the estimated source location. The output coordinates are the coordinates of the center of the determined voxel. Instead of error ellipsoids, the visualization of the normalized error matrix is used to present the reliability and expected accuracy of the determined solution.

The results for source S6 determined with the data provided by sensor layout E are displayed in Fig. 4. A three-dimensional representation of the outcome of the three source localization algorithms has turned out to be impractical. Instead, three cross sections are used to visualize the projection of the three-dimensional error ellipsoids superimposed with the result of the normalized error matrix. The cross sections are positioned at the source location estimated with *FastWay*. The error matrix is visualized for the voxels located in the displayed cross section only. The Geiger error ellipsoids, estimated source location determined with the two mentioned Geiger methods, and sensor locations are displayed on the cross sections. Figure 4 shows one of the most satisfying out of all 30 results. The three presented methods estimated the source location with maximum deviations of less than 7 mm (see Fig. 6). The determined error ellipsoids were very small, and the predefined source location lies within both error ellipsoids. The voxels with a normalized error matrix value (e_{norm}) of 0.11 or smaller form a spatial area, in which the source is located with a high probability. The voxels are displayed in colors ranging from violet ($0 \leq e_{\text{norm}} \leq 0.016$) to a greenish yellow ($0.095 \leq e_{\text{norm}} \leq 0.111$). The voxels with $e_{\text{norm}} \geq 0.111$ are colored ranging from green to gray (see Figs. 4 and 5).

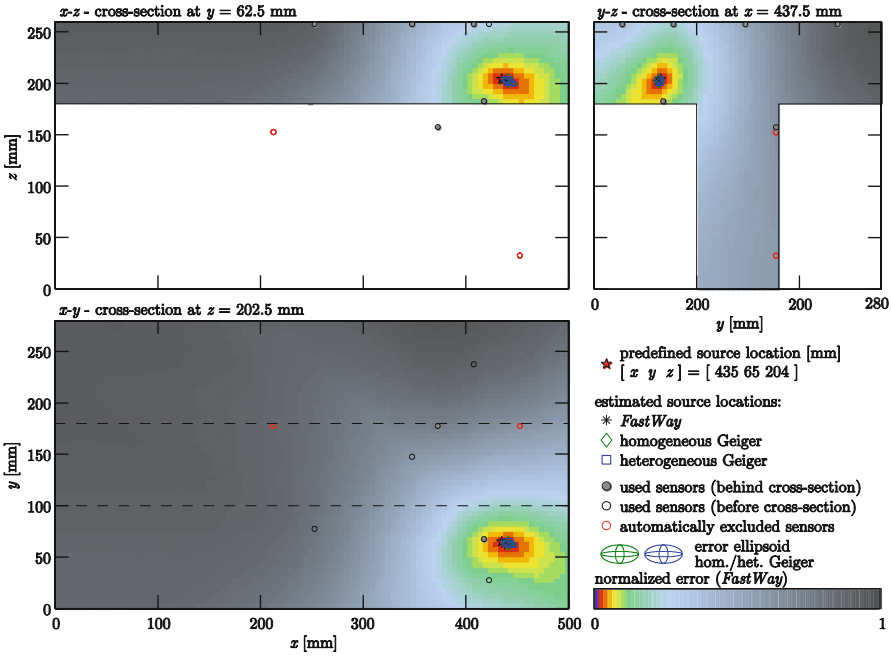

Fig. 4 Cross sections displaying normalized error matrix, error ellipsoids for the Geiger methods, locations of the used sensors, estimated sources, and predefined source (S6) marked, using sensor layout E

The area with $e_{\text{norm}} \leq 0.111$ should be as small as possible if the reliability of the accuracy of the determined source location is high. In case of Fig. 4 the area is very small and two voxels are colored in violet. One of the two voxels hosts the predefined source. Figure 5 represents an unsatisfying result. It is clearly visible that the determined error ellipsoids are larger than the specimen itself. Obviously, the predefined source is located within both error ellipsoids. However, the large error ellipsoids indicate that the accuracy of the determined source location is very low. The deviation between the predefined and the estimated source location is 263.3 mm and 200.6 mm for the homogeneous and the heterogeneous Geiger method, respectively. The estimated source locations determined with *FastWay* also differ considerably from the predefined source locations. The deviation is 41.8 mm, which can still be considered as satisfyingly accurate. The visualization of the normalized error matrix in Fig. 5 indicates that the source is located at the upper-left corner of the flange (y–x cross section). A preference of the z-location within the web, however, cannot be identified. The predefined source is located within the spatial area formed by the voxels with $e_{\text{norm}} \leq 0.111$. In case of Fig. 5, however, this area is significantly larger than in Fig. 4. Summarizing, the error ellipsoids and the visualization of the normalized error are a reliable way to demonstrate the expected accuracy of the determined source location.

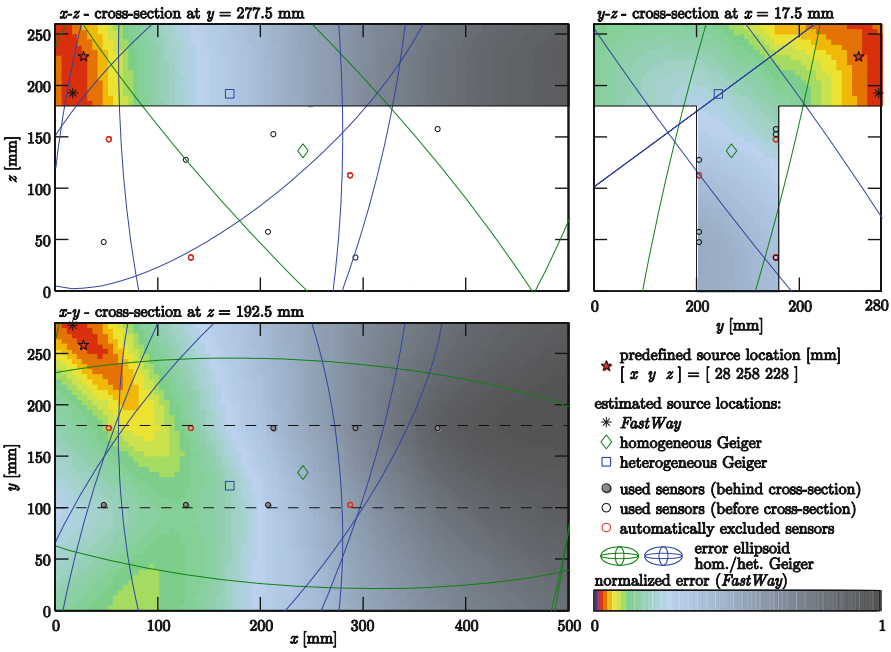

Fig. 5 Cross sections displaying normalized error matrix, error ellipsoids for the Geiger methods, locations of the used sensors, estimated sources, and predefined source (S3) marked, using sensor layout C

4.3 Localization Accuracy

The deviation between the estimated source location and the controlled, predefined one is significantly lower if the estimated one was determined with *FastWay*. The mean deviation between the predefined source location and the source location estimated with *FastWay* (of all 30 source localization setups) was 20.7 mm. The homogeneous Geiger method and the heterogeneous Geiger method provide estimated source locations with a mean deviation from the predefined one of 119.7 mm and 89.6 mm, respectively. The localization error of *FastWay* was approximately one-fifth of the localization error of the Geiger methods. *FastWay* provides 25 of the 30 estimated source locations with the smallest deviation from the predefined source location. The homogeneous Geiger method provides four of the most accurate source location predictions and the heterogeneous Geiger method only one. If *FastWay* did not provide the most accurate solution, the localization error of the source location predicted with *FastWay* was between 0.3 and 5.0 mm larger than the most accurate prediction. Figure 6 visualizes the deviations between the estimated and the predefined source locations for all six sources, five sensor layouts, and three localization methods. The bar diagram, which displays the deviation, is limited to a maximum of 100 mm. A localization error of more than 100 mm was

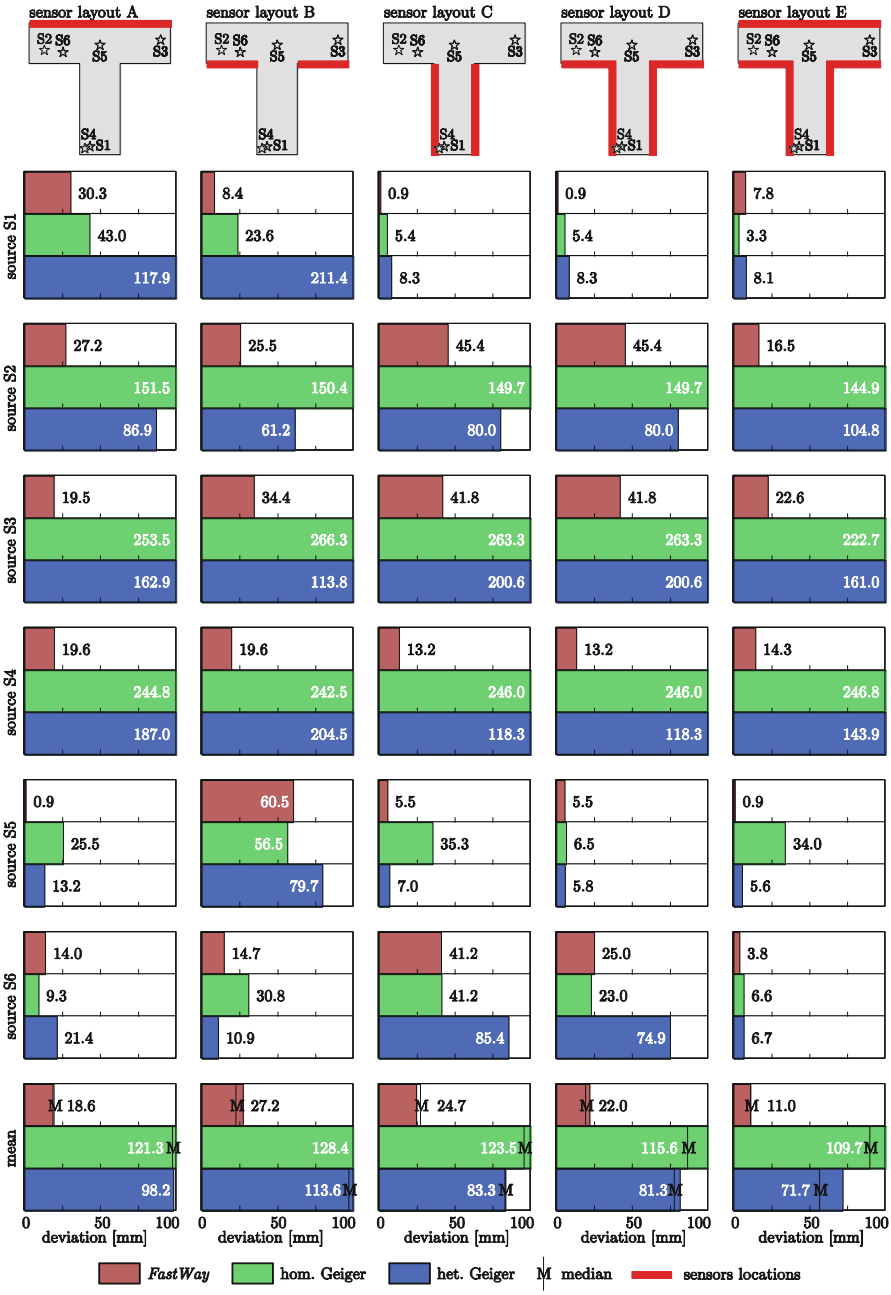

Fig. 6 Visualization of the deviation between the estimated and the predefined source locations. In the last segment the mean (*colored bar*) and the median of the deviations for all six sources are visualized

considered as unsatisfying. Determining a satisfying source prediction for sources S2, S3, and S4 was not possible using the homogeneous Geiger method, regardless of the sensor layout. These sources were located in both the web (S4) and the flange (S2 and S3). The localization error of S3 and S4 was about 250 mm, which is half of the largest specimen's dimension ($l_x = 500$ mm). The heterogeneous Geiger method was not able either to predict the source location of S3 and S4 satisfyingly, regardless of the sensor layout. Nevertheless, the localization error was smaller compared to that of the homogeneous Geiger method. In addition, the localization error for source S1 in combination with sensor layout A and B, as well as source S2 in combination with sensor layout E, was more than 100 mm when determined with the heterogeneous Geiger method.

5 Conclusion

The last row of Fig. 6 emphasizes that *FastWay* provides significantly more accurate source predictions than the two applied Geiger methods with regard to the investigated experimental setups. Moreover, *FastWay* was the only method that provided a satisfyingly accurate estimation of the source location for every source and sensor layout. Nevertheless, the deviations of more than 10 mm point out that *FastWay* bases on a simplified wave propagation model and does not reflect the real physical wave propagation behavior entirely. However, the accuracy of the estimated source locations can be improved significantly by means of *FastWay*.

References

1. G.K. Kocur, T. Vogel, E.H. Saenger, Crack localization in a double-punched concrete cuboid with time reverse modeling of acoustic emissions. Int. J. Fract. **171**, 1–10 (2011)
2. F. Schubert, Ausbreitungsverhalten von Ultraschallpulsen in Beton und Schlussfolgerungen für die zerstörungsfreie Prüfung, Ph.D. dissertation, Technical University of Dresden, 1999
3. S. Gollob, G.K. Kocur, T. Schuhmacher, T. Vogel, Source localization of acoustic emissions using multi-segment path analysis combined with a heterogeneous velocity model. Ultrasonics **74**, 48–61 (2015)
4. E.H. Saenger, N. Gold, S.A. Shapiro, Modeling the propagation of elastic waves using a modified finite-difference grid. Wave Motion **31**(1), 77–92 (2000)
5. B. Schechinger, T. Vogel, Acoustic emission for monitoring a reinforced concrete beam subject to four-point-bending. Constr. Build. Mater. **21**(3), 483–490 (2007)
6. L. Geiger, "Herdbestimmung bei Erdbeben aus der Ankunftszeit," Nachrichten von der Königlichen Gesellschaft der Wissenschaften zu Göttingen. Math. Phys. Klasse **4**, 331–349 (1910)
7. M. Ge, Analysis of source location algorithms, part II: iterative methods. J. Acoustic Emission **21**, 29–51 (2003)

8. S. Gollob, T. Vogel, Localisation of acoustic emission in reinforced concrete using heterogeneous velocity models, in *31st Conference of the European Working Group on Acoustic Emission (EWGAE)* (2014)
9. S. Stein, M. Wysession, *An Introduction to Seismology, Earthquakes, and Earth Structure* (Blackwell Publishing Ltd., Malden, MA, 2003)
10. E.W. Dijkstra, A note on two problems in connexion with graphs. Numer. Math. **1**, 269–271 (1959)

Pattern Recognition for Acoustic Emission Signals of Offshore Platform T-Tube Damage Based on K-means Clustering

Peng Jiang, Luying Zhang, Wei Li, and Xiao Wang

Abstract An experiment on offshore platform about the damage of the T-tube-node is performed to determine the signal characteristics of different damage stages by monitoring the acoustic emission and analyzing K-means clustering of the acoustic emission. The acoustic emission signal is used as an input to determine the characteristic parameter of damages through correlation analysis. The method can realize the recognition of T-type pipe-node damage from the AE signal. The reference for damage monitoring of T-type pipe node and identification of different damage stages can also be provided.

1 Introduction

T-type welded tubes are widely used in offshore oil platforms. The stability of the overall structure of these tubes is greatly affected by the active extension of cracks in tubular joints. Acoustic emission monitoring is a type of dynamic nondestructive testing technique. The detected source sound energy originates from active defects of tested components. Acoustic emission technique can be used to monitor the extension of dynamic cracks in T-type tubular joints, thereby enabling judgment on the severity of the damage of tubular joints [1]. However, tubular joints on offshore oil platforms experience interference from various signals in a complicated manner. Due to the influence from these external sources the detection of a crack needs to be investigated. Therefore, identifying different damage types accurately by using the traditional acoustic emission parameter approach is difficult.

In this study, K-means clustering and correlation analysis are combined to form a pattern recognition technique to analyze the acoustic emission signals of T-type tubular joint damages. The recognition technique is used as a comparative analysis with damage mechanics analysis to confirm the characteristics of acoustic emission signals in different stages of damage. The result of this study confirms that it can provide a basis for T-type tube damage monitoring of offshore oil platforms.

P. Jiang (✉) • L. Zhang • W. Li • X. Wang
Northeast Petroleum University, Daqing 163318, China
e-mail: jpnepu@163.com

G. Shen et al. (eds.), *Advances in Acoustic Emission Technology*, Springer Proceedings in Physics 179, DOI 10.1007/978-3-319-29052-2_5

2 K-means Clustering

K-means clustering refers to a clustering method to minimize the square of a distance from all data set vectors to the center of data set, namely minimum distance is regarded as the classification criterion [2]. K-means clustering uses the principle of error sum squares for repeated iteration, thereby achieving clustering result optimization. Thus, the distance sum squares of all samples to the centers of their own categories are minimized [3]. The concrete steps are as follows:

1. K objects are chosen from *m* data samples to be the initial clustering centers.
2. The distance between each sample and the clustering center is calculated one by one, and the corresponding samples are divided based on the minimum distance criterion.
3. The sample mean vector is included in each clustering domain. The latest mean vector is made as a new clustering center, which can ensure that the clustering criterion function is minimized.
4. The calculation is finished if the algorithm convergence that the center obtained from clustering meets the requirements of the standard density function. Otherwise, it must return to the second step and recalculate the aforementioned distance one by one. The K-means clustering flowchart is shown in Fig. 1.

3 Experiments

Q345 steel samples are selected as experimental specimens. One is a defect-free T-type tube, and another is a precracked T-type tube, with a stripe 1 mm deep and 4.2 mm distant to welding root. SANS 300 KN electronic universal testing machine is selected to load. PCI-8 acoustic emission monitoring system is selected as the experimental system. Two WD broadband sensors are installed up and down the node. Force load is selected as a loading way with speed of 10 N/s. The experiment system is shown in Fig. 2.

4 Analysis and Discussion

4.1 Analysis on Acoustic Emission Parameter

Figures 3 and 4 show amplitude experience figures during the process in which T-shaped tubes are compressively injured. Figure 3 shows many microcrack initiations at the beginning of loading for the defect-free T-type tube, with a large number of low amplitude and small signal energy. The signals are rare in the early injury process because of the existence of prefabricating cracks, as shown in Fig. 4, that is, nearly no microcrack initiation signal existing. In the second stage, the

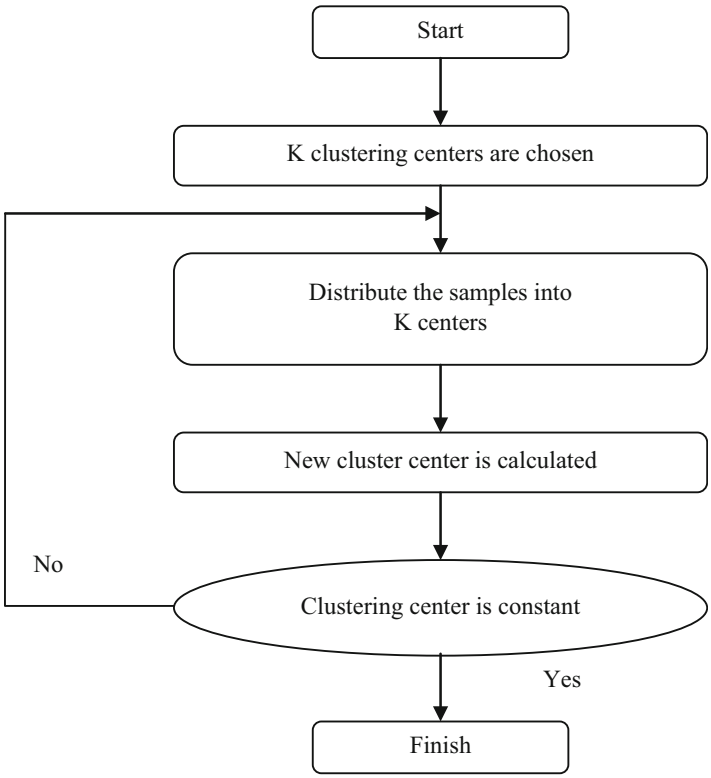

Fig. 1 K-means clustering algorithm flowchart

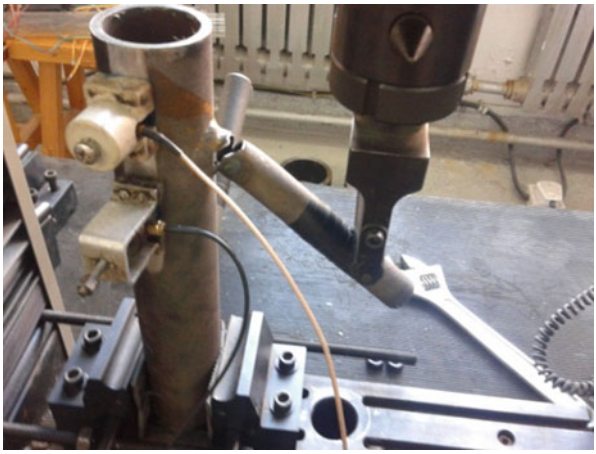

Fig. 2 Experimental system diagram

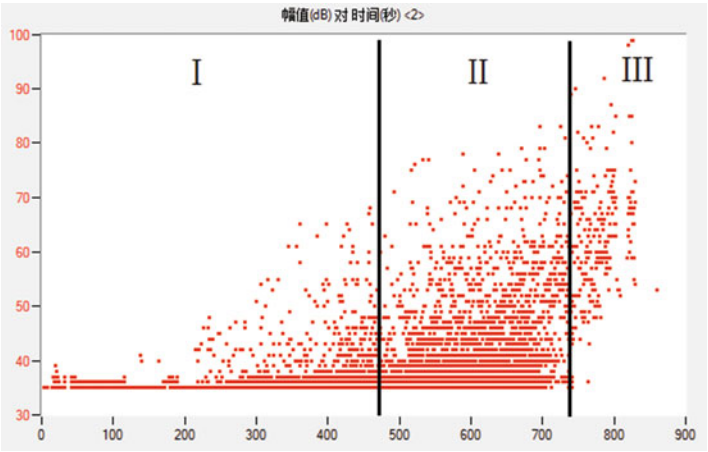

Fig. 3 Defect-free T-type tube damage amplitude figure

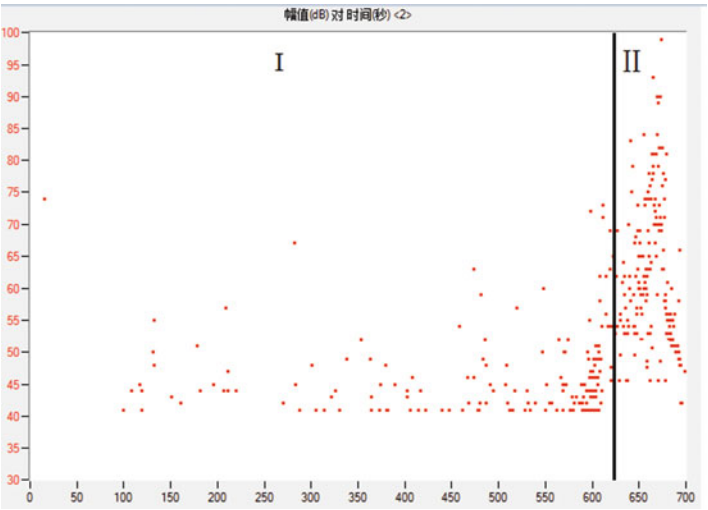

Fig. 4 Precracked T-type tube damage amplitude figure

microcrack extends continuously along with the load increase. The specimen enters the active crack propagation stage. The acoustic emission signal amplitude increases rapidly at the same time with the largest amplitude increasing to 80 dB. Vast amounts of energy released in the expansion of the microcracks many large amplitude signals.

The specimen enters the stage of macroscopic crack initiation and structural failure when the load increases continuously. The signal amplitudes can reach more

than 85 dB and the number of hits in this stage has a large drop compared with that in the microcrack extension stage, as the specimen completely failed.

As shown in the diagram of acoustic emission parameters during this damage experience, various stages of damaged specimen can be roughly distinguished. However, extracting acoustic emission signals in different damage stages accurately and effectively only relying on time is difficult because of the existence and concentrated distribution of numerous acoustic emission signals in the whole process of loading failure. Thus, the related acoustic emission parameter analysis must be associated with clustering parameter analysis to identify the acoustic emission signal characteristic of different damage stages.

4.2 Analysis on K-means Clustering

K-means clustering accuracy mainly depends on the selection of characteristic parameters. Thus, it must select the most relevant parameters as input vectors from various acoustic emission ones in front of the clustering analysis [4]. Amplitude, energy, duration, and other parameters of the acoustic emission signal of a T-type tube damage form a hierarchical clustering tree, and then get the correlation between the parameters, as shown in Fig. 5. The figure indicates that the correlation coefficient among energy, rise time, central frequency, and count is below 0.5, which is lower than that among other parameters. This result is determined as the feature vector for clustering analysis.

The optimal number of K-means clustering is determined via BD criterion. If DB is the smallest, then the corresponding k is superior. Fig. 4 shows a line chart of DB

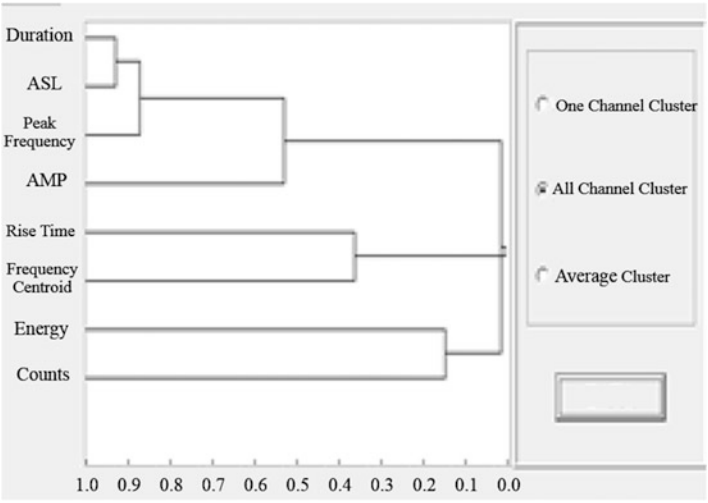

Fig. 5 Acoustic emission parameter correlation diagram

coefficient to a clustering number k after k-means clustering. Figure 6 indicates that the optimal clustering number is 3.

Figure 7 shows the connection diagram of ringing count and rise time for class 1 to class 3. The counts in class 1 are below 50, and the rise time is no more than 1000. Ringing counts in class 2 increase with the range of 50–250, and the rise time increases obviously. Signal strength is high but decays quickly. It belongs to the strong excitation signal. However, signals in class 3 have the characteristics of not

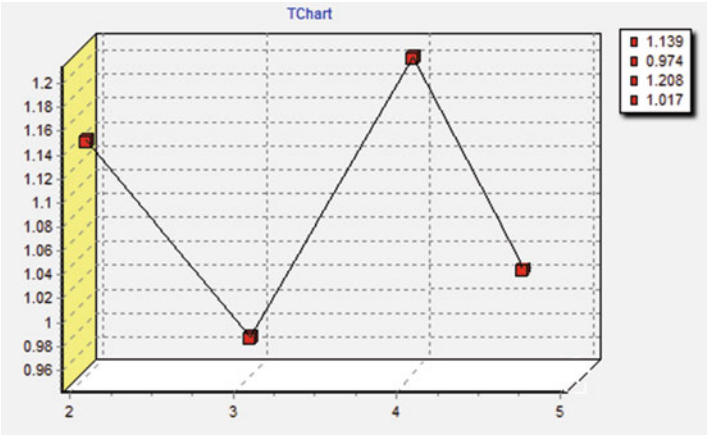

Fig. 6 Optimal clustering number

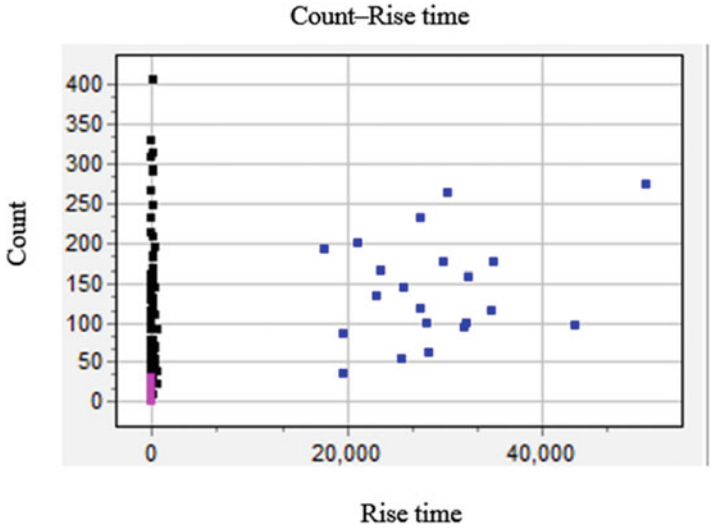

Fig. 7 Count-rise time clustering diagram

only a small rise time but also a large ringing count. This observation shows that such signals have a small amplitude but a long duration. The preceding analysis combined with the loading damage types of materials indicates that the signals in class 1, 2, and 3 belong to microcrack initiation, macroscopic crack initiation, and microcrack spread signals, respectively.

The energy with the highest correlation is selected for clustering analysis. The characteristic parameters after clustering are also used to conduct analysis intuitively and conveniently by corresponding to the time of specimen damage process.

Figures 8 and 9 show the clustering distribution of two different specimens. These illustrations indicate that the signals in the overall damage process are divided into three types. Red Class 0 signal accounts for the majority of total signals showing low energy. This kind of signal becomes gradually dense over time. The overall specimen damage process is accompanied by the continuous occurrence of microcracks. Thus, a comparison with acoustic emission signal in damage process is performed to judge an acoustic emission signal as microcracks occur. Energy distribution shows that purple class 1 signal is higher than the crack-occurring signal in energy value. Based on the characteristics and occurring time of a signal, this result can be judged as a concentrated phase of microcrack extension.

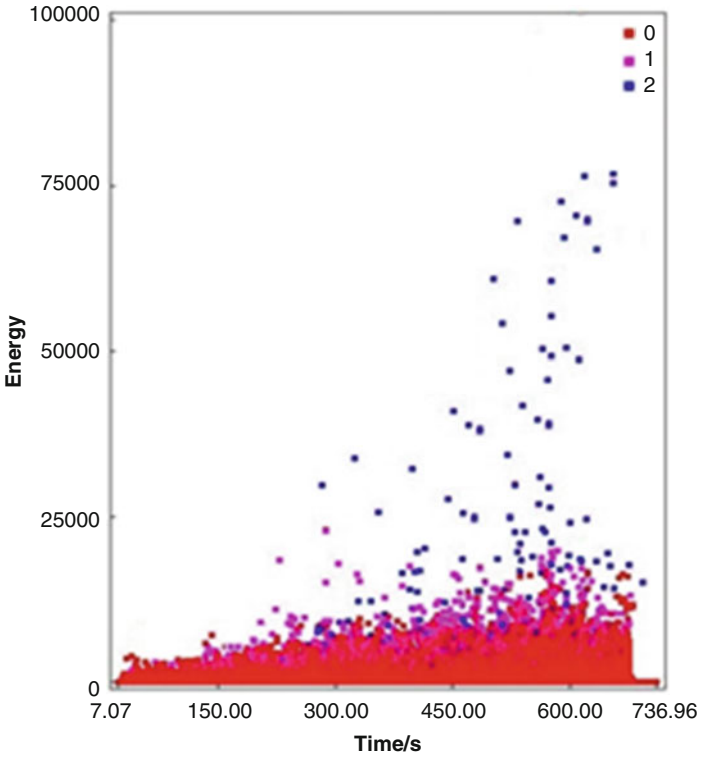

Fig. 8 Defect-free T-type tube damage clustering result

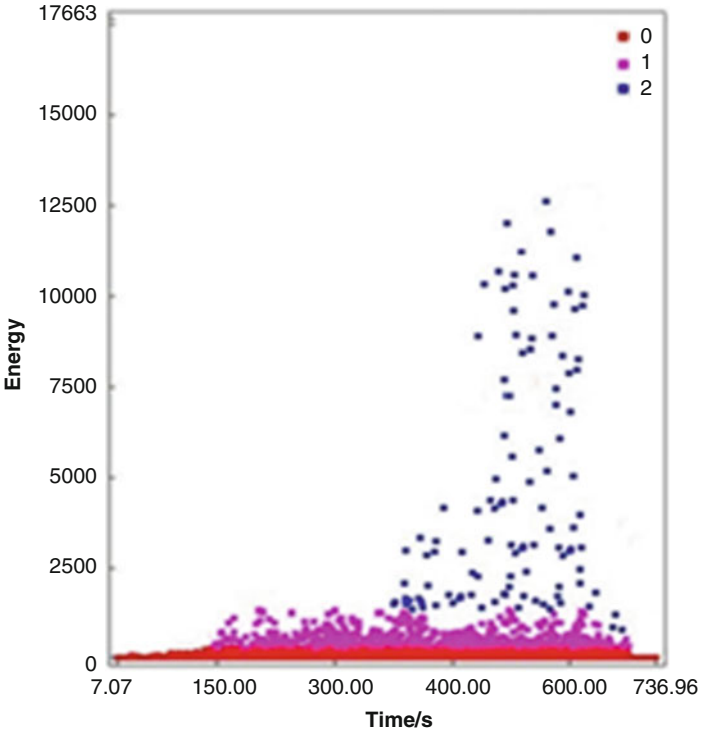

Fig. 9 Precracked T-type tube damage clustering result

Class 2 signal is significantly higher than the previous two signal types in terms of energy. It also increases with the loading process. Meanwhile, this signal is widely distributed in the middle and late stages of damage, which show macrocrack characteristics.

5 Conclusion

This study uses K-means clustering to achieve the pattern recognition of an acoustic emission signal of T-type tubes on an offshore platform. According to the analysis of correlation analysis and clustering correlation of acoustic emission signal of damage, we can obtain the occurrence of macrocrack, macrocrack extension, and macrocrack extension of specimens. Clustering analysis is also used to analyze and confirm the distribution law of the acoustic emission signals of different damage types in a damage loading process. The result shows that K-means clustering method can be used to achieve an effective recognition of the damage patterns of T-type tubes and to distinguish the acoustic emission signals of different damage

types. Acoustic emission parameter analysis can be combined with clustering parameter analysis to obtain the dynamic distribution of damage on materials. This analysis can provide a basis to recognize and evaluate the acoustic emission signals of T-type tube damages on offshore platforms.

References

1. D. Guang, Acoustic emission detection technique in China—to celebrate the thirty anniversary of the establishment of nondestructive testing Branch, the China Mechanical Engineering Society. Nondestruct. Test. **30**(7), 389–394 (2008)
2. Z. Shibin, Z. Xu, T. Xuqing, New K-means algorithm for confirming the optimal clustering number. Comput. Eng. Appl. **46**(16), 27–31 (2010)
3. Li Jinjiao, Wang Aixia, Wang Jiao, et al., *Recognition pattern*, 4th edn. (Beijing Electronics Industry Press, 2010), pp. 431–432
4. A.A. Pollock, *Acoustic emission inspection*, ASM handbook: nondestructive evaluation and quality control, vol 17 (ASM International, Materials Park, 1989), pp. 278–294

Fault Analysis for Low-Speed Heavy-Duty Crane Slewing Bearing Based on Wavelet Energy Spectrum Coefficient

Yang Jiao, Guanghai Li, Zhanwen Wu, Huipo Geng, Jian Zhang, and Li Cheng

Abstract By use of the custom-built crane model, loads, acoustic emission instrument, and sensor, AE tests for the slewing bearing with no defect, the slewing bearing with outer race defect, and the slewing bearing with roller defect had been conducted under the operating conditions of low speed and heavy duty. A lot of AE signals had been acquired and processed. AE signal acquired under different working conditions had made wavelet decomposition using Daubechies wavelet. All wavelet energy spectrum coefficients under every working condition had been calculated. The judgment basis for the slewing bearing fault had been obtained by the distribution law of wavelet energy spectrum coefficients under different working conditions. This study lays a theoretical foundation for the fault diagnosis of crane slewing bearing working at low speed and heavy duty.

1 Introduction

Heavy-duty slewing bearing is the key component of gantry crane, tower crane, and arm crane. These hoisting equipment run in low-speed, heavy-load, intermittent operation. In operation a large-impact load is supported by them. Their operational status directly affects the performance of the whole system. If they get out of order, the production efficiency of the whole equipment can be influenced, and the safety of personnel and equipment is threatened. Commonly used methods [1] for crane detection are metal magnetic memory testing, electromagnetic detection, ray

Y. Jiao (✉) • L. Cheng
School of Information Science and Technology, Hebei University of Science and Technology, Shijiazhuang 050018, China
e-mail: jyang939@163.com

G. Li • Z. Wu
China Special Equipment Inspection and Research Institute, Beijing 100013, China

H. Geng • J. Zhang
Hebei Supervision and Inspection Institute of Boiler and Pressure Vessel, Shijiazhuang 050061, China

G. Shen et al. (eds.), *Advances in Acoustic Emission Technology*, Springer Proceedings in Physics 179, DOI 10.1007/978-3-319-29052-2_6

detection, ultrasonic testing, acoustic emission testing, vibration testing, etc. Acoustic emission detection technology is used in this study.

By use of the custom-built crane model, AE tests for the slewing bearing with no defect (ND), the slewing bearing with outer race defect (ORD), and the slewing bearing with roller defect (RD) had been done, respectively. AE signal acquired from different slewing bearing at different working conditions had made wavelet decomposition and energy spectrum coefficient analysis. The slewing bearing fault judgment had been obtained.

2 Wavelet Decomposition and Energy Spectrum Coefficient

Wavelet analysis [2–4] is the localization analysis in time (space) and frequency. Signal is multiscale refined gradually by expansion and translation operation. Finally, time subdivision can be achieved in high frequency, and frequency subdivision in low frequency. It can automatically adapt to the requirements of time-frequency signal analysis, and focus to any details of the signal, and to solve the difficult problem of Fourier transform. At present, wavelet analysis is widely used in denoising, feature extraction, signal recognition, and location of the acoustic emission signal.

By wavelet analysis, the signal was decomposed into low-frequency and high-frequency components. In the decomposition, the lost information in low-frequency part is captured by high frequency. In the next layer decomposition, the decomposed low-frequency part is decomposed into low-frequency and high-frequency components again, and the lost information in low-frequency part is also captured by high frequency. By analogy, a deeper level of decomposition can be completed. From the structure of wavelet decomposition, the frequency resolution of wavelet transform decreases with the increase of frequency.

2.1 Wavelet Decomposition

In view of the characteristics of acoustic emission signal, such as sudden, transient, diversity of acoustic emission source signal and diversity of interference noise, the selection of wavelet basis functions needs to be considered as follows [5, 6]:

1. In order to capture the acoustic emission signal in the low-speed and heavy-load crane, the sampling time is longer and the data is huge, so the discrete wavelet transform is needed to improve the data processing speed.
2. In order to embody the burst and transient characteristics of acoustic emission signals, the wavelet bases with a certain degree of order vanishing moment are

required to highlight all kinds of singular characteristics of acoustic emission signals.
3. In order to eliminate or weaken the distortion of the signal in wavelet decomposition and reconstruction, the wavelet basis function must be with symmetry.
4. In order to guarantee the smooth degree of the curve of wavelet decomposition, the wavelet basis function with regularity can be given priority.
5. In order to guarantee the local analysis ability of wavelet bases in the frequency domain, the wavelet base is required to have a fast decay in the frequency domain. The selected wavelet basis should have a tight support in time domain and has a fast attenuation in the frequency domain.

In some common wavelet bases, Daubechies wavelet, Symlets wavelet, and Coiflets wavelet all can be wavelet bases for acoustic emission signal analysis. Db8 wavelet is selected to make wavelet decomposition. According to the principle of wavelet multi-resolution analysis and signal sampling rate, the decomposition scale $J = 7$ is selected.

2.2 Wavelet Energy Spectrum Coefficient

The wavelet energy spectrum coefficient [7–9] is defined as the ratio of the energy of each wavelet decomposition scale to the total energy. The energy distribution of the acoustic emission signal in each frequency band after wavelet decomposition is characterized by it. For example, the J scale wavelet decomposition of the signal is decomposed into a component of $J + 1$ frequency range. Because of differences in the acoustic emission source, the energy distribution of acoustic emission signal in every decomposition scale after the wavelet decomposition is different, and the wavelet energy spectrum coefficients can describe the characteristics of acoustic emission source.

Wavelet analysis is used to decompose the signal into the frequency range of $J + 1$, and to define the energy of the signal in each wavelet decomposition scale according to the following formula:

$$\begin{cases} E_j^A f(n) = \sum_{n=1}^{N} [A_j f(n)]^2 \\ \qquad\qquad\qquad\qquad j = 1, 2, \cdots, J \\ E_j^D f(n) = \sum_{n=1}^{N} \left[D_j f(n)\right]^2 \end{cases} \tag{1}$$

where the f(n) is acoustic emission signal to be processed, the $A_j f$(n) is the reconstructed signal of low frequency component after J wavelet decomposition, and the $D_j f$(n) is the reconstruction signal of high frequency component after the j wavelet decomposition, $E_j^A f(n)$ is expressed as the energy of the low-frequency

signal component on the decomposed scale J, and $E_j^D f(n)$ is expressed as the energy of the signal in the high-frequency signal component on the decomposed scale j.

The total energy of the signal is defined:

$$Ef(n) = E_J^A f(n) + \sum_{j=1}^{J} E_j^D f(n) \tag{2}$$

The wavelet energy spectrum coefficients of each wavelet decomposition scale are, respectively, represented with ηE_J^A and ηE_j^D:

$$\eta E_J^A = \frac{E_J^A f(n)}{Ef(n)} \quad \eta E_j^D = \frac{E_j^D f(n)}{Ef(n)}, j = 1, 2, \cdots, J \tag{3}$$

In the formula, the wavelet energy spectrum coefficient of the low-frequency signal on J is represented by ηE_J^A, and the wavelet energy spectrum coefficient of the signal in the high frequency on j is represented by ηE_j^D.

3 Experimental Setup, Sensor Placement, Defect Setting, and Experimental Scheme

3.1 Experimental Setup

The experimental setup consists of crane model, loads, testing instrument, computer, and sensors. The main part of the crane model and loads are shown in Fig.1. The crane model consists of foundation, slewing bearing, control cabinet, etc. Each load weights 2.2 tons. 0 ton (no load), 4.4 tons (half load), and 8.8 tons (full load) are used as three kinds of loading conditions in the experiment. Through the control cabinet, the slewing bearing speed can be adjusted. In the test, the low speed (1 r/min), the medium speed (2 r/min), and the high speed (3 r/min) are set.

Fig. 1 The crane model and loads

The German company Vallen AMSY-6 is used as testing instrument. The VS150-RIC resonant sensors are adopted. The threshold is set to 40 dB to shield the outside noise, the sampling frequency $f_s = 5$ MHz, and sampling points $n = 8192$.

3.2 Sensor Arrangement

The inner ring of the crane model is stationary. As the inner ring of the rolling track is close to the rolling bearing, the three sensors are arranged on the inner ring to enhance acquisition signal. Three sensors were separated by 120° and placed in the rolling bearing inner ring, as shown in Fig. 2.

3.3 Defect Setting

Outer race defect types are approximately the same, so the defect is set on interface between the outer ring surface and maximum diameter of roller. The slot was used as the outer race artificial defect which is shown in Fig. 3a.

In slewing bearing, the largest diameter of rings is most prone to failure, so the defect will be set in this row of rollers. The simulation of defects is to cut 1/4 roller in end, as shown in Fig. 3b.

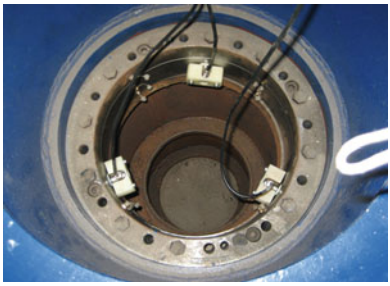

Fig. 2 Sensor layout

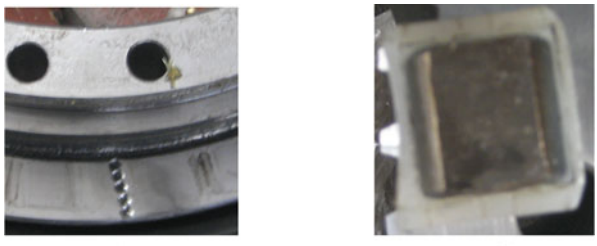

Fig. 3 The outer race defect and roller defect. (**a**) The outer race defect. (**b**) The roller defect

3.4 Experimental Scheme

The AE signals in the slewing bearing with ND, the slewing bearing with ORD, and the slewing bearing with RD are acquired at three loads and three speeds.

The AE data in this paper is acquired in the slewing bearing with ND, the slewing bearing with ORD, and the slewing bearing with RD in half load and medium speed conditions.

4 Wavelet Decomposition and Energy Spectrum Analysis for Acoustic Emission Signals

4.1 The Slewing Bearing with ND

Crane model run at half load and medium speed: The acoustic emission signal acquired from the slewing bearing with ND and its frequency spectrum is shown in Fig. 4.

The spectrum of the signal is mainly distributed in the range of 30–200 kHz, There is the peak in the vicinity of 60 and 80 Hz, and also in the vicinity of 150 and 160 Hz.

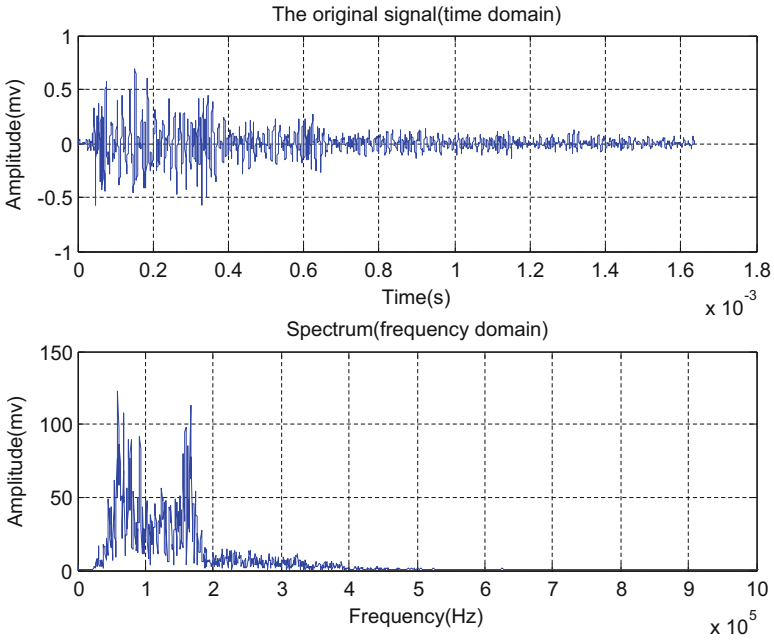

Fig. 4 AE signal and frequency spectrum of the slewing bearing with ND

Firstly, the wavelet denoising of the signal is carried out, and then 7-scale wavelet decomposition for the signal after denoising has been conducted, and the results are shown in Fig. 5.

According to the solving method of wavelet energy spectrum coefficient of acoustic emission signal, the decomposition signal from the slewing bearing with ND has been calculated and the wavelet energy spectrum coefficient distribution map has been obtained. It is shown in Fig. 6.

The energy after wavelet decomposition for the acoustic emission signal acquired from the slewing bearing with ND is mainly distributed in d4, d5, and d6 layers.

4.2 The Slewing Bearing with ORD

The slewing bearing with artificial ORD was used in crane model. The acoustic emission signal was acquired at half load and medium speed. Its waveform and spectrum corresponding to peak signal are shown in Fig. 7.

The spectrum of the signal is mainly distributed in the range of 30–240 kHz, There is the peak in the neighborhood of 40, 160, and 230 kHz.

Firstly, the wavelet denoising of the signal is carried out, and then 7-scale wavelet decomposition for the signal after denoising has been conducted. Limited to the length of this chapter, the results of the decomposition are omitted.

According to the solving method of wavelet energy spectrum coefficient of acoustic emission signal, the decomposition signal from the slewing bearing with ORD has been calculated and the wavelet energy spectrum coefficient distribution map has been obtained. It is shown in Fig. 8.

It can be seen from the figure that the energy after wavelet decomposition for the acoustic emission signal acquired from the slewing bearing with ORD is mainly distributed in d4, d5, d6, and d7 layers.

4.3 The Slewing Bearing with RD

The slewing bearing with artificial RD was used in crane model. The acoustic emission signal was acquired at half load and medium speed. Its waveform and spectrum corresponding to peak signal are shown in Fig. 9.

The spectrum of the signal is mainly distributed in the range of 30–350 kHz. There is the peak in the neighborhood of 100, 170, and 240 kHz.

Firstly, the wavelet denoising of the signal is carried out, and then 7-scale wavelet decomposition for the signal after denoising has been conducted. Limited to the length of this chapter, the results of the decomposition are omitted.

According to the solving method of wavelet energy spectrum coefficient of acoustic emission signal, the decomposition signal from the slewing bearing with

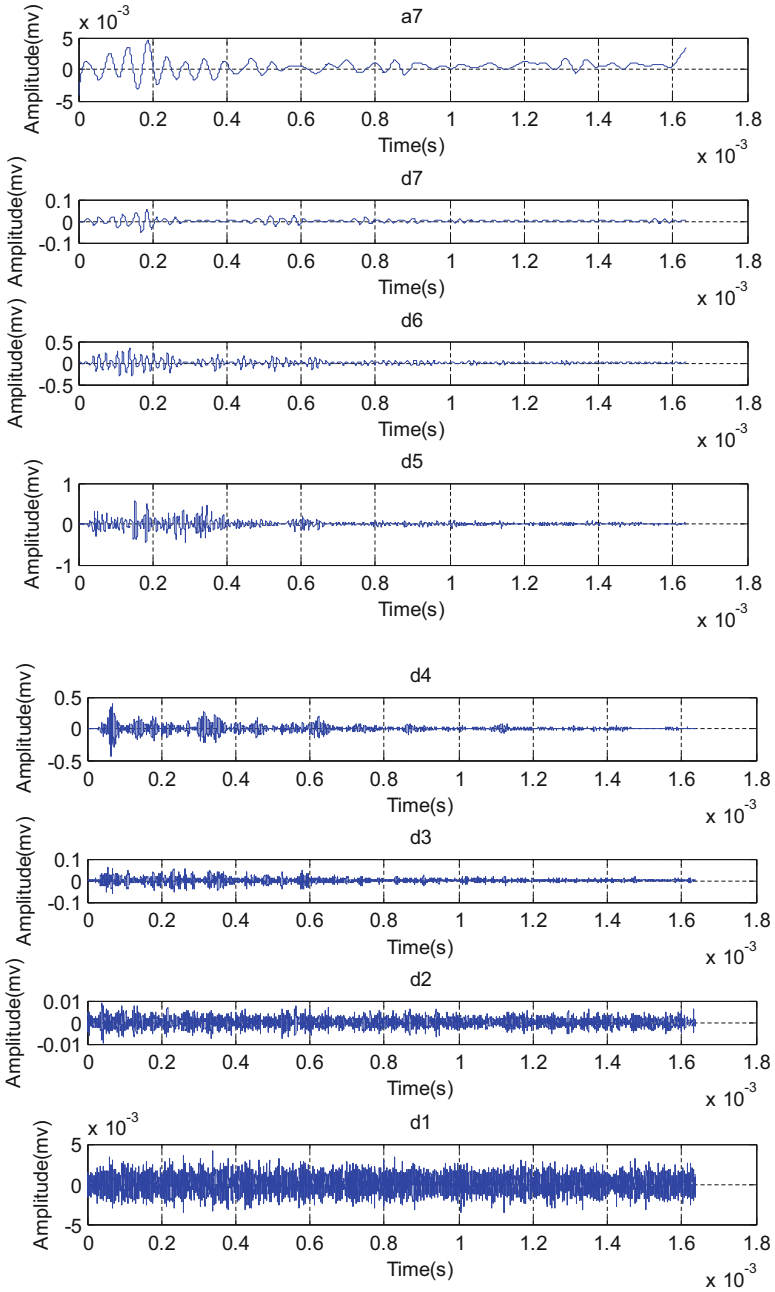

Fig. 5 Wavelet decomposition for the AE signal acquired from the slewing bearing with ND

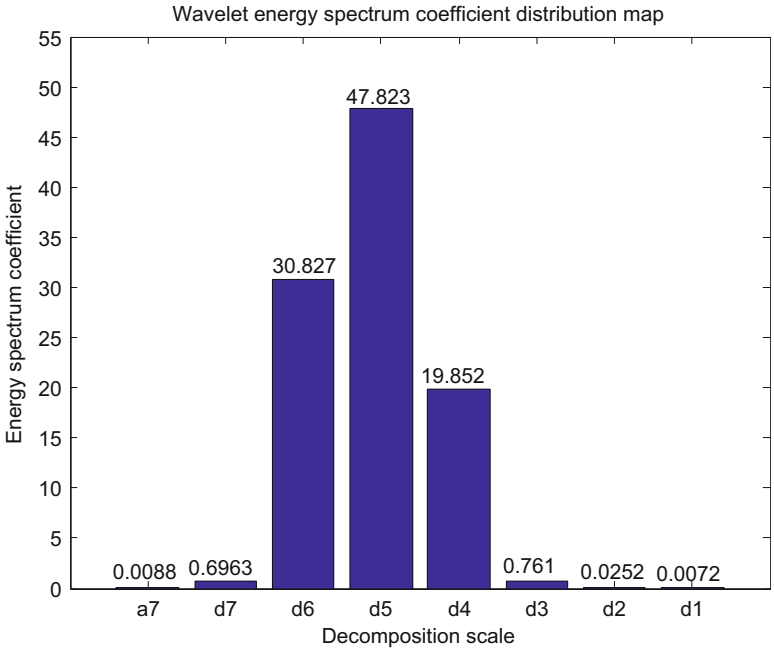

Fig. 6 Wavelet energy spectrum coefficient distribution of the slewing bearing with ND

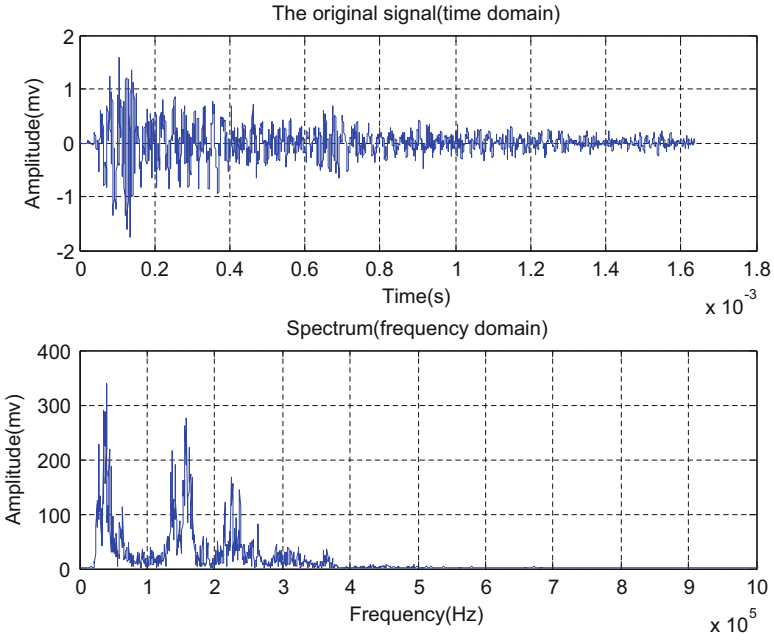

Fig. 7 AE signal and frequency spectrum of the slewing bearing with ORD

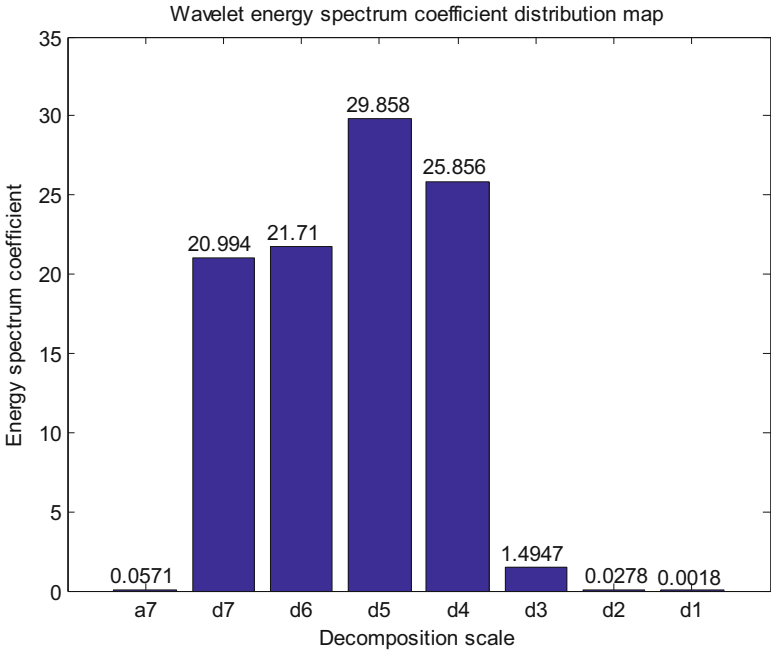

Fig. 8 Wavelet energy spectrum coefficient distribution of the slewing bearing with outer race defect

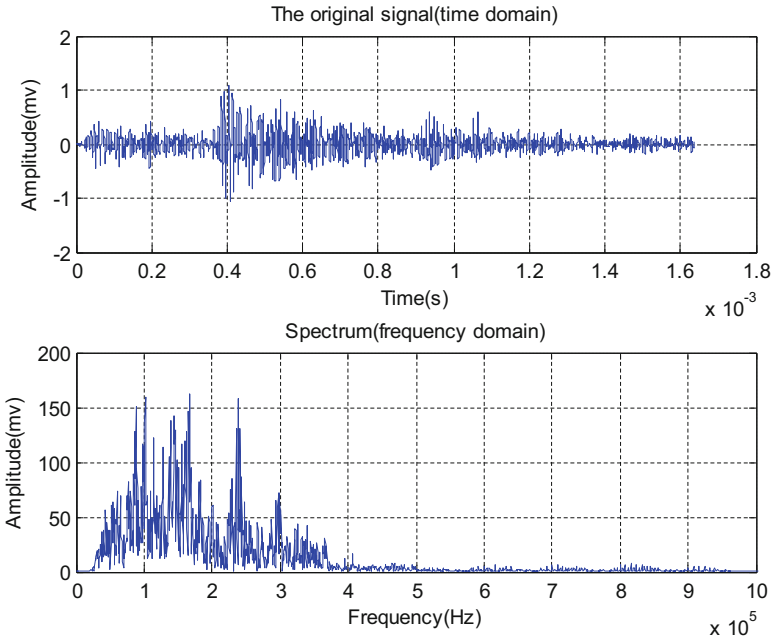

Fig. 9 AE signal and frequency spectrum of the slewing bearing with RD

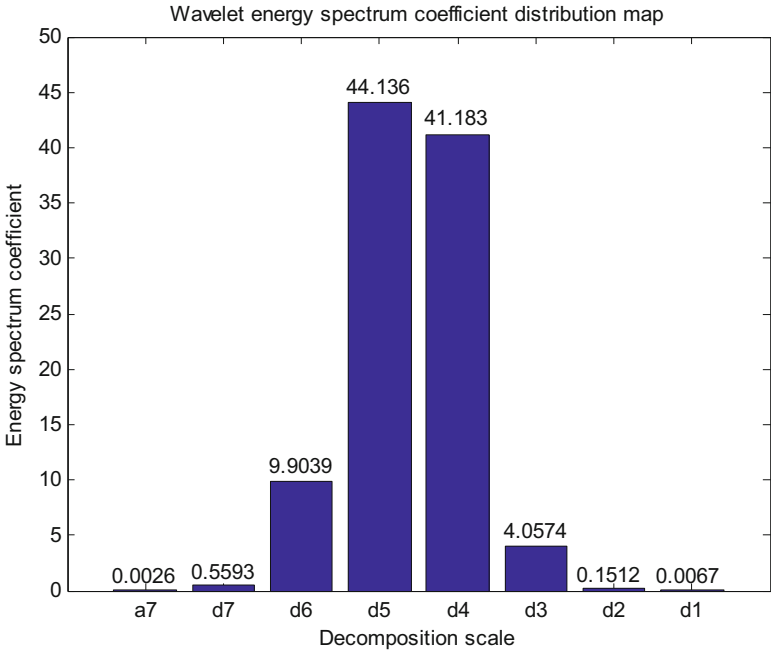

Fig. 10 Wavelet energy spectrum coefficient distribution of the slewing bearing with roller defect

RD has been calculated and the wavelet energy spectrum coefficient distribution map has been obtained. It is shown in Fig. 10.

It can be seen from the figure that the energy after wavelet decomposition for the acoustic emission signal acquired from the slewing bearing with RD is mainly distributed in d4 and d5 layers.

Compared with the wavelet energy spectrum distribution of the acoustic emission signal acquired from the slewing bearing with ND, the wavelet energy spectrum distribution of the acoustic emission signal acquired from the slewing bearing with ORD and with RD has obvious characteristics.

The wavelet energy spectrum coefficient distribution of the acoustic emission signal acquired from the slewing bearing with ORD mainly concentrates in the d4, d5, d6, and d7 layers. D4 layer and d5 layer accounted for less than 56% of the total energy; they are half of the total signal energy. D6 layer and d7 layer accounted for more than 42% of the total energy; they are close to half of the total energy.

The wavelet energy spectrum coefficient distribution of the acoustic emission signal acquired from the slewing bearing with RD mainly concentrates in the d4 and d5 layers. D5 layer and d4 layer accounted for more than 85% of the total energy; they are absolute subject of signal energy. The other layer accounted for only 15% of the total energy; they are auxiliary components of signal energy.

5 Conclusions

By use of the custom-built crane model, AE tests for the slewing bearing with ND, the slewing bearing with ORD, and the slewing bearing with RD had been done, respectively. The wavelet analysis to acoustic emission signal acquired from every slewing bearing has been conducted. The conclusions are as follows:

The acoustic emission signal is a burst-mode signal. For the slewing bearing with ND, signal frequency is mainly concentrated in 30–240 kHz range. For the slewing bearing with ORD and the slewing bearing with RD, the band broadens, and signal frequency is mainly concentrated in 30–350 kHz range.

Feature extraction method for defect of the slewing bearing based on wavelet energy spectrum coefficient has been presented. The acoustic emission signal features from the slewing bearing with ND, the slewing bearing with ORD, and the slewing bearing with RD are extracted, respectively. The results show that the acoustic emission signal acquired from two kinds of defect can be identified correctly by this method.

Acknowledgment The research work was supported by National Key Technology Support Program No. 2011BAK06B03-03.

References

1. C. Chen, J. Yang, L. Guanghai, et al., Application of acoustic emission technology to crane inspection. Hebei J. Ind. Sci. Technol. **30**(3), 199–202 (2013)
2. G. Rongsheng, G. Shen, L. Shifeng, An overview on the development of acoustic emission signal processing and analysis technique. NDT **24**(1), 23–28 (2002)
3. J. Yang, J. Hou, L.I. Guanghai, et al., Acoustic emission signal processing technology and the application status in rolling bearing test. J. Hebei Univ. Sci. Technol. **34**(4), 313–317 (2013)
4. Z. Ping, K. Shi, R. Geng, et al., Application of wavelet transform to acoustic emission test. Nondestr. Test. **24**(10), 436–439 (2002)
5. J. Xie, L. Le, L. Wenfeng, Research on wavelet base selection for vibration signal denoising. Sci. Technol. Eng. **11**(25), 5997–6000 (2011)
6. S. Tan, Q. Shuren, T. Baoping, Time-frequency characteristic of wavelet base and its application transient signal detection. J. Chongqing Univ. **21**(2), 12–17 (2001)
7. Z. Wu, S. Wang, G. Shen, Extraction of acoustic emission resource characteristics based on wavelet transform. J. Wuhan Univ. Technol. **32**(1), 85–87 (2008)
8. Z. Jingchuan, Z. Zhoumo, L. Ping, et al., A recognition method with wavelet energy spectrum and wavelet information entropy for abnormal vibration events of a petroleum pipeline. J. Vib. Shock **29**(5), 1–5 (2010)
9. T. Shoufeng, T. Minming, Y. Pan, et al., Energy spectrum coefficient analysis of wavelet features for coal rupture microseismic signal. Chin. J. Sci. Instrum. **32**(7), 1521–1527 (2011)

Analysis of the Fractional S Transform

Yang Yu, Tiepeng Xu, and Ping Yang

Abstract The acoustic emission (AE) signals of corrosion are non-stationary and random. Time frequency analysis is the best approach for extracting the features of corrosion AE signals. The fractional S transform (FRST) combines the advantages of the S transform (ST) and the (FRFT). The window size of an ST can be adjusted by the signal frequency and the window width can be increased when higher frequency resolution is needed. With optimal matching order, which is the order corresponding to the FRFT maximum peak value, a FRFT can get a better fractional time-frequency representation by rotating the fractional frequency axis to the optimal place. Simulation results show that the FRST is better than the ST both in time-frequency concentration and precision, and the FRST is able to accurately extract the characteristics of a corrosion AE signal.

1 Introduction

Acoustic emission (AE) is the phenomenon of parts of materials emitting instantaneous elastic waves due to fast release of energy. The methods of AE signal processing are mainly parameter analysis and waveform analysis [1]. For parameter analysis, the characteristics of AE signals are represented by a number of simplified waveform feature parameters that are then analyzed and processed. In waveform analysis, the analysis of the waveform is based on the storage and recording of AE signals. Of the available spectrum analysis methods, such as modal AE analysis, time-frequency analysis is commonly used to analyze AE signal waveforms. Time-frequency analysis is short for joint time-frequency analysis. It combines the time domain and frequency domain to describe and observe the signal, which at

Y. Yu (✉) • T. Xu • P. Yang
School of Information Science and Engineering, Shenyang University of Technology, Shenyang 110870, China
e-mail: yuy@sut.edu.cn

G. Shen et al. (eds.), *Advances in Acoustic Emission Technology*, Springer Proceedings in Physics 179, DOI 10.1007/978-3-319-29052-2_7

a given time constitute the time-frequency spectrum of the signal [2]. For stationary signal processing the most common method is the Fourier transform (FT), which is a bridge between the time domain information and the frequency domain information of the signal [3]. However, the Fourier transformation is a global transformation that cannot describe the local characteristics of time and frequency. For non-stationary signal processing the most common methods are short-time Fourier transform (STFT), Gabor transform and wavelet transform. These methods are based on the idea of windowing the signal, and assuming that the signal is stationary in the window. However, due to the constraint of the Uncertainty Principle the time width and bandwidth of the window function cannot be arbitrarily narrow at the same time, therefore it is impossible to simultaneously get acceptably accurate time and frequency resolution. In 1996 the American geophysicist Stockwell proposed the ST, which combines the advantages of the STFT and the wavelet transform. The ST overcomes the problem in which the time frequency resolution is fixed when the window function is selected in the short time Fourier transform. Because it doesn't need to satisfy the permissible condition of the wavelet transform, the ST doesn't have the cross term interference of the quadratic time-frequency distribution. Its window function is inversely proportional to frequency (i.e. scale). Because of these advantages, the ST has been widely used in various fields.

The FRFT is a generalized form of Fourier transformation which was developed in the 1980s [4, 5]. In recent years it has become an important tool in signal analysis and processing. The FRFT is determined by a parameter, α, which relates to the rotation angle of the signal in the time-frequency phase space. When $\alpha = 0$, the rotation angle is zero; at this time the FRFT is equivalent to the unit operator. When $\alpha = 1$, rotation angle is $\pi/2$; at this time the FRFT is equivalent to the ordinary Fourier transform. The general value of α is given to the distribution of a corresponding line in the time-frequency plane. So the time frequency distribution can be defined from the FRFT, which is a special time frequency distribution based on the parameter of order a.

On the basis of previous studies, in 2012, Xu Deping proposed the FRST, which is a combination of the ST and the FRFT. In this chapter, the FRST is studied and investigated. We verify the superiority of the FRST in nonstationary signal processing by comparison with the ST, discuss methods of how to find the optimal fractional domain order, and show that when the optimal fractional order is selected, the FRST has perfect time-frequency concentration. Finally, a corrosion AE signal is processed by FRST and ST.

2 Fractional S Transform

FRST is a new time-frequency analysis method, it is derived from the combination of ST and FRFT. It is a continuation of the ST in the fractional domain.

2.1 S Transform

For a signal $x(t)$, its ST is defined as [6],

$$s(\tau,f) = \int_{-\infty}^{\infty} x(t)\,{}^{|f|}\!/_{\sqrt{2\pi}}\, e^{-{}^{(\tau-t)^2 f^2}\!/_{2\pi}} e^{-j2\pi ft} dt \tag{1}$$

$$\text{The basic wavelet is } w(\tau,f) = {}^{|f|}\!/_{\sqrt{2\pi}} \exp\left(\frac{-t^2 f^2}{2}\right)\exp(-j2\pi ft) \tag{2}$$

$$\text{Window function is } g(t,f) = {}^{|f|}\!/_{\sqrt{2\pi}} \exp({}^{-t^2 f^2}\!/_{2}) \tag{3}$$

In (1), t is the time, τ is a parameter that controls the window function's position on the t axis and f is the frequency. In (3) the window function is related to time t and frequency f. Its width is $\sigma(f) = {}^{1}\!/_{|f|}$. At low frequency, a wide window can be used to get higher frequency resolution, while at high frequency a narrow window can be applied to get higher time resolution. Therefore, the ST has higher time-frequency precision than the Fourier transform.

2.2 Fractional Fourier Transform

Generally speaking, for a signal $x(t)$, an order FRFT is defined as [7, 8]:

$$X_a(u) = F^a(x(t)) = \int_{-\infty}^{\infty} x(t) K_a(t,u) dt \tag{4}$$

$$\text{where } K_a(t,u) = \begin{cases} A_\alpha \exp[j\pi(u^2\cot\alpha - 2ut\csc\alpha + t^2\cot\alpha)], & \alpha \neq n\pi \\ \delta(t-u), & \alpha = 2n\pi \\ \delta(t+u), & \alpha = (2n\pm 1)\pi \end{cases} \tag{5}$$

is the kernel function for the FRFT, $A_\alpha = \sqrt{1 - j\cot\alpha}, \alpha = {}^{a\pi}\!/_{2}$, n is an integer, and u is the fractional frequency. When fractional order $a = 1, \alpha = {}^{\pi}\!/_{2}, A_\alpha = 1$, by (4) and (5),

$$X_1(u) = \int_{-\infty}^{\infty} x(t)\exp(-2j\pi ut) dt \tag{6}$$

It can be seen that $X_1(u)$ is the ordinary FRFT of $x(t)$ from (6). Similarly $X_{-1}(u)$ is the ordinary inverse FRFT of $x(t)$. Thus, the FRFT can be considered as a generalized Fourier transform.

2.3 Fractional S Transform

2.3.1 Definition of Fractional S Transform

For a signal $x(t)$, an order FRST is defined as [9]:

$$FRST_x^a(\tau,u)=\int_{-\infty}^{+\infty}x(t)g(\tau-t,u)K_a(t,u)dt \tag{7}$$

Where $K_a(t,u)$ is the kernel function of the fractional Fourier transform, $g(\tau-t,u)$ is the Gauss function about time t and frequency u, $g(t,u)={}^{|\mu\csc\alpha|^p}\!/_{\sqrt{2\pi}q}\cdot\exp\left({}^{-t^2(\mu\cdot\csc\alpha)^{2p}}\!/_{2q^2}\right)$. In (7) u is the fractional frequency, rotating factor $a\in[0,4)$, $\alpha=a\cdot{}^{\pi}\!/_2$, p, q are the adjustment factors of the Gauss window. When a takes different values, the frequency axis is rotated correspondingly. Especially when the value of a, p, and q are all 1, $\alpha={}^{\pi}\!/_2$,

$$K_a(t,u)=A_\alpha\exp\left[j\pi\left(u^2\cot\alpha-2ut\csc\alpha+t^2\cot\alpha\right)\right]=\exp(-2j\pi ut) \tag{8}$$

$$g(t,\mu)={}^{|\mu\cdot\csc\alpha|^p}\!/_{\sqrt{2\pi}q}\cdot\exp\left(-{}^{t^2(\mu\cdot\csc\alpha)^{2p}}\!/_{2q^2}\right)={}^{|\mu|}\!/_{\sqrt{2\pi}}\cdot\exp\left({}^{-t^2\mu^2}\!/_2\right) \tag{9}$$

At this point the FRST is the ordinary ST. That is, the FRST extends the ST to the fractional domain after adding adjustment factors to the Gauss window of the ST.

2.3.2 Selection of Optimal Rotation Factor *a*

The time-bandwidth product is one of the most important indexes for evaluating the concentration of a time-frequency analysis. To find the optimal order of time-frequency analysis in the fractional domain, we must find the optimal rotation factor a that minimizes the signal's fractional time bandwidth.

In time-frequency analysis, after adding window to the signal, the time width and bandwidth becoming the windowed signal's time width and bandwidth. If we let T_s and B_s stand for the original signal's time width and bandwidth and we let T_h and B_h stand for the window function's time width and bandwidth, then the windowed signal's time width T_{sp} and bandwidth B_{sp} are defined as [10]:

$$T_{\mathrm{sp}}=T_s\sqrt{1+\left({}^{T_h}\!/_{T_s}\right)^2}\quad B_{\mathrm{sp}}=B_s\sqrt{1+\left(\sqrt{{}^{B_h}\!/_{B_s}}\right)^2} \tag{10}$$

This function's compact support set is shown in Fig. 1.

In 2002, Durak proposed the concept of a generalized time-bandwidth product (GTBP), which is defined as [11],

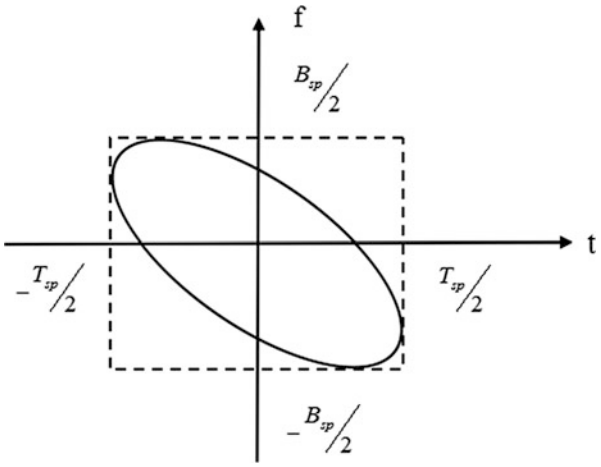

Fig. 1 The compact support set of signal in time-frequency plane

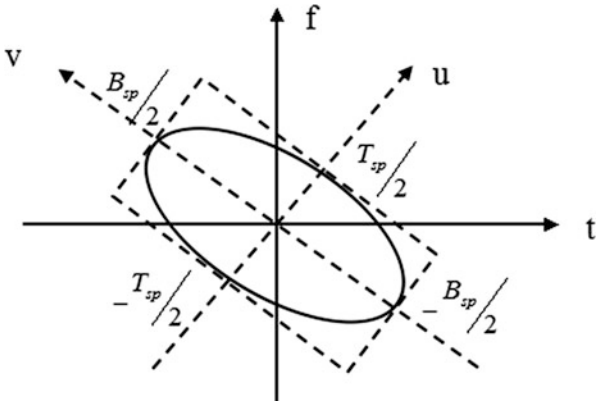

Fig. 2 Compact support set for optimal order

$$\mathrm{GTBP}\{x(t)\} = \min_{0 \le a < 4} \mathrm{TBP}\{x_a(t)\} \tag{11}$$

In (11), $x_a(t)$ is the a order FRFT of signal $x(t)$. The minimum order a is the optimal order, or a_{opt}, when the rotation angle is $a_{\mathrm{opt}} \cdot \pi/2$, the signal's time-frequency concentration is the best. The compact support set of the signal at this point is shown in Fig. 2,

However, when there is a large amount of data it takes too much time to calculate Eq. (11). In reference [12], a method is proposed of searching the a_{opt} for the optimal fractional Gabor transform, as the FRST is a fractional time-frequency analysis which conforms to the Parseval theorem of FRFT. According to Figs. 1 and 2, when a is at its optimal order, the signal would have the largest peak model value in the fractional domain. Therefore, calculating the signal FRFT under different orders, finding the maximum peak value and the corresponding order gives the optimal order for the FRST.

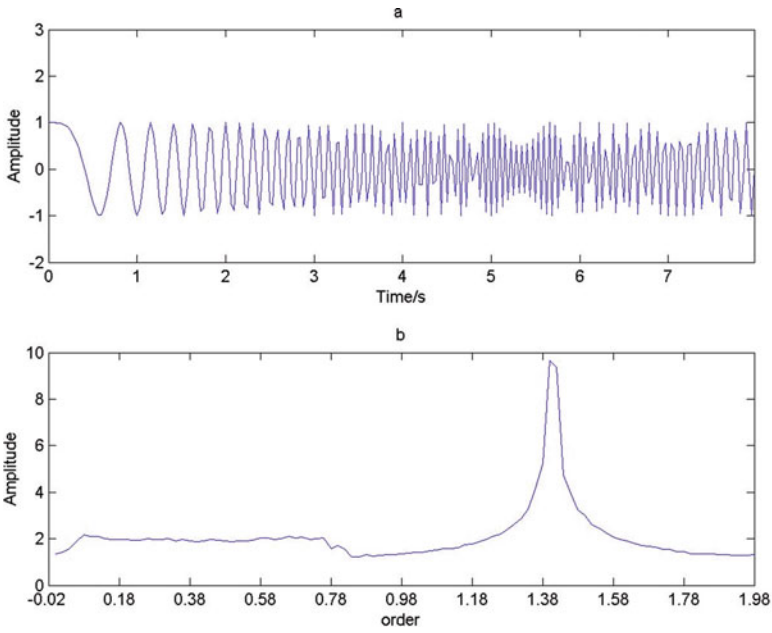

Fig. 3 Chirp signal and order-peak mode curve

3 Simulation

3.1 Selection of Optimal Rotation Factor a

Figure 3 shows a chirp signal and order-peak mode curve. Fig. 3a is the chirp signal and Fig. 3b is the order-peak mode curve for a module where the order takes values only from 0 to 2. From Fig. 3b when the peak value is the maximum, the corresponding optimal order $a_{\text{opt}} = 1.4$. Figure 4 compares the time frequency concentration of the ST with different order FRSTs. Figure 4a is the ST, Fig. 4b is the optimal order FRST, $a = 1.4$, Fig. 4c is the FRST, $a = 1.5$, and Fig. 4d is the FRST, $a = 1.6$. The time-frequency concentration of Fig. 4b is obviously better than others. That is to say, the method as mentioned above of how to select the optimal order a is feasible in the FRST.

3.2 Time Frequency Analysis of a Theoretical Signal with Fractional S Transform and S Transform

Fig. 5 is the time frequency graph of ST and FRST for a cross-chirp signal, where the cross-chirp signal is defined as:

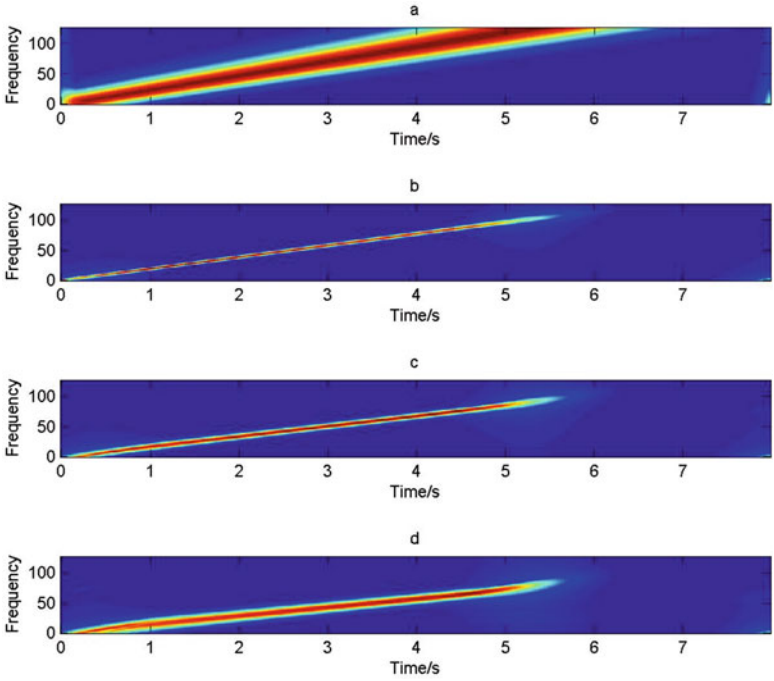

Fig. 4 ST and different order FRST

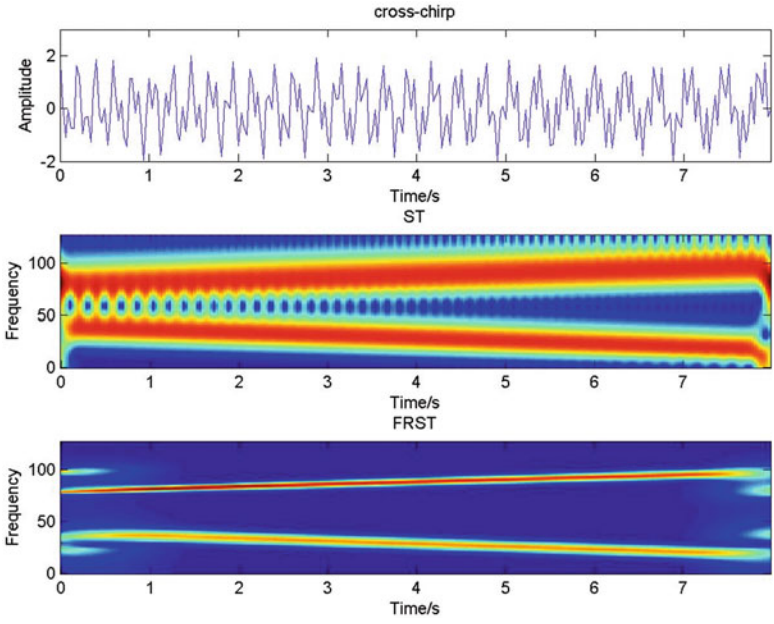

Fig. 5 Time frequency graph of ST and FRST for a cross-chirp signal

$x(t) = \cos(2\pi t(10 + \%)) + \cos(2\pi t(2.8 - \%))$. It can be seen that the signal contains two parts, the frequency of one part increases with time, and the frequency of the other part decreases with time. With the passage of time, the two signals frequency difference gradually increases. When the frequency difference is relatively small, the ST of the signal has a frequency aliasing phenomenon but the FRST is completely avoided. The time frequency analysis of the FRST is obviously better than that of the ST.

3.3 *Time Frequency Analysis of Corrosion Acoustic Emission Signals with Fractional S Transform and S Transform*

The ST and FRST transforms for a group of 2048 AE signals were measured in laboratories. Figure 6 is the waveform and power spectrum for the signals, the time domain and frequency domain of the signals are respectively displayed as waveforms and power spectra. The relationship between the frequency and time of the signal cannot be obtained. Figure 7 is the time frequency graph of the ST and the FRST for the AE signal. We can clearly see from the signal's peak and the time and frequency information of the signal that the peak value of the time frequency graph

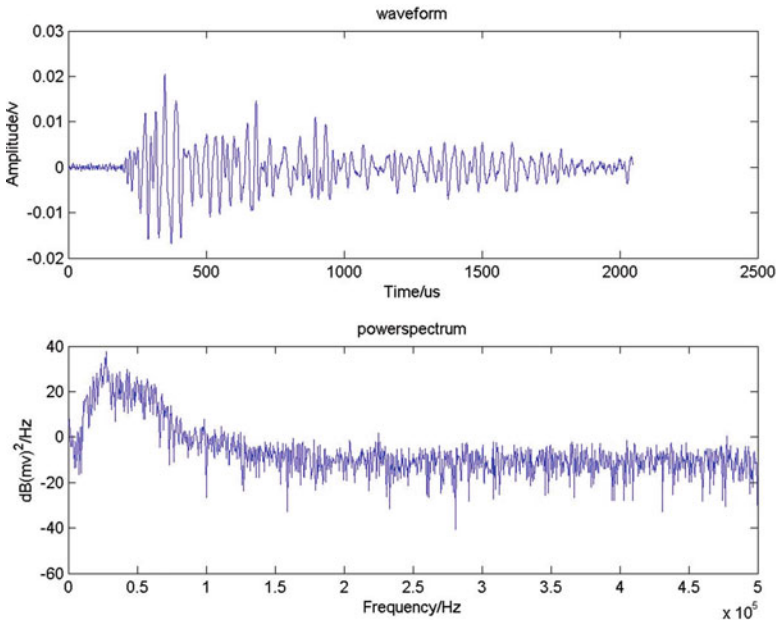

Fig. 6 Waveform and power spectrum for the Acoustic Emission Signal

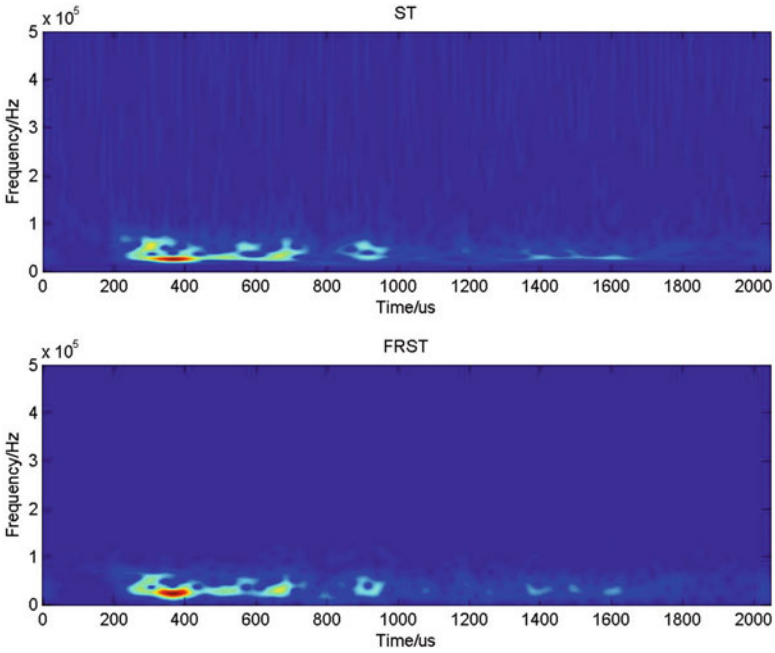

Fig. 7 Time frequency graph of ST and FRST for the Acoustic Emission Signal

corresponds to the signal in time and frequency. Comparing the time frequency graph of the ST and the FRST, the FRST is superior to the ST in both time-frequency concentration and analysis precision.

4 Conclusion

In this paper, we introduced the FRST as a new time-frequency analysis method that is derived from the combination of ST and FRFT. On the basis of previous studies, calculating the peak mode of a FRFT to seek its optimal order is feasible and is verified by simulation. When the optimal order a is used, the time-frequency concentration of the FRST gives the best result. Simulation results of a theoretical signal shows the FRST is more accurate than the ST in the non-stationary signal analysis, so more ideal analysis results can be obtained. The simulation of a corrosion AE signal indicated that both the ST and the FRST can be used in time-frequency feature analysis of AE signal, but FRST is better than the ST both in time-frequency concentration and precision.

References

1. M. Yang, *Acoustic Emission Detection* (Machinery Industry Press, Beijing, 2005), pp. 8–10
2. L. Liu, *Time Frequency Analysis Technology and Its Application* (Chengdu University of Technology, Chengdu, 2008), pp. 16–17
3. X. Zhang, B. Zheng, *Non-stationary Signal Analysis and Processing* (National Defense Industry Press, Beijing, 1998), pp. 37–40
4. V. Namias, The fractional order Fourier transform and its applications to quantum mechanics. J. Inst. Math. Appl. **25**, 241–265 (1980)
5. A.C. McBride, F.H. Kerr, On Namias's fractional Fourier transform. IMA J. Appl. Math. **39**, 159–175 (1987)
6. R.G. Strockwell, L. Mansinha, R.P. Lowe, Localization of the complex spectrum: the S transform. IEEE Trans. Signal Process. **44**(4), 998–1001 (1996)
7. H.M. Ozaktas, O. Arikan, M.A. Kutay, G. Bozdagi, Digital computation of fractional Fourier transform. IEEE Trans. Signal Process **44**(9), 2141–2150 (1996)
8. C. Candan, M.A. Kutay, H.M. Ozaktas, The discrete fractional Fourier transform. IEEE Trans. Signal Processing **48**(5), 1329–1377 (2000)
9. D. Xu, K. Guo, Fractional S transform—Part I: Theory. Appl. Geophys. **9**(1), 73–79 (2012)
10. Y. Liu, *Introduction to Non-stationary Signal Analysis* (National Defense Industry Press, Beijing, 2006), pp. 37–40
11. L. Durak, O. Arikan, in *Generalized Time Bandwidth Product Optimal Short Time Fourier Transform*, vol. 2 (IEEE Conference Publications, 2002), pp. 1465–1468
12. Y. Chen, Z. Peng, Z. He, T. Lin, D. Zhang, The optimal fractional Gabor transform based on the adaptive window function and its application. Appl. Geophys. **10**(3), 305–313 (2013)

Research of Tank Bottom Corrosion Acoustic Emission Simulation

Yang Yu, Xinyuan Qian, and Ping Yang

Abstract Acoustic Emission is a useful tool for on-line detection of tank bottom corrosion. The finite element software COMSOL is used to model the tank bottom. The rules of acoustic emission signal spread from corrosion are studied by analyzing signals from different directions in various positions. Digital filters and wavelet transforms are used to extract features of the acoustic emission signals. Simulation results showing acoustic emission signals spreading in different directions with different frequency spectrum characteristics and varies attenuation rules contribute significantly to the research on acoustic emission mechanisms of tank bottom corrosion and offer guidance for sensor selection.

1 Introduction

Most storage tanks for storing petroleum products are built in the open air environment. A free-standing tank is subject to wear and tear from exposure to the natural environment, and the most affected part is the bottom plate of the tank. The present technology for detecting the condition of a tank and clearing it for further use requires stopping production and incurs a high cost. Acoustic emission technology can detect bottom corrosion phenomena in real time and detect problems without stopping production, greatly improving production efficiency.

The classical method, determined primarily after extensive research on acoustic emission, uses parameters such as the impact and ring count to describe acoustic emission signals. The standards for testing have been established by using this method. To research a tank bottom's acoustic emission, the work using algorithms to extract and recognize acoustic emission signal characteristics is strong, but our ability to analyze the tank bottom acoustic emission signal is weak.

The finite element method can be applied in acoustic emission simulation analysis as a method for finding approximate solutions of boundary value problems for partial differential equations. Foreign countries have proposed the use of the

Y. Yu (✉) • X. Qian • P. Yang
School of Information Science and Engineering, Shenyang University of Technology, Shenyang 110870, China
e-mail: yuy@sut.edu.cn

G. Shen et al. (eds.), *Advances in Acoustic Emission Technology*, Springer Proceedings in Physics 179, DOI 10.1007/978-3-319-29052-2_8

finite element method for the simulation of acoustic emission signals [1]. M.A. proposed that finite element analysis is an effective method for the analysis of acoustic emission signals [4]. W.H. proposed that the acoustic emission source could be simulated with good success by using the finite element method [2]. P. Hora simulated different acoustic emission sources using finite element simulation software [3]. To conclude, finite element analysis is an effective method for the analysis of acoustic emission signals [4].

In this chapter, the tank bottom plate model is simulated by using COMSOL finite element simulation software. The corrosion acoustic emission signal spread rules are studied by analyzing signals from different directions in various positions. Wavelet analysis is carried out to obtain the time-frequency to further extract the signal characteristics. Using this mechanism, simulated acoustic emission signals are decomposed into displacement components in all directions to determine the tank bottom's characteristics. These results can provide theoretical guidance for sensor distribution and feature extraction.

2 Wave Theory

The ASTM defines acoustic emissions as "the class of phenomena whereby transient elastic waves are generated by the rapid release of energy from localized sources within a material, or the transient elastic waves so generated". The essence of acoustic emission is a transient elastic wave caused by the fast release of energy in a material's interior [5]. The problem of acoustic emission in the bottom of a tank is equivalent to the problem of fluctuation in a plate, which needs to be introduced into the wave equation.

The relationship between stress, strain, displacement and force in any point in the elastic body has been described based on the basic equations of elasticity. The equilibrium equation, geometric equation and physical equation are used, which separately described the relationship between stress and force, strain and displacement, stress and strain.

The elastic wave equation in the X direction can be expressed by the following equations.

The stress compatible equation in the X direction is (1)

$$\frac{\partial \sigma_x}{\partial x} + \frac{\partial \tau_{xy}}{\partial y} + \frac{\partial \tau_{xz}}{\partial z} + P_{vx} = 0 \tag{1}$$

where σ_x is normal stress in the x direction, τ_{xy}, τ_{xz} are two shear stresses in the x direction and P_{vx} is external force in the x direction.

The geometric equation in the x direction is (2)

$$\varepsilon_x = \frac{\partial u}{\partial x} \tag{2}$$

where u is the displacement in the x direction and ε_x is the strain in the x direction.

The physical equation is (3)

$$\begin{cases} \varepsilon_x = \dfrac{1}{E}(\sigma_x - u\sigma_y - u\sigma_z) \\ v_{xy} = \dfrac{\partial u}{\partial y} + \dfrac{\partial v}{\partial x} = \dfrac{1}{G}\tau_{xy} \end{cases} \tag{3}$$

where v is the displacement in the y direction, E is the modulus of elasticity and G is the shear elastic modulus.

The relationship between E and G can be expressed as

$$G = \frac{E}{2(1+\mu)} \tag{4}$$

where μ is the Poisson's ratio of the material.

By correlating those equations, 15 equations were obtained in three directions, corresponding to six components of stress, six components of strain, three components of displacement. Those variables can be calculated by solving those differential equations.

Those generalized dispersion equations are suitable only for the case of bulk waves, which means waves propagate only in the medium and far away from boundaries. The bottom plate of the tank is not thick, fixed at the bottom in cement, which means the phenomenon of reflection and refraction may appear, usually when waves propagate in the bottom plate. Waves in plates are guided waves which need to be added as constraints on the generalized dispersion equations to account for interaction with boundaries.

The most common guided waves include Rayleigh waves (a type of surface acoustic wave that travels on solids) and Lamb waves (which propagate in solid plates). Figure 1 shows a Reyleigh-Lamb wave's dispersion curves [6].

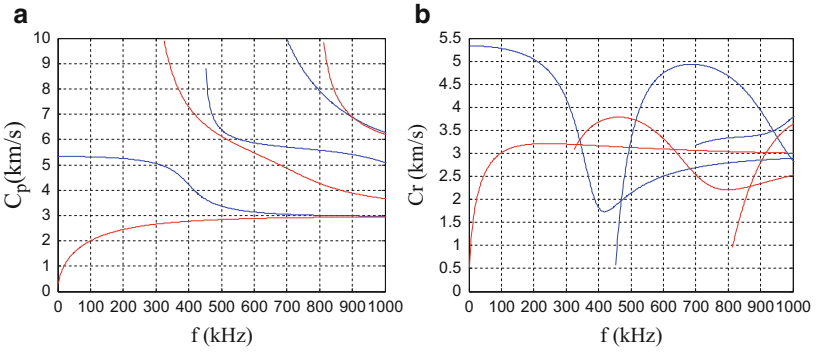

Fig. 1 (**a**) group velocity curve of 6 mm steel plate, (**b**) phase velocity curve of 6 mm steel plate

The modal analysis which we already have can't be used because of different boundary conditions corresponding to different constraint equations. This must be addressed as a boundary value problem for differential equations.

Two common way to solve these kinds of problems are difference methods and variable methods. The finite element method may be the best way to solve this problem when it is complicated. Compared with the traditional method, simulation by the finite element method has the advantages of easy computing and programming.

3 The Finite Element Model of Tank Bottom Plate

3.1 Finite Element Simulation

We used the finite element analysis software COMSOL to establish the three-dimensional finite element model of a tank bottom plate. Finite element simulation analysis software can simulate the different conditions of the model by setting different values, and it has degrees of freedom and flexibility which are difficult to physically measure by experiment. The characteristics of acoustic emission signal propagation in the steel plate can be calculated by changing conditions such as the receive distance, the position of acceptance, sensor placement method and so on. These calculations are helpful in the research and practical application of acoustic emission theory. In order to establish a suitable model, the sampling rate and boundary conditions of the model must be set up first.

Sampling rate includes time sampling rate and spatial sampling rate. When the sampling rate is small, effective acoustic emission information will e missed. When the sampling rate is large, it can lead to tedious calculations, wasted time and poor efficiency, so it is important to choose a suitable sampling rate.

Time sampling rate is:

$$\Delta t = \frac{1}{kf_{\max}} \tag{5}$$

where Δt is the time interval, the reciprocal of sampling rate, $f_{\max}$ is the highest frequency of the signal. K is the multiple of sampling which need equal to ten times the Δt in order to get a more accurate value; here k is 10.

Spatial sampling rate is:

$$\Delta l = \frac{\lambda_{\min}}{k} \tag{6}$$

where Δl is the minimum unit length, $\lambda_{\min}$ is the minimum wavelength, k is the multiple of sampling.

Boundary conditions are the conditions for the solution of the equations on the moving boundary. Boundary conditions include materials, boundaries, constraints and so on. Different boundary conditions correspond to different equations. The correct equations can be obtained only by choosing the correct boundary conditions.

3.2 Finite Element Model of Tank Bottom Plate

Figure 2 is the finite element model of a steel plate whose size is 100 × 100 × 6 mm. The model uses structural mechanics for a solid material, and a time dependent analysis. The black spots represent the sampling points.

The physical model adds prescribed displacement; here, displacements in the bottom are prescribed to be 0 in the z direction, which simulates a fixed steel plate. The domain material is linear elastic material. Table 1 shows the material parameters.

3.3 The Simulation of Acoustic Emission Excitation Signal

A driving point of size is 1 × 1 × 6 mm is built into the central position of the steel. Body load is used as a form of excitation and the total force is 1 N. The acoustic emission excitation signal is simulated for a simplified calculation, as in

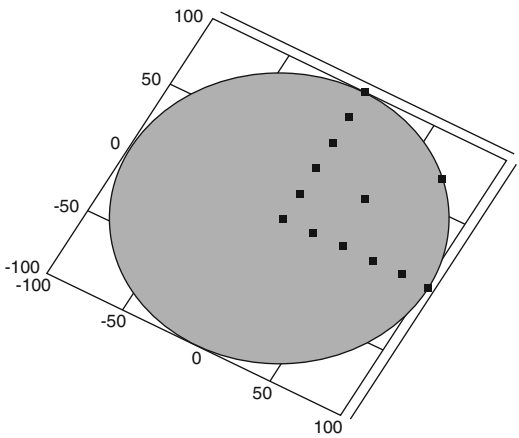

Fig. 2 The finite element model of a steel plate

Table 1 Material parameters of steel plate

Density	Poisson's ratio	Young's modulus
7870 kg/m^3	0.29	200 × 10^{9}N/m^2

$$T(\tau) = \begin{cases} 0 & t \le 0 \\ 1 - \cos(2\pi t/\tau) & 0 < t \le \tau \\ 0 & t > \tau \end{cases} \tag{7}$$

where τ is the release time of the acoustic emission signal and $\tau = 200$ μs for the simplified calculation.

4 The Extraction Method of Acoustic Emission Signal Features

Simulation of the receiving point of acoustic emission signal is shown in Fig. 3. The signal waveform is changed significantly and the frequency is lower in the picture because the attenuation of high frequency signal is fast and the amplitude is small. Effective acoustic emission signals could not be obtained without signal processing.

Filtering processing should be carried out in order to obtain an effective acoustic emission signal. This study uses a combination signal processing method includes digital filtering and wavelet transform. The first Chebyshev filter was used because it is easy to realize.

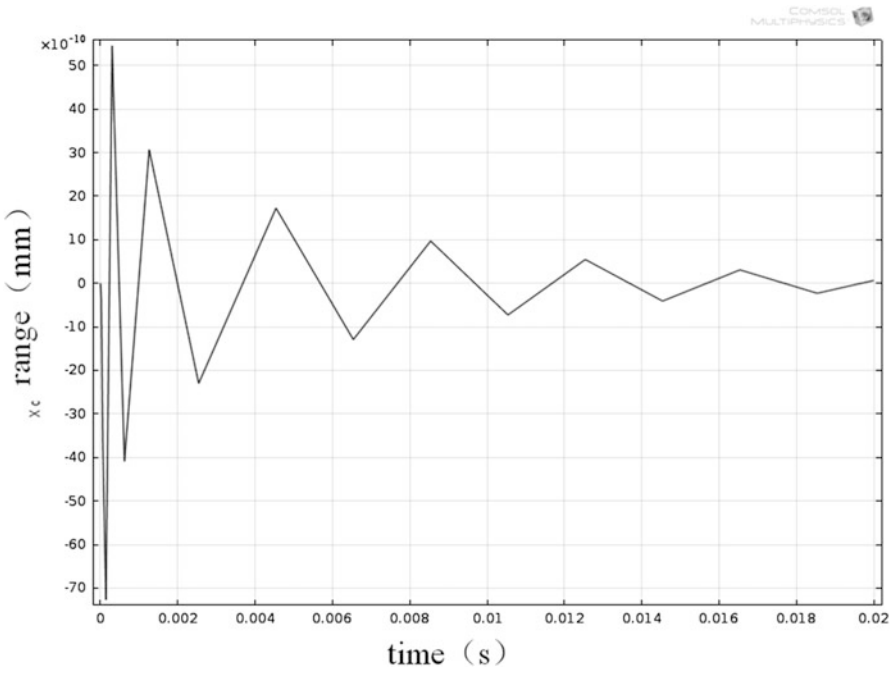

Fig. 3 The simulation acoustic emission signal at the receiving point

The following Equation is the first Chebyshev filter of the amplitude frequency characteristic curve

$$G_n(\omega) = |H_n(j\omega)| = \frac{1}{\sqrt{1 + \varepsilon^2 T_n^2\left(\frac{\omega}{\omega_0}\right)}} \tag{8}$$

Figure 4 is the frequency characteristic of the digital filter amplitude with a 1700–2400 passband frequency.

An acoustic emission signal is non-stationary. There are many modes in the signal, and the frequency components are complex. Methods used to analyze acoustic emission signals must include both time and frequency domain analysis. Fourier transformation has no positioning in the time domain, and so is not suitable for analysis of an acoustic emission signal.

Wavelet transform is a time-frequency analysis method of variable resolution. A key advantage it has over Fourier transforms is temporal resolution: it captures both frequency and location information (location in time). It can be used to analyze a non-stable signal at different frequencies, which is needed in analysis of acoustic emission signals because of multi-scale refinement of such signals through expansion and translation [7].

The wavelet transform method calculates the inner product of wavelet analysis $\varphi(t)$ and signal analysis $f(t)$ in a scale.

$$W(a,b) = \int_{-\infty}^{+\infty} f(t)\frac{1}{\sqrt{a}}\varphi\left(\frac{t-b}{a}\right)\mathrm{d}t \tag{9}$$

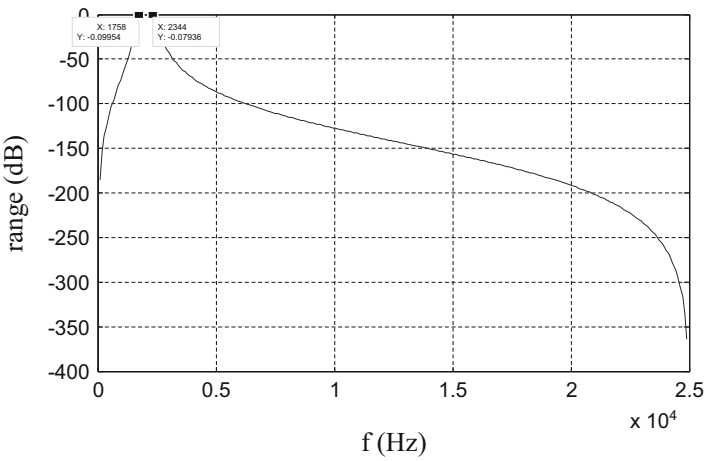

Fig. 4 The filter passband curve

Morlet wavelets have been used because of their higher frequency domain resolution. [8]

The plane wave is modulated by the Gauss function of the unit length and the Morlet wavelet is obtained.

$$\varphi(t) = \pi^{-1/4} e^{iw_0 t} e^{-t^2/2} \tag{10}$$

Morlet wavelets are expressed through wavelet transforms for time frequency charts of acoustic emissions, which are helpful in spread characteristic analysis.

5 Simulation Analysis of Acoustic Emission Signal Spread

A tank's bottom plate model (no weld, weld conditions) is established using the finite element software COMSOL. By simulation, we study the spread of acoustic emissions by signals received from six points equidistant on the X axis and different directions (x, y, z directions). Digital filtering is used to observe the distribution of single point signals. Wavelet analysis is carried out to obtain the time-frequency for further extracting the signal characteristics.

5.1 Normal Displacement

Take samples c(0 0 6), $x1$(20 0 6), $x2$(40 0 6), $x3$(60 0 6), $x4$(80 0 6), $x5$(100 0 6) in the X direction in the model. The normal displacement obtained from the points in the direction of X axis can be seen in Fig. 2.

The wavelet time-frequency diagrams of each point are shown in Fig. 5.

Taking into account the impact of scale changes on graphics, the $X1$ point is the strongest signal. Signals are mainly concentrated in two regions, the frequency ranges $f = 500$ and $f = 2000 \sim 4000$. With an increase of the propagation distance, the signal obviously divides into three parts, the frequency ranges $f = 2000$, $f = 1200$ and $f < 300$. The original signal is strong where $f = 500$ has no signal. The $x5$ signal spectrum is shown in Fig. 6. The frequency of different points is different in the propagation. With the increase of the distance, the signal spectrum also changes.

The signal of the $X5$ points is concentrated in the areas of $f = 195.3$, $f = 830.1$ and about 3000. By using a Chebyshev filter on the signal obtained from the simulation, we obtain the frequency spectrum. The spectrum after filtering in the X direction (normal direction) is received in the $x5$ point, Fig. 7.

The left side of the picture is the filtered signal, and the right is the signal spectrum. The first line in the picture is the signal in the low frequency range with slow change and long oscillation time. The second line in the picture is the signal in the frequency range $f = 800$.

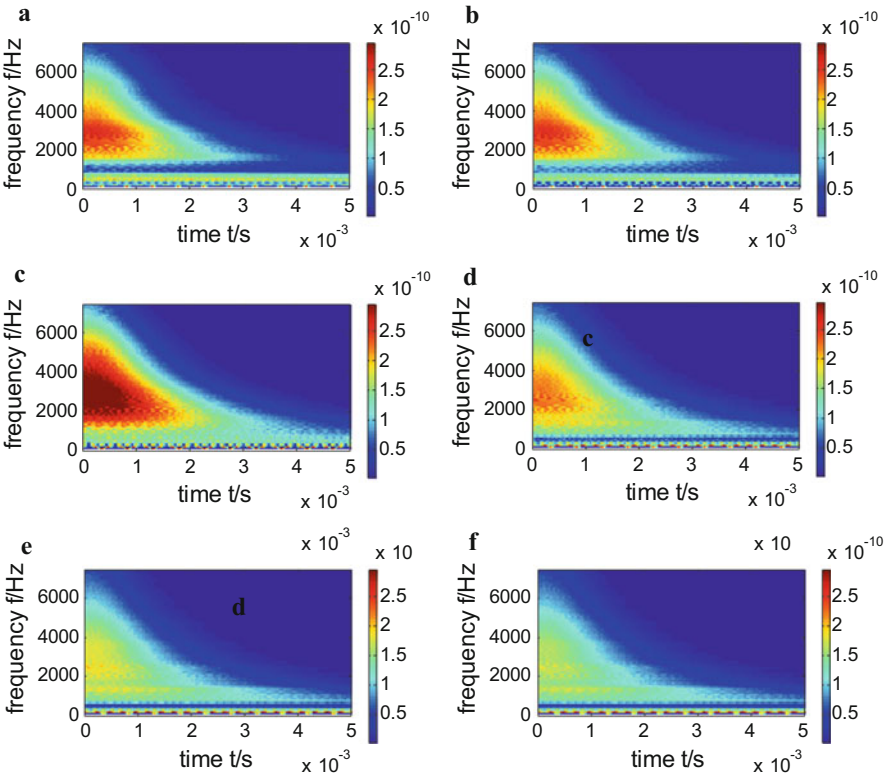

Fig. 5 The wavelet time-frequency diagrams of each point on the X axis. (**a**) c point scale 3×10^{-10}, (**b**) $x1$ point scale 4×10^{-9}, (**c**) $x2$ point scale 1.5×10^{-9}, (**d**) $x3$ point scale 1.5×10^{-9}, (**e**) $x4$ point scale 1.5×10^{-9}, (**f**) $x5$ point scale 1.5×10^{-9}

The scale has been changed for easy viewing. The signal change is faster than the signal in low frequency and not smoother than the signal in low frequency. The third line in the picture is the signal in the frequency range $f = 3000$.

The oscillation time is short and the phenomenon of signal superposition is obvious. This indicates that with increasing distance, the frequency is higher, the wider frequency band is larger and the frequency dispersion phenomenon becomes more obvious. The frequency components also increase and the phenomenon of signal superposition is obvious.

5.2 *Tangential Displacement*

Now we examine by simulation the tangential displacement on the spread of acoustic emission by signals received from six points equidistant on the X axis. The wavelet time-frequency diagrams of each point are shown in Fig. 8.

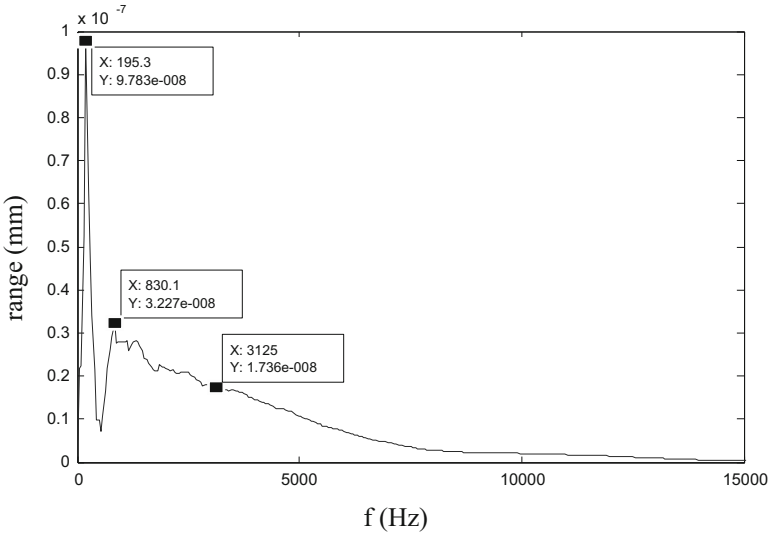

Fig. 6 *x*5 spectrum in normal displacement

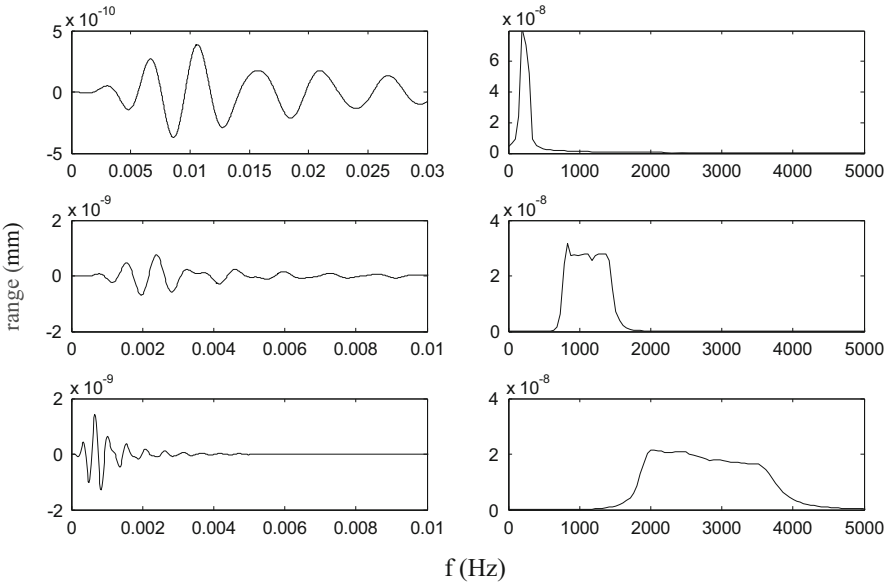

Fig. 7 *x*5 segmented filtering in normal displacement

It can be observed in the picture that the signal is stable and vigorously attenuated with increased distance except at the *x*3 point. The signal is very weak at the *x*5 point. The signal spectrum is unchanged with the increase of distance.

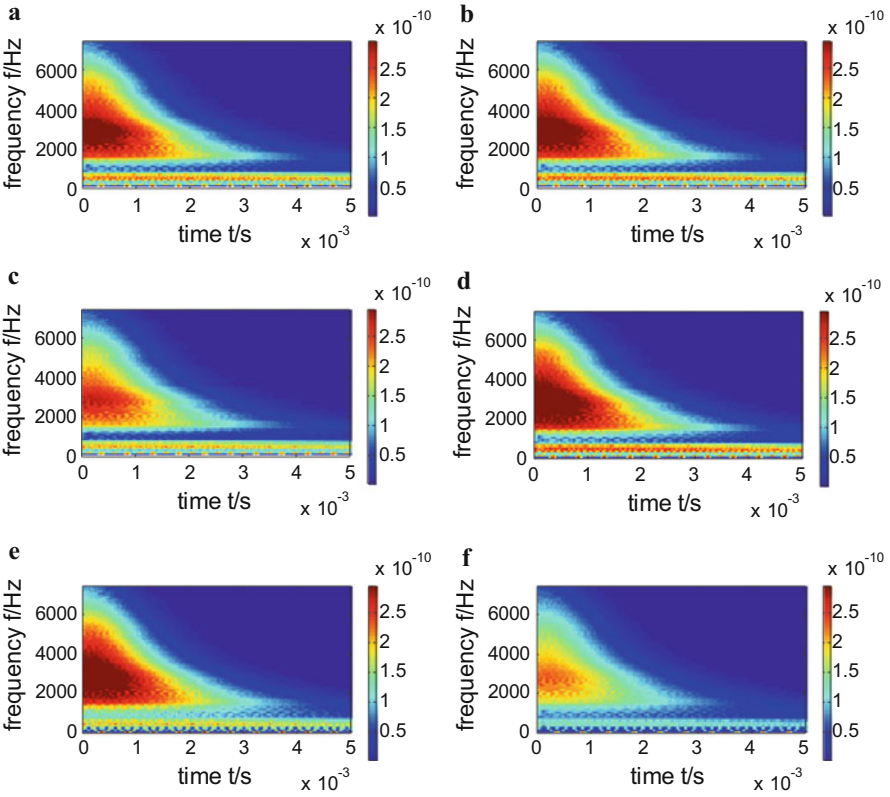

Fig. 8 The wavelet time-frequency diagrams of each point on the X axis. (**a**) c point scale 6×10^{-10}, (**b**) $x1$ point scale 7×10^{-12}, (**c**) $x2$ point scale 5×10^{-14}, (**d**) $x3$ point scale 1×10^{-13}, (**e**) $x4$ point scale 6×10^{-14}, (**f**) $x5$ point scale 3×10^{-14}

The signal decays obviously between the c point and the $x1$ point, which differs with the normal direction. The signal of $f = 500$ is more obvious than that of the other frequency areas, and the signal at $f = 500$ is not significantly attenuated.

5.3 Displacement in Z Direction

Now we examine by simulation the Z direction displacement on the spread of acoustic emissions by signals received from six points equidistant on the X axis. The wavelet time-frequency diagrams of each point are shown in Fig. 9.

The signal in the Z direction is rich in low frequencies and its intensity is strong. It can be observed that in the middle part of the plate, the high frequency signal has low intensity and the low frequency signal has high intensity, but in the edge of plate the signal with low frequency is obviously attenuated and the higher

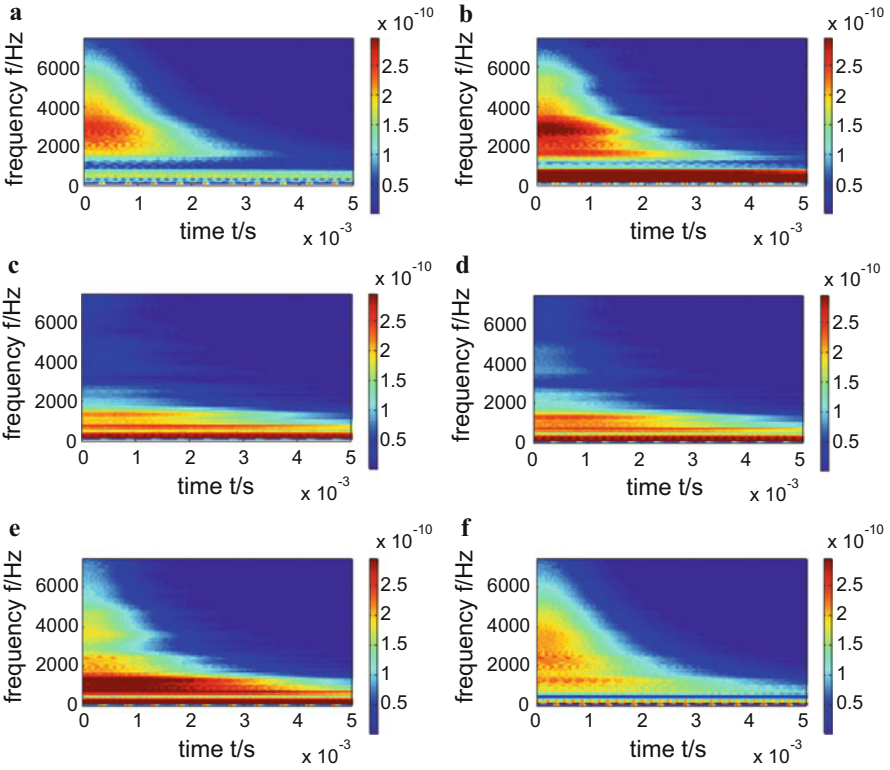

Fig. 9 The wavelet time-frequency diagrams of each point on the X axis. (**a**) c point scale 4×10^{-7}, (**b**) $x1$ point scale 1×10^{-10}, (**c**) $x2$ point scale 6×10^{-11}, (**d**) $x3$ point scale 4×10^{-11}, (**e**) $x4$ point scale 2×10^{-11}, (**f**) $x5$ point scale 2×10^{-11}

frequency signal is replenished. The difference in the phenomenon shown in Fig. 5f compared to other image spectra may be the result of the influence of the model boundary conditions.

6 Simulation Analysis of Tank Bottom Plate

6.1 Model of Tank Bottom Plate

For further research, some welds are added based on the circular plate and the simulation of the bottom plate of the tank. Four welds of 2 mm were constructed at $x = 30$ mm, 70 mm, -30 mm, -70 mm to simulate the weld seams on the bottom plate.

The COMSOL model of tank bottom plate is shown in Fig. 10.

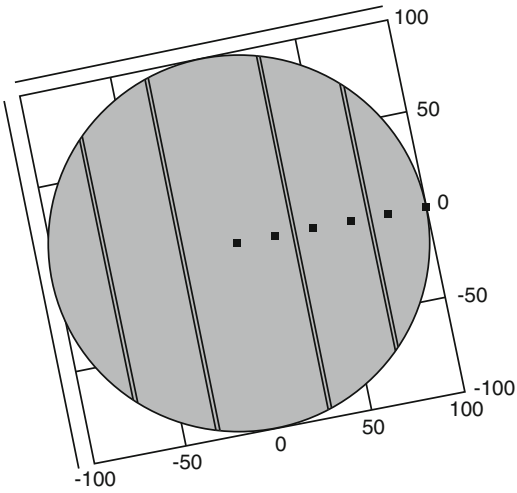

Fig. 10 The COMSOL model of tank bottom plate

Table 2 Material parameters of weld

Density	Poisson's ratio	Young's modulus
9000 kg/m^3	0.4	10×10^9N/m^2

The COMSOL built in material "solder, 60Sn-40Pb" was used as the material of weld. Table 2 shows the material parameters of the weld.

6.2 Simulation Analysis of Tank Bottom Plate

According to the observation of the steel plate experiment, the displacement in the normal direction is the main form of displacement. We examine by simulation the normal direction displacement on the propagation of acoustic emissions by signals received from six points equidistant on the X axis. Wavelet analysis is carried out to obtain the time-frequency for further extracting the signal characteristics.

The wavelet time-frequency diagrams of each point are shown in Fig. 11.

It can be seen that after adding welds to our model, the overall frequency has been significantly decreased, which may be caused by structural changes. As the picture illustrates, signals are still mainly concentrated in two regions, the frequency ranges $f = 500$ and $f = 2000 \sim 4000$. Between $x1$ and $x2$, $x3$ and $x4$, the signals crossing the weld show a partial attenuation. When a signal crosses the weld, the signal is attenuated 50%. But unlike the steel plate, the normal direction frequency remains the same at all times.

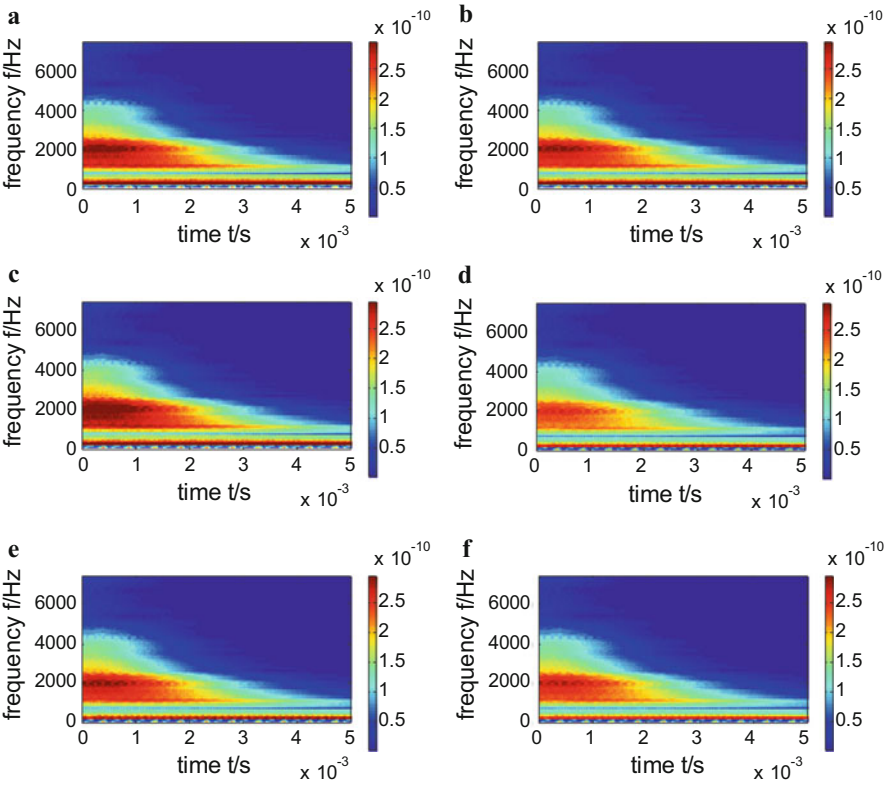

Fig. 11 The wavelet time-frequency diagrams of each point on the X axis. (**a**) c point scale 1.5×10^{-9}, (**b**) $x1$ point scale 9×10^{-9}, (**c**) $x2$ point scale 4×10^{-9}, (**d**) $x3$ point scale 4×10^{-9}, (**e**) $x4$ point scale 3×10^{-9}, (**f**) $x5$ point scale 3×10^{-9}

7 Conclusion

We studied the propagation of acoustic emission signals in different directions by finite element modeling with digital filtering and wavelet transforms and reached the following conclusions: The signal spreads in the X, Y, and Z directions with different attenuation rules and various frequency spectrum characteristics. Signals in the normal direction (X direction) with small attenuation and large strength is the main transmission mode, and is also the best way to accept a signal. Sensors should be placed in the normal direction of the receiving point. The signal in the tangent direction (Y direction) is the weakest, but its spectrum is the same, as the signal intensity decreases only with increased distance. The signal in the tangent direction can be used as an auxiliary signal to determine the distance of the acoustic emission source. The signal in the Z direction is a little weaker than the signal in the normal direction, and its frequency characteristics change considerably in transmission. Multi-point measurements can be used to help understand the status of the bottom plate.

References

1. W.H. Prosser, M.A. Hamstad, J. Gary, et al., Finite element and plate theory modeling of acoustic emission waveforms. J. Nondestruct. Eval. **18**(3), 83–90 (1999)
2. M.A. Amstad, Acoustic emission signals generated by monopole (pencil-lead break) versus dipole sources: finite element modeling and experiments. J. Acoust. Emission **25**, 92–105 (2007)
3. P. Hora, O. Cervena, Acoustic emission source modeling. Appl. Comput. Mech. **4**, 25–36 (2012)
4. Yang Yu, Ping Yang, Lijian Yang, Analysis the rotor rubbing based on parameters of acoustic emission. J. Converg. Inf. Technol. 7(23), 780–787 (2012), EI:20130215879990
5. Yang Yu, Ping Yang, Lijian Yang, Observations of changes in acoustic emission signal partial power spectrum for rotor rubbing, in *World Conference on Acoustic Emission-2011 Beijing*, Beijing, 2011, pp. 500–505
6. S. Yan, H. Zhang, Y. Meng, Number calculation and experimental validation for lamb wave dispersion curves. J. Huazhong Univ. Sci. Technol. **27**(1), 1–4 (2010)
7. Y. Yu, P. Yang, L. Yang, C. Liang, Research on acoustic emission signal characteristic of local corrosion on Q235 steel. Acta Acustica **40**(4), 546–554 (2015)
8. J. Zhang, S. Cui, G. Li, Frequently-used wavelets and their time-frequency properties. Earth Sci. Front. **19**(2), 1–6 (2012)

Extracting the Fault Features of an Acoustic Emission Signal Based on Kurtosis and Envelope Demodulation of Wavelet Packets

Li Lin, Qiang Xu, and Yong Zhou

Abstract This chapter presents an envelope demodulation method based on wavelet packets and kurtosis to extract the fault features of an acoustic emission signal. De-noising was performed first to reduce the noise. Then, we calculated the coefficients of wavelet packet nodes and the kurtosis value after wavelet packet decomposition. Finally, we performed an envelope spectrum analysis on the reconstructed signal based on the maximum degree of kurtosis. To correctly extract fault features of the acoustic emission signal, we compared the maximum amplitude of different nodes' envelope spectra and the kurtosis value. The method can improve the accuracy of fault diagnosis.

1 Introduction

Acoustic emissions, also called stress wave emissions, are releases of strain energy in the form of transient elastic waves. This phenomenon also occurs when a material deforms and fractures under external force, or when internal stress exceeds the yield limit and the material undergoes an irreversible plastic deformation. An acoustic emission signal takes the form of a voltage signal, which can then be picked up by sensors. The signal is obtained through processing with front amplifier gain, and can be classified as an emergency type or a continuous type. According to the research of the German Kaiser, acoustic emission technology has many advantages: (1) It is a dynamic nondestructive test method; (2) It is very sensitive to linear defects; (3) Proximity to the measured component is not required; (4) It is not sensitive to the geometrical size of components, and so on. Usefulness of acoustic emission data depends on how the signals are processed, as the emissive source can be uncertain, diverse, and unpredictable [1, 2].

National Science Foundation (51275066).

L. Lin (✉) • Q. Xu
College of Transportation Engineering, Dalian Jiao Tong University, Dalian 100240, China
e-mail: 173670324@qq.com

Y. Zhou
Dalian University of Technology, Dalian 110023, China

G. Shen et al. (eds.), *Advances in Acoustic Emission Technology*, Springer Proceedings in Physics 179, DOI 10.1007/978-3-319-29052-2_9

Kurtosis index analysis was first reported in the literature when it was used for early detection of faults in roller bearings [3]. Wavelet decomposition was used to eliminate noise and interference signals. After that, the wavelet signal was reconstructed and focused with energy. Finally, the Hilbert envelope spectrum was constructed, and the envelope signal was found to reflect the fault characteristic frequency.

In reference [4], kurtosis was used to analyze whether a fault had occurred or not. The fault signals, which were non-stationary and modulated, were decomposed at different levels by wavelet packet. The envelope spectrum of reconstructed signals at different levels was illustrated. By contrasting the frequency of spectrum peak and the fault frequencies of inner race, outer race, balls and rolling element, the auto-diagnosis of the rolling bearing fault was realized by the minimum distance principle.

The wavelet packet method was used to decompose the vibration signal in the references [5, 6]. The kurtosis of the wavelet packet coefficient was calculated in different frequency bands. The resonant frequency bands caused by bearing defects were determined automatically, based on the kurtosis value maximum principle. Finally, the failure frequency was determined by the spectral envelope analysis of the wavelet packet coefficient.

To solve this problem, a method for incipient fault diagnosis of gears was proposed in the literature [7–10] using kurtosis, wavelet packet energy features extraction and discriminative weighted probabilistic neural networks. The method used the kurtosis statistics in the impact load feature extraction method and wavelet packet decomposition in extracting energy characteristics of various frequency bands. A discriminative weight probabilistic neural network (DWPNN) was introduced to solve the problem of scene noise pollution.

In order to extract the fault characteristics of acoustic emission signals, this chapter uses integrated methods, including kurtosis, wavelet packets and spectral envelopes. Each has its own merits, but this chapter focuses on wavelet packets and kurtosis. First, this chapter looks at the acoustic emission signal. The acoustic emission signal is an ultra-high frequency stress wave pulse signal, which is caused by the distortion crack of the molecular lattice in metal processing and materials in plastic deformation, so there is no need to determine a failure for reducing error, one should perform de-noising using wavelets then perform wavelet packet decomposition and calculate the wavelet packet coefficient of the node and kurtosis. After that, one should reconstruct the wavelet packet coefficient according to the kurtosis value maximum principle. Lastly, one should perform the envelope spectrum analysis. In contrast to the literature [5, 6], de-noising by wavelet is performed earlier than decomposition and reconstruction of wavelet packets in this chapter. The envelope spectrum analysis with the wavelet packet coefficient was performed after band-pass filtering in literature [6, 11–13]. The wavelet packet threshold quantization was carried out on the wavelet packet coefficient of node in literature [5–13].

So, this paper tried to use the kurtosis and wavelet packet method to extract the fault features effectively and accurately.

2 The Fundamental Theory

2.1 The Wavelet Filtering of Wavelet Packet

The application effect of wavelet packet theory is very significant on the non-stationary signal. It can decompose the signal into different levels of 2^n spectrum. It can decompose the low frequency part as same as the high frequency part.[4] But, the wavelet analysis works on the low frequency, not on the high frequency. Therefore, this thesis chooses wavelet packet filtering. The decomposition process of the wavelet and wavelet packet is shown as Fig. 1:

The signal is decomposed into eight signals of different frequency bands by using three layers of wavelet packet decomposition after de-noising. The frequency of different frequency bands is shown in Table 1:

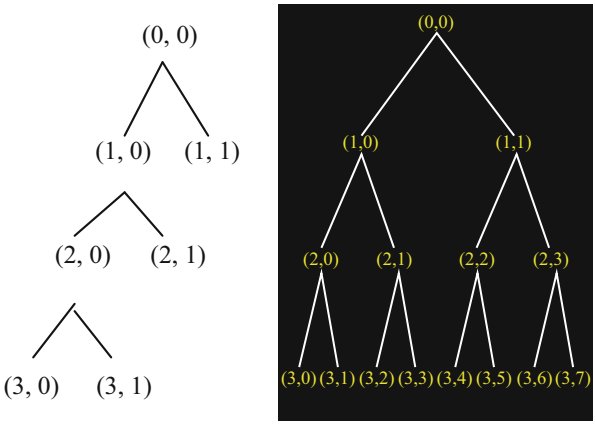

Fig. 1 The drawing of wavelet/wavelet packet

Table 1 The frequency range for different frequency bands

Frequency band	Frequency range (kHz)
(3,0)	0–62.5
(3,1)	62.5–125
(3,2)	125–187.5
(3,3)	187.5–250
(3,4)	250–312.5
(3,5)	312.5–375
(3,6)	375–437.5
(3,7)	437.5–500

2.2 Kurtosis [6–8]

Kurtosis uses numerical statistics to reflect the distribution characteristics of signal amplitude. It is the normalized four-order central moments. Based on the comparison between the related literature and the records of experimental data -, kurtosis values can clearly reflect the fault information when failure vibration generates the large amplitude pulse signal. Therefore, it is more effective to extract the fault feature signals by using kurtosis.

The kurtosis value of the vibration signal is seen as follows:

$$K = \frac{\int_{-\infty}^{+\infty} [x(t) - \bar{x}]^4 p(x) dx}{\sigma^4} \tag{1}$$

The discrete formula is:

$$K = \frac{1}{N} \sum_{i=1}^{N} \left(\frac{x_i - \bar{x}}{\sigma_i} \right)^4 \tag{2}$$

In formula, $\bar{x}$ is the average value, $p(x)$ is the probability density, σ and is the standard deviation.

2.3 The Envelope Demodulating Analysis

1. The principle of envelope demodulating.

   The envelope demodulation method is the comprehensive application of signal envelope detection and spectral analysis, which judges the fault information according to the spectral envelope peak. When the vibration signal is a high-frequency vibration, envelopment analysis is indispensable. It is the technology based on the traditional power spectrum analysis.

2. The principle of Hilbert transform [9, 10].

   The Hilbert transform is used in the signal envelope. It is essentially envelope transformation. It is that the vibration signal that has a 90°phase shift is combined with the primary signal to form a new signal. And the new signal is the envelope signal.
   Hilbert transform $x_h(t)$ of a real signal $x(t)$ is defined as follow:

$$X_{\mathrm{h}}(t) = H[x(t)] = \frac{1}{\pi} \int_{-\mu}^{+\mu} \frac{x(\tau)}{t - \tau} d\tau = x(t) \times \frac{1}{\pi t} \tag{3}$$

$x_h(t)$ can be regarded as the output of real signal $x(t)$ through a filter, the unit impulse response of the filter is as follows:

$$h(t) = 1/\pi t \tag{4}$$

Analytical signal of $x(t)$ is as follows:

$$g(t) = x(t) + jx_h(t) \tag{5}$$

The amplitude $A(t)$ and the phase $\varnothing(t)$ of the analytic signal $g(t)$ are as follows:

$$g(t) = A(t)e^{j\varnothing(t)} \tag{6}$$

In formula:

$$A(t) = \sqrt{x^2(x) + x_h{}^2(t)} \tag{7}$$

$$\varnothing(t) = \tan^{-1}\left[\frac{x_h(t)}{x(t)}\right] \tag{8}$$

In the formula, amplitude A(t) is the envelope signal of signal x(t) and can be obtained by the Hilbert transform and envelope detection. This signal filters out the high frequency part of the primal signal. Then one performs frequency spectrum analysis on the envelope signal A(t). The fault diagnosis can be based on this analysis, which is better to get the failure frequency.

3 The Analysis and Processing of Acoustic Emission Signals

3.1 The Acquisition of Acoustic Emission Signals

According to the experiment, we can get the time-frequency images of the knocking acoustic emission signal and the flaw acoustic emission signal, [14] which are as shown as Fig. 2:

3.2 Signal Processing

Acoustic emission signals will be affected by noise in the collection. Therefore, in order to reduce the error, de-noising should be applied to the collected knocking acoustic emission signal and flaw acoustic emission signal. Then, the original signal

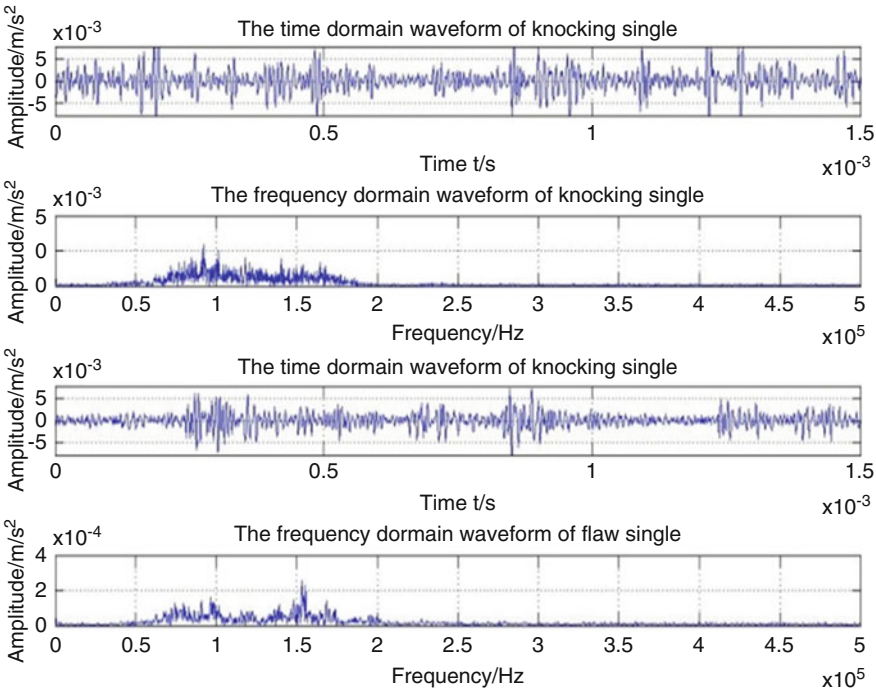

Fig. 2 Time-frequency diagrams of the knocking signals and flaw signals

can be decomposed into eight signals of different frequency bands with three-step wavelet packet decomposition. Afterwards, we can calculate the wavelet packet coefficients for each frequency spectrum. The frequency range is shown in Table 1. The wavelet packet coefficients of each frequency band are shown in Figs. 3 and 4 below.

After wavelet packet decomposition coefficients are obtained, we can calculate the kurtosis value of different spectrums and judge the scope of failure frequency by using the sensitivity of kurtosis and the principle of the kurtosis maximum. The kurtosis diagram is as shown in Fig. 5.

Because of the zero padding between one of the knocking signal's source , we take the several former wavelet packet coefficients into account. Through the analysis of the kurtosis figure, seen in Fig. 5, the knocking signals' wavelet packet coefficient of the node (3, 3) and the flaw signals' wavelet packet coefficient of the node (3, 2) are reconstructed based on the principle of kurtosis maximum, which show in Fig. 6.

We can then obtain their envelope-spectra after envelope demodulation as shown in Figs. 7 and 8.

As can be seen from above, one cannot obtain the failure frequency completely. According to preliminary judgment, the failure frequency of the knocking signal is for low-frequency parts. And the failure frequency of the flaw signal is for

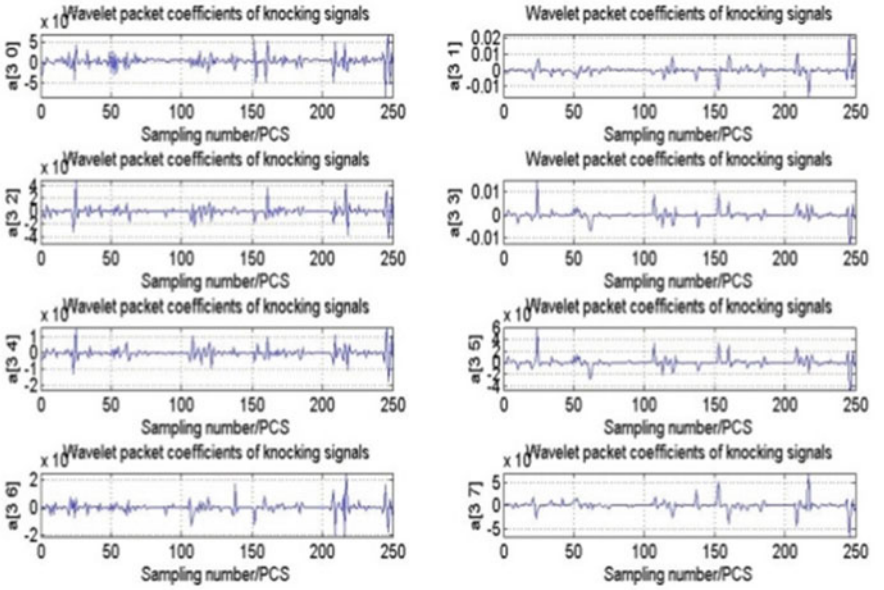

Fig. 3 Wavelet packet coefficients of the knocking signals

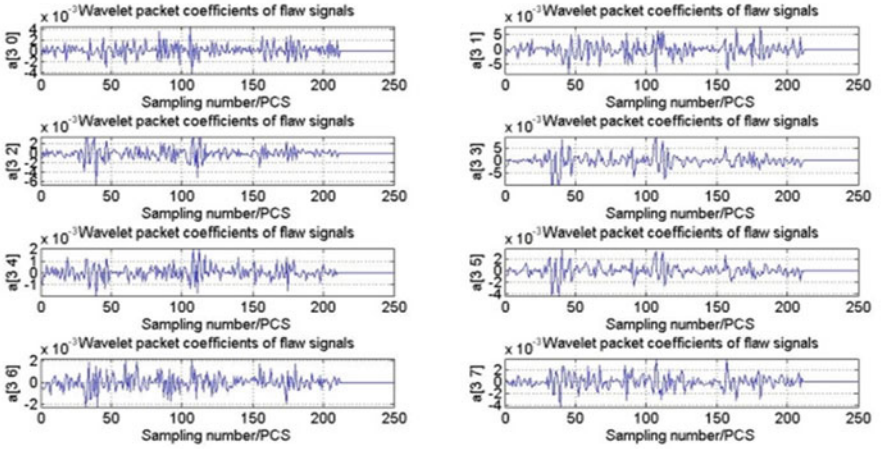

Fig. 4 Wavelet packet coefficients of the flaw signals

high-frequency parts. Thus, one needs to make the comparison for the envelope-spectra between the different frequency bands of the two signals, which is shown in Figs. 9 and 10.

In order to analyze the fault frequency, we make a comparison for the maximum amplitude of different nodes' envelope spectra by using the scatter plot, seen in

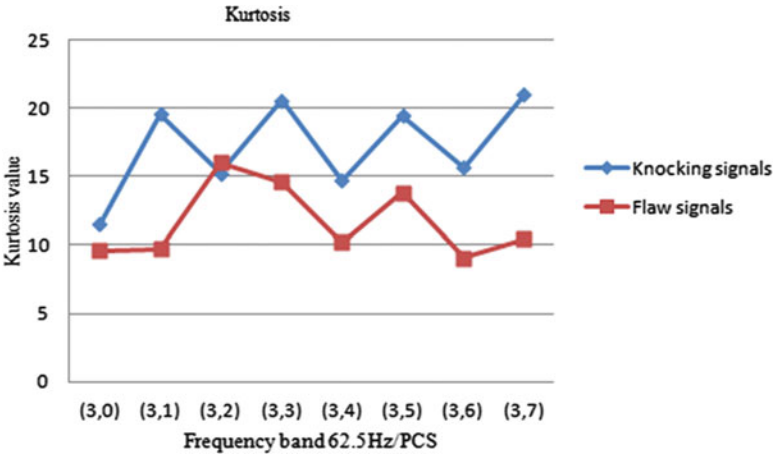

Fig. 5 Kurtosis figure

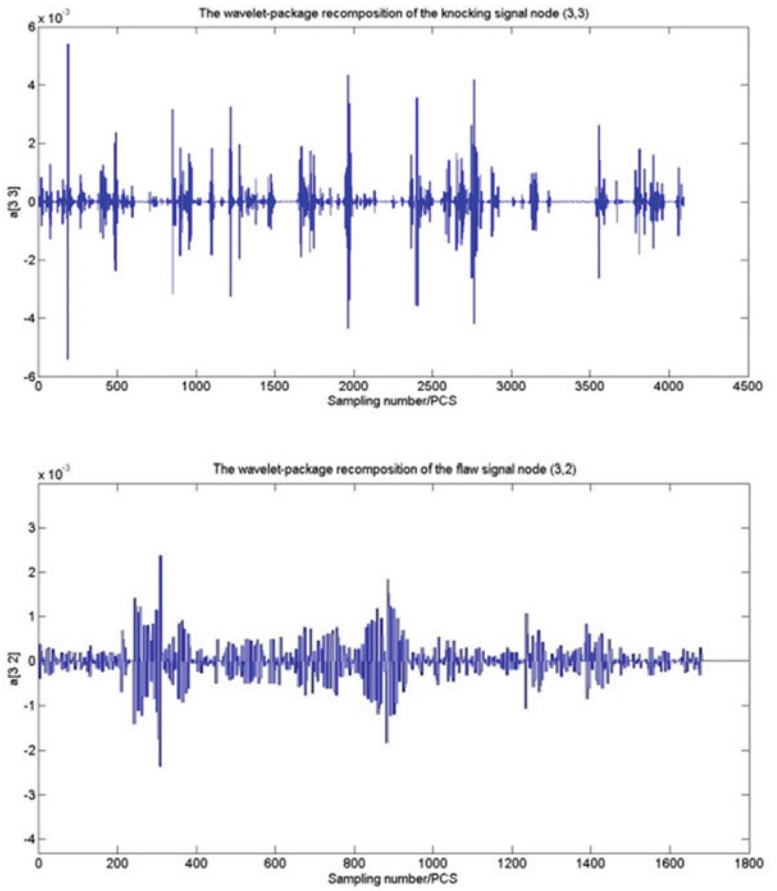

Fig. 6 The reconstruction of wavelet-package coefficients

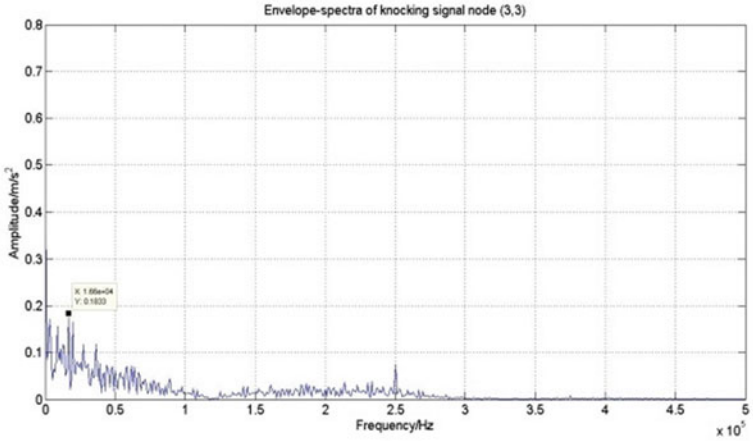

Fig. 7 Envelope-spectra of the knocking signal node (3,3)

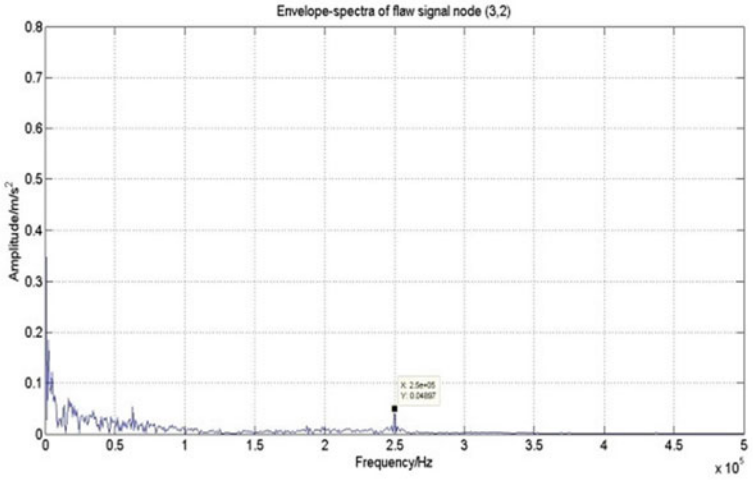

Fig. 8 Envelope-spectra of the flaw signal node (3,2)

Figs. 9 and 10. In the two figures, each circle represents a maximum, plotted by frequency band on the horizontal axis and frequency on the vertical. Others, the different colors represent the different amplitude values. The red is deeper; the value is higher. The blue is deeper; the value is smaller. Therefore, from Fig. 9, we can obtain the maximum amplitude of all nodes in knocking signals is in low-frequency parts. And the maximum amplitude of node (3,3) is most prominent, which is about 17 kHz. For the flaw signals, seen in Fig. 10, the maximum amplitude of all nodes is in the high-frequency part, and most of the maximum

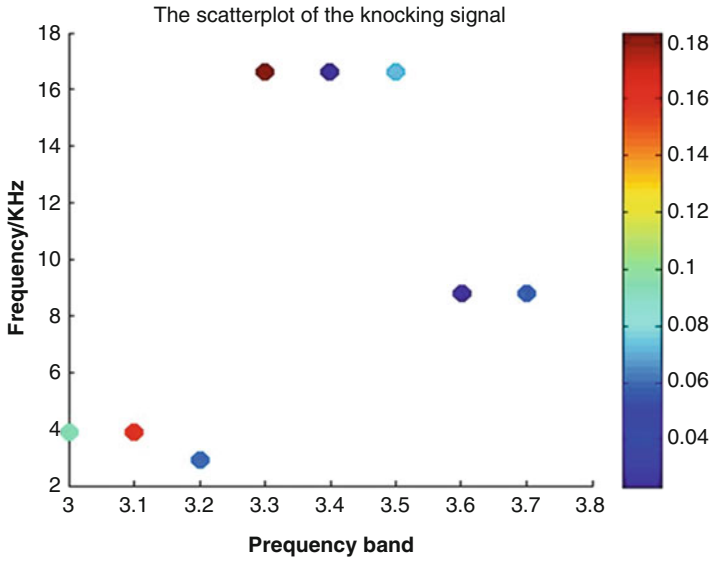

Fig. 9 The scatter plot and of knocking signals

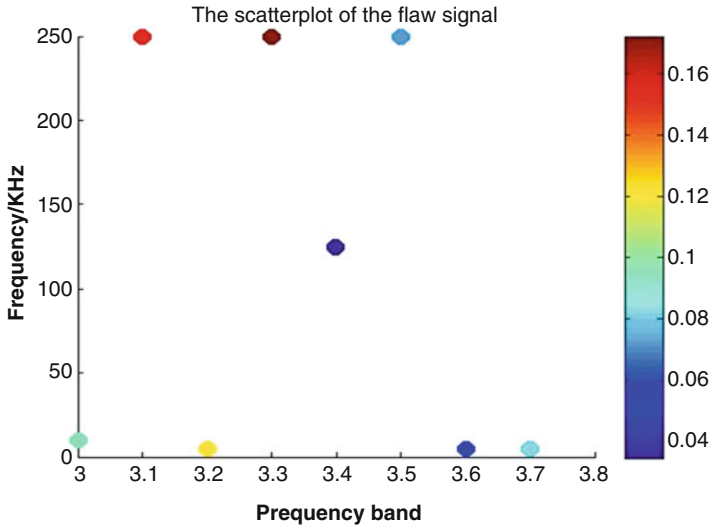

Fig. 10 The scatter plot and of flaw signals

amplitude is at 250 kHz. And the highest is 250 kHz at the node (3,3). Then, compared with the kurtosis figure in Fig. 5, the conclusion is in line with the kurtosis outcome. Thus, through the analysis and comparison, it reserves that the different fault frequency of the knocking signal and the flaw signal should be around about 17 kHz and 250 kHz.

4 Conclusions

Although there is a similar approach in literature [3], de-nosing after wavelet packet decomposition may result in boundary error. For this reason, the authors made changes. Compared with the method in the literature, mine is simple but not correct.

First of all, I perform de-noising for the collected knocking acoustic emission signal and flaw acoustic emission signal with the wavelet method in my chapter. Then I obtain eight different signals of decomposition and work out coefficients of each wavelet packet using three-step decomposition of wavelet packets. After that, I figure out the kurtosis of each wavelet packet coefficient. Ultimately, the filtered signal that contains the fault signature signal component is determined, by using the principle of kurtosis maximum. Of course, in order to make sure of the correctness and the kurtosis availability, it is necessary to compare all of the reconstructed signal nodes' envelope spectra for the two signals. Then we can draw the conclusion after envelope demodulation analysis.

The kurtosis and wavelet packet method is verified by the experiment. It is usable to judge the failure frequency rapidly and reduce the influence of noise. It is conducive to extract fault features of the acoustic emission signals.

References

1. C. Yang, Y. Shutian, C. He, et al., The rolling bearing fault diagnosis based on kurtosis and wavelet envelope analysis. Mach. Manuf. **2**(52), 594 (2014)
2. J. Junfeng, G. Yang, L. Xinhua, Z. Wu, The rolling bearing fault diagnosis based on wavelet packet and envelope analysis. Oil Field Equip. **35**(5), 18–22 (2006)
3. R. Xueping, P. Zhen, X. Xiangzhi, X. Yitong, Kurtosis and wavelet packet is applied to analysis the incipient faults of a rolling bearing. Bearing **3** (2014)
4. Ma Chuan, Li Hongkun, Zhao Lihua, Guo Zhenggang. The fault diagnosis of a rolling bearing based on wavelet packet envelope and kurtosis. Vib. Test. Diagn. 31(6), 12 (2011)
5. C. Shuixuan, Z. Jun, Y. Jiming, D. Xie, The incipient fault diagnosis and ante-noise research of gearbox based on kurtosis and wavelet packet energy feature. Mech. Drive **36**(11) (2012)
6. A.M. Al-Ghamdi, D. Mba, A Comparative experimental study on the use of acoustic emission and vibration analysis for bearing defect identification and estimation of defect size. Mech. Syst. Signal Process. **20**(7), 1537–1571 (2006)
7. J. Hualong, *The Application of Acoustic Emission in the Defects of Mechanical Structure* (Kunming University of Science and Technology, Kun Ming, 2014)
8. G.Y. Gary, C.L. Kuo, Wavelet packet feature extraction for vibration monitoring. IEEE Trans. Indust. Electron. **47**(3), 650–667 (2000)
9. S. Xiaomei, M. Fanchao, Y. Zhang, The research of rolling bearing fault diagnosis based on the envelope demodulation analysis. Instrum. Anal. Monitor. **1**, 1–4 (2012)
10. H. Li, u.-p. Zhang, H.-q. Zheng, Hilbert-Huang transform and spectrum for detection and dia - gnosis of localized defects in roller bearing. J. Mech. Sci. Technol. **23**(2), 291–301 (2009)
11. H. Zhen Nan, X. Shibo, L. Jinbao, Detection of incipient localized gear faults in gearbox by complex continuous wavelet transform. Chin. J. Mech. Eng. **16**(4), 363–366 (2003)
12. M. Yang, G. Rongsheng, *Acoustic Emission Testing* (China Machine Press, Beijing, 2004)
13. M. Li, Z. Shang, H. Chai, G. Dong, et al., *Acoustic Emission Testing and Signal Processing* (Science Press, Beijing, 2010)
14. L. Lin, F. Chu, HHT-based AE characteristics of natural fatigue cracks in rotating shafts. Mech. Syst. Signal Process. **26**, 181–189 (2012)

Research on the Diagnosis Method Based on the Waveform Streaming Signal of Rolling Bearing

Ying Zhang, Ruixiao Fan, Rui Cong, and Wei Li

Abstract The internal relations are analyzed between the different types of rolling bearing fault characteristic frequency and the cumulative peak count of acoustic emission waveform streaming. And the fault diagnosis method is established for the fault diagnosis of rolling bearing based on the periodic acoustic emission waveform streaming. Noncontact acoustic emission testing technology is used to analyze the faults of rolling elements, inner ring, and outer ring under the condition of working. According to the quantitative relationships between the cumulative peak count of periodic acoustic emission waveform streaming and the characteristic frequency of rolling bearing, the early diagnosis of rolling bearing can be carried out.

1 Introduction

Rolling bearings are critical components of rotating machine; monitoring their conditions is important to avoid catastrophic failures and reduce the machinery downtime [1]. When the rolling bearing is in the early fault stage, the characteristic signal is weak, and is seriously affected by the environment noise, so the fault feature is difficult to extract [2]. In the vibration detection method, the vibration signal of the bearing fault is very weak, which is often overwhelmed by a relatively large-frequency noise signal, so it is difficult to extract the information of the fault. When the rolling bearing is faulty, the abnormal sound is produced; it belongs to the category of acoustic emission, and the technology of acoustic emission can be used to the noncontact detection online [3, 4], and the early diagnosis and prediction of the fault can be realized. Acoustic emission method has obvious advantages compared with vibration method in the condition monitoring and fault diagnosis [5]. While the traditional acoustic emission signal is discontinuous (only below a few milliseconds), the periodic signal of low speed can't be collected completely. Aiming at the shortage of traditional acoustic emission signals, a continuous means of acoustic emission waveform streaming technology for the signal acquisition is

Y. Zhang (✉) • R. Fan • R. Cong • W. Li
College of Mechanical Science and Engineering, Northeast Petroleum University, Daqing 163318, China
e-mail: aezy163@163.com

G. Shen et al. (eds.), *Advances in Acoustic Emission Technology*, Springer Proceedings in Physics 179, DOI 10.1007/978-3-319-29052-2_10

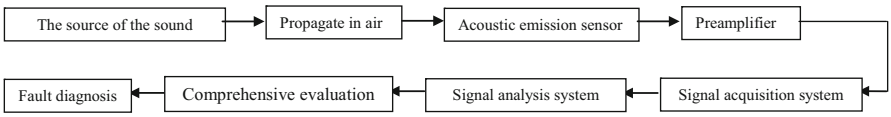

Fig. 1 The principle for the technology of acoustic emission waveform streaming

used; by this means the continuous periodic signal of the complete failure of the rolling bearing can be obtained. The corresponding relationship between the fault characteristic frequency of the rolling bearing and the cumulative fault peak value of the acoustic emission waveform streaming is used to establish a diagnosis method for the fault of rolling bearing based on the technology of the acoustic emission waveform streaming.

2 The Principle for Noncontact Acoustic Emission

When the rolling bearing is fault, the defect position in the operation process will produce a sudden impact signal, and it is cyclical. In the absence of fault, the signal generated is stationary. The basic principle of acoustic emission testing technology is to use sensitive instrument to receive the acoustic emission signals, then apply modern waveform processing technology for the adopted signals, and extract all kinds of typical fault features to analyze the location, the range of the state, and the development of the defect in the material or structure; the basic principle is shown in Fig. 1.

3 Advantage and Periodic Characteristic of Acoustic Emission Waveform Streaming

The technology of acoustic emission waveform streaming has the advantages as the traditional acoustic emission, and also has its own advantages. Acoustic emission waveform streaming can be used to complete the whole traditional acoustic emission test with high sampling rate. These waveforms can then be extracted from the time domain and frequency domain as the traditional acoustic emission for analysis. The acquisition technology of acoustic emission waveform streaming makes the recording of the acoustic emission signal from only discontinuous, burst, and finite length (only a few milliseconds) to the same as the vibration, it can obtain continuous acoustic emission signals. Thus the complete periodic signals of the rolling bearing are acquired, so that the acoustic emission waveform streaming technique is more accurate for the diagnosis of bearing faults, and more suitable for low-speed and heavy-load detection; meanwhile the test in real time can be realized.

The typical fault frequency of rolling bearing is characterized by the number of abnormal collisions in the unit time of failure. Each collision with the generation of waveform streaming peak counts. Rolling bearing belongs to the category of rotating machine, and the acoustic emission signal generated by the rotation of the rolling bearing is periodic, so the technology of acoustic emission waveform streaming is more capable to reflect the advantage in the fault diagnosis. Therefore, the cumulative fault peak counts obtained by the technology of acoustic emission waveform streaming can be used to compare to the fault characteristic frequency calculated by the theory. And then we can determine whether the rolling bearing is fault, and also we can determine the type of the fault.

4 Calculation for the Fault Characteristic Frequency of Rolling Bearing

The rolling bearing is made up of inner ring, outer ring, cage, rolling element, and so on. When some faults such as crack and flake emerged in these parts, the other parts will impact the damage point in the operation, and the periodic acoustic emission signal is generated.

The frequency when the contact points passing the defects are not the same with the different parts of the defects. In case the outer ring is fixed, the inner ring and the shaft rotate together. When the rolling element, outer ring, and inner ring appear as local defects, respectively, the typical failure impact frequency of rolling bearings can be calculated according to the following formula:

The frequency when a defect in the rolling elements impacts with the inner and outer ring rolling:

$$f_r = \frac{D}{2d}\left[1 - \left(\frac{d}{D}\cos\alpha\right)^2\right] f_s \tag{1}$$

The frequency when a defect found in rolling body impacts with a defect in the outer ring:

$$f_0 = \frac{z}{2}\left(1 - \frac{d}{D}\cos\alpha\right) f_s \tag{2}$$

The frequency when a defect found in rolling body impacts with a defect in the inner ring:

$$f_i = \frac{z}{2}\left(1 + \frac{d}{D}\cos\alpha\right) f_s \tag{3}$$

Type: D—the pitch diameter of roller bearing, mm
α—contract angle

Z—the number of rolling elements
f_s—spindle rotating frequency

5 Experiment

The tapered roller bearing 32,217 is selected in the test; the basic parameters are as follows: $D = 115.8$ mm, $Z = 19$, $d = 16.9$ mm, and $\alpha = 14.6°$; there is a defect of strip shape in the inner ring, outer ring, and roller with 2 mm length, 2 mm width, and 0.5, 1, 1.5, and 2 mm depth, respectively.

In the process of the experiment, the system of SAMOS PCI-2 is adopted for the collection of the sound, the broadband sensor type of WD is selected, and the preamplifier type of 2/4/6 is used. The threshold value is 30 dB to shield the noise outside. The basic parameters of the acoustic emission waveform streaming signal acquisition device are as same as traditional acoustic emission, and other settings remain unchanged.

The method of noncontact acoustic emission is used to detect the faults. In noncontact acoustic emission testing, sound waves propagate to the outer surface of the bearing. Airborne acoustic emission waves directly translate to the surface of piezoelectric crystal, and sensor eventually receives a longitudinal wave from the air, converted into electrical signals. The signal amplitude of contact and noncontact in two different distances is as in Fig. 2; the signal amplitude of noncontact is less than the contact type, but the count of sound emission impact is close to the theoretical value, which provides the experimental basis for the single-fault diagnosis of rolling bearing. Considering that the process of the acoustic emission generated by the collision of defects is pointed, the distances between the noncontact testing sensor and the rolling bearing are 100 mm, 200 mm, 300 mm,

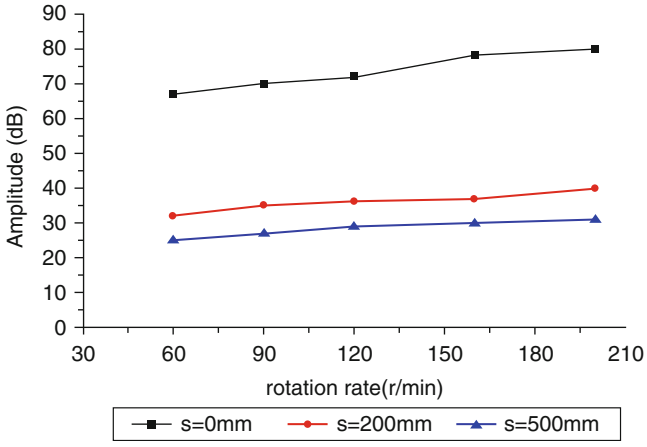

Fig. 2 The signal amplitude comparison of contact and noncontact acoustic emission

400 mm, and 50 mm. The test is carried out on the test rig with adjustable speed, and the speed of n is 60 r/min, 90 r/min, 120 r/min, 160 r/min, and 200 r/min; different types of faults for the test have been set ahead of the time.

6 Data Analysis

The theoretical impact number of the rotation is calculated, and at the same time the counts of the actual waveform streaming peak counts are calculated for comparison; the data are listed in Table 1. Taking the speed $n = 60$ r/min, the distance between the sensor and the bearing $s = 200$ mm, and the depth of the prefabricated defect is 1 mm for example for analysis. As is shown in Fig. 3a, by the analysis of the acoustic emission waveform streaming data, we can see that the peak voltage of the acoustic emission waveform streaming exceeds 30 mv is 3 within 1 revolution, and it has been connected with a red line, it represents the counts of failures in 1 revolution is 3 in the actual test. By comparison with the theoretical value, it is concluded that the failure is the roller fault. Other results are shown in Table 1.

From Table 1 it can be seen that the error rate of the rolling element failure, the error rate of the inner ring failure, and the error rate of the outer ring failure are less than 10%. The error rate increased gradually with increasing number of revolutions, and the real number of the waveform peak count is generally lower than the theoretical impact number; this is due to the rolling bearing leakage and impact overlapping phenomenon existed in the rotation process. At the same time, according to the data in Table 1 it can be seen that the error rate of real impact and the theoretical number of waveform peak count are relatively small in 1 revolution and in 5 revolutions; especially in 1 revolution, the real number and the theoretical number is completely consistent. Therefore, the single-fault diagnosis of rolling bearing can be realized according to the numbers of acoustic emission waveform peak value.

6.1 Analysis for the Test Results of the Acoustic Emission Waveform Roller Fault

By analyzing and processing the acoustic emission data for the test of the roller fault, the cumulative fault peak counts of the noncontact acoustic emission waveform streaming can be concluded, and it is shown in Fig. 2. By comparing the typical frequency of the roller with the theoretical calculation, it can be seen that the cumulative peak waveform counts are compliant with the theoretical calculation completely in 1 revolution, 5 revolutions, and 10 revolutions. While the waveform counts of 20 revolutions are 66, and it is less than the theoretical data, the error rate is 1.49%. The results above show that there is a corresponding relationship between

Table 1 The number of waveform streaming counts in different revolutions for different type of failures

Rotation speed (r/min)	Revolutions	Rolling element failure			Outer ring failure			Inner ring failure		
		Theoretical counts	Measured counts	Error rate/%	Theoretical counts	Measured counts	Error rate/%	Theoretical counts	Measured counts	Error rate/%
$n = 60$	1	3	3	0	8	8	0	11	11	0
	5	17	17	0	41	39	4.88	54	52	3.70
	10	34	34	0	81	78	3.70	108	103	4.63
	15	50	49	2.00	122	117	4.10	162	155	4.32
	20	67	64	4.48	163	157	3.68	217	211	2.76
$n = 90$	1	5	5	0	12	12	0	16	16	0
	5	25	25	0	61	60	1.63	81	79	2.50
	10	50	49	2.00	122	119	2.46	162	158	2.50
	15	76	73	3.94	184	180	2.17	244	234	4.10
	20	100	95	5.00	245	239	2.45	325	310	4.62
$n = 120$	1	7	7	0	16	16	0	22	22	0
	5	34	34	0	82	81	1.22	108	105	2.78
	10	67	65	2.99	161	159	1.24	217	209	3.69
	15	101	97	3.96	245	240	2.04	325	312	4.00
	20	134	128	4.47	326	314	3.68	434	416	4.18
$n = 160$	1	9	9	0	22	22	0	29	29	0
	5	45	45	0	109	107	1.83	145	143	1.38
	10	90	88	2.22	218	213	2.29	289	281	2.77
	15	134	131	2.24	326	311	4.60	434	419	3.46
	20	179	173	3.35	435	410	5.75	578	555	3.98
$n = 200$	1	11	11	0	27	27	0	36	36	0
	5	56	56	0	136	134	1.47	181	175	3.31
	10	112	110	1.78	272	266	2.21	361	350	3.04
	15	167	163	2.40	408	394	3.43	542	516	4.80
	20	224	216	3.57	544	519	4.60	723	683	5.53

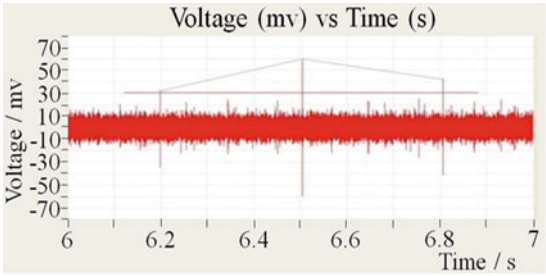

(a) 1 revolution

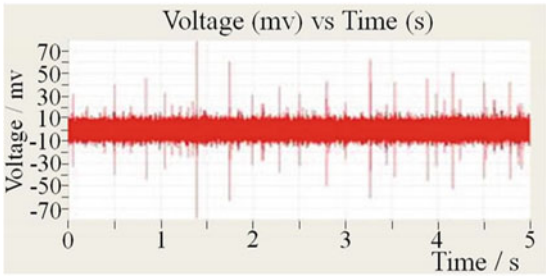

(b) 5 revolutions

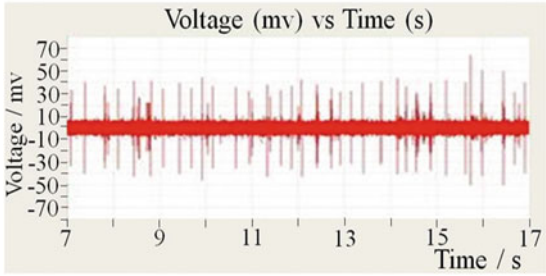

(c) 10 revolutions

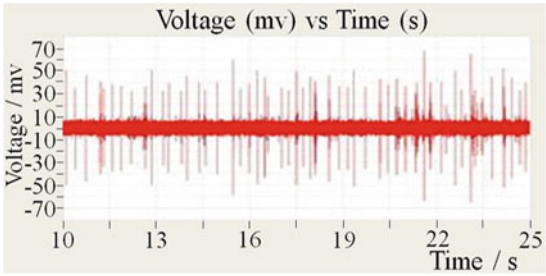

(d) 15 revolutions

Fig. 3 Data for noncontact detect of the failure of rolling body in different revolutions

the cumulative fault peak counts and the characteristic fault frequency. The results of the test are highly consistent with the theoretical value in the small cycles. While in the multiperiod the test is affected by the attenuation of the sound propagation process and the effect of the superposition effect, the cumulative peak counts are less than the theoretical value.

6.2 *Comparative Analysis for the Test Results of Different Types of Faults*

By effective analyzing and processing the acoustic emission waveform streaming data of the inner ring and outer ring, the cumulative waveform peak counts of the fault defects in 5 revolutions can be obtained, as shown in Figs. 4 and 5.

It can be seen that the cumulative peak waveform counts of the outer ring fault are completely consistent with the theoretical calculation of the bearing fault characteristic frequency in 1 revolution and 5 revolutions from Fig. 3. While the cumulative peak count of 10 revolutions is 80, and the error rate is 1.23%. The cumulative peak waveform streaming counts of the inner ring fault are completely consistent with the theoretical calculation of the bearing fault characteristic

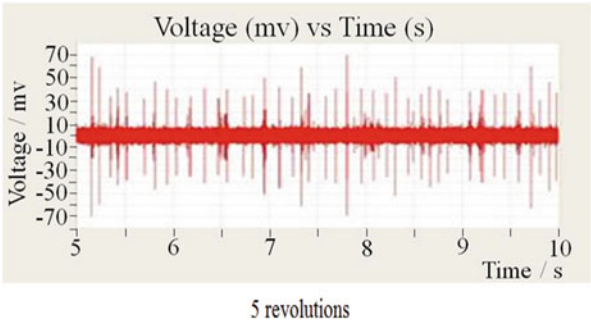

Fig. 4 Data of detection of inner ring fault in 5 revolutions

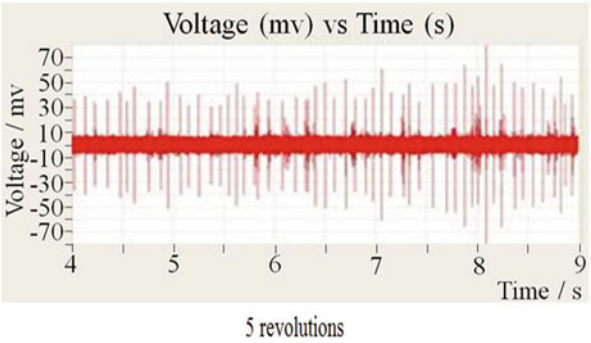

Fig. 5 Data of detection of outer ring fault in 5 revolutions

frequency in 1 revolution and 5 revolutions, and the cumulative peak count of 10 revolutions is 106, and the error rate is 1.85%.

By the analysis of noncontact acoustic emission test of rolling element fault with Fig. 3, the corresponding relationship between the peak waveform counts and the fault characteristic frequency can be used in the same test period for the fault diagnosis of the rolling bearing. Although in the case of a few revolutions the fitness between the cumulative waveform peak counts and the fault characteristic frequency is high, due to the influence of the attenuation of the acoustic propagation process and the superposition effect in practice, the cumulative waveform peak counts are less than the theoretical value. So it is better to adopt multiperiod test result for analysis to reduce the test error; it will not affect the fault diagnosis.

7 Conclusion

The technique of acoustic emission waveform streaming can complete the whole traditional acoustic emission test with high sampling rate, collect the complete date of the acoustic emission waveform, and determine whether the rolling bearing is faulty and the fault type; this technique makes the test results more accurate; it can be used to test and diagnose the fault of the rolling bearing under the working condition.

Acknowledgment I would like to thank "Innovation Foundation For Postgraduate of Northeast Petroleum University (No. YJSCX2015-027NEPU)" for its financial support.

References

1. J.L.F. Chacon, V. Kappatos, W. Balachandran, T.-H. Gan, A novel approach for incipient defect detection in rolling bearings using acoustic emission technique. Appl. Acoust. **89**, 88–100 (2015)
2. G. Tang, X. Wang, The method of maximum correlation kurtosis deconvolution with 1.5 dimension spectrum for early fault feature extraction of rolling bearing. Vib. Impact **12**, 79–84 (2015)
3. F. Li, Y. Shen, J. Xiong, Acoustic emission testing technology of rolling bearing fault. Nephrol., Dial., Transplant. **11**, 583–586K. Elissa, "Title of paper," unpublished
4. X. Wang, Z. Liu, G. Zhang, W. Dou, The fault diagnosis for the rub of tilted-pad journal bearing based on the acoustic emission. Chin. J. Mech. Eng. **8**, 64–69 (2009)
5. X. Zhang, Y. He, R. Hao, F. Chu, Parameters optimization of continuous wavelet transform and its application in acoustic emission signal analysis of rolling bearing. Chin. J. Mech. Eng. **2**, 104–108 (2007)

Part IV
Material Characteristics

Acoustic Emission Behavior of 12MnNiVR under Corrosion

Guanghai Li and Xinjian Wang

Abstract Large atmospheric storage tanks play an important role in the petrochemical, energy, and logistics industries. Improvements in materials and manufacturing processes have enabled larger tank volume capacity, leading to increased material performance requirements as well. 12MnNiVR is a material typically used in the fabrication of large-scale atmospheric tanks. However, serious tank bottom corrosion can occur, not only from the medium inside the tank, but also from soil erosion of the tank foundation. Testing of corrosion on the tank floor is usually conducted using nondestructive methods such as magnetic flux leakage (MFL) to determine an equivalent bottom corrosion indication, but this requires cleaning of the tank and access to a large area for inspection, which is costly. In recent years, acoustic emission (AE) testing methods have been frequently used to determine the qualitative corrosion condition of the tank floor. However, according to researchers, only a few simple parameters of AE signals, tank bottom corrosion severity grade, the lack of concrete storage tank under the conditions of material effect, corrosion materials research AE signal spectrum and characteristic parameters, and thus the corrosion status of materials for quantitative analysis and assessment. This study simulates corrosion conditions for 12MnNiVR, a typical material used in the construction of atmospheric tanks. The Devanathan–Stachurski technique is used, with electrolytic hydrogen charging corrosion on one side of the surface material and simulated soil solution soaking on other. AE signals were collected and analyzed over time under corrosive conditions, and the empirical mode decomposition (EMD) and Hilbert–Huang transform (HHT) methods of signal processing were used to obtain AE signal characteristics from the beginning to various stages of corrosion, providing an experimental basis for online AE measurement and qualitative assessment of large atmospheric tanks.

G. Li (✉)
China Special Equipment Inspection and Research Institute, Beijing 100029, China
e-mail: liguanghai@csei.org.cn

X. Wang
Beijing University of Technology, Beijing 100022, China
e-mail: wangxj@bjut.edu.cn

G. Shen et al. (eds.), *Advances in Acoustic Emission Technology*, Springer Proceedings in Physics 179, DOI 10.1007/978-3-319-29052-2_11

1 Introduction

Large atmospheric storage tanks (AST) play an important role in the petrochemical, energy, and logistics industries, with improvements in materials and manufacturing processes enabling greater AST capacity. 12MnNiVR is a material that is often used for the construction of large AST; however, tanks constructed with carbon steel are susceptible to serious corrosion. The tank bottom suffers the greatest corrosive effects, both on the product side (internal corrosion) and the soil side (external corrosion) of the tank bottom. The detection of these corrosion defects is commonly performed using nondestructive testing (NDT) methods, such as magnetic flux leakage testing, after tank clean-up. Such offline detection techniques, however, are costly. In recent years, acoustic emission (AE) testing methods have become a frequent means of determining the qualitative condition of the tank bottom. AE parameters such as amplitude, count, and energy can be utilized to analyze the levels of corrosion under controlled operating environments. Various laboratory and field studies have used AE signal and parameter analysis to classify different types of corrosion, such as uniform corrosion, pitting, and stress corrosion cracking. The major cause of corrosion is the dynamic force generated from tank filling and discharge, which induces stress corrosion cracking and electrochemical corrosion from the formation of a water layer by the collection of water droplets. Corrosion processes such as cracking, surface oxide formation and spalling, and hydrogen blistering can release stress waves, which produce AE signals. AE testing is also widely used for the grading of tank floor corrosion for in-service AST. The AE signal characteristics are largely dependent on the material properties. This study simulates corrosion conditions of a tank bottom constructed of 12MnNiVR, and AE signals are collected over the course of the experiment. Advanced signal processing methods are used to analyze the AE signals, and the signal characteristics of various corrosion states are obtained.

2 Experiments

2.1 Experimental Setup

Corrosion occurs from both the product side (internal corrosion) and the soil side (external corrosion) of AST bottoms constructed of carbon steel. The soil type is an important factor affecting tank floor corrosion. In this work, we created a corrosion test device for both sides of the specimen. The experimental design is based on the Devanathan–Stachurski method, the principle of which is to subject the left side of the specimen surface to electrolytic hydrogen charging corrosion, while the surface of the right side is soaked in a simulated soil solution. The electrolytic hydrogen permeation test apparatus is shown in Fig. 1. The specimen was fixed between two containers, with an exposed area of 10 cm^2. A National Association of Corrosion

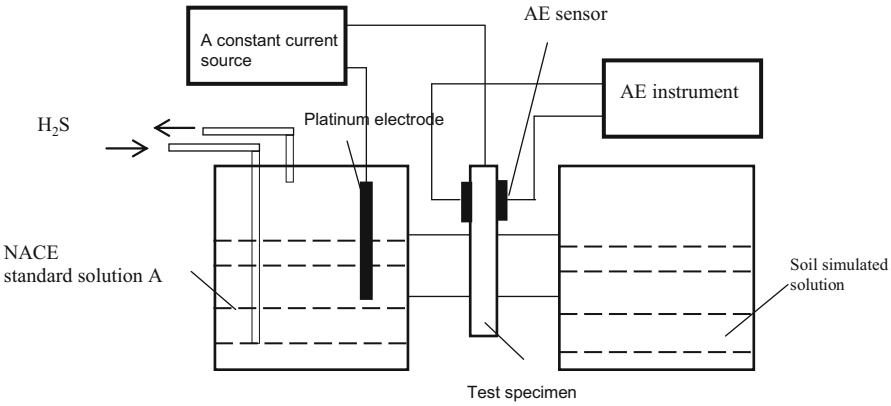

Fig. 1 Schematic of the experiment

Engineers (NACE) Standard solution and simulated soil solution were used for the cathode and anode sides of the device, respectively.

For the cathode side, the NACE TM0284-2003 Standard Solution A was used, which is an aqueous solution containing 5% sodium chloride and 0.5% glacial acetic acid. Hydrogen sulfide gas was obtained through the reaction of a mass percentage of 30% H_2SO_4 solution and Na_2S. The H_2S concentration in the soaking solution was determined by 0.1 N sodium thiosulfate ($Na_2S_2O_3$) and 0.1 N iodine (I_2) and 5% starch solution. Typical domestic seaside saline soil was selected for the simulated soil solution. The composition of the solution was based on physical and chemical soil salinity formulated as follows: 0.426% (mass fraction) Cl^-, 0.1594% SO_4^{2-}, 0.0439% HCO_3^-, pH value of 7.76.

The main test supplies included the following: a sealed Plexiglas container, constant current power supply, AE sensors, AE instrument, cables, couplant, and pH meter. A schematic of the experiment is shown in Fig. 2.

2.2 Experimental Procedure

The main test steps were as follows:

1. The specimen was fixed between the two containers, bolted, and sealed with silicon sealant. Sensors were mounted on a conduit connecting the inlet and outlet;
2. Standard A solution and simulated soil solution were poured into the two devices;
3. The AE testing system was calibrated using break tests with 0.3 mm (2H) lead next to the sensor. The breaks were performed with the lead at an angle of

Fig. 2 Experiment equipment

approximately 30° to the surface and with a 2.5 mm lead extension. Before and after the test, measurements were made of the peak amplitude response of each sensor to a repeatable simulated AE source at a specific distance from the sensor. (The measured peak amplitude should not vary more than 3 dB from the average of all the sensors);

4. Nitrogen gas was introduced into the solution for about 30 min to remove oxygen;
5. Background noise was measured before the specimen was placed into the corrosive environment;
6. Hydrogen sulfide gas was piped into the container for 30 min. The constant current source was turned on, and the AE signals of the electrolytic hydrogen charging process were collected.

3 Results and Discussion

3.1 Parametric Analysis of Acoustic Emission Signals

With regard to the amplitude of the AE signals, the signal amplitude of the entire corrosion process was less than 65 dB. The presence of a crack in the material causes the signal amplitude to weaken. With regard to signal attenuation and propagation path (through the bottom plate or the operating medium), the amplitudes should be large enough for the AE receiver equipment. If we adopt AE testing for large-scale AST in-service inspection, the effective testing area should cover the entire tank floor in order to enable complete evaluation of the tank bottom corrosion condition.

The cumulative number of AE signal hits vs. time is presented in Fig. 3, which shows that the corrosion process can be divided into two stages. In the first stage,

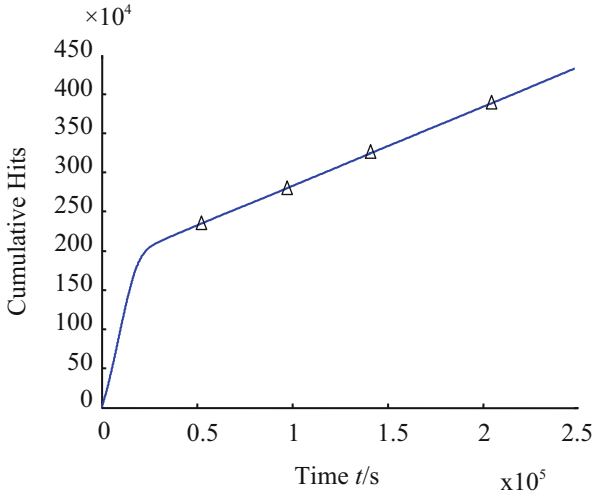

Fig. 3 AE signal hits cumulative vs. time

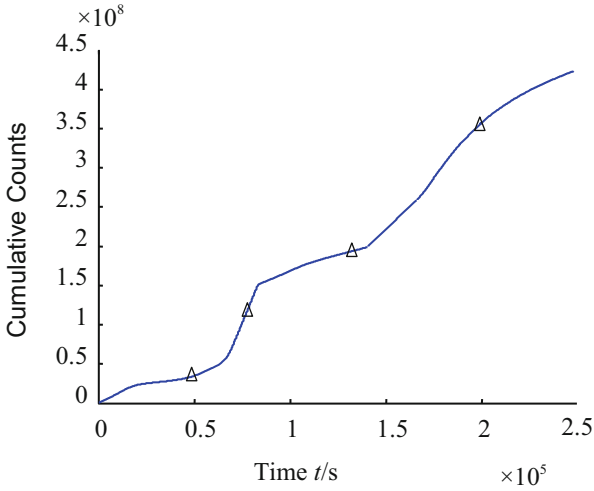

Fig. 4 AE signal counts cumulative vs. time

t = 0–2000 s, the corrosion rate is faster, and the hit rate accelerates, reaching 100 hits/s. In the second stage, which occurs after t = 2000 s, the hit rate is reduced to 11/s. When corrosion reaches a certain point, the compact oxidation film deposited on the surface prevents further corrosion and slows the AE hit rate. In Fig. 4, which shows the cumulative AE signal counts vs. time, the entire corrosion process can be divided into four periods: t = 0–6500 s, t = 6500–8000 s, t = 8000–14,500 s, and t = 14,500–25,000 s. The count rate in the first and third periods is essentially the same, and the count rate is substantially the same in the second and fourth periods. The count rates are 115 counts/s and 150 counts/s.

3.2 *Hilbert–Huang Transform Analysis of Acoustic Emission Signals*

Using AE signal analysis, we have been able to determine the basic parameters of the AE signals during the material corrosion process. To extract corrosion features during the individual corrosion phases, we can utilize AE waveforms to further determine the corrosion state of the material.

For extraction of AE signal characteristics during the different corrosion phases, we selected four typical AE signal phases, as shown in Fig. 4, with time points of $t = 5000$ s, $t = 7000$ s, $t = 14{,}000$ s, and $t = 20{,}000$ s. The triangular mark is used in Fig. 4. These four AE signals are investigated using time–frequency analysis. The signals are received by a broadband probe (VS45-H) at a sampling rate of 2.5 MHz, with 4096 sampling points.

Figure 5 presents four typical signal corrosion process time-domain waveforms and spectra. The time-domain diagram shows that the four signals belong to a continuous AE signal. With regard to signal amplitude, the signal amplitude shown in Fig. 5a is largest, with peak amplitude of approximately 0.5 mV. The signal

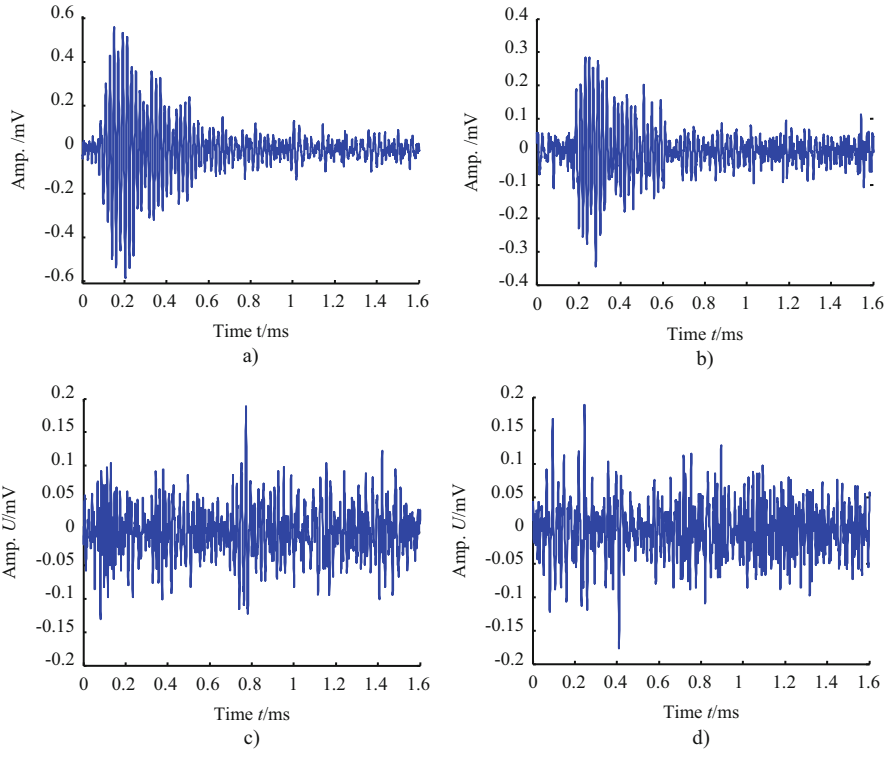

Fig. 5 AE waveform and spectrum in corrosion periods: (**a**) first period, (**b**) second period, (**c**) third period, and (**d**) fourth period

amplitudes during the third and fourth periods, however, are only 0.1 mV. The four signal frequency bandwidths are almost the same, ranging from 30 to 180 kHz. The AE signals show a peak emerging near 50 kHz for the first and the second periods, but this phenomenon is not present in the last two signals, which show multiple peaks (Fig. 6).

To determine additional AE signal characteristics, the intrinsic mode functions (IMF) of the four periods were obtained. Based on the energy of this eight-layer decomposition, we can obtain the proportion of total energy, as presented in Table 1. The results show that the sum of the first four components is more than

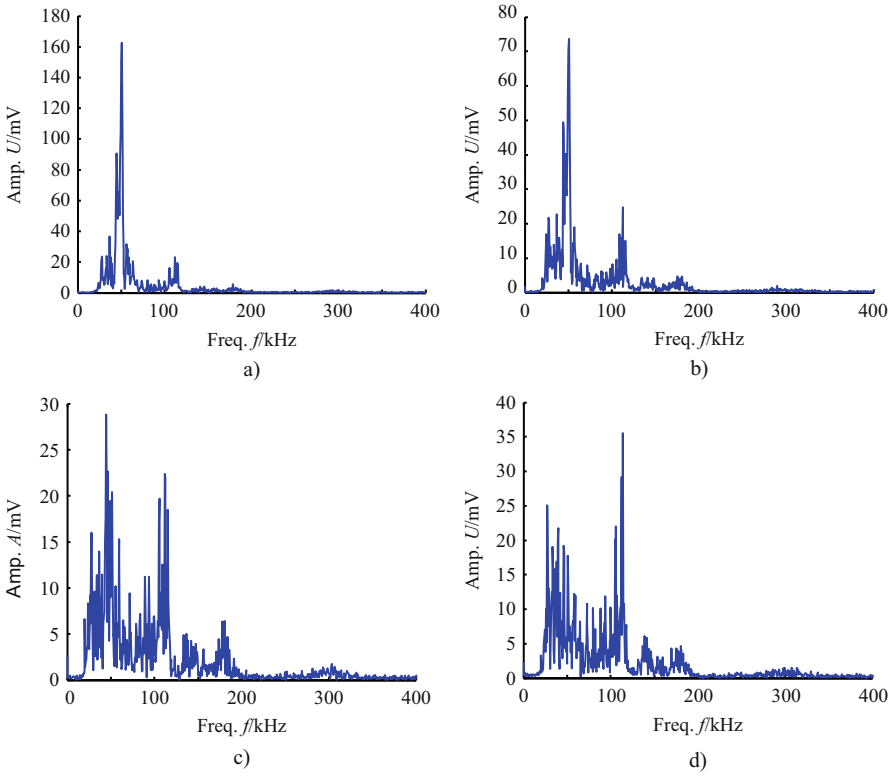

Fig. 6 AE waveform and spectrum in corrosion periods: (**a**) first period, (**b**) second period, (**c**) third period, and (**d**) fourth period

Table 1 IMF results in corrosion experiment

	IMF1 (%)	IMF2 (%)	IMF3 (%)	IMF4 (%)	Other IMF (%)
0–6500 s	45	32	14	7	1
6500–8000 s	65	29	3	1	2
8000–14,500 s	58	26	13	2	1
14,500–25,000 s	50	30	13	4	3

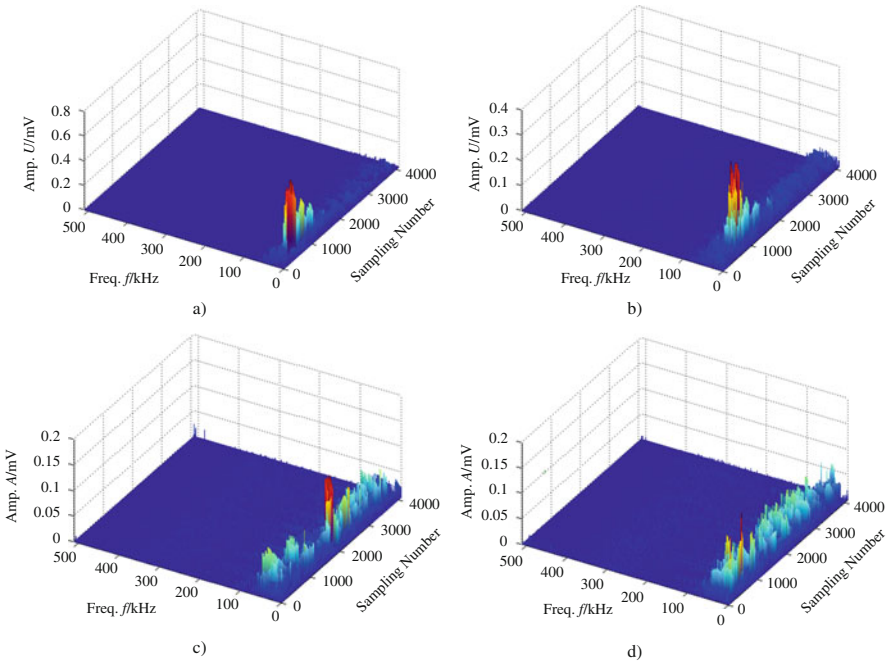

Fig. 7 AE 3D spectrum in corrosion periods: (**a**) first period, (**b**) second period, (**c**) third period, and (**d**) fourth period

98% of the total energy, with the sum of the other components accounting for only about 2%.

Further analysis of the AE signals was performed using the 3D Hilbert spectrum, which is an excellent time–frequency analysis method. Three elements (sampling points, frequency, and energy) can be seen in the 3D plot, which shows many time–frequency characteristics (Fig. 7a–d). The first AE signal frequencies are concentrated in the range of 0–50 kHz., with an energy peak of 0.53 mV, and number of sampling points in in the range of 80–1100. The second signal frequencies are similarly distributed from 0 to 50 kHz, with an energy peak of 0.22 mV, and 80–1500 sampling points. The AE signal frequencies of the third and fourth distributions are more widely dispersed, ranging from 0 to 80 kHz, with sampling points ranging from 0–4000. The third AE signal peak is 0.13 mV, and sampling points are distributed in the range of 1800–2200, with frequencies of 30–80 kHz. The fourth signal energy peak is 0.09 mV, with a frequency range of 0–80 kHz, and sampling points in the range of 800–1000.

4 Conclusions

In this work, AE signals were analyzed using the Hilbert–Huang transform (HHT) method, which revealed that the signals could be divided into four stages according to the corrosion state. The AE signal frequencies in the first and second stages were concentrated in the range of 0–50 kHz. The peak amplitudes were s 0.53 mV and 0.22 mV in the first and second stages, respectively. The signal frequency distribution in the third and fourth stages was more widely dispersed, ranging from 0 to 80 kHz. The amplitude was 0.13 mV in the third stage and 0.09 mV in the fourth stage.

HHT and empirical mode decomposition (EMD) methods were then used for analysis of the AE signals, and the stages of the tank material corrosion were obtained by analyzing the AE signal characteristics. Through analysis of the features of corrosion AE signals, the corrosion stages were successfully identified. These results provide an experimental basis for qualitative assessment of tank bottom corrosion stage.

Acknowledgments This work was supported by the Special Fund for AQSIQ Scientific Research in the Public Interest (Grant No. 201510066), National Key Technology Research and Development Program, China (Grant No. 2011BAK06B03-03).

B-Value Characteristics of Rock Acoustic Emission Under Impact Loading

Xiling Liu, Mengcheng Pan, Xibing Li, and Jinpeng Wang

Abstract *B*-Value characteristics of rock acoustic emission which is based on split-Hopkinson pressure bar system are studied in this chapter. The signals collected on rock samples contain both the signals generated by rock fracturing and the signals generated by elastic wave propagation. The parameter peak frequency can be used to distinguish two typical signals. As the signals can be divided into two groups based on peak frequency, in order to study the evolution process of rock failure under the impact loading, the *Hb*-value of each signal is calculated with the algorithm same as the *b*-value.

1 Introduction

Rock failure by stress is a process in which microcracks appear in the material, expand, and then fracture; this process is accompanied by an acoustic emission (AE) phenomenon. The phenomenon was discovered in the 1930s by L. Obert of the US Bureau of Mines, who applied AE technology to the monitoring of mine rock pillar stability and forecasting of rock burst [1]. Since then there have been many developments and achievements in the study of rock AE characteristics, among them *b*-value analysis.

The concept of *b*-value was derived from seismology research. In 1941, Gutenberg and Richter [2] first derived the rule that the frequency of earthquake occurrence decreases exponentially with magnitude. They proposed the widely used *G–R* formula:

$$\log N = a - bM$$

where M is the earthquake magnitude and N is the number of the corresponding earthquakes; a and b are constants and b is the so-called *b*-value. Similar to earthquakes, the elastic wave emissions produced by cracking inside brittle rock

X. Liu (✉) • M. Pan • X. Li • J. Wang
School of Resources and Safety Engineering, Central South University, Changsha 410083, China
e-mail: lxlenglish@163.com

G. Shen et al. (eds.), *Advances in Acoustic Emission Technology*, Springer Proceedings in Physics 179, DOI 10.1007/978-3-319-29052-2_12

are related to the occurrence of frequency and amplitude, and this relationship can be used to evaluate the changes of the crack scale [3]. Thus, *b*-value analysis has become an effective way to study the AE characteristics of rock.

Many researchers have intensively studied the changes and mechanisms of *b*-value of rock AE. Early studies focused mainly on the factors affecting the *b*-value. Experimental studies showed that the *b*-value is affected by the nonuniformity of the medium, stress, strain, temperature, rock moisture content, and many other factors [4–8]. Moreover, some researchers examined the effect of the number of events selected for analysis [9], number of groups [10], and the steps [11] on the results of the calculation of the *b*-value, and concluded that the selection can reflect the process of rock fracture under stress intuitively, but does not affect the general trend of the *b*-value. Using the statistical distribution characteristics of AE signals, Shiotani [12] proposed an improved *b*-value (the *Ib*-value), and Rao [13] compared the *Ib*-value and *b*-value and found that their general trends were similar and that the *Ib*-value can identify the moment of rock fracture. In terms of *b*-value behavior, many studies [14–18] showed that the *b*-value changes during the rock loading process: it decreases with increasing levels of stress, and reaches its minimum values at peak stress. However most studies examined the *b*-value of rock AE under static loading or low strain rate loading, while the *b*-value characteristics of rock AE under impact or high strain rate loading have rarely been investigated. Therefore, in this study we focus on the behavior and significance of the rock AE *b*-value under impact loading, and discuss the difference between the *b*-value under impact and under static loading conditions.

2 Experiment and *B*-Value Calculation Algorithm

2.1 Experimental Setup

Because its loading rate matches that of drilling and blasting, the 50-mm-diameter split-Hopkinson pressure bar (SHPB), recommended by the International Society for Rock Mechanics Commission on Rock Dynamics [19], was employed in this study as the impact-loading device (Fig. 1). A PCI-2 system (Physical Acoustic Corporation, NJ, USA) and an ultra-mini Pico-type sensor were used to record the AE signals. The Pico-type sensor has 250 kHz resonant frequency, and was directly glued onto the rock specimen. The AE signals detected by the sensor were pre-amplified by 40 dB; the detection threshold and sampling rate were set at 45 dB and 40 Msps, respectively. Four types of rock (granite, limestone, sandstone, and skarn) were selected for the experiment, and five specimens of each rock type with a length (25 mm) to diameter (50 mm) ratio of 0.5:1 were prepared for the tests.

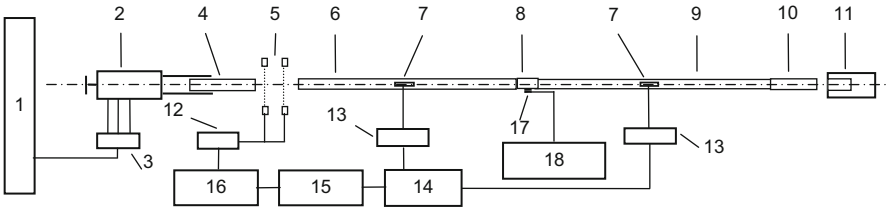

Fig. 1 Schematic of split-Hopkinson pressure bar system with acoustic emission (AE) testing device. (*1*) Gas tank; (*2*) pressure vessel; (*3*) control valve; (*4*) striker; (*5*) light beams; (*6*) input bar; (*7*) strain gauge; (*8*) specimen; (*9*) output bar; (*10*) absorption bar; (*11*) dashpot; (*12*) electronic counter; (*13*) bridge; (*14*) ultra-dynamic strain gauge; (*15*) transient wave memory; (*16*) data-processing unit; (*17*) AE sensor; (*18*) AE signal recording and processing unit

2.2 B-*Value Calculation*

To calculate the *b*-value of rock AE using the *G–R* formula, the magnitude is replaced by amplitude:

$$\log N = a - b\frac{A_{\mathrm{dB}}}{20}$$

where A_{dB} is the peak amplitude of the AE hit in decibel, $A_{\mathrm{dB}} = 20 \lg A_{\max}$, and $A_{\max}$ is the maximum amplitude of the AE hit in microvolt.

Compared with static loading, the loading time under impact loading is much shorter, with less hits recorded by the PCI-2 system; therefore, a larger step size is needed to obtain reliable statistical results. Thus, we selected a 5 dB step size in our tests, and used the least squares method to calculate the *b*-value.

3 Results and Discussion

3.1 *Analysis of* B-*Value Characteristics*

Figure 2 shows the amplitude-frequency distribution of the four types of rock samples, and the *b*-values and goodness-of-fit R^2 are listed in Table 1. All the rock samples have a linear amplitude-frequency relationship, with R^2 values being higher than 0.95, which is in line with the *G-R* relationship. The *b*-values for the four types of rock samples under impact load were all less than 1.

Studies of rock failure [20–24] showed that at the initial stages of AE in hard brittle materials under static loading, the *b*-value ranges from 1.5 to 2.5 because of the emergence of a number of small cracks and the stress concentration caused by the cracks. It then falls below 1.0, indicating that considerable cracking occurs.

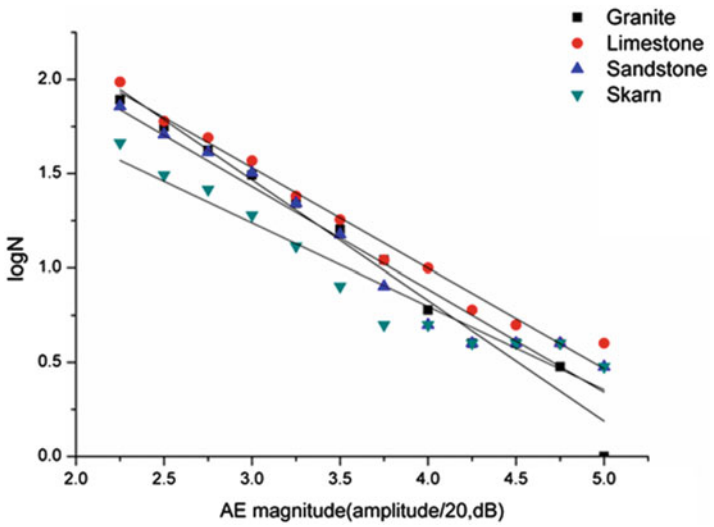

Fig. 2 The relation between the amplitude of the AE hits and their occurrence frequency for the four types of rock samples. *N* is the number of AE hits

Table 1 *B*-value and the goodness-of-fit R^2 of each specimen

	Granite	Limestone	Sandstone	Skarn
B-Value	0.6392	0.5323	0.5444	0.5913
R^2	0.9785	0.9839	0.9581	0.9907

However, under impact loading, small cracks do not have enough time to form because of the significantly shortened loading time and incomplete stress concentration as well as high strength impact; this leads to the emergence of significant cracks and more energy release which results in more wave hits with larger amplitudes and a decrease in the *b*-value.

The distribution of the AE hit amplitudes from the static loading and impact loading tests (Fig. 3) shows that under static loading the majority of hits had an amplitude of around 50 dB. The distribution pattern of the amplitude of the hits is dominated by 50 dB amplitudes and resembles a normal distribution pattern. The amplitude distribution of the hits under impact loading is more dispersed, with more hits of significantly large amplitude; however, the most frequently occurring hits are still the 50 dB amplitude hits. The amplitude-frequency pattern under impact loading is more widely distributed, with a smaller *b*-value.

3.2 B-*Value Analysis of Hits Grouped by Peak Frequency*

The AE wave has a very wide frequency range, from infra-acoustic frequency to supra-acoustic frequency, which can range from several Hz to several MHz. The

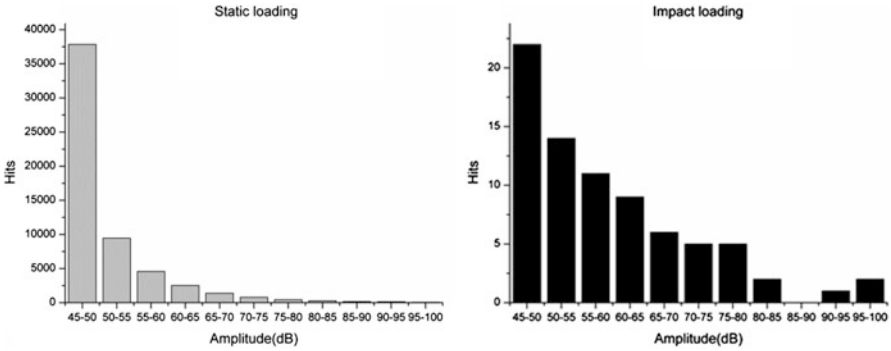

Fig. 3 The amplitude distribution under static loading (*left*) and impact loading (*right*)

AE can be generated from a range of sources, from microscopic dislocation movement to macroscale fractures, with amplitudes between several μV and several 100 mV. Generally, AE signals can be divided into two types, namely, burst type and continuous type. Initiation and propagation of cracks can generate burst-type acoustic waves and plastic deformation can generate continuous acoustic waves [25].

Impact loading can produce stress waves; the AE sensor will detect the signals generated by a stress wave propagating in a rock specimen. Hence, the recorded signals can be those generated by stress waves or by rock fracturing. The signals generated by stress waves in a rock specimen should be similar in waveform and frequency components to the signals recorded on the input elastic pressure bar of the SHPB system. Figure 4 shows the waveform of a typical signal recorded on the input elastic pressure bar. The peak frequency (f_p) was less than 100 kHz for all such signals. Signals with f_p below 100 kHz were also recorded on the rock samples (Fig. 5); these signals have a similar waveform to that of the signals recorded on the input elastic pressure bar. A discussion of these two types of signals can be found in reference [26]. Although 100 kHz cannot be used as a boundary to distinguish the signals generated by stress-wave propagation and those generated by rock fracturing, other measures such as the *b*-value can be used to analyze these signals which have different peak frequencies.

For the *b*-value analysis we divided all the acoustic signals of the rock sample into two groups based on their peak frequency: the hits with $f_p > 100$ kHz and those with $f_p < 100$ kHz. The calculated *b*-values of each group are listed in Table 2; the amplitude-frequency distribution for the four rock types represents a good linear relationship, with $R^2 > 0.9$, which is in line with the *G–R* relationship. The *b*-value of the hits with $f_p < 100$ kHz is smaller than that of the hits with $f_p > 100$ kHz, indicating an even distribution for the amplitudes of the hits with $f_p < 100$ kHz while those with $f_p > 100$ kHz are clustered. The amplitude distribution of the two groups of hits (Fig. 6) shows that the amplitudes of hits with $f_p < 100$ kHz are distributed throughout the amplitude scale range from the 45 dB threshold to the

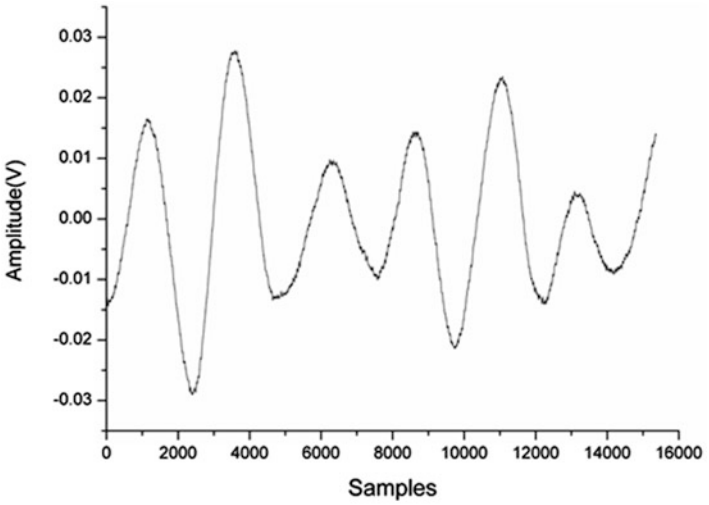

Fig. 4 A typical waveform of a hit recorded on the elastic pressure bar

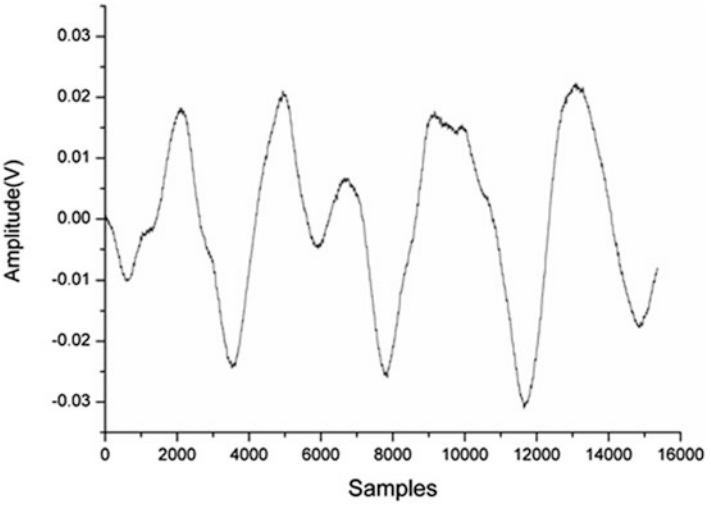

Fig. 5 A typical waveform of a hit from a rock sample with peak frequency less than 100 kHz

Table 2 B-value and the goodness-of-fit R^2 for peak frequencies below and above 100 Hz for four specimen types

	Granite	Limestone	Sandstone	Skarn
$b_{\text{P-FRQ}<100}$	0.5332	0.5258	0.4108	0.4705
R^2	0.9720	0.9704	0.9348	0.9856
$b_{\text{P-FRQ}>100}$	0.7661	0.5678	0.6226	0.8720
R^2	0.9307	0.9742	0.9207	0.9459

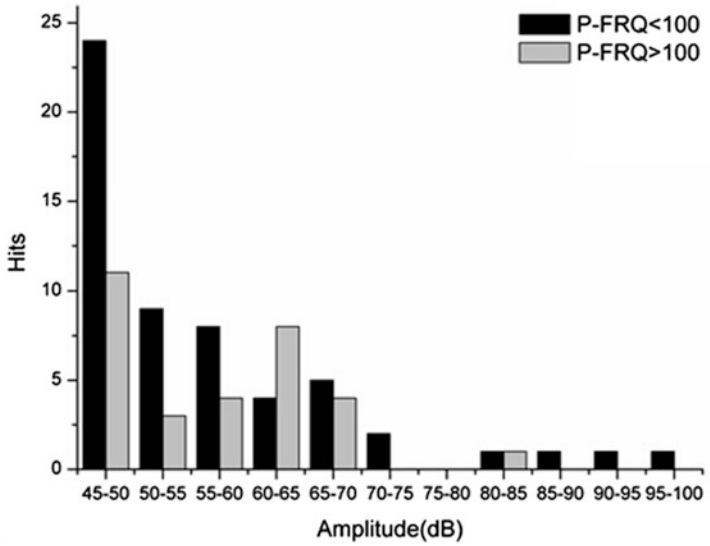

Fig. 6 The amplitude distribution of hits with peak frequencies below (*black bar*) and above (*gray bar*) 100 Hz

100 dB maximum value, while the amplitudes of hits with $f_p > 100$ kHz are mostly in the range of 45–70 dB.

3.3 Analysis of Hb-*Value*

In AE testing, the amplitude is the largest peak in the AE signal waveform. Each sample point of the AE signal waveform corresponds to a voltage magnitude, customarily expressed in decibels relative to 1 μV at the preamplifier input, assuming a 40 dB preamp. For this case, the voltage magnitudes of the AE signal waveform can also be used to calculate the relationship between the occurrence frequency and magnitude of a single signal using the same algorithm as that used to derive the *b*-value; we denote this calculated value the *Hb*-value. The change in *Hb*-value for a series of hits is shown in Fig. 7 for the four rock types; also shown are the corresponding counts. For most of the hits, the magnitude–frequency distribution of their waveform shows a good linear relationship with high goodness of fit.

The first two *Hb*-values (Fig. 7) are always small, especially the first one, which corresponds to the hit with the largest values of amplitude, counts, signal strength, and absolute energy. The waveform of this hit is similar to the ones recorded on the input elastic pressure bar of the SHPB system as well as the frequency spectra. These similarities indicate that this waveform is generated by an impact of stress wave propagating in the rock sample; detailed analysis can be found in our

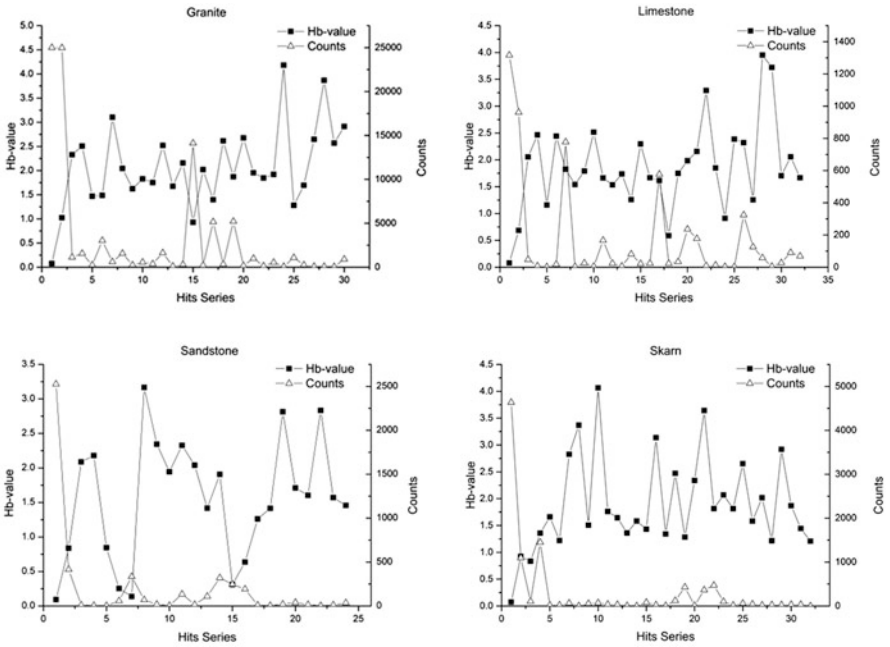

Fig. 7 The *Hb*-value and the corresponding counts for a series of hits in the four rock types

publication [26]. The very small *Hb*-value corresponding to the hit with the largest values of amplitude, counts, signal strength, and absolute energy can be regarded as further evidence that this hit is generated by a stress wave propagating in the rock sample.

4 Conclusions

The *b*-value of rock AE under impact loading is less than 1, which is much smaller than the *b*-value obtained in rock AE tests under static loading. Under impact loading conditions, small cracks do not have enough time to form because of the shortened loading time; incomplete stress concentration as well as high strength impact lead to the emergence of significant cracks and more energy release which results in more high-amplitude wave hits and a decrease in the *b*-value.

The recorded hits were divided based on their peak frequency, corresponding to different *b*-value characteristics. The *b*-values of the hits with $f_p < 100$ kHz were smaller than the *b*-values of the hits with $f_p > 100$ kHz. This suggests that hits with $f_p < 100$ kHz were generated by stress-wave propagation, while those with $f_p > 100$ kHz were generated by rock fracturing under stress-wave loading. Moreover, this also indicates that the rock sample is continuously cracking during the

stress-wave loading process unlike the case of rock samples under static loading where microcracks propagate accompanied by energy accumulation that develops into macroscale damage.

We define the *Hb*-value as the magnitude–frequency distribution of a single hit, which is calculated with the same algorithm used to derive the *b*-value. However, the *Hb*-value does not have a regular pattern in the hits series, except for the one corresponding to the hit with the largest amplitude, counts, signal strength, and absolute energy; this hit is significantly smaller than the others. This may be further evidence that this hit is generated by stress-wave propagation.

Acknowledgments This work is supported by the National Natural Science Foundation of China (Grant Nos. 51204206 and 41272304); the authors are very grateful for the financial support provided by these funds.

References

1. W. Blake, Microseismic applications for mining-a practical guide, [s. l.]:[s. n.], 1982.
2. B. Gutenberg, C.F. Richter, Frequency of earthquakes in California. Bull. Seismol. Soc. Am. **4**, 185–188 (1944)
3. L. Yuanhui, L. Jianpo, Z. Xingdong, Y. Yujiang, Study on b-value and fractal dimension of acoustic emission during rock failure process. Rock Soil Mech. **20**, 2559–2563 (2009)
4. K. Mgoi, Study of elastic cracks caused by the fracture of heterogeneous materials and its relations to earthquakes phenomena. Bull. Earthquake Res. Inst. **40**, 125–173 (1962)
5. C.H. Scholz, The frequency-magnitude relation of microfracturing in rock and its relation to earthquake. Bull. Seismol. Soc. Am. **58**, 399–415 (1968)
6. K. Mogi, *Earthquake Prediction in Japan, Chinese edition translated by Zhuang Cantao* (Seismological Press (in Chinese), Beijing, 1986)
7. N. Warren, G. Latham, An experimental study of thermally induced microfracturing and its relation to volcanic seismicity. J. Geophys. Res. **75**(23), 4455–4464 (1970)
8. F. Yaru, C. Daien, L. Xiaohong, L. Jihan, H. Jinsheng, G. Naiguang, The change of b-value of acoustic emission before ruptures of water-bearing rocks. Earthquake **2**, 2–6 (1986)
9. I.S. Colombo, I.G. Main, M.C. Forde, Assessing damage of reinforced concrete beam using "b-value" analysis of acoustic emission signals. J. Mater. Civ. Eng. **15**, 280–286 (2003)
10. R. Vidya Sagar, S. Shantha Kumar, B.K. Raghu Prasad, Comparison of acoustic emission b-values with strains in reinforced concrete beams for damage evaluation. Bridge Eng. **165**, 233–244 (2012)
11. A. Farhidzadeh, S. Salamone, B. Luna, A. Whittaker, Acoustic emission monitoring of a reinforced concrete shear wall by b-value-based outlier analysis. Struct. Health Monit. **1**, 3–13 (2012)
12. T. Shiotani, K. Fujii, T. Aoki, K. Amou, Evaluation of progressive failure using AE sources and improved b-value on slope model tests. Progr. Acoust. Emiss. **7**, 529–534 (1994)
13. M.V.M.S. Rao, K.J. Prasanna Lakshmi, Analysis of b-value and improved b-value of acoustic emissions accompanying rock fracture. Curr. Sci. **89**, 1577–1582 (2005)
14. Q.I.N. Siqing, L.I. Zaodin, Fractals distribution in space of rock acoustic emission events. Appl. Acoust. **4**, 19–21 (1992)
15. P.R. Sammonds, P.G. Meredith, S.A.F. Murrel, *Modelling the damage evolution in rock containing pore fluid by acoustic emission, Eurock'94* (Balkerna, Rotterdam, The Netherlands, 1994)

16. D.O.N.G. Yuli, X.I.E. Heping, Z.H.A.O. Peng, Study on b-value and fractal dimension D_f of concrete under complete process compression. J. Exp. Mech. **11**, 273–276 (1996)
17. X.L. Lei, Typical phases of pre-failure damage in granitic rocks under differential compression. Geol. Soc. **261**, 11–29 (2006)
18. L.I. Hongyan, K.A.N.G. Lijun, X.U. Zijie, et al., Precursor information analysis on acoustic emission of coal with different outburst proneness. J. China Coal Soc. **39**, 384–388 (2014)
19. Y.X. Zhou, K. Xia, X.B. Li, H.B. Li, G.W. Ma, J. Zhao, Z.L. Zhou, F. Dai, Suggested methods for determining the dynamic strength parameters and mode-I fracture toughness of rock materials. Int. J. Rock Mech. Min. Sci. **49**, 105–112 (2012)
20. S.J.D. Cox, P.G. Meredith, Microcrack formation and material softening in rock measured by monitoring acoustic emission. Int. J. Rock Mech. Min. Sci. Geomech. Abstr. **30**, 11–21 (1993)
21. C.G. Hatton, I.G. Mainand, P.G. Meredith, A comparison of seismic and structural measurements of scaling exponents during tensile sub-critical crack growth. J. Struct. Geol. **15**, 1485–1495 (1993)
22. M.V.M.S. Rao, in *Proceedings of the 14th World Conference on Non-Destructive Testing (14th WCNDT)*, ed by C. G. Krishnadas Nair et al. Significance of AE-based b-value in the study of progressive failure of brittle rock: some examples from recent experiments, vol 4 (Oxford & IBH, New Delhi, 1996), pp. 2463–2467
23. P.R. Sammonds, P.G. Meredith, I.G. Main, Role of pore fluids in the generation of seismic precursors to shear fracture. Nature **359**, 228–230 (1992)
24. X. Lei, K. Kusunose, M.V.M.S. Rao, O. Nishizawa, T. Satoh, Quasi-static fault growth and cracking in homogeneous brittle rocks under triaxial compression using acoustic emission monitoring. J. Geophys. Res. **105**, 6127–6139 (2000)
25. G.T. Shen, *Acoustic emission technology and application* (Science Press, Beijing, 2015)
26. X.L. Liu, X.B. Li, L. Hong, T.B. Yin, M. Rao, Acoustic emission characteristics of rock under impact loading. J. Cent. South Univ. **22**, 3571–3577 (2015)

Evaluation of Acoustic Emission from Damaged CFRP Sheets for Air Industry Applications

M. Bardadyn, R. Karczewski, P. Sobczak, L. Golebiowski, L. Sarniak, K. Paradowski, and A. Zagorski

Abstract In this chapter we propose a new methodology for CFRP and GFRP composite testing. One of the most important factors describing such materials is the shear modulus. The test we have carried out included a shear test with digital image correlation and acoustic emission. We proposed to use the acoustic emission method to determine degradation of fiber-reinforced composites.

In our test we used a plane localization of acoustic emission events to show places where the first stage of degradation occurs. In this test, two different materials and two fiber arrangements were used. On top of that, we introduced a few kinds of damage into materials to check how the degradation changed. We wanted to check if the degradation mechanism is changed with the change of material structure and defect presence.

We proved that the degradation mechanism is different. What is more, we determined which mechanism is the reason of destruction in particular materials. The acoustic emission results presented showed that for −45/45° fiber placement, where fibers are longitudinal to main directions of the loaded force, there are places where stresses are concentrated. For 0/90° fiber placement, where fibers are at the angle of 45° to the main force direction, all fibers are involved in transmission of the force. It was also proved that the acoustic emission is suitable for fiber composite testing. Comparing the acoustic emission results obtained during shear test and computer simulation using the finite element method, we can clearly see that the detected acoustic emission sources are found in places where they were predicted by simulations.

M. Bardadyn (✉) • P. Sobczak • L. Golebiowski • A. Zagorski
Faculty of Materials Science and Technology, Warsaw University of Technology, Woloska 141 Street, 02-507 Warsaw, Poland
e-mail: michal.bardadyn@inmat.pw.edu.pl

R. Karczewski • L. Sarniak • K. Paradowski
Faculty of Materials Science and Technology, Warsaw University of Technology, Woloska 141 Street, 02-507 Warsaw, Poland

Materials Engineers Group Sp. z o. o., Woloska 141 Street, 02-507 Warsaw, Poland
e-mail: lukasz.sarniak@inmat.pw.edu.pl

G. Shen et al. (eds.), *Advances in Acoustic Emission Technology*, Springer Proceedings in Physics 179, DOI 10.1007/978-3-319-29052-2_13

To characterize defects in shear samples, we conducted ultrasonic test and SEM observation. It proved that the mechanical defect influenced layers under the surface. Comparing it with the acoustic emission results, we can conclude that we registered friction which was caused by delamination stemming from the mechanical defect.

1 Introduction

The aerospace industry has always been introducing new technologies and materials. The main idea to develop capacity and durability of such structures was to decrease the weight of materials and keep the strength needed to ensure safe use. The driving force behind the development of technology in this case is also the constant change of the manufacturers' requirements. Another important reason is to create airplanes which are more environmentally friendly, decrease the level of exhaust fumes produced by machines, and use materials that are eco-friendlier. It is why air industry materials have changed so much over the past century.

Materials used for spaceships have to cope with quite serious environmental changes (especially temperature and pressure). Additionally, they are exposed to collisions with different kinds of objects during the flight, e.g., birds and ice crystals, and throughout landing and takeoff, like stones coming from under the wheels. Therefore, materials in such applications are expected to be strong, corrosion resistant, impact resistant, rigid, and durable.

The milestone was the invention of fiber-reinforced plastic composites. First used in civil aircrafts in 1957, composites are the fastest developing type of material now. There are two major types of fiber-reinforced composites used in modern flying structures: glass fiber-reinforced polymers (GFRP) and carbon fiber-reinforced polymers (CFRP). For both types of materials the most important aspect is the direction and placement of fibers [1].

Modern aircrafts are subjected to a number of drawbacks that could lead to failures during the flight. Knowledge about them is collected and analyzed, so that places where such defects occur can be identified. It helps to counteract failures by periodic inspections of most exposed parts.

Design of such structures presupposes that all materials will be subject to shear stress. Consequently, the shear stress parameter is the most crucial criterion describing the material in such application. We identified shear stress using a nondestructive method, i.e., acoustic emission (AE) [2]. AE can be used in structure health monitoring (SHM) and during periodic inspections as well. Taking into account theory, AE entails creation and propagation of elastic waves produced by defects within materials. The source of such waves can be crack, release of internal energy, as well as delamination or fiber breaking in composites. In other words, if there is a defect in material, and the material is loaded, the defect generates detectable elastic waves. On top of that, AE is able to locate the source of waves with the accuracy of centimeters. The main advantage of AE is the ability to examine a whole object using sensors placed on the surface of the examined material.

In this chapter we analyzed the behavior of composite structures exposed to shear stress during static loads using acoustic emission and digital image correlation (DIC) [3]. We used AE to check if this method is able to locate and determine places of damage caused by shear stress. We also prepared simple finite element method (FEM) [4] model to determine the distribution of the stress in glass-epoxy composites.

On top of that, we used ultrasonic testing (UT) to characterize the defects and to check what the AE source was.

2 Pure Shear Stress in the Inclined Section

The shear test method, which we use here, lends itself to determine the shear modulus of thin samples. This test method is most useful for determining the shear modulus of orthotropic materials for which shear modulus cannot be computed from Young's modulus and Poisson's ratios. Shear modulus obtained in this kind of test is the result of planar deformation of the sample.

Pure shear can be represented as a special case of biaxial stress state [5]. Assuming that the cross section is inclined at an angle of 45° to the axis of symmetry, shear stress "τ" equal to the absolute value of the input stress "σ_1" and "σ_2" is the main stress affecting the sample damage. Then, in the shear planes there is the following equation:

$$|\sigma_1| = |\sigma_2| = \sigma = \tau \tag{1}$$

The graphical presentation of this condition is Mohr's circle. The maximum stress shear in the planes inclined at the angle of 45° to the main directions is $\tau_{max} = \pm\sigma$, and the normal stresses in those directions are zero.

The deformation of the square-shape sample is shown in Fig. 1a. Since there is no normal stress at the edges of the sample, the length of edges does not change

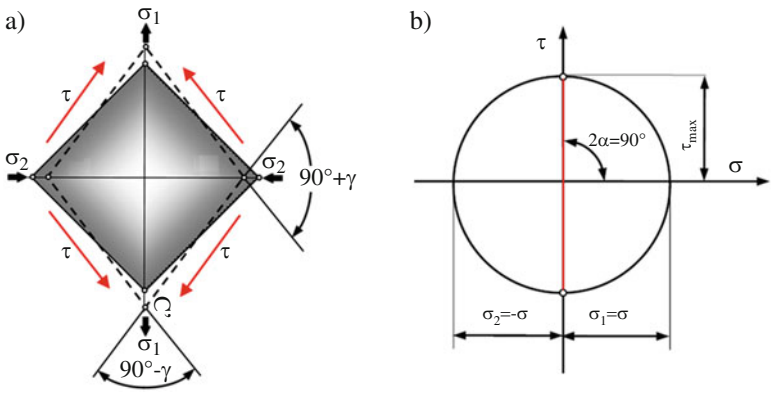

Fig. 1 The biaxial state of stresses: schematic exploration of the dependencies deformation (**a**), Mohr's circle (**b**)

during the test. The vertical diagonal is extended and the horizontal diagonal is shortened. The shape of the deformed element is shown by phantom lines. The angles of the deformed element corners are $(90^\circ + \gamma)$ and $(90^\circ - \gamma)$, where "γ" is the angular deflection. In the elastic strain range, it can be assumed that the angular deflection "γ" is proportional to the shear stress τ:

$$\gamma = \frac{G}{\tau} \tag{2}$$

where G is a shear modulus. Considering pure shear, there is no volume change during the element deformation. The only change is its form. For a square-like sample of the length "a" and the thickness "b," the relationship between shear stress "τ" and applied force "P" is given by the following equation:

$$\tau = \frac{P}{\sqrt{2}ab} \tag{3}$$

3 Tested Material and Testing Method

We have tested two kinds of materials: GFRP and CFRP. Each sample had the thickness of 2.4 mm and side length of 170 mm. There were two kinds of fiber placement: 0/90° and −45/45°. Figure 2 shows the way of cutting samples from composite plates.

We also introduced four kinds of defects into specimens. The samples are labeled as follows:

- LA—Sample without defect
- LA_D—Sample with square delamination (30 × 30 mm)

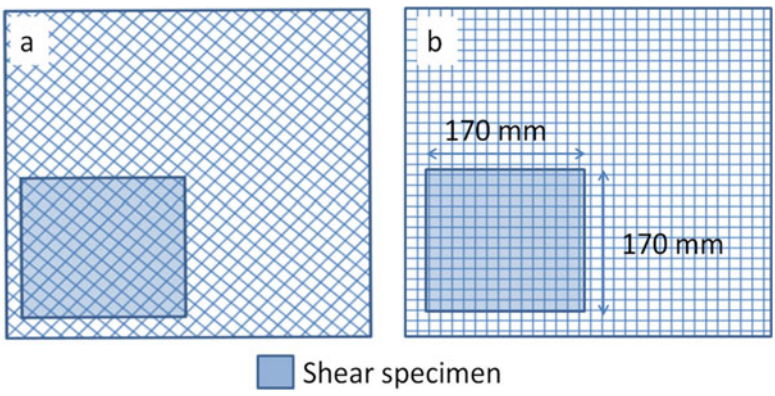

Fig. 2 Shear specimen cutting methodology. (**a**) −45/45°, (**b**) −0/90°

- LA_01—Sample with the drilled hole (8 mm diameter)
- LA_02—Sample with a square cutout (30 × 30 mm)
- LA_ID—Sample with an impact damage (hammer tapping)

A drilled hole was created to simulate a defect produced by the riveting process. Impact damage is a typical defect of such kind of materials. It is very dangerous, because sometimes it is very hard to find from the surface. Delamination usually appears under the surface.

We conducted the shear test using uniaxial static testing machine Zwick/Roell Z250. Thanks to the clamp design, there were two kinds of force applied to the sample: stretching in vertical direction and compressing in horizontal direction. We also placed four VS150-RIC piezoelectric AE sensors on the surface of the tested material. We used AE to identify places where fibers start to crack. We had to use more than one sensor because we wanted to obtain planar localization of AE sources. In this case, sources included matrix and fiber breaks, tightening of the fibers, and friction produced by delaminations. The acoustic test is able to detect all those phenomena.

On the backside, samples were painted to obtain DIC maps. We painted them with black spray and then made black dots. We used two cameras to take photos during the test. After the test, we used VIC-2D software to process the data.

4 Results and Discussion

As mentioned before, we tested two kinds of materials: GFRP −45/45° and CFRP 0/90°. The main idea was to determine differences deriving from various fiber placement. GFRP −45/45° material was introduced with three kinds of defects described above (LA_D, LA_01, and LA_02). In case of CFRP 0/90°, two kinds of defects were used (LA_01 and ID). The results for GFRP −45/450 are shown in Fig. 3.

Shear tests of composite materials were carried out with acoustic emission recording. The measuring instruments used in the study included a multichannel AE measurement system AMSY-5: M6-2 produced by Vallen Systeme GmbH with six dual-channel acoustic signal processor ASIP-2 for recording and processing of AE signal, with software Vallen AE-Suite R2011.1115.1. We used four AE VS150-RIC sensors with resonant frequency $f_s = 150$ kHz. For each AE signal exceeding the threshold value of 59.9 dB, AE parameters were stored. Additionally, transient waveforms of signals with amplitude greater than 59.9 dB are recorded for later more detailed analysis. The sampling rate was set to 10 MHz. We carried out stress measurements with static testing machine Zwick/Roell Z250, Fig. 4.

After the shear test, we prepared FEM simulation to find places where stress concentration occurred. For FEM model, we used maximum stress criterion (biaxial criterion). According to this criterion, a unidirectional composite is not destroyed if the normal stresses σ_1 and σ_2 and the shear stress τ do not exceed the values corresponding to their orientations to the strength [6].

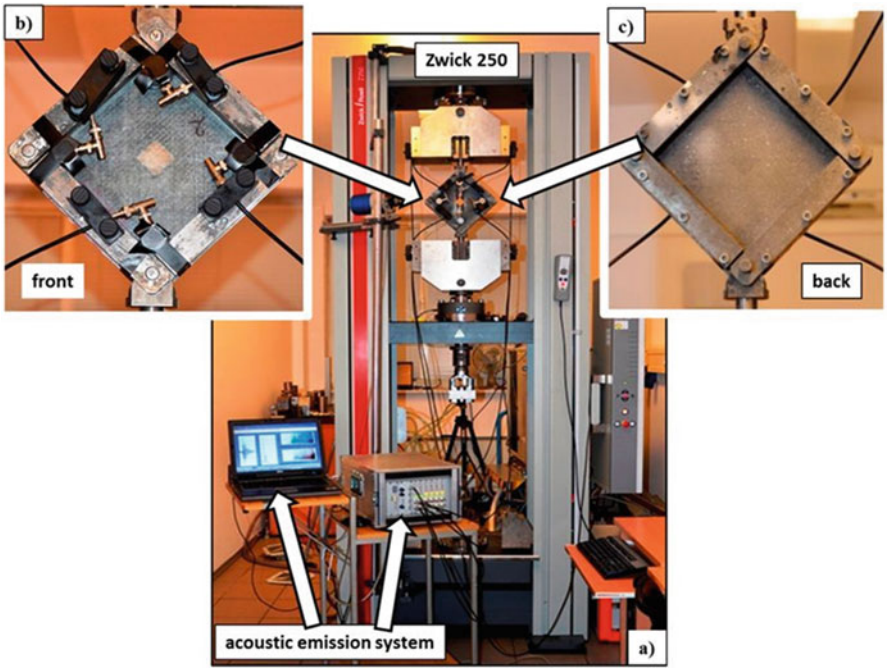

Fig. 3 Shear stress distribution of GFRP −45/45° obtained from FEM simulation

It can be described in the following form:

$$-X_c \leq \sigma_1 \leq X_t \tag{4}$$

$$-Y_c \leq \sigma_2 \leq Y_t \tag{5}$$

$$\tau \leq S \tag{6}$$

where:

X_t—Longitudinal tensile strength
X_c—Longitudinal compressive strength
Y_t—Transverse tensile strength
Y_c—Transverse compressive strength
S—Longitudinal shear strength (shear strength)

Failure criteria for composite laminates are mainly analytical approximations or curve fittings of experimental results. They allow to check the failure of the whole layer. If any of the above conditions are met, it is considered that the material may be damaged. The evolution of independent damage variables begins when the corresponding failure criterion for damage initiation is satisfied. We used the failure criteria of maximum stress, which involve the strength of the matrix in tension and compression, in longitudinal and transverse directions. It will be denoted as X_t, X_c, Y_t, and Y_c, respectively, and in-plane shear strength as S_{LT} [5].

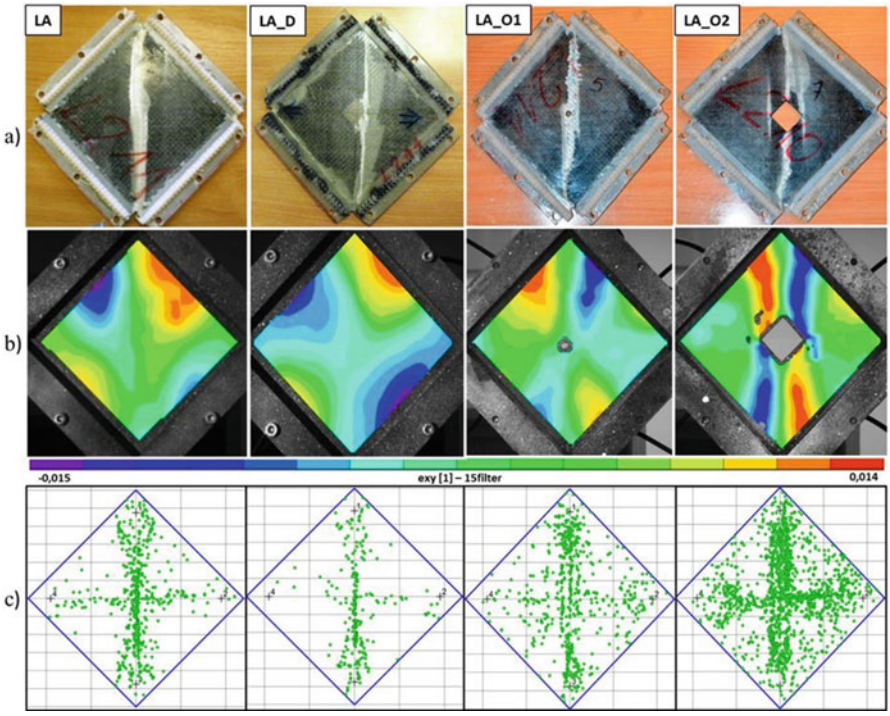

Fig. 4 AE tests bench: (**a**) uniaxial static testing machine Zwick/Roell Z250, AMSY-5 AE system; (**b**) AE VS150-RIC sensors mounted on the sample; (**c**) sample coated with a paint for the measurement of DIC

Table 1 Material properties adopted for the FEM model

Material	EX (Mpa)	EY (Mpa)	EZ (Mpa)	VXY (Mpa)	VYZ (Mpa)	VXZ (Mpa)	GXY (Mpa)	GYZ (Mpa)	GXZ (Mpa)
GFRP	25,000	8000	8000	0.14	0.3	0.3	4000	4000	4000

A geometric model simulating the samples used for testing mechanical properties was developed using the finite element method. Numerical analysis of stresses was carried out using the calculation package ANSYS 13.0. We employed four-node element with 6° of freedom type "shell 181" (Table 1).

In the numerical models a laminar configuration [0/90°] consisting of six layers of unidirectional with a thickness of 0.4 mm was considered. We prepared models of defective sample and the load capacity under shear stresses was tested.

After the shear stress of GFRP −45/45° we can say that there are two axes where stress is concentrated. Those axes are diagonals of samples. As we can see clearly in Fig. 5, AE testing proved that sources of AE signals came from diagonals. On top of that, the test showed that the defects increased AE activity. The most significant

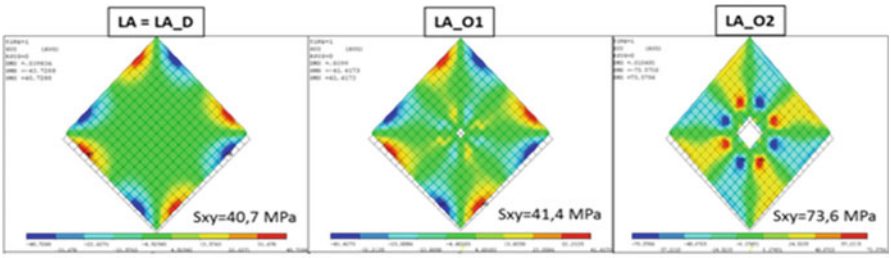

Fig. 5 The results of the shear test for GFRP −45/45°: (**a**) specimens after the test, (**b**) the summary deformation maps obtained by DIC, (**c**) localization of AE events

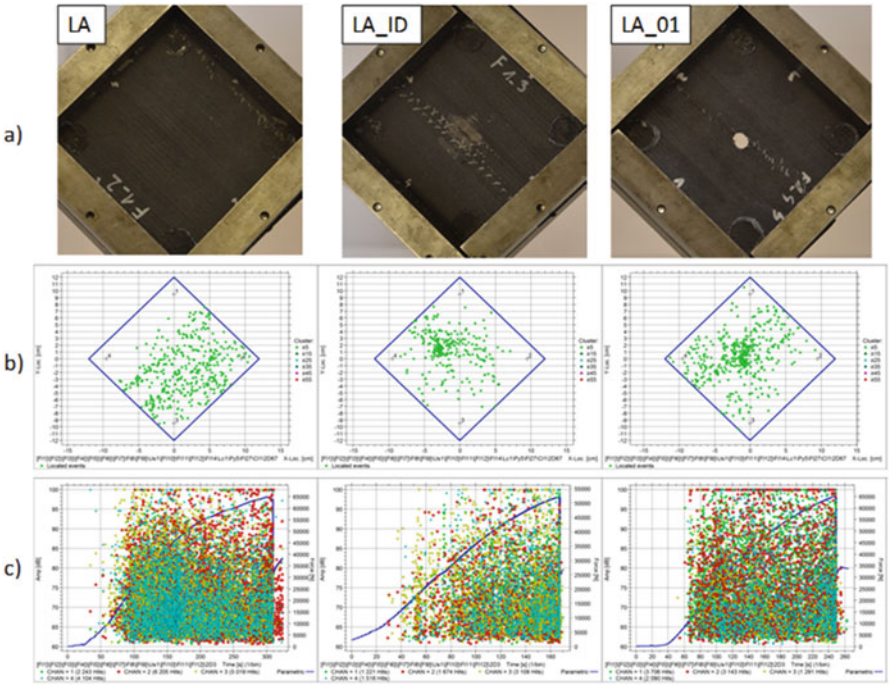

Fig. 6 The results of the shear test for CFRP 0/90°: (**a**) specimens after the test, (**b**) localization of AE events, (**c**) amplitude of localized AE events as a function of a time of loading

change in AE response was caused by the square hole (LA_02). The reason was sharp corners of the defects. Corners of the square were places of crack initiation.

Basic FEM simulation showed that in case of samples we used, the degradation occurred in diagonals' directions (red areas). We can also say that such a fiber direction is improper. Stresses are concentrated and only part of fibers were carrying the loads.

In the second part of the study we tested CFRP 0/90° composite. We assumed that a different fiber arrangement will cause different stress distribution.

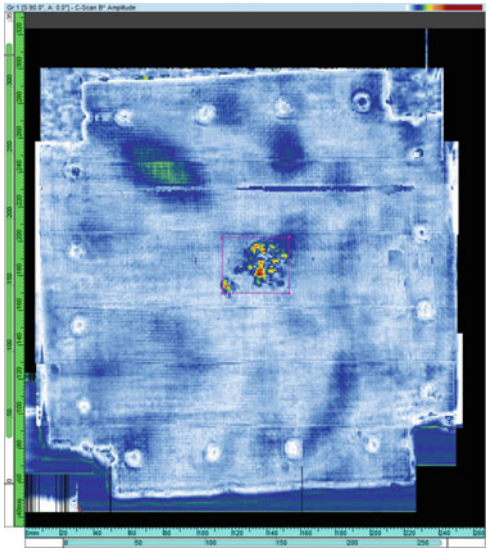

Fig. 7 UT visualization of impact damage (LA_ID)

In Fig. 6b and c we presented localization and intensity of AE signals obtained from CFRP composites, respectively. Compared to GFRP, we can distinguish two degradation types. In case of GFRP samples, degradation occurred locally on diagonals, along the load axis. In case of CFRP, the distribution of AE events is more uniform on the whole area of the sample. The difference is caused by a changed fiber arrangement.

It should be noticed that in the second test the load direction is not longitudinal to the fibers. Thanks to that, more fibers are involved in load transmission. It can also be seen on AE signal localization (Fig. 6b) that the sources are more dispersed. It means that the composite degradation occurs in various places. There is no stress concentration in any particular place or even direction. Even in case of defected samples, degradation is not concentrated in one place. It plays a significant role especially in materials which are used for aircraft, because they are designed to carry shear stress.

In order to characterize the defects, especially impact damage, we conducted the ultrasonic test. As we can see in Fig. 7, in case of impact defect (LA_ID) more than one layer was damaged. Under the surface, there were delaminations and cracks in several layers. Considering the results of the AE, there was a local increase of AE sources, the area of which was similar to the area of mechanical defect. We know also that during the shear test, there was a deformation of the sample. Taking it into account, we can conclude that what we registered by AE was friction between damaged layers or pulling of damaged fibers. The area where we registered more signals was not in the exact middle of the sample, so we incline to say that it was either friction caused by pulled damaged fibers or friction due to mechanical defect in the middle. Not so exact localization of the source might be caused by changed wave propagation due to defects in the composite microstructure.

5 Conclusions

We proved that the acoustic emission method is suitable for testing GFRP and CFRP composites. As it can be seen in Figs. 5 and 6, AE system located AE event sources right where the degradation was suspected. We can conclude that this type of nondestructive test is proper for periodic checks of composite structures. Using it, we can observe advancing degradation, not only the occurrence of irreversible defects. Unfortunately, it is not an ideal solution. To prepare the test, the tested material/construction has to be loaded with some force which is sometimes hard or even impossible to do.

Secondly, we proved that fiber arrangement plays a significant role in such materials. Differences in degradation localization are significant. It is even more important if there is a defect in the sample. For $-45/45^{\circ}$ fiber orientation, if we damage fibers in the diagonal direction, the whole composite is less resistant to stress, because only a part of fibers transfers the applied loads.

Acknowledgments This work was partially supported by the grant no. PBS1/B6/8/2012 (KOMPNDT project) of Polish National Centre for Research and Development (NCBiR).

References

1. J. C. Raia, "Natural fibre composites and its potential as building material," Development Officer, BMTPC, New Delhi.
2. EN 1330-9:2009, "Non-destructive testing. Terminology. Part 9: terms used in acoustic emission testing."
3. M. Stamborska, Application of two-dimensional digital image correlation for measurement of plastic deformations, Transcom (2011), pp. 195–198, ISBN: 978-80-554-0375-5.
4. I. Ivanov, T. Sadowski, Numerical modelling and investigation of plywood progressive failure in CT tests. Comput. Mater. Sci. **45**, 729–734 (2009)
5. M. Zochowski, A. Jaworski, G. Krzesinski, T. Zagrajek, Mechanika materiałów i konstrukcji Tom 2, wydawnictwo: Oficyna Wydawnicza Politechniki Warszawskiej (2013), p. 175.
6. F. Grexa, D. Poutch, H. Manikova, A. Martvonova, A. Bartekova, Intumescence in fire retardancy of lignocellulosic panels. Polym. Degrad. Stab. **82**, 373–377 (2003)

Acoustic Emission Study of Ti–Ni Shape-Memory Alloy in Loading–Unloading

Hongyan Xing, Cheng Zhu, Yasunari Tamari, Gang Qi, and Shuichi Miyazaki

Abstract Stress-induced martensite transformation in Ti–Ni shape-memory alloys is a well-known phenomenon. In this work, acoustic emission (AE) data acquisition was conducted simultaneously with mechanical testing (loading–unloading) at room temperature. In addition to the mechanical properties of the Ti–Ni shape-memory alloy, the AE parameters of the specimen tensile process were analyzed. The results showed that AE parameters such as count, amplitude, and energy can indicate the damage process.

1 Introduction

Acoustic emission (AE) is a method for observing rapid dynamic material processes with elastic waves. The technique has rapidly gained attention and is being extensively explored as a tool for investigating the micromechanics of deformation and fracture during mechanical testing [1, 2]. It has also been applied as a nondestructive evaluation technique for detecting and locating flaws in mechanical structures that are able to predict stress and premature failure [2–4]. Shape-memory alloys are widely used in engineering applications because of their high superelasticity [5–7]. AE signals have been observed in superelasticity [8–10], which occurs by the stress-induced martensitic transformation during deformation of the austenite phase.

H. Xing (✉) • C. Zhu • G. Qi
College of Mechanical Engineering, Tianjin University of Science and Technology, Tianjin 300222, China

Tianjin Key Laboratory of Integrated Design and On-line Monitoring for Light Industry & Food Machinery and Equipment, Tianjin 300222, People's Republic of China
e-mail: xhy02@126.com

Y. Tamari • S. Miyazaki
Institute of Materials Science, University of Tsukuba, Tsukuba, Ibaraki 305-8573, Japan

G. Shen et al. (eds.), *Advances in Acoustic Emission Technology*, Springer Proceedings in Physics 179, DOI 10.1007/978-3-319-29052-2_14

In this study, stress-induced phase transformations were evaluated by examining the signal characteristic parameters of the AE in order to understand the characteristics of the Ti–Ni alloy phase change process.

2 Experimental Methods

2.1 Materials and Specimens

The test materials in this experiment were provided by the Miyazaki-Kim Laboratory of Tsukuba University, Japan. The chemical composition of the experimental material is 49.1Ti–50.5Ni–0.4Fe (at %). The shape of the sheet specimen (thickness of 1 mm) is shown in Fig. 1. The martensitic transformation was monitored by thermal measurement with a differential scanning calorimeter, the results of which confirmed that the sample was 100% austenite at room temperature. Tensile testing was carried out at a constant crosshead velocity of 0.5 mm min^{-1}, and showed superelasticity. When the tensile stress is 530MPa, the load is finished, then unload is beginning, when the stress reached 20MPa, the cycle is over, and in all processing, AE signal is also observed.

2.2 AE Measurement

All testing of mechanical properties was performed on a computer-controlled electronic universal testing machine (model MTS E45), and the entire process was monitored using the Micro-II Digital AE system (Physical Acoustics Corporation, NJ, USA). During the experiment, two sensor probes were attached to the sample surface with a coupling agent. A schematic of the experimental set-up, which consisted of a sensor, an amplifier, a signal conditioner, and an oscilloscope connected in series in that order, is shown in Fig. 2. This measurement set-up was designed for the purpose of counting the number of AE signals. These AE signals, including the fundamental parameters (e.g., rise time, duration, count, energy, and amplitude) derived from the waveforms, were digitized, recorded, and stored in a large data set.

The loading and unloading process (the equal displacement) is controlled by computer. The loading and unloading speed of the material testing machine was set to 0.5 mm min^{-1} uniform stretching. In this study, interference signals were eliminated by setting an appropriate acquisition threshold. Mechanical noise was filtered using a threshold value of 30 dB, below which no detectable AE signals exist at zero loading. The preamplifier gain was set at 40 dB. Emission signals were synchronously acquired by the emission acquisition system at a sampling rate of one megasample per second.

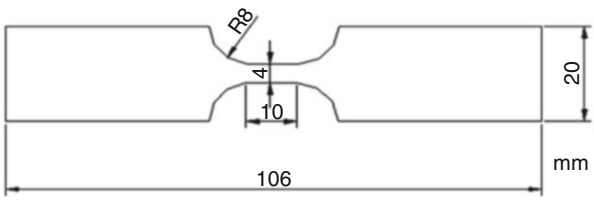

Fig. 1 Shape and the size of the specimen

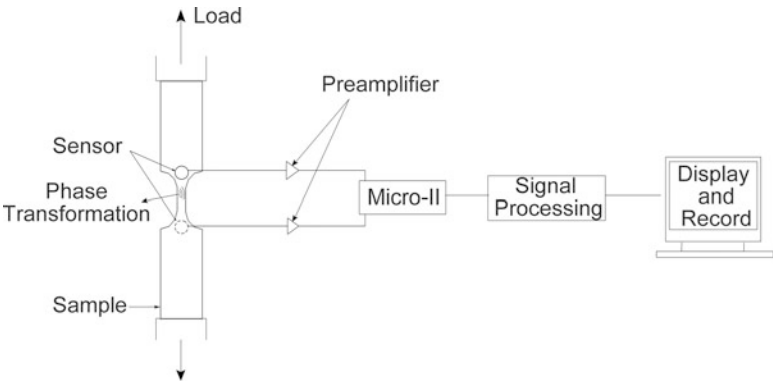

Fig. 2 Block diagram of the two-sensor method for locating the source of the acoustic emission signal

3 Results and Discussion

3.1 Characterization of AE Signals during Loading

The AE and stress–strain curves were measured simultaneously. Figure 3 shows the count and the stress–strain curve during loading. The AE count displays the discrete distributions as load increases, with the total number of count signals reaching 2094. Based on the distribution pattern of the count signals, the entire stretching process can be divided into three stages, with corresponding strain ranges of 4.2–5.8%, 8–12.1%, and 16–18% for stages I, II, and III, respectively. The AE signals illustrate the microscopic changes inside the materials, which were found to be significant. Thus the AE study of shape-memory alloys is entirely feasible, reflecting the martensite transformation in the internal materials over time.

Figure 4 shows the amplitude and stress–strain curve during loading. Here, the AE signals can be clearly seen during the various stages. A large number of AE signals are observed during loading, and the amplitude changes as the load is increased. The stretching intensity during the various stages of the AE signals is clearly shown. The signal amplitudes were concentrated in a certain range of 30 dB to 45 dB, as shown as Fig. 4. Higher signal amplitude was found in the strain from 8% to 12.1%, and the maximum value reached 79 dB.

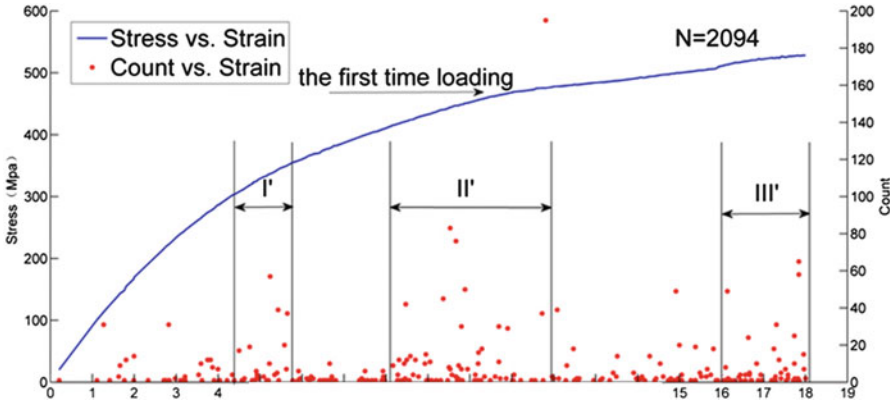

Fig. 3 The stress–strain curve and the count of AE measured during loading

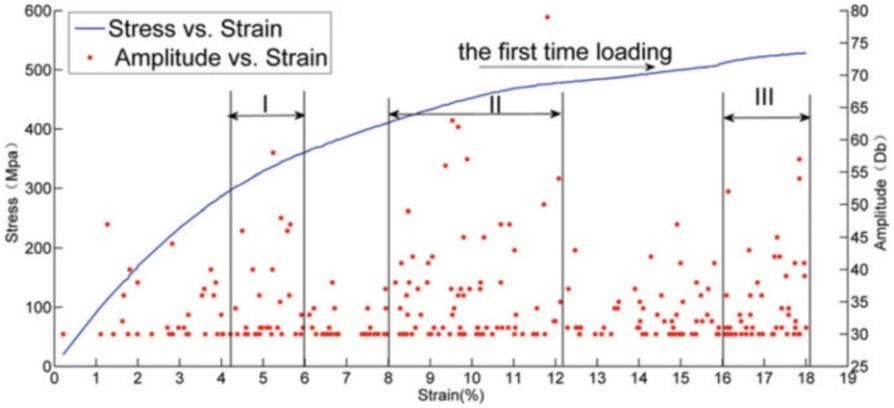

Fig. 4 The stress–strain curve and the amplitude of AE measured during loading

Figure 5 shows the relationship between the absolute energy of the signals and the stress–strain during the loading process. The sum of the absolute energy emitted is 98,211. It can be seen from the graph that most of the AE signals are very small, almost close to zero. However, at different stages, the larger AE energy values appear. The absolute energy values of the three peak signals were 701, 8.86×10^4 and 774.5, respectively. There was a large strain energy signal (in order to better reflect the other signal, this energy value is labeled separately) at 11.81%. The AE energy signal is directly related to the important physical parameters (mechanical energy, strain rate, deformation mechanism, etc.).

In summary, from Fig. 3 and 4, it can be seen that all of the AE signal can be divided into three stages by monitoring the loading process, and the signal distribution trends appear in the three stages are consistent. It showed that the AE signals

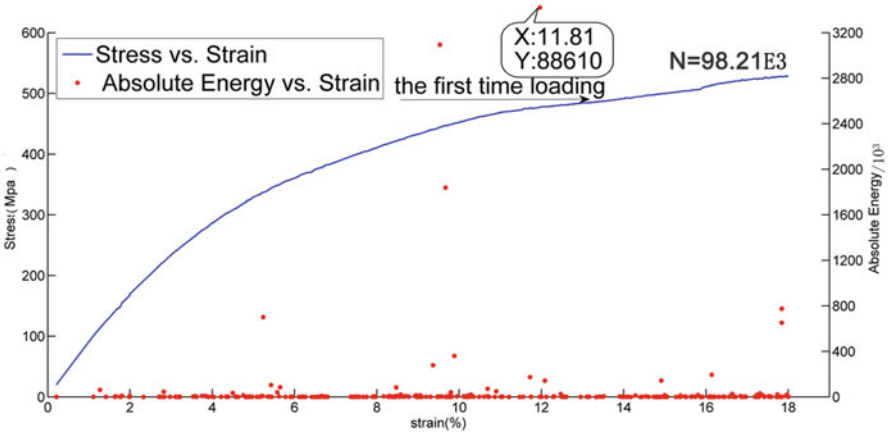

Fig. 5 The stress–strain curve and the count of AE measured during loading

is burst-type signals during the loading, then the signal amplitude and count strength are bigger, at the same time the energy signal occur bigger peak in the three stages. It is due to the deformation of the material lattice [11–13]. The AE signals were active, so the count and amplitude generally increased through the progression of the three stages. These three stages can be characterized as corresponding to the stress-induced *R* phase transformation (I), the stress-induced martensite transformation (II), and the martensite growth phase (III).

3.2 Characterization of AE Signals during Unloading

Figure 6 shows the count and the stress–strain curve during unloading. Here, the number and size of signals differs significantly different from that during loading, with a total of only 51 count signals. The size of a single signal is between 1 and 2, reflecting the significant reduction in the amount and frequency of AE events during unloading compared to loading. The microscopic changes in the internal structure of the material thus clearly differ from those during loading.

Figure 7 shows the amplitude and the stress–strain curve during unloading, where the AE signals during the various stages are clearly observed. Fewer AE signals were observed during unloading, with most located in the signal threshold at 30 dB. High amplitude was observed only at a strain of 8.5%, as shown as Fig. 7, and the maximum value reached 50 dB.

Figure 8 shows the relationship between the absolute energy signals and the stress–strain during the process of unloading. Here, the energy during the entire process is very low, essentially zero, with accumulated energy of only 25.62. The proportion of AE energy signals was lower during unloading than during loading.

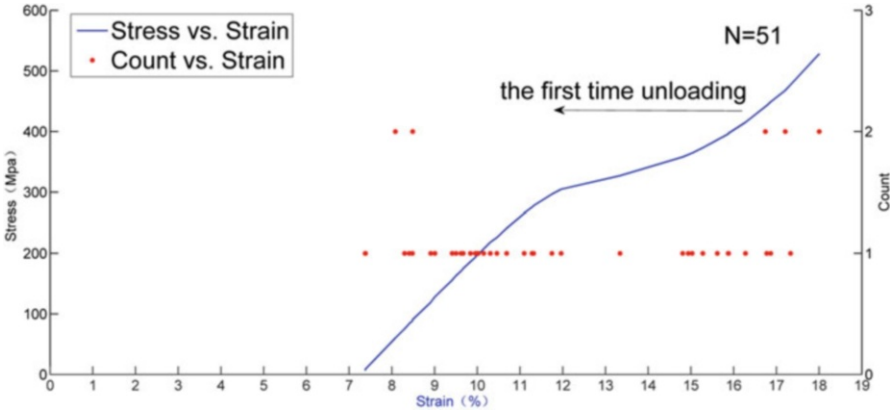

Fig. 6 The stress–strain curve and the count of AE measured during unloading

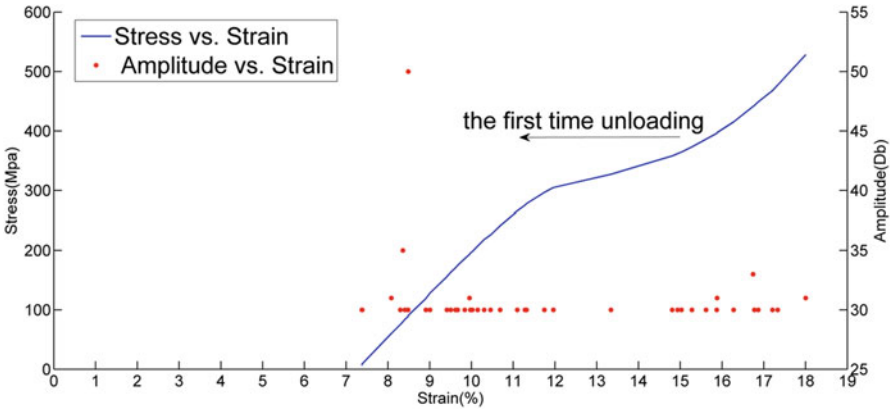

Fig. 7 The stress–strain curve and the amplitude of AE measured during unloading

High energy was observed only at a strain of 8.5%, as shown as Fig. 8, and the maximum value reached 18.12. This indicates that the energy released was much higher during loading than unloading.

4 Conclusions

In this study we have proposed a method for using the AE signal of a shape-memory alloy to monitor stress-induced martensite transformation. The following conclusions may be made:

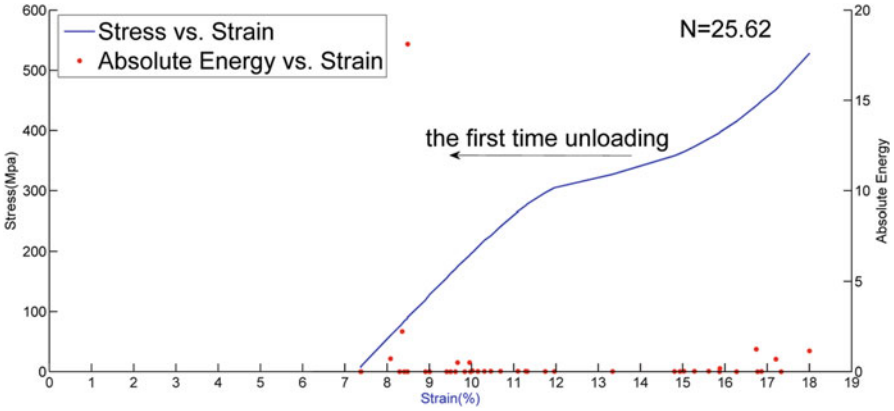

Fig. 8 The stress–strain curve and the count of AE measured during loading

1. The AE signal was clearly confirmed during both the loading and unloading processes. The number of AE counts was significantly higher during loading than during unloading.
2. The number of AE signals in unloading was less than loading. This was due to having residual deformation in the material, the inverse transformation of martensiteand is less, it also lead to the reduction of the strain energy.
3. According to the AE signals during loading, the deformation of material can be divided into three stages: the stress-induced *R* phase transformation (I), the stress-induced martensite transformation (II), and the growth of the martensite phase (III).

Acknowledgments This investigation was supported by the National Natural Science Foundation of China under Grant No. 11272234. The authors also thank the Miyazaki-Kim Laboratory, University of Tsukuba, Japan, for sample preparation and conditioning.

References

1. M. Enoki, S. Ohtake, T. Kishi, Classification of micro-fracture process type in glass matrix composites by quantitative acoustic emission method. Mater. Trans. **42**(1), 108–113 (2001)
2. Smagin G, Nonlinear absorption of longitudinal elastic waves in dislocationless crystals. In: Proceedings of the 1999 I.E. Ultrasonic Symposium (1999), vol. 1, pp. 553–556.
3. J.A. Simmons, H.N.G. Wadley, Theory of acoustic emission from phase transformations. J. Res. Natl. Bur. Stand. **89**(1), 55–64 (1984)
4. H.N.G. Wadley, R. Mehrabian, Acoustic emission for materials processing. Mater. Sci. Eng. **65**, 245–263 (1984)
5. E. Vives, D. Soto-Parra, L. Manosa, R. Romero, A. Planes, Driving-induced crossover in the avalanche criticality of martensitic transitions. Phys. Rev. B **80**, 180101 (2009)

6. C.M. Hwang, M. Meichle, M.B. Salamon, et al., Transformation behaviors of a Ti50Ni47Fe3 alloy II. Subsequent premartensitic behavior and the commensurate phase. Philos. Mag. A. **47**, 31–36 (1983)
7. G.B. Olson, M. Cohen, in *Dislocation in Solids*, ed. by F. R. N. Nabarro. Dislocation theory of martensitic transformations, vol 7 (Eslevier, New York, 1986), pp. 297–407
8. A. Planes, L. Manosa, E. Vivea, Acoustic emission in martensitic transformations. J. Alloys Compd. **577S**, S699–S704 (2013)
9. T. Cernoch, M. Landa, V. Novák, P. Sedlák, P. Šittner, Acoustic characterization of the elastic properties of austenite phase and martensitic transformations in CuAlNi shape memory alloy. J. Alloys Compd. **378**, 140–144 (2004)
10. M. Shaira, N. Godin, P. Guy, L. Vanel, J. Courbon, Evaluation of the strain-induced martensitic transformation by acoustic emission monitoring in 304L austenitic stainless steel: Identification of the AE signature of the martensitic transformation and power-law statistics. Mater. Sci. Eng. A **492**, 392–399 (2008)
11. Y. Liua, T. Geraldine, S. Miyazakib, Deformation-induced martensite stabilisation in [1 0 0] single-crystalline Ni–Ti. Mater. Sci. Eng. A **438–440**, 612–616 (2006)
12. A. Vinogradov, A. Lazarev, M. Linderov, A. Weidner, H. Biermann, Kinetics of deformation processes in high-alloyed cast transformation-induced plasticity/twinning-induced plasticity steels determined by acoustic emission and scanning electron microscopy: influence of austenite stability on deformation mechanisms. Acta Mater. **61**, 2434–2449 (2013)
13. B. Strnade, S. Ohashi, H. Ohtsuka, T. Ishihara, S. Miyazaki, Cyclic stress-strain characteristics of Ti–Ni and Ti–Ni–Cu shape memory alloys. Mater. Sci. Eng. A **202**, 148–156 (1995)

Glass Fiber-Reinforced Plastic Composite Acoustic Emission Signal Detection and Source Localization

Qiang Wang, Xiaohong Gu, Xinwei Fan, and Rongyao Ye

Abstract This chapter investigates failure process in glass fiber-reinforced plastics (GFRP) using acoustic emission (AE) technique. The GFRP panels were tested in three-point bending in a series of loading–unloading cycles with the experimental platform consisting of WDW-100 universal testing machine and Physical Acoustic Corporation acoustic emission instrument. Parameter analysis and wavelet packet decomposition were used to process collected AE signals accomplished with damage process. Moreover, according to time reversal operator, AE source localization method was tested in GFRP panel with one AE sensor. The imaging results of impact localization have shown that it is able to detect impact point position in complex anisotropic GFRP structure.

1 Introduction

Glass fiber-reinforced plastic (GFRP) composite materials are widely used in the field of aerospace, construction, and special equipment with its high specific strength, and corrosion resistance. Because of complicated manufacturing process and harsh working conditions of GFRP composite, they are not immune to different structural defects. Since the composites are microscopically inhomogeneous represented by spatially irregular array of fiber and matrix, statistical distributions of fiber strength as well as the defects are arising mainly from the manufacturing process. Over time, these defects grow and lead to a catastrophic failure of the structure [1]. Acoustic emission (AE) technology is a dynamic nondestructive testing technology, which is able to analyze the damage process of GFRP timely and effectively. Previous studies on AE monitoring of GFRP just have focused on

Q. Wang (✉) • X. Fan • R. Ye
Department of Quality and Safety Engineering, China Jiliang University, Hangzhou 310018, China
e-mail: qiangwang@cjlu.edu.cn

X. Gu
Department of Mechanical and Electrical Engineering, China Jiliang University, Hangzhou 310018, China
e-mail: xhgu@cjlu.edu.cn

G. Shen et al. (eds.), *Advances in Acoustic Emission Technology*, Springer Proceedings in Physics 179, DOI 10.1007/978-3-319-29052-2_15

AE signals due to the structures being subjected to cracking under service loads. The significant advantage of AE over other NDE techniques lies in the fact that it is passive, which means that the information detected comes from localized sources (i.e., plastic deformation, cracking, corrosion within the structure provided that some form of external loading is provided) [2].

The AE signals from GFRP composites are collected during the standard quasi-static tensile testing and transformed by the Daubechies discrete wavelets. In the study of GFR composite fracture behavior, classical linear fracture mechanics method is used for comparison [3, 4]. The experimental investigations of thin-walled channel section column GFRP subjected to static compression are described by Kubiak et al. [5]. The acoustic emission-aided experimental tests of composite columns under compression have proven that the AE method is useful in monitoring the damage along the whole loading path—both critical and post-critical. Some representative features such as the energy, counting, and amplitude are extracted with the load history to study the controlling failure mechanisms of composites. The acoustic emission method was allowed to investigate the behavior of composite structures in the phase prior to their collapse. Ten glass-reinforced, rubber-toughened polymer laminate panels were tested in three-point bending in a series of loading–unloading cycles, with increasing deflection. The AE was monitored by four sensors on the compressive side of the GFRP samples [6]. Furthermore, influence of attenuation on acoustic emission signals in carbon fiber-reinforced polymer (CFRP) cross-ply and quasi-isotropic panels is examined. The AE signals generated by damage mechanisms are modified as they propagate across composite laminates [7].

The conventional AE source localization is based on the arrival time at a number of AE sensors. Based on the arrival time differences, observed in an array of three sensors, an exact solution for the configuration of three sensors in a planar surface was derived [8]. However, it often happens that AE waves are not clearly detected, resulting in a failure of source location. The two-dimensional source location with two AE sensors by using wavelet transform for thin CFRP plate was proposed to improve location accuracy [9].

To dispersive and angular dependent group velocity, multiple scattering, boundary reflections, and mode conversion in geometrically complex composite structures, the TOA will cause the wrong results. Recently, acoustic emission source localization method was examined through a time reversal (TR) process [10]. In a time reversal acoustic experiment, an input signal can be focused back on the original source if the output received by a set of transducers is time reversed and emitted back to the excitation point. The idea of using TR as a focusing method for impact source localization was proposed by Ing et al. [11], in which a prior knowledge of the wave velocity about the properties and structures of the specimen and the transducer was not required. The TR approach exploits the superposition principle in a homogenous medium, while the Rayleigh's reciprocity theorem utilizes the equation of motion and the stress–strain relation in the space-frequency domain to obtain the Green's function. Time reversal and reciprocal time reversal are applied to achieve the focusing of the source with high resolution in

geometrically complex anisotropic structure with diffuse field condition (a dissipative stiffened carbon-fiber composite panel) [12, 13]. Also the impact localization of a composite plate using TR and inverse filtering focusing with a single receiving transducer was discussed in [14].

The purpose of this work is to analyze AE signal characteristics during GFRP total damaging process. The GFRP panels were tested in three-point bending in a series of loading–unloading cycles, and the fiber-damaging AE signal was explored with hit strength and wavelet packet decomposition (WPD). After AE signal WPD, the feature packets of AE signals in time-frequency domain were extracted. Lastly, the TR for acoustic emission source localization with one AE sensor test was carried out in GFRP panel (80 × 80 cm).

2 Methods

2.1 AE Signal Characteristics Based on WPT

Wavelet packet analysis is an extension of wavelet analysis. It is a multilevel decomposition in whole frequency bands (including the high-frequency and the low-frequency parts). It can achieve effective separation of useful information and unwanted information of acoustic emission signal. The wavelet packet transform (WPT) decomposed the signal utilizing both low-frequency and high-frequency components [15]. This flexibility of a rich collection of abundant information with arbitrary joint time-frequency resolution allowed extraction of features that combine nonstationary and stationary characteristic. Let acoustic emission signal $S(t)$ be the digitized signal in the time domain with length N; the value of N must be a power of two. Db4 wavelet packet basis (*Daubechies* series with $N = 5$) is selected to decompose signal. If signal is directly decomposed into three or more levels with AE signals, it will produce 2^3 packets or more packets. The frequency resolution is sensitive enough to different GFRP fiber fracture conditions, but it induces high computational cost and reduces classification speed in application [15]:

$$\begin{cases} d^{(\mathrm{j}+1,2n)} = \sum_l h_{2j-k} d_l^{(j,n)} \\ d^{(\mathrm{j}+1,2n+1)} = \sum_l g_{2l-k} d_l^{(j,n)} \end{cases}, \tag{1}$$

$d^{(j,n)}$ is the nth wavelet packet coefficient in the jth level; j is a positive integer; and $n = 0, 1, \ldots, 2^{i-1}$; l and k are parameters related to the scaling function with compact support; and g and h are wavelet filters related to wavelet functions and scaling functions. After being decomposed, each wavelet packet corresponds to a specific sub-band and contains different information of target signals with different resolutions and different time windows.

The energy $E_{j,n}$ of each frequency band signal in the jth level is as follows:

$$E_{jn} = \int \left|S_{jn}(t)\right|^2 dt = \sum_{k=1}^{n} |x_{nk}|^2, \tag{2}$$

where S_{jn} is the reconstructed signal of $d^{(j,n)}$, and x_{nk} ($n = 0, 1, \ldots, 2^{i-1}$, $k = 0, 1, \ldots$) represents discrete amplitude of the reconstructed data.

2.2 AE Source Localization Based on TR

Based on the principle of time reversal invariance and spatial reciprocity of the acoustic wave equation in a lossless medium, in a TR experiment, the elastic waves diverging from a point-like target can be focused back to the original source if the output measured by a set of transducers is time reversed and reemitted back onto the excitation point. Nevertheless, a perfect localization would require a totally covering array of sensors (closed cavity), which is impossible to obtain in practice [12]. Jeong et al. have proposed the impact source localization method [14], which includes three steps. Firstly, the impulse response functions are obtained by hitting every grid within the composite panel grid area (in Fig. 1). The impulse response functions are received by AE sensor in a fixed position and stored in a database. Secondly, for an actual AE event happening at any grid point, then the impact signal was gathered by the AE sensor. Thirdly, the actual AE signal is processed by time reversal and multiplied by impulse response functions. The grid with the maximum amplitude (focus point) is the AE source localization.

2.2.1 The Propagation Operator H

The AE source localization test was performed in a GFRP composite panel (anisotropic material). According to reference [12], the specimen region of interest was divided into $M = 12 \times 5$ excitation points distributed along a regular grid interval in Fig. 1. At each point, the AE was generated by impact loads. The hammer was used to impact at each grid point and the corresponding impulse response function at a receiving AE sensor was gathered.

Due to linearity, the acoustic field measured by the AE sensor for the mth excitation point is given by [13]:

$$f(t) = \sum_{m=1}^{M} \mathbf{h}_m(t) * \mathbf{e}_m(t) = \int_{-\infty}^{+\infty} \sum_{m=1}^{M} \mathbf{h}_m(\tau) * \mathbf{e}_m(t-\tau) \mathrm{d}\tau, \tag{3}$$

where * is a temporal convolution operator, $\mathbf{e}_m(t)$ is the input signal, and $\mathbf{h}_m(t)$ is the signal received on the mth control point after a temporal Dirac function is applied

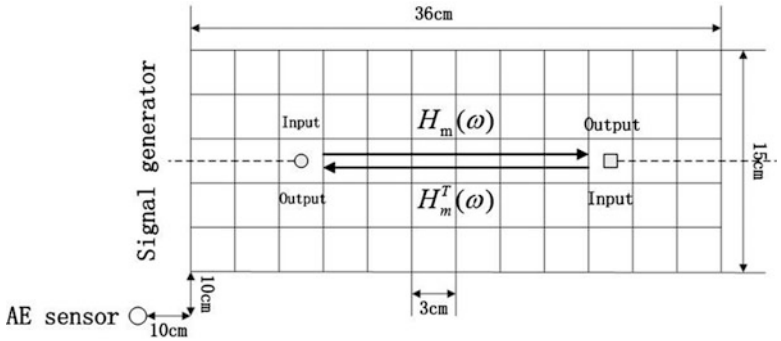

Fig. 1 Acoustic emission experimental layout of composite material

on the transducer (impulse response function). M is the number of excitation points. This response includes all the propagation effects through the medium under investigation. The $f(t)$ is the output signal measured by the transducer at each instant in time.

A temporal Fourier transform leads to the following relation, and (3) leads to the simplified matrix form [12]:

$$F(\omega) = \sum_{m=1}^{M} \mathbf{H}_m(\omega)\mathbf{E}_m(\omega). \tag{4}$$

The transfer matrix $\mathbf{H}_m(\omega)$ describes the propagation in the medium from the array to the set of excitation points and thus is called the propagation operator, which is Fourier transform of the Green's function.

Due to the spatial reciprocity, the equation can be written as, if we regard the input signal $\mathbf{E}_m(\omega)$ as output signal $F(\omega)$,

$$\mathbf{E}_m(\omega) = \mathbf{H}_m^T(\omega)F(\omega). \tag{5}$$

The transfer matrix $\mathbf{H}_m^T(\omega)$ is the transpose of $\mathbf{H}_m(\omega)$, which describes the propagation in the medium between the transducer and the excitation points (in Fig. 1):

$$\mathbf{E}_m(\omega) = \mathbf{H}_m^T(\omega)F(\omega). \tag{6}$$

Therefore, the M signals representing a library of impulse responses $\mathbf{H}_m(\omega)$ of the GFRP structure were recorded by AE sensor and further recorded by the computer.

2.2.2 Time Reversal Method

Our object is to focus a short pulse in the mth element of control array (60 impulse points). According to (4), the acoustic wave received by AE transducer to the actual impact event at $m0$ point:

$$F_{m0}(\omega) = \mathbf{H}_{m0}(\omega)\mathbf{E}_{m0}(\omega). \tag{7}$$

A time reversal operation of the impulse transform function $\mathbf{h}_{m0}(-t)$ in the time domain is equivalent to taking complex conjugation in the Fourier domain $\mathbf{h}^*_{m0}(\omega)$ where the asterisk notates the complex conjugation; then we can calculate the signals received on the AE sensor after propagation as

$$F^*_{m0}(\omega) = \mathbf{H}^*_{m0}(\omega)^*_{m0}(\omega) = \mathbf{H}^*_{m0}(\omega)\mathbf{E}_{m0}(\omega). \tag{8}$$

Based on (6) and (8), after time reversal emission and propagation, the new acoustic source focusing point is [13]:

$$\mathbf{E}_{TR}(\omega) = \mathbf{H}^T_m(\omega)F^*_{m0}(\omega) = \mathbf{H}^T_m(\omega)\mathbf{H}^*_{m0}(\omega)\mathbf{E}_{m0}(\omega), \tag{9}$$

where $\mathbf{H}^T_m(\omega)\mathbf{H}^*_{m0}(\omega)$ is time reversal operator, when $m_0 = m$, $\mathbf{E}_{TR}(\omega)$ has a maximum value at the focus point, which is related to the acoustic emission source location [12].

3 GFRP AE Signal Testing Experiment

The tested GFRP composite panel was fabricated from Enric Energy Equipment Holdings Limited. The GFRP winding processing is shown in Fig. 2. An AE suite manufactured by Physical Acoustic Corporation is used. The R15I-AST piezoelectric AE sensors are used with an operating frequency range of 50–400 kHz. The sample damaging acoustic emission was detected by two PAC transducers (Fig. 3), with integral preamplifiers, connected to a Physical Acoustics four-channel PCI system. The gain selector of the preamplifier was set to 40 dB. The test sampling rate was 1 MHz with 16 bits of resolution between 10 and 100 dB. The acquisition parameters for the material are calibrated using the pencil lead break test: a pencil break is broken on the surface of the specimen and the acquisition parameters are adjusted so that the signal is well defined.

According to the national code of GB/T1449-2005, the three-point bending experiments with glass fiber specimens were achieved in the condition of two types of loading rate, respectively, 2 and 10 mm/min. Two panels were subjected to three-point bending as shown in Fig. 3, using a WDW-100 universal testing machine. To avoid breaking the fiber near the holders, each end of the sample was glued to the sample holder.

Fig. 2 The reinforced glass fiber-winding process

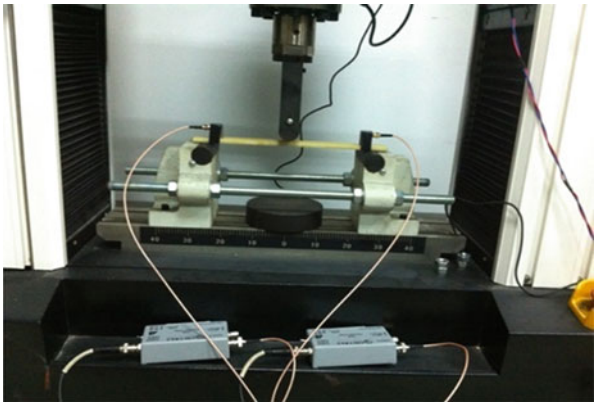

Fig. 3 Schematic of specimen three-point bending loading

3.1 GFPR AE Signal Characteristics

The AE signals monitored contain complicated information on the fracture process. AE signals were captured during mechanical testing. Signal descriptors, such as amplitude, duration, rise time, counts, and energy, were calculated by the AE software (AEwin) in Fig. 4. To identify the type of damage corresponding to the AE events, AE signal is decomposed into three levels; that is, it is split into eight wavelet packets with their frequency band ranging from 0 to 93.75 kHz for the lowest, and 656.25 to 750 kHz for the highest (Table 1). The sampling frequency F is 1.5 MHz.

The damage forms of glass fiber mainly consist of matrix cracking, interfacial damage, and fiber breakage. The performance of these stages of AE signal parameters ranges from matrix cracking with low amplitude (40–65 dB), low duration (less than 1000 μs), and low energy (less than 5000 μs) to fiber breaking with high

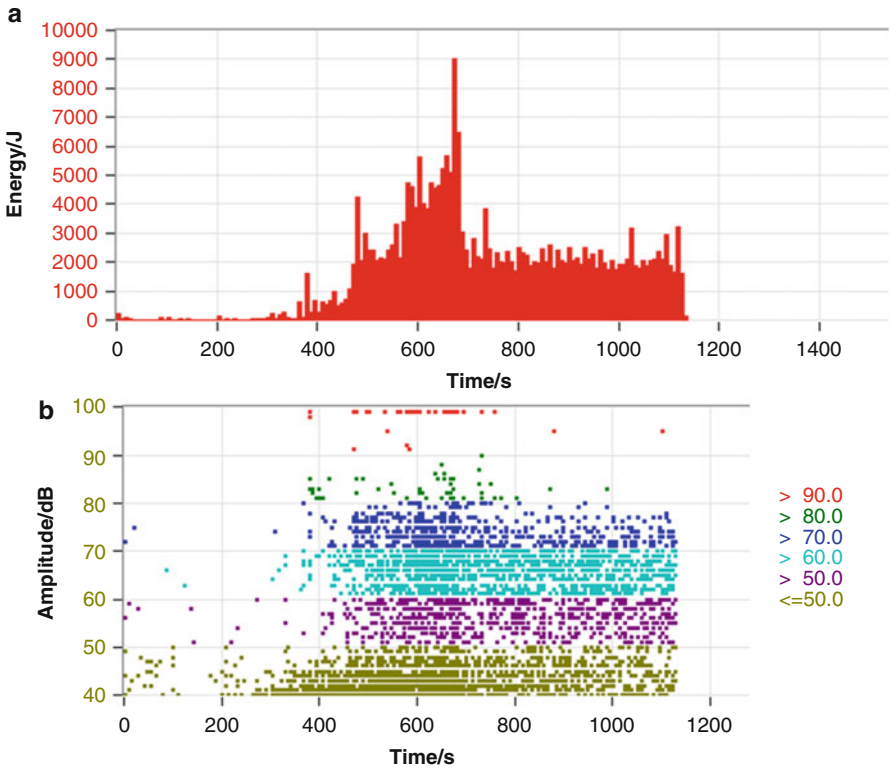

Fig. 4 Acoustic emission response for composite of fracture, (**a**) energy–time curve, (**b**) amplitude–time curve at the moment

Table 1 Wavelet packet frequency bands

Wavelet packet bin	Frequency band (kHz)	Wavelet packet bin	Frequency band (kHz)
(3, 1)	0–93.75	(3, 5)	375–468.75
(3, 2)	93.75–187.5	(3, 6)	468.75–562.5
(3, 3)	187.5–281.25	(3, 7)	562.5–656.25
(3, 4)	281.25–375	(3, 8)	656.25–750

amplitude (greater than 95 dB), high duration (greater than 3000 μs), and high energy (more than 10,000 μs). The intensity of AE signal variation process was discussed. Based on a parametric method, a wavelet packet energy method was used to analyze the AE signal waveforms. AE signal frequency feature distribution was obtained by wavelet packet decomposition. The different damage patterns and stages during the process of glass fiber composite material deformation were successfully recognized, as shown in Fig. 5. Three failure modes are identified with wavelet levels centered as follows: matrix cracking (0–93.75 kHz), interfacial damage (93.75−187.5 kHz), and fiber breakage (281.25−375 kHz). AE monitoring

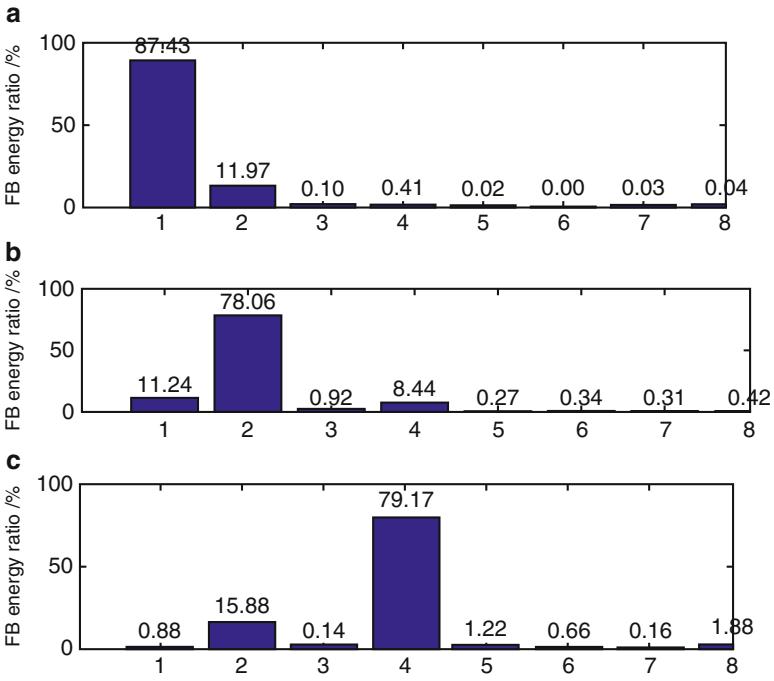

Fig. 5 Acoustic emission signal frequency band energy ratio after wavelet packet decomposition, (**a**) matrix cracking process, (**b**) interfacial damage process, (**c**) fiber breakage, FB-frequency band

of pure matrix cracking under tensile loading shows that the dominant frequency range of signals is at a lower level, and first packet (0–93.75 kHz) contains most of total energy. Fiber breakage process AE signal energy was focused on the 281.25−375 kHz range, and the energy of fourth packet becomes predominant.

3.2 AE Source Localization-Based TR

In Fig. 6, the panel dimension is 80 × 80 cm, and thickness 0.5 cm, which consists of four panels. The density is 2.55 g/cm^3. The testing localization area of interest is 36 × 15 cm, which was divided into $M = 12 \times 5$ grids. As shown in Fig. 1, each grid size is 3 × 3 cm. The impulse signal was generated by hammer. The impacts were applied to 60 grid points spaced 3 cm apart using an impact hammer. The impacts were applied to 60 grid points spaced 3 mm apart using an impact hammer. The experimental impulse response function from each grid point was acquired using only one AE sensor. Figure 7 shows the typical raw waveforms of hammer impact-simulated AE signals in the time domain. The true impact hit point position is (6, 9 cm). Amplitude is calculated peak amplitude of the TR signal at each point,

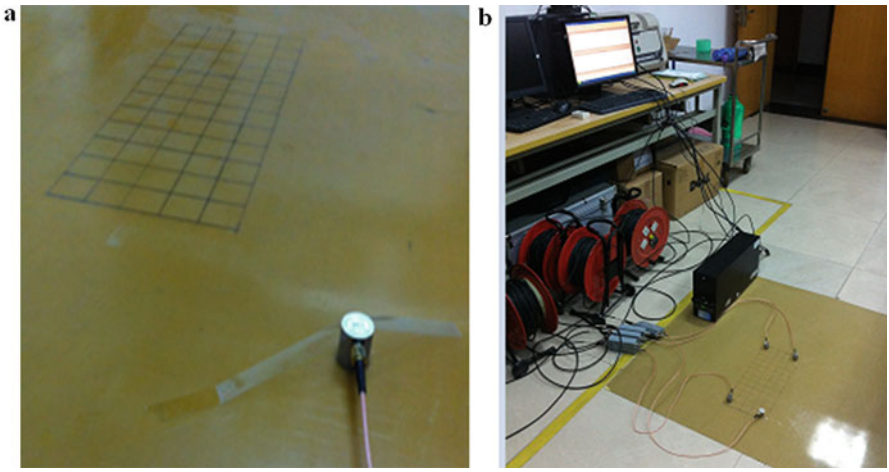

Fig. 6 GFRP plate defect acoustic signal detection, (**a**) testing area, (**b**) AE data-gathering system

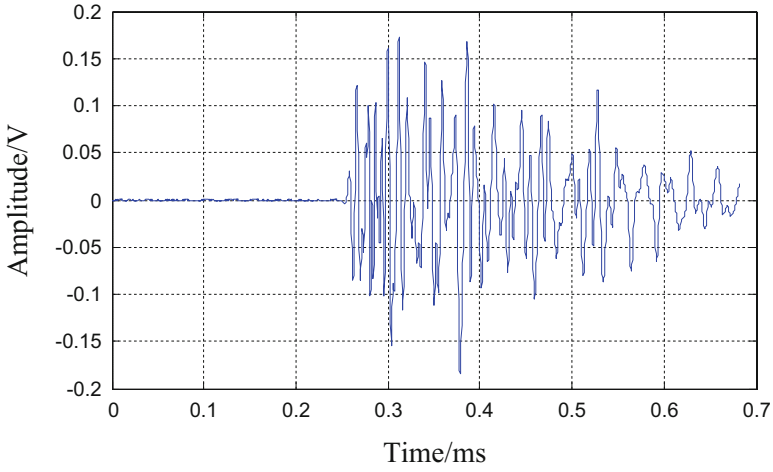

Fig. 7 Response signal of the hammer excitation at (6, 9 cm)

normalized to the maximum calculated amplitude. The imaging result of impact location is illustrated in Fig. 8. The refocusing wave fields at the source position were represented by a normalized 2D map. From Fig. 8, the TR accurately estimates the true impact source as they provide a maximum normalized value of one in the true impact source. The TR method imaging the AE source on panel provides the correct position and enhances its positioning accuracy.

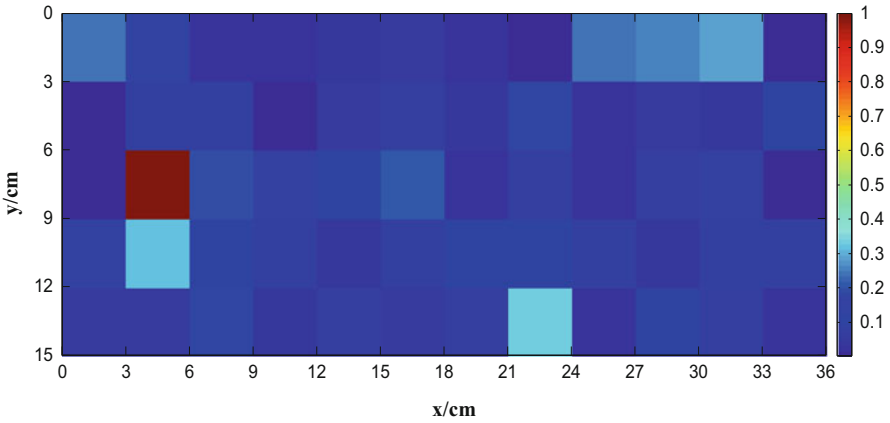

Fig. 8 The maxima normalized correlation coefficient with time reversal analysis localization results

4 Conclusion

For the characteristics of GFRP material with its inhomogeneous and anisotropic nature, AE signal characteristics were analyzed. To identify the type of damage corresponding to the AE events, the events were separated into those with coincident hits' recorded data. The matrix cracking (0–93.75 kHz), interfacial damage (93.75−187.5 kHz), and fiber breakage (281.25−375 kHz) processes are identified. Based on the wavelet packet method, the different damage patterns and stages during the process of glass fiber composite material deformation were successfully recognized. On the basis of a standard time reversal approach, the AE source localization method based on one sensor was used to enhance a higher level of focusing of the source accuracy, and it does not require priori knowledge of the mechanical properties of the GFRP structure and anisotropic group speed. We exploit the benefits of a diffuse wave field and the reciprocity condition of acoustic field to achieve the focusing of the source with a high accuracy in a GFRP board.

Acknowledgments This work was supported by National Quality Supervision and Inspection Public Welfare Project of China under Grant No. 201410027 and Zhejiang Provincial Natural Science Foundation of China under Grant No. LY14E040002.

References

1. I. Amenabar, A. Mendikute, A.L. Arraiza, M. Lizaranzu, J. Aurrekoetxea, Comparison and analysis of non-destructive testing techniques suitable for delamination inspection in wind turbine blades. Compos. Part B: Eng. **42**(5), 1298–1305 (2011)
2. J. Cuadra, P.A. Vanniamparambil, D. Servansky, I. Bartoli, A. Kontsos, Acoustic emission source modeling using a data-driven approach. J. Sound Vib. **341**, 222–236 (2015)

3. P.F. Liu, J.K. Chu, Y.L. Liu, J.Y. Zheng, A study on the failure mechanisms of carbon fiber/epoxy composite laminates using acoustic emission. Mater. Des. **37**, 228–235 (2012)
4. G. Qi, Wavelet-based AE characterization of composite materials. NDT&E Int. **33**, 133–144 (2000)
5. T. Kubiak, S. Samborski, A. Teter, Experimental investigation of failure process in compressed channel-section GFRP laminate columns assisted with the acoustic emission method. Compos. Struct. **133**, 921–929 (2015)
6. K.W. Campbell, P.H. Mott, Damage tolerance in glass reinforced polymer laminates. Compos. Sci. Technol. **95**, 21–28 (2014)
7. K. Asamene, L. Hudson, M. Sundaresan, Influence of attenuation on acoustic emission signals in carbon fiber reinforced polymer panels. Ultrasonics **59**, 86–93 (2015)
8. A. Tobias, Acoustic-emission source location in two dimensions by an array of three sensors. Non-Destruct. Test. **9**(1), 9–12 (1976)
9. N. Toyama, J.-H. Koo, R. Oishi, M. Enoki, T. Kishi, Two-dimensional AE source location with two sensors in thin CFRP plates. J. Mater. Sci. Lett. **20**(19), 1823–1825 (2001)
10. C. Prada, F. Wu, M. Fink, The iterative time reversal mirror: A solution to self-focusing in the pulse echo mode. J. Acoust. Soc. Am. **90**(2), 1119–1129 (1991)
11. R.K. Ing, N. Quieffin, S. Catheline, M. Fink, In solid localization of finger impacts using acoustic time-reversal process. Appl. Phys. Lett. **87**, 204104 (2005)
12. F. Ciampa, M. Meo, Acoustic emission localization in complex dissipative anisotropic structures using a one-channel reciprocal time reversal method. J. Acoust. Soc. Am. **130**(1), 168–175 (2011)
13. F. Ciampa, M. Meo, Impact detection in anisotropic materials using a time reversal approach. Struct. Health Monit. **11**(1), 43–49 (2011)
14. H. Jeong, S. Cho, Impact localization for a composite plate using the spatial focusing properties of advanced signal processing techniques. J. Korean Soc. Nondestruct. Test. **32**(6), 703–710 (2012)
15. S. Mallat, *A wavelet tour of signal processing*, 2nd edn. (Academic Press, Beijing, 2002), pp. 208–211

Evaluating Freeze-Thaw Damage in Concrete with Acoustic Emissions and Ultrasonics

Heather N. Todak, Marisol Tsui, M. Tyler Ley, and W. Jason Weiss

Abstract The purpose of the experiments described in this chapter was to apply acoustic emission technology in a passive mode to identify crack development in concrete specimens exposed to thermal cycling. Acousto-ultrasonics techniques, or using the acoustic emission sensors in an active mode to function as both pulse generators and receivers, were applied to periodically measure the speed of an ultrasonic wave sent across the specimen throughout thermal cycling. The observed reduction in wave velocity can be correlated to the degrading elastic properties of the concrete matrix due to damage development. These experiments were performed on concretes with a wide range of entrained air volumes which were conditioned to various degrees of saturation to identify the critical degree of saturation (S_{crit}) required for deterioration. As predicted, concrete specimens conditioned to high levels of saturation showed more damage than samples at or below the critical degree of saturation. This was made clear by studying the activity parameters of the recorded hit data from passive acoustic emission methods as well as by comparing the damage parameter determined from the acousto-ultrasonic method. Large amounts of acoustic emission activity were observed during periods of freezing resulting from cracking due to volume expansion as well as during thawing due to friction during crack closure. Small fluctuations in pulse velocity which clearly correlated to the temperature cycles were observed during testing of a control aluminum sample, showing a minor dependence of pulse velocity on temperature effects on the coupling agent alone. The combined approach using both active and passive acoustic emission proved to be highly

H.N. Todak (✉)
Wiss, Janney, Elstner Associates, Inc., Pasadena, CA 91106, USA
e-mail: htodak@wje.com

M. Tsui
Oregon State University, Corvallis, OR 97331, USA
e-mail: tsuicham@oregonstate.edu

M.T. Ley
Structural Engineering, 319C Engineering South, Stillwater 74078, OK, USA
e-mail: tyler.ley@okstate.edu

W. Jason Weiss
Oregon State University, Corvallis, OR 97331, USA
e-mail: Jason.weiss@oregonstate.edu

G. Shen et al. (eds.), *Advances in Acoustic Emission Technology*, Springer Proceedings in Physics 179, DOI 10.1007/978-3-319-29052-2_16

informative, making it possible to quantify bulk material damage development while observing trends in acoustic emissions throughout multiple freezing and thawing cycles.

1 Introduction

Concrete that is sufficiently saturated and exposed to freezing and thawing temperatures is highly subjectable to premature deterioration. Air-entraining admixtures are often used to promote durability in concrete by stabilizing air bubbles (approximately 0.01–1.25 mm in size) within the paste portion of concrete during the mixing process. Air-entrainment serves an important purpose to maintain a lower degree of saturation and provide a relief outlet for the hydraulic pressure created during the expansion of water during the freezing phase change. Both the total volume of air and the quality of the air void spacing are important aspects of a well-entrained concrete system. These experiments utilize a new piece of equipment called the super air meter (SAM), which outputs an SAM number that quantifies the quality of the air void distribution in fresh concrete [1, 2]. This device is similar to a standard ASTM C231 pressure meter; however it outputs both the total air volume and the SAM number, an indicator of air void spacing. The SAM utilizes additional pressure events and the SAM number is then defined as the difference between the first and second equilibrium pressures [3]. Despite the use of air-entraining admixtures, it has been determined that once concrete exceeds a critical degree of saturation (estimated to be approximately 86%), the material is vulnerable to damage after even a single freeze-thaw cycle [4–6]. The degree of saturation (DOS) is defined as the ratio of the volume of liquid in the pores (V_{filled}) and the total pore volume (V_{total}), as shown in (1):

$$\text{DOS} = \frac{V_{\text{filled}}}{V_{\text{total}}} \tag{1}$$

2 Method

When concrete is saturated to levels that exceed the critical degree of saturation and is exposed to freezing conditions, there is high potential for damage development. This is attributed to having insufficient void space to accommodate the volume expansion of the freezing liquid, resulting in hydraulic pressure and highly emissive microcracking. Acoustic emission (AE) testing involves the interpretation of transient elastic waves which are generated by the rapid release of energy from localized sources within a material [7]. Unlike other nondestructive testing techniques, AE testing requires that the material is stressed to serve as a stimulus to

generate flaw growth. By applying thermal cycles as the stimulus, AE testing can be used to detect emissions produced when the pressure relief system provided by an air-entrainment system fails in highly saturated concretes. Stress is generated within the saturated pores due to cracking as a result of the ice formation and fluid movement during freezing. Acoustic emission waves propagate from the flaw site through the concrete material and are detected by sensors. The waveform features can then be studied to draw conclusions about the flaw type and location.

Acoustic emission equipment can also be used in an active sense by applying the concepts behind ultrasonic testing. This involves emitting a pulse with known properties from a sensor. The pulse is then transmitted to another sensor located a known distance away. Both sensors can be used as transmitters and receivers in a send/receive setup. For the purposes of this chapter, this technique will be referred to as acousto-ultrasonics. The measurement of ultrasonic velocity (the speed of the pulse sent from one sensor to the other) is a conventional method to estimate the elastic constants of the material [8, 9]. This is found by simply sending a pulse from one sensor to another at a known/measured distance across the medium. Ultrasonic pulse velocity can be used to detect deterioration in materials because the velocity of the wave is dependent upon the elastic properties and density of the medium as shown in (2):

$$V_{\mathrm{p}} = \sqrt{\frac{E_{\mathrm{d}}(1-v)}{\rho(1+v)(1-2v)}} \tag{2}$$

where V_{p} is the pulse velocity, E_{d} is the dynamic modulus of elasticity, ρ is the density, and v is the Poisson's ratio. This relationship between ultrasonic pulse velocity and modulus of elasticity can then be correlated to the level of damage incurred by a concrete specimen assuming that the Poisson's ratio remains constant. The dynamic modulus is a measure of the structural integrity of the concrete, and a reduction in the modulus of elasticity corresponds to increased damage in a solid due to the stiffness reduction caused by microstructural deformities. Therefore, the damage parameter (D) is directly related to the change in the modulus of elasticity. By assuming no change in Poisson's ratio or material density, the damage parameter can therefore be computed in terms of the reduction in pulse velocity, as shown by (3):

$$D = 1 - \frac{E}{E_0} = 1 - \left(\frac{V}{V_0}\right)^2 \tag{3}$$

3 Materials and Specimen Preparation

In order to accomplish the task of determining whether the critical degree of saturation is dependent upon total air content, it was desired to observe the freeze-thaw behavior for samples covering a wide spectrum of air content as well as the quality of the air void spacing within the matrix. All of the specimens for this set of experiments were prepared in a laboratory environment at Oklahoma State University. This chapter examines the results from the testing of 11 concrete mixtures with the properties shown in Table 1. Type I ordinary Portland cement was used with a specific gravity of 3.15 and Blaine fineness of 386 m^2/kg. The coarse aggregate used was a locally available crushed limestone with a maximum nominal aggregate size of 3/4″ that met a 57 stone gradation with an SSD-specific gravity of 2.70 and absorption of 0.73%. The fine aggregate used was natural sand with an SSD-specific gravity of 2.65 and 0.44% absorption. A wood rosin air-entraining admixture was used in accordance with ASTM C260-10 to obtain the desired spectrum of air properties. Mixtures 9–11 also contain a high-range water-reducing admixture. For reference, an SAM number of 0.20 or below is expected to have an adequate air void system, with a spacing factor lower than 0.200 mm (0.008 in.) and specific surface above 15,240 mm^{-1} (600 $in.^{-1}$) [1–3].

Each mixture was tested at three degrees of saturation (99%, 93%, and 88% ±2 DOS). These were all above the predicted S_{crit} of 86% in order to provide sufficient moisture content for damage development to be detected by acoustic emission testing [5, 10]. The concrete was cast into sealed cylindrical molds and conditioned for at least 180 days after casting. Samples were prepared for testing by coring and cutting each cylinder into three samples 51 mm tall with 57 mm diameter. Each specimen then had two opposing sensor pads ground on each side of the sample to provide a 24 mm long, 20 mm wide, 1.5 mm deep smooth flat surface for each acoustic emission sensor. Next, the concrete specimens were oven dried in a 110 °C ± 5 °C oven for 3 days and the oven dry mass was recorded. Full saturation (i.e., 100% degree of saturation) for each sample was achieved by holding the concrete under vacuum (approximately 7–10 Torr) for 3 h before adding a saturated lime-water solution while the sample remained under vacuum for an additional 1 h [11]. The samples remained under water for at least an additional 18 h to reach 100% degree of saturation. The desired degree of saturation was achieved for each test specimen by letting the fully saturated samples dry in a controlled environment until the necessary mass loss was achieved. The concrete was then sealed and placed in a temperature-controlled environment for 7–10 days to allow the moisture content to equilibrate within the pore structure before testing. Samples being tested at full saturation were tested directly after the 18-h submerged period following vacuum saturation.

Table 1 Material properties

Mixture ID	w/c	Total air content (%)	Coefficient of variation	SAM number	Coefficient of variation
1	0.45	6.58	0.01	0.11	0.39
2	0.45	2.59	0.01	0.55	N/A
3	0.45	3.88	0.04	0.24	0.15
4	0.40	1.97	0.00	0.49	0.19
5	0.40	3.65	N/A	0.20	N/A
6	0.40	7.2	0.01	0.17	0.01
7	0.40	4.31	0.00	0.39	0.02
8	0.40	2.44	N/A	0.58	N/A
9	0.35	4.04	0.04	0.32	0.09
10	0.35	9.24	0.01	0.16	0.14
11	0.35	5.26	0.01	0.46	0.34

[a]Mixture designs are based on target batch quantities. All mixtures include a wood rosin air-entraining admixture that meets the requirements of ASTM C 260-10, AASHTO M 154, and CRD-C 13. COV determined from measurements collected from 2 to 3 different SAMs. N/A indicates that only one measurement was taken

4 Experimental Procedures

Following conditioning, the air-entrained concrete specimens were tested in a longitudinal guarded comparative calorimeter (LGCC) which was constructed in accordance with ASTM E1225-13 and ASTM D5470-12. This setup was equipped with two acoustic emission sensors (AE-LGCC) as shown in Fig. 1 [12]. This test setup is designed to simulate freeze-thaw cycles and to capture phase changes and damage development simultaneously. A cold plate (Fig. 1b) was used to regulate three thermal cycles between 24 °C and −20 °C. The setup is fully insulated both inside and outside the aluminum cylindrical guard with rigid extruded polystyrene to limit heat loss and to establish one-dimensional heat flow. As illustrated in Fig. 1, type T perfluoroalkoxy-insulated (PFA) thermocouples measured the temperature at seven locations. The concrete specimen was positioned between two 25.4 mm tall pieces of Pyroceram Code 9606 which were used as meter bars in this study due to their known thermal properties and effective heat transfer. With this information, the heat flow consumed or released by the concrete sample during phase change could be estimated. Within the LGCC, specimens remained fully sealed with a plastic wrapping to prevent any reduction in the degree of saturation during testing. Despite these measures, posttest mass measurements indicated a decrease in DOS of approximately a 1–2% during the 5-day test, and therefore the average degree of saturation during testing is reported.

Imbedded within the insulation are two VS375-M cylindrical broadband sensors capable of withstanding low temperatures with a frequency range of 250–700 kHz and peak frequency of 375 kHz [13]. Vallen Systeme AEP4 external preamplifiers with 34 dB gain capable of pulse through capabilities up to 450 V_{pp} (peak-to-peak

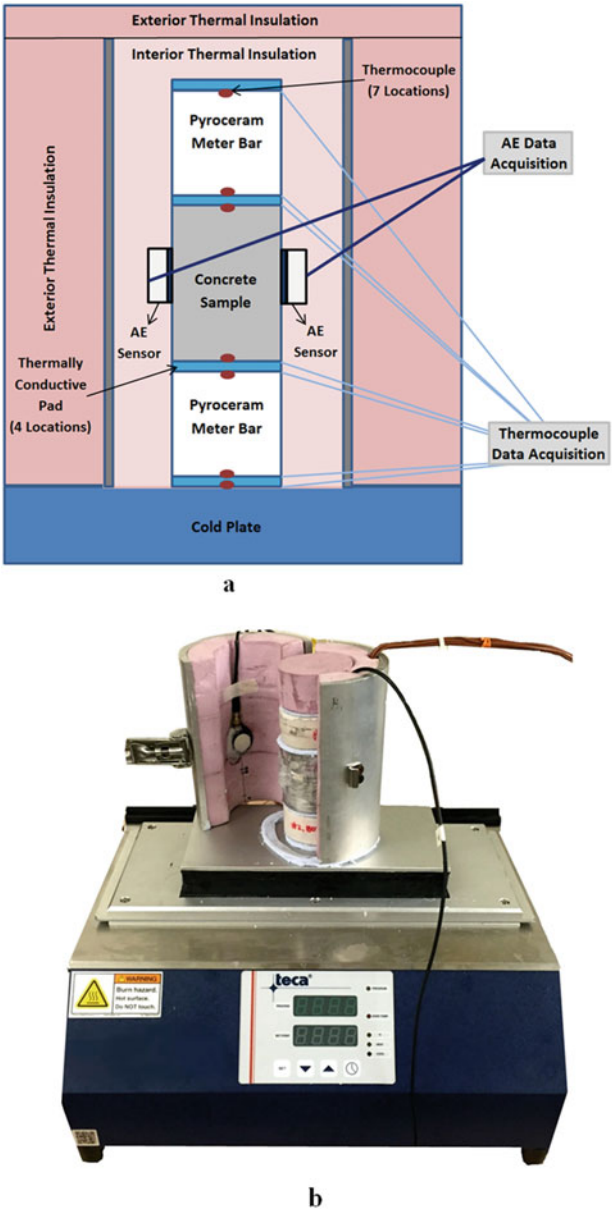

Fig. 1 Longitudinal guarded comparative calorimeter with acoustic emission (**a**) diagram and (**b**) test setup

voltage) [14] were used with Vallen AMSY5 acoustic emission system with transient recording for data collection [15]. To limit background noise, front-end filters were applied to each transducer including a 40 dB threshold and the duration

discrimination time (DDT) was set to be 200 ns less than the rearm time (RAT) due to the small sample size. During analysis, an additional plausibility filter was applied. One of the following criteria had to be met in order for the data to be retained: (1) hit duration less than 1000 μs with greater than four counts (2) rise time greater than or equal to 30 μs or (3) duration greater than 100 μs. Additionally, all send/receive signals induced by the automatic pulsing were rejected from the data set during hit analysis.

Cutouts were made in the plastic sheeting where the AE sensors made contact with the specimen. To ensure an effective transfer of stress between the test specimen and the sensor pad, a high-vacuum grease was applied to both the sensor and the concrete surface. This contact medium was determined to be best due to the strong coupling performance and low freezing point. Prior to testing, the cylindrical longitudinal guard is clamped shut which ensured good contact pressure between the sensor and the concrete. This model is an update to the original AE-LGCC [16] which is suitable for small, prismatic samples and is equipped with a single AE sensor for passive monitoring only.

With two AE sensors imbedded within the LGCC insulation, periodic acousto-ultrasonic testing throughout the 5-day, three-cycle test was made possible. Each hour, signal pulses were sent between the two sensors across the cylindrical specimen. With the distance between sensor pads known, the variation in pulse velocity over time could be monitored to later make conclusions about damage development. For automatic pulsing, the pulse peak-to-peak amplitude was 100 volts with 1 pulse per burst at a burst interval of 1000 ms over a normal (90–210 kHz) pulse frequency range. The average velocity computed for each burst was used for each channel, and the average pulse velocity between the two opposing channels was used to monitor the degrading elastic properties throughout the freeze-thaw test. It is important to note that wave speed resolution is dependent on distance travelled and larger sample size may provide improved wave speed resolutions. Strong agreement between the pulse velocity measured by the two opposing sensors was required before testing initiated to ensure good coupling at each interface enclosed within the LGCC. Additionally, one acousto-ultrasonic measurement was made external to the test setup before and after the freeze-thaw cycling for comparison and identifying coupling or temperature concerns.

5 Experimental Results

The purpose of this set of experiments was to determine whether the critical degree of saturation required for damage development is dependent upon the air entrainment qualities of a concrete system. This was accomplished by quantifying the freeze-thaw damage development for various mixtures at three levels of saturation, assuming a linear trend, and projecting the degree of saturation associated with a damage index of 0%. In order to accurately assess these results, it was essential to compare the acoustic emissions and acousto-ultrasonic measurements to a control

sample (aluminum) undergoing the same procedure. This comparison provides valuable information about (1) acoustic emission activity generated by phenomena other than freeze-thaw-related flaw development and (2) changes in wave velocity due to temperature effects alone.

5.1 Passive Acoustic Emission Results

Three levels of saturation above S_{crit} (approximately 99%, 93%, and 88%) were chosen for testing to ensure that damage development would occur for acoustic emission testing to be effective. Table 2 shows the specimen temperature and associated test time for each phase change of one representative complete data set. These values have been determined from sudden spikes in heat flow caused by the endothermic and exothermic phase changes. Fig. 2 shows the acoustic emission activity generated by these samples throughout the course of three freeze-thaw cycles. By applying the values in Table 2 to Fig. 2, it is clear to see a distinct correlation between phase changes (and all associated cracking emissions) and quantity and intensity of the collected signals. The most drastic peak in acoustic activity is observed at the onset of the first freezing cycle. The accumulation of lower amplitude emissions prior to the first freeze has been attributed to friction generated due to a mismatch in thermal expansion coefficients between the concrete matrix and the aggregate [16, 17]. It is evident that acoustic emission is also produced during thawing. These emissions are attributed to nonhomogeneous stress relief during thawing or frictional rubbing caused by crack closure following the volume reduction of the saturation solution during phase change. This activity was more apparent for samples tested at high degrees of saturation. As expected, very few hits passed through the front-end filter and posttest plausibility filters for the aluminum specimen due to lack of freeze-thaw damage development. It is hypothesized that the acoustic activity shown for this control sample may be due to pressure against the transducer due to temperature-related volume changes, bursting air bubbles in the vacuum grease couplant, or unintentional external forces near the experimental setup.

Another important feature of Fig. 2 is the cumulative signal strength (1eu = 1 nV s), which is a measure of energy recorded by the acoustic emission software. For high levels of saturation (i.e., 94% and 99%), this graph illustrates a gradual rise in energy prior to the first freeze, an obvious jump associated with the first freezing event, another significant step associated with the first thaw, and additional steplike increases associated with the second and third thermal cycles. It was a common observation across all sample sets that the amount of acoustic emission activity reduced with each thermal cycle. The total cumulative energy recorded for the fully saturated specimen is nearly five times that of the 89% degree of saturation sample (just over S_{crit}) and is an entire order of magnitude greater than the minimal cumulative energy recorded for the control. This observation creates confidence that the acoustic emission activity is generated primarily by freeze-thaw-related

Table 2 Average sample freezing temperature (±0.2 °C), thawing temperature (±0.4 °C), and testing time (±0.2 h.) at phase change

	Cycle 1		Cycle 2		Cycle 3	
Average D.O.S. (%)	Freeze temperature, °C (time, h)	Thaw temperature, °C (time, h)	Freeze temperature, °C (time, h)	Thaw temperature, °C (time, h)	Freeze temperature, °C (time, h)	Thaw temperature, °C (time, h)
99	−2 (17.0)	1.5 (33.7)	−2.2 (57.1)	2.1 (73.8)	−2.2 (97.1)	2.0 (113.8)
94	−2.7 (17.2)	1.7 (33.8)	−2.7 (57.3)	1.6 (73.8)	−2.9 (97.3)	1.7 (113.8)
89	Not detectable	0.9 (33.2)	−4.6 (57.8)	1.5 (73.4)	−6.1 (98.4)	0.8 (113.2)

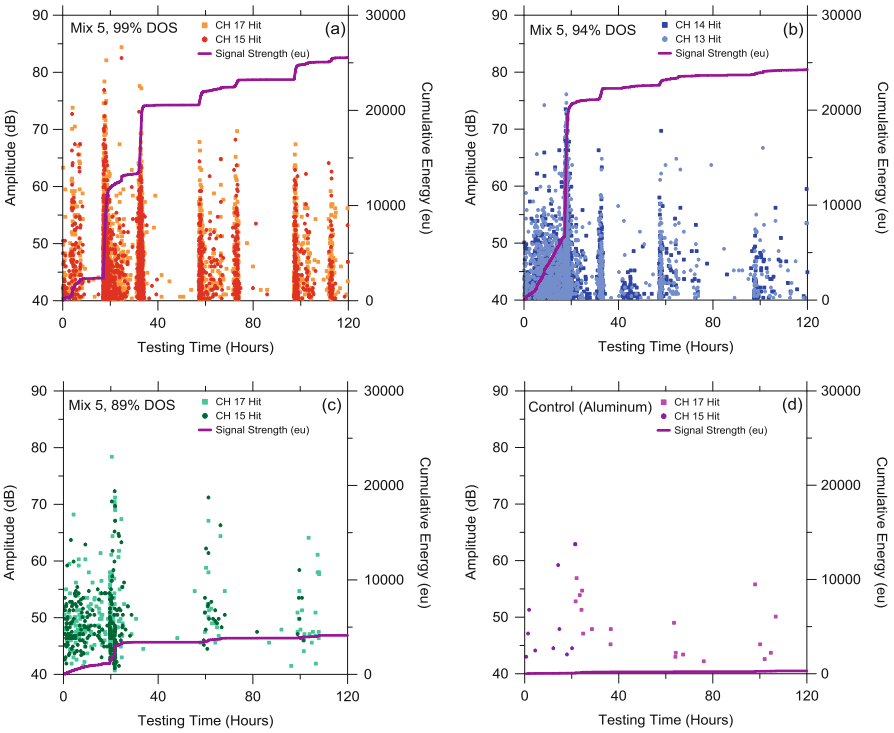

Fig. 2 Acoustic emission hits and cumulative signal strength (1eu = 1 nV s) for (**a**) fully saturated, (**b**) 94% saturated, and (**c**) 89% saturated concrete undergoing three freeze-thaw cycles compared to (**d**) an aluminum sample with no freeze-thaw-related damage

damage. It is important to note that the hit data is shown for both sensors located on opposing sides of the cylindrical sample and that the signal strength shown is the average cumulative signal strength between the two sensors.

5.2 Acousto-Ultrasonics Results

The trends observed in pulse velocity over time are most informative for quantifying damage development and extrapolating a critical degree of saturation for each air-entrained concrete mixture. Both the continuous pulse measurements taken once hourly within the LGCC during the 5-day freeze-thaw test and measurements taken external to the test setup before and after testing are displayed for concrete at all three levels of saturation and the aluminum control specimen in Fig. 3. This acousto-ultrasonic data (Fig. 3) indicates (1) expected rise in pulse velocity corresponding to time periods when the saturation solution was frozen; (2) reductions of various intensities in room-temperature pulse velocity after the first,

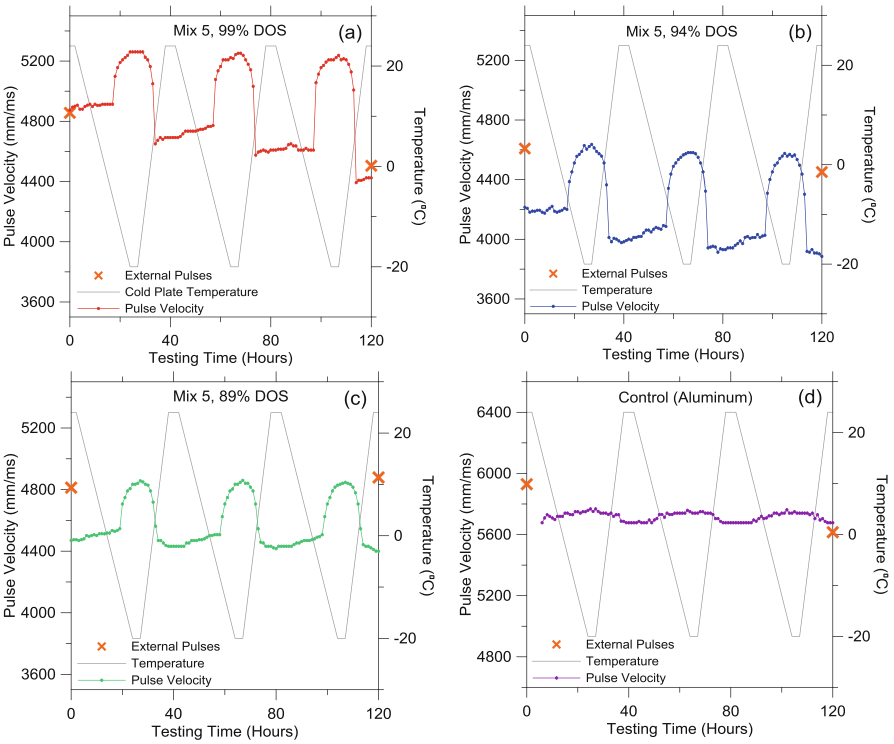

Fig. 3 Changes in wave velocity throughout three thermal cycles for (**a**–**c**) concrete saturated to three different degrees of saturation compared to (**d**) a control aluminum sample. (Note: Pulse velocity primary scale difference is due to different material properties between concrete and aluminum)

second, and third thermal cycles; and (3) differences in internal and external measurements related to coupling effects.

All concrete mixtures, at each tested level of saturation, displayed significant increases in pulse velocity when the solution within the pore structure was frozen. This observation can be simply attributed to waves traveling more quickly through a solid medium (i.e., concrete with ice-filled porosity) than a composite medium containing solid and liquid (i.e., concrete saturated with water). Similarly, it was a frequent observation that samples of higher saturation showed slightly faster overall pulse velocities than samples of the same mixture with lower saturation due to waves moving very slowly through the associated empty void space. Much less significant bumps in pulse velocity are shown at each freezing cycle for the control aluminum sample (due to there being no solution to undergo freezing and thawing phase changes), which indicates a slight dependence of pulse velocity on temperature effects alone (Fig. 3d). This may be caused by temperature effects on the coupling agent itself or changes in contact strength between the sensor and sample as the aluminum sample undergoes thermal expansion and contraction. This minor

fluctuation should be considered when studying the trends in pulse velocity for the saturated concrete specimens.

As explained previously, the damage incurred by a sample was quantified using the reduction in room-temperature pulse velocity after each thermal cycle. The fully saturated specimen shown in Fig. 3a shows a drastic reduction in room-temperature wave velocity throughout the test. This reduction becomes less intense for lower levels of saturation, and is not apparent for the control aluminum specimen due to the absence of damage development.

The pulse velocities recorded external to the LGCC before and after testing (shown with cross symbols in Fig. 3) often did not show good agreement with the continuous internal measurements. As shown in Table 3 for Mix 5 and the aluminum control, in many causes the damage index determined by these two methods showed significant discrepancies. It was of interest to determine which measurements (internal or external) provided a more accurate quantification of damage development. In order to evaluate the integrity of the internal and external measurements, it is important to consider the differences in coupling each method incurred. Both approaches used the same high-vacuum grease couplant at the same locations on the specimen; however the external measurements required that the sensors were attached, used for measurement, then uncoupled, and reattached at the end of the experiment. Although the couplant was reapplied, differences in couplant thickness, exact sensor position, and contact pressure could have major implications on the resulting velocity measurements [18, 19]. A benefit of the internal measurements is that once contact between the transducer and the specimen was applied, the sensor remained in place for the duration of the test. However, the couplant was subjected to the range of testing temperatures between 23 and −20 °C which may have altered its properties despite being a silicon-based grease stable above temperatures of −40 °C. Additionally, due to the nature of the LGCC test setup, changes in sample volume due to thermal expansion may have caused changes in contact pressure between the transducer and the concrete during temperature cycling. Typically, higher pulse velocity measurements are an indicator of better coupling. By this standard, it appears that in some cases including those shown in Fig. 3, the external measurements have superior coupling. However, it is important to remember that the damage index is a relative measurement and therefore consistency in coupling may outweigh the desire to achieve higher pulse velocity measurements. Inconsistent coupling before and after the test for the external measurements is likely the cause of the unrealistic negative damage index reported for the 89% saturated Mix 5 specimen. Ultimately, the external measurements were determined to be less reliable due to the unreasonably high damage index measured for the control sample, whereas the internal measurements indicated nearly no damage, as anticipated. Another benefit of using the pulse velocity trends determined from internal LGCC measurements was having the full spectrum of pulse velocities during all three freeze-thaw cycles rather than before and after measurements only.

Table 3 Damage parameter determined from pulse velocities determined both internal and external to the LGCC

	Cycle 1 damage index (%)	Cycle 2 damage index (%)	Cycle 3 damage index (%)	
Specimen ID (%)	Internal	Internal	Internal	External
Mix 5, 99	4.0	5.8	9.7	7.2
Mix 5, 94	4.8	6.1	6.9	3.4
Mix 5, 89	1.4	1.6	1.9	−1.4
Aluminum	0.3	0.4	0.4	5.3

5.3 *Critical Degree of Saturation Projections*

In order to determine whether the critical degree of saturation required for damage development is dependent upon the air-entrainment properties of a concrete system, the damage index for the 11 mixtures outlined in Table 1 at three levels of saturation was studied against measures of air quantity and quality. S_{crit} was extrapolated using the damage index calculated for cycle 1, cycle 2, and cycle 3. For the purpose of this study, the super air meter (SAM), a device that applies multiple pressure events to fresh concrete to determine the spacing quality and the total volume of air voids, was used to measure these parameters [20]. The outputted SAM number correlates with the spacing factor of the entrained air, an important quality for freeze-thaw durability. For reference, lower SAM numbers are indicators of more well-distributed air void systems, and an SAM number of 0.20 or below is typically a good indicator of strong freeze-thaw performance.

The projected S_{crit} fell within a range of 80–90% degree of saturation, which is consistent with previous studies [4–6]. This was anticipated due to the 9% volume expansion water undergoes during phase change. There exists a positive trend in the critical degree of saturation as the total air volume is increased (Fig. 4a). An inverse relationship between S_{crit} and the SAM number is shown in Fig. 4b. A stronger correlation with S_{crit} was observed for SAM numbers than for total air volume. This suggests that concretes with higher quality air void systems, quantified by lower SAM numbers, may resist freeze-thaw damage at higher levels of saturation (S_{crit}) than those with poorly distributed air void systems. This trend is apparent for the projections made for all three cycles and is strongest for the three-cycle projection. This data suggests a dependence of S_{crit} on void spacing quality, and therefore it is recommended that future specifications take this into account by treating S_{crit} as a function of air properties when assessing durability. However, the critical degree of saturation is consistently between 80 and 90%, and therefore it would be a conservative approach to assume the lower bound of S_{crit} across all mixtures when creating specifications. Additional mixtures and a larger range of degree of saturation are required to confirm these results and to develop an empirical relationship which quantifies S_{crit} as a function of air void properties.

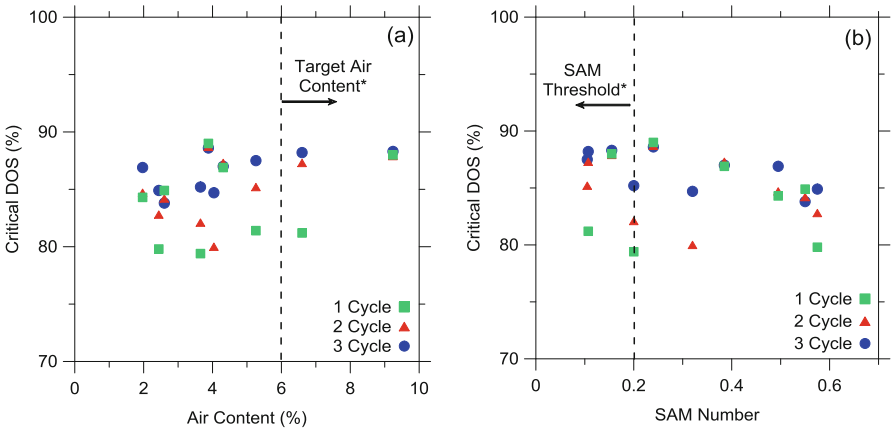

Fig. 4 Projected critical degree of saturation for concrete mixtures with (**a**) total air content and (**b**) air quality (SAM number). *Target air content specification for concrete with 3/4–1″ nominal maximum aggregate size in exposure class F2 or F3 [21]. *SAM threshold indicates the proposed upper limit for adequate freeze-thaw performance

6 Conclusions

As predicted, concrete specimens conditioned to high levels of saturation showed more damage than samples at or below the critical degree of saturation. This was made clear by studying the acoustic activity parameters of the recorded hit data from the passive method as well as by comparing the damage parameter determined from the acousto-ultrasonic method. Small fluctuations in pulse velocity observed during testing of the aluminum sample which clearly correlated with the temperature cycling show that there is a minor influence of temperature on the recorded pulse velocity. It was determined that the damage index determined by continuous AE measurements taken internally in the LGCC experimental setup was more consistent with the expected results than before and after measurements taken external to the setup. The combined approach using both active and passive acoustic emission proved to be highly informative, making it possible to quantify bulk material damage development while collecting waveform data to fully understand the cracking behavior of the concrete during thermal cycling. Lastly, a trend between the critical degree of saturation and the air void spacing quality was observed. This relationship between critical DOS and SAM number suggests that higher quality air void distributions may provide improved protection of the paste against freeze-thaw damage.

Acknowledgments This work was supported in part by the National Pooled Fund Study titled "Improving Specifications to Resist Frost Damage in Modern Concrete Mixtures." The work described in this chapter was conducted at Oklahoma State University and in the Pankow Materials Laboratory at Purdue University and the authors would like to acknowledge the support that has made its operation possible. The contents of this chapter reflect the views of the authors, who are

responsible for the facts and the accuracy of the data presented herein, and do not necessarily reflect the official views or policies of the Federal Highway Administration, the Indiana Department of Transportation, and the Oklahoma Department of Transportation, nor do the contents constitute a standard, specification, or regulation.

References

1. D. Welchel, *Determining the air void distribution of fresh concrete with the sequential pressure method* (Oklahoma State University, Oklahoma, 2014)
2. M. T. Ley, B. Tabb, "A test method to measure the freeze thaw durability of fresh concrete using overpressure," in TDI Congress.
3. J. Tanesi, H. Kim, M. Beyene, A. Ardani, Super air meter for assessing air-void system of fresh concrete, in *Proceedings of the 94th TRB, Transportation Research Board of the National Academies* (2015).
4. G. Fagerlund, in *The long-time water absorption in the air-pore structure of concrete*, 1993.
5. W. Li, M. Pour-ghaz, J. Castro, J. Weiss, Water absorption and critical degree of saturation relating to freeze-thaw damage in concrete pavement joints. J. Mater. Civ. Eng. **24**, 299–307 (2012)
6. G.G. Litvan, Freeze-thaw durability of porous building materials. ASTM Spec. Tech. Publ. **691**, 455–463 (1980)
7. "Standard terminology for nondestructive examinations," Am. Soc. Test. Mater., No. ASTM E1316 (2014).
8. S. Kawamoto, R. S. Williams, Acoustic emission and acousto-ultrasonic techniques for wood and wood-based composites, Chemistry (2002), pp. 1–16.
9. H. Shimada, K. Sakai, G. G. Litvan, Acoustic emissions of mortar subjected to freezing and thawing, Second Int. Conf. Durab. Concr. (1991), pp. 263–278.
10. Y. Farnam, H. Todak, R. Spragg, J. Weiss, Electrical response of mortar with different degrees of saturation and deicing salt solutions during freezing and thawing. Cem. Concr. Compos. **59**, 49–59 (2015)
11. Y. Bu, R. Spragg, W.J. Weiss, Comparison of the pore volume in concrete as determined using ASTM C642 and vacuum saturation. Adv. Civ. Eng. Mater. **3**, 308–315 (2014)
12. Y. Farnam, D. Bentz, A. Hampton, W.J. Weiss, Acoustic emission and low-temperature calorimetry study of freeze and thaw behavior in cementitious materials exposed to sodium chloride salt. Transp. Res. Rec. J. Transp. Res. Board. **2441**, 81–90 (2014)
13. Acoustic emission sensors specification (Vallen Systeme, Icking, Germany, 2012).
14. Acoustic emission preamplifiers specification (Vallen Systeme, Icking, Germany, 2013).
15. AMSY-5 system specification (Vallen Systeme, Icking, Germany, 2011), pp. 1–15.
16. Y. Farnam, D. Bentz, A. Sakulich, D. Flynn, J. Weiss, Measuring freeze and thaw damage in mortars containing deicing salt using a low-temperature longitudinal guarded comparative calorimeter and acoustic emission. Adv. Civ. Eng. Mater. **3**, 1 (2014)
17. D.-J. Yoon, W.J. Weiss, S.P. Shah, Detecting the extent of corrosion with acoustic emission. Transp. Res. Rec. **1698**, 54–60 (2000)
18. P. Finkel, Experimental study of 'auto sensor test–self test mode' for acoustic emission system performance verification. AIP Conf. Proc. **509**, 1995–2002 (2000)
19. "Standard guide for determining the reproducibility of acoustic emission sensor response," ASTM Int. (2010), pp. 1–7.
20. M. T. Ley, "Producing freeze-thaw durable concrete," No. January CP Road Map (2015).
21. *Building code requirements for structural concrete and commentary (ACI 318-14)*. ACI Committee 318-14 (2014).

Evaluation of Tensile Failure Progress in FRP Using AE Tomography and Digital Image Correlation

Takahiro Nishida, Tomoki Shiotani, Yoshikazu Kobayashi, Hisafumi Asaue, Hiroshi Nakayama, and Kai-Chun Chang

Abstract Recently some applications of Fiber Reinforced Plastics (FRP) in actual structures have been reported. However progresses of failures in FRP are still not well known. Additionally the evaluation/inspection methods against defects of FRP in actual structures are of high demand. In this study failure progresses in a FRP sampled from an actual bridge were evaluated using Acoustic Emission Tomography (AET) and Digital Image Correlation (DIC) during a tensile test considering the applicability of these methods as future inspection methods in actual structures.

1 Introduction

Steel is widely used as civil engineering material around the world from the benefits of mechanical properties or economical aspects. However steel materials also have negative aspects as civil engineering materials such as its heavy weight and low durability against corrosion. Therefore a lightweight and high durable material taking place of steel is required. Recently some applications of FRP in actual civil engineering structures such as a footbridge member or reinforcing material have been discussed and reported. However progresses of failures in FRP especially exposed to outer sever environment for several years are still not well known. Also the evaluation/inspection methods against defects of FRP in actual structures are of high demand.

Here, there are plenty of reports related to inspection methods for civil engineering structures based on several kinds of theory or experience. Visual inspection is one of common non-destructive inspection methods. However, it is difficult to find defects of FRP by visual inspection before its failure because FRP tends to be brittle fracture. Therefore a reliable and sensitive non-destructive inspection

T. Nishida (✉) • T. Shiotani • H. Asaue • H. Nakayama • K.-C. Chang
Kyoto University, C-Cluster, Katsura Campus, Nishikyo, Kyoto 615-8540, Japan
e-mail: nishida.takahiro.6e@kyoto-u.ac.jp

Y. Kobayashi
Nihon University, 1-8-14, Kanda-Surugadai, Chiyoda-ku, Tokyo 101-83-8, Japan

G. Shen et al. (eds.), *Advances in Acoustic Emission Technology*, Springer Proceedings in Physics 179, DOI 10.1007/978-3-319-29052-2_17

method for FRP is required. Related to this issue, authors have investigated non-destructive inspection methods such as Acoustic Emission Tomography (AET) and Digital Image Correlation (DIC) against failure of FRP as well as other types of civil engineering materials.

From above backgrounds, in present study, the failure progress in a FRP sampled from an actual bridge was evaluated using AET and DIC during a tensile test considering the applicability of these methods as a future inspection method of FRP in actual structures.

2 Experimental and Data Analysis Procedures

2.1 Outline of Test Piece

The outline of FRP test pieces used in this study is shown in Fig. 1. This test piece was taken from FRP plate, which was sampled from an existing footbridge as shown in Fig. 2. This footbridge was located at Okinawa prefecture, southern part of Japan. The mean temperature there is 23 °C and relative humidity is over 80%. The bride was constructed in the year of 2000 and used for 12 years.

The length of test piece was 480 mm and the parts up to 140 mm from the edges were reinforced by attaching two pieces of additional FRP for the grip parts. The thickness of test piece was 4 mm. The width of center of the test piece was 100 mm. The area of cross section at A, B, and C shown in Fig. 1 were 400 mm^2, 560 mm^2, and 480 mm^2 respectively. Therefore the failure of tensile test might be occurred around the point of A (center of test piece). Also this FRP has anisotropy of velocity distribution as shown in Fig. 3. The wave velocity of vertical (tensile) direction was 0.7 times lower than that of horizontal direction.

2.2 Tensile Test

The edges of specimens (grip parts) were fixed on loading equipment though jacks as shown in Fig. 4. Incremental cyclic tensile load as shown in Fig. 5 was applied to the specimen by 2 kN up to 12.7 kN (seventh cycle), which was failure load of test piece. During tensile test, AE activities obtained by AE sensors and surface pictures for evaluating the strains by DIC are recorded. The front side of test piece was mottled by black spry as shown in Fig. 6a in order to evaluate the surface strains of test piece by DIC. On the other hand, four of AE sensors were located on the back side of test piece as shown in Figs. 1 and 6b.

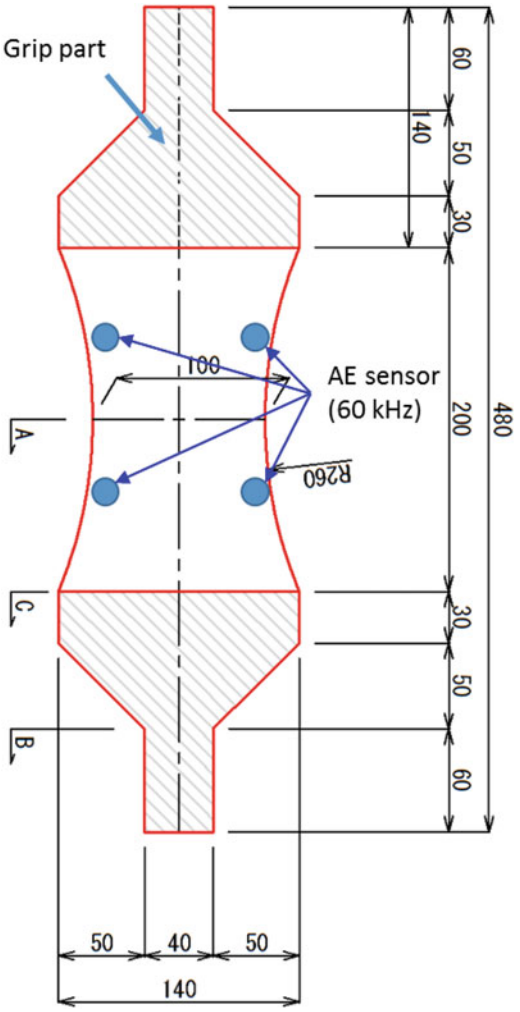

Fig. 1 Outline of test piece

2.3 Digital Image Correlation

In the case of DIC, five pictures in every 1 s were captured using two of correlated digital cameras during tensile test. The surface strain behaviors of test piece were calculated by digital correlation system based on the movements of mottled points recorded by correlated cameras. The schematic figure of calculation of strain is shown in Fig. 7. The strain was calculated by the movements of the mottled points on the surface of the test piece based on following equations.

Fig. 2 Over view of existing footbridge

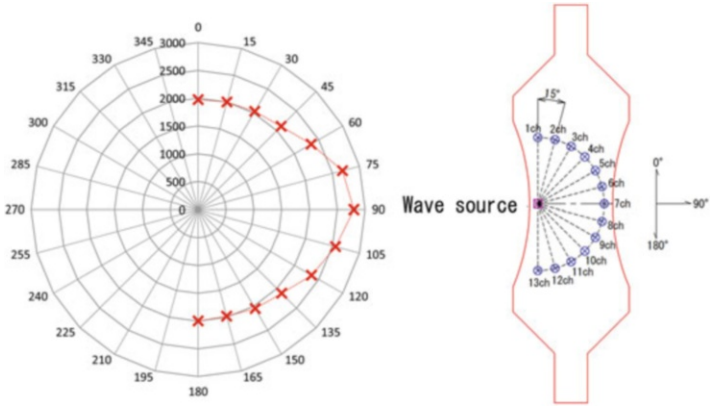

Fig. 3 Wave velocity distribution in each direction

$$\begin{aligned}\varepsilon_x &= \frac{(Xa' - X0)/X0 + (Xb' - X0)/X0}{2} \\ \varepsilon_y &= \frac{(Ya' - Y0)/Y0 + (Yb' - Y0)/Y0}{2} \\ \varepsilon_{xy} &= \frac{(\delta X_1/Ya' + \delta Y_1/Xa') + (\delta X_2/Yb' + \delta Y_2/Xa')}{2}\end{aligned} \tag{1}$$

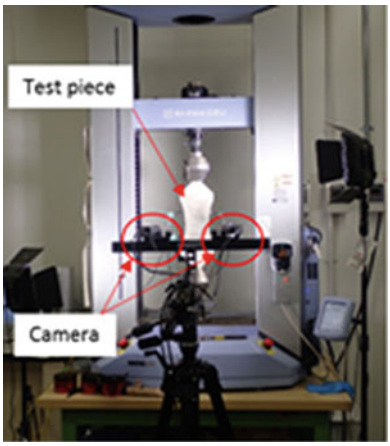

Fig. 4 Tensile loading situation

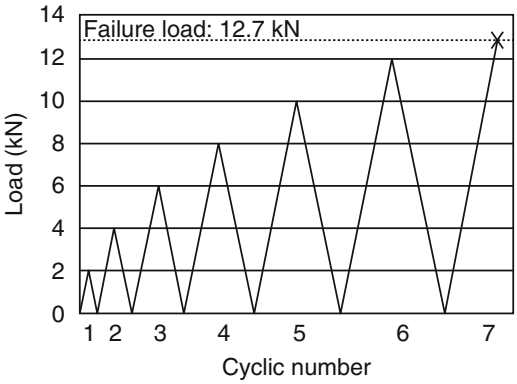

Fig. 5 Incremental cyclic tensile load

2.4 AE Activities and AE Tomography for Anisotropic Materials

AE activities were recorded by AE sensors located on the back side of specimen. The distance of AE sensors in horizontal direction was 80 mm, and that of vertical direction was 100 mm. The sensors were put on the test piece through grease and fixed by packing tape. AE win for Express 8 produced by MISTRAS group was used for data correction. The sampling rate, threshold, and resonant frequency were 2M sampling per second, 50 dB, and 60 kHz respectively.

The AE tomography method was applied to the tensile test of FRP using AE signals. This AE tomography method was developed by Shiotani and Kobayashi [1] and was based on elastic wave tomography. The details of elastic wave tomography and AE tomography are shown below.

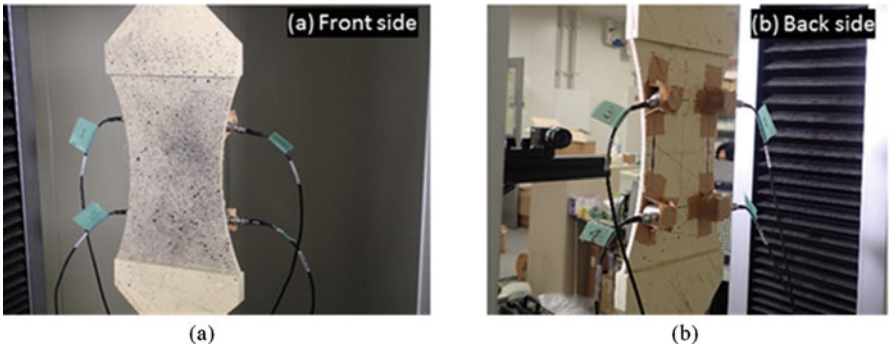

Fig. 6 Front side and back side of test piece during tensile test. (**a**) Mottled points for DIC on front side of test piece. (**b**) AE sensors on back side of test piece

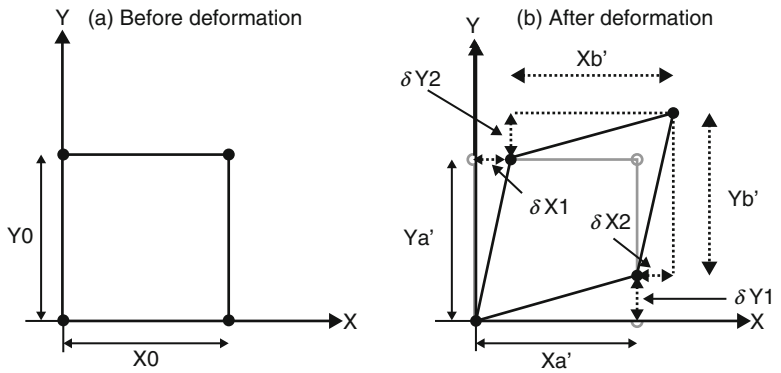

Fig. 7 Schematic outline of calculation of strain by DIC

Elastic wave tomography has been used as a technique to identify elastic wave velocity distribution on cross section or volume of interest. In elastic wave tomography, the elastic wave velocity distributions are reconstructed as an identification problem based on following equation.

$$\Delta T = f(V(r)) \tag{2}$$

where ΔT is a vector of first travel times of an elastic waves between a source and a receiver, $V(r)$ is elastic wave velocity at r, and f is a nonlinear function that computes the first travel times on the given information. Generally, the first travel time ΔT is computed as differences between arrival times of the elastic waves at receivers and emission times of the elastic waves at source locations as follows.

$$\Delta T = A - O \tag{3}$$

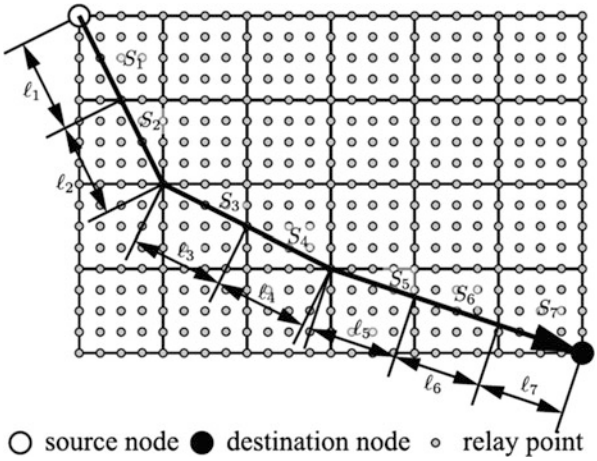

Fig. 8 Representation of ray-path on two-dimensional mesh [1]

where A is a vector of arrival times of the elastic waves at receivers, O is a vector of emission times of the elastic waves at source locations. Hence, the elastic wave velocity tomography is actually an identification problem that reconstructs the elastic wave velocity distribution from the first travel times ΔT and the function f. The function f is constructed on the basis of ray-trace technique in the techniques. In case of two-dimensional problems, a cross section of interest is meshed as well as finite element analysis and ray-path is approximated as polylines as illustrated in Fig. 8. On the approximation, relay points are installed on the mesh to raise the accuracy of ray-path representation in the presented technique [2]. If it is assumed that elastic wave velocity is constant in each cells and materials of a cross section is isotropic, a travel time between a source and a receiver is shown as follows.

$$A - O = \Delta T = \sum_{i=1}^{n} S_i \ell_i \tag{4}$$

where S_i is slowness that is a reciprocal of elastic wave velocity of cell i, and ℓ_i is a length of a ray-path between the source and the receiver on cell i. Thus, travel times on any ray-paths between two points on the cross section can be computed using Eq. (4). The ray-path is sought from all of the potential ray paths between the two points, so that a ray-path that gives minimum travel time is required for the elastic wave velocity tomography. This is the shortest path problem, and Dijkstra's algorithm is adopted for the seeking in the present technique. Consequently, the observation equations are given as

$$\begin{Bmatrix} \Delta T_1 \\ \Delta T_2 \\ \vdots \\ \Delta T_n \end{Bmatrix} = \begin{bmatrix} \ell_{00} & \ell_{01} & \cdots & \ell_{0m} \\ \ell_{10} & \ell_{11} & \cdots & \ell_{1m} \\ \vdots & \vdots & \cdots & \vdots \\ \ell_{n0} & \ell_{n1} & \cdots & \ell_{nm} \end{bmatrix} \begin{Bmatrix} S_0 \\ S_1 \\ \vdots \\ S_m \end{Bmatrix} \tag{5}$$

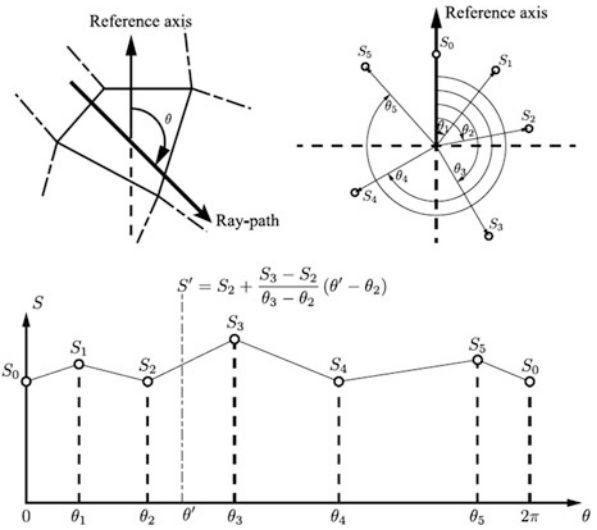

Fig. 9 Slowness profile [1]

where ΔT_i is a travel time of ray-path i, ℓ_{ij} is a length of the ray-path i on cell j. On the basis of the observation equations, the slowness vector is identified by an identification technique. In this study, SIRT (Simultaneous Iterative Reconstruction Technique) is adopted as the identification technique.

To apply the elastic wave velocity tomography for anisotropic bodies, the anisotropy of materials is implemented in the elastic wave velocity tomography by defining the slowness S_i as a function of an angle of a ray-path. The function $S(\theta)$ is set to the individual cells on the mesh, and each of the function is represented by a slowness profile as shown in Fig. 9. In this profile, the directivity of the slowness is set by specifying slowness at specified angles to a reference axis that is defined in each cell. It should be noted that the slowness between the specified angles are given by linearly interpolating the slowness at the adjacent specified angles as shown in Fig. 9. The function is actually described as follows in this study.

$$S(\theta) = \mathrm{Sm}a(\theta) \tag{6}$$

where Sm is the minimum slowness on the profile, i.e. this corresponds to maximum velocity in the profile, and $a(\theta)$ is a coefficient that is represented as $S(\theta)$/Sm. Consequently, Eq. (4) is rewritten as follows to consider the anisotropy.

$$\{\Delta T\} = [\ell]\{\mathrm{Sm}\} \tag{7}$$

where,

$$\{\Delta T\} = \begin{Bmatrix} \Delta T_1 \\ \Delta T_2 \\ \vdots \\ \Delta T_n \end{Bmatrix} \tag{8}$$

$$[\ell] = \begin{bmatrix} \ell_{00}a_{00} & \ell_{01}a_{01} & \cdots & \ell_{0m}a_{0m} \\ \ell_{10}a_{10} & \ell_{11}a_{11} & \cdots & \ell_{1m}a_{1m} \\ \vdots & \vdots & \cdots & \vdots \\ \ell_{n0}a_{n0} & \ell_{n1}a_{n1} & \cdots & \ell_{nm}a_{nm} \end{bmatrix} \tag{9}$$

$$\{\mathrm{Sm}\} = \begin{Bmatrix} S_0 \\ S_1 \\ \vdots \\ S_m \end{Bmatrix} \tag{10}$$

where a_{ij} is the coefficient of the ray-path i in cell j. The vector Sm is identified by applying the identification technique to (7), and elastic wave velocity distribution is visualized by using the vector. It is noteworthy that this observation equations assume that the directivities of the slowness, actually the ratios of the slowness to the minimum slowness at specified angles, does not change even if the Sm is changed to simplify its computational procedure.

On the other hand AE Tomography is a technique that uses AE as signals, i.e. this technique uses only arrival time of AE at receivers, to identify elastic wave velocity distribution on the basis of the elastic velocity tomography. As introduced in above, elastic wave velocity tomography reconstructs elastic wave velocity distribution from first travel times that are computed from emission times and arrival times of elastic waves and ray-paths that are determined by ray-trace technique between source locations of the elastic waves and locations of receivers. However, AE is inappropriate as the signals for the identification since it is impossible to compute the travel times and determine the ray-path because emission times and source locations of AE are generally unknown. Therefore, in AE-Tomography, the source locations and the emission times are identified prior to the reconstruction of the elastic wave velocity distribution by using the AE source location technique. The source locations have been identified by assuming that elastic wave velocity distribution is homogeneous and ray-paths can be approximated as straight lines between the source location and receivers in the conventional AE source location techniques to simplify its computational procedure. However, the assumptions are violated if deterioration of the cross section is localized and severe since the elastic wave velocity locally decline in this case, and consequently, it leads to degrade the accuracy of the identified AE source locations. Hence, the authors proposed a source location technique based on the ray-trace technique to avoid the difficulty [3]. And further, the anisotropy was implemented in the source location technique to extend its applicability for AE-Tomography on anisotropic materials [4]. In this technique, firstly potential emission times P_{ij} of AE are computed at individual nodal points and relay points on the mesh as follows by executing the ray-trace from all of receivers on the mesh.

$$P_{ij} = T_i - \delta T_{ij} \tag{11}$$

where i is a receiver number, j is a serial number of the nodal points, and relay points and δT_{ij} is a travel time from the receiver i to the point j that is computed by the ray-trace technique. It should be noted that the anisotropy is automatically considered in the source location technique because the anisotropy is already implemented in the ray-trace technique. Therefore, each of the nodal points and relay points has n potential emission times where n is number of receivers. The potential emission times are identical at the source location if the elastic wave velocity distribution and shape of the ray-path are exactly represented. However, the point generally does not exist since the representation is normally insufficient due to limitations of meshing of the cross section. Thus, a point that gives minimum variance of the potential emission times is chosen as the source location, and average of the potential emission times at the source location is used as the emission time. The first travel time and the ray-path can be determined by using the estimated source locations and emission times, and the observation (7) can be formulated by using the results. Finally, the elastic wave velocity distribution with the anisotropy is identified by applying identification technique for the observation equations.

3 Results and Discussions

3.1 Surface Strain Distribution Detected by DIC

The surface strain distributions detected by DIC in each loading cycle are shown in Fig. 10. Hence color contrast in the figure is shown the strain of vertical (tensile) direction. From Fig. 10, the constant strain distributions over the surface of test piece were observed up to fifth cycle (Maximum load was 10 kN) of tensile test, although the strain of the surface increased as the applied load became large. Then the two lines of localized strain parts were observed during sixth cyclic of loading. The positions of the localized parts were 12.9 mm and 36.4 mm upper from center line of test piece. Finally the test piece was broken at the point around 12.9 mm from center line.

3.2 AE Activities During Tensile Test

The behaviors of vertical strain and AE parameters such as accumulated AE energy and or peak frequency are shown in Fig. 11a, b. According to Fig. 11a, it was confirmed that the accumulated AE energy gradually increased after fifth cycle. Especially the AE energy became large at sixth and seventh cycles when the localized deformations were observed by DIC. Also from Fig. 11b, some of large peak frequencies were observed after fifth cycles.

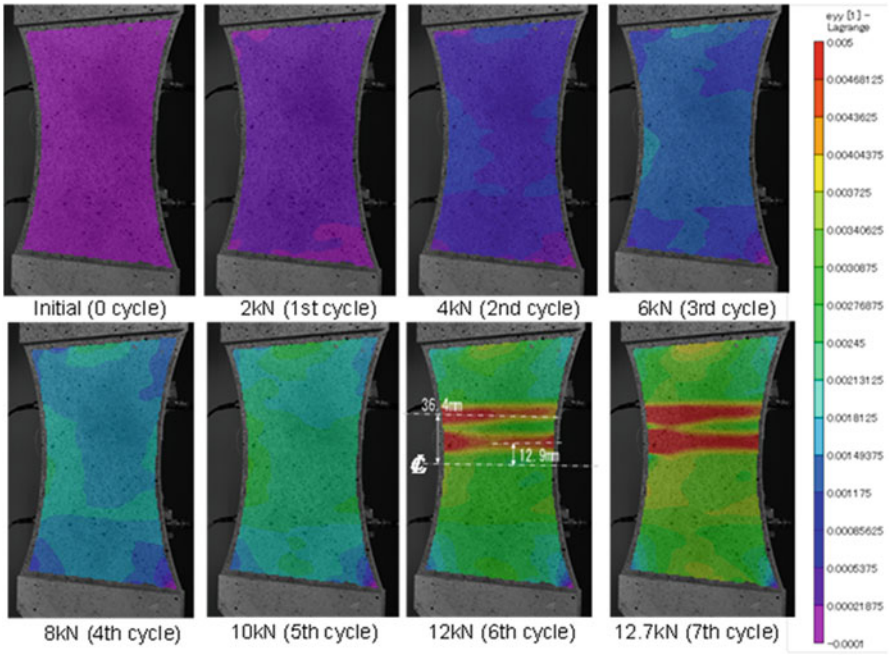

Fig. 10 Surface strain distribution on test piece detected by DIC

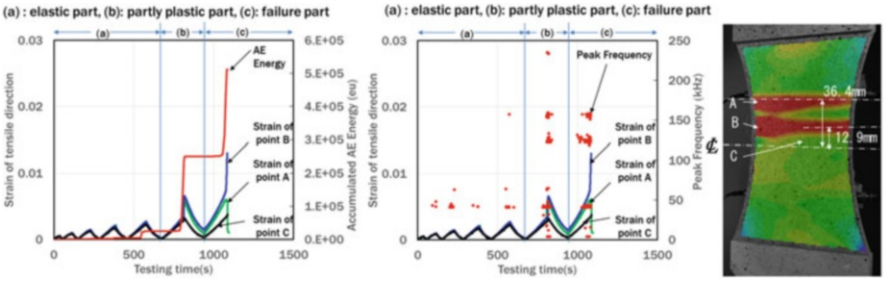

Fig. 11 Behavior of vertical strain and AE parameters such as (**a**) accumulated AE energy and or (**b**) peak frequency

Figure 12 shows the relationship between peak frequency and RA value obtained by AE parameters. Here RA value was calculated from the rise time divided by the maximum amplitude. According to the literature review [5], the relationship between frequency and RA value is highly related to the crack modes, tensile or shear, and tensile crack tends to high frequency and low RA value. From the results of Fig. 12, it was confirmed that most of data tended to be plotted in the tensile mode. From above results, it was supposed that the tensile failure of epoxy resin or fibers occurred at the minute region in test piece after fifth cycles.

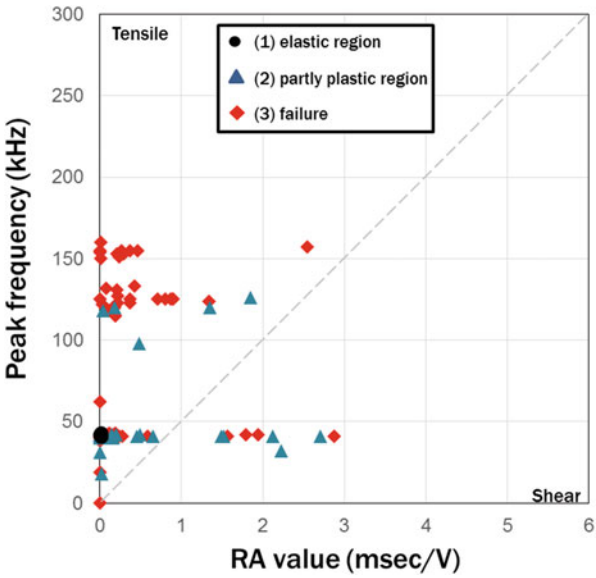

Fig. 12 Relationship between peak frequency and RA value

3.3 AE Tomography

The AE tomography method described in Sect. 2.4 was applied to the obtained AE activities during tensile test. The results were shown in Fig. 13. Figure 13a shows the results that the initial velocity distribution in FRP test piece was isotropy. On the other hand, Fig. 13b shows the results that the initial velocity distribution was followed by Fig. 3, where the velocity of vertical direction was 0.7 times of that of horizontal direction. Also "☆" and "+" in figures mean the AE source obtained by four sensors and three sensors respectively. The data of tensile test was separated into three parts, (1) elastic region, (2) partly plastic region and (3) failure based on the results of surface strain.

In the case of (1) elastic region, the velocity distribution was almost constant regardless of conditions of initial velocity, isotropy and anisotropy. However in the case of (2) partly plastic region and (3) failure, the results of two cases were quite different depending on the condition of initial velocity distributions, that is isotropy or anisotropy. In the case of the isotropy velocity distribution, the velocity of lower part of test piece became higher than that of elastic region although middle and upper part of velocity decreased. On the other hand, in the case of anisotropy, the lower part of test piece almost constant during tensile test and it was confirmed that the velocity of the upper part (failure part) of test piece was decreased. According to the surface strain of test piece shown in Fig. 10, the defected part of test piece is localized from 0.01 to 0.04 m upper from center line and the results of AET considering with anisotropy followed with this results. Therefore it was considered that the results shown in Fig. 13b correctly represented the velocity distribution of tensile failure of test piece.

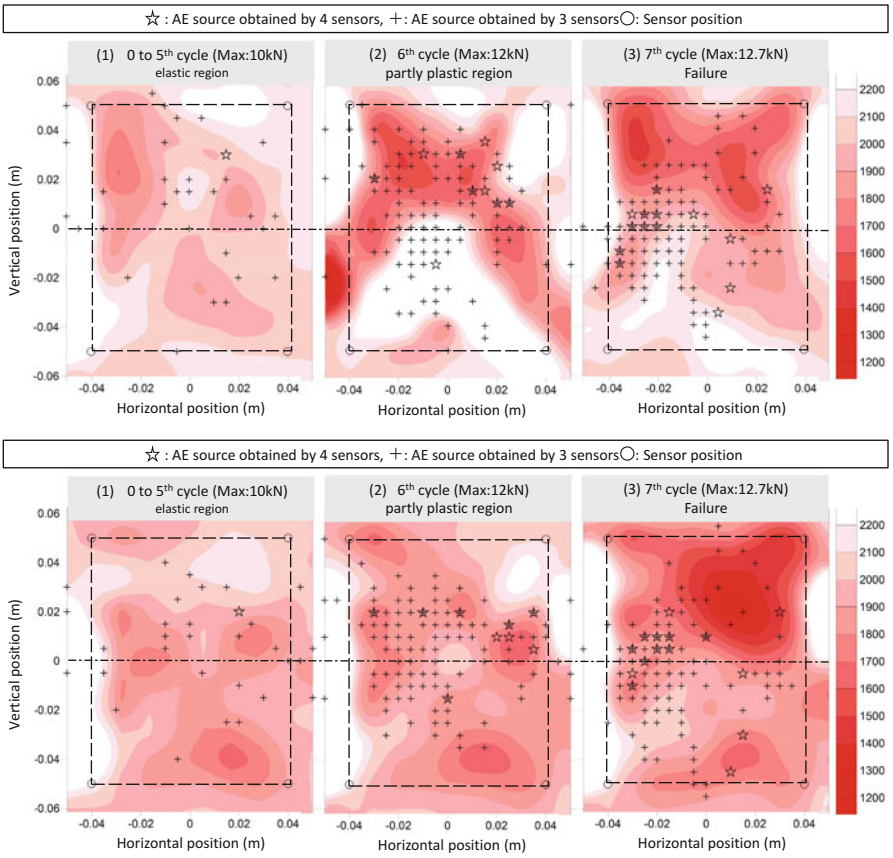

Fig. 13 AE source and velocity distribution of test piece during tensile test considering (**a**) isotropic or (**b**) anisotropic velocity

4 Summary

The following results were obtained from present study.

1. The surface strain of FRP during tensile test could be obtained by digital image correlation.
2. The energy and peak frequency of AE in tensile failure progress of FRP were increased with the surface strain increasing during tensile test and it was considered that the tensile failure process of FRP could be properly detected by evaluating AE parameters.

3. The AE tomography method could be applied to detection of the failure part of FRP successfully. Especially the case of results considering anisotropy velocity distribution were followed by the results of the surface strain behaviors.
4. From above results, it was assumed that the evaluation of AE parameters and AE tomography method could be applied to future inspection of FRP structures as well as digital image correlation.

Acknowledgment This research was promoted by COI program Construction of next-generation infrastructure using innovative materials—Realization of a safe and secure society that can coexist with the Earth for centuries—supported by MEXT and JST.

References

1. Y. Kobayashi, T. Shiotani, in *Two-Dimensional AE-Tomography Based on Ray-trace Technique for Anisotropic Materials*. 6th edition of the International Conference on Emerging Technologies in Non-destructive Testing, May 2015 (To be published)
2. Y. Kobayashi, Mesh-independent ray-trace algorithm for concrete structures. Construct. Build. Mater. **48**, 1309–1317 (2013)
3. Y. Kobayashi, T. Shiotani, K. Oda, in *Two-dimensional Ray-trace Technique for Anisotropic Materials*. The 6th Asia and Pacific Young Researchers and Graduates Symposium (2014)
4. Y. Kobayashi, Shiotani, in *Two-dimensional Source Location Technique on Anisotropic Medium on the Basis of Raytracing*. The 22nd International Acoustic Emission Symposium (2014)
5. K. Ohno, M. Ohtsu, Crack classification in concrete based on acoustic emission. Construct. Build. Mater. **24**, 2339–2346 (2010)

Assessment of Damage Evolution in Paper Material Based on Acoustic Emission: An Experimental and Statistical Method

Liang Zhang, Jianyu Li, Gang Qi, Yingli Zhu, Ming Fan, and Yuxin Qi

Abstract Assessments of damage evolution in paper material are essential to understand, predict, and control this material failure, to which has been paid a great attention in the field of pulp and papermaking. However, for many reasons the evaluation of mechanical performance was not the primary concern in the paper industry previously. The most important points lie in lack of experimental means to obtain the complex damage information and hardness of deterministic mechanical formulas in modeling such a heterogeneous material. This chapter introduces an experimental and a statistical method under a multivariate framework to assess the damage evolution of paper material based on acoustic emission (AE). The intrinsic dynamics of material microstructure during damage evolution were captured with high-resolution, high-speed visualization in real time. Certain pivotal AE parameters (such as timing, quantity, and AE amplitude) extracted from the recorded AE signals were used as inputs to establish a multivariate D_A including scale and observation vectors. Based on the multivariate D_A, information entropy is applied to evaluate damage states quantitatively, and Andrews plot is utilized to cluster damage data with applied stress/strain in different damage stages. Results show that the damage evolution in packaging paper specimen under uniaxial tensile loading mode characters multistage progression, which is evidenced by Andrews plot and optical damage recognition of paper specimen surface topography using scanning electron microscope (SEM) during loading history.

L. Zhang • J. Li (✉) • Y. Zhu
Tianjin Key Laboratory of Integrated Design and On-line Monitoring for Light Industry and Food Machinery and Equipment, Tianjin University of Science and Technology, Tianjin 300222, China
e-mail: lijianyu@tust.edu.cn

G. Qi • M. Fan • Y. Qi
Tianjin Key Laboratory of Integrated Design and On-line Monitoring for Light Industry and Food Machinery and Equipment, Tianjin University of Science and Technology, Tianjin 300222, China

Department of Mechanical Engineering, The University of Memphis, Memphis, TN 38152, USA

G. Shen et al. (eds.), *Advances in Acoustic Emission Technology*, Springer Proceedings in Physics 179, DOI 10.1007/978-3-319-29052-2_18

1 Introduction

Paper material has been extensively used in goods packaging and transporting for its low cost, lightweight, ease of shape and design, recyclability and biodegradability, and also excellent mechanical properties [1–3]. Actually during its lifetime, paper products are exposed to various kinds of loadings including transportation and handling impart load from shocks, vibrations, and compression forces and likewise tension from printing process. All these may produce severe physical damage, such as cracking, rupturing, twisting, shearing, creasing, as well as combination of all these damages, which ultimately accelerated its failure time. Hence, it is of profound significance to understand the damage behavior of the paper material.

The evaluation and characterization of damage evolution during fracture process of paper material, however, are still staying in a "smeared-out" sense. Many traditional experimental methods are still kept developing and using today. Mechanical indicators of paper, such as tensile strength, bursting strength, tearing resistance, and folding endurance, arising from standard test methods and procedures, have been proved to be valuable for reflecting the mutual relationships between mechanical properties and manufacture of paper material [4]. However, these methods didn't dig deep into the progressive damage process leading to final failure.

Currently, successful application of deterministic mechanical models combined with experimental data in other solid material provides much important reference for the study of paper material. Suhling J. C. et al. (1985) began to apply tensorial type failure criteria with linear and quadratic terms to calculate the strength of paper board under plane stress [5]. Correlated with experimental data and operational simplification, the criteria became attractive for predicting the strength of paperboard. Isaksson P. et al. (2004) developed a model for isotropic strain-hardening elastic anisotropic plasticity coupled to anisotropic damage, which properly simulates the failure of packaging paper material subjected to tensile loading [6]. Verified by experimental parameters, the model was efficient to model irreversible deformations calibrated of tensile-loaded paper. Harrysson A. et al. (2007) provided a large strain orthotropic elasto-plastic constitutive model by calibration with biaxial tension tests, and worked satisfactorily in simulation of a creasing operation of corrugated boards [7]. However, the agreement between formula and experiment does not necessarily ensure that the mechanical model accurately can accurately describe and characterize the authentic physical nature of mechanical damage. The artificial calibration in simulation just highlighted the reliability and applicability of experimental data.

In essence, the damage evolution of paper material involves variability, diversity, and interactivity of events of random damage (ERD) existing over various scales ranged from micro- to macroscopic. ERD refers to the failure mechanism residing in material microstructure, such as fiber breakage, fiber pullout, inter-ply failure, and crack formation or crack propagation. The size, shape, energy, and

magnitude of ERD are unpredicted and randomly distributed. The occurrence of ERD releases strain energy rapidly in forms of stress waves. This phenomenon is usually termed as acoustic emission (AE), and can be measured and recorded as acoustic signatures [3, 8]. The obtained AE parameters including amplitude, quantity, and time map to these physics of ERD. Knowing the correlation between a detected AE signatures and ERD, statistical analysis of AE parameters is also "physics." To distinguish the different influence of scales ERD on the material structure, we establish a multivariate D_A coupling multiscale and time effects [9–11]. The establishment of D_A enables us for further multivariate analysis of AE data for identifying and characterizing damage evolution.

The objectives of this investigation are as follows: (1) the quantification of the evolving damage states involving randomness but rule based; (2) clustering of damage modes for further exploring the correlations and interactions of ERD under the influence of multiscale and multi-physics coupling; and (3) the optical recognition of damage physics.

2 Experimental Procedure

2.1 Materials and Specimens

In this investigation, the clay-coated kraft back (CCKB), one typical grade of recycled paper for packaging, is chosen as the case study. Schematics of CCKB (its grammage is 200 g/m^2 and clay-coated one side) are shown in Fig. 1, which depicts a complex heterogeneous structure in three dimensions. During manufacturing, most fibers tend to line up in the running direction of web, and this direction refers to as machine direction (MD); the fibers are presumably hydrogen-bonded side-by-side cross the running web, and consequently this direction is called the cross direction (CD); the out-of-plane direction (ZD) refers to thickness direction of paper material, cf. Fig. 1 [3, 7, 12]. The verso of this paper material shows a stochastic network of plant fibers, while its recto showing a blackened flat surface refers to coating plane with fillers in the porosity of network. Along the cross section the two major layers included fibrous layer and coating layer which are distinguished distinctly, and even the internal structure of the fibrous layer is multilayered.

We cut paper samples from CCKB into rectangular tensile specimens of effective dimensions of 140 mm × 25 mm. An initial crack of length 1 mm was pre-fabricated at one edge and along centerline edge of the specimen. Here, 30 specimens in MD (the long side corresponds to MD of this paper material) were made.

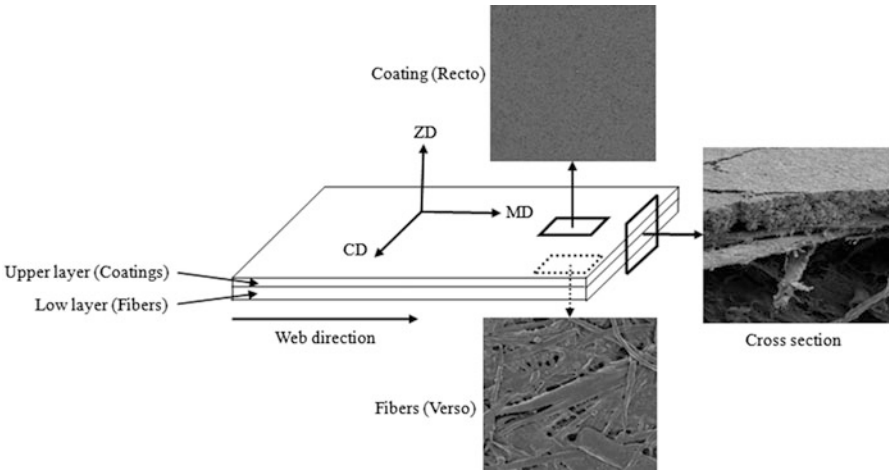

Fig. 1 The basic structure of paper material, obtained from the clay-coated kraft back (CCKB)

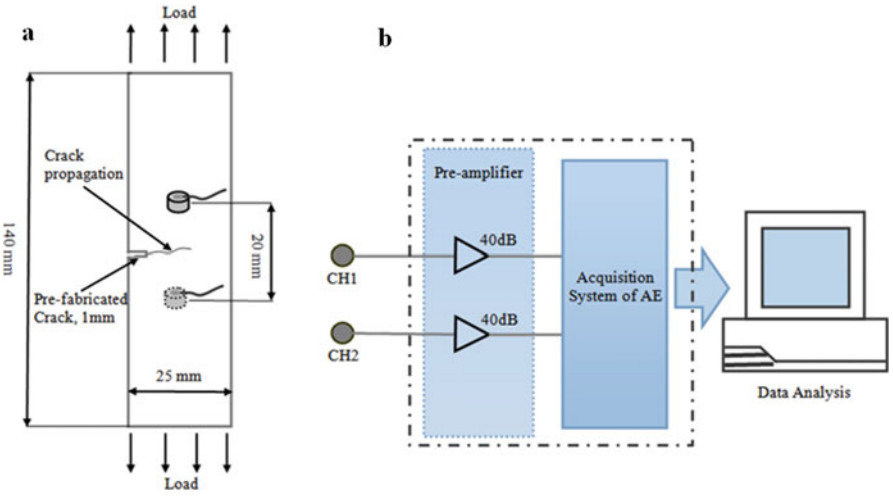

Fig. 2 The schematic of AE measurement setup: (**a**) the specimen is clamped to MTS Universal Tensile Testing Machine, (**b**) AE data acquisition system

2.2 Measurement of Acoustic Emission During Damage Evolution

In current experimental work, AE data acquisition was simultaneous with mechanical testing (in mode-I loading) under certain laboratory conditions (at about 26 °C, 60% RH). Schematics of experimental setup are shown in Fig. 2. Two piezoelectric

sensors were symmetrically glued to the surface of the specimen at locations about 10 mm far from the pre-fabricated crack line.

All the paper specimens were loaded to rupture uniaxially at movement (CMT4304). Meanwhile AE was real-timely monitored during this uniaxial tensile test by Micro-II digital AE system of Physical Acoustics Corporation (PAC), with a sample rate of 1 MSPS and a 40 dB preamplifier (PAC, its band-pass filter is about 20–1200 kHz). Two Nano-30 miniature AE sensors with a resonant response at 300 kHz and a good frequency response over the range of 125–750 kHz were used. The mechanical noise was filtered using a threshold value of 32 dB, below which no detectable AE signals exist at zero loading.

In experimental practice, AE signals caused by the ERD started to emerge when the specimens were strained to certain level. These AE signals including that essential parameters (rise time, duration, counts, energy, amplitude, etc.) deriving from the waveforms were then recorded, and stored into a big data set. Furthermore, scanning electronic microscopy (SEM) techniques were used to overview the skin topography of damage surface of paper specimen.

3 Data Analysis

3.1 *Establishment of the Multivariate* $\mathbf{D_A}$ *Based on Multiple Scales of Events of Random Damage*

The ERD originated from material failure have been captured, recorded, and stored as AE signals timely and continuously. Hence, the valuable information of ERD, i.e., their initiation, growth, localization, and magnitude, could be successfully characterized as AE features. Primary AE parameters, such as timing, quantity, and amplitude, were extracted as input variables of D_A [9, 10, 13]. Ultimately, we obtained a matrix D_A, composed of observation and scale vectors, which equal to quantify the evolution of ERD. Actually, the matrix D_A-based AE presented progressive process of damage evolution in paper material, and especially laid fundamentals for further multivariate analysis to explore the intrinsic physics of damage evolution (Fig. 3).

The formula of D_A is given by [9, 10, 13]

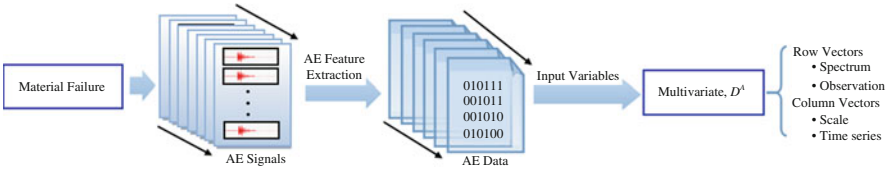

Fig. 3 The sketch of the establishment of the multivariate D_A based on multiple scales of events of random damage

$$D_A = \left[\alpha_{ij}\right]_{M\times N} = \begin{pmatrix} \alpha_{11} & \cdots & \alpha_{1j} & \cdots & \alpha_{1N} \\ \vdots & \ddots & \vdots & \iddots & \vdots \\ \alpha_{i1} & \cdots & \alpha_{ij} & \cdots & \alpha_{iN} \\ \vdots & \iddots & \vdots & \ddots & \vdots \\ \alpha_{M1} & \cdots & \alpha_{Mj} & \cdots & \alpha_{MN} \end{pmatrix} \tag{1}$$

where the matrix element α_{ij} = counts (AE events lie in the j^{th} amplitude-scale subinterval, and the i^{th} observation subinterval). The sign N, the total number of column vectors of D_A matrix, indicates the number of divided scales based on amplitude. The sign M, the total number of row vectors, indicates the number of observation vectors (or spectrums) based on varying time level:

$$D_A = \begin{pmatrix} Y_1^A \\ \vdots \\ Y_i^A \\ \vdots \\ Y_M^A \end{pmatrix}, \quad Y_i^A = \left(\alpha_{i1}, \alpha_{i2}, \cdots, \alpha_{ij}, \cdots, \alpha_{iN}\right) \tag{2}$$

where Y_i^A ($i = 1, 2, \ldots, M$) represents the i^{th} row vector, and indicates the damage state at specified time level.

3.2 Application of the Entropy Value to Quantify the Evolving Damage States

As already stated, the observation vectors of D_A actually represent the distribution of numbers and scales of obtained ERD at specified time level, which reflect the damage state to some degree. The damage state can be assessed by applying probability entropy according to our previous work.

Firstly a normalized form of D_A is given by

$$\overline{D_A} = \left(p_{ij}^A\right)_{M\times N} = \begin{pmatrix} p_{11}^A & \cdots & p_{1N}^A \\ \vdots & \ddots & \vdots \\ p_{M1}^A & \cdots & p_{M\times N}^A \end{pmatrix}, \quad p_{ij} = \alpha_{ij} / \sum_{j=1}^{N} \alpha_{ij} \tag{3}$$

Then a probabilistic entropy s is [9, 10, 13, 14]

$$s \approx \sum_{j=1}^{N} p_{ij}(x) \ln\left(1/\left(N_{P_{ij}}(x)\right)\right) \tag{4}$$

Several concrete important properties of entropy s are described as follows [9]:

1. Increasing entropy: $\partial s/\partial t > 0$. The higher the value of s, the greater the uncertainty of occurrence of multiscale ERD, and then the material microstructure is more vulnerable to failure.
2. Near-equal entropy (knee transition): $\partial s/\partial t \approx 0$. The stable value of s indicates the immutability of the propagation of multiscale ERD.
3. Decreasing entropy: $\partial s/\partial t < 0$ or sharp uncertainty. The smaller value of s indicates the less uncertainty of occurrence of multiscale ERD. In other words, the occurrence of ERD gathers in less scale interval. Or the value of entropy s fluctuates wildly due to the destabilization of material structure for ultimate failure.

One point to note is that generally it is the relative value of s that should be focused on, because only in certain source physics the meaning of s is valuable. When the entropy s is correlated with the varying time, trajectory of damage state (TDS) is obtained. It has been evidenced that application of TDS to describe whole damage evolution process is effective and practical.

3.3 Application of Andrews Plots to Cluster Damage Modes

An exploratory data analysis, Andrews plot, is employed to visualize the spectrum of multivariate D_A, which helps us to find the similarity of different damage modes with increasing time and clustering them precisely. Here, the algorithm of Andrews plot is defined by the following trigonometric function [15]:

$$\begin{aligned} f_{Y_i^A}(t) = \; & \frac{\alpha_{i1}}{\sqrt{2}} + \{\alpha_{i2}\sin(2\pi t) + \alpha_{i3}\cos(2\pi t) \\ & + \cdots + \left\{ \begin{array}{l} \alpha_{ij}\sin(j\pi t), \;\; \text{if } j \text{ is even} + \\ \alpha_{ij}\cos((j-1)\pi t), \;\; \text{if } j \text{ is odd} \end{array} \right\} + \cdots \end{aligned} \tag{5}$$

where the continuous dummy variable, t, belongs to the interval [0, 1]. Here, before making the plots, we should standardize every Y_i^A (zero mean and unit standard deviation), so the resulting α_{ij} is represented by $\alpha^s{}_{ij}$. The modified algorithm is given by

$$\begin{aligned} f_{Y_i^A}(t) = \; & \frac{\alpha_{i1}^s}{\sqrt{2}} + \{\alpha_{i2}^s\sin(2\pi t) + \alpha_{i3}^s\cos(2\pi t) \\ & + \cdots + \left\{ \begin{array}{l} \alpha_{ij}^s\sin(j\pi t), \;\; \text{if } j \text{ is even} + \\ \alpha_{ij}^s\cos((j-1)\pi t), \;\; \text{if } j \text{ is odd} \end{array} \right\} + \cdots \end{aligned} \tag{6}$$

This formula can be regarded as the projection of the observation vector $Y_i^A = ()$ $Y_i^A = \left(\alpha_{i1}^s, \alpha_{i2}^s, \ldots, \alpha_{ij}^s, \ldots, \alpha_{iN}^s\right)$ onto the vector $\left(1/\sqrt{2}, \sin(2\pi t), \cos(2\pi t), \ldots, \left\{ \begin{array}{l} \sin(j\pi t), \;\; \text{if } j \text{ is even} + \\ \cos((j-1)\pi t), \;\; \text{if } j \text{ is odd} \end{array} \right\}, \ldots\right)$.

Hence, in this data spectrum visualization, those individual vectors Y_i^A featuring similarity will dance similar in the form of curves correspondingly. Use of Andrews plot to identify clusters of damage modes graphically is based on advantages that this data transformation maintains many useful inherent properties of the original ERD-based damage data, such as mean preservation, distance preservation, one-dimensional projections, and linear relationships.

4 Results and Discussion

4.1 Acoustic Emission Behavior of Paper Material Under Tensile Test

Figure 4 shows the plot of applied load and AE amplitude against time relationship from all 30 specimens in MD. During the initial loading stage (the time is before 150 s, and the load is less than 75 N), there are no detected AE signals exceeding the threshold, which means that little of ERD occur or the released energy is too weak to measure. For paper material, these results were primarily attributed to the ductility and malleability of fibers, mutual connection of hydrogen bond among fibers, and even inherent cushioning property of fibered network structure [3, 11]. Essentially all these properties contribute to the absorption of mechanical energy done by external force. Hence, this stage can reasonably be identified as the elastic deformation. Before approaching maximum loading, acoustic emission

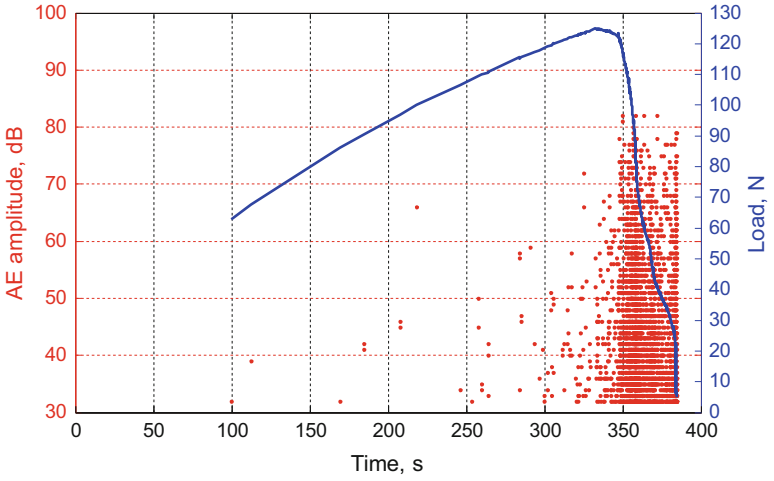

Fig. 4 The representation of AE signal amplitude vs. time during loading. As shown in Fig. 3, we detected many AEs before the final fracture

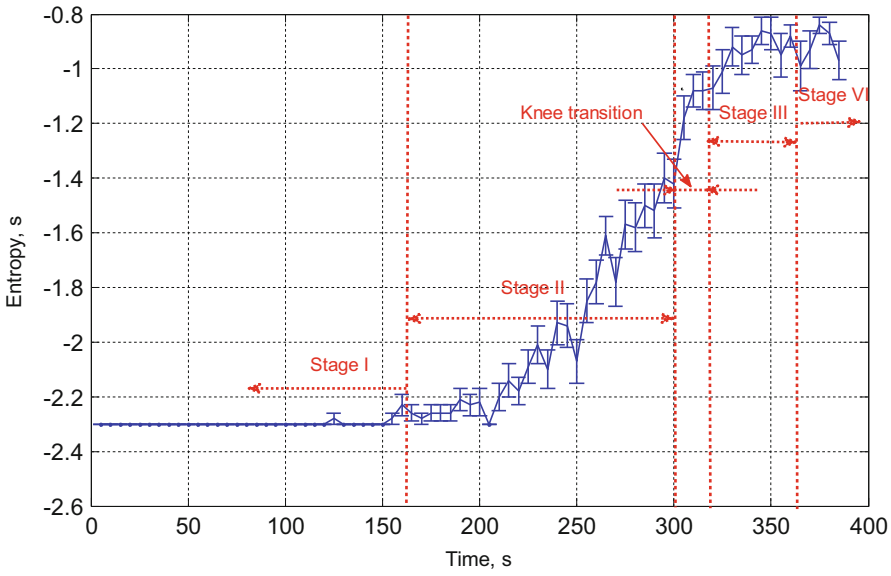

Fig. 5 Trajectory of damage state for paper material

events begin to occur. It is worth noting that initiation of AE activities indicates one "critical point" in damage evolution, after which damage exerts significant influence on the mechanical performance of paper material. The count of AE events increases rapidly after the maximum load, suggesting more ERD counts in this loading stage. During this loading stage, cracks form, propagate, and extend until ultimate fracture of the paper specimen. Actually, the process of damage accumulation, coalescence, and development illustrates a gradual loss of instability of material's fibered network structure.

4.2 The Multistage Progression of Damage Evolution in Paper Material

Figure 5 illustrates results of TDS for 30 paper specimens under tensile test. As is shown Fig. 5, the entire loading in tensile test can be divided into four stages following the tendency of s according to Section 3.2. As shown in Fig. 6, the clustering results of Andrews plot present that the four groups of plots correspond to the four stages. From the detailed analysis of the damage ensemble of each stage, it is possible to associate these different stages with typical variation of ERD and source physics. All following observations are made:

Stage I ($t \leq 160$ s in Fig. 5): $s_{\min} = \ln(1/10)$ and $\partial s/\partial t \approx 0$. During the initiation of loading, this does not indicate immutability of the occurrence of multiscale ERD

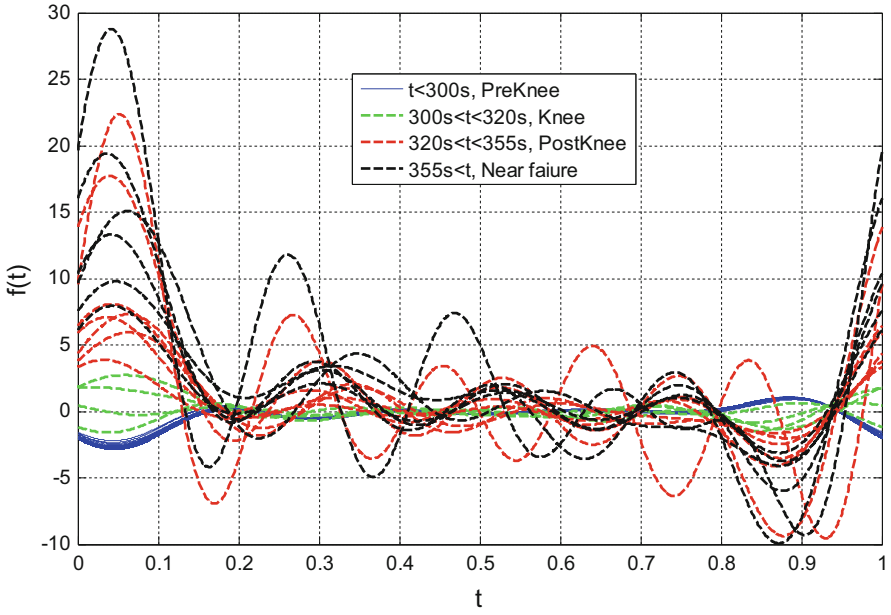

Fig. 6 Andrews plots of paper material

but represents that there exists little occurrence of ERD, cf. Fig. 4. Andrews curves marked blue in this stage in Fig. 6 cluster together. For paper material, these results were primarily attributed to the ductility and malleability of fibers, interaction of hydrogen bond among fibers, and even porous network structure, which all contribute to absorb the energy of mechanic work by external force without any irreversible damage. Additionally, the damage-related variables of this stage also associate to in-plane stiffness and other elasticity-related parameters for strength evaluation of paper material, but further data analysis is needed to find these variables or indicators.

Stage II (160 s $< t \leq$ 300 s in Fig. 5): $\partial s/\partial t > 0$ and $\partial^2 s/\partial t^2 > 0$. During this stage s begins to accelerate at higher and higher speed rate, which suggests that distribution of multiscale ERD becomes more and more uniform. From this stage, ERD begin to occur and spread ranging from low scale to high scale. Here the ERD residing in paper structure begin to influence the plastic performance and other mechanical properties of paper material. Andrews carves of this stage are also marked blue in Fig. 6, which show high similarity with stage I. It shows that the increase of entropy s doesn't necessarily identify the increase of severity of the damage state; on the contrary it demonstrates the enhancement of material tolerance to tensile load. From the perspective of source physics, occurrence of multiscale ERD was driven by the expansion of the force or strain field beginning from the vicinity of a pre-fabricated crack tip to volume. In other words, the influenced region by ERD began to propagate radially from crack line. It is

reasonable to infer that at the onset of the damage process those ERD of lower energy occur in the failure mechanism such as fragile nodes or weak de-bonding of network structure, fibril breakage, and other initiation of low energy-intensive micro-damage. Note that this damage state presents an initiation of plastic deformation.

Knee transition (300 s $< t \leq$ 320 s in Fig. 6): transition from $\partial^2 s/\partial t^2 > 0$ to $\partial^2 s/\partial t^2 < 0$, which slows down the increasing speed of value of s. During this knee transition, the Andrews curves marked green dance together in the transition zone. If we define the midpoint of this stage as the knee point, i.e., $t_{\text{knee}} \approx 310$ s in Fig. 6, it corresponds to $\sim$80% of the paper material's tensile loading time. It can be anticipated that this finding may have in-depth relationships with mechanical properties of paper material. The underlying physics of the knee transition deserves further data analytics.

Stage III (320 s $< t \leq$ 355 s in Fig. 6): $\partial s/\partial t > 0$, from $\partial^2 s/\partial t^2 < 0$ to $\partial s/\partial t \approx 0$. This means immutability of the occurrence of multiscale ERD in damage process of paper specimens and damage states tend to become more stable. But the stable stage is very short and features local fluctuation in paper material. In Fig. 6, the family Andrews curves (marked red) of this stage are 180° in the phase angle parting from previous two stages. The crack line has formed cross the specimen and the distribution of ERD in the range of all scales becomes unchangeable. The radial region of multiscale ERD stops from expanding, and moves following the crack tip until ultimate failure. The occurrence of fundamental micro-damage mechanism, such as fiber breakage, fiber-fiber bond failure, delamination between fibers and non-fibrous components, failure of non-fibrous components, and even "fretting" between different components (especially the friction in dislocation of fibers), becomes relatively constant without significant occurrence of new damage modes.

Stage IV ($t >$ 355 s in Fig. 6): $\partial s/\partial t < 0$ or sharp uncertainty, when the paper specimens approach failure. Sometimes the shape of the TDS curves changes rapidly due to the loss of stability for tolerating the driven force. This stage was empirically regarded as precursors of failure.

4.3 Optical Damage Recognition of Paper Specimens Under Tensile Loading

Figure 7 shows the topography of surface damage of paper specimens in MD at different stages during loading history. As shown in Fig. 7a, the main micro-crack was initiated. Actually, in experimental practice AE observations showed that ERD occurred before the onset of main crack. At the beginning, the internal ERD were excited by the elastic deformation or preexisting defects in paper microstructure but not be observed visually. Also radical cracks on coating surface in the vicinity of the main crack indicate the regions of multiple stress fields. This stage corresponds to the first two stages (stages I and II in Fig. 5), when the occurrence of ERD doesn't

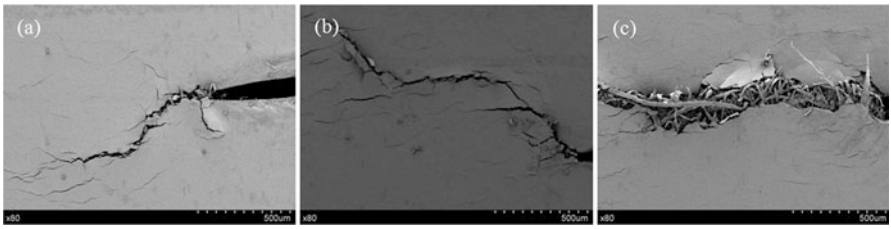

Fig. 7 The SEM evaluation of paper specimen surface topography: (**a**) initial damage; (**b**) significant damage; (**c**) approach fracture

necessarily identify the increase of severity level of the damage state or the loss of tolerance to driven force. As shown in Fig.7b, as the external force was increasing, the main crack began to propagate macroscopically and simultaneously many radical secondary cracks initiated randomly from main crack line and finally some parts of them coalesced. During this stage, the region of stress field around the crack tip and crack line stopped expanding, all fundamental damage mechanisms were included, and then damage evolution process was relatively stable. Finally, catastrophe failure was approached, when a nonlinear trace of rupture is behind as shown in Fig. 7c.

5 Conclusions

In this investigation, we develop an experimental and statistical method under multivariate framework to assess the damage evolution of paper material based on AE. Experimentally, AE technology is a powerful tool to investigate the damage evolution of paper material. Application of entropy to quantify the evolving damage state with time levels based on D_A shed additional light to assessment of damage evolution in paper material. The obtained TDS present that the process of damage evolution in paper material under tensile load characters multistage progression. This is also evidenced by the Andrews plot cluster, which distinguished different groups of curves. Additionally, optical damage recognition using SEM also provides the experimental evidence for our statistical analysis.

Acknowledgment The authors are indebted to all who have contributed to this chapter. Special thanks to S. F. Wayne (University of Memphis) for many helpful discussions. Authors gratefully acknowledge the support of National Natural Science Foundation of China under Grant No. 11272234.

References

1. Paper and paperboard packaging technology, Wiley, 2008
2. P. Samyn, J. Van Erps, H. Thienpont, et al., Paper coatings with multi-scale roughness evaluated at different sampling sizes. Appl. Surf. Sci. **257**(13), 5613–5625 (2011)
3. P. Isaksson, R. Hägglund, P. Gradin, Continuum damage mechanics applied to paper. Int. J. Solids Struct. **41**(16), 4731–4755 (2004)
4. D.F. Caulfield, D.E. Gunderson, Paper testing and strength characteristics. 1988 Paper preservation symposium: Capital Hilton, Washington, DC, October 19–21, TAPPI Press, 1988, pp. 31–40
5. J.C. Suhling, R.E. Rowlands, M.W. Johnson, et al., Tensorial strength analysis of paperboard. Exp. Mech. **25**(1), 75–84 (1985)
6. P. Isaksson, R. Hägglund, P. Gradin, Continuum damage mechanics applied to paper. Int. J. Solids Struct. **41**(16), 4731–4755 (2004)
7. A. Harrysson, M. Ristinmaa, Large strain elasto-plastic model of paper and corrugated board. Int. J. Solids Struct. **45**(11), 3334–3352 (2008)
8. L. Salminen, *Aspects of Fracture Processes in Paper* (Helsinki University of Technology, Espoo, 2003)
9. G. Qi, S.F. Wayne, A framework of data-enabled science for evaluation of material damage based on acoustic emission. J. Nondestruct. Eval. **33**(4), 597–615 (2014)
10. G. Qi, J. Li, M. Fan, et al., Assessment of statistical responses of multi-scale damage events in an acrylic polymeric composite to the applied stress. Probabilist. Eng. Mech. **33**, 103–115 (2013)
11. L. Zhang, M. Fan, J. Li, *Statistical Analysis of Events of Random Damage in Assessing Fracture Process in Paper Sheets Under Tensile Load*, Advances in Acoustic Emission Technology (Springer, New York, 2015), pp. 267–281
12. Q.S. Xia, M.C. Boyce, D.M. Parks, A constitutive model for the anisotropic elastic–plastic deformation of paper and paperboard. Int. J. Solids Struct. **39**(15), 4053–4071 (2002)
13. G. Qi, S.F. Wayne, M. Fan, Measurements of a multicomponent variate in assessing evolving damage states in a polymeric material. Instrum. Meas. Mag. **60**(1), 206–213 (2011)
14. J.W. Gibbs, *Elementary Principles in Statistical Mechanics* (Courier Corporation, North Chelmsford, 2014)
15. D.F. Andrews, Plots of high-dimensional data. Biometrics **28**, 125–136 (1972)

Innovative AE Measurement by Optical Fiber Sensing for FRP

H. Asaue, T. Shiotani, T. Nishida, K.C. Chang, and H. Nakayama

Abstract Recently, composite materials are widely applied to the civil structures due to their high corrosion resistance, lightweight, and high mechanical strength. Along with these conditions, a long-term and periodic measurement for damage monitoring for civil structures is imperative by fiber-reinforced plastics (FRP). The advantages of optical fiber sensing technology have attracted the attention in FRP measurement such as its long life, ready embeddedness, large-scale measurements, lack of disturbance by electrical noise, and excellent harmonization with FRP. In this study, detection of AE activity was confirmed for evaluation of precursory damage as a break using the FBG of optical fiber sensing with high-speed data sampling.

1 Introduction

Recently, fiber-reinforced plastic (FRP) composite material has been widely used in civil structures. Civil structures made of reinforced concrete demand a special attention to the corrosion protection components exposed to the corrosive environments such as coastal area. In order to meet the demand, maintenance costs increase. Nevertheless, FRP for civil structures provide solutions for problems because FRP have high corrosion resistance, lightweight, and high mechanical strength. Therefore, FRP composites replaced traditional materials, i.e., steel and concrete, for bridge became a tendency in civil applications. However, due to the poor reliability on long-term durability and insufficient data of physical properties for its short usage history in Japan, FRP for civil structures in bridges are generally more likely to use light-load designs. Hence, for pervasiveness of FRP, it is necessary to evaluate damage progress and physical behavior in actual structures made by FRP. Consequently, long-term and periodic measurement methods must be developed in order to extend the performance and service life of infrastructure.

H. Asaue (✉) • T. Shiotani • T. Nishida • K.C. Chang • H. Nakayama
Kyoto University, Katusra campus, Kyoto 615-8540, Nishikyo, Japan

Oriental Consultants Kyushu Branch, Fukuoka 812-0011, Japan
e-mail: asaue.hisafumi.7a@kyoto-u.ac.jp

G. Shen et al. (eds.), *Advances in Acoustic Emission Technology*, Springer Proceedings in Physics 179, DOI 10.1007/978-3-319-29052-2_19

The benefits of optical fiber sensing technology have attracted the attention because of its long life, ready embeddedness, large-scale measurement, lack of disturbance by electrical noise, and excellence with FRP. Currently, although static monitoring of FRP can be performed with multiple numbers of fiber Bragg gratings (FBG), e.g., time-division multiplexing (TDM) or wavelength-division multiplexing (WDM) technology [1], dynamic monitoring to the level of acoustic emission is still in progress [2]. The feasibility of acoustic emission (AE) detection for FRP by dynamic measurement using high-speed FBG monitoring system was evaluated and discussed in this study.

2 Optical Fiber Sensing

2.1 Optical Fiber Sensing by FBG

An optical fiber sensing system consists of an optical source, a fiber as transmission path, a measuring section, and an optical receiver. The system has been widely used to measure various physical parameters including strain, vibration, and temperature. Optical fiber sensing is divided into two groups called distribution and multipoint. The former is applied for continuous longitudinal direction, and the latter can be used as an existing sensor because of high-speed data sampling and high accuracy. One great advantage of multipoint measurement is that the measurement provides a convenient evaluation of AE detection activity by optical fiber sensing. For this reason, FBG sensors for multipoint measurement are a suitable method to be used for this purpose. WDM and TDM are two major multipoint measurements for FBG sensors. The WDM can provide high-speed data sampling and high accuracy, but the number of FBG sensors in a single line is limited about ten FBG sensors. On the other hand, the TDM can markedly increase the number of FBG sensors, i.e., a hundred FBG sensors in a single line, but the disadvantages of TDM over WDM are that it needs at least 2 m spacing between FBG sensors, and large time-consuming process in one-time measurement. Therefore, due to high-speed data sampling and importance of AE detection, the technique of WDM was selected in this study.

2.2 Outline of FBG

An FBG is an optical fiber sensor created by periodic variation of the refractive index which is induced by ultraviolet ray irradiation within the core of optical fiber. The overview and schematics of FBG sensors are shown in Fig. 1. The grating acts as a mirror on the variation of the real part of the refractive index. The change of

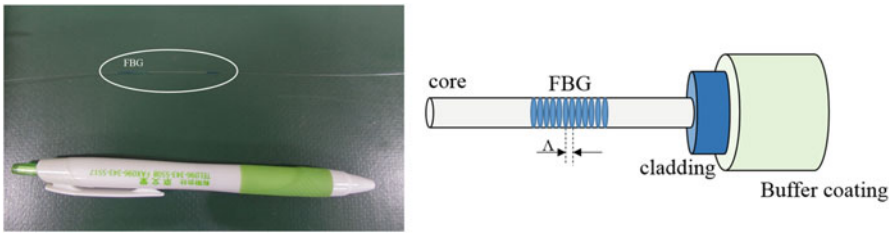

Fig. 1 Overview and schematics of FBG

refractive index works as a grating. The grating reflects that optic source is satisfied with the condition for Bragg reflection. Bragg wavelength λ_b is defined by

$$\lambda_b = 2n\Lambda \tag{1}$$

where n and Λ are effective refractive index in the core of optical fiber and grating spacing, respectively [3]. For example, when FBG sensor is strained, Bragg wavelength is shifted to the long-wavelength direction. A number of FBG can be set in one fiber by changing Λ of each FBG.

3 Experiment Condition

3.1 Outline of Specimen

In this study, FRP was sampled from undersurface plate of an existing footbridge as shown in Fig. 2. The footbridge was located in Okinawa Island in southern Japan. The bridge was constructed in 2000 and has been used for 12 years. A schematic diagram of FRP specimen is shown in Fig. 3. Two pieces of additional FRP were attached as grip parts on the end of a specimen. The length, width of center, and thickness of it were 480 mm, 100 mm, and 4 mm, respectively. AE sensors and strain gauges were set up on the specimen in addition to FBG. Spacing of sensors was 80 mm in direction of short axis and 100 mm in direction of long axis.

3.2 Cyclic Tensile Test

The cyclic tensile test was carried out by AG-50kNX (Shimadzu Co., Ltd.) in this study. Load capability of the equipment is 50 kN. The equipment can be controlled by dedicated software using a computer. The edges of specimen (grip parts) were fixed on loading equipment through jacks as shown in Fig. 4. Incremental cyclic tensile load as shown in Fig. 5 was applied to the specimen by 2 kN up to 12.7 kN. 12.7 kN was failure load of the specimen. The layout of sensors is shown in Fig. 6.

Fig. 2 FRP footbridge

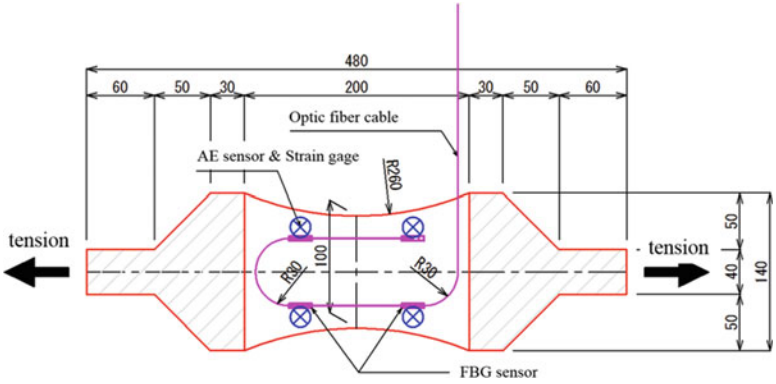

Fig. 3 Outline of specimen

3.3 AE Activity Measurement

During tensile test, the results of AE activities were obtained by FBG and general AE measurements. FBG measurement was carried out by AR5011B FBG monitoring system (Anritsu Co., Ltd.) incorporated with WDM and AWG (arrayed waveguide grating) (Fig. 7).

The FBG system specifications are summarized as follows. Usually, the range of sampling rate is from 1 to 1 kHz. However, detection of AE activity is required at least nearly 1 MHz of the sampling rate. Therefore, the FBG system which enables high-speed sampling rate of 806.45 kHZ was developed, and was used in this study. Acquisition time is 0.01 s per event. Measurement ranges of spectrum wavelength and FBG peak are from 1530.334 to 1580.350 nm and from 1531.116 to 1579.518 nm, respectively. Reproducibility of wavelength is 5 pm. In this study, optical signal port is applied in one of the connected ports. In some case, it can be

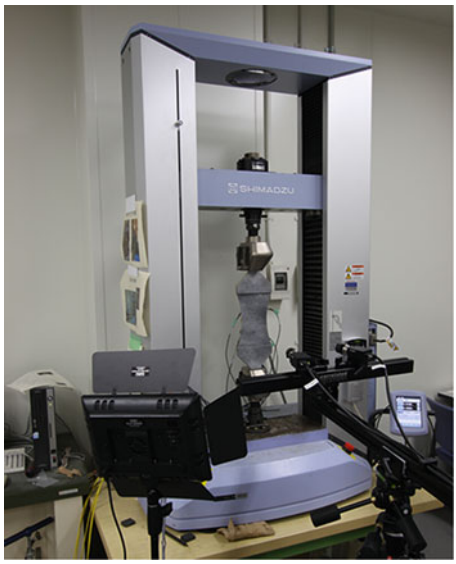

Fig. 4 Tensile loading situation

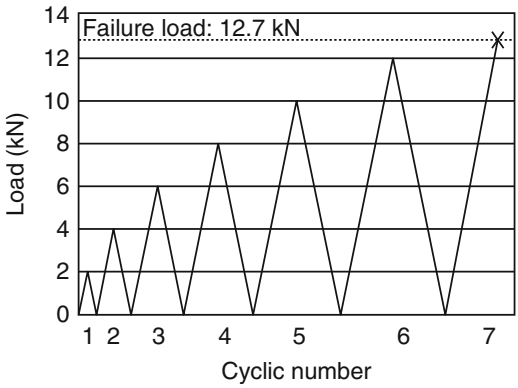

Fig. 5 Incremental cyclic tensile load

extended up to eight connected ports. Many types of fiber connector have been developed for different purposes. Both SC and PC (not angled PC) fiber connectors are used in this study. Adapted fiber is a single-mode fiber which has the size of 426 (W) × 177(H) × 451(D) mm, and the weight of 10.6 kg. Configuration diagram of AR5011B is shown in Fig. 8.

Optical signal for FBG is divided into each wavelength into AWG. Then, the optical signal is transduced into electrical signal by photodetector (PD) array, and analog signals are converted into digital signals in ADC field-programmable gate array (FPGA), and finally sent to control PC. In the case of AE system, it consists of Micro-II Express (Physical Acoustics Co., Ltd.) with four AE sensors with resonance frequency of 60 kHz incorporated with integral preamplifier. Dynamic data acquisition system was specifically used for AE measurement in both systems. It

Fig. 6 Specimen with sensors

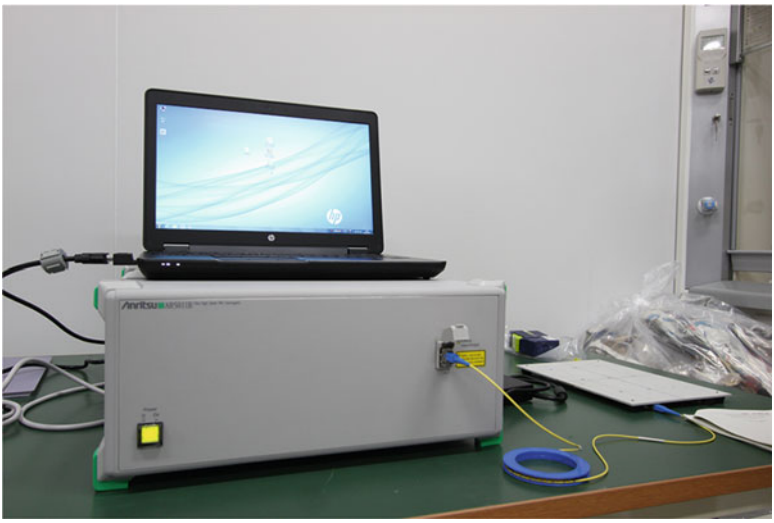

Fig. 7 Overview of FBG observation instrument (AR5011B)

means that AE activity data can be obtained when activity exceeded a certain predefined threshold level, 20 picometers in FBG measurement, and 40 dB preamplifier in AE system in this study.

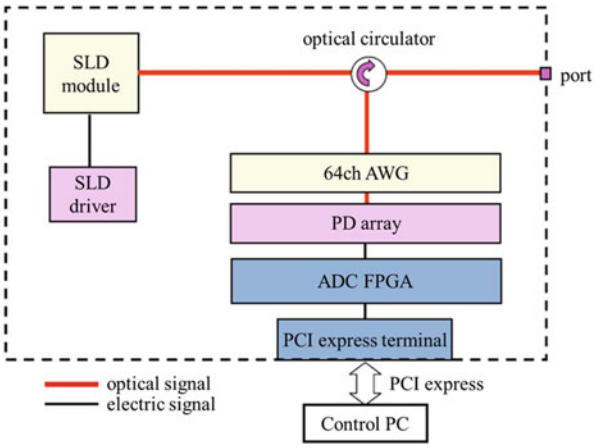

Fig. 8 Configuration diagram of AR5011B

4 Results and Discussions

According to the test results, the FRP was damaged at 390.7 s from test start. It is important to note that the strain curve has linear relationship with tensile loads. The experimental results show that FRP was damaged after applying 12.7 kN loading on a specimen. The results of the AE amplitude and wavelength difference of FBG over the time are shown in Fig. 9a, b, respectively. As shown in Fig. 9, a gap of strain curve at 383 s corresponding yield point occurred immediately prior to final brakeage. The detection of AE activities before 350 s cannot be measured by dynamic FBG, while the detection of AE activities corresponding to the emergence of large-energy AE event was obtained after 350 s as shown in Fig. 9c. Despite less sensitivity for AE activity measurements, the applied AE activity measurements by dynamic FBG were sufficient to obtain the results.

Relatively sharply defined waveforms were obtained by FBG measurement when the elapsed times are 383.5, 384.57, and 390.7 s. The former two were wavelength difference of FBG over 1.5 nm after reaching corresponding yield point, and the last measurement was at brakeage. FBG waveforms and AE waveforms obtained at same period are plotted in Fig. 10a–c. High-frequency fluctuation in AE activities and FBG waveforms can be detected in 500 μs from arrival time (it means 1500 to 2000 μs in the graph) at the case of 383.51 and 384.57 s. In addition, long-wave period fluctuation appeared after high-frequency fluctuation, which corresponds to the later phase in the AE system. As the reason to this, it is thought that AE sensor has a resonance frequency of 60 kHz but the FBG do not set off the resonance frequency. Different waveforms from the above were obtained at the case of 390.7 s in both AE system and FBG. According to this, both large variations of up to 2500 μs are common. Thus, the possibility of AE waveform discrimination of even FBG is indicated. Based on the test results, waveforms of AE activity would be obtained by dynamic FBG measurements. However, FBG waveforms are biased to the direction of short wavelength. For this reason, it is thought

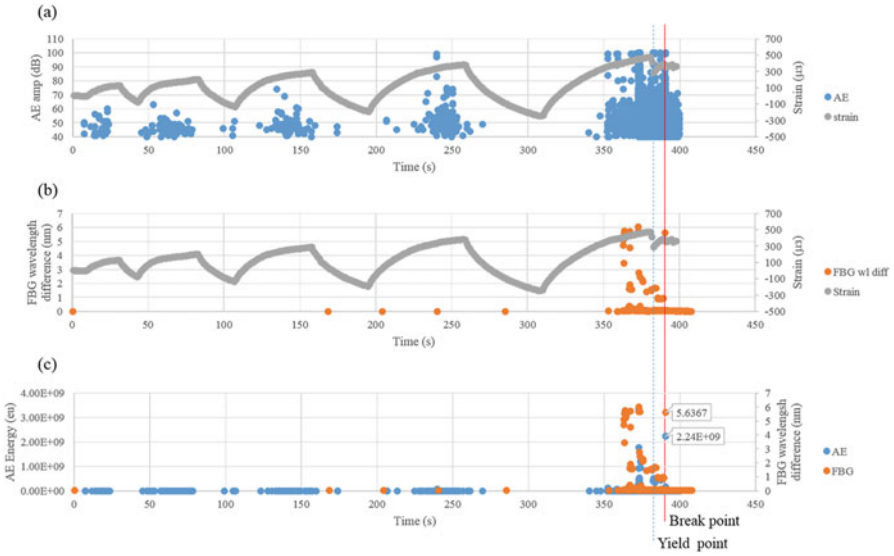

Fig. 9 (**a**) Relationship between AE amplitude and strain, (**b**) wavelength change by FBG, and (**c**) increment of AE energy was conformity with that of FBG wavelength change

that FBG were affected by constraint bonding to FRP. FBG were difficult to extend so that FBG waveforms are biased.

These results indicate that the feasibility of AE detection by dynamic measurement using FBG sensors is recommended to perform at this generation, although suitable installation and resonance frequency of FBG sensors should be considered carefully on FRP for high-sensitive measurement.

5 Conclusion

The following results were obtained from the present study:

1. AE activity before final breakage of FRP can be confirmed by dynamic FBG measurements.
2. Large-energy AE activity on yield point and final breakage would be detected by waveform of dynamic FBG measurement.
3. FBG data quality would be affected by its installation.

From above results, feasibility of AE detection using dynamic FBG measurement would be demonstrated.

Acknowledgment This research was promoted by COI program "Construction of next-generation infrastructure using innovative materials - Realization of a safe and secure society that can coexist with the Earth for centuries" supported by MEXT and JST.

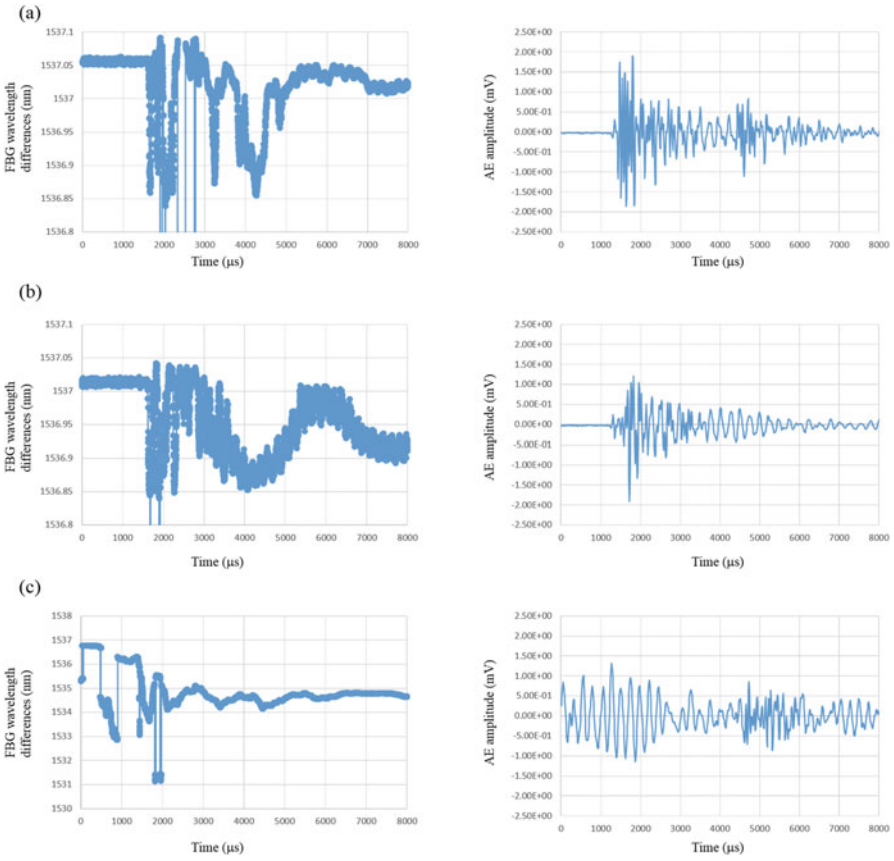

Fig. 10 Waveforms by FBG monitoring system and AE system, (**a**) at 383.51 s, (**b**) at 384.57 s, and (**c**) at 390.7 s from test start

References

1. K.T.V. Grattan, T. Sun, Fiber optic sensor technology. Sensor. Actuat. **82**, 40–61 (2000)
2. K.O. Hill et al., Bragg Gratings fabricated in monomode photosensitive optical fiber by UV exposure through A phase mask. Appl. Phys. Lett. **62**(10), 1263–1276 (1993)
3. A. Othonos, K. Kalli, *Fiber Bragg Grating* (Artech House Publishers, Norwood, MA, 1999), pp. 95–99

Fracturing Behaviors of Unfavorably Oriented Faults Investigated Using an Acoustic Emission Monitor

Xinglin Lei, Shinian Li, and Liqiang Liu

Abstract In order to shed light on the mechanism and characteristics of the reactivation of unfavorably oriented faults due to natural or man-made stress changes, we investigated the stick-slip behavior of precut faults having different angles to the greatest principal stress in granite rock samples using an acoustic emission (AE) technique under well-controlled laboratory conditions. The results show that the friction coefficient of a precut fault depends only on its stick-slip history, being independent of fault angle. In all cases, the fault friction drops from ~0.75 to 0.6 after a few stick-slip iterations. Many AE events preceding each stick-slip event were observed. We mapped both on-fault and off-fault microcracks in detail with their AE hypocenters. A tendency toward decreased AE activity was observed. Experimental results suggest that there are two competing mechanisms governing the evolution of the frictional properties and the damage zone characteristics of such faults. On the one hand, the fault plane is smoothed by fault slippage as a result of asperities failing on the fault plane and a fault gauge is created. On the other hand, the fault plane is roughened by new damage. As a result, both AE activity and fault friction tend to decrease, but with significant fluctuations.

1 Introduction

Reactivation of preexisting favorably and unfavorably oriented faults is an important issue in earthquake seismology and petroleum applications. It is particularly important in seismicity induced by fluid injection or extraction in various applications such as oil/gas production, shale gas fracking, geological storage of CO_2 and other wastes, and enhanced geothermal systems [1, 2]. Reshearing of favorably oriented faults provides the lower limiting bound to overpressures, which is a key

X. Lei (✉)
Geological Survey of Japan, AIST, Ibaraki 305-8567, Japan
e-mail: xinglin-lei@aist.go.jp

S. Li • L. Liu
State Key Laboratory of Earthquake Dynamics, Institute of Geology, China Earthquake Administration, Beijing 100029, China

G. Shen et al. (eds.), *Advances in Acoustic Emission Technology*, Springer Proceedings in Physics 179, DOI 10.1007/978-3-319-29052-2_20

parameter in the design and management of injection applications. At the same time, unfavorably oriented faults are also important because they are stable and show very low levels of background seismicity under regional stress conditions, but might be reactivated due to man-made local stress changes. Therefore, we should pay special attention to such faults, both known and unknown, in geomechanical analyses and risk assessments of related applications.

Rocks with foliated structures also have weak planes, so they exhibit fracturing behaviors similar to some natural faults [3]. It has been observed that the orientation of foliations within a given stress regime, which weaken the structure of some sedimentary and metamorphic rocks, plays a governing role in the fracturing process of the rock [3]. In earthquake seismology, seismicity on unfavorably oriented faults is considered to be evidence of over-pressurized fluids and has attracted researchers' attention for a long time (e.g., [4–7]). Thus, explaining the fracturing properties of faults under various stress conditions is important.

Acoustic emission (AE) events have been observed during frictional sliding on precut faults in laboratory rock samples. Besides the lithology of the blocks, the roughness of surface, geometries (bend and orientation) of the fault, gouge, and loading speed have been investigated (see review in [8]). Most published studies are motivated by the need to provide frictional models for faults, which are required for earthquake cycling simulation, so either most experiments are performed under pure shear conditions or the samples tested are favorably oriented for rupture under triaxial compression conditions. So far, AE activity related to the stick-slip of unfavorably oriented faults has not been systematically investigated in the laboratory. Motivated by these facts, we carried out a systematic study using rock samples containing artificially precut faults as well as naturally created faults and acoustic emission technology in well-controlled laboratory conditions. Here, we present our experimental results using granite samples precut at 45° and 50° orientations.

2 Test Samples and Experimental Setup

2.1 Test Samples

The test samples were prepared in two steps. First, cylindrical samples 50 mm in diameter and 125 mm long were cored from a granite block. The granite is fine-grained and has a relatively low density of preexisting microcracks. It thus demonstrates a high P-wave velocity, ~6.0 km/s under atmospheric conditions. The cylindrical samples were then cut along a given angle (θ) with respect to the axis, which is the direction of greatest principal stress under the experimental conditions. We simply call the precut angle the "fault angle" and refer to the test sample with it. For example, "D45#1" indicates sample number 1 with a fault angle of 45°. We completed a series of experiments using samples with these precut faults. Some experiments were designed to investigate the repeatability of the experimental

results. In this chapter, we focused mainly on results for three samples with unfavorable angles, D45#1, D45#2, and D50#1. The commonly accepted typical range of frictional coefficient for faults in the upper crust is ~0.6–0.75. Therefore, based on the Mohr-Coulomb failure criteria, the optimal angle, at which faults show minimum frictional strength, is ~25°–30°. The faults in our test samples are thus deemed to be unfavorably oriented, and the friction strengths of D45 and D50 samples are expected to be 50% and 100% greater than for an optimally oriented fault, respectively. The test samples and fault planes are homogeneous at the mesoscale, but random inhomogeneity on the grain scale is significant.

To record ultrasonic signals radiating from microcracking events and stick-slip events and for making velocity measurements, up to 24 piezoelectric transducers (PZT), each 5 mm in diameter, having a resonant frequency of 2 MHz were mounted to the curvilinear surface of the sample. The sample and two end pieces were either coated with silicone sealant or jacketed with a 3 mm thick heat-shrunk tube of silicone rubber to prevent confining oil from leaking into the sample. In the first method, we mounted PZTs and strain gages on the rock surface, and then carefully coated the sample and two end pieces with silicone sealant. The coating work takes a few weeks. In the second method, the sample and two end pieces were jacketed with a heat-shrunk tube. Then, ~8 mm diameter holes were opened by cutting the tube for mounting the PZT sensors. After all the sensors were properly mounted, the holes were filled with silicone sealant. The second method requires a much shorter sample preparation time. The jacketed samples can suffer relatively large shear displacement (at least ~5 mm) compared to the coated samples.

2.2 Experimental Setup and Procedure

Figure 1 shows a block diagram of the loading and AE monitoring systems, which are basically similar to those used in fracture testing intact rock samples [9, 10]. When loading, the axial force is controlled by a spring-force balancing system, and the spring is simply compressed by a stepping motor. After a stress drop, the force of the spring does not change, so the reloading speed is very fast, reaching ~40 MPa/s. The loading system will be replaced soon with a servo-control system. In the present study, time-dependent healing is not considered, so the loading speed is not important for our purposes.

The recently updated waveform-recording system has 24 A/D channels to digitize the analog signals with a sampling rate up to 100 MHz, a dynamic range of 16 bits, and onboard buffer memory of 256 mega words per channel. The AE signal from every sensor is pre-amplified by 40 dB and then fed to the recording system. In this study, we digitized the AE signals with a sampling rate of 25 MHz and a sample length of 4096 words (~160 μs). Two peak detectors were used to capture the values of the maximum envelope amplitudes from two artificially selected sensors after 20 dB preamplifiers. An automatic switching subsystem was used to sequentially connect selected sensors (eight sensors in the present

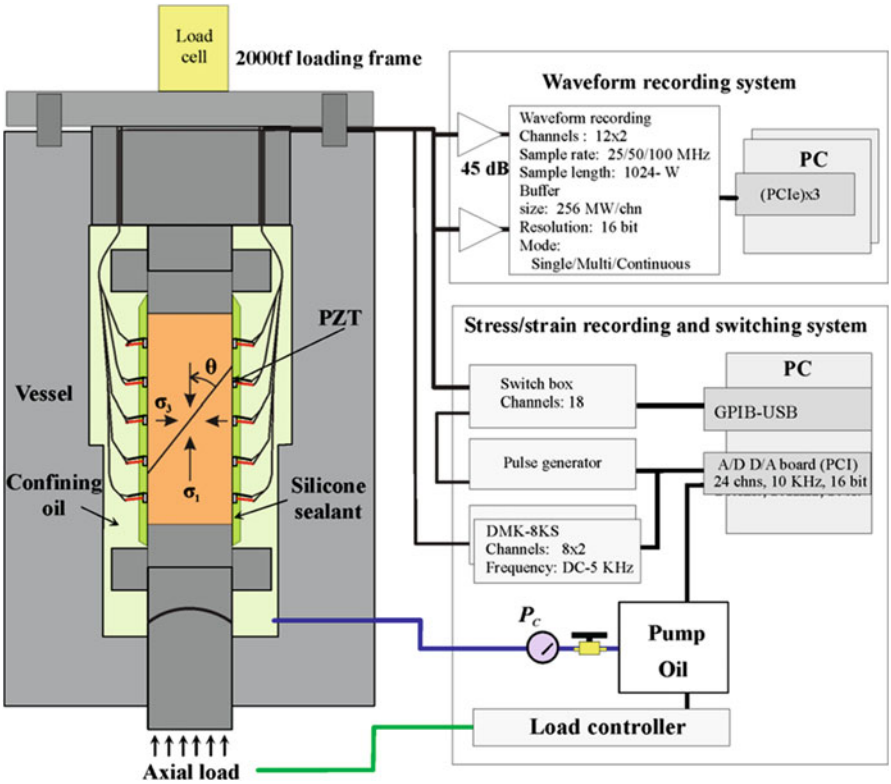

Fig. 1 Block diagram of the renewed experimental apparatus and data acquisition systems used for rock fracture test and acoustic emission monitoring

study) to a pulse generator to generate ultrasonic pulses for velocity measurement. During the velocity measurement, signals from the source sensor were recorded by all the other sensors. The time required to measure eight sources is less than 1 s. Therefore, losing AE events during velocity measurement using this system is very rare.

In our laboratory, the mixed noise level for AE signals is ~40 dB after applying the 20 dB preamplifiers. The threshold for the peak detectors was thus set to be 45 dB. The effective dynamic range is 45–100 dB, corresponding to a relative magnitude range of 2.75, equivalent to earthquake magnitude [11]. Due to attenuation, some events that had insufficient energy could be recorded by only the one detector nearest to the AE hypocenter. As a result, the number of events counted by two detectors could be different. Data recorded by the peak detectors are used to calculate seismic *b*-values, which are very useful in characterizing the pre-failure damage phases [8, 12]. Waveform data were recorded for the purposes of hypocenter determination and source mechanism solution, which require clear first motions at more than four sensors. Hence, we designed a complicated triggering

logic for the waveform-recording system. First, three pairs of neighboring sensors were selected as triggering sensors. To avoid biased triggering, the three pairs needed to be homogeneously distributed on the sample surface. An OR logic is used within each pair, and an AND logic is used among the three pairs. Then, a triggering threshold level is determined, which is ~10 times higher than that of the peak detectors. As a result, the AE hypocenter data constitute a subset of relatively large events among the AE count data and only a few percent of the peaks detected have AE waveform data. Higher thresholds and multiple homogeneously distributed trigger channels ensure that sufficient AE hypocenter data are collected throughout the sample space.

The new waveform-recording system has three working modes: single event, multi-event, and continuous mode. In this study, we mainly used the multi-event mode, in which the system can record up to ~5000 events per second since digitized waveform data are directly stored in the onboard memory. Its very short dead time, during which new events cannot be recorded, ensures that event loss during AE bursts is not important. Its onboard memory can store all the waveform data of 65,536 events under the aforementioned sampling conditions. Velocity measurements were performed at artificial intervals. The velocity data were used in hypocenter determination. First, P wave arrival times were picked up and hypocenters were determined automatically. The arrival time pickup is advanced by utilizing an autoregressive (AR) model and the Akaike information criteria (AIC) as proposed in 1973 (see reprint [13]). Careful checks could be manually performed using an interactive interface in the Windows operation system. We were able to determine the detailed locations of microcrack and stick-slip events with a location error of less than 2–3 mm in most cases. In order to guarantee such precision, we use only AE hypocenters determined by at least eight arrival times. Focal types, including shear cracks, shear-dominated wing cracks, tensile cracks, and pore closures, were obtained statistically for all located events based on the method of Lei et al. (2000) [9]. At the same time, detailed focal mechanism solutions including P and T directions were determined for relatively larger shear events recorded at multisensors with clear first motions.

In our experiments, the normal stress σ and shear stress τ acting on the fault plane are functions of the fault angle θ given by

$$\begin{aligned} \sigma &= \sigma_1 \sin\theta + \sigma_3 \cos\theta \\ \tau &= \sigma_1 \cos\theta - \sigma_3 \sin\theta \end{aligned} \tag{1}$$

The static and dynamic frictional coefficients are estimated from the peak and minimum stress during a stick-slip event by

$$\mu = \tau/\sigma \tag{2}$$

Based on Coulomb failure law, the critical condition for rupturing on a preexisting fault of a friction μ and an effective normal stress σ_e is

$$\tau = \sigma_e \mu \tag{3}$$

Another relevant conception in the present study is "slip tendency." The slip tendency of a fault to undergo slip under a given stress pattern depends on the frictional coefficient of the surface and the ratio of shear to normal stress acting on the plane [14]:

$$T_s = {}^{(\tau/\sigma_e)}/_{\mu} \tag{4}$$

It is clear that fault reactivation occurs when its slip tendency equals 1.

3 Results

3.1 Typical D45 Sample Results

Figure 2 shows the major parameters against time from the experiment on sample D45#1. In total, 17 stick-slip events were recorded in a single run. The total shear displacement on the fault plane is ~5 mm. To get more events, the test sample would need to be reset. As seen from Fig. 2, the first stick-slip event occurred when the peak axial stress reached 253 MPa, leading to a stress drop of ~123 MPa. The peak stress of later stick-slip events decreased gradually with some fluctuations to a relatively stable value of ~130 MPa.

As shown in Fig. 2b, the static frictional coefficient during the first stick-slip events is ~0.75, which reduced to a stable mean value of ~0.6 after several stick-slips. In this sample, the dynamic frictional coefficient fluctuates between 0.45 and 0.55.

AE activity was initiated when the axial stress reached ~100 MPa. The event rate increased with increasing stress until the first stick-slip event occurred. After every stick-slip, there is a quiescent period showing very low AE activity. When the axial stress reached 80–90% of the peak stress of the previous stick-slip event, AE activity was reinitiated and continued, with the event rate increasing until the next stick-slip occurred. In total, the number of AE events per stick-slip cycle shows a gradual decrease as the number of previous stick-slips events increases, indicating the role of slip smoothing.

Figures 3 and 4 show the basic results from sample D45#2. The peak axial stress is 290 MPa, 37 MPa higher than that of D45#1. We stopped the experiment after seven stick-slip events occurred. Compared with later stick-slips, the first event shows the largest stress drop and the residual shear stress acting on the fault is almost zero, so this is an overshot event. Both the peak and the minimum show some fluctuations. From the second stick-slip on, the peak stress falls in the range of 180–215 MPa, while the minimum stress varies from 80 to 110 MPa. AE activity is in agreement with D45#1. Following a quiescent period after each stick-slip, AE

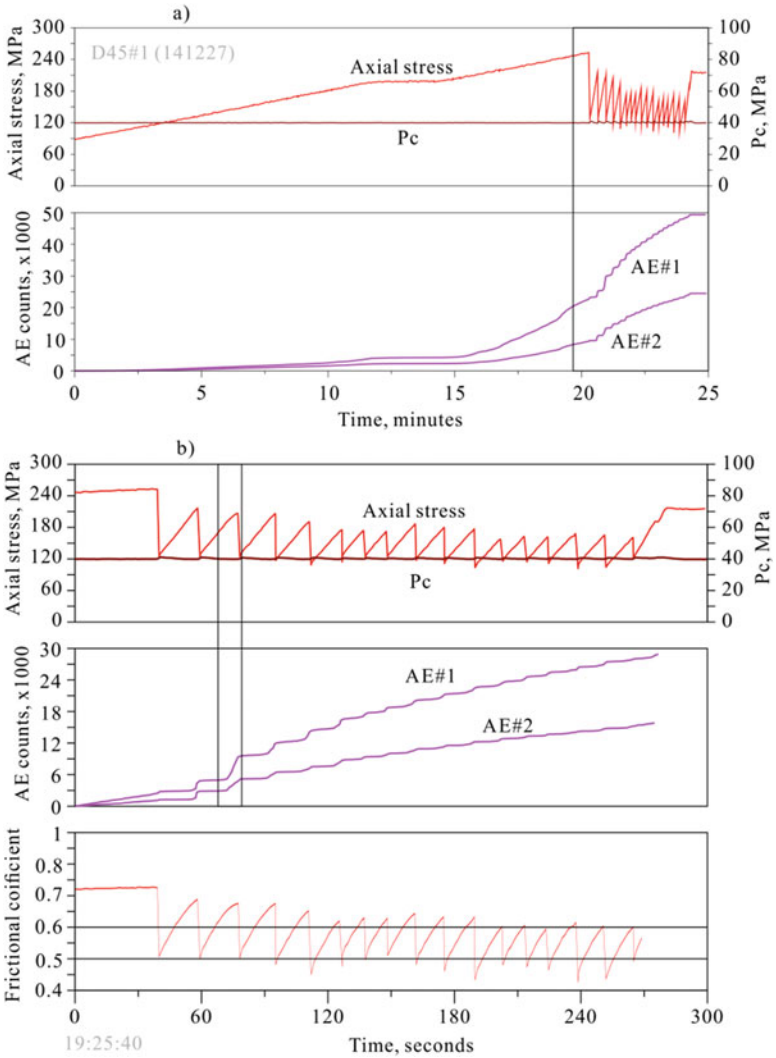

Fig. 2 Results for sample D45#1 with a precut fault of 45°. (**a**) Plots show axial stress, confining pressure (Pc), and AE counts recorded at two selected sensors against time. (**b**) Plots show zoomed views of the period of stick-slip events with additional plots of frictional coefficients calculated from axial and confining pressure data

activity was reinitiated when the axial stress reached 80–90% of the peak stress of the previous stick-slip event. As the number of previous stick-slip events increased, the number of AE events in a stick-slip cycle tended to decrease.

In Fig. 4, the AE hypocenters preceding each stick-slip are projected onto two orthogonal planes: the fault plane and the vertical profile perpendicular to the fault plane. Most AE hypocenters are clustered in a narrow zone along the fault plane. Cases of off-fault damage, especially in the footwall, are also observed.

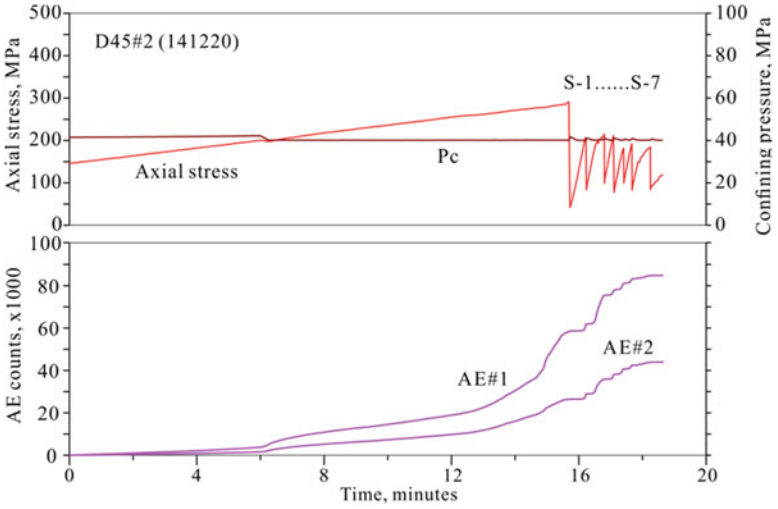

Fig. 3 Results for sample D45#2 with 45° precut. Axial stress, confining pressure (Pc), and AE counts recorded at two selected sensors are plotted against time

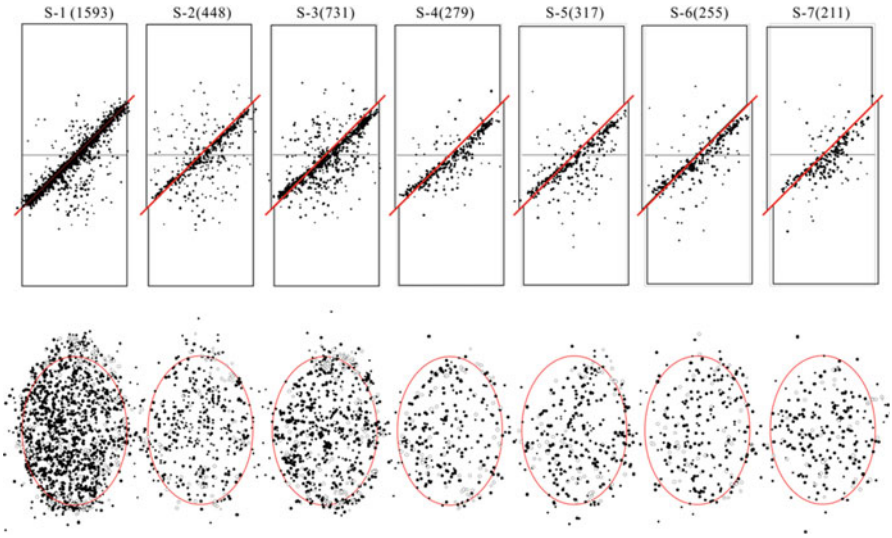

Fig. 4 The *top row* shows the distribution of AE hypocenters on a vertical profile perpendicular to the precut fault. The *lower row* shows AE hypocenters projected on the dipped fault plane. Each column shows AE hypocenters preceding stick-slip events indicated by sequential numbers from S-1 to S-7. In the *bottom row*, *open* and *closed circles* indicate tensile-dominated and shear-dominated microcracks, respectively. Note that most AE hypocenters are concentrated in a narrow zone along the fault plane, but off-fault damage is also important, especially in the footwall

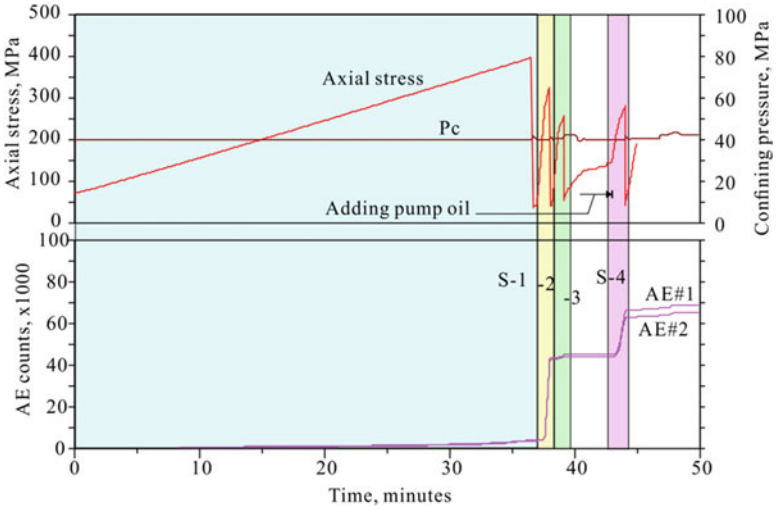

Fig. 5 Results for sample D50#1 with 50° precut showing axial stress, confining pressure (Pc), and AE counts recorded at two selected sensors against time

3.2 Typical D50 Sample Results

The basic results for sample D50#1 are shown in Figs. 5 and 6. As seen in Fig. 5, the peak axial stress was 397 MPa. The first stick-slip event then occurred, leading to a large stress drop. We stopped the experiment after four stick-slip events occurred to avoid overly damaging the sample, allowing confining oil to leak into the sample, making it impossible to ensure that no leakage occurred during the early stick-slips. It is very interesting that the dynamic stress drops during the stick-slip events are very large, and the residual shear stress on the fault is almost zero. Before the first stick-slip, the peak detectors recorded ~5000 AE events. More than 40,000 AE events were observed preceding the second stick-slips. AE activity before the third stick-slip is very low. More than 20,000 AEs were observed preceding the fourth stick-slip. Similar to the results from samples D45#1 and D45#2, a clear quiescent period was observed following all stick-slip events. When the axial stress reached ~60% of the peak stress of the most recent previous stick-slip event, intensive AE activity began and continued until the next stick-slip occurred.

Figure 6 shows the AE hypocenter distributions projected onto two orthogonal planes: the fault plane and the vertical profile perpendicular to the fault plane. The AE hypocenters are limited to a narrow zone along the fault plane before the first stick-slip. After that, off-fault damage became more important than on-fault damage and several AE clusters appeared along an angle of ~30° to the greatest principal stress axis, i.e., the optimal orientation for shear fracturing. Such aligned AE clusters demonstrate the nucleation of sub-faults. Increased AE event rates before the second and fourth stick-slips, therefore, resulted from intensive microcracking activity associated with the formation and growth of these aligned sub-faults.

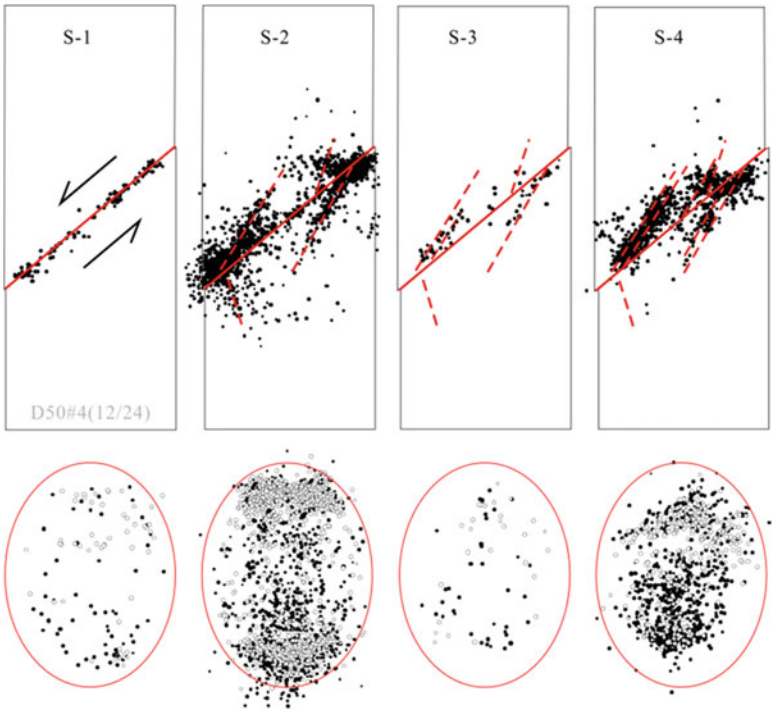

Fig. 6 The *top row* shows the distribution of AE hypocenters on a vertical profile perpendicular to the precut fault. The *bottom row* shows AE hypocenters projected on the dipped fault plane. Each column shows AE hypocenters preceding stick-slip events indicated by sequential numbers from S-1 to S-4. In the *bottom row*, *open* and *closed circles* indicate tensile-dominated and shear-dominated microcracks, respectively. Note that AE hypocenters are limited to a narrow zone along the fault plane, while in later events, off-fault damages are more important and some sub-faults with an optimal orientation are created

4 Discussion and Conclusions

From (1) and (3), the rupture strength expressed in differential stress, for convenience, can be obtained as a function of fault angle for different (static) frictional coefficients. Figure 7 shows plots of experimental data and theoretical data for friction coefficients of 0.6, 0.65, 0.7, and 0.75. In all tests, the first stick-slip event has a relatively large frictional coefficient, ~0.7–0.75, and then a decreasing tendency is observed. Finally, the fictional coefficient becomes rather stable at a mean value of ~0.6 with some fluctuations. Thus, our experimental results agree very well with the commonly accepted values of (dry) fault friction in the upper crust. Due to the formation of sub-faults in the D50 samples, stick-slips in D50 samples are complicated and show larger fluctuation amplitudes than the D45 samples. Decreasing frictional coefficient is an indicator of fault surface smoothing,

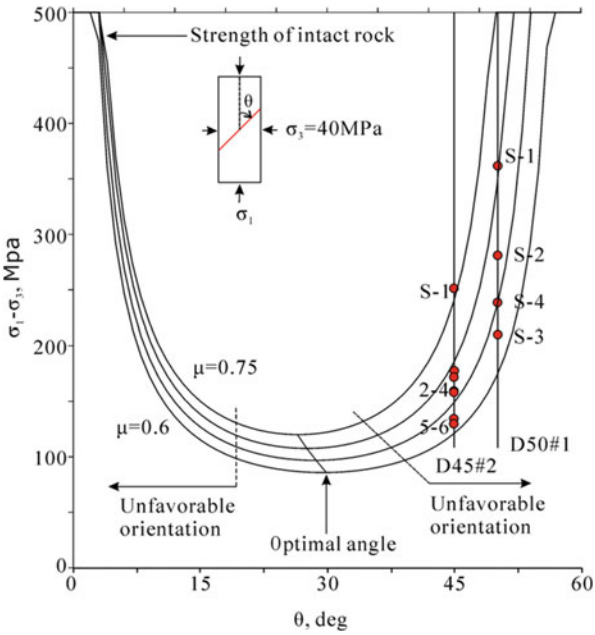

Fig. 7 Fault strength as a function of angle to the maximum principal stress, for different (static) frictional coefficients from 0.6 to 0.75. Circles represent experimental data of this study. In all tests, the first stick-slip event shows a relatively high frictional coefficient, ~0.7–0.75. Then a decreasing tendency is observed. Finally, the frictional coefficient becomes stable at 0.6–0.65 with some fluctuations, in agreement with the commonly accepted mean value of natural faults in the upper crust

which might result from the failure of geometric and mechanical asperities on the fault surface. After the tests, we observed some fault gauges. As indicated by the fluctuation of the frictional coefficient, both on-fault and off-fault damage could play a role in roughening the fault surface.

Our experimental results clearly demonstrated that, in the case of the D50 samples, after the first stick-slip event some sub-faults are created along an optimal direction, say ~30° to the greatest principal stress. Due to their optimal orientation, the newly created faults grow and rupture more easily since the slip tendency on these faults is a maximum. After a few stick-slips on the old fault, further fracturing is governed by these faults. It is therefore reasonable to assume that at field scale, activity on the old unfavorably oriented fault would be supplanted by activity on the new favorably oriented fault.

For $\theta = 45°$, no sub-faults were created for up to ~20 stick-slip iterations, which is the limit allowed in a single run under our conditions. However, the fault zone could be widened by off-fault damage.

In conclusion, the frictional behaviors and on-fault/off-fault damage observed in these tests demonstrate that there are two competing mechanisms. On the one hand, the fault plane is smoothed by fault slippage as asperities on the fault plane fail. Thus, we can see a decreasing tendency in AE activity and friction coefficient. The friction coefficient of the precut fault depends only on the history of stick-slip, independent on fault angle. In all cases, the fault friction drops from ~0.75 to 0.6 after a few stick-slips. On the other hand, the fault plane is roughened by new damage, which leads to fluctuations in AE activity and frictional behavior. In the

D45 samples, the smoothing mechanism plays a dominant role, while in the D50 samples, the roughening mechanism and formation of sub-faults in optimal directions are important.

Acknowledgment This work is partially supported by National Science Foundation of China (NSFC 41174046).

References

1. X. Lei, S. Ma, W. Chen, C. Pang, J. Zeng, B. Jiang, A detailed view of the injection-induced seismicity in a natural gas reservoir in Zigong, southwestern Sichuan Basin, China. J. Geophys. Res. Solid Earth **118**(8), 4296–4311 (2013)
2. X.-L. Lei, X.-Y. Li, Q. Li, S.-L. Ma, B.-H. Fu, Y.-X. Cui, Role of immature faults in injection-induced seismicity in oil/gas reservoirs-a case study of the Sichuan Basin, China. Geol. Seismol. **36**(3), 625–643 (2014)
3. X. Lei, T. Funatsu, and E. Villaescusa, in *Fault formation in foliated rock—insights gained from a laboratory study,* ed. By A. Malovichko, D. Malovichko. Proceedings of the 8th International Symposium on Rockbursts and Seismicity in Mines (RaSim8), Russia Saint-Petersburg-Moscow, pp. 41–49 (2013)
4. T. Terakawa, C. Hashimoto, M. Matsu'ura, Changes in seismic activity following the 2011 Tohoku-Oki earthquake: effects of pore fluid pressure. Earth Planet. Sci. Lett. **365**, 17–24 (2013)
5. R.H. Sibson, F. Robert, K.H. Poulsen, High-angle reverse faults, fluid-pressure cycling, and mesothermal gold-quartz deposits. Geology **16**(6), 551 (1988)
6. T. Terakawa, A. Zoporowski, B. Galvan, S.A. Miller, High-pressure fluid at hypocentral depths in the L'Aquila region inferred from earthquake focal mechanisms. Geology **38**(11), 995–998 (2010)
7. R.H. Sibson, Brittle-failure controls on maximum sustainable overpressure in different tectonic regimes. AAPG Bull. **87**(6), 901–908 (2003)
8. X. Lei, S. Ma, Laboratory acoustic emission study for earthquake generation process. Earthq. Sci. **27**(6), 627–646 (2014)
9. X. Lei, K. Kusunose, M.V.M.S. Rao, O. Nishizawa, T. Satoh, Quasi-static fault growth and cracking in homogeneous brittle rock under triaxial compression using acoustic emission monitoring. J. Geophysic. Res. **105**(B3), 6127 (2000)
10. X. Lei, X. Li, Q. Li, *Insights on Injection-induced Seismicity Gained from Laboratory AE Study—Fracture Behavior of Sedimentary Rocks.* in *8th Asian Rock Mechanics Symposium,* Sapporo, Japanese Committee for Rock Mechanics, Japan (2014)
11. X. Lei, Dragon-Kings in rock fracturing: Insights gained from rock fracture tests in the laboratory. Eur. Phys. J. Spec. Top. **205**(1), 217–230 (2012)
12. X. Lei, Typical phases of pre-failure damage in granitic rocks under differential compression. Geol. Soc. Lond., Spec. Publ. **261**(1), 11–29 (2006)
13. H. Akaike, *Information theory and an extension of the maximum likelihood principle*, in *Selected Papers of Hirotugu Akaike*. 1998, Springer. p. 199–213
14. A. Morris, D.A. Ferrill, D.B. Brent Henderson, Slip-tendency analysis and fault reactivation. Geology **24**(3), 275 (1996)

Part V
Structure

Investigation of Acoustic Emission Characteristics on Harbor Portal Crane

Zhanwen Wu, Gongtian Shen, Junjiao Zhang, Xuerong Tao, and Dajin Ni

Abstract Acoustic emission (AE) testing was carried out for the inspection of A-frame structure in a harbor portal crane and its testing areas were the repair welding on the A-frame. The acoustic emission localization characteristics, parameter distribution, and frequency spectrum characteristic are analyzed in this chapter. Also, the magnetic particle testing was used for reinspection of the AE location areas. The results indicated that the AE linear location method could be used well on the A-frame of the harbor portal crane during the loading test, which AE sources was produced by the surface crack defects of the repair welding. During the loading process, the maximum AE signal amplitude of the located events is about 69 dB, and the AE signal frequency mainly in 100–250 kHz range. During the load-keeping process, the maximum AE signal amplitude of the located events is about 55 dB, and the AE signal frequency mainly in 100–400 kHz range with a peak at about 160 kHz.

1 Introduction

Nowadays, harbor portal crane is one of the important equipment in the ports and docks. There are thousands of port cranes in use of the coastal and inland port in China, and about 20,000 cranes are in the later stage of service or extended stage. Cracks and deformation generally exist in the metal structure of these cranes, especially in the area of slewing platform and A-frame which is under the cyclic fatigue loading [1]. These may lead to failure and even the overall collapse of the crane with costly downtime.

At present, there is no effective method of crack detection and its activity evaluation in the nondestructive testing of the port crane metal structure [2]. There are some investigations for the AE technology applied in the inspection

Z. Wu • G. Shen (✉) • J. Zhang • X. Tao
China Special Equipment Inspection and Research Institute, Beijing 100029, China
e-mail: shengongtian@csei.org.cn

D. Ni
Nanjing Special Equipment Safety Supervision and Inspection Institute, Nanjing, China
e-mail: nidajin2005@yahoo.com.cn

G. Shen et al. (eds.), *Advances in Acoustic Emission Technology*, Springer Proceedings in Physics 179, DOI 10.1007/978-3-319-29052-2_21

of the crane structure in China and abroad [3–5], but the reports are also rare in the crack detection of the real crane.

In this chapter, the acoustic emission technique was used to obtain the AE signal characteristics of the crack in the A-frame structure of the harbor portal crane. The testing areas on the A-frame were the repair welding. Normally, these areas were susceptible to cracks.

2 Testing Object and Methods

2.1 Testing Object

The testing was practiced on a portal crane TQ 10-33, which was made in 2002, with its rated lifting capacity of 10 tons, radius from 10 to 33 m, and working level A6. The slings for lifting loads are both the hook and grab. The A-frame structures were mainly inspected and focused on the repair welding areas where cracks have been found. The welds with cracks have been repaired 2 months before this test. The main material of the A-frame is Q235B steel. The appearance of the tested crane is shown in Fig. 1.

One of the testing areas is located in the right-side pull rod of A-frame structure, which is to the right side facing the hook. The pull rod is a box structure. The repair welding is in the middle of the pull rod which is the connection between the pull rod

Fig. 1 Appearance of the portal crane

and the platform of the radius-changing mechanism with gear. Vibration and impact are often produced in the platform, which could be the cause of the fatigue cracks. The length of the repair welding area is about 200 mm; the thickness of the steel is 8 mm.

The other testing area is located in the left side supporting frame of A-frame structure which is to the left side facing the hook. The supporting frame is also a box structure. The repair welding is in the end of the supporting frame which is the connection between the supporting frame and the top platform of the A-frame. The length of the repair welding area is about 200 mm; the thickness of the steel is 12 mm.

2.2 *Instrument and Sensor Arrangement*

In the test, a fully digital multichannel AE system series AMSY-5 was used, which includes the sensors, preamplifier, computer software, and cables. The sensor model is VS150-RIC, and the gain is 34 dB.

According to the previous research, the linear location method was used in this test. The sensor arrangements in the structure with the repaired welds are shown in Fig. 2.

Before the AE testing, the simulated AE sources of lead break were applied in the repair welding. The simulated AE sources could be located correctly between the adjacent sensors.

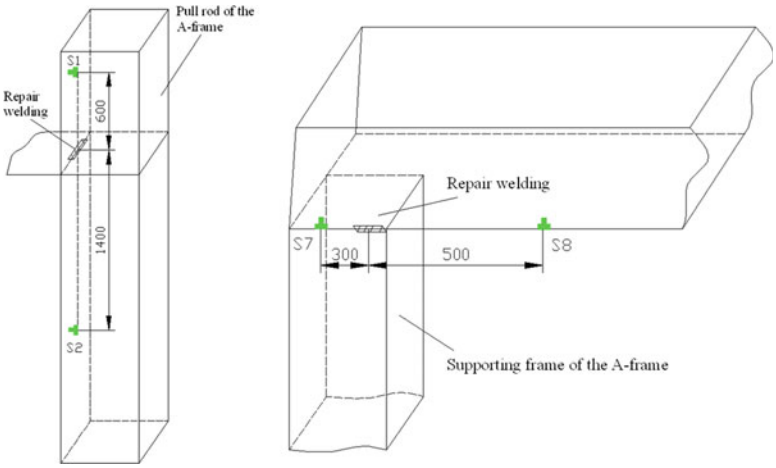

Fig. 2 Sensor arrangement in the pull rod and supporting frame of the A-frame

2.3 Loading Procedures

The loads of the portal crane daily are 6 tons. The test load is 9.2 tons. The twice-loading tests are carried out. The load-keeping circle of the first time is 10 min, and the second circle is 5 min. The AE signals of the two loading tests are recorded.

3 Testing Results and Discussion

3.1 AE Location During the Testing

During the two loading tests, many AE signals appeared in the repaired welding areas. These AE signals could be located. Figures 3 and 4 show the AE located events of the two testing areas. Table 1 shows the statistics of the AE events in the two detection areas. The magnetic particle testing was used for reinspection of the AE location areas. The results show that in these two repair welding, there are new cracks generated.

From the AE location events of the pull rod of the A-frame, we can see that there are 118 AE events in the first loading process, but only 20 events in the second time. At the same time, eight AE events appeared in the first load-keeping process, but only three events in the second time. It shows that the crack surface friction produced a large number of AE events in the repair welding area during the loading process. But there are only a few AE events in the load-keeping process.

From the AE location events of the supporting frame of the A-frame, we can see that there are 67 AE events in the first loading process and 30 AE events in the first load-keeping process, but only 1 AE event in the second process. It shows that there are many AE events generated by the crack during the load keeping.

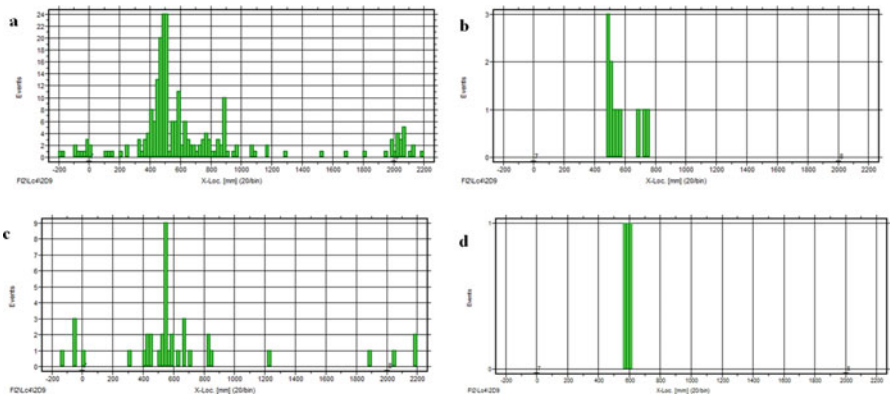

Fig. 3 Distributive AE events vs. location in the pull rod: (**a**) first loading process; (**b**) first load-keeping process; (**c**) second loading process; (**d**) second load-keeping process

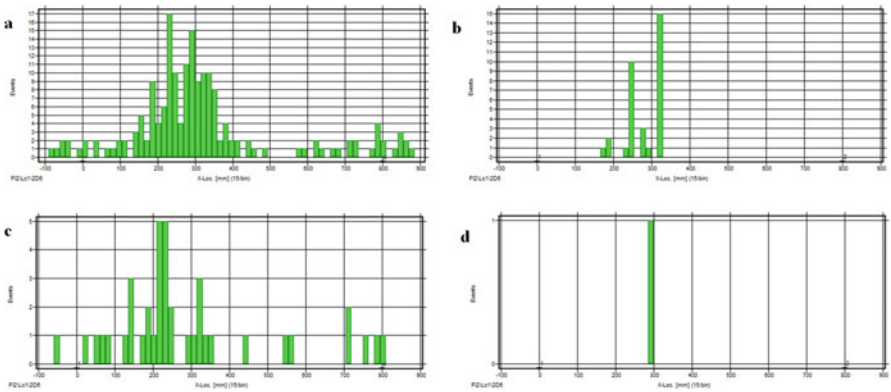

Fig. 4 Distributive AE events vs. location in the supporting frame: (**a**) first loading process; (**b**) first load-keeping process; (**c**) second loading process; (**d**) second load-keeping process

Table 1 Statistics of the AE events in the two detection areas

Areas	First loading process	First load-keeping process	Second loading process	Second load-keeping process
Pull rod (400–600 mm)	118	8	20	3
Supporting frame (200–400 mm)	67	30	20	1

Table 2 Average AE amplitude of the five maximum located events

Areas	First loading process	First load-keeping process	Second loading process	Second load-keeping process
Pull rod (dB)	67.2	51.1	68.9	44.5
Supporting frame (dB)	69.5	55.3	68.6	41.5

Comparing the two areas' AE location events, there are many AE events in the first testing circle in both areas, but only a few AE events in the second testing circle.

3.2 Distribution AE Location Signal Parameters

For the analysis of the AE event intensity, Table 2 shows the average AE amplitudes of the five maximum located events. The AE intensity value of the located events is about 68.9 dB during the loading process and about 51.1 dB during the

load-keeping process in the repair welding of the pull rod. For the supporting frame, these two AE intensity values, respectively, are 69.5 dB and 55.3 dB.

3.3 AE Waveform Behavior of the AE Location Events

Figures 5, 6, and 7 show several typical AE signals' waveform and frequency spectrum characteristics of the AE location events. From these figures, these show that:

(a) In the loading process, the frequencies of the AE signals are mainly distributed in the range of 100–250 kHz. There are two main peaks at 100 and 160 kHz. And the energy at the peak of 100 kHz is bigger than the energy at 160 kHz.
(b) In the load-keeping process, the frequencies of the AE signals are mainly distributed in the range of 100–400 kHz. There are four main peaks, at 100, 160, 250, and 350 kHz. And the maximum energy peak appears nearly at 160 kHz.

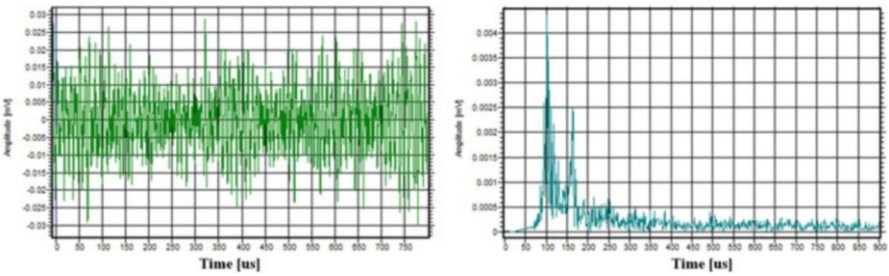

Fig. 5 AE waveform and frequency spectrum for pull rod during the loading process

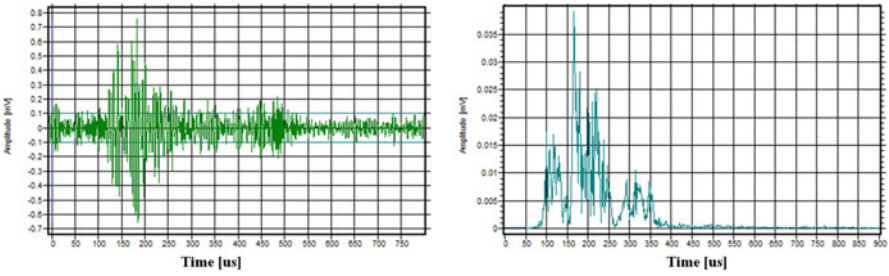

Fig. 6 AE waveform and frequency spectrum for pull rod during the load-keeping process

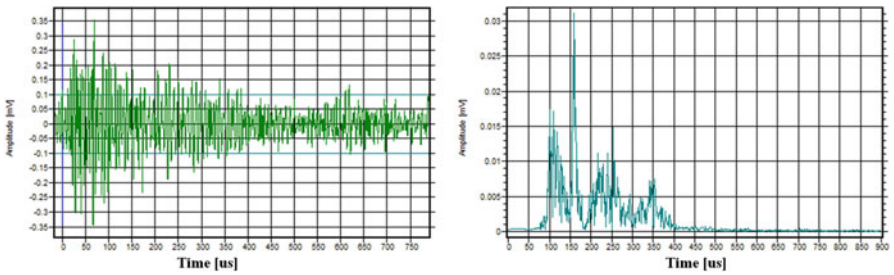

Fig. 7 AE waveform and frequency spectrum for supporting frame during the load-keeping process

4 Conclusion

According to the testing results, we can get the conclusions that:

1. The AE events of the crack propagation on the A-frame of the portal crane could be correctly located by using the AE linear location method. The magnetic particle testing results also show that there are surface crack defects in the AE location area which are the repaired welds.
2. Due to the existence of crack defects, there are many acoustic emission location events in the loading process. But there are less AE events in the load-keeping process than the loading process.
3. During the loading process, the AE intensity value of the located events is about 67–69 dB. And the AE intensity value is about 51–55 dB during the load-keeping process.
4. The frequencies of the AE signals are mainly distributed in the range of 100–250 kHz during the loading process, and its maximum energy peak is nearly at 100 kHz. But the frequencies of the AE signals during the load-keeping process are mainly distributed in the range of 100–400 kHz, and its maximum energy peak is nearly at 160 kHz. The AE events in the loading process are mainly generated by the crack surface friction, but the AE events in the load-keeping process are mainly generated by the growth of the crack.

Acknowledgments This study was financially supported by the national natural science fund of China (No. 51205292), Chinese 12th 5-year science and technology supporting project (No. 2011BAK06B05), and China Special Equipment Inspection and Research Institute research projects (No. 2015-15).

References

1. Z. Zhangyan, S. Guozheng, Faults distribution of port cranes' metal structure. J. Wuhan Transport. Univ. **23**(6), 679–680 (1995)
2. W. Yan, S. Gong-tian, G. Sen, Nondestructive testing of lifting appliances. Nondestr. Test. **28** (7), 367–372 (2006)

3. L. Hongyun, Z. Zheng, Z. Qunpeng, et al., The application of AE technique in the safety assessment on handling facility. Hoisting Conveying Machinery **1**, 36–39 (2005)
4. T. Jian-jun, W. Fu, D. Yong-gang, et al., Application of acoustic emission testing technology in truck crane girder detection. China Meas. Technol. **33**(4), 30–32 (2007)
5. W. Zhanwen, S. Gongtian, W. Shaomei, Study on the characteristic of acoustic emission during the propagating of external crack on the crane box beam. Nondestr. Test. **30**(9), 635–639 (2008)

Fatigue Failure Evaluation of RC Bridge Deck in Wheel Loading Test by AE Tomography

Tomoki Shiotani, Takahiro Nishida, Hiroshi Nakayama, Hisafumi Asaue, Kai-Chun Chang, Toyoaki Miyagawa, and Yoshikazu Kobayashi

Abstract In Japan, remediation and replacement of reinforced-concrete (RC) bridge decks consumes a major part of the road structure maintenance budget, and numerous studies have explored ways to expand the service life of the deck. Traditionally, corrective maintenance procedures and repairs have been conducted when noteworthy deterioration becomes visible to the naked eye, for example, as crack patterns on the deck surface. However, from the perspective of life cycle cost, to reduce maintenance budgets, the deterioration and damage should be evaluated before the damage reaches the surface (J Struct Eng 123: 1390–1401, 1997). Accordingly, in this study, internal damage of an RC deck due to fatigue failure is reproduced by a wheel loading testing apparatus, and the damage progress is evaluated by AE measurements as well as by elastic wave/AE tomography analysis.

1 Introduction

Bridge deck replacement consumes a large share of road investment costs. A principal cause of damage, fatigue failure, often goes unnoticed until the deterioration becomes so remarkable as to be observable on the bridge deck surface. Crack characteristics, including the direction of the cracks and the density of the surface, are used to determine the degree of the fatigue failure damage. Bridge owners, however, have long believed that their investment could be reduced if internal damage could be evaluated with nondestructive testing (NDT) approaches, so the degree of damage could then be reasonably contained [1]. NDT methods for visualizing internal damage described in the literature include elastic wave tomography and AE tomography [2, 3], and X-ray tomography [4]. However, these methods involve considerable time and expense, and can be harmful to human

T. Shiotani • T. Nishida (✉) • H. Nakayama • H. Asaue • K.-C. Chang • T. Miyagawa
Kyoto University, C-Cluster, Katsura Campus, Nishikyo, Kyoto 615-8540, Japan
e-mail: shiotani.tomoki.2v@kyoto-u.ac.jp; nishida.takahiro.6e@kyoto-u.ac.jp

Y. Kobayashi
Nihon University, 1-8-14, Kanda-Surugadai, Chiyoda-ku, Tokyo 101-83-8, Japan
e-mail: kobayashi.yoshikazu@nihon-u.ac.jp

G. Shen et al. (eds.), *Advances in Acoustic Emission Technology*, Springer Proceedings in Physics 179, DOI 10.1007/978-3-319-29052-2_22

health, so they have not been widely used. Acoustic emission measurements are now considered the only solution capable of tracking damage continuously [5]. But because AE monitoring requires multiple specific sensors, preamplifiers, and corresponding multi-channel systems, it is reserved for only a limited number of important structures. In addition, the external environmental frequently presents unavoidable noise signals that interfere with long-term monitoring, so that real-time fatigue damage monitoring with AE techniques has been conducted only for experimental purposes [6]. In contrast to AE monitoring, ultrasonic approaches, in which signal excitation and detection can be implemented with as few as one pair of excitation and receiver sensors, are more convenient for exploring internal damage. In this ultrasonic technique, the locations of defects can be measured by propagation time under the assumption that there exist unique or spatially homogeneous values of ultrasonic wave velocity. In the case where the wave propagation length of the media is already known, overall deterioration can be estimated by a calculation involving wave velocity and propagation time. In order to identify AE sources that indicate damage positions or areas, wave velocity is necessarily determined in advance of the test. Sources are then determined based on differences in the arrival times of waves at various sensors given a specific velocity value—for example, 4000 m/s. Innovative AE tomography, which the authors have been developing for more than a decade, enables us to determine both the wave velocity and the location of AE sources, and even to determine whether the damage is evolving or already exists within the materials of interest. In this paper, the progress of fatigue failure of RC decks is reproduced by a wheel loading apparatus, and AE measurements and elastic wave excitations for tomography analysis are executed at proper timings throughout the test. Finally, the internal progress of fatigue damage is visualized and quantified by elastic wave velocity, followed by comparison with resultant surface crack conditions.

2 Wheel Loading Program

To induce fatigue failure quantitatively, an RC deck specimen was subjected to repeated wheel loading with a steel wheel as shown in Fig. 1. The apparatus contains a steel wheel 300 mm in diameter and 400 mm wide, which can be applied to a load of up to 250 kN in the case of dynamic loads and 534 kN in the case of static loads in the vertical direction. Contrary to the conventional wheel loading machines with a movable loading wheel [7], the foundation and the specimen it holds are moved in a longitudinal direction within $\pm$500 to $\pm$1000 mm ($\pm$500 mm in this test). The repetition rate can be set between 0.897 and 9.97 rpm/min (8.97 rpm in this test). The test specimen was 3000 $\times$ 2000 $\times$ 210 mm in size with steel reinforcement arranged as shown in Fig. 2.

Stepwise cyclic loading was performed as shown in Fig. 3. First, a load of 98 kN was repeatedly applied 100000 times, then the test was suspended to excite elastic waves for elastic wave tomography. Subsequently, AE monitoring with static load

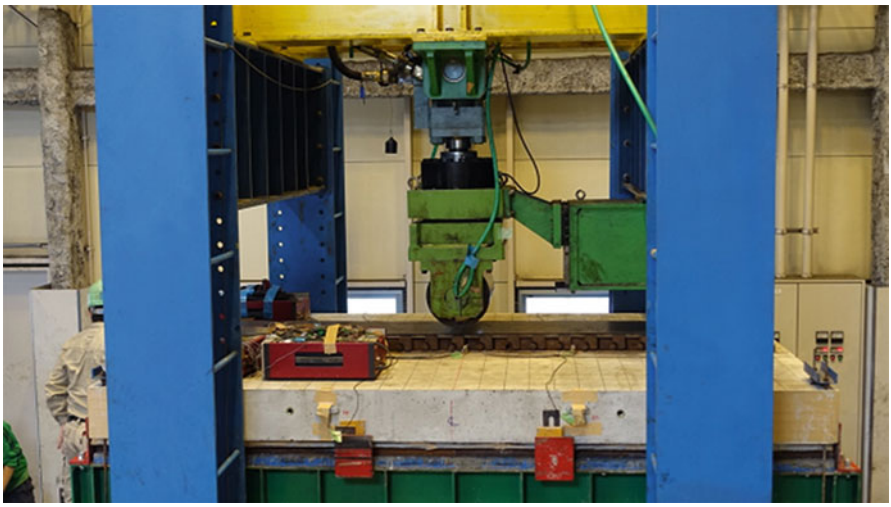

Fig. 1 Wheel loading test machine

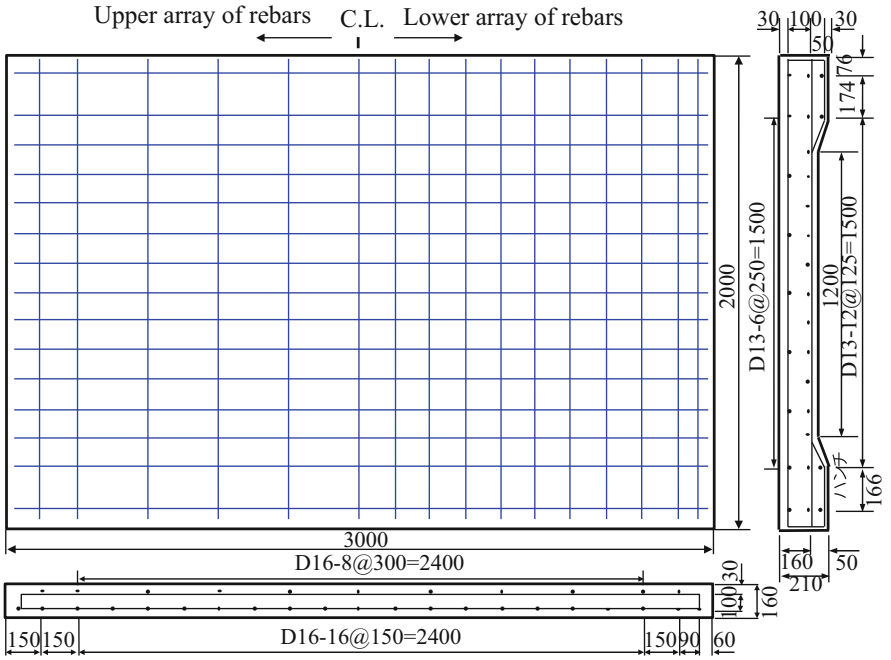

Fig. 2 Configuration of RC deck specimen

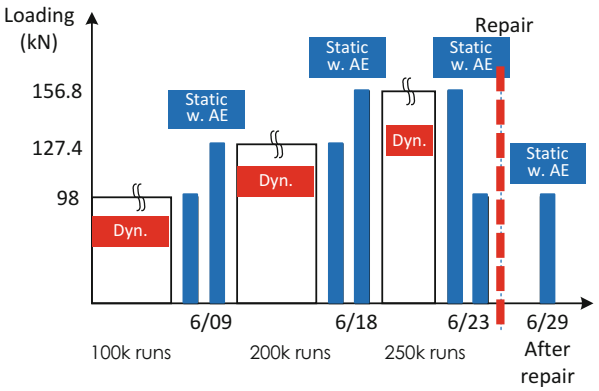

Fig. 3 Load application program in wheel loading test

Fig. 4 After repair agent execution

application to the previous maximum of 98 kN was conducted only once for AE tomography, assuming no further damage. An AE measurement was again conducted for the next loading step of 127.4 kN for reference, and further load repetitions of 200000 cycles were applied. Elastic wave excitations and AE monitoring were subsequently performed after this loading step, applying static loads up to 127.4 kN. AE monitoring was then performed during the next loading of 156.8 kN. With this 156.8 kN load, cyclic loading was conducted 250000 times. The same manner of elastic wave excitations for elastic wave tomography and AE measurements were repeated after this loading step, and the specimen failed during the following loading step. As shown in Fig. 4, cracks generated during the test were repaired by injecting epoxy-acrylate high-penetration resin. The agent was also expected to shield the specimen against water infiltration. After repair, elastic wave excitations were conducted for tomography, and then load application matching that which was first applied, i.e., 98 kN, was carried out with AE monitoring.

3 Monitoring

Damage evolution can be visualized by plotting accumulated AE sources through the whole failure process. However, as there are few cases in which AE sensors were installed at the time of bridge construction, cumulative damage interpretation cannot be performed with in situ AE activity; therefore, tomographic approaches have been employed using elastic wave tomography through the thickness of the structure. In conventional elastic wave tomography, the excitations are made at designated locations with accurate time records of excitation, leading to time-consuming measurements and the need for a large numbers of sensors. In bulky 3D structures for which there is no access to the rear area, 3D visualization of damage requiring sensor placement on the rear side cannot be implemented by conventional tomography. As a solution for this difficult configuration, the authors' research group has proposed a new approach, 'acoustic emission tomography' (hereafter referred to as AET). In AET, the calculation of both source locations and velocity distributions are implemented simultaneously [3]. We recently successfully applied this approach in addressing three-dimensional problems [8].

In order to monitor AE activity as well as artificial excitations, 32 AE sensors of 60 kHz resonance were placed onto the four planes: 10 on the top, 14 on the bottom and 2 each on the four sides. Artificial excitations were made by a 35 mm diameter hammer at 12 designated points on the top and 14 points on the bottom surface. The wheel loads were applied in the longitudinal direction shown as the area surrounded by green lines in Fig. 5. In each phase-suspension of wheel loads, the specimen was subjected to static vertical loads at the central area shown by a blue rectangle. Both AE signals and elastic wave signals due to excitations were amplified at the sensor-integrated pre-amplifier by 40 dB and acquired by an AE monitoring system, 48-ch Express 8 PAC with a 16 bit A/D conversion rate and a 1 MHz sampling rate.

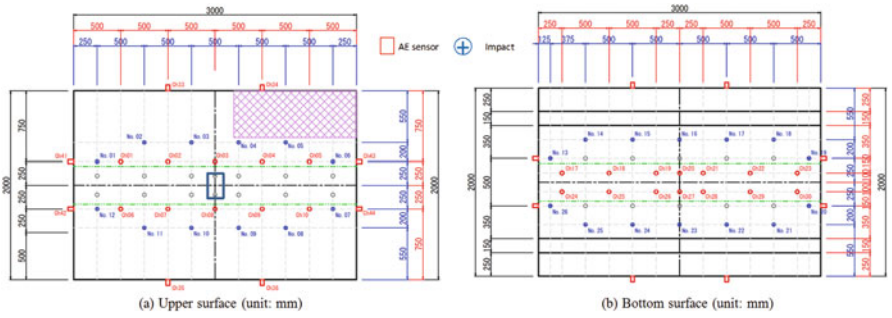

Fig. 5 Arrangement of AE sensors. (**a**) *Upper* surface (unit: mm) (**b**) *Bottom* surface (unit: mm)

4 AE Tomography

As shown above, in AET, both source locations and velocity distributions are calculated simultaneously, using the procedure described here. Here, we describe the source location algorithms, leaving detailed tomographic procedures to the other literature [2].

The source location technique is based on a ray-tracing algorithm [9]. This algorithm is characterized by installation of relay points in each cell as illustrated in Fig. 6. In a conventional ray-tracing algorithm, because the ray paths are formed by segments among nodal points, its resolution depends on the mesh characteristics, implying that high accuracy in source location requires a fine mesh. This leads to incrementing the number of degrees of freedom, since slowness, which is a reciprocal of velocity, is defined in each cell, and consequently makes the identification procedure more complicated. In this ray-tracing algorithm, the relay points between nodes are proposed, and a ray path is formed by segments among nodal and relay points, as shown in Fig. 7.

By using this approach, the resolution of ray tracing is increased without incrementing the degrees of freedom. As one role of the relay points is to relay the signals, the relay points should be distributed uniformly on the surface, but this can be difficult due to the heterogeneous shapes of the cross sections of concrete structures. To solve this problem, the relay points are installed by using the iso-parametric mapping that is used in the ray-tracing algorithm. Since each cell is mapped to an isosceles right triangle, the relay points can be uniformly installed in the mapped cell, as shown in Fig. 8. Although this algorithm does not provide

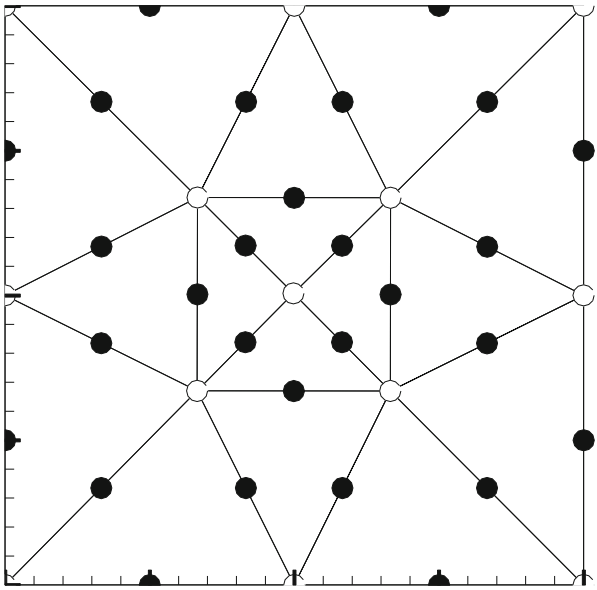

Fig. 6 Conventional set of relay points

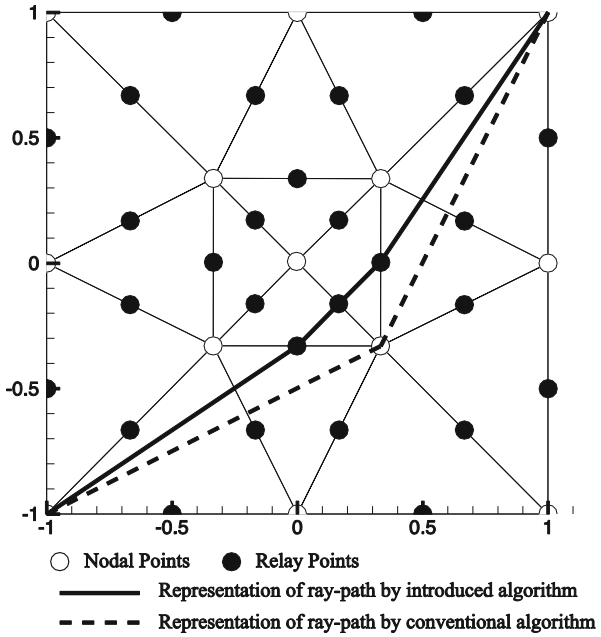

Fig. 7 Revised ray path in consideration of proposed relay points

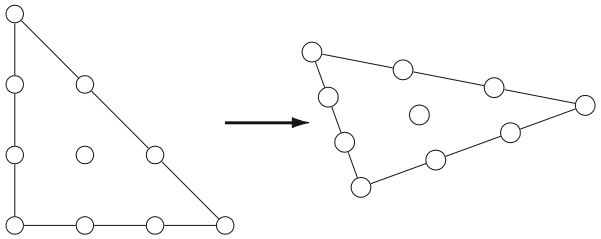

Fig. 8 Mapping to the global coordinates of set relay points

exactly uniform distribution of relay points if the shape of the cell is skewed, the distribution is improved by avoiding the use of strongly skewed cells. The source location is estimated using this ray-tracing algorithm.

The procedure for estimating source location is briefly described in Fig. 9. As the first step in estimating the source location, ray tracing is carried out for a receiver as illustrated in Fig. 10. This procedure calculates travel times t_{ij} from a receiver i to all nodal and relay points that are numbered as j. Since the first travel time T_i at receiver i is known, the possible emission time of the signal E_{ij} is computed by (1) at a nodal or relay point j.

$$E_{ij} = T_i - t_{ij} \tag{1}$$

This step is applied to all receivers, and then variance of the E_{ij} is computed as follows.

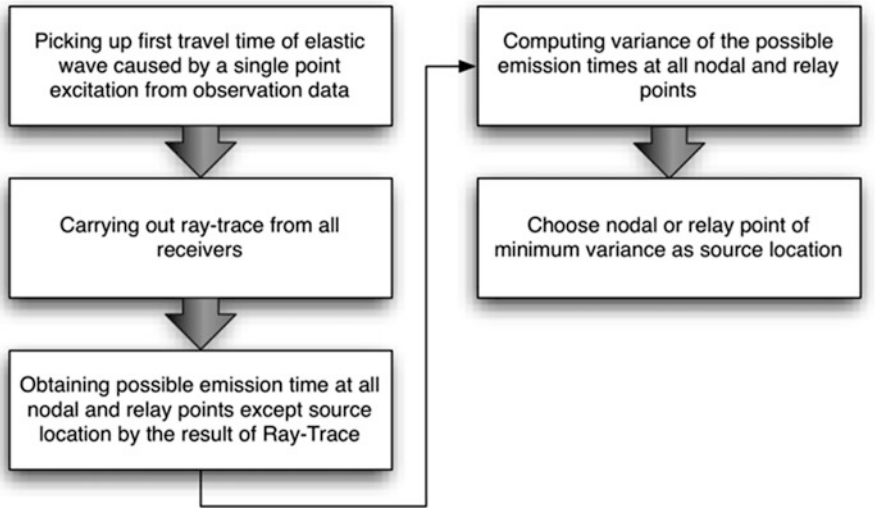

Fig. 9 Procedure to estimate source locations

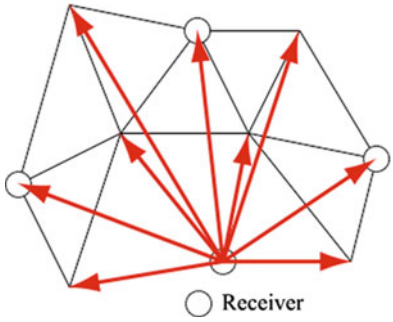

Fig. 10 Mapping to the global coordinates of set relay points

$$\sigma_j = \frac{\sum_i \left(E_{ij} - m_j\right)^2}{N} \tag{2}$$

in which

$$m_j = \frac{\sum_i E_{ij}}{N} \tag{3}$$

where N is the number of receivers. To estimate the source location, the variance σ_j is evaluated. If the slowness distribution is identical to the real slowness distribution, σ_j must be equal to zero at the source location and m_j must be the emission time. Due to discretization errors of the slowness distribution and insufficient

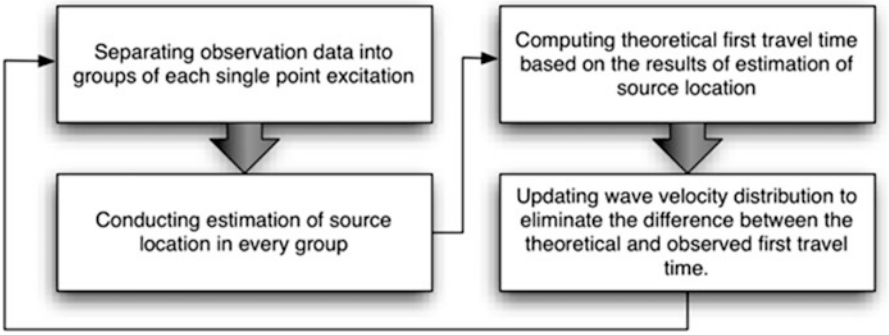

Fig. 11 Procedure to estimate source locations and velocity distributions

resolution of ray tracing, σ_j is generally not zero, even at the source location, as with the identification procedure of seismic tomography. However, it is predicted that σ_j is at a minimum at the source location. Hence, in this procedure, the source location is determined as a nodal or relay point of minimum variance $\sigma_{j\min}$. Additionally, m_j is used as the possible emission time. The accuracy of the estimation of the source location is controlled by the density of the nodal and relay points, because the source location is assigned to a nodal or relay point in the proposed algorithm. Furthermore, by applying this technique to the iterative procedure of identifying wave velocity structures, the source locations are updated in every iterative step, improving the accuracy of the source location. This approach can be applied not only to AE signals but also to signals that are generated by any excitation point.

Seismic tomography requires source location, emission time and travel time to the receiver. However, signals having neither emission time nor source location can be used for seismic tomography; source location and emission time can be estimated from travel times to the receivers under the wave velocity distribution determined by the method introduced in the previous section. Based on these facts, we introduce a seismic tomography procedure that uses estimated source location, as shown in Fig. 11. In seismic tomography with estimated source location, the first step is to estimate the source locations and emission times. If the observed travel times can be separated into groups that are associated with individual excitation points, the estimation of source location and emission time can be carried out for each observed travel time group. The second step is to apply ray tracing to all estimated source locations. In this step, ray tracing is carried out for all of the estimated source locations, and the travel time from the estimated source locations to the other nodal or relay points is calculated. Adding the computed travel time to the estimated emission time, the theoretical travel times at receivers are given by the following equation:

$$T_i' = m_j + t_{ij} \tag{4}$$

In the third step, the slowness distribution is updated to eliminate the difference between the theoretical and observed travel times by an identification technique.

In order to apply this 2D AET practically, 3D AET has been proposed [8]. First, elements in the 3D AE tomography are expressed in three dimensions, differently from those of 2D AE tomography. The greatest difference between 2D AET and 3D AET is the ray-tracing technique in the algorithms. In the developed ray-tracing technique, the waves in 3D AET are expressed by (5) and (6), which are expanded to three dimensions and are different from (7), the formula used in 2D AET.

$$a_1x + b_1y + c_1z + d_1 = 0 \tag{5}$$

$$a_2x + b_2y + c_2z + d_2 = 0 \tag{6}$$

$$ax + by + c = 0 \tag{7}$$

To use this developed ray-tracing technique, it must be possible to verify the AE source location and the deterioration of elastic wave velocity in three dimensions.

5 Results and Discussions

The velocity distributions are referred to as 'tomograms,' and are exhibited for the cases with artificial excitation and with AE sources in Fig. 12a, b. The circles and the stars in the figure indicate the locations of the AE sensors and AE sources, respectively, used for AE tomography. These are the tomograms after the first load step, that is, after 100 k runs of 98 kN. As shown in the figures, no remarkable damage could be estimated by the velocity distributions. Note that the tomogram resulted from the 2D AE tomography, i.e., all the AE sources were projected on the top surface, and the velocity distributions were obtained based on the projected AE sources on the surface, so that neither exact areas nor source locations could be addressed by these results.

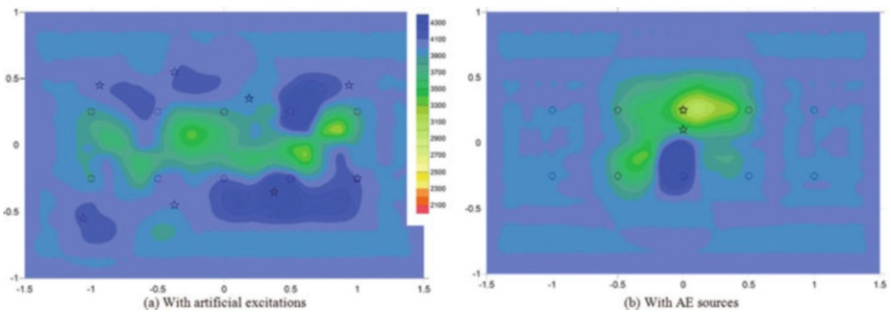

Fig. 12 Tomograms with two types of sources (figures are shown by the unit of meters/second): (**a**) with artificial excitations, (**b**) with AE sources

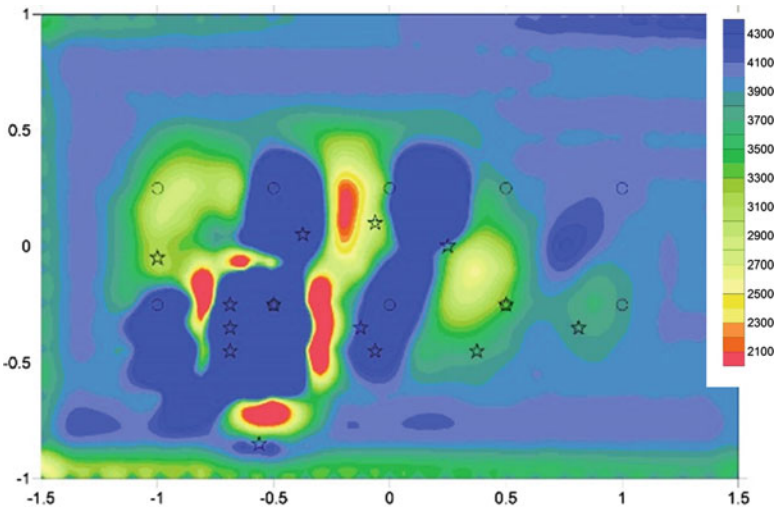

Fig. 13 Tomogram with AE sources during load application of 127.4 kN

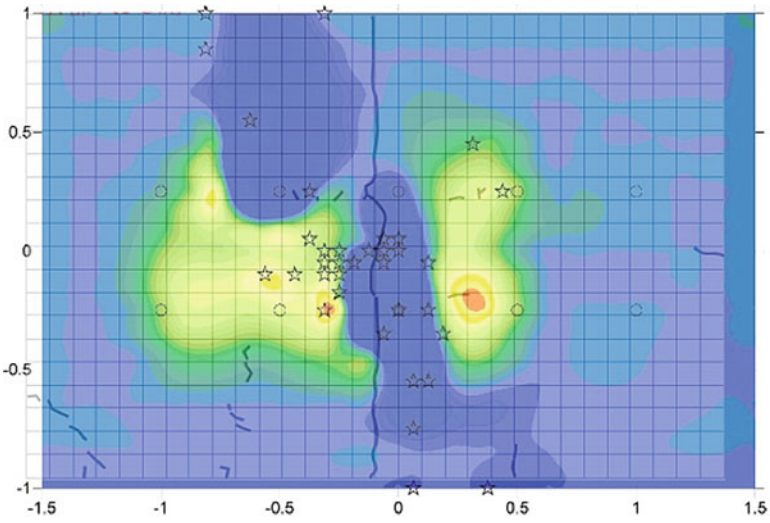

Fig. 14 Tomogram with AE sources after 250 k runs of 156.8 kN

The tomogram using several AE sources during the subsequent static load application of 127.4 kN is shown in Fig. 13. At this step, obvious vertical damage areas are represented by the low-velocity zones. For the subsequent loading steps, similar low-velocity zones appear in the tomograms. During AE monitoring after the 250 k runs of 156.8 kN, intensive AE activity is observed around central area of the specimen and resultant vertical cracks at −0.10 m and −0.75 m in the longitudinal direction have emerged, as shown in Fig. 14. Surprisingly, these

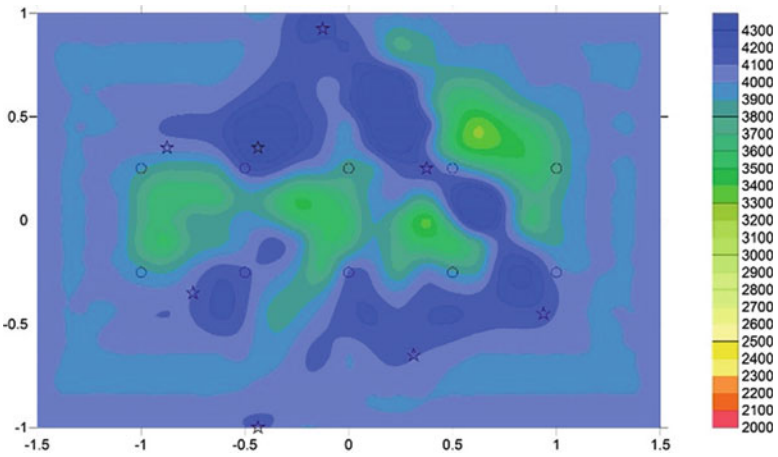

Fig. 15 Tomogram with artificial excitations after repair

characteristics of damage have already been estimated by the tomogram obtained during load application of 127.4 kN (see Fig. 13). The tomogram revealed no correlation between the location of the principal vertical crack generated in −0.1 m in the longitudinal direction and the low-velocity areas. This discrepancy seemed to be generated by two factors. One is that the tomogram was based on the AE sources projected to the top surface and exhibited one of the distributions within the specimen, i.e., Fig. 14 seemed to exhibit one of the internal and narrow damage areas. The other is due to the form of the principal vertical crack, i.e., it seemed to be generated perpendicular to the surface; however, it is possible to form diagonal damage in the thickness direction. Besides the central area, the low-velocity area in Fig. 13 was expanded to the left side in Fig. 14, and therefore fatigue damage evolution due to cyclic loads was manifested by those tomograms.

The tomogram with artificial excitations after repair can be found in Fig. 15. Two expanded low-velocity zones in Fig. 14 have disappeared, and overall recovery of the velocity can be observed. The repair effect is thus verified with velocity distributions. After repair, a static small load of 98 kN was applied to the specimen, and unexpectedly a large number of AE sources were acquired around the loading area as show in the stars of Fig. 16. These AE activities appeared to be generated by the failure of the thin repair agent on the surface. The resultant tomogram based on these AE sources accorded well with the AE activity. Low-velocity zones emerged around the loading plate (see Fig. 5a for the location of the plate). From these findings it can be implied that the repair agent did not improve the surface protection against water infiltration, although the recovery of the crack could not be examined in this study, and will be studied with 3D AE tomography.

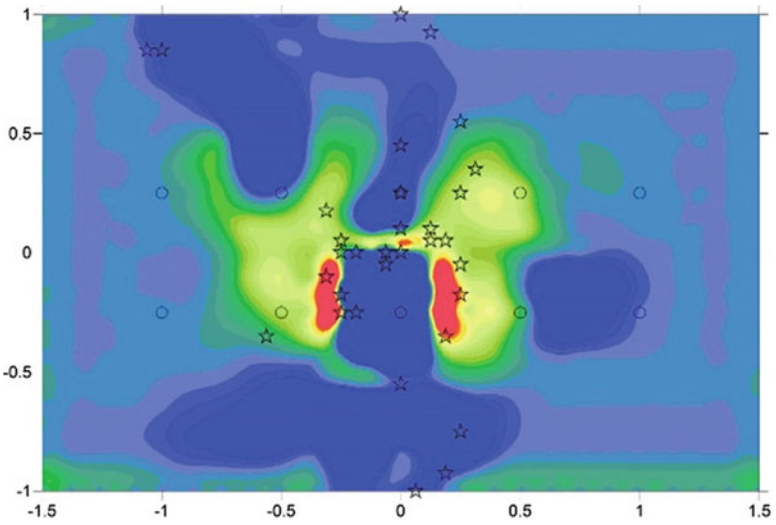

Fig. 16 Tomogram with AE sources during the first loading after repair

6 Conclusions

Elastic wave and AE tomography were applied to the quantification of fatigue damage in an RC deck. The damage was reproduced by a wheel loading apparatus and these tomographic approaches were conducted in every loading phase. Consequently, although 3D approaches will be presented in the follow-up paper, it was concluded that internal damage can be evaluated by tomograms on the surface, and visible cracks on the surface can be predicted by the tomograms in previous phases. With the tomographic approaches, repair evaluation for establishing lifetime scenarios for concrete structures, seems to be possible.

Acknowledgment In this study, experimental works were principally conducted in the College of Engineering of Nihon University under the support of the Cross-Ministerial Strategic Innovation Promotion Program (SIP). The authors extend special thanks to Prof. I. Iwaki and Associate Prof. Y. Koda with Nihon University as well as Associate Prof. Y. Tanaka with the University of Tokyo.

References

1. D. Frangopol, K. Lin, A. Estes, Life-cycle cost design of deteriorating structures. ASCE J. Struct. Eng. **123**(10), 1390–1401 (1997)
2. Y. Kobayashi, T. Shiotani, H. Shiojiri, Damage identification using seismic travel time tomography on the basis of evolutional wave velocity distribution model, Engineering Technics Press, in *Proceedings of Structural Faults and Repair 2006*, 2006 (CD-ROM)

3. T. Shiotani, S. Osawa, S. Momoki, H. Ohtsu, *Visualization of Damage in RC Bridge Deck for Bullet Trains with AE Tomography*, Advances in Acoustic Emission Technology (Springer, New York, 2014), pp. 357–368
4. J. Otani, Y. Obara (eds.), *X-ray CT for Geomaterials, Soils, Concrete, Rocks* (A.A. Balkema, Rotterdam, 2004)
5. U. Grosse, M. Ohtsu (eds.), *Acoustic Emission Testing* (Springer, Heidelberg, 2008)
6. T. Shiotani, D.G. Aggelis, O. Makishima, Global monitoring of large concrete structures using acoustic emission and ultrasonic techniques: case study. ASCE J. Bridge Eng. **14**(3), 188–192 (2009)
7. T. Shiotani, H. Ohtsu, S. Momoki, H.K. Chai, H. Onishi, T. Kamada, Damage evaluation for concrete bridge deck by means of stress wave techniques. ASCE J. Bridg. Eng. **17**(6), 847–856 (2012)
8. T. Shiotani, S. Osawa, Y. Kobayashi, S. Momoki, Application of 3D AE tomography for triaxial tests of rocky specimens, in *Proceedings of 31st Conference of the European Working Group on Acoustic Emission* (EWGAE), 2014, CD-ROM
9. F. Schubert, Basic principles of acoustic emission tomography. J. Acoustic Emission **22**, 147–158 (2004)

Testing the Node of a Railway Steel Bridge Using an Acoustic Emission Method

Marek Nowak, Igor Lyasota, and Dawid Kisała

Abstract Research on bridge construction elements was conducted as part of a joint project by the Cracow University of Technology and PKP Polish Railway Lines, funded by the NCBiR. In the first phase, the material properties were defined, and modeling calculations for the bridge and node were performed. In the next phase, the node was loaded using a scheme corresponding to the real loading conditions of this part of the bridge.

Tests were performed on the prepared test stand with the registration of acoustic emission signals. The recorded measurement data were analyzed to determine the signal characteristics, the signal parameters used for assessing defects, and the most effective system for locating signals.

1 Introduction

Many operated railway steel bridges in Poland are in poor condition from many years of use, and appropriate diagnostics are needed for bridge structural assessment. Some of the bridges are small, but very often they are long, so visual diagnostic methods are typically used, and in exceptional cases, other nondestructive testing is performed. Therefore, in many cases, a complete evaluation of the conditions of these steel bridges lacking, and studies are needed to determine the most effective and accurate diagnostic approach.

The Cracow University of Technology, together with PKP Polish Railway Lines—the owner of the majority of railway infrastructure in Poland—conducted a project funded by the National Centre for Research and Development in order to explore diagnostic methods for assessing the steel railway bridges using an acoustic emission method.

M. Nowak (✉) • I. Lyasota
Laboratory of Applied Research, Cracow University of Technology, Cracow, Poland
e-mail: nowak@mech.pk.edu.pl

D. Kisała
Cracow University of Technology, Cracow, Poland

G. Shen et al. (eds.), *Advances in Acoustic Emission Technology*, Springer Proceedings in Physics 179, DOI 10.1007/978-3-319-29052-2_23

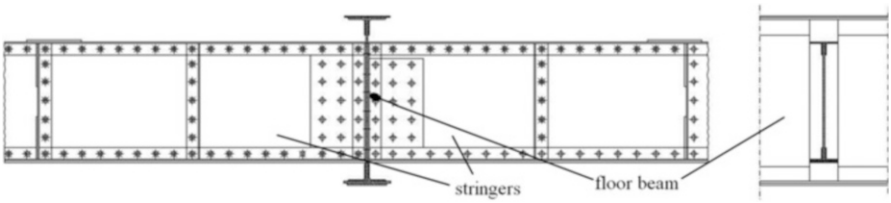

Fig. 1 The scheme of the test object

One stages of the project involved laboratory studies on the elements of a real bridge structure.

2 Test Object

In order to carry out the laboratory tests, an element was obtained for rebuilding from the riveted truss of a single-span bridge with a drive bottom, which was built in 1905. The joint consisted of two sections of stringers about 3 m in length and a total of 0.67 m with additional reinforcements, and a section of floor beam measuring about 0.7×0.95 m. The scheme of the element for testing is shown in Fig. 1.

3 Material Tests and Model Analysis

Due to the incomplete documentation regarding the type and properties of the material, studies were conducted prior to the implementation of stress testing to determine the chemical composition, mechanical properties, and metallographic microstructure using both fixed and portable microscopes. These studies showed that the individual elements of the node differed in terms of the chemical composition and structure of the material.

The chemical composition test showed that the material had very low carbon content (0.03–0.07%). Figure 2 shows images of the microstructure of the web stringer after Nital etch, indicating a ferritic structure, with cementite on grain boundaries and a large number of non-metallic inclusions.

The intention was to create a test with loading conditions representing the working conditions of that element. For designing the test stand and loading conditions, the bridge construction and node were evaluated using finite element analysis. The bridge analysis was carried out using Robot Structural Analysis on the rod model in a spatial structure with dimensional elements in three-dimensional space.

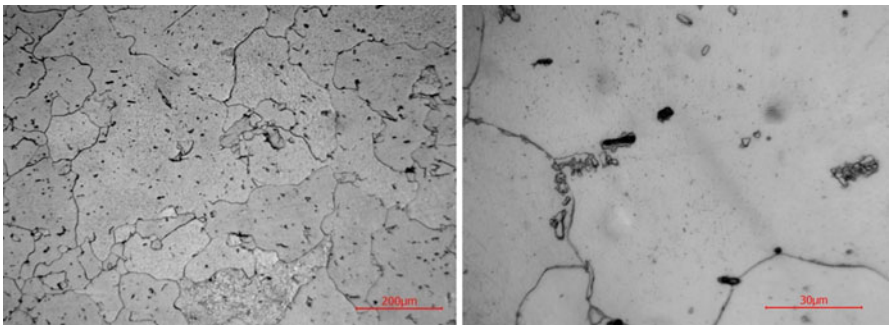

Fig. 2 The microstructure of the web stringer material (×250 and ×800 magnification)

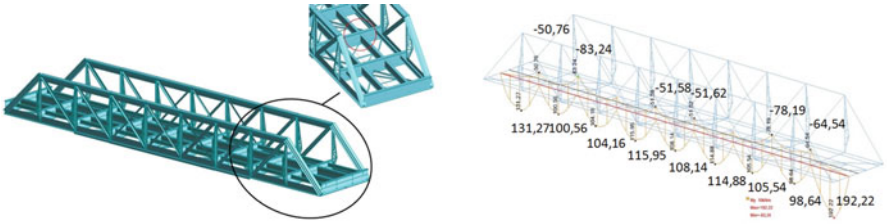

Fig. 3 Visualization of the model, the location of the joint on the model, and the envelope characteristic bending moments in the stringers (kNm)

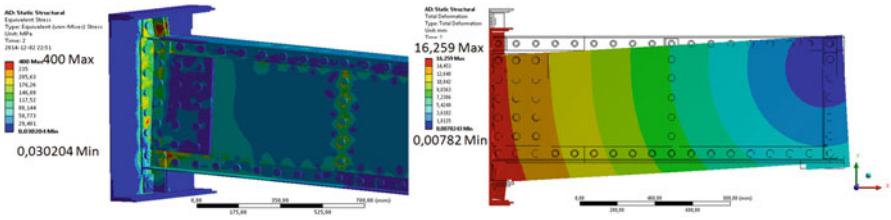

Fig. 4 Stress distribution by the HMH hypothesis and deformation simulation for loading of node

For the assumed load from railway stock, a chart of the envelope of bending moments in the string from constant weight and load moving rolling stock was determined. The characteristic values are shown in Fig. 3.

Numerical calculations were carried out (in ANSYS Workbench 13 software) to determine the deformations and zones of maximum stresses in a loaded node. Calculations were performed for individual elements of complex construction and for determination of the stresses in the main directions. Examples of visualizations are presented in Fig. 4. Due to the symmetry of the object relative to the plane of the floor beam, the simulations shown in the figure are for one part of the element.

The maximum values of stresses by the HMH hypothesis (up to 400 MPa) are at the top and bottom of the stringer–floor beam connections. In the area of the rivets, the stresses have medium values (180–230 MPa), but the stresses in the rest of the web area are low. The calculated maximum displacement for the assumed force value of 120 kN in the middle part of the node was about 16 mm.

4 Equipment and Test Methodology

The above-mentioned tests and calculations made it possible to design a test stand and to determine the type of loading of the node. The registration of AE signals was carried out by three-point bending using an Instron tensile testing machine (Instron Schenck Testing Systems) with a hydraulic cylinder (IST PL1000) with maximum force of 1000 kN. Both static and dynamic tests were performed. A view of the joint on the test stand is shown in Fig. 5.

To register the AE signals during the joint loading tests, two types of resonant sensors were used (total of 34 sensors), which were attached to the joint by magnetic holders. These included the VS150-RIC AE sensors with resonant frequency of 150 kHz and an integrated preamplifier (34 dB gain), and the VS75-V sensors with resonant frequency of 75 kHz and an additional preamplifier (AEP4; 34 dB). The Vallen AMSY-6 measuring system was used, with software contained in the Vallen control panel.

The layout of the sensors was similar among the tests, but the positions of some sensors were changed in individual tests. The main sensor layout is presented in Fig. 6.

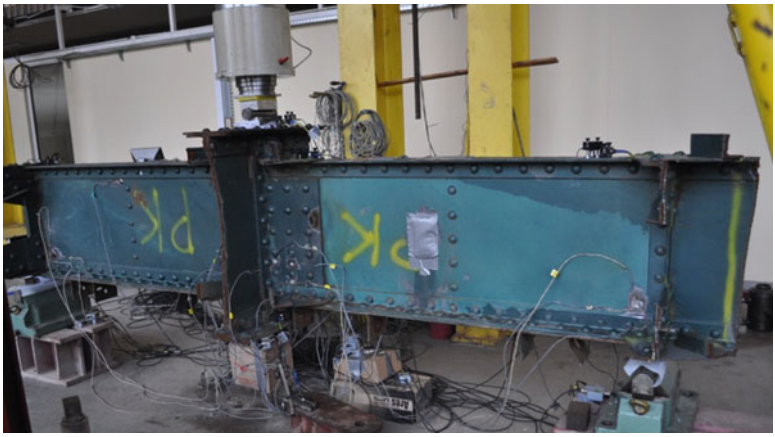

Fig. 5 View of joint on test stand

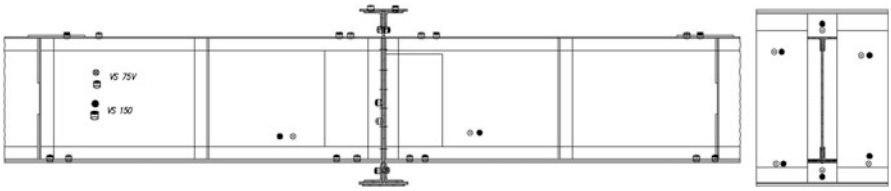

Fig. 6 Layout of sensors on node

5 AE Tests

The three main objectives of the laboratory tests with the acquisition of AE signals on steel bridge elements are presented below. In these tests, the AE signals were acquired with the following parameters: threshold range of 46–49 dB; frequency range of 50–300 kHz for VS75-V sensors and 95–300 kHz for VS150-RIC resonant sensors; rearm time = 0.4 ms; duration discrimination time = 400 μs.

5.1 Tests of Node with Corrosion Products

One of the purposes of this research was to separate acoustic signals generated by cracks and material defects from the signals caused by corrosion products remaining in confined spaces and elements of bridge structures subjected to loading.

For this purpose, two series of measurements were performed, one during the dynamic loading of the node with corrosion products, and the other after their removal at the upper part of the node. This allowed us to determine the emission characteristics of the signals generated by the remaining corrosion products during loading of the structure. Figure 7a shows the locations of AE signals in the area with large quantities of corrosive products, and Fig. 7b shows the same area after removal. These locations relate to signals recorded by sensors with a frequency of 75 kHz during two identical time sequences of the cyclic loading of the node to the maximum force of 240 kN.

The recorded signals were analyzed to determine their parameters and frequency characteristics. The basic parameters of these signals in different correlations used during the analyses are shown in Fig. 8.

In general, the frequency at the maximum amplitude of the spectrum (FmaxAmp) for signals recorded during loading of the node with corrosion products was 88–90 kHz, but the center of gravity of the frequency spectrum for those signals was in a range of 84–88 kHz.

The correlation graphs show the amplitudes of the located signals of up to 75 dB (a few signals up to 87 dB), with signal duration in a range of 200–1100 μs. The number of counts generally does not exceed 40, and only a few signals have signal strength values exceeding 180 nVs.

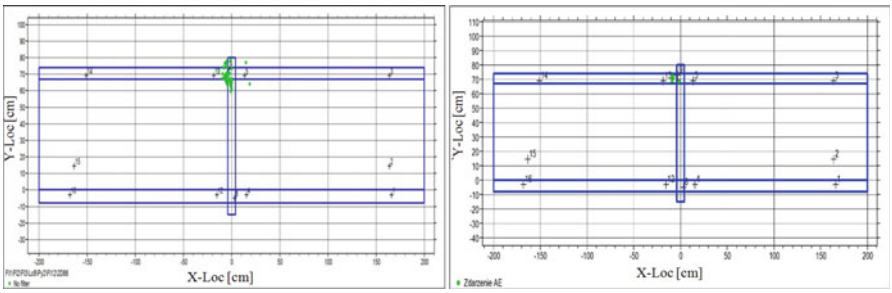

Fig. 7 AE signal location for loading structure (**a**) with a large covering of corrosion products, and (**b**) after removal of corrosion products

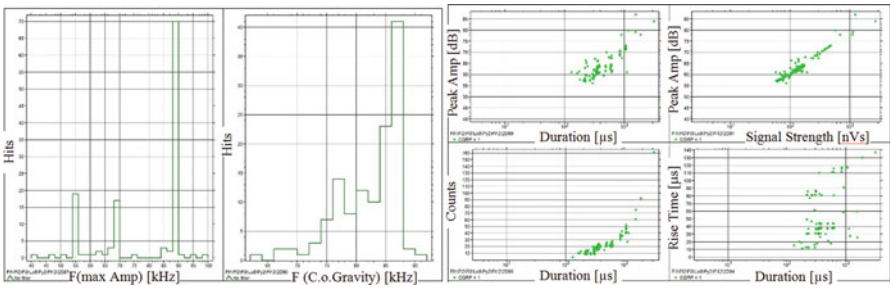

Fig. 8 AE signal parameters recorded during loading of the node in the area of the overhang of corrosive products

5.2 *Location of AE Signals on Complex Construction Elements*

Complex geometries were also investigated to explore the possibility of using different variants of layouts, groups, and algorithms available in Vallen software for the location of AE signals, using planar and linear algorithms. These tests were carried out using a Hsu-Nielsen artificial source to generate signals in a selected area of the node. The sensors were assembled on stringers and floor beams. The results were compared in terms of the number of localized signals and location accuracy as specified by the parameter LUCY (location uncertainty). This parameter describes how well a calculated source position fits with the measured arrival time differences. It is the value of the standard deviation of distances from the *i*th sensor to the signal source (S_i) and the same distances calculated according to speed and difference in signal arrival time Dst_i, as follows:

$$\mathrm{LUCY} = \sqrt{\frac{1}{N-1}\sum_{i=1}^{N}\left(D\mathrm{st}_i - (S_i - S_1)\right)^2}$$

where

$$D\mathrm{st}_i = \Delta t_i \bullet V;$$

Δt_i is the difference in signal arrival time between the first and the ith sensor, and V is the speed of signal propagation.

Figure 9 shows the location signals for different location configurations (sensors on stringer and floor beam, only on stringers, etc.) and the number of localized signals (location events) for these configurations, as well as the number of localized signals for which the location error (LUCY) does not exceed 10% of the maximum distance between the sensors participating in the location.

The analysis allowed us to determine the most effective system for locating signals for geometrically complex steel structures. For algorithm with sensors on floor beam (Fig. 9a) the number of located signals is 34 but only for 18 of them the LUCY parameter does not exceed 10% of the maximum distance between the sensors. The system with two location groups (Fig. 9c) is effective (52 located events, and 50 with low LUCY), but it requires a greater number of sensors. The combination with sensors on the stringer and floor beam was most effective (Fig. 9b). This system can be used for monitoring of objects with defects.

A linear location algorithm using sensors mounted large distances apart was also used, and the results are presented in Fig. 9d. This system enabled the detection of sources, but it was less accurate.

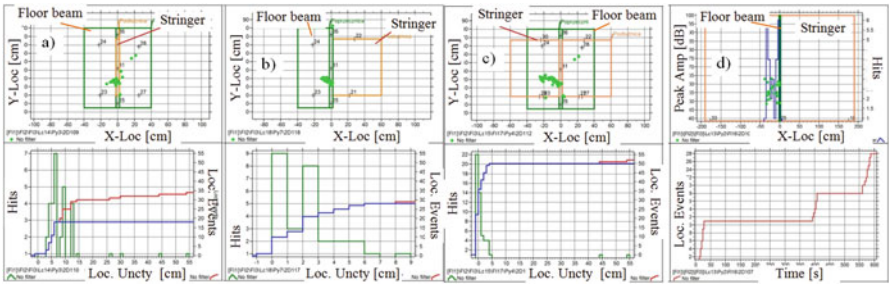

Fig. 9 Location of signals, number of localized signals, and location accuracy for different variants of locating systems: (**a**) sensors on the floor beam, (**b**) sensors on both stringers and floor beam, (**c**) system with two location groups (**d**) linear location

5.3 *Determination of the AE Signal Parameters Describing the State of Structural Defects*

During loading of the elements of the composite structure, a large number of AE signals are generated, especially in the case of severe corrosion damage or material defects. Thus it is important to select a parameter or combination of AE parameters that enable the detection of active structural defects that threaten the integrity of the structure. This task was the last stage of the laboratory tests.

Numerical calculations were used to determine the zone with the greatest stress values of the node, which was the area with the largest number of localized AE signals during static and cyclic loading of the node (Fig. 10).

For realization of the tasks in the zone with lower stress values, artificial discontinuities (cuts) were created in the flange of the stringer. After a series of loading with measurement of AE signals, discontinuity was increased.

Figure 10 shows the location of the AE signals during cyclic loading of the node without artificial defects. A large number of signals are detected in the area with the highest stress values.

The introduction of artificial defects—the discontinuity of the lower flange of the stringer (as indicated in the figures)—generates AE sources during subsequent loading cycles. Figure 11a illustrates the location of the signals after the introduction of a discontinuity (cutting), and Fig. 11b shows the increase in the number of signals located in the area of the defect after a second discontinuity is performed.

A multi-parametric analysis of the recorded AE signals was carried out to define the parameters describing the state of structural damage. Sample graphs created for analysis using the standard signal parameters and grading processor parameters are

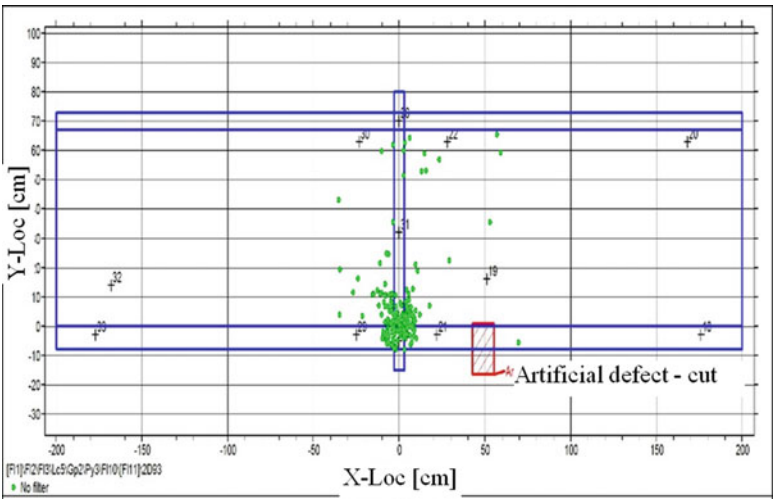

Fig. 10 Location of AE signals for loading of node without artificial defects

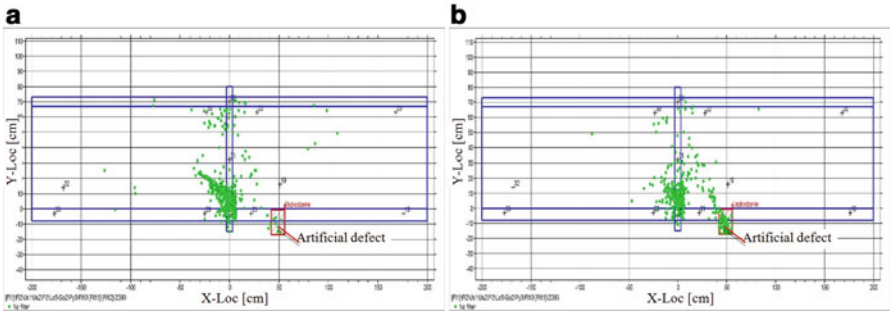

Fig. 11 Location of AE signals for a node with artificial defects: (**a**) first step of discontinuity, (**b**) second phase

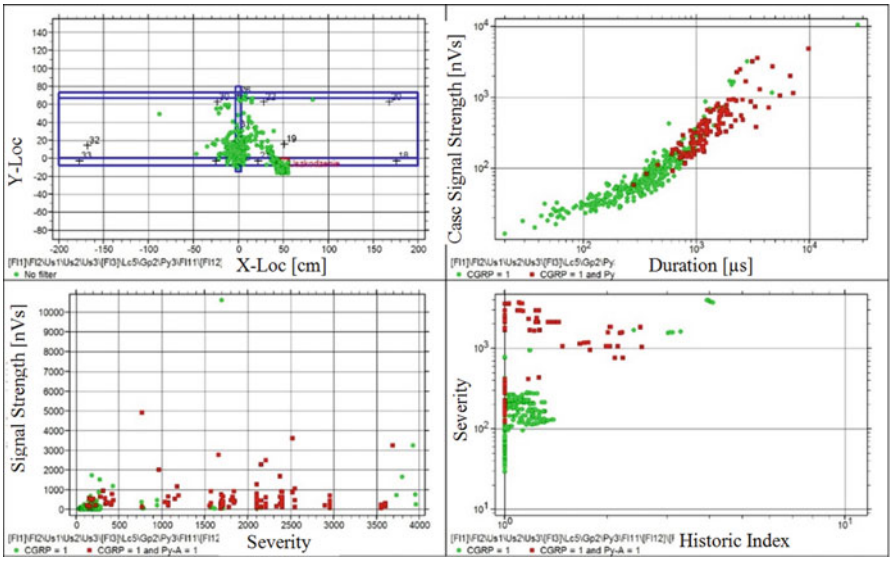

Fig. 12 Parameters of the signals recorded during loading of the node with artificial defects located around the node (CGRP = 1) and in the area with defects (CGRP = 1 and Py-A = 1)

shown in Fig. 12. The red points denote signals in the artificial defect area and the green points denote signals located in other areas.

For example, on the graph titled Cascade Signal Strength vs. Duration, the signals located in the area with defects are not separated, but are in one part of the correlation graph. Better separation is seen on the Severity vs. Historic Index graph, where higher severity values are found for signals detected in the zone with artificial defects.

The use of selected signal parameters as a filter for separation of the recorded AE signals enabled the elimination of most of the signals generated at the time of

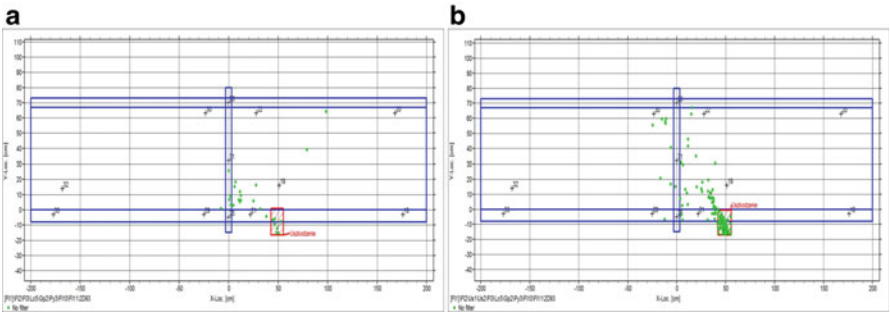

Fig. 13 AE signal location after filtering for nodes with (**a**) one discontinuity, (**b**) two discontinuities

loading before the introduction of discontinuities, without damaging the material. The results of the filtering for nodes with one and two discontinuities are shown in Fig. 13.

6 Conclusions

Analysis of the recorded signals allowed us to define the characteristics of the signals generated by corrosion products arising during the loading of structural elements.

The application and verification of location accuracy for different locating systems enabled the selection of the most effective system for use in monitoring the measurement of objects with defects.

Measurements performed during the loading of elements after the introduction of artificial defects and multi-parametric analysis were the basis for determining the parameters and their values indicating the degree of structural damage.

Laboratory tests conducted on elements of bridge structures were pretests for the study of real objects using acoustic emission analysis, which is ongoing.

References

1. J. Bień, Uszkodzenia i diagnostyka obiektów mostowych, Wydawnictwa Komunikacji i Łączności (2010)
2. K. Szadkowski, Raport o stanie technicznym kolejowych obiektów inżynieryjnych PKP Polskie Linie Kolejowe S.A. według stanu na dzień 31 grudnia 2013 roku, Biuro Dróg Kolejowych PKP Polskie Linie Kolejowe S.A., Warszawa, 2014
3. C.U. Grosse, M. Ohtsu, *Acoustic Emission Testing* (Springer, Berlin, 2008)
4. R.K. Miller, E.v.K. Hill, P.O. Moore, *Nondestructive Testing Handbook*, Acoustic Emission Testing, vol 6, 3rd edn. (American Society for Nondestructive Testing, Columbus, 2005)

5. D. Robert Hay, J.A. Cavaco, V. Mustafa, Monitoring the civil infrastructure with acoustic emission: bridge case studies. J. Acoustic Emission **27**, 1–10 (2009)
6. Kanji Ono, Application of acoustic emission for structure diagnosis, 56 Konferencja Naukowa Komitetu Inżynierii Lądowej i Wodnej PAN oraz Komitetu Nauki PZITB, Kielce-Krynica (2010)
7. Schultz A., *Development of an advanced structural monitoring system*, Research Project (Department of Civil Engineering, University of Minnesota, 2010)
8. Vallen Systeme GmbH, AMSY-6 user's manual
9. Kaphle, Manindra R., Tan Andy, Thambiratnam David, & Chan, Tommy H.T., Analysis of acoustic emission data for structural health monitoring applications, in *6th Australasian Congress on Applied Mechanics (ACAM 6)*, Australia (2010)
10. EN 1330-9:2009, Non-destructive testing. Terminology. Terms used in acoustic emission testing
11. Evgrafov A., Advances in mechanical engineering, in *Selected Contributions from the Conference "Modern Engineering: Science and Education"*, Saint Petersburg (2014)

Evaluation of Deterioration of Concrete Due to Alkali-Aggregate Reaction Based on Through-the-Thickness Elastic Waves

S. Uejima, T. Nishida, T. Shiotani, H. Asaue, T. Miyagawa, S. Furuno, and K. Hirano

Abstract There are many reports related to concrete structures deteriorated by alkali-aggregate reaction (ASR). In order to evaluate the progress of deterioration, a visual inspection of the structure has been principally carried out. However, this visual inspection cannot detect internal defects of the concrete structure, so that sometimes the results of inspection mislead maintenance or asset management. Therefore, the evaluation method which can assess the internal damage should be established. Authors have studied wave velocity tomography as indices to evaluate inside concrete damage.

In this study, actual concrete bridge piers which have been damaged by ASR were experimented. Based on the velocity distribution namely tomogram, the internal defects of concrete affected by ASR could be visualized. Furthermore, the progress of deterioration could be evaluated by the resultant tomogram as well.

1 Introduction

Alkali-aggregate reaction (ASR) is one of the serious forms of deteriorations of concrete structures around the world. Therefore, there are many reports related to concrete structures deteriorated by ASR. In order to evaluate the progress of deterioration, a visual inspection of the structure has been principally carried out as nondestructive evaluation. In other words, the conventional evaluation has often been carried out based on the surface information of the structure. However, this visual inspection cannot always evaluate the state of concrete structure satisfactorily because of lack of inside damage information. Destructive evaluation with cored concrete samples is thus employed as an inspection of actual concrete structures in order to obtain the internal information. However information obtained by such destructive tests is so localized and limited that the whole of deterioration progress in concrete structures cannot be studied. Therefore, the

S. Uejima (✉) • T. Nishida • T. Shiotani • H. Asaue • T. Miyagawa • S. Furuno • K. Hirano
Department of Urban Management, Kyoto University, Katsura Campus, Nishikyo-ku, Kyoto 615-8540, Japan
e-mail: uejima.shinsuke.85v@st.kyoto-u.ac.jp

G. Shen et al. (eds.), *Advances in Acoustic Emission Technology*, Springer Proceedings in Physics 179, DOI 10.1007/978-3-319-29052-2_24

evaluation method which can assess the internal damage in large concrete structures should be established.

Elastic wave tomography [1] using several parameters of the wave is one of the solutions against those issues. This is a method for evaluating the concrete characteristic using a specified elastic wave feature in each set element over the structure based on variations of elastic wave parameters through the propagation. For example, velocity and attenuation of amplitude in elastic waves are some kinds of elastic wave features. Among those parameters, the elastic wave velocity has been well used to relate the deterioration because the elastic waves are regarded to be associated with the elastic moduli, implying information of internal damages such as voids or cracks in the materials. Under the existence of such defects as voids or cracks, the elastic waves will result in scattering, reflection, and diffraction, leading to the decrease of elastic wave velocity. Therefore, the paths showing lower velocity were assumed to be deteriorated in the structure. This theory supports the algorithm of elastic wave tomography and finally tomogram was represented as elastic wave distributions. In this study, the actual concrete bridge piers which have been damaged by ASR were focused on and these ASR damages were evaluated based on obtained tomogram.

2 Methodology

2.1 Measurement

In this study, two bridge piers were evaluated using through-the-thickness elastic waves. This bridge is located in Toyama Prefecture, Japan, and has been used for 46 years. Based on the visual inspection, one of the piers (P2) was deteriorated by ASR severely, although another pier (P3) was not so much deteriorated. The condition of surface cracks of P2 is shown in Fig. 1.

Elastic waves were excited by impacting a steel sphere ball as shown in Fig. 2. First, 45 acceleration sensors were arranged on three sides of the concrete bridge pier as shown in Fig. 3. Secondly, elastic waves were generated from the other large side of concrete surface as shown in Fig. 3. Here, an acceleration sensor was placed in the vicinity of each impact point in order to measure the input waveform and impact time. Seventy-three excitation points are also indicated in Fig. 4. The diameter of impact hammer was φ100 mm. With this sensor arrangement as well as manner of impact, P2 and P3 were measured and evaluated by using through-the-thickness elastic waves.

Fig. 1 Condition of surface cracks of bridge pier and sensor-attached situation (*left*)

Fig. 2 Elastic wave excitation with impacting a ball on concrete surface (*right*)

2.2 Data Analysis

In order to determine wave velocity distributions of the bridge pier, several analysis steps are necessary as shown below.

First, arrival time of each sensor is determined with Akaike Information Criterion (AIC) picker [2]. AIC picker can determine the arrival time of detected AE waveforms or elastic wave. For the seismogram x of length N, the AIC value is defined as (1)

$$\mathrm{AIC}(k) = k \times \log\{\mathrm{var}(x[1, k])\} + (N - k - 1) \times \log\{\mathrm{var}(x[k + 1, N])\} \quad (1)$$

where k ranges through all the seismogram samples.

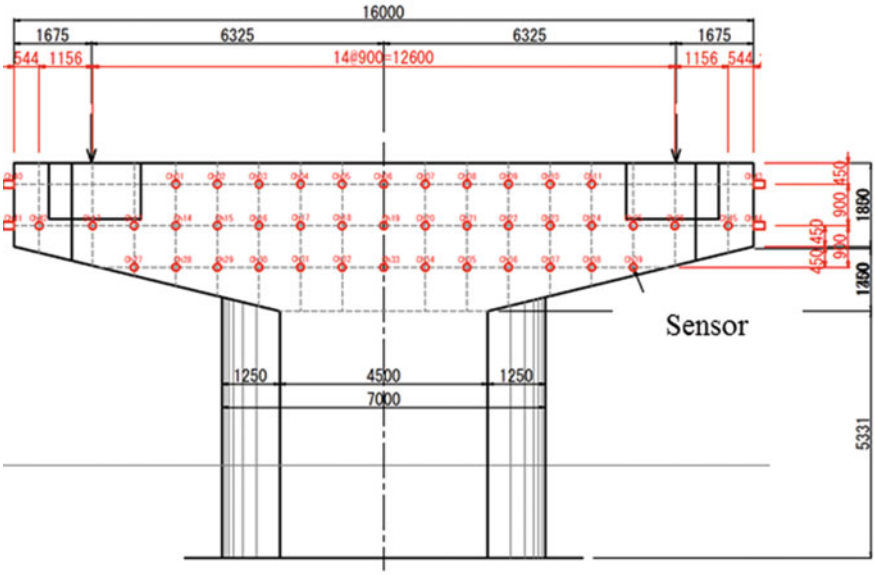

Fig. 3 Arrangement of sensors on concrete surface

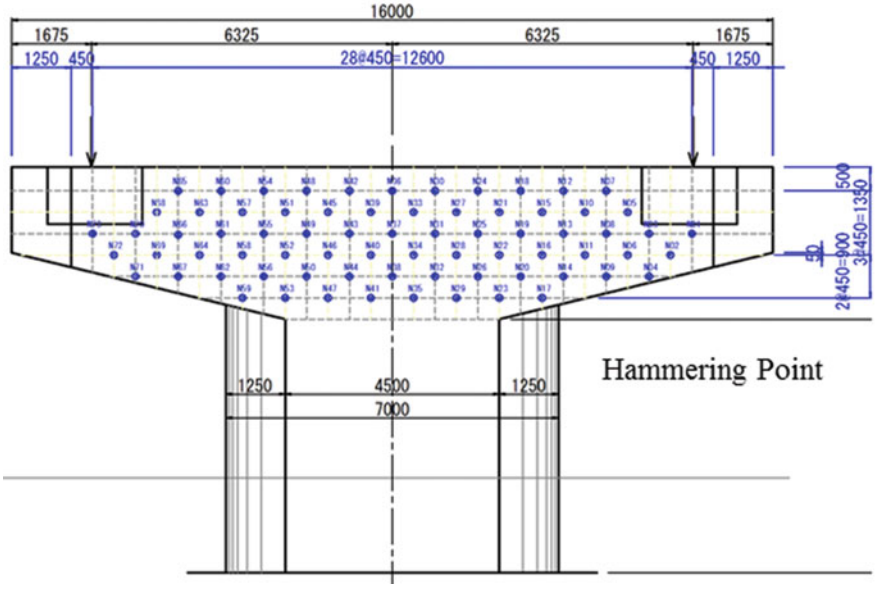

Fig. 4 Hammering point arrangement

The point where the AIC is minimized with the least squares method determines the optimal separation of the two stationary time series, and thus this is interpreted as the phase onset. That is why noise is well represented by a relatively low AIC value, whereas input wave signals gradually require a higher AIC value. Thus, arrival time of each sensor is found with AIC picker.

After each arrival time is determined, the propagation velocity of through-the-thickness elastic wave is calculated by both of the distance from the excitation point to the receive point and T_{obs} (observed propagation time) which is obtained by (2)

$$T_{obs} = T_o - T_s \tag{2}$$

where T_s is the excitation time and T_o is the arrival time [3].

On the other hand, in the algorithm of the elastic wave tomography, the inverse of velocity, which is specifically referred to as the "slowness," is given as an initial parameter into each element as shown in Fig. 5. Next, T_{cal} (theoretical propagation time) obtained by a finite element model is the total of the propagation time calculated by the slowness and the distance in each element (refer (3)). Third, ΔT which defines the difference between observed propagation time (T_{obs}) and theoretical propagation time (T_{cal}) is obtained by (4)

$$T_{cal} = \sum_j s_j \times l_j \tag{3}$$

$$\Delta T = T_{obs} - T_{cal} \tag{4}$$

where l_j is the length crossing each element and s_j is the slowness of each element.

Then the slowness in each element is revised in order to reduce ΔT which defines the difference between observed propagation time and theoretical propagation time. The slowness correction amount is obtained by (5). In addition, the revised slowness is obtained by (6)

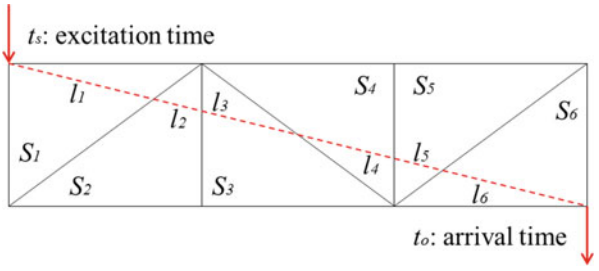

Fig. 5 Slowness for calculation of propagation time

$$\begin{bmatrix} \Delta s_1 \\ \Delta s_2 \\ \vdots \\ \Delta s_j \end{bmatrix} = \begin{bmatrix} \sum_i \frac{\Delta T_i \times l_{i_1}}{L_i} / \sum_i l_{i_1} \\ \sum_i \frac{\Delta T_i \times l_{i_2}}{L_i} / \sum_i l_{i_2} \\ \vdots \\ \sum_i \frac{\Delta T_i \times l_{i_j}}{L_i} / \sum_i l_{i_j} \end{bmatrix} \tag{5}$$

$$s'_j = s_j + \Delta s_j \tag{6}$$

where L_i is the total distance of the wave in the i-element. In other words, L_i is the sum of wave distances in i-element.

The iteration calculation from (5) to (6) enables to obtain the accurate slowness and finally the velocity in each element corresponding to the observed propagation time of multiple waves over the structure, resulting in forming the tomogram of the elastic wave velocity over the target area. Through these steps, wave velocity distributions were determined in this research.

3 Results

3.1 Input Waveform Result

An example of input waveforms which were obtained from input accretion sensor is shown in Fig. 6. Some of the maximum amplitudes were around 1–4 V with φ100 mm hammer. Moreover, Fig. 7 shows the fast Fourier transform results of

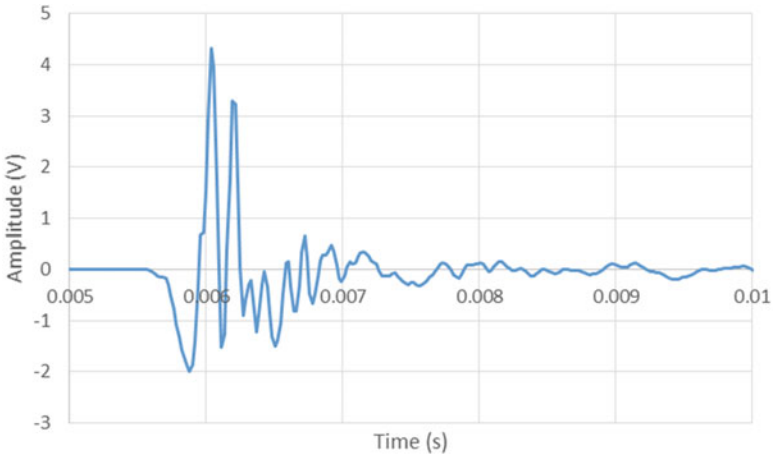

Fig. 6 Input waveform with impact hammer of φ100 mm

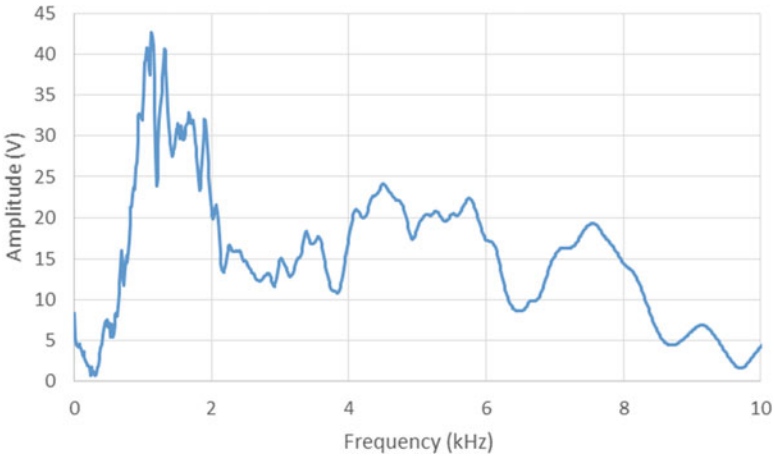

Fig. 7 FFT power spectrum

the input waveforms of impact hammer. As shown in Fig. 7, the dominant frequency of the impacted wave with φ100 mm is about 1 kHz.

3.2 Wave Velocity Distribution

First, P2 bridge pier is analyzed and evaluated. According to the visual inspection, this bridge pier seemed seriously damaged by ASR. The situation of surface damage about P2 is shown in Fig. 8. A large number of continuous horizontal cracks could be found at the center of bridge pier. The result of elastic wave tomography of P2 is shown in Fig. 9. In general, the elastic velocity of intact concrete is 4500 m/s. However, that of P2 shows remarkably low values in contrast. Moreover, extremely low-velocity distribution can be seen at the areas where the large cracks on the bridge surface were presented. As for the internal structure of P2, lower velocity area can be seen at the center ($x = 4$ to 5 m, $y = 0.9$ m, and $z = -0.5$ to -2 m). It is noted that such deterioration could not be found with the visual inspection.

On the impact side, the surface crack at the center of bridge pier (see Fig. 8) can be found from the result of tomogram, which is $Y = 0.9$ m of Fig. 9. On the other hand, the surface crack on the sensor side cannot be found clearly from the result of tomogram. Therefore, the other excitation must be needed on the opposite side and the data should be analyzed.

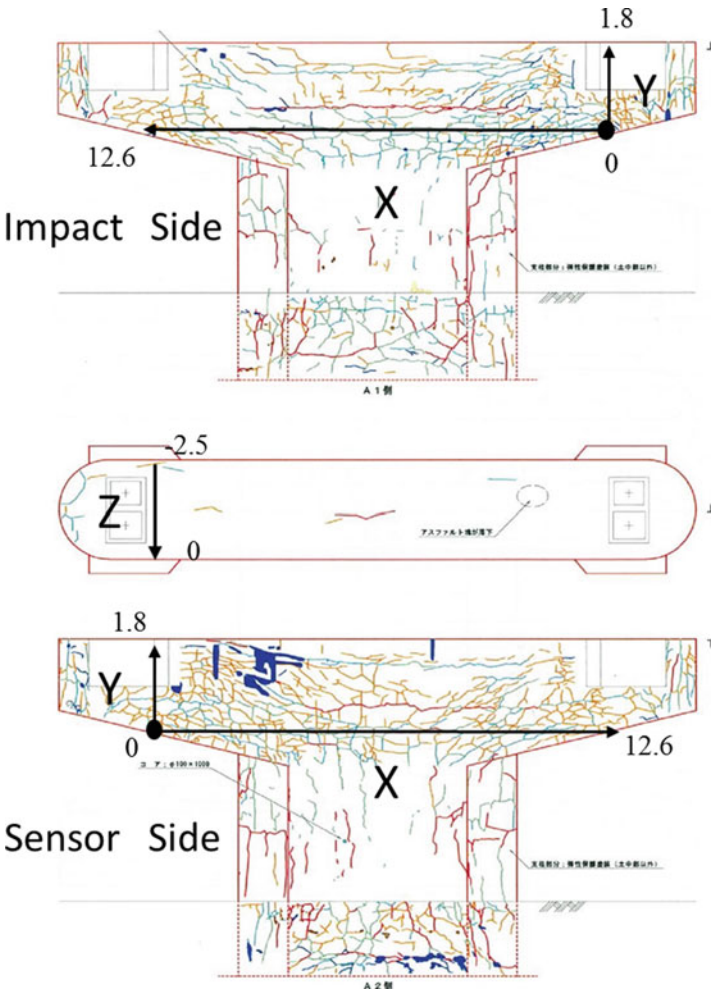

Fig. 8 Surface damage of P2 and coordinate of bridge pier

Second, P3 bridge pier was analyzed and evaluated. This bridge pier has not been damaged so much based on the visual inspection. The situation of surface damage about P3 is shown in Fig. 10. The result of elastic wave tomography of P3 is shown in Fig. 11 (with φ100 mm impact hammer). The elastic velocity of P3 is higher than that of P2. Therefore, P3 is a better situation than P2. However, the elastic velocity of P3 also shows remarkably low values in contrast and the areas of surface crack on the impact side show the lower velocity in each height ($Y = 0$ m, 0.9 m, and 1.8 m). Moreover, the internal deterioration has been found in the area

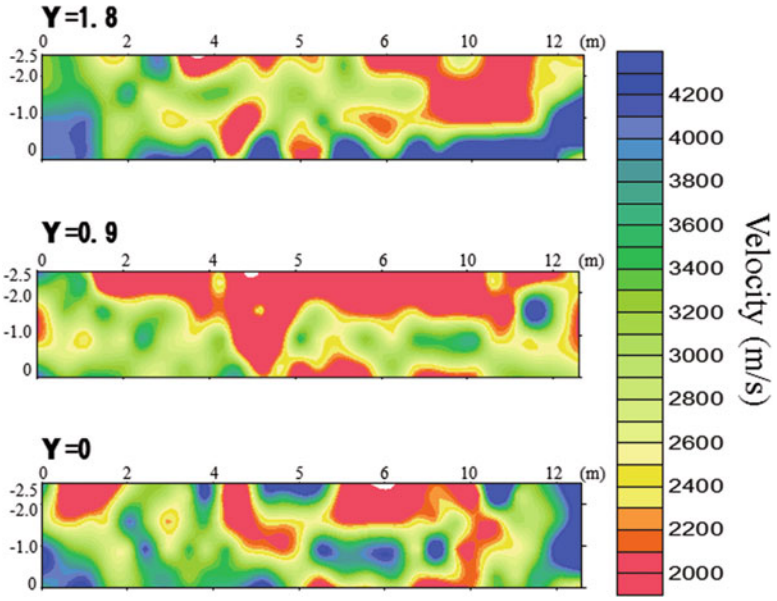

Fig. 9 Tomogram of P2 with φ100 mm impact hammer (cross figure)

from $X = 2$ to $X = 4$. Compared to the cross figures of $Y = 0$ m and 1.8 m, the internal concrete has not been damaged so much in the cross figure of $Y = 0.9$ m while some surface cracks can have been found apparently. It means that the situation of surface crack does not correspond to the internal defect.

4 Conclusion

In this research, the deterioration due to ASR in actual concrete bridge piers was evaluated using elastic wave tomography using velocity distributions. This analysis was performed with through-the-thickness waves. From the results of tomograms, the internal defects of concrete affected by ASR could be successfully visualized. Conclusions can be made as follows:

- The internal defects of concrete affected by ASR could be visualized by using elastic wave tomography with velocity distributions.
- In general, the elastic velocity of intact concrete is 4500 m/s. However, as for the bridge piers in this study, the average of elastic wave is about 2000 m/s. Therefore, overall these concrete structures have been damaged by ASR.

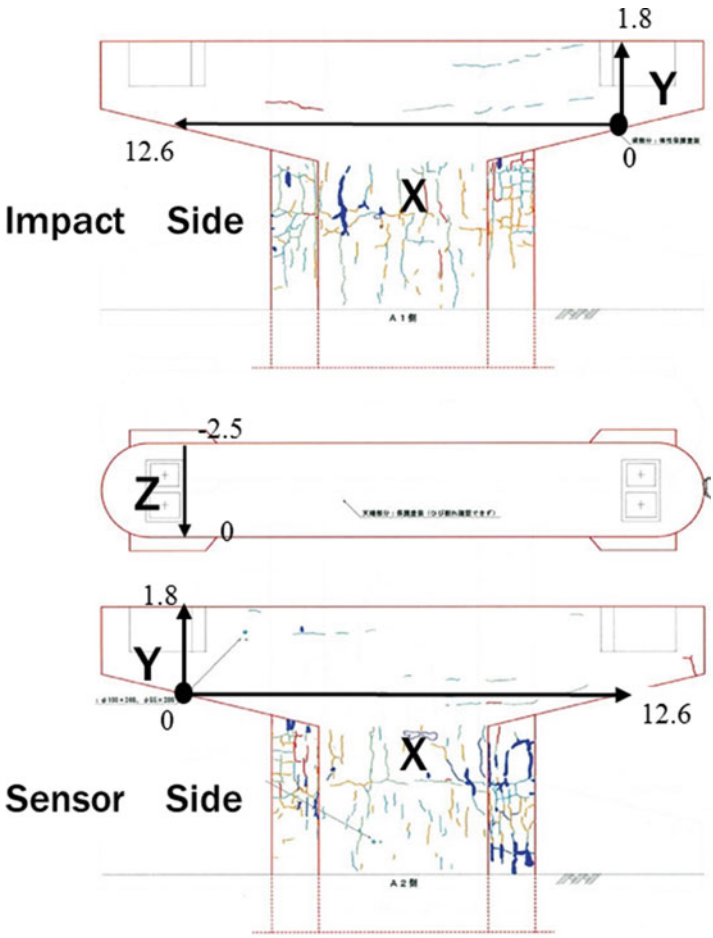

Fig. 10 Surface damage of P3 and coordinate of bridge pier

- The result of internal damage does not always correspond to the surface visual inspection result. Therefore, it might be considered that not only surface information but also internal information with employing this elastic wave tomography must be carried out when the ASR damage and defect are evaluated quantitatively.
- In order to examine this study, the experimental study has been conducted, which is related to the internal deterioration due to ASR and this elastic velocity distribution.

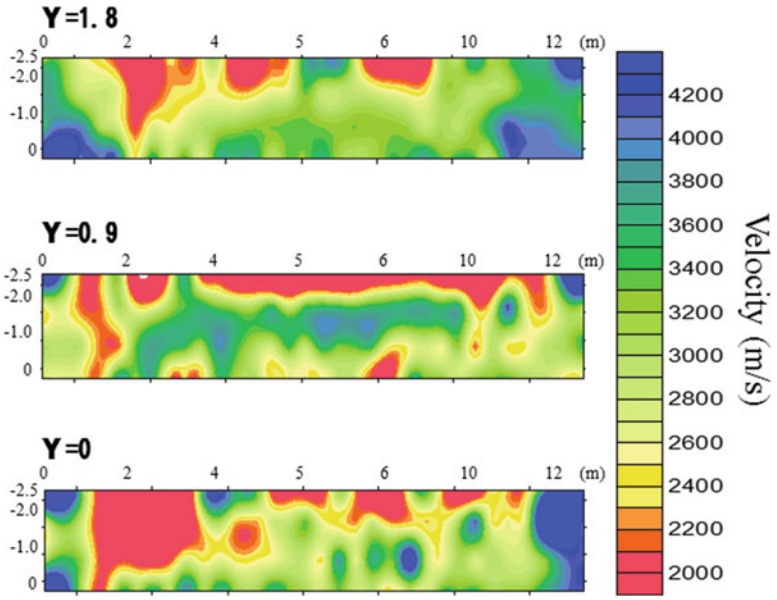

Fig. 11 Tomogram of P3 with φ100 mm impact hammer (cross figure)

References

1. S. Momoki, H.K. Chai, T. Shiotani, Y. Kobayashi, T. Miyanaga, Evaluation of concrete structures with three-dimensional elastic wave tomography. J. Struct. Eng. **57A**, 959–966 (2011). (in Japanese)
2. H. Zhang, C. Thurber, C. Rowe, Automatic P-Wave arrival detection and picking with multiscale wavelet analysis for single-component recordings. Bull. Seismol. Soc. Am. **93**(5), 1904–1912 (2003)
3. S. Osawa, T. Shiotani, H. Kitora, Y. Momiyama, Damage visualization of imperfectly-grouted sheath in PC structures. 31st Conference of the European Working Group on Acoustic Emission, German Society for Non-Destructive, Sept 2014. http://www.ewgae2014.com/portals/131/bb/fr1b3.pdf

Assessing Deterioration of an In-field RC Bridge Deck by AE Tomography

M. Fukuda, K.C. Chang, H. Nakayama, H. Asaue, T. Nishida, T. Shiotani, T. Miyagawa, K. Watabe, and T. Oshiro

Abstract Deterioration of aging infrastructures is an important issue in many developing and well-developed countries. For maintenance of the infrastructures in limited budgets, proactive inspections and countermeasures are important before severe structural damage occurs. To assess the deterioration of those structures in a reliable and preferably nondestructive manner is highly demanded. Responding to the demand, acoustic emission (AE) tomography can be regarded as a powerful method since it builds the elastic-wave velocity distribution of the medium that AE waves propagate through while simultaneously locating AE sources. Such a method has been widely tested in laboratories but not yet fully realized in fields. In the present study, the applicability of two-dimensional (2D) and three-dimensional (3D) AE tomography techniques to the evaluation of internal damages in existing RC bridge deck was examined using the data obtained by single-side AE measurement. The overlay of 2D elastic-wave velocity distribution with AE source locations reveals that AE was active in moderate-velocity areas and the boundaries of low-velocity areas, which were regarded as deteriorated areas with progressing defects. Moreover, in the AE measurement, a large number of AE with small amplitudes were observed in the severely deteriorated panel; amazingly, primary AEs were captured, which implied the propagation of an internal crack in the deck.

M. Fukuda • T. Oshiro
West Nippon Expressway Company Limited, 1-6-20 Dojima Kita, Osaka, Japan
e-mail: m.fukuda.ac@w-nexco.co.jp

K.C. Chang • H. Nakayama • H. Asaue • T. Nishida (✉) • T. Shiotani • T. Miyagawa
Kyoto University, Nishikyo, Kyoto, Japan
e-mail: nishida.takahiro.6e@kyoto-u.ac.jp; shiotani.tomoki.2v@kyoto-u.ac.jp

K. Watabe
Toshiba Corporation, Komukaitoshiba 1, saiwai, Kawasaki, Kanagawa, Japan
e-mail: kazuo.watabe@toshiba.co.jp

G. Shen et al. (eds.), *Advances in Acoustic Emission Technology*, Springer Proceedings in Physics 179, DOI 10.1007/978-3-319-29052-2_25

1 Introduction

Recently, deterioration of aging infrastructures like RC bridge decks is becoming a major concern around the world. As available budgets and manpower are always limited, effective maintenance of infrastructures is highly demanded. Proactive inspections and countermeasures are important before severe structural damage occurs. In addition to the conventional visual inspections, nondestructive testing techniques that can evaluate interior damage of the infrastructures are widely investigated. Here acoustic emission (AE) tomography can be regarded as one of the efficient nondestructive testing techniques mentioned above [1]. In the visualized velocity distribution, lower-velocity zones may indicate deteriorated areas in acknowledging the fact that damage like cracks or voids in concrete structures may force elastic waves bypass and therefore decrease their observed velocities. Such a method has been widely tested in laboratories but not yet fully realized in fields [2, 3].

In the present study, the applicability of two-dimensional (2D) and three-dimensional (3D) AE tomography techniques to the evaluation of internal damages in existing RC bridge deck was examined using the data obtained by single-side AE measurement. In addition, basic evaluations based on AE parameters are implemented.

2 Outline of AE Measurement in Actual RC Deck

The surface condition of the target RC deck is shown in Fig. 1. This RC deck is supported by steel girder and has been served for 40 years as a part of a highway in Nara Prefecture, Japan.

AE measurement system is AMSY-6 MB19 by Vallen Systeme GmbH. Twelve AE sensors of 30 kHz resonant frequency (VS30-V by Vallen Systeme GmbH) were installed on the bottom surface of the highway bridge deck, 6 on the panel severely deteriorated (upper panel in Fig. 1) and 6 on another panel slightly deteriorated (lower panel) by visual inspection. AE activities under normal traffic loadings were monitored from 10:08 AM, 24th Dec., 2014 to 9:28 AM, 26th Dec., 2014 and a total of 29,438,265 AE events were acquired. Most of AE data obtained in-situ measurements are secondary AE induced by traffic loads. The relationship between the AE peak amplitude and LUCY (Location Uncertainty, defined in VisualAE®) [4] is shown in Fig. 2. It shows that as the peak amplitude increases, the number of AE events and LUCY decrease. Herein, the threshold was set as 60 dB for peak amplitude and 0.3 m (half of sensor spacing) for LUCY, i.e., AE events with peak amplitude smaller than 60 dB and a LUCY larger than 0.3 m are filtered out for further analysis.

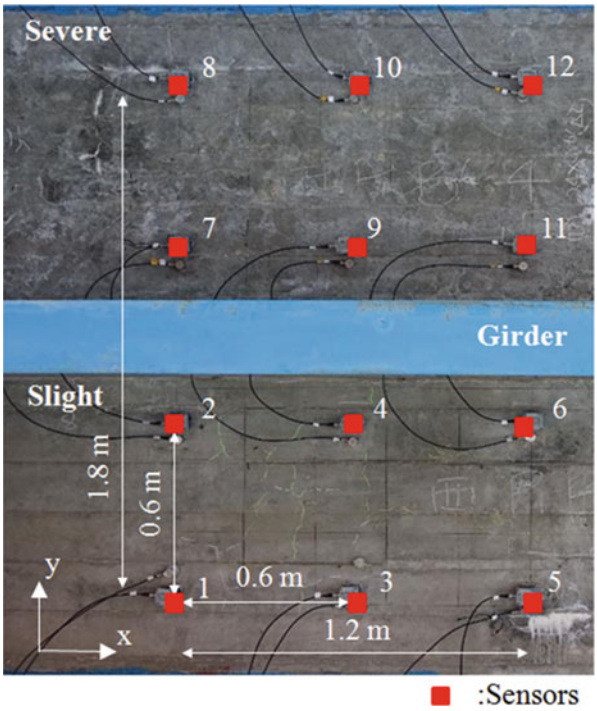

Fig. 1 Target RC deck and sensor layout

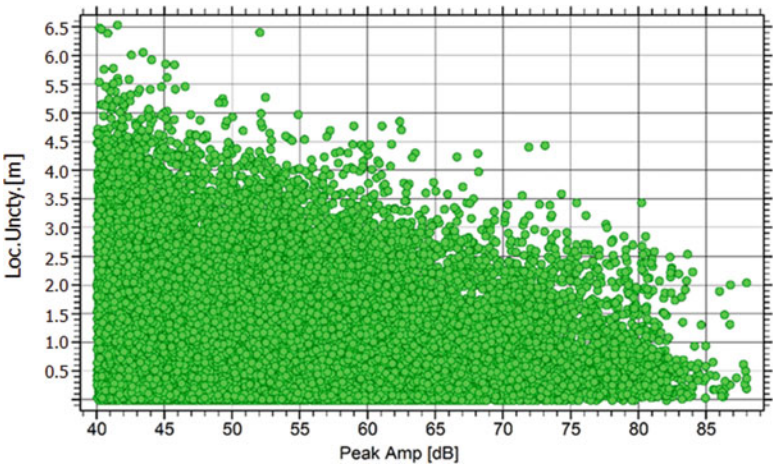

Fig. 2 Relation between peak amplitude and LUCY

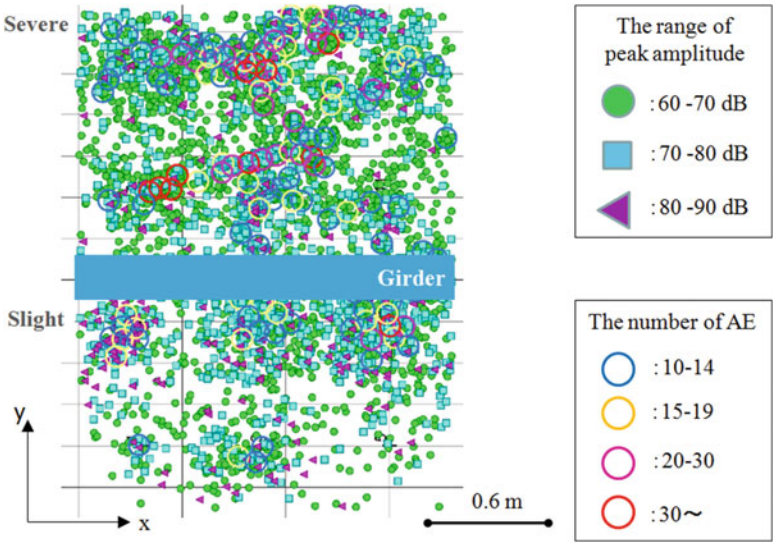

Fig. 3 AE source locations

3 AE Analysis

3.1 Source Location Analysis

AE source locations are shown in Fig. 3, where the AE peak amplitudes are labeled as follows: 60–70 dB in green circle, 70–80 dB blue square, and 80–90 dB in purple triangle. Also, the numbers of AE events clustering in a circular area of 0.1 m in diameter are marked in hollow circles as follows: 10–14 events in blue, 15–19 events in yellow, 20–30 events in pink, and more than 29 events in red. It is observed that AE activities were denser and generally of smaller peak amplitude in the severely deteriorated panel than the slightly deteriorated panel.

3.2 Crack Propagation Detected in AE Measurement

In order to investigate the AE source locations in detail, the measured area was divided into small area of 0.1 m $\times$ 0.1 m and AE sources were counted for each area. Among those small areas, we were interested in a specific area where extraordinarily many AE events (383 in number) were captured. The cumulative number of AE events in this area is shown in Fig. 4a, where the full time-span was separated into 5 intervals: Interval 1 is from 10:00, 24th Dec. to 18:30, 25th Dec., Interval 2 is from 18:30 to 20:20, 25th Dec., Interval 3 is from 20:20 to 22:30, 25th Dec., Interval 4 is from 22:30, 25th Dec. to 1:30, 26th Dec., and Interval 5 is from

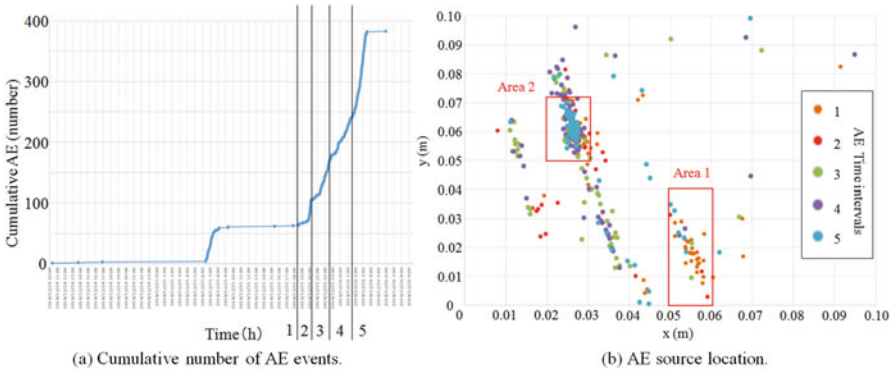

Fig. 4 AE events in a specific 0.1 m × 0.1 m area. (**a**) Cumulative number of AE events. (**b**) AE source location

1:30 to 9:28, 26th Dec. In this area, AE occurred from 6:00 to 9:00, 25th Dec. (in Interval 1 of Fig. 4a), calmed down once and then occurred continuously from 18:30, 25th Dec. to 3:30, 26th Dec. (intervals 2–5).

The AE sources location is shown in Fig. 4b. Amazingly the majority of the sources distributed in two belt zones. Let us take a closer look at Area 1 (x = 0.05–0.06 m, y = 0–0.04 m, Fig. 4b) and Area 2 (x = 0.02–0.03 m, y = 0.05–0.07 m). In Area 1, a large number of AE events were observed in Interval 1. In Area 2, AE events were observed continuously in all intervals and they extended towards upper-left side of this area. Although the frequency characteristics or other AE parameters have not been comprehensively studied yet, the rapidly increasing number (Fig. 4a) and spatial concentration (Fig. 4b) of AE events in Area 2 might imply a propagating internal crack, which released primary AE waves.

4 2D AE Location and Elastic Wave Velocity Distribution

Elastic wave tomography analysis (see [1, 2] for detailed algorithm) was also implemented using hammering impacts. Area of tomography analysis and hammering points are shown in Fig. 5. In the elastic wave tomography analysis, velocity distribution of surface or measured media is acquired. It is known that the velocities tend to be high when the media is uniform and sound. The elastic wave velocity distribution overlaid with AE sources location is plotted in Fig. 6. It is observed that AE of large amplitude occurred at moderate-velocity areas (3300–3800 m/s) and the boundaries of low-velocity areas (3300 m/s or lower); fewer AE occurred at high-velocity areas (4100 m/s and higher) and low-velocity areas.

This observation can be explained in mechanical sense as follows. In high-velocity areas, which are generally regarded as sound areas, AEs are inactive and

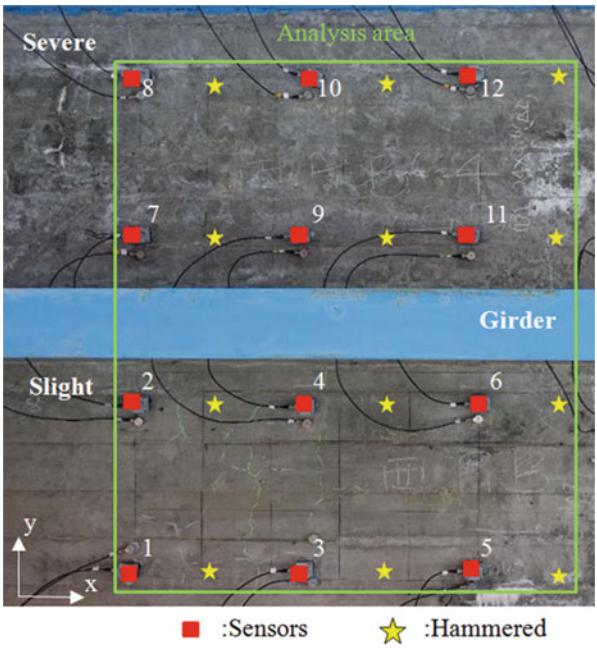

Fig. 5 Area of tomography analysis and hammering points

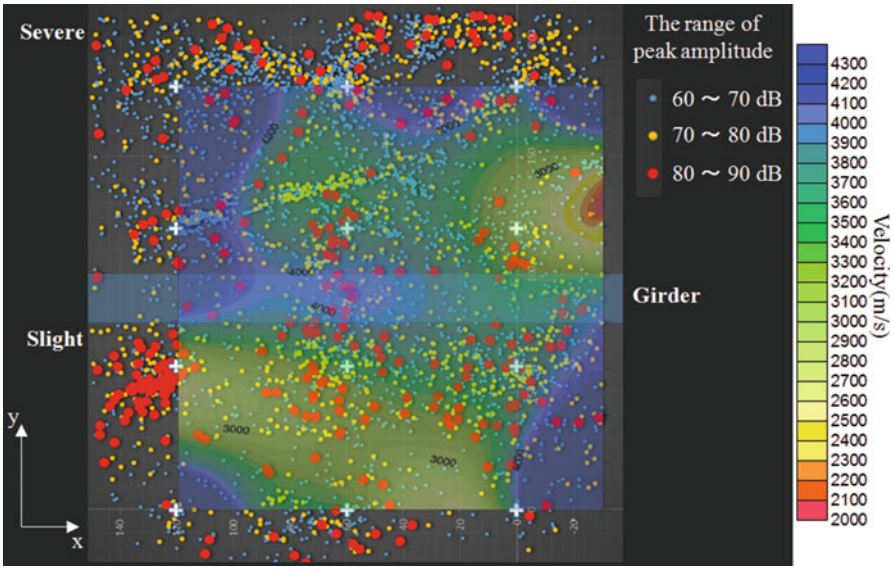

Fig. 6 Comparison of AE location and elastic wave velocity

their amplitudes are small because there are little defects causing internal frictions. It means that crack interface is mostly contact in this area. Therefore, this result indicates less defects area. In the low-velocity areas, which are regarded as highly deteriorated areas, AEs are inactive as well since the defects like cracks have fully developed and little new defects propagating. This area can be estimated as crack interface with less contact; AEs are difficult to generate because of less friction. The area is regarded as a defected area.

As for the moderate-velocity areas and the boundaries low-velocity areas, AEs are active and their amplitudes are large due to the propagation and frictions of newly developing defects. It is estimated that the results of velocity structures indicate edge of clacks. AEs are easy to generate in the area because clacks will make progress at this area. Fatigue damage by traffic load has been progressing during the measurement.

5 3D AE Tomography Analysis

A 3D AE tomography was performed, using the obtained AE events. The same area as that for 2D analysis as shown in Fig. 7 was considered, which is confined by the sensors No. 1, 5, 8, and 12. The area was discretized into $6 \times 8 \times 2$ meshes in the $X \times Y \times Z$ dimensions. Forty AE events that had large amplitude and were measured by at least four sensors at the same event were used for the 3D AE tomography analysis, to obtain 3D AE source locations and elastic wave velocity distribution. AE sources located by 3D AE tomography analysis are compared with those by 2D AE tomography analysis, as shown in Fig. 7. From these results, it could be said that similar source locations were identified in 2D and 3D analysis. 3D analysis is more powerful in that AE sources can be located inside the deck.

3D elastic wave velocity distribution from 3D AE tomography analysis is shown in Fig. 8, where variations of the internal velocity can be observed. The elastic wave velocity distributions extracted at the horizontal planes $z = -0.05$ and -0.15 m are shown in Fig. 9. Near the bottom surface of the deck ($z = -0.05$ m), low velocity areas were observed and those areas were considered as deteriorated areas. On the other hand, at the plane $z = -0.15$ m, high velocity was observed in most areas, which indicated the internal deterioration was less progressed than the surface. The velocity distributions at cross-section of $x = 0.45$ m, 0.75 m and $y = -0.45$ m, -1.35 m, are shown in Fig. 10. It was observed that velocity distributions were not uniform in the concrete deck and low velocity (around 2000 m/s) areas were distributed below the depth of 0.1 m measured from the bottom surface (the sensor side). As mentioned above, 3D AE tomography analysis would be able to visualize the interior distribution of concrete quality, which is unavailable by both the 2D AE tomography analysis and conventional visual inspection.

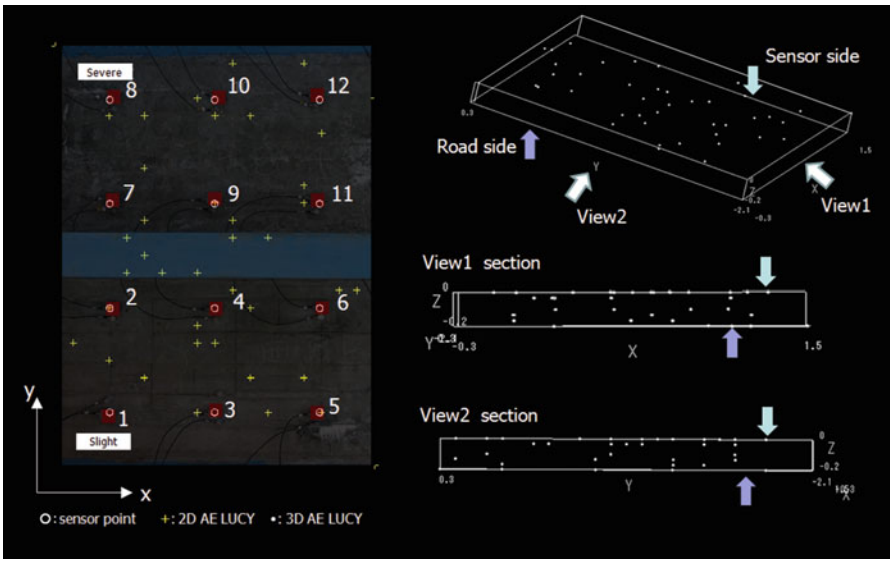

Fig. 7 AE source location detected by 2D and 3D tomography

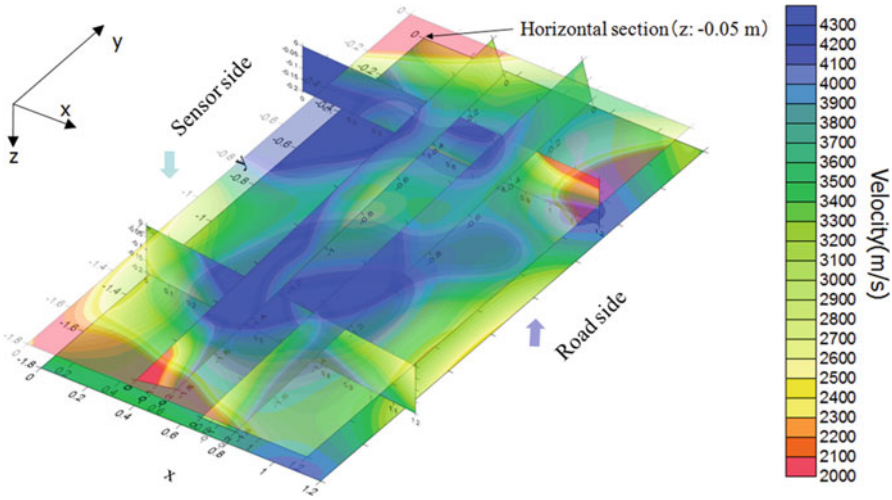

Fig. 8 Panel diagram of 3D analysis

6 Summary

Following conclusions could be drawn from the present experimental study.

1. In the AE measurement on the real RC deck, a large number of AE with small amplitudes were observed in the severely deteriorated panel and a smaller

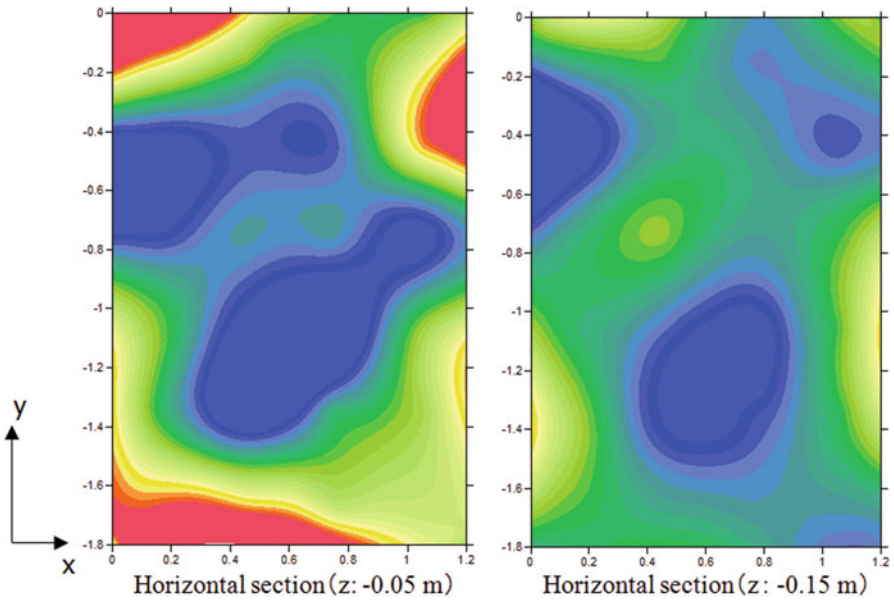

Fig. 9 Elastic wave velocity distribution (*z*-axis)

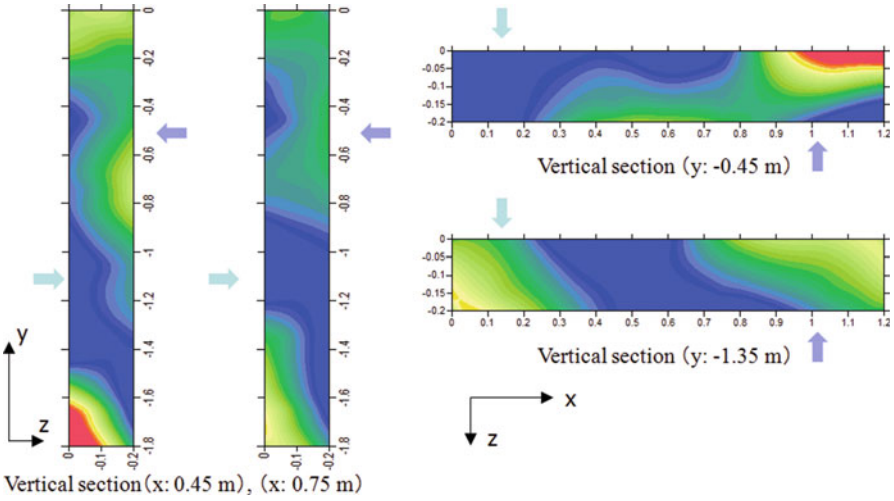

Fig. 10 Elastic wave velocity distribution (*x*-axis and *y*-axis)

number of AE with large amplitudes were detected in the slightly deteriorated panel. Amazingly, primary AEs were captured during the measurement, which implied the propagation of an internal crack.

2. The overlay of 2D elastic-wave velocity distribution with AE source locations reveals that AE was active in moderate-velocity areas and the boundaries of

low-velocity areas, which were regarded as deteriorated areas with progressing defects. Contrarily, AE was less active in high- and low-velocity areas, which were regarded as sound areas and deteriorated areas with fully developed defects, respectively.

3. The present AE tomography works well for the in-field RC bridge deck as illustrated above. It is available to assess deteriorations of the target deck in either 2D or 3D elastic-wave velocity distribution, which encourages a further practicability study along this line.

Acknowledgment A part of field measurements was financially supported by NEDO, New Energy and Industrial Technology Development Organization.

References

1. T. Shiotani, D.G. Aggelis, O. Makishima, Global monitoring of large concrete structures using acoustic emission and ultrasonic techniques: case study. J. Bridg. Eng. **14**(3), 188–192 (2009)
2. Kobayashi, Y., Shiotani, T., Oda, K., in *System identification for three-dimensional AE-tomography with Kalman Filter, Proceedings of the 31th Conference of the European Working Group on Acoustic Emission*, 2014
3. Shiotani Tomoki, Okude Nobuhiro, Momoki Shohei, Yoshikazu Kobayashi, in *Proposal of soundness evaluation method for infrastructure construction by AE tomography, Japan Non-destructive Inspection Association, the 18th AE General Conference Papers*, 39–42, 2011 (in Japanese)
4. M.A. Hamstad, Acoustic emission source location in a thick steel plate using lamb modes. J. Acoustic Emission **25**, 194–214 (2007)

A Preliminary Study on Application of AE Methods to Detecting Aggregation Regions of RC Bridge Decks

T. Shiotani, T. Nishida, K.C. Chang, T. Miyagawa, M. Ohara, and H. Yatsumoto

Abstract Nowadays, numerous "aggregation" problems are reported in existing RC bridge decks. Since aggregation is known as a main factor that decreases the serviceability and safety of the decks, it is highly demanded to detect and recover it as early as possible. However, those regions are invisible from asphalt pavement surfaces, so the aggregation parts are recognized after severely deteriorated. Facing this challenge, this study is devoted to develop a nondestructive testing method that the aggregation regions can be detected from asphalt pavement surfaces by capturing the acoustic emissions (AE) under traffic loads. As a preliminary experimental study, a laboratory-scale specimen was conducted with one end equipped with and the other end without modelled aggregation regions. From incremental cyclic loading tests, it is verified that, firstly, the aggregation regions may yield a great amount of AE activities, significantly more than the non-aggregation regions, under loads of similar order to traffic loads, and, secondly, most measured AE waves, dominated by low frequencies, are those likely caused by the frictions between aggregated particles.

T. Shiotani • T. Nishida (✉) • K.C. Chang • T. Miyagawa
Kyoto University, C-Cluster, Katsura Campus, Nishikyo, Kyoto 615-8540, Japan
e-mail: nishida.takahiro.6e@kyoto-u.ac.jp

M. Ohara
West Nippon Expressway Company Limited, Dojima Avenza 18F 1-6-20 Dojima Kita-ku, Osaka 530-0003, Japan
e-mail: m.ohara.ab@w-nexco.co.jp

H. Yatsumoto
Hanshin Expressway Company Limited, 4-1-3 Kyutaro-machi, Chuo-ku, Osaka 541-0056, Japan
e-mail: hitoshi-yatsumoto@hanshin-exp.co

G. Shen et al. (eds.), *Advances in Acoustic Emission Technology*, Springer Proceedings in Physics 179, DOI 10.1007/978-3-319-29052-2_26

1 Introduction

Nowadays, numerous "aggregation" problems are reported in existing RC bridge decks and related investigation was widely conducted around the world by means of nondestructive testing such as GPR, Impact Echo, Ultrasonic wave, and Half-cell potential [1]. It is considered that the main factor of aggregation in RC decks is fatigue damage caused by repeated traffic loads and rain. Aggregation may greatly decrease the serviceability/durability of RC deck and it is necessary to detect/recover the aggregation region at an early stage.

AE wave is an elastic wave generated by the release of energy by the formation of micro-cracks or frictions of materials [2, 3]. In general, primary AE is generated by the fracture of materials, while secondary AE is generated by the frictions between cracked and fractured surfaces. Based on the above phenomenon, this study proposed the application of AE methods to detect aggregation regions of RC bridge decks when subjected to traffic loading. To preliminarily investigate its feasibility, laboratory experiment were conducted on a pair of test specimens, one being sound and the other one with an artificial aggregation region. In addition, the sensitivity of AE measurement to different levels of loading and AE sensors of different resonance frequencies were also investigated.

2 Experiment Procedures

2.1 Outline of Specimen Preparation

Two types of concrete specimens, aggregation test specimen and sound test specimen, were prepared in this study. Mixture proportion for the test specimen is listed in Table 1. The test specimens were 200 mm in thickness, 300 mm in width, and 700 mm in length as shown in Fig. 1. This 200 mm thickness resembled the actual thickness of RC bridge decks in Japan. Also, the specimens were paved, with a layer of 80 mm thick, dense graded asphalt as shown in Fig. 2.

The aggregation region is experimentally simulated by filling course aggregates with the maximum size of 20 mm in a part of concrete. The dimension of the aggregation region was 200 mm × 200 mm × 45 mm as shown in Fig. 3.

Table 1 Concrete mixture proportion

Merging ratio (kg/m^3)					
		Sand	Gravel		
Cement	Water	Type (1)	Type (2)	Admixture	
295	168	443	431	978	2.95
W/C (%)			Sand ratio (%)		
57%			47.40%		

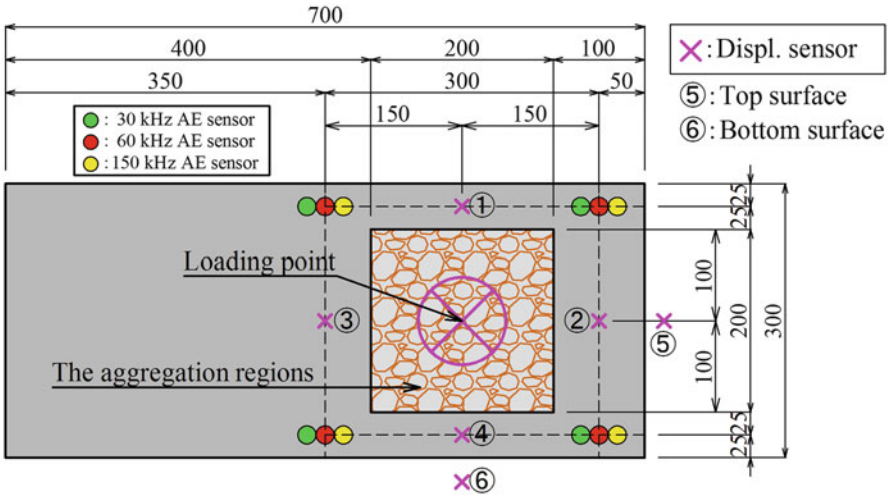

Fig. 1 Dimension of the test specimen and sensor layout

Fig. 2 Overview of the test specimen

The aggregation region was simulated exclusively with gravels for simplicity, although real aggregation regions in RC decks may consist of fine and coarse particles.

2.2 Loading Patterns

As shown in Fig. 4, a universal loading machine with the maximum loading capacity of 2000 kN was used to apply external loads. Cyclic loading and unloading

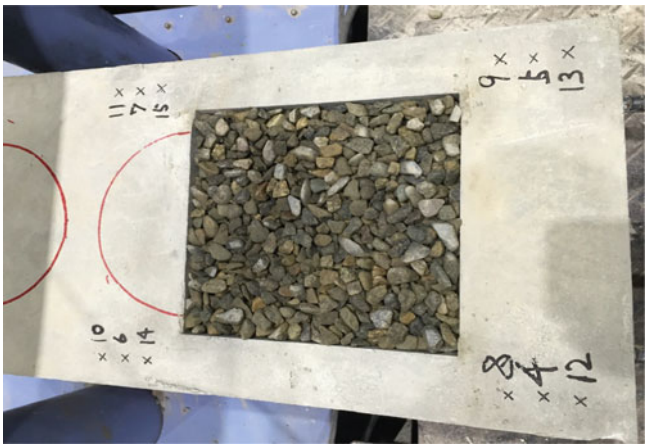

Fig. 3 Simulated aggregation regions under asphalt layer

Fig. 4 Universal loading machine used

were applied to specimens manually. Thin rubber pads of 3 mm in thickness were installed between the bottom surface of specimen and loading plate to reduce the horizontal gap of the surface of the test specimen, to avoid stress concentration at certain points, and to avoid the friction between the contact surfaces.

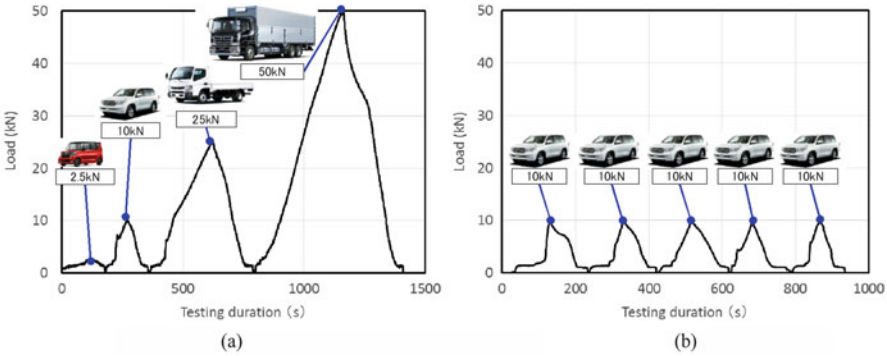

Fig. 5 Loading patterns (**a**) Incremental cyclic loading (**b**) Constant cyclic loading

A static cyclic loading was applied to specimens considering general vehicle weights. Two types of loading cases were applied: an incremental cyclic loading for resembling general vehicle loadings (Fig. 5a) and a constant cyclic loading at 10 kN for examining Kaiser effect (Fig. 5b). During the tests, loads and displacements (see Fig. 1 for loading and sensor location) were recorded by data loggers.

2.3 Sensor Location

In this study, three types of AE sensor, 30, 60, and 150 kHz in resonance frequency, were attached on the asphalt surface, to clarify frequency characteristics of AE waves obtained from aggregation regions. These AE sensors were placed in the range of aggregation regions in every direction (see Fig. 1 for sensor layout). In addition, displacement sensors around a loading point were installed to examine the deformation behavior of test specimens.

3 Experimental Results and Discussions

3.1 Deformation Characteristic

The displacement sensors around a loading point were set up to evaluate the deformation behavior of both sound test specimen and aggregation test specimen under loading and unloading conditions. The test processes and test results are shown in Fig. 6.

From the results, it can be found that the displacement in aggregation test specimen was two times larger than that in sound specimen. The displacement of sound test specimen at 50 kN of load was approximately 1 mm, while the displacement in aggregation test specimen became 2 mm under the same loading

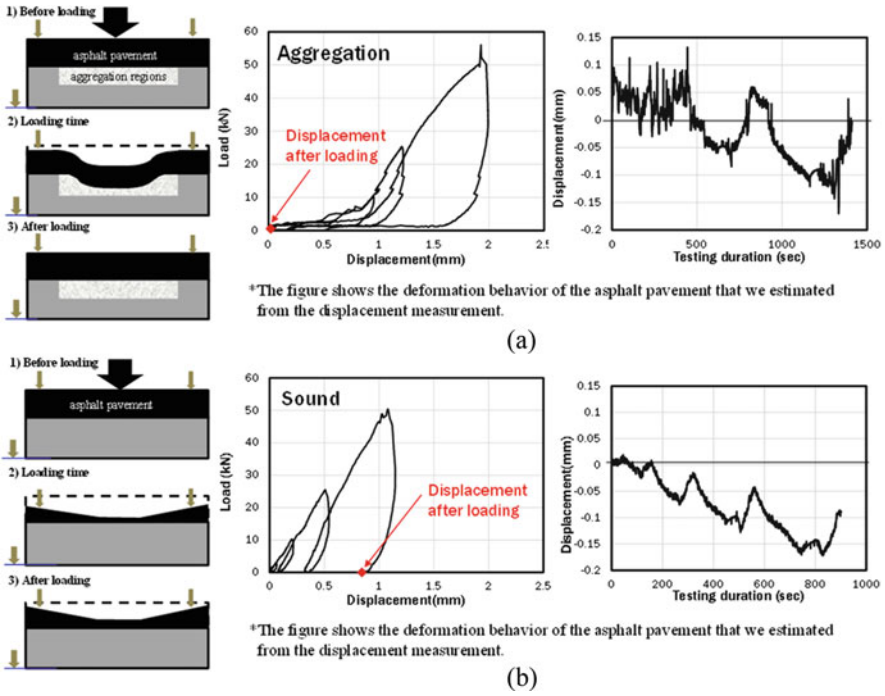

Fig. 6 Displacement during loading and unloading (**a**) The aggregation test specimen (**b**) The sound test specimen

magnitude. On the other hand, almost 1 mm of residual deformation in sound test specimens was found after unloading, while the displacement in aggregation test specimen was back to zero. It is assumed that the asphalt layer had bending behavior in elastic state as shown in Fig. 6, so that there was a gap between asphalt layer and gravels simulating aggregation region. On the other hand, the sound test specimen presented consolidation deformation at a certain point due to the existence of concrete under asphalt layer and the displacements of specimen show plastic behavior. Considering above, it can be explained that frictions between aggregates are main causes of the AE generation in the aggregation test specimen.

3.2 Kaiser Effect

Kaiser effect was discussed using the data of constant cyclic loading. As shown in Fig. 7, the number of the AE hits rarely decreased after second cycle AE activity in aggregation test specimen, while the results of the sound test specimen exhibited remarkable reduction of AE hits after second cycle AE activity. Based on the above data, it was considered that the occurrences of AE in sound test specimen were affected by consolidation deformation during initial loading. Otherwise, when the

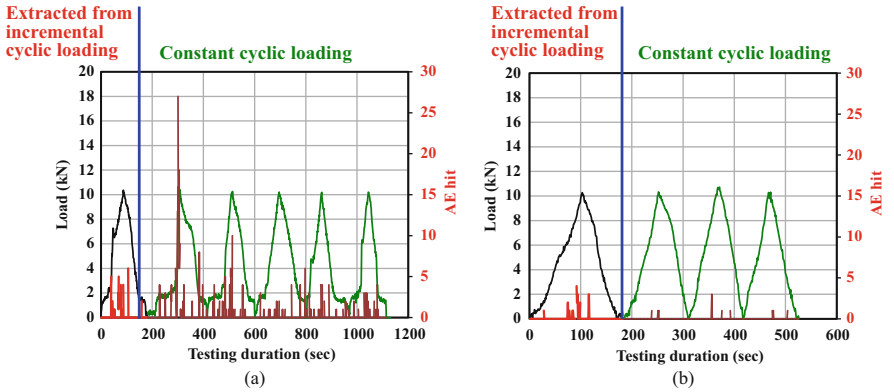

Fig. 7 The number of AE hits in the constant cyclic loading of 10 kN (**a**) The aggregation test specimen (**b**) The sound test specimen

aggregation part was subjected to the constant cyclic loading repeatedly, it was confirmed that AE waves can be captured and recorded due to frictions between aggregates.

3.3 Relations of Load and AE Parameters Such as AE Hits or AE Energy

Figure 8 shows the relationship between load and cumulative AE hits for the aggregation test specimen and the sound test specimen and Fig. 9 shows the relationship between load and cumulative AE energy.

It seems that AE hits gradually increased when the applied load exceeded the previous cycle in Fig. 8. This tendency is also confirmed in the results of energy shown in Fig. 9. Here the rapid growth of AE energy was observed around the 650th second of testing duration in Fig. 9, although the number of AE hits gradually increased in Fig. 8. It is considered that large cracks with large energy AE occurred in the sound test specimen at this moment.

Also, from these graphs, it can be seen that both the number of AE hits and energies in the aggregation test specimen were larger than those in the sound test specimen. Especially, the accumulated energy for the sound test specimen and aggregation test specimen was around 5.5×10^3 eu and 6.5×10^5 eu, respectively (eu: energy unit $=10^{-18}$ J), by using 30 kHz resonance-type AE sensor at 50 kN of loading. The accumulated energy was about 120 times larger in the aggregation test specimen than the sound test specimen. In addition, the number of accumulation AE hits of the aggregation test specimen was approximately ten times more than that of the sound test specimen.

In addition, three kinds of AE sensor were set up to examine the corresponding energy. Based on the observation, it can be concluded that the level of accumulated energy was high when low-frequency resonance sensor was selected.

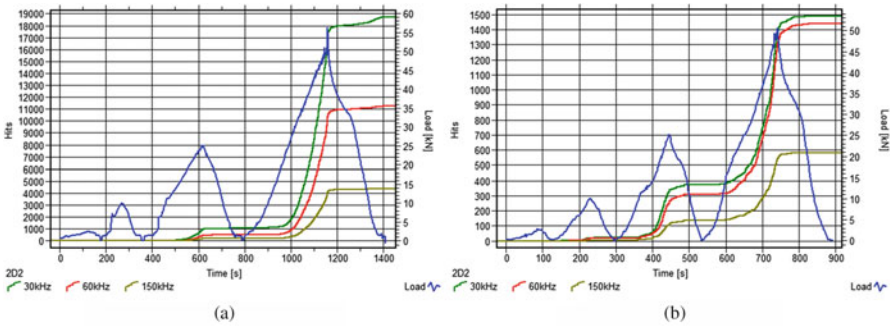

Fig. 8 Load vs. AE hits (**a**) The aggregation test specimen (**b**) The sound test specimen

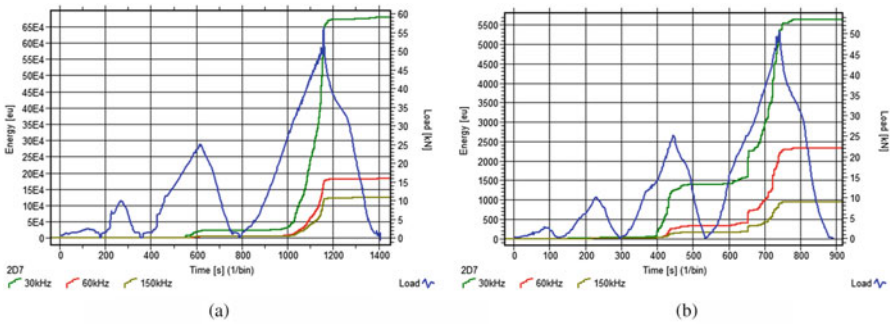

Fig. 9 Load vs. AE energy (**a**) The aggregation test specimen (**b**) The sound test specimen

3.4 Influence of Sensors on AE Detections

Generally, an AE can be classified into primary emissions and secondary emissions. For example, when particle breakage occurs, an AE wave (primary AE) is characterized by essentially higher frequency and larger energy [4]. However, it is known that an AE wave (secondary AE) generated through particle friction is characterized by lower frequency. In this study, incremental loading on the aggregation test specimen was adopted to identify frequency characteristics of the AE waves. The peak-frequency histograms during loading and unloading processes for three types of AE sensors are given in Fig. 10.

As known in Fig. 10, low-frequency band of 10–30 kHz dominated the AE waves in both the loading and unloading processes due to the friction between the aggregates occurred in the aggregation test specimen. The similar frequency distributions in loading and unloading processes indicate that the AE monitored in this specimen is mainly secondary AE. Therefore, it is more appropriate to adopt lower frequency resonance sensor.

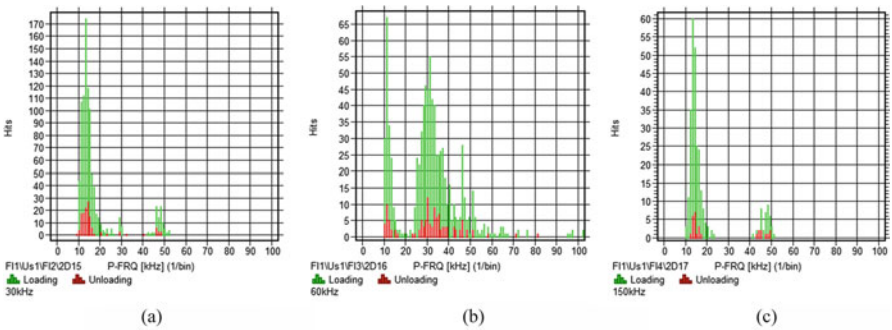

Fig. 10 Peak frequency vs. the number of AE hits in aggregation test specimen (**a**) 30 kHz AE sensor (**b**) 60 kHz AE sensor (**c**) 150 kHz AE sensor

Table 2 Minimum loads for AE activities to be observable

(a) The aggregation test specimen (unit: kN)			
Loading step	Sensor type		
	30 kHz	60 kHz	150 kHz
1 Cycle (max: 2.5 kN)	–	2.5	–
2 Cycle (max: 10 kN)	2.5	5.2	7.8
3 Cycle (max: 25 kN)	6.8	11.1	13.1
(b) The sound test specimen (unit: kN)			
Loading step	Sensor type		
	30 kHz	60 kHz	150 kHz
1 Cycle (max: 2.5 kN)	–	–	–
2 Cycle (max: 10 kN)	1.5	3.8	8.4
3 Cycle (max: 25 kN)	4.2	6.5	9.4

The minimum loads for AE activities to be observable in each test specimen are listed in Table 2. From this table, it can be found that the minimum load for AE detections increased as the cycle number increased. Also lower frequency resonance sensors such as 30 or 60 kHz can detect the first AE in smaller loads.

From the above observations, it can be concluded that AE sensors with resonance frequency less than 60 kHz would be more suitable for detecting aggregation regains under asphalt pavements.

3.5 Peak Frequency and Peak Amplitude

Figure 11 shows the relationship between peak frequency and peak amplitude. In the case of aggregation test specimen, it is observed that the maximum peak amplitude of test specimens was more than 80 dB, implying a strong possibility that the location of aggregation regions under general traffic loads can be detected by measuring AE activities.

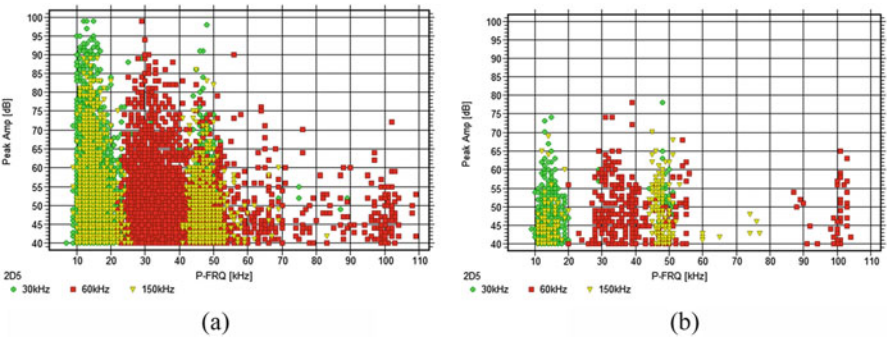

Fig. 11 Peak frequency vs. peak amplitude (**a**) The aggregation test specimen (**b**) The sound test specimen

4 Conclusions

The following conclusions can be derived from this experimental study.

1. The feasibility of applying AE methods to detecting aggregation regions under general traffic loads was verified, in observing that the peak amplitudes of AE waves were more than 80 dB at the aggregation region and were larger than those at the sound region.
2. It is considered that AE hits at the sound part were generated by consolidation of asphalt pavement and the number of AE hits decreased with cyclic loads growth due to Kaiser effect. On the other hand, at the aggregation part, the frictions of aggregates were detected by AE sensors with small asphalt consolidation.
3. AE sensors with resonance frequency less than 60 kHz would be suitable for detecting AE activities occurred in aggregation regions.

References

1. Transportation Research Board 2012 Executive committee of the National Academies, "Non-destructive Testing to Identify Concrete Bridge Deck Deterioration Strategic Highway Research Program 2, Renewal Research", Report S2-R06A-RR-1, 2013.
2. P.E. Mix, Ch. 2 Acoustic Emission, in *Introduction to Nondestructive Testing- A Training Guide*, 2nd edn. (Wiley, 2005)
3. J. Bohse, Acoustic Emission, in *Handbook of Technical Diagnostics*, ed. By H. Czichos (Springer-Verlag, 2013), pp. 137–160
4. G. S. Robinson, Method of Detecting the Formation and Propagation of Microcracks in Concrete, in *Proceeding of the International Conference on the Structure of Concrete*, London, 1965, pp. 131–145

Acoustic Emission Testing on Aluminum Alloy Pressure Vessels

Jun Jiang, Cheng Ye, Zhongzheng Zhang, and Yongliang Yu

Abstract To study the acoustic emission (AE) signal characteristics of aluminum alloy pressure vessels, a small aluminum pressure vessel containing a groove defect was tested using AE methods. The conventional parameter-based approach and signal-based analysis were combined to analyze recorded AE signals. The results show that AE signals induced by residual stress relief have lower amplitude and frequency, and joint cracks and expansion can produce a large number of high-energy and high-amplitude signals, with peak frequencies mainly in the range of 100–300 kHz. The quantity of location points is less, mainly caused by crack propagation, but accurate location can be determined. The research results have certain reference value for AE testing of aluminum alloy pressure vessels.

1 Introduction

Acoustic emission (AE) technology, an important nondestructive testing technique, has been successfully applied in the field of pressure vessel inspection. Current AE testing investigations are primarily aimed at carbon and low-alloy steel material [1–5], and applications for aluminum alloy are rare [6, 7]. Aluminum alloy pressure vessels often find important uses in some special conditions. To further expand AE techniques to the field of aluminum pressure vessel testing, it is very important to understand the AE characteristics of aluminum alloy pressure vessels.

In this chapter, a small aluminum pressure vessel containing a groove defect was tested by AE technology. The AE signals were recorded and analyzed during the loading process in order to obtain the AE signal characteristics of the aluminum pressure vessel.

J. Jiang • C. Ye • Z. Zhang (✉) • Y. Yu
Nanjing Boiler & Pressure Vessel Supervision and Inspection Institute, Nanjing 210019, China
e-mail: anyan2227@163.com

G. Shen et al. (eds.), *Advances in Acoustic Emission Technology*, Springer Proceedings in Physics 179, DOI 10.1007/978-3-319-29052-2_27

2 Test Procedure

Figure 1a shows the small aluminum alloy pressure vessel we tested. It was a new pressure vessel and built with aluminum alloy 5754. The vessel was 600 mm in diameter and 950 mm high, with wall thickness of 8 mm. The design pressure of the vessel was 0.85 MPa. Two nozzles, one in the middle of the vessel top head and one in the lower part of the cylinder, provided connection points for a hydraulic test machine and a pressure gauge. The vessel was supported by three legs evenly arranged along the cylinder. One groove was made with a grinding machine at the vessel vertical weld middle position with length of 50 mm, depth of 4 mm, and width of 7 mm.

The AE equipment was an AMSY-5 model of German company Vallen Systeme. This system consists of 50 separate monitoring channels for gathering AE information. There are three kinds of AE sensors used. The first sensor was an SR150 resonant sensor of resonant frequency 150 KHz with bandwidth of 100–850 KHz for S1, S2, S3, S4; the others were bandwidth sensors with bandwidths of 100–850 KHz for S5 and with bandwidth of 40–450 KHz for S6.

The sensors were arranged as follows: S1 and S2 were symmetrically mounted circumferentially on two sides of the groove. With the groove centered, the distance of two sensors was one third of the cylinder circumferential length on each side of the groove. S3 and S4 were arranged in the center of the vessel head, one up and one down, and the distance from the center of the groove was about 70 cm. S5 and S6 were asymmetrically mounted axially on two sides of the groove. The exact axial distance from S5 and S6 to the groove center was designated as x cm; the exact value was not important as the S5 and S6 broadband sensors were used only for signal frequency analysis and comparison, and were not involved in the detection of AE characteristics parameter analysis or location calculations. Figure 1b shows a schematic of the arrangement of sensors on the pressure vessel.

The channel group corresponding to the S1, S2, S4, and S5 sensors was used in the test for detection and location. Location was determined by time difference, and the detection threshold was set to 40 dB. During the pressure cycle, the loading process followed a ladder pattern, as listed in Table 1. When the load value was

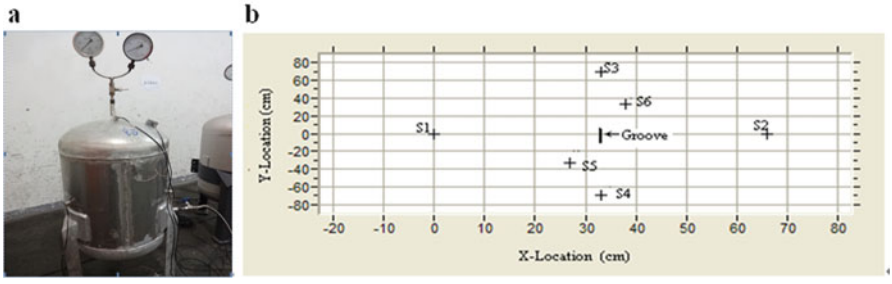

Fig. 1 The tested aluminum alloy pressure vessel and sensor arrangement diagram: (**a**) the test vessel; (**b**) AE sensor arrangement

Table 1 Load versus time in test

Pressure (MPa)	Time (s)	Load state	Pressure (MPa)	Time (s)	Load state
0	0–412	Hold pressure	3.3	2437–2807	Hold pressure
0–0.8	412–474	Rising pressure	3.3–3.8	2807–2832	Rising pressure
0.8	474–775	Hold pressure	3.8	2832–3167	Hold pressure
0.8–1.6	775–857	Rising pressure	3.8–4.2	3167–3168	Rising pressure
1.6	857–1147	Hold pressure	4.2	3168–3881	Hold pressure
1.6–2.0	1147–1177	Rising pressure	4.2–4.7	3881–3953	Rising pressure
2.0	1177–1493	Hold pressure	4.7	3953–4556	Hold pressure
2.0–2.4	1493–1532	Rising pressure	4.7–4.9	4556–4625	Rising pressure
2.4	1532–1892	Hold pressure	4.9	4625–5159	Hold pressure
2.4–2.8	1892–1923	Rising pressure	4.9–5.4	5159–521	Rising pressure
2.8	1923–2405	Hold pressure	5.4	5210–5873	Hold pressure
2.8–3.3	2405–2437	Rising pressure			

0 Map, it means that the vessel was filled with water but the pressure gauge read zero. The whole test procedure referenced GB/T 18182-2012 [8]. The detected AE signals were observed during the test, and penetration methods were used to confirm crack initiation and propagation in the groove.

3 Results and Discussion

3.1 Characteristic Parameters Distribution and Analysis

The main method currently used to characterize and evaluate AE testing of pressure vessels uses AE characteristic parameters. The conventional characteristic parameters include amplitude, rise time, duration, energy, and counting. Figure 2 shows the test results of characteristic parameters including amplitude, rise time, energy, and counting versus load history schematic for the four channels corresponding to the S1, S2, S3, and S4 sensors. Figure 3 illustrates the history of AE hits versus load. Figure 4 shows the appearance of cracks within the groove during different load stages using a penetration test.

Amplitude is a very important characteristic in AE testing, and it can be directly associated with AE source mechanisms, and is often used to identify and determine the type of AE sources and to evaluate test results. As shown Fig. 2a, when the load is 0 MPa, an aluminum alloy pressure vessel containing grooves can produce a greater number of AE signals, but the amplitude is low. With the load increasing, the AE hit signals are significantly reduced, but at a higher amplitude with rising pressure. When the pressure reached 2.4 MPa, there was a sharp increase in the number of AE signals, especially high-amplitude (>55 dB) signals in larger quantities, and we saw high-amplitude signals even up to 100 dB. After the pressure

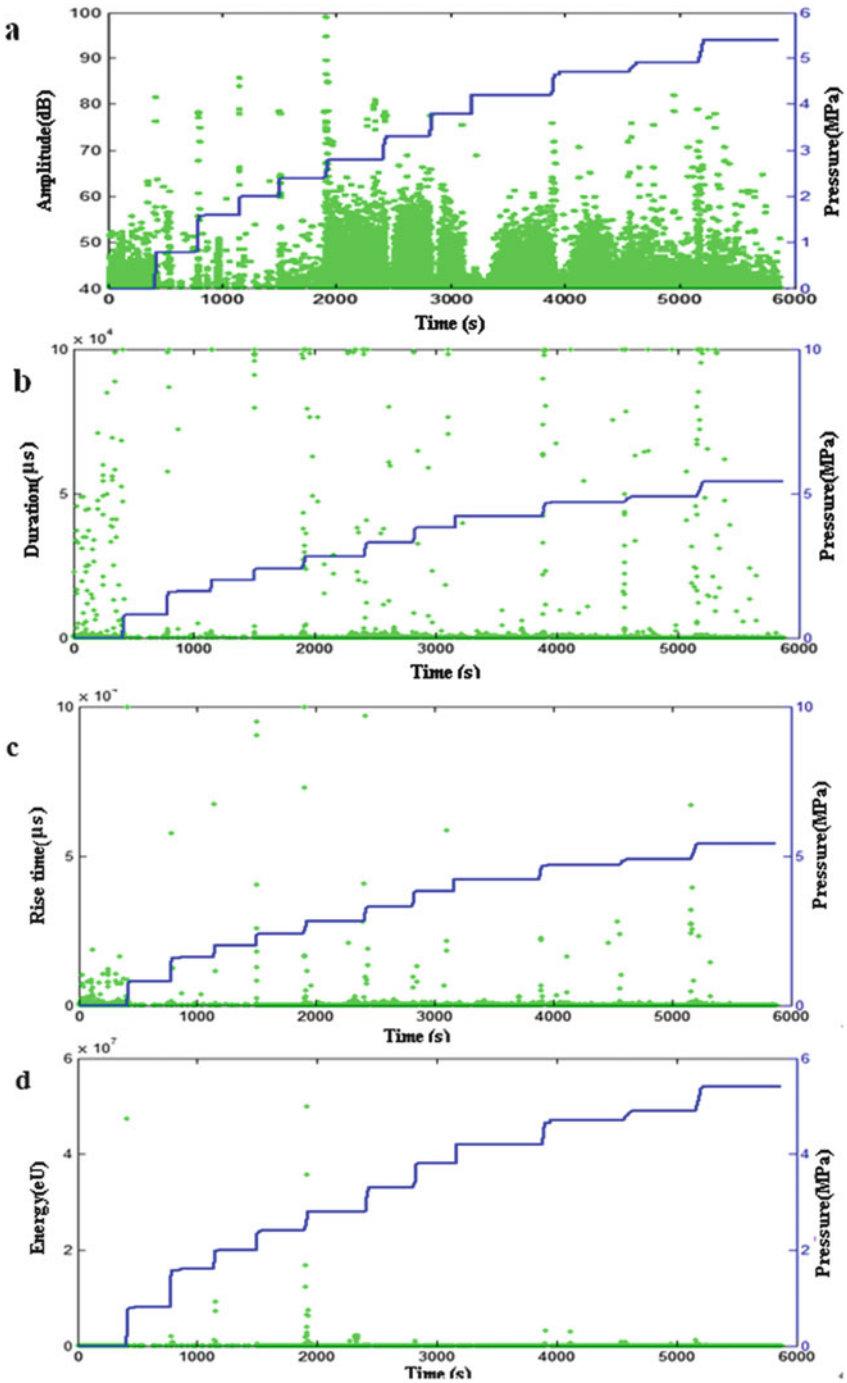

Fig. 2 Diagram of conventional AE characteristic parameters versus load history: (**a**) amplitude and load history; (**b**) duration and load history; (**c**) rising time and load history; (**d**) energy and load history

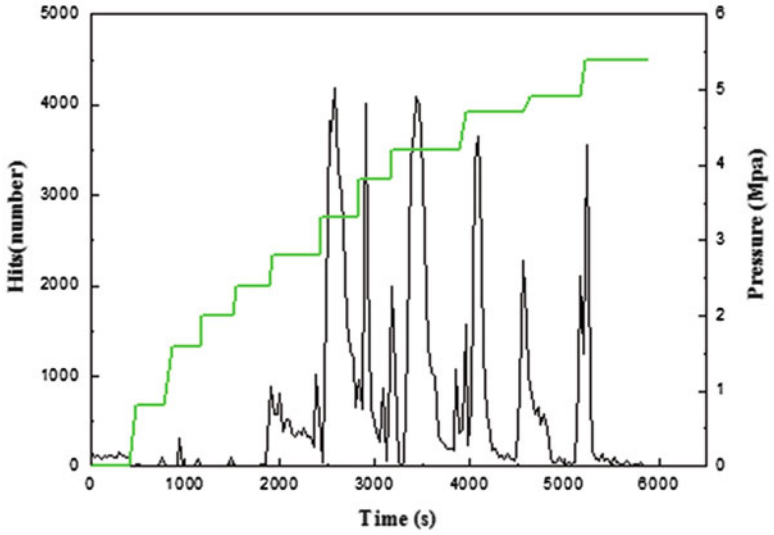

Fig. 3 Diagram of acoustic emission hits versus load history

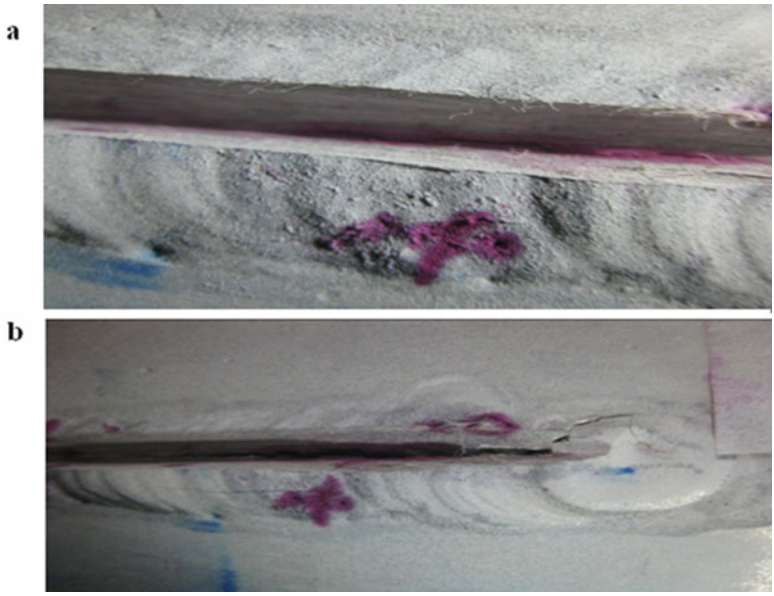

Fig. 4 Appearance of cracks within the groove by penetration test. (**a**) Holding pressure stage for 2.8 MPa. (**b**) Holding pressure stage for 5.4 MPa

exceeded 2.8 MPa, the number of AE signals maintained a high level as the pressure rose, but showed a slow decreasing tendency, though the number of high-amplitude (>55 dB) signals still maintained their higher level. The amplitude value of AE

signals was significantly higher in the rising pressure phase than in the sustained phase. The results are shown in Fig. 3, which displays the AE hits quantity distribution with time and load.

The AE testing procedure can be roughly divided into three phases according to the quantities, amplitudes, and magnitudes of the AE signals with load and time: 0 MPa, 0–2.4 MPa, and 2.4–5.2 MPa. The tendency of the amplitude with regard to magnitudes of load and time reflect the evolving deterioration of the aluminum alloy pressure vessel containing a groove defect. When the gauge read 0 MPa, the device was in fact bearing a load caused by the weight of the water. Rolling and welding of the pressure vessel fabrication process unavoidably produces residual deformation and stress. When the vessel is filled with water, the residual stress is released and results in many AE signals with lower amplitude. In the second stage, the pressure vessel undergoes elastic deformation with increasing loading, relieving residual deformation and residual stress, but due to stress concentration the groove portion, which produces only a small part of the plastic deformation, shows the initiation of a small amount of micro-cracks, forming lower-amplitude signals. In the rising pressure stage, the amplitude value increases sharply and shows significant linear segment shape. These signals maybe induced by crack initiation and propagation in the groove and a current rush caused by the wall when the pressure is rising. These kind of noise signals induced by current rush in the low pressure stage obviously, with the pressure increases, gradually weakened. How to exclude the interference noises during rising pressure requires further research. Application of location functions of acoustic the emission testing system and pattern recognition technology may be effective methods for distinguishing between crack growth signals and noise signals induced by current rush. In addition, in the holding pressure stage, current rush did not exist, and more signals originated from material damage and defect extension. Extracting such signals to analyze is more representative, and is an important method to exclude the disturbance of current rush noise signals.

The third stage, with the pressure increasing, the groove site materials occurred on a larger plastic deformation, micro-cracks jointly formed a large crack and continued to expand, resulting in a large number of high-amplitude AE signals. Figure 4a shows a visible crack revealed by penetration testing at the holding pressure phase of 2.4–2.8 MPa. The crack clearly consists of small cracks from the joint, corresponding to relatively high-amplitude AE signals. Figure 4b illustrates crack morphology in the groove at a holding pressure stage within 5.4 MPa. Compared to Fig. 4a, the crack length and width of the opening become larger, indicating a significant expansion of the crack.

Figure 2b–d shows a diagram of the AE signal duration, rise time, and energy characteristic parameters versus load time history. Combining the above-mentioned three stages, divided by amplitude in Fig. 2a, we can summarize parameter characteristics as follows: In the first phase, the AE signals induced by residual stress and strain relief have longer duration and rise time, with lower energy and amplitude. In the second stage, AE signals are mainly caused by micro-crack formation, and most of the signals have short duration, short rise time, and low-energy and

low-amplitude characteristics. The third phase is the crack growth stage, where most signals shows short rise time, long duration, and high-energy and high-amplitude characteristics. During the loading process, especially the rising pressure phase, there are always some signals with long duration, long rise time, high energy, and high amplitude; these signals are likely to be caused by the current rush to the wall.

3.2 Location Analysis

One of the important functions of AE testing system is source location. The current common location method is the plane time difference location method. The source positions are obtained by calculating the differences in the times at which different sensors receive a given signal. In the AE test, when at least three sensors receive AE signals from a single source simultaneously, the AE test system can find the source's position.

When acoustic emission signals produced by one AE source are received by four sensors of a channel group, the source position can be determined by multiple regression algorithms. The AE signals generated by current rush can be distinguished from those generated by actual crack growth by applying location functions. Sources of current rush can be located, but the positioning results are not necessarily located in the actual groove defect, while AE events generated by crack growth will be located at the groove's position.

The AE testing location results are shown in Fig. 5. Most of the AE location points are in the middle of the diamond composed by the S1, S2, S3, and S4 sensors,

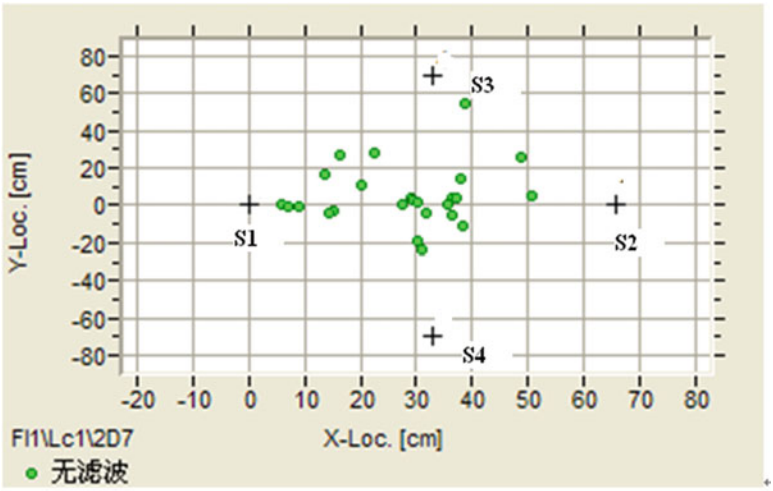

Fig. 5 Acoustic emission source location detection experiment results picture

which is the actual region of the crack in the groove. There are also location points deviating from the groove position. These location points, distributed in the vicinity of the sensor S1, located near the container legs and on the opposite side of the outlet pipe, may be inconsistencies of deformation for the container body and leg pad or may be current rush with the wall by inlet flow. The probability exists that the localization algorithm result contains some uncertainty in the deviation when the crack signals are simultaneously received by four sensors.

Compared with the number of channel groups that received AE events, the AE location points are fewer in quantity and composed of higher-amplitude signals. By the positioning principle known when the AE signal is not simultaneously received, three or more sensors are unable form the source location. The main reason for this situation is that aluminum alloy has good plasticity and toughness compared to high-strength steel and is not easy to crack, which results in AE signals with lower amplitude and energy induced by the initiation and propagation of cracks. In addition, the signal attenuation in the material is large. As shown in Fig. 6, the maximum attenuation can reach 37 dB for 600 mm, which means that if the crack AE signal amplitude is below 77 dB, it cannot be received by S3 and S4, and therefore cannot be located. All of these factors lead to many signal being unable to cross amplitude thresholds and be received by at least three sensors simultaneously to form a location point.

During the experiment, each stage yields some location points, but most occur in the visible crack joint positioning and expansion stage. These signal characteristic parameters were extracted and constitute the location points listed in Table 2. Most signals have high amplitude (above 60 dB), short rise time, longer duration, and high-energy characteristics. These features are very important in AE test results analysis, especially for defect identification and evaluation.

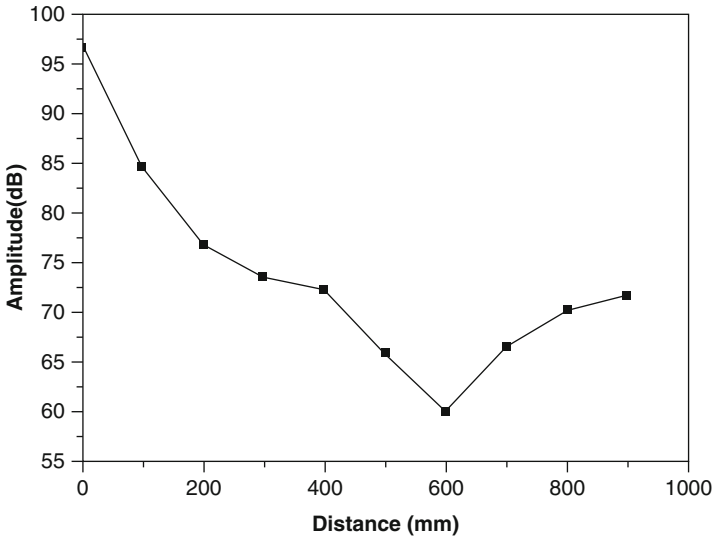

Fig. 6 Acoustic emission signal attenuation cure for aluminum alloys material

Table 2 Load versus time in test

First hit channel	Amplitude (dB)	Rising time (μs)	Energy (eU)	Duration (μs)	Pressure (MPa)	Time (s)
1	63.3	14.2	1.27E + 05	98995.2	0	343.049242
1	45.6	375.8	9.40E + 01	403.8	0	373.746913
1	78.4	1380	4.74E + 04	1874.4	1.3623762	779.276211
1	75	733	8.06E + 05	99,999	1.5207921	788.413637
2	84	18.8	7.33E + 06	99,999	1.9325301	1147.07275
1	89.7	1078	1.68E + 07	99,999	2.5139108	1906.75982
2	94.9	1086.4	3.57E + 07	99,999	2.5417323	1907.87139
2	84.8	727.6	6.41E + 06	99,999	2.6703412	1917.95982
1	69.3	739.8	1.68E + 05	99,999	2.6929134	1918.42814
2	71.2	723.2	3.73E + 05	99,999	2.8	1953.87581
1	54.7	11.6	3.77E + 02	419.2	2.8	2185.27166
1	76.9	734.8	9.81E + 05	99174.4	2.8	2265.88829
1	79.1	20.6	2.30E + 06	98995.2	2.8	2316.03555
2	74.6	1080	9.78E + 05	99,999	2.8	2329.89637
2	76.5	1090.4	1.65E + 06	99,999	2.8	2337.35513
1	77.2	329.8	2.57E + 04	1630.8	2.8441928	2408.299
4	69	9.2	1.30E + 04	12883.2	3.3	2604.18761
1	77.6	321.8	2.21E + 04	1992	3.3780886	2809.5878
2	52	28.4	1.37E + 02	40	4.7	4217.51452
2	73.1	1077.6	6.19E + 05	99,999	4.7537705	4569.24508
1	62.6	214.2	1.91E + 04	63052.8	4.9	4642.00745
1	78.7	226.6	5.04E + 05	99,999	4.9	4966.38797
1	79.1	83.8	1.34E + 04	1293.2	4.9	5151.57865
1	75	227	1.69E + 05	99,999	5.4	5307.42742
1	67.8	218.2	2.84E + 04	61772.8	5.4	5399.48755
1	58	10.6	1.53E + 03	5724.8	5.4	5543.01396
1	61.4	47.6	5.68E + 03	24121.6	5.4	5618.37626

3.3 Signal Waveform Analysis

Three types of sensors are used to analyze signal waveforms in the test process. It was found that continuous and burst-type signals both exist in the test, but the burst-type signals are dominant. The frequency band of such signals is rich and distributed within the 20–1200 KHz range.

During different load stages, there are some differences in frequency distributions for AE signals. In the first stage, namely at 0 MPa, most signals have a peak frequency of less than 100 KHz, which indicates that the signals generated by residual stress release have lower frequency. In the second stage, i.e. in the 0–2.4 MPa loading range, the peak frequency of most signals is also less than 100 KHz, which shows that the frequency of signals caused by plastic deformation are lower. In the third stage, while pressure rises from 2.4 MPa to 5.4 MPa, the

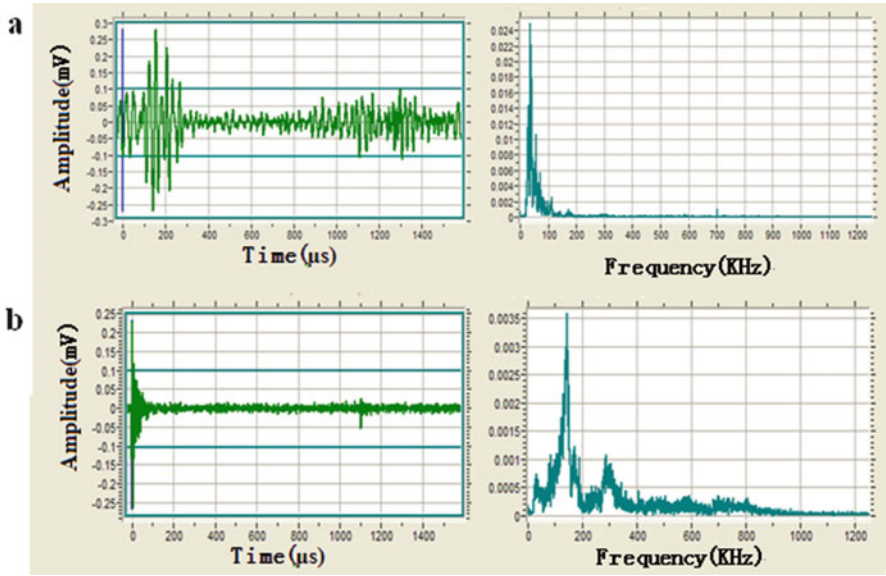

Fig. 7 Typical acoustic emission signals and spectrum

corresponding peak frequency of signals is widely distributed, although most are in a range of 100–200 KHz. There is a big crack joint and expansion in this stage, which shows the frequency features of crack joint and propagation. In addition, the high-amplitude AE signals caused by current rush have a lower peak frequency, and the peak frequency of those high-amplitude signals consisting of location points are mainly in the ranged of 100–200 KHz.

Modal AE theory holds that when the power source is perpendicular to the board, it mainly produces bending waves in a lower-frequency range, and when the power source is parallel to the plate it will produce higher-frequency expansion waves in the plate [9]. The signals caused by plastic deformation and micro-cracks that form in the second stage have lower frequency and should belong to bending waves, while the signals produced by crack joint and expansion in the third stage consist of expansion waves. Typical low-frequency and high-frequency AE signals and spectrum are shown in Fig. 7.

4 Conclusions

1. When an aluminum alloy pressure vessel containing a groove defect is loaded, residual stress release produces low-amplitude signals A small amount of plastic deformation and initiation of micro-cracks produce fewer signals with lower amplitude. Joint cracks and expansion generates a large number of high-amplitude signals.

2. Applying time difference location methods, only a few high-amplitude signals can be located.
3. The peak frequencies of signals generated by residual stress release and plastic deformation and micro-crack initiation are mainly distributed in a range less than 100 KHz. Signal frequencies caused by joint cracks and expansion are rich, with peak frequencies mainly distributed in the range of 100–300 kHz.

Acknowledgment The present study was partly performed with the help of Professor Shen Gongtian and Miss Zhang Chunjiao of China Special Equipment Inspection and Research Institute. The authors thank them for their guidance and suggestions for the research work.

References

1. Z. Zhong-zheng, G. Jian-Ming, L. Hua, The application of acoustic emission technology on coke tower inspection. Nondestruct. Test. **32**(2), 143–148 (2010)
2. K. Jeong-Rock, L. Geun-Jun, L. Tae-Hee, K. Jee-Yoon, Acoustic emission testing of repaired storage tank. Int. J. Press. Vessel. Pip. **78**, 373–378 (2001)
3. F. Hong-wei, Y. Ya-lin, L. Sheng-hua, Acoustic emission testing on 1000 m^3 LPG pressure vessel. Press. Vessel Technol. **22**(5), 56–58 (2005)
4. S. Gong-tian, Z. Yu-feng, D. Qing, Acoustic emission sources from field test of pressure vessels. Nondestruct. Test. **21**(7), 321–325 (1999)
5. L. Li-fei, S. Gong-tian, Z. Wan-ling, Acoustic emission analysis and pattern recognition on hydrogen induced cracking of mild steel. Nondestruct. Test. **31**(10), 773–776 (2009)
6. G. Rongsheng, F. Gangqiang, Evaluation of corrosion damage using acoustic emission testing. Acta Acustica **29**(1), 6–11 (2004)
7. L.M. Spasova, M.I. Ojovan, Characterisation of AL corrosion and its impact on the mechanical performance of composites cement wasteforms by the acoustic emission technique. J. Nucl. Mater. **375**, 347–358 (2008)
8. GB/T 18182—2012, Acoustic Emission Examination and Evaluation of Metallic Pressure Vessels
9. G. Rongsheng, G. Shen, L. Shifeng, Acoustic emission signal processing. Nondestruct. Test. **24**(8), 341–345 (2002)

Development of Damage Evaluation Method for Concrete in Steel Plate-Bonded RC Slabs

N. Ogura, H. Yatsumoto, K.C. Chang, and T. Shiotani

Abstract The steel plate bonding method has been conventionally used on reinforced concrete (RC) slabs of road bridges in Japan as a protection from fatigue damage. As more than 30 years have passed since the first application of this method, some of the RC slabs previously repaired by steel plate bonding started to show debonding of the steel plates (detected by dully sounds) or internal damage of concrete of the slabs. A steel plate-bonded RC slab forms a composite structure of steel and concrete. Its flexural rigidity and other capacities will decrease if the adhesive agent or other material combining the steel and concrete is deteriorated. If the concrete slab itself is damaged significantly, the resistance performance of the composite structure will be affected, irrespective of the bonding condition. However, although the presence or extent of debonding of adhesive agent can be roughly estimated from the change in sound observed during inspection by the hammer impact test, there are no decisive methods for detecting or evaluating the internal damage of the concrete. This study proposes a method for evaluating damage in concrete of RC slabs bonded with steel plates on road bridges in service, using the anchor bolts, which had been installed for holding the steel plates temporarily until complete setting of adhesive agent, as ultrasonic probes.

N. Ogura (✉)
Engineering Department, CORE Institute of Technology Corporation, Tokyo 111-0053, Japan
e-mail: ogura.nori@coreit.co.jp

H. Yatsumoto
Engineering Department, Hanshin Expressway Company Limited, Osaka 541-0056, Japan
e-mail: hitoshi-yatsumoto@hanshin-exp.co.jp

K.C. Chang • T. Shiotani
Laboratory on Innovative Techniques for Infrastructures, Department of Civil and Resources Engineering, Kyoto University, Kyoto 615-8540, Japan
e-mail: chang.kaichun.4z@kyoto-u.ac.jp; shiotani.tomoki.2v@kyoto-u.ac.jp

G. Shen et al. (eds.), *Advances in Acoustic Emission Technology*, Springer Proceedings in Physics 179, DOI 10.1007/978-3-319-29052-2_28

1 Introduction

Fatigue damage to reinforced concrete (RC) slabs under cyclic loading from vehicle traffic has been a problem to road bridges which are mostly made of concrete. Many of the existing bridges in Japan were built during the rapid growth period after the WWII, and the fatigue problem is frequently found in their slabs, especially those built before 1970. Many field surveys and researches have been made, and various strengthening measures have been developed using the results. One of such results is the steel plate bonding method. Steel plates are bonded to the slab bottom surfaces by using anchor bolts, resin, or other means to improve load carrying performance of the structure. This technique has become popular and has been used on many bridges including those of the Hanshin Expressway, an important urban expressway network in the Kyoto-Osaka-Kobe area. The RC slabs of the Hanshin Expressway built to the old design standards are thinner than those of today, having a lower load carrying capacity or durability. About a half of them, or about 70,000 panels (about 2–3 m on each side per panel) in total, have been repaired by this technique. However, over 30 years have passed since its first practical application, with unexpected increases in traffic volume and vehicle load beyond the initially estimated design levels. The previously repaired slabs are often found to have debonding of the steel plates which is evaluated by dully sounds during hammer impact tests.

The relative authorities of the Hanshin Expressway and other urban expressway networks have started to strengthen inspections; however, internal damage of concrete of slabs bonded with steel plates cannot be observed by the visual inspection because of the steel plates covering the bottom concrete surfaces. Although the presence and extent of debonding can be roughly estimated from the change in sound observed during inspection by the hammer impact test, there are no decisive methods for detecting or evaluating the internal damage of concrete [1, 2].

This study attempts to establish a method for evaluating damage in concrete of RC slabs bonded with steel plates on road bridges in service. Focus was put on the anchor bolts which had been installed for holding the steel plates temporarily until complete setting of adhesive agent. Those temporarily set anchors were utilized as ultrasonic probes. Figure 1 shows a picture and a schematic view of an RC slab bonded with steel plates.

2 Sensing Technique Using the Temporary Set Anchors

2.1 Background of the Anchor Bolt Sensing Technique

To evaluate the soundness of the steel plate-bonded RC slabs, some techniques need to be developed for evaluating the soundness of the concrete slabs themselves

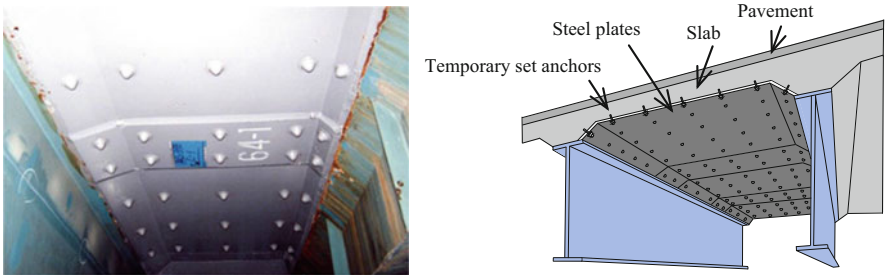

Fig. 1 A picture and a schematic view of RC slab bonded with steel plates

as described in the previous section. Since the evaluation is to be made on bridges in service, it is desirable from the viewpoint of public impact to avoid coring, chipping, or other destructive techniques which inevitably require traffic restrictions. The authors investigated the applicability of existing nondestructive testing techniques as well as means of access from the bottom surface of the slab to eliminate impact on traffic on the roads.

The steel plate bonding method uses adhesive agent (epoxy resin) to combine the RC slabs and the steel plates. The steel plates need to be held in place temporarily until adequate adhesion develops during construction. The anchor bolts are the temporary retainers installed for the steel plates and usually driven to a depth of about 50–60 mm in cover concrete of the slabs to securely hold the steel plates, making a full contact with the inside of the concrete slabs.

This study focused on the anchor bolts installed in all steel plate-bonded RC slabs and developed a sensing technique utilizing them as ultrasonic probes.

2.2 *Outline of the Internal Damage Detection System*

Figure 2 shows a schematic of the proposed internal damage detection system which utilizes the anchor bolts as sending probes. An impact elastic wave is generated by hitting an anchor bolt at the head which is protruding about 20 mm from the surface of the steel plate with a hammer or similar tool. Propagation of the

Fig. 2 Schematic diagram of measurement

generated wave is analyzed to determine internal damage of concrete present in the propagation path inside the RC slab. The propagated wave is received by a sensor installed on the head of the other anchor bolt. Since the anchor bolt on the impact side is hit at the head, it is impossible to mount a sensor like the one on the receiving side. Instead, the sensor is installed on the surface of the steel plate in the vicinity of the impact-side anchor bolt in the proposed system. The authors carried out demonstration experiments using artificial specimens as well as a sample taken out of a slab of an existing bridge to investigate applicability of the proposed damage detection system to existing structures. The results are reported in the following sections.

3 Preliminary Experiment Using Artificial Specimens

3.1 Outline of the Experiment

In order to examine various factors in using the anchor bolts as sensing probes, the authors prepared control specimens having a design strength of 24 N/mm^2 and defect specimens having a simulated defective part in the surface area. They had a rectangular shape of 300 mm × 300 mm × 2200 mm as shown in the schematic diagrams of Fig. 3. The defective part in the defect specimens was created by placing poorly proportioned concrete to a depth of 20 mm from the surface. Other materials used in the specimens include SS400 steel plates with a thickness of 4.5 mm which are commonly used for steel plate bonding in the field, M12 concrete anchors for the temporary set anchors, and epoxy resin for steel plate bonding. Steel plate debonding was reproduced by dividing each specimen into two parts at the center and leaving the gap between the steel plate and concrete surface of the right half ungrouted to create a poor bond zone. The gap in the left half was grouted fully with epoxy resin to make a full bond zone. Table 1 shows measured compressive strength and static modulus of elasticity of the concrete used. Holes were drilled to a depth of 60 mm as specified, and the anchor bolts were spaced at 400 mm as commonly practiced in the field.

3.2 Measurement Method

An elastic wave was generated by hitting an anchor bolt and received by an acoustic emission (AE) sensor (resonant frequency of 150 kHz), which was installed on the head of the other anchor bolt to obtain the waveform data as shown in Fig. 2. The other AE sensor was installed on the surface of the steel plate at a distance of 30 mm from the anchor bolt on the impact side to obtain the input waveform data. The former was referred to as the receiving sensor, and the latter was the impact-side

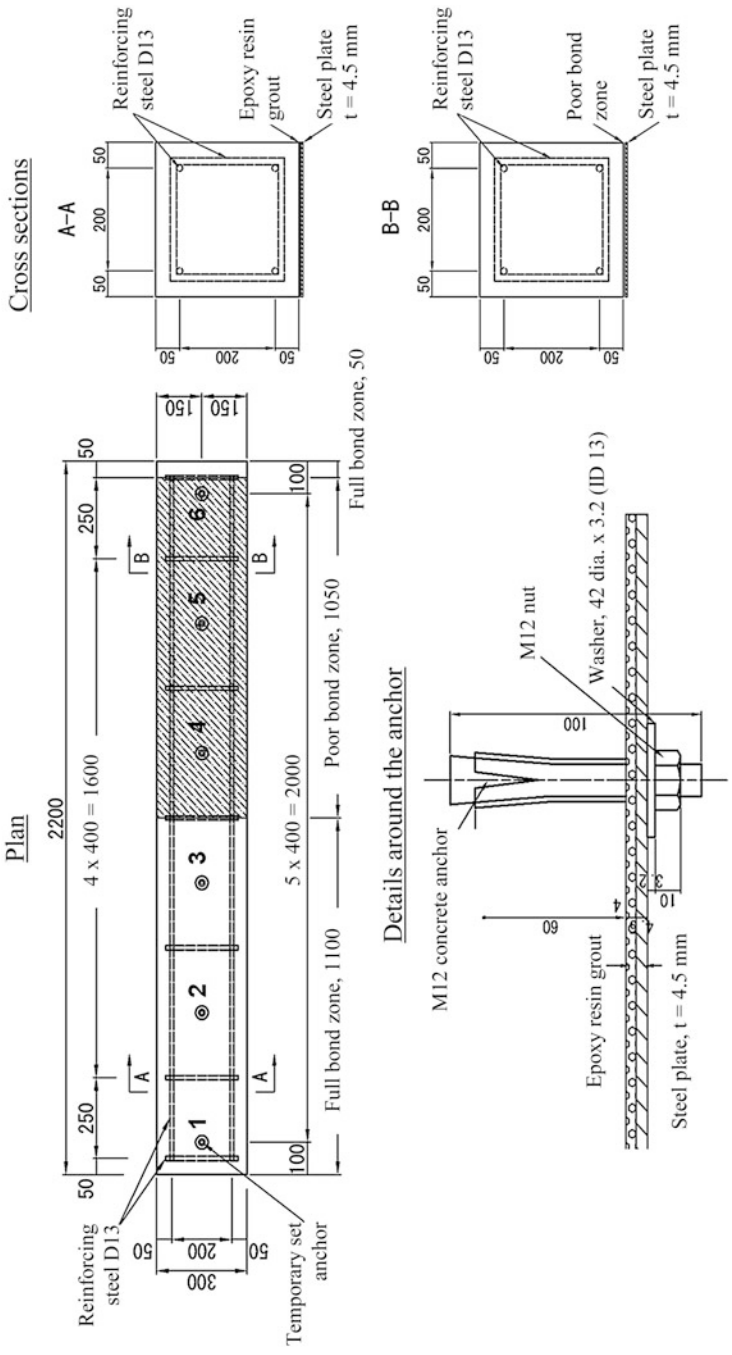

Fig. 3 Schematic diagrams of the specimens

Table 1 Physical property test results of the specimens

	Compressive strength (N/mm^2)		Static elastic modulus (kN/mm^2)	
	Measured value	Average	Measured value	Average
Control specimens	33.9	33.7	28.7	28.6
	33.4		28.3	
	33.9		28.9	
Defect specimens	22.3	23.3	25.4	25.2
	23.9		25.0	
	23.8		25.1	

sensor afterwards. The waveform recorder recorded the input waveforms generated by the impact as well as the output waveforms after propagation through the steel plates and concrete. Sampling period was 0.2 μs, and the number of samplings was 25,000. A steel ball with a diameter of 15 mm was used to apply the impact to the head of the anchor bolt and generate the elastic wave. The diameter of 15 mm was selected through a preliminary test which revealed that the receiving sensor could not detect time history response waveforms at a distance of 2 m or longer between the sensors when steel balls smaller than 15 mm were used.

3.3 Propagation Velocity Before and After Steel Plate Bonding

It is well known that propagation velocity of an elastic wave decreases when the concrete has a decrease in compressive strength or rigidity, cracks or other damage by deterioration. The authors measured propagation velocity in this study, expecting that there should be significant change in propagation velocity of the elastic wave traveling through the concrete. Figure 4 shows the measured propagation velocities with respect to measurement pair. The solid dots in the diagram represent the velocity before steel plate bonding, and the hollow dots represent the velocity after steel plate bonding. Theoretically, propagation time should be equal when the impact-side and receiving-side measurement points are interchangeable, like Measurement pairs 2–3 and 3–2. Therefore, in calculating propagation velocity by dividing measurement-pair distance with propagation time, the average of those pairs was taken as their representative; for example, the average of Measurement lines 2–3 and 3–2 for Measurement line 2–3. Propagation velocity in the absence of steel plates was found to be 4200–4300 m/s in all measurement lines in the control specimens. In contrast, that in the defect specimens was 4000–4100 m/s in all measurement lines, decreasing by about 5% from that in the control specimens. This proves that propagation velocity decreases in deteriorated concrete as described in previous studies. Propagation velocity in the presence of steel plates was about 5500 m/s in all measurement lines in the control and defect specimens. Steel plate bonding conditions were changed at the center of the specimens as

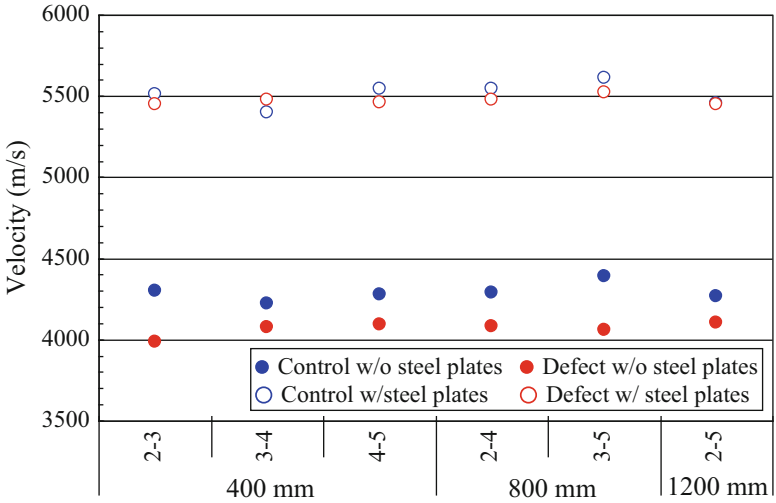

Fig. 4 Propagation velocity by measurement line

described in the previous section. For example, Measurement lines 2–3 and 3–4 are same in measurement distance, 400 mm, but different in the steel plate bonding conditions. The similarity in propagation velocity observed between the measurement lines with different structural conditions was likely attributable to the extremely fast propagation in the steel plates which could override the influence from the concrete or epoxy resin. It would be possible to evaluate damage in concrete from the difference in elastic wave propagation velocity measured by using the anchor bolts as sensing probes. However, it was found difficult to determine the velocity of an elastic wave propagated through concrete bonded with steel plates because of the extremely high velocity of propagation in steel plates.

3.4 Frequency Analysis Before and After Steel Plate Bonding

Figure 5 shows the frequency analysis results with respect to measurement pairs on the waveforms recorded at the impact-side and receiving sensors in the control and defect specimens before and after steel plate bonding.

Spectral centroid was used as an evaluation index in the frequency analysis. It is an analysis technique focused on elastic wave energy which can express attenuations in the elastic wave in low and high frequency components during propagation quantitatively. The spectral centroid used here is a weighted average of the frequency spectrum obtained by Fourier transform.

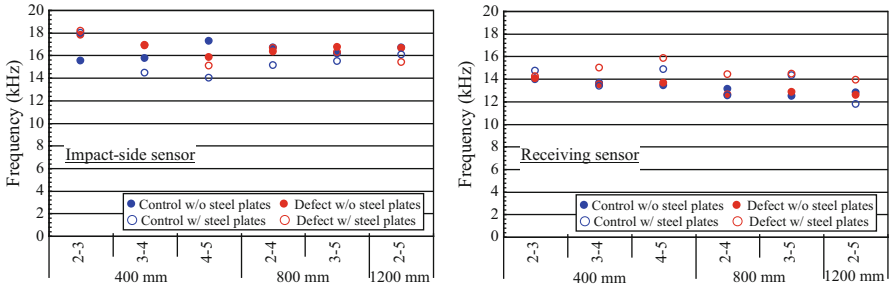

Fig. 5 Spectral centroid by measurement line

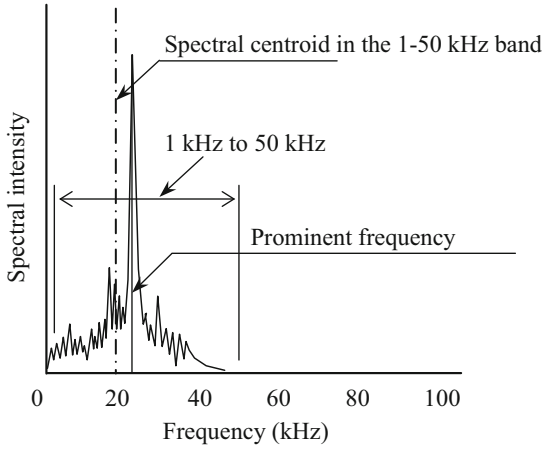

Fig. 6 Illustration of the spectral centroid

The spectral centroid was calculated with (1), by weighting the average with frequency components between 1 kHz and 50 kHz (0.15 kHz increment) so that influence of noise or minor vibration of the specimens would be reduced (Fig. 6).

$$\text{Spectral centroid (kHz)} = \frac{\sum Ei \cdot Fi}{\sum Ei} \tag{1}$$

where Fi: frequency of the i-th segment, Ei: magnitude corresponding to Fi.

As shown in Fig. 5, spectral centroid on the impact side showed no significant differences between the control and defect specimens in the absence of steel plates. However, comparison between the measurement lines within or crossing the boundary of the full and poor bond zones after steel plate bonding showed a decrease in spectral centroid, indicating the effect of bonding condition of the epoxy resin. Spectral centroid on the receiving side decreased with the increase of the sensor-to-sensor distance in the absence of steel plates. This was likely

because of the effect of distance attenuation. Propagation energy attenuation was more significant at longer distances because the impact was applied in the same direction as the anchor bolts and also because the signals were received through the medium of the anchors. These suggest that this method is applicable to a comparison at a same distance but not to a comparison at different distances. In contrast, this tendency did not appear after steel plate bonding, suggesting the strong influence of the presence of steel plates.

3.5 Wavelet Analysis After Steel Plate Bonding

The preliminary experiments above provided the following findings: (1) soundness/deterioration of concrete can be readily determined from propagation velocity when steel plates are absent; (2) when the temporarily set anchors are used for measurement, distance attenuation has a major influence in the frequency-based evaluations due to dispersion and reduction of input energy; and (3) although the influence of the presence of epoxy resin does not appear in the propagation velocity which is more influenced by elastic waves propagating through steel plates, frequency analysis on the elastic waves at the receiving sensor provides quantitative evaluation.

These findings suggested that time domain evaluation would provide more significant differences for evaluating internal damage of steel-bonded concrete. To eliminate the influence of the waves propagated through the steel plates, the wavelet analysis was performed to waveforms recorded at the receiving sensor.

Figure 7 shows the analysis results for Measurement pair 5–2 (sensor-to-sensor distance: 1200 mm) in the control and defect specimens after steel plate bonding. A peak appeared at around 12 kHz in the wavelet analysis results. The authors extracted change in the time-history spectrum, focusing on the frequency of 12 kHz as the prominent frequency. A difference was found in time to reach the peak between the control and defect specimens. Based on the finding, another index was proposed in this study. A velocity index defined as dividing the measurement-pair distance (the distance wave propagation) with the time to the peak; such an index expresses the velocity at which the wave of the prominent frequency was transmitted (hereinafter referred to as the "prominent frequency transmission velocity"). Figure 8 shows the prominent frequency transmission velocity obtained for all measurement pairs. General decrease in velocity was observed in both of the control and defect specimens. Propagation velocity of an elastic wave is known to decrease when concrete is damaged and affected in rigidity. It would be possible to determine transmission of the waves in concrete to some extent by focusing on an appropriate frequency and determining transmission of the peak of the wave corresponding to the focused frequency.

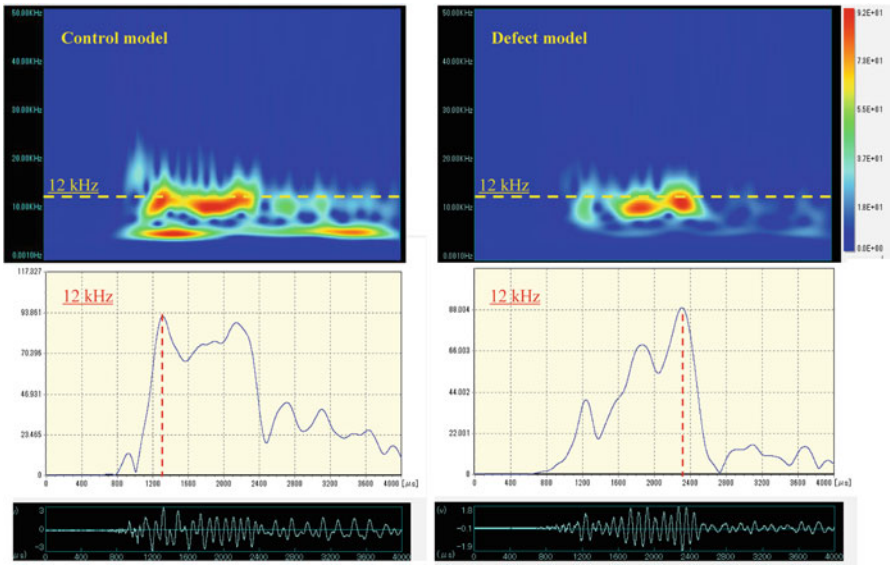

Fig. 7 Wavelet analysis results for the control and defect specimens after steel plate bonding

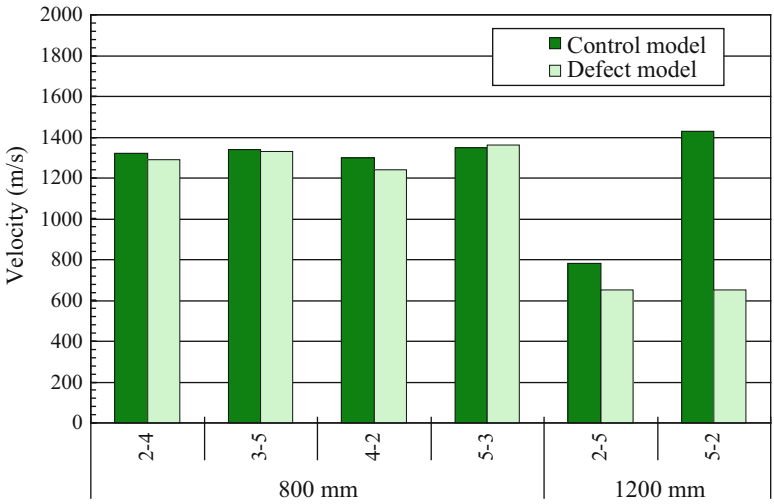

Fig. 8 Prominent frequency transmission velocity by the wavelet analysis

4 Verification Experiment Using a Slab Extracted from an Existing Bridge

4.1 Overview of the Verification Experiment

An experiment was carried out by using a sample of steel plate-bonded RC slab extracted from an existing bridge to verify the applicability of the proposed method to real structures. The target slab had been in service for about 50 years on the Hanshin Expressway. The sample slab was cut out for soundness evaluation and subjected to a moving-wheel loading test as shown in Fig. 9. Measurement using the anchor bolts as sensing probes was carried out two times at the same locations: one before the moving-wheel loading test and the other after 4000 cycles of moving-wheel loading.

Figure 10 shows the measurement locations on the steel plate-bonded RC slab sample. Using the 12 anchor bolts numbered in the diagram, 12 measurement pairs

Fig. 9 Cutting out a steel plate-bonded RC slab sample (*left*) and carrying out moving-wheel loading test (*right*)

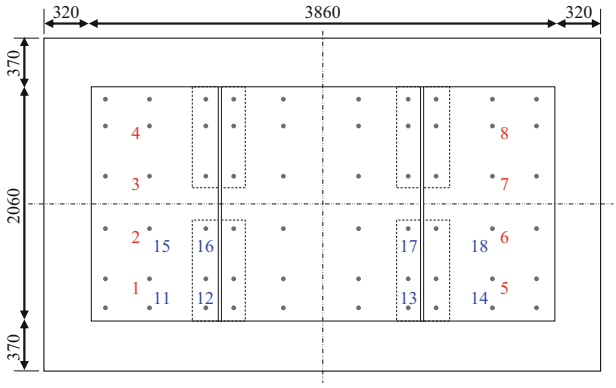

Measurement lines	Distance (mm)
1-2	456
2-3	433
3-4	473
5-6	382
6-7	498
7-8	473
11-12	434
12-13	1525
13-14	751
15-16	440
16-17	1525
17-18	742

Fig. 10 Measurement lines on the steel plate-bonded RC slab sample for the moving-wheel loading test

with different distances were set in longitudinal and transverse directions. For the purposes of safety, the steel plates were temporarily removed in the field during the cutting of the slab, with the anchor bolts left in position. They were reinstalled before starting the moving-wheel loading test. Poor bonding condition was reproduced by applying release agent to the interface between the steel plates and the concrete.

4.2 Verification Results

Figure 11 shows the changes in the two proposed indices after 4000 cycles of moving-wheel loading. The transmission velocity of the prominent frequency (12 kHz) in focus, which was the index specially defined for detecting internal concrete damage, showed a decrease in 10 of the 12 measurement pairs after the 4000 cycles of loading. Although the reason for the increase in 2 of 12 measurement pairs is still under investigation, the general tendency of decrease in most measurement pairs suggested the applicability of the proposed method to real steel plate-bonded RC slabs. The spectral centroid on the receiving side also showed a decrease in most measurement pairs after 4000 cycles of loading as compared to the initial values.

The simultaneous change in those two indices could be illustrated in a scatter plot, as shown in Fig. 12, where the solid triangles represent the status before loading, the hollow triangles represent the status after the 4000-cycle loading, and the solid and hollow circles are their means respectively. In the scatter plot, the points after 4000 cycles of loading are distributed in the bottom left, and those before loading are distributed mostly in the upper right. Suppose that internal damage had occurred in concrete during the moving-wheel loading test, cracks should have occurred inside the slab, causing a decrease in propagation velocity. Such cracks could have also led to damping of the high-frequency components of

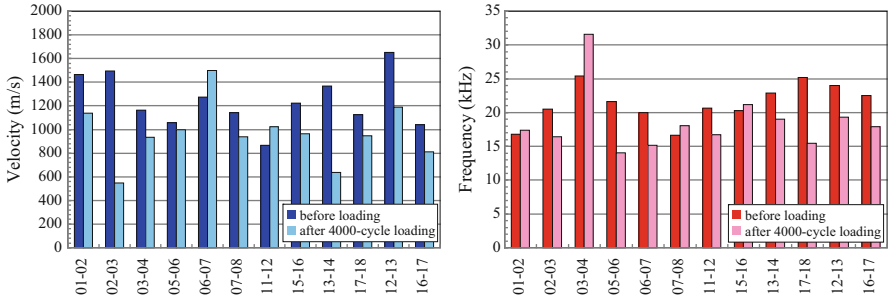

Fig. 11 Changes in prominent frequency transmission velocity and spectral centroid before and after the moving-wheel loading test

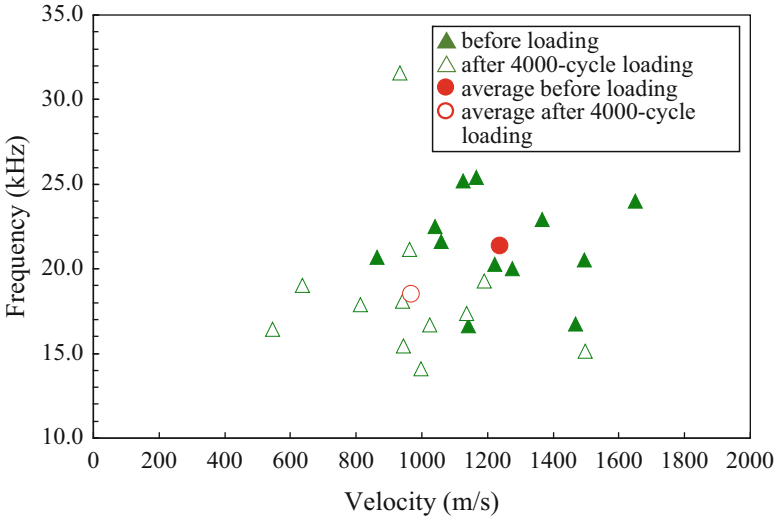

Fig. 12 Correlation diagram between the two proposed indices before and after the moving-wheel loading test

elastic waves. Consequently, scatter plots using the proposed two indices might be practical to evaluate internal damage of concrete of steel plate-bonded RC slabs and determine priorities for repair or strengthening.

5 Conclusions

In this study we proposed a method for evaluating damage in concrete of steel plate-bonded RC slabs on road bridges in service. The focus was placed on the anchor bolts penetrating the steel plates into the concrete which had been installed for temporary use in steel plate bonding. We developed a sensing technique and an internal damage detection system, utilizing the temporary set anchors as ultrasonic probes. Experiments were carried out using laboratory specimens as well as a sample extracted from an existing bridge slab. The results showed that internal soundness of concrete of steel plate-bonded RC slabs could be evaluated successfully by utilizing the temporarily set anchors as sensing probes, without removing the steel plates.

Acknowledgment This study was implemented in collaboration with the Laboratory of Innovative Techniques for Infrastructures, Kyoto University. Their great assistance and support to this research are gratefully acknowledged.

References

1. M. Sano, K. Yamashita, S. Matsui, T. Horikawa, Y. Hisari, T. Niina, Evaluation of fatigue resistance and re-injection of resin for uplifted reinforced concrete deck slabs reinforced by steel plates bonding. J. Jpn Soc. Civ. Eng. **67**(1), 27–38 (2011)
2. T. Maekawa, Y. Hisari, K. Sasaki, A. Higatani and Y. Aoki, in *Examination about the maintenance of the RC deck slab reinforced with steel plate bonding method, Proceeding of 7th Symposium on Decks of Highway Bridge, Japan Society of Civil Engineers*, pp. 13–18, June, 2012

Acoustic Emission Testing Research of Blowout Preventer

Junru Zhao and Wei Li

Abstract This chapter explores the application of acoustic emission (AE) testing technique in blowout preventor (BOP) shell. Two problems are presented in this dissertation. First, a tensile test is implemented, using a specimen made of BOP shell material ZG25GrNiMo, and the AE characteristics of the shell material during tensile process are obtained. Then, a pressure test of a BOP shell with crack performed with water and the AE characteristics of the BOP shell during pressure process are obtained. The research shows that the AE frequency spectrums characteristics of BOP shell material are different at different damage stages, and the AE technique can be used to test the damage of BOP shell.

1 Introduction

The BOP is an important well control equipment in oil drilling process, used to control the wellhead pressure and to ensure that oil drilling is safe and of high efficiency. In using this, cracks will occur mostly in the inner surface of the shell because of impact, corrosion, wellhead pressure, and repeated pressure experiment, and mostly the cracks and defects will be at the transition of the shape for the complex structure. Because the shell of the BOP is thick, magnetic particle testing and penetrate testing cannot detect internal defects of the shell. The testing of the BOP shell lacks effective method, and mostly relies on our senses and experience. If the internal cracks of the shell exist for a long time and develop gradually, then the BOP shell will leak or even fail, which will bring costly damage for drilling production, even personnel casualties.

The AE technique offers the unique opportunity to monitor components in real time and detect sudden changes in the integrity of the monitored element, which is a dynamic nondestructive testing method. The principle is that dynamic input sources cause a stress wave to form, travel through the body, and create a transient surface displacement that can be recorded by piezoelectric sensors located on the surface.

J. Zhao (✉) • W. Li
Northeast Petroleum University, Daqing 163318, China
e-mail: zhaojunru2007@126.com; 13845909333@163.com

G. Shen et al. (eds.), *Advances in Acoustic Emission Technology*, Springer Proceedings in Physics 179, DOI 10.1007/978-3-319-29052-2_29

The monitoring range of the sensor is only related with its receiving radius, material attenuation, and quantity of the sensor, which ideally can monitor any complex components without being affected by their shapes and sizes. In this research, we firstly carried out AE testing to BOP shell material ZG25CrNiMo during its tensile test to obtain the characteristics of the AE signals during its deformation, yield, and fracture process. Then, a BOP shell with a defect was tested by using AE technique when it was pressurized.

2 AE Tensile Testing of Small-Scale Specimens

2.1 Research Significance

In this experiment, AE technique was employed to study the failure process of small-scale specimens under axial tensile loading, and the AE characteristics of the process were analyzed. The specimens were made of BOP shell material ZG25CrNiMo. While performing the AE monitoring of the specimen during its tensile process, we can obtain the characteristics of the AE signals during its yield, plastic deformation, and fracture process, and the relation between AE signal parameters and mechanical behavior of the specimen, which can lay a foundation for the result evaluation of AE testing of BOP shell.

2.2 Experiment Specimens

For purpose of this research experiment, a total of ten specimens were tested to study the AE characteristics of the BOP shell material ZG25CrNiMo. The shape of the specimens is shown in Fig. 1, the ends of which are cylinders for being clamped by the fixture. The surface of the ends must be flat and smooth to paste the sensors.

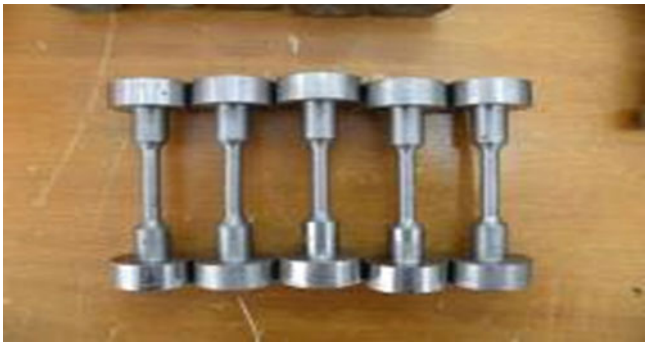

Fig. 1 Figure of the experiment specimens

Fig. 2 The experiment equipment and sensor arrangement

2.3 Experiment System

In this experiment, the major equipment was the SAMOS-II AE detection instrument, produced by Physical Acoustics Corporation (PAC) in the USA. Software controlling the monitoring process was AEWin, which enables filtering, storage, and graphical replay of all AE data. The tensile process was carried out in the SHT4605 computer-controlled electrohydraulic servo-type 10-ton universal tensile testing machine, and the moving speed of the load cell was 0.5 mm/min. The sensors were broadband sensors, and the preamplifier was set for 40 dB. Experiment equipment and sensor arrangement are shown in Fig. 2.

2.4 Data Analysis of the Experiment

2.4.1 The AE Characteristics of the Specimen During the Tensile Process

It can be seen from Fig. 3 that the material has typically four stages of mechanical properties: elastic stage, yield stage, plastic deformation stage, and the last fracture stage.

Figures 4 and 5 show the relation of amplitude and energy of acoustic emission signals against time, respectively.

As the tensile process advances, in the elastic deformation stage, AE activity events were frequent, but the damage energy and the amplitude were relatively low, mainly because of the influence of the noise signal produced by the friction between

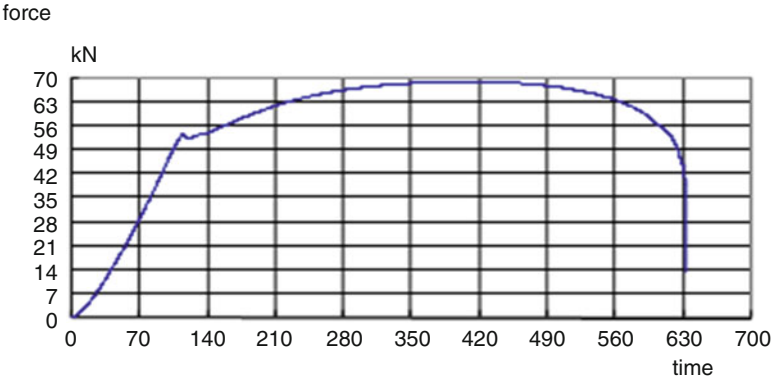

Fig. 3 Diagram of force according to time

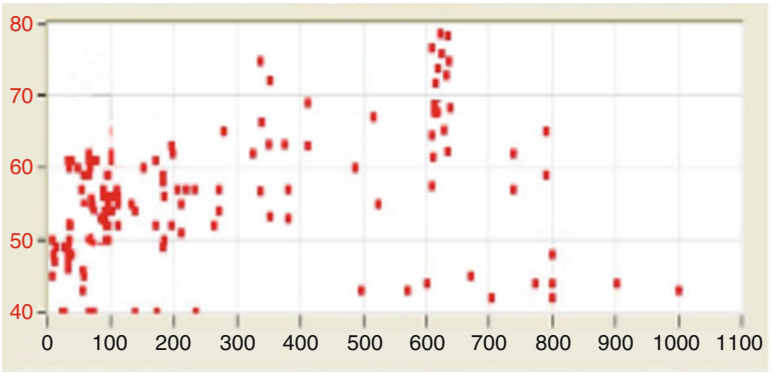

Fig. 4 Diagram of amplitude against time

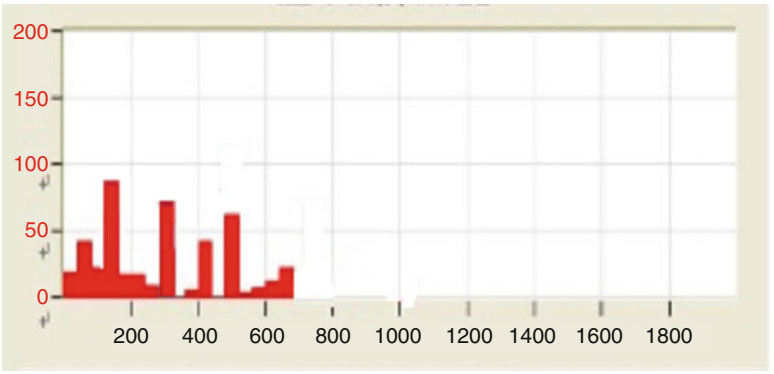

Fig. 5 Diagram of energy against time

the specimen and the fixture. At the ending of the elastic stage, the yield stage began, and an increase in AE activity was observed in all specimens. Elastic resistance to the stretch broke, the specimen released a great amount of elastic potential energy, and a peak of AE amplitude and energy appeared. In the plastic deformation stage, after the energy release of the yield stage, the material entered the work-hardening stage, no great amount of energy was released, but the energy accumulated again; therefore, the AE activity was weak until fracture, when large mount of lattice was damaged and then the AE amplitude and energy increased significantly.

Different types of acoustic emission sources will produce different characteristics of acoustic emission signals. In fact, the acoustic emission sources are very complicated during the specimen tensile process, and the acoustic emission source types of every stage are not unique, but superimposed by several sources. The above analysis only shows the most important type of acoustic emission source of every stage.

2.4.2 The Waveform and Spectrum Analysis

Wavelet de-noising to the collected signals reduced effectively the influence of the electrical noise and mechanical friction. The time-frequency analysis based on fast Fourier transform was carried out for the signals and the typical signal at each damage stage was investigated. Figure 6 shows the waveform and spectrum characteristics of every damage stage of the BOP shell material after wavelet de-noising.

As can be seen from Fig. 6, the signals generated during the tensile process are all burst acoustic emission signals, but the waveform and spectrum are different. Yield process produces signals with minimum amplitude and multiple frequency peaks; the amplitude of plastic stage increases, and the frequency is mainly in the vicinity of 90–150 kHz. Fracture stage produces the maximum signal amplitude and frequency, and the peak concentrates in the vicinity of 100–150 kHz. This shows that yield process produces broadband and minimum amplitude signals, and in the plastic deformation and fracture process, the signals have focused frequency, and fracture process produces maximum amplitude.

3 AE Crack Detection of BOP Shell

The experiment is carried out in a testing pressure room for well control workshop, using an annular BOP with a crack. Because the shell is too thick, corrosion cracking and leaking cannot occur, so we cut a crack of 100 mm length and 5 mm width, then welding on the surface and polishing are performed, as shown in Figs. 7 and 8. The BOP shell was pressured by the pneumatic pump and AE signals from the defects were collected at different pressure holding steps.

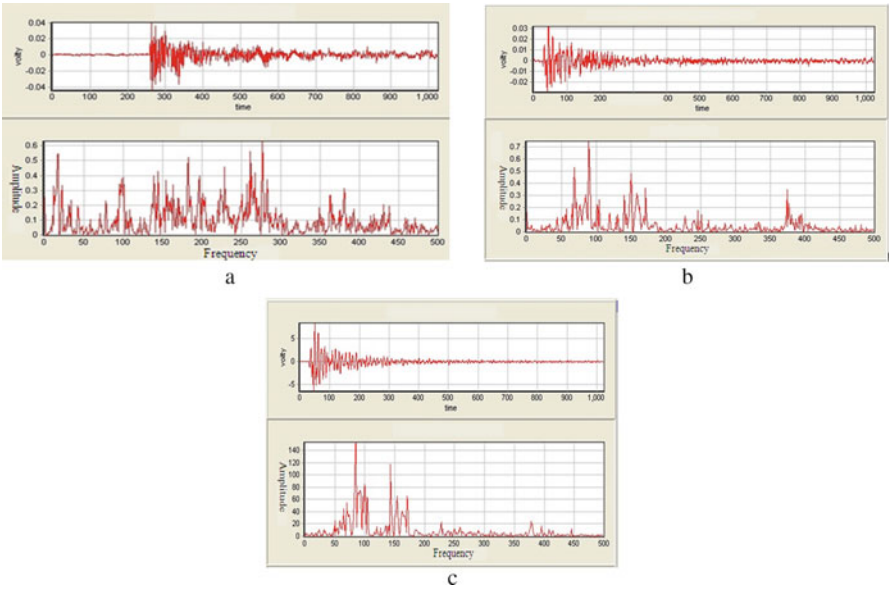

Fig. 6 Waveform and frequency spectrum figure at different damage phases during tensile process of the shell material of blowout preventer. (**a**) Yield. (**b**) Plastic deformation. (**c**) Fracture

Fig. 7 Cutting breach in the BOP

Fig. 8 Polishing the breach after welding

3.1 Experiment Equipment

The experiment uses the same equipment as in Sect. 2.3. The sensors use the US WD broadband AE sensor, in order to get more wide frequency range of signal. Using the 2/4/6 preamplifier produced by the US PAC company, and the gain set to 40 dB.

3.2 Sensor Placement

According to the shell shape of the annular BOP, we arrange two groups of sensor arrays; each array makes up of three sensors, respectively, for the 1-2-3 and 4-5-6 sensors, using triangle location method.

3.3 Experiment Process

At the locations of the sensors, polish some 30 mm diameter areas on the BOP shell for pasting the sensors. Set data collection procedure, calibrate the sensitivity of every channel, and make sure that the differences between every channel and the average are less than 3 dB.

The loaded medium of the BOP is water and the pressurized equipment is pneumatic pumps. The loading process is shown in Fig. 9. The maximum pressure is the hydrostatic test pressure. There are four pressure holding steps: The first one is 10% of the maximum value for detecting the background noise. The other three are 80% of design pressure and the maximum pressure. Collect the data of the last three processes as the experiment data.

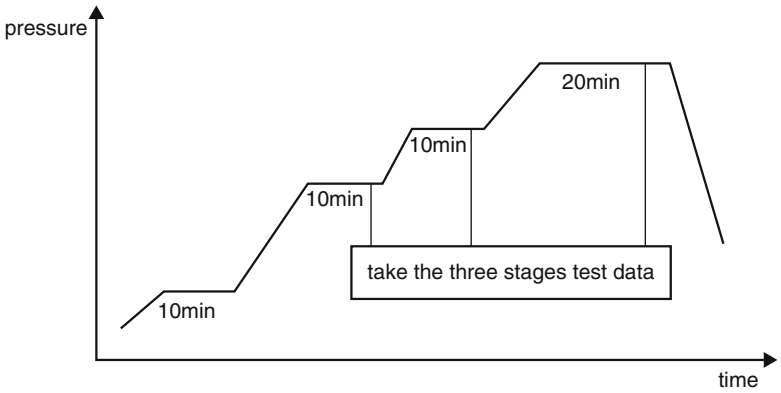

Fig. 9 Schematic diagram of BOP pressurization process

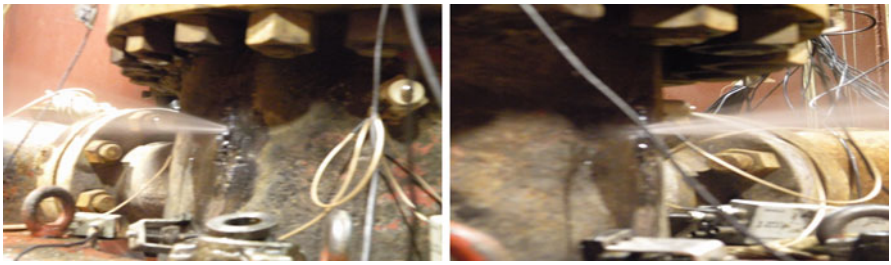

Fig. 10 The appearance when BOP shell is leaking

3.4 Data Analysis

At each pressure holding phase, the data analysis results showed a clear correlation between AE characteristics and crack growth. At the first pressure holding step, there are only several AE signals, and the activity and strength of the sound source are weak; at the second pressure holding step, there are active, high-strength sound sources; at the third pressure holding step, there are strong-activity, high-strength sound sources. Through the inspection, as shown in Fig. 10, the BOP has obvious leak, and the leaking location coincides with the AE position. Results show that AE technique can detect the different stages of the crack propagation and effectively locate possible areas. A novel application has been developed.

4 Conclusions

From the result, we can conclude that AE event rate and generation behavior showed different characteristics depending on the different damage stages, using acoustic emission technology to monitor BOP shell during hydrostatic testing is

feasible, and the AE technique is a good tool which can be used to monitor the initiation and expansion of the fatigue crack, and improve the online inspection level of BOP shell.

References

1. Z. Wu, G. Shen, S. Wang, in *The Acoustic Emission Monitoring During the Bending Test of Q235 Steel Box Beam[C], 17th World Conference Non-Destructive Testing*, 2008
2. T.M. Roberts, M. Taletbzadeh, Acoustic emission monitoring of fatigue crack propagation. J. Constr. Steel Res. **59**(6), 659–712 (2003)
3. L.F.Q. Deng YongGang, Z. LiGong, L. Jungang, Y. Xiulan, Application of AET technology in oilfield BOP inspection. Drill. Prod. Technol. (3), 83–85 (2009)
4. Z.X. Jun, W. Yi, Application of acoustic emission inspection in an annular blowout preventer. J. nondestruct. test. **12**(6), 359–362 (2009)

Part VI
Condition Monitoring and Diagnosis

Acoustic Emission Testing of Cryogenic Pipelines in Operating Conditions

T. Lusa, J. Płowiec, M. Szwed, Ł. Sarniak, and A. Zagórski

Abstract This chapter presents some selected results of application of the acoustic emission method for diagnostics of technical condition of cryogenic pipelines in working conditions. The aim of the research performed was to create a solution suitable for online testing of pipeline performance using acoustic emission testing method (AT) in service, under constant working parameters of operation or with a slight working pressure overload.

1 Introduction

Process pipelines that operate in sub-zero temperatures are an essential element of the production installations in the petrochemical industry. Depending on the transferred medium, the material and structure of the pipeline must meet the conditions in which safety of use is ensured. Said pipelines, constructed in the 1960s, frequently fail to meet the requirements currently set for materials. Additionally, the conditions of operation are usually conducive to gradual degradation manifested, for instance, by accumulation of defects resulting from material fatigue [1]. Control tests conducted in operating conditions, with the use of non-destructive testing methods, have a limited scope of application due to the operating temperature of the pipelines, frequently below −100 °C. Furthermore, the methods and procedures currently in use do not allow for the assessment of all essential pipeline elements, including welds, resulting from both the time of their being exposed to the natural conditions and technical limitations arising from difficult access to the investigated zone [2].

This chapter presents some selected results of the research work on the application of the acoustic emission technique for diagnostics of cryogenic pipelines during operation, without the necessity of shutting down the system. Laboratory tests were mostly associated with the development of a dedicated couplant, AE

T. Lusa (✉) • J. Płowiec • M. Szwed • Ł. Sarniak • A. Zagórski
Faculty of Materials Science and Engineering, Warsaw University of Technology,
141 Woloska St., 02-507 Warsaw, Poland
e-mail: tlusa@inmat.pw.edu.pl

G. Shen et al. (eds.), *Advances in Acoustic Emission Technology*, Springer
Proceedings in Physics 179, DOI 10.1007/978-3-319-29052-2_30

sensor and holder. Work was performed under industrial conditions employing as a verification method the acoustic emission method and ultrasonic defectoscopy *phased array* method.

2 Testing

2.1 Acoustic Emission Sensor

The first stage of laboratory research work involves the development of a dedicated acoustic emission sensor that is capable of providing stable operation in a temperature as low as −185 °C.

This acoustic emission sensor designed for operation in extremely low temperatures was developed in cooperation with the manufacturer of acoustic emission test equipment—*Score Atlanta Inc*. The main criterion for selection of sensor was the frequency response. Sensors with 150 kHz resonant frequency were selected as they are characterised with the highest sensitivity in terms of crack detection [3]. Table 1 presents the operating parameters of the sensor (Fig. 1).

Table 1 Operating parameters of the sensor for low-temperature testing

Parameter	Description
Resonant frequency	150.9 kHz
Preamplifier	Non-integrated
Case	Stainless steel
Cable	Integrated (without connector)
Cable length	1 meter
Average sensitivity	−65.5 dB ref 1 V/µBar in range 100–200 kHz
Dimensions	ϕ20 mm × 22 mm
Working temperature	−185 °C ÷ +80 °C

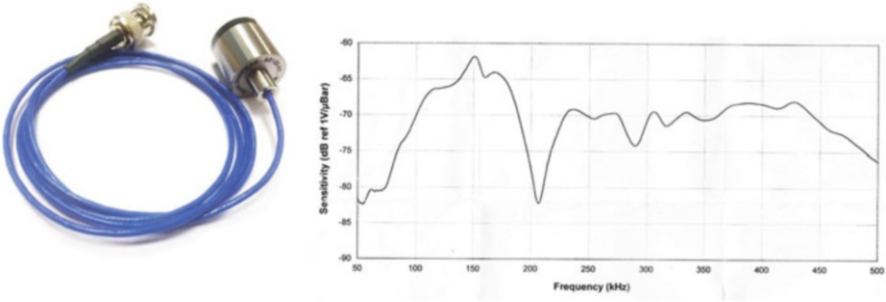

Fig. 1 Low-temperature AE sensor and its frequency response

Integration of the cable with the sensor case was to eliminate noises generated on the connector due to the freezing of water steam from the air.

The conducted laboratory tests confirmed that the sensor operates in a stable manner in the temperature of −185 °C.

Due to the fact that the thermal shocks generated in the course of installation of the sensor on the pipeline surface can cause fractures of the piezoelectric crystal, it is necessary to first cool the sensor down in the liquid nitrogen environment with the cooling rate not exceeding 10 °C/min prior to its installation.

2.2 Development of the Low-Temperature Couplant

The couplant in acoustic emission tests provides proper acoustic coupling between the measuring sensor and the surface of the tested object for the reason that it is necessary that it preserves its properties throughout the entire measuring cycle. The studies regarding development of the coupling agent involved tests at a laboratory site of the couplants available on the market that can operate in low temperatures as well as the couplants developed within the scope of the project. In order to verify the effectiveness of various types of coupling agents, the thermal conditions to be found on the wall of the process pipeline were simulated and the couplants were tested in such conditions. For the purpose of complex laboratory tests, it was necessary to design and construct a special cold box ensuring a stable maintenance of the required sub-zero temperature. The thermos was made of 6 mm thick 304 austenitic steel plate and thermally insulated lining. A 20 mm thick 300 mm × 100 mm steel plate sample was placed inside the cold box and the measurements were conducted on it. Liquid nitrogen was used as the cooling agent. The temperature inside the cold box and on the surface of the cooled sample was monitored by means of a thermocouple.

Tests for effectiveness of the coupling agents were conducted upon removal of the sample from the thermos, followed by mounting it in the special handle made of graphite EPS in the temperature of −160 °C. Due to nitrogen boiling and, as a consequence, generation of a high-level noise, it was impossible to carry the measurements out directly in the thermos. Table 2 presents the results of average

Table 2 Coupling agents used in testing

Coupling agent	Average noise level (dB)	Sensitivity (dB) (20 mm from the sensor)
MOLYKOTE 33 grease	33	96
AEROSPEC 200 grease	38	98
Ethyl alcohol	41	97.6
Silicone oil	36	98
Machine tool coolant	34	94.5
AG-1 couplant	30	98.7

noise levels and sensitivity of AE sensor. The tests involved the use of the Hsu-Nielsen source with a 0.5 mm graphite rod.

The laboratory tests showed that only the machine tool coolant and developed AG-1 couplant did not freeze. The required coupling conditions were obtained only for the developed AG-1 couplant that is a mixture of glycerine and propanol in volumetric proportions of 1/50. The obtained results of an average noise level and average AE amplitude for the wall temperature of −160 °C for the developed couplant indicate the possibility of its application even in lower temperatures.

2.3 Sensor Holder

The design work on a structural model of the mounting handle was conducted at a laboratory site, using a model pipeline. The objective of the research work was to develop a handle that provides equal tension of the acoustic emission sensor on the surface of the investigated object, with a constant force [3]. Due to the fact that pipelines operating in temperatures lower than −100 °C are mostly made of austenitic stainless steels, i.e. paramagnetic materials, the designed handle takes into account that it will be mounted on the thermal insulation of the pipeline. Such insulation consists of an insulating material secured with aluminium plate sheets. The structure of the mounting handle also takes into account thermal insulation in the form of polyurethane foam which prevents formation of thermal bridges resulting from temperature differences between the pipeline surface and its surrounding. The head of the developed mounting handle which keeps the acoustic emission sensor can move in two planes, independently from the other parts of the handle. This allows the sensor to, somehow, "adjust itself" to the curves of the pipeline surface, improving the accuracy of signal detection. The couplant is pumped directly onto the contact surface of the sensor and pipeline wall through a special handle in-built duct (Fig. 2).

The suggested structural solution was tested in industrial conditions on a section of an actual process pipeline selected for the tests. The obtained results are satisfactory in the context of mounting stability, tension, as well as efficiency of couplant application.

2.4 Pipeline Testing with AE

A section of an actual technological pipeline in active operation was selected for the purpose of the research work that is the subject of the implemented project. Detailed data are presented in Table 3.

The pipeline is used to transfer gaseous state of the hydrogen, carbon monoxide, carbon dioxide, hydrogen sulphide and methane mixture in the operating temperature of −163 °C.

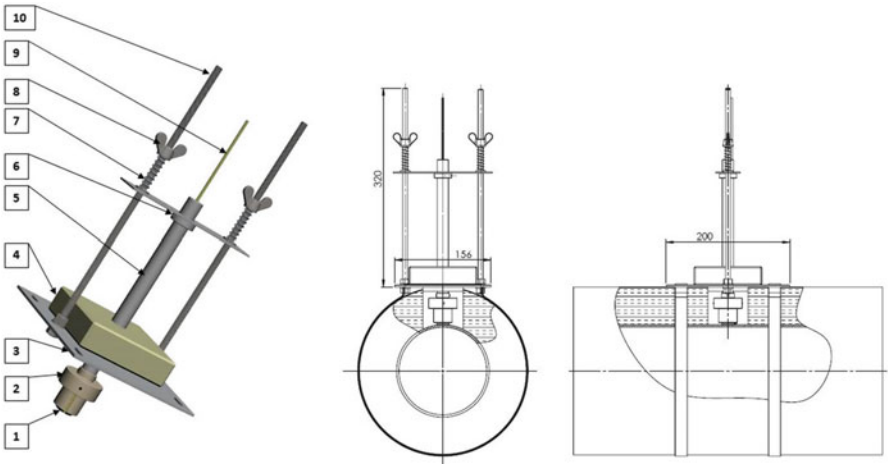

Fig. 2 Scheme of the mounting handle for the acoustic emission sensors and the installation method of mounting it to the thermal insulation. *1*—AE sensor, *2*—head, *3*—aluminium plate, *4*—thermal insulation, *5*—tube, *6*—spacer ring, *7*—spring, *8*—set screw, *9*—couplant cable, *10*—pin with thread

Table 3 Parameters of the process pipeline selected for the tests

Parameter	Value
Year of construction	1979
Length/diameter	110 m/152.4 mm
Wall thickness	7.1 mm
Working pressure	4 MPa
Medium flow rate	2166 kg/h
Min. temperature	−163 °C
Material	Stainless steel 304
Medium (gas)	$H_2 + CO + CO_2 + H_2S + CH_4$

The tests conducted on the selected process pipeline were performed using the acoustic emission method in the operating conditions. The first stage involved determination of the attenuation curve by means of the Hsu-Nielsen source and background noise level. The work included also development of a method of sensor arrangement on the tested pipeline, measurement time and selection of the acoustic signal acquisition parameters. The measurements were carried out with the use of the designed mounting handles and AE sensors as well as the AG-1 couplant. Table 4 presents a specification of acoustic signal acquisition parameters.

As mentioned above, the pipeline operating pressure was 4 MPa and it was constant for the last 6 months of operation. The AE tests involved an increase of the pipeline pressure to the value of 4.16 MPa, i.e. 104% of the nominal operating pressure. In connection with the characteristic of the conducted technological process, pressure fluctuation was found ranging from 4.09 to 4.16 MPa. In that case the use of the pipeline load scheme with stable holds at several levels was

Table 4 Settings of the measurement system and measurement data acquisition

Parameter	Description
Background noise level	42–50 dB
Max. sensor spacing	3 m
Threshold	56 dB
Filters	95–850 kHz
Number of measuring sensors	38
AE sensors	150 kHz resonant
AE system	Vallen AMSY-5
Preamplifier/gain	AEP4/34 dB

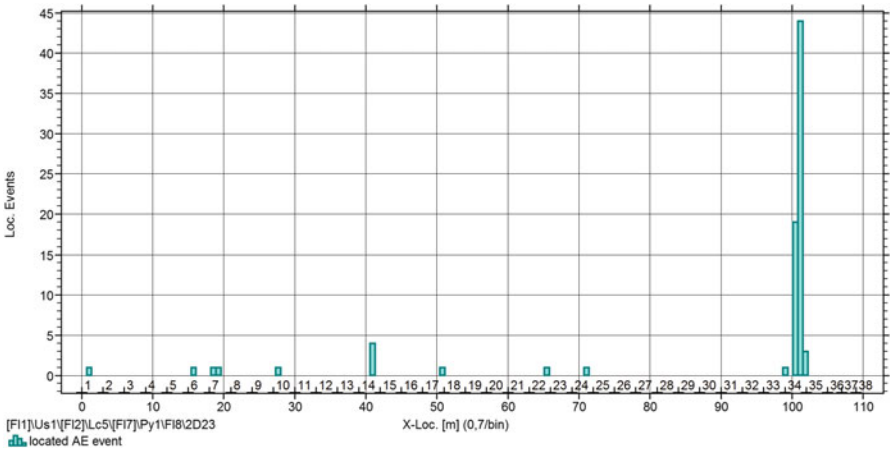

Fig. 3 Results of linear localisation of acoustic emission signals on the investigated pipeline

impossible. A decision was made to conduct two 6-h-long measuring sessions with an increased pressure and then to compare the recorded acoustic signals from both sessions. Figures 3 and 4 present results of linear localisation of signals on the entire pipeline and in a located AE source. The presented results are representative for both measurement sessions.

2.5 Verification of Acoustic Emission-Located Source

The conducted measurements resulted in the localisation of only one acoustic emission source between sensors 34 and 35, as presented in Fig. 4. The source was registered in both measurement sessions. The average signal amplitude at the located source was 64 dB. The tests of the pipeline welds were commenced upon removal of thermal insulation at the site of the located source. Weld inspection was carried out in operation conditions using a *phased array* ultrasonic flaw detector. A

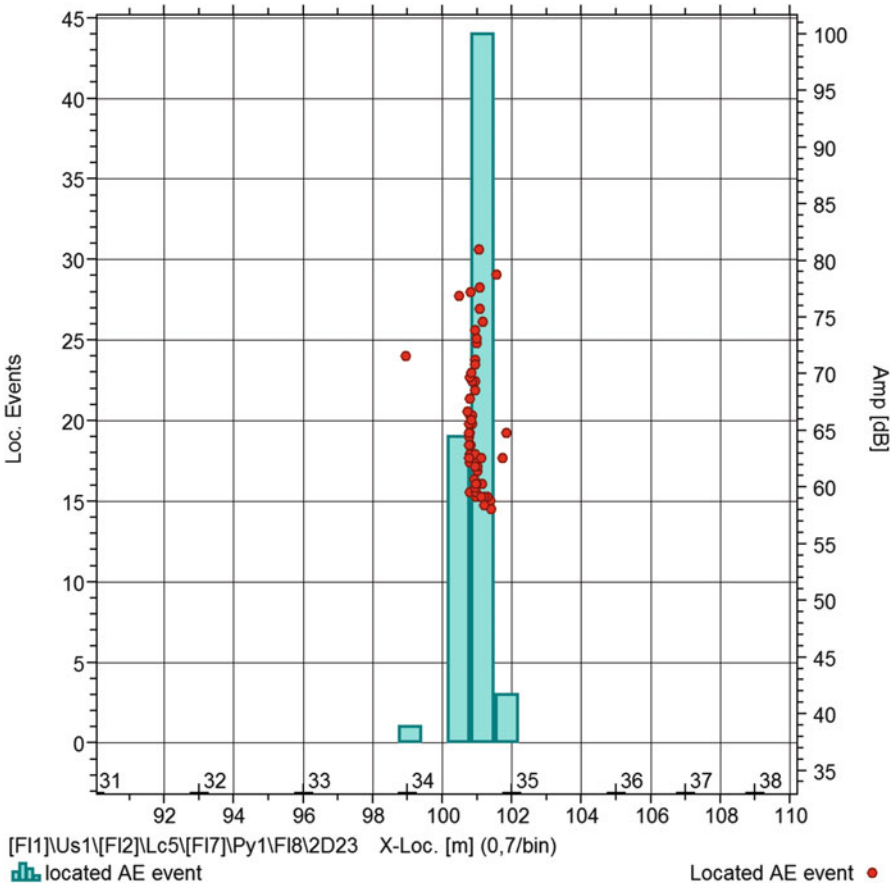

Fig. 4 Number of located events and signal amplitude at the located AE source

10 MHz, 32-element *phased array* probe with a 45° wedge was applied in a sectorial scan mode. The benefits of *phased array* technology over conventional UT come from its ability to use multiple elements to steer, focus and scan beams with a single-transducer assembly [4]. Beam steering can be used for mapping components at appropriate angles. This can greatly simplify the inspection of components with complex geometry. Electronic focusing permits optimising the beam shape and size at the expected defect location, as well as further optimising probability of detection. The ability to focus at multiple depths also improves the ability for sizing critical defects for volumetric inspections. Focusing can significantly improve signal-to-noise ratio, and electronic scanning across many groups of elements allows for C-Scan images to be produced very quickly [5].

As a result of ultrasonic testing, a flaw located near the outer surface of the pipe was detected. The flaw (crack) was about 5 mm long and 1 mm high. The obtained results are presented in Fig. 5.

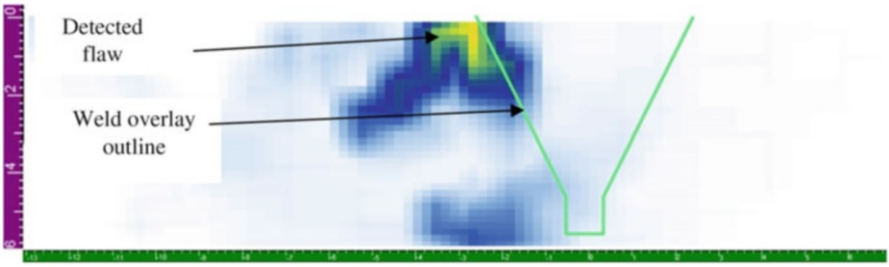

Fig. 5 End view (D-Scan) obtained by volumetric merge of ultrasonic testing results

3 Conclusions

The aim of the research work presented in this chapter was to develop a research method of testing cryogenic pipelines in their operating conditions.

In effect, conditions required for acoustic coupling of the developed AG-1 couplant in the temperature range of −160 °C were obtained as confirmed by the acoustic emission tests and ultrasonic defectoscopy in the operating conditions of the pipeline.

The developed acoustic emission sensor allows testing technical objects, the wall temperature of which reaches down to −185 °C, as shown by tests conducted at the laboratory and industrial sites. For the purpose of preventing any thermal shock it is, however, necessary to first cool the sensor down to the required operating temperature with the cooling rate not exceeding 10 °C/min.

The design of the mounting handle for the AE sensor ensures its stable pressure throughout the test period, facilitates application of the couplant on the sensor contact surface and prevents formation of thermal bridges.

The tests of the pipeline conducted in operating conditions under the pressure increased to 104% of the operating pressure revealed the presence of a single acoustic emission source identified as a weld crack by means of the ultrasonic defectoscopy *phased array* technique.

The results of the research confirmed that it is possible to evaluate the technical condition of cryogenic pipelines in operating conditions using the proposed methodology.

The obtained results constitute a base for elaboration of test procedures of acoustic emission and ultrasonic *phased array* technique for in-service cryogenic pipeline investigation. Nowadays, research work is focused on separation of signals generated by various noise sources and cracks using the *pattern recognition* method.

Acknowledgment The research work presented in this chapter was fully funded by the National Centre for Research and Development within the framework of the LIDER III Programme No. - LIDER/18/44/L-3/NCBR/2012 entitled “The methodology for the characterization, in the actual

state of degradation, of the material and welded joints of technological pressure pipelines used for transporting chemical substances maintained at temperature levels of below minus 100°C, using the Acoustic Emission method".

References

1. K. Paradowski, W.L. Spychalski, J. Plowiec, T. Lusa, A. Zagórski, K.J. Kurzydłowski, *Application of Acoustic Emissions to Technical Evaluation of New Pressure Devices* (European Working Group on Acoustic Emission, Kraków, 2008)
2. R.K. Miller, P. McIntire, in *Nondestructive Testing Handbook,* vol. 5, Acoustic Emission Testing (ASNT, Columbus, 1987), pp. 12–14, 17, 18
3. M. Nowak, I. Baran, Z. Nicewicz, J. Schmidt, A. Zagórski, in *Problem of test of double—wall storage tank for liquid ethylene with Acoustic Emission method*", The 20th International Acoustic Emission Symposium, (Progress in Acoustic Emission XV), 2010
4. N.D.T. Olympus, *Introduction to Phased Array, Ultrasonic Technology Applications*, R/D Tech Guide, 2007
5. M. Wielgat, Ł. Sarniak, W. Spychalski, W. Manaj, K. J. Kurzydłowski, in *Monitoring of degradation of a pipeline of hydrocracking installation by Phased Array and Acoustic Emission methods*", *5th Middle East Nondestructive Testing Conference & Exhibition*, 9–11 Nov 2009, Bahrain

Hit-Based Acoustic Emission Monitoring of Rock Fractures: Challenges and Solutions

Zabihallah Moradian and Bing Qiuyi Li

Abstract The two common AE measurement techniques are continuous-based streaming and hit-based triggering. In the continuous streaming method, the system records the emissions over longer periods of time. As a result, the data file may consume significant memory. Since rock fractures produce burst (discrete) signals, the hit-based method is commonly used. In this method, the system saves as much information as is reasonably required, and therefore the technique is cheaper in cost and in storage space. This method also allows the system to calculate the AE parameters of each hit in real time, simplifying the analysis process. Defining a proper setup for parameters such as threshold, sampling rate, file length, PDT, HDT, HLT, and Max duration is a critical step in data acquisition by the hit-based method especially close to the time of rock failure, when the AE activity is very high and signals may overlap each other. The aim of this paper is to discuss hit-based AE monitoring of experimental rock mechanics tests in terms of requirements and limitations and providing some solutions. Issues include data loss due to mask time, miscalculation of the AE parameters due to improper parametric setup, and system saturation due to high AE activity close to the rock fracture.

1 Introduction

When a microseismic event occurs, each sensor individually detects the AE event as an AE hit. The path that a signal takes from the point of origin to the digitized waveform consists of source, propagation through the material, material boundary, coupling, sensor, cable, preamplifier, and analog to digital conversion in the data acquisition (DAQ) system. The effects on the signal waveforms through this path can be categorized as source effect, propagation effect, and instrumentation effect. Along this path some phenomena such as attenuation, reflection, refraction, and mode conversion change the shape and the properties of the original signal.

Z. Moradian (✉) • B.Q. Li
Department of Civil and Environmental Engineering and Earth Resources Lab (ERL), Massachusetts Institute of Technology (MIT), Cambridge, MA, USA
e-mail: moradian@mit.edu

G. Shen et al. (eds.), *Advances in Acoustic Emission Technology*, Springer Proceedings in Physics 179, DOI 10.1007/978-3-319-29052-2_31

If small test specimens are used, the geometry may cause signal reflection such that the resulting detected signal will be a superposition of the directly propagating signal from the source, along with all reflections. Another important factor affecting the characteristics of the detected signals is the material and the thickness of the coupling used between sensors and the surface of the specimen. For minimizing the effect of coupling on the AE signals a thin material with low attenuation should be used to attach the sensors to the specimen. Nevertheless, the efficiency of the coupling should be verified by artificial sources such as a pencil lead break (PLB) or an active sensor pulse. The breaking of the pencil lead creates a very short-duration, localized impulse that is similar to a natural AE source such as a crack. An active pulse works similarly in that an impulse can be generated by the sensor and detected by itself or another sensor.

Acoustic emission sensors are generally piezoceramic and are made from lead zirconium titanate (PZT). They generate a voltage upon surface displacement, and as such are able to transform elastic waves into an electrical signal. The key parameters for sensors are the range of signal frequencies that the sensor can detect, as well as how sensitive it is in that range. The sensitivity of sensors is defined in decibels as $\mathrm{dB} = 20 \log(V/a)$, where V is the output voltage of the sensor in response to a reference movement of magnitude a. In acoustic emissions this is either a movement of 1 m/s or a pressure of 1 μbar. Within sensors, there are two broad categories: resonant and broadband (wideband) sensors. Resonant sensors typically have higher sensitivity, lower frequency range, and lower cost. They are also not useful for waveform analysis because (1) they may not accurately detect other frequencies beyond their resonance frequency and (2) as their name implies, they are prone to resonance and significantly distort the source signal. As a result only first arrivals and some parameters such as amplitude can be gathered from resonant sensors. Broadband sensors, on the other hand, are damped and so have lower sensitivity but cover a larger frequency range. They are also less prone to resonance due to the damping block in the sensor design.

With regard to low frequencies (nominally below 20 KHz), ambient noises can interfere with low amplitude signals while for high frequency signals attenuation problems can be encountered since they decay much faster. A trade-off must be applied in this regard. Considering this, Hardy [1] has suggested a general frequency range for geotechnical materials from 1 to 500 KHz; however for eliminating low and high frequency components a band-pass filter of 20–400 KHz is usually recommended.

In most systems preamplifiers are required since the voltages from the sensors are low and would acquire too much noise if the signal is sent directly to the DAQ. The boost from the preamplifier is expressed similarly to sensor sensitivity as $\mathrm{dB} = 20 \log G$, where G is the gain factor. Thus, signal conditioning at or near the sensor is necessary to allow transmission to and detection by the DAQ system. For this purpose, low noise preamplifiers are usually placed at a cable distance of no more than 1.2 m from the source. Forty decibel is commonly used, and corresponds to an amplification factor of 100.

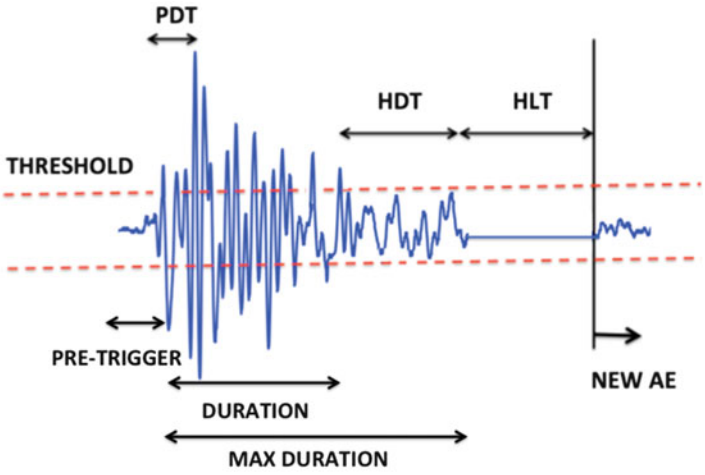

Fig. 1 Important parameters in hit-based data acquisition setup

When the voltage read by the acquisition system passes the threshold, a hit is triggered and the time of arrival is recorded. When the signal amplitude reaches a maximum and starts to decline, the DAQ card records the maximum amplitude, and waits an additional peak definition time (PDT) to see if the previous signal amplitude is exceeded (Fig. 1). If it is, the measurement continues, otherwise the previous amplitude is defined as the peak amplitude. As the signal continues, the card always records the time of the last threshold crossing. If there is no further crossing within the hit definition time (HDT), the last recorded time defines the end of the signal. If signal never goes under the threshold within the HDT, the system continues registration of the waveform until a certain time period (maximum duration) and then it automatically defines the end of the signal. After either the HDT or maximum duration has been reached, the DAQ card waits until the HLT (hit lockout time) expires. At this point, the DAQ card is reset and ready to acquire the next signal.

In addition to recording the number of acoustic hits the DAQ system records certain properties of the AE waveforms. Common parametric features include hits, amplitude, counts, duration, energy, and rise time. Frequency domain features such as peak frequency and frequency centroid are also determined from the fast Fourier transform (FFT) of the recorded waveforms, although these parameters are very sensitive to the resonant frequency of the sensors. Figures 2 and 3 show the common AE features in the time and frequency domains.

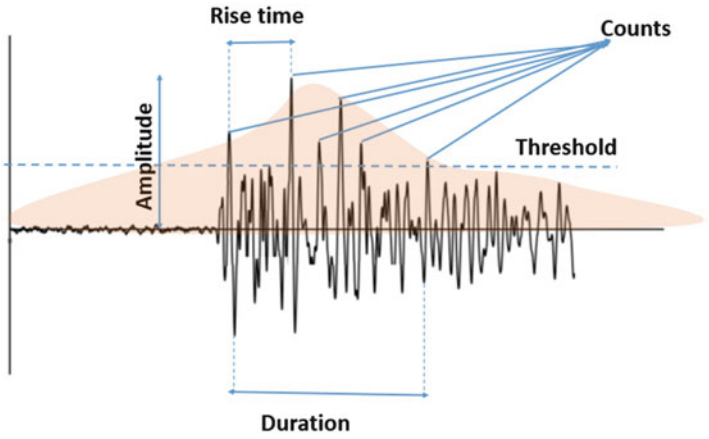

Fig. 2 Common parameters of an AE waveform in time domain. Amplitude is the highest peak voltage of the signal, counts are the number of the times that the signal crosses the threshold, duration is the time interval between the first and the last threshold crossing, rise time is the time interval between first threshold crossing and the signal peak, and energy is the area under the envelope of the signal (*colored area*)

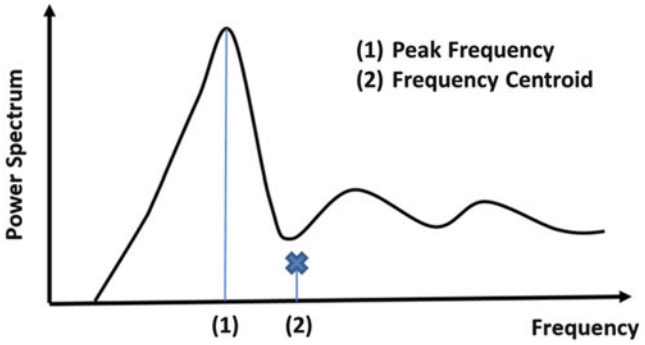

Fig. 3 Peak frequency is the point where the power spectrum is greatest and frequency centroid is the center of mass of the power spectrum graph

2 The Importance of the AE Setup

In the following sections, the importance of the AE setup in hit-based AE method will be evaluated in terms of requirements and limitations. Limitations include miscalculation of the AE parameters due to improper parametric setup of PDT, HDT, and max duration and data loss due to HLT.

2.1 Threshold

In the hit-based method, the system only saves data when the signal satisfies a certain condition such as a threshold value. As a result, the method only saves as much information as is reasonably required, making it cheaper in cost and in storage space. One disadvantage is that if the save condition is not properly specified, useful data may be lost. If a simple threshold is used, a balance should be struck between setting signal threshold limits high enough to filter out the majority of the background noises, yet low enough to pick up small desirable signals [2], though there are certain mechanical and hydraulic noises which have broad spectral content like small acoustic emission signals. In rock fracture testing, 40 dB is a reasonable threshold for most of the experiments but if the level of noise is low, a lower threshold like 35 dB can also be used. If the noise level is high, a higher threshold such as 45 or 50 dB can be used but then after the test especially for source location the threshold must be reduced, if threshold passing is used for arrival time detection.

2.2 Peak Definition Time (PDT)

High PDT is recommended to detect the maximum amplitude of the signal. A low PDT (close to the signal wavelength) can also be used to set the first motion amplitude as the parameterized amplitude. In either case the PDT parameter is less important than the HDT and HLT as it doesn't affect the triggering and end condition of hits.

2.3 Hit Definition Time (HDT)

If a long HDT is considered in the setup, several signals coming from different sources can be detected as a single hit. In this case, the number of AE hits decreases and other parameters such as duration, counts, energy, and signal strength will be approximately the sum of the contributed signals in the registered hit (Fig. 4). As a solution, one can reduce the HDT, or alternatively increase the threshold. In the case of a short HDT, a single signal can be detected as several hits. Large signals with their reflections can cause such a situation. Using a longer HDT, increasing HLT or applying some damping material to reduce reverberation can mitigate this problem.

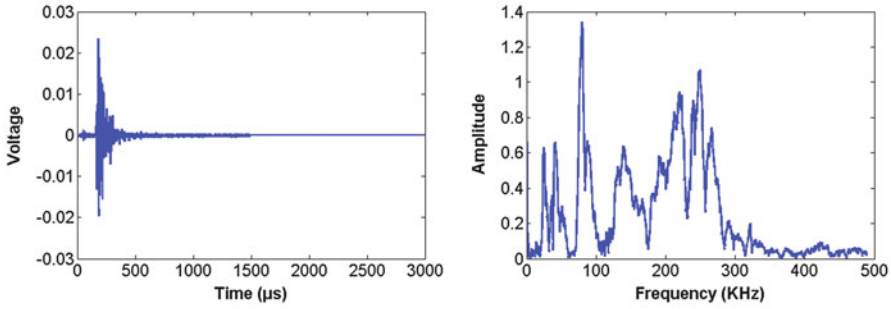

(a) A single hit defined by HDT

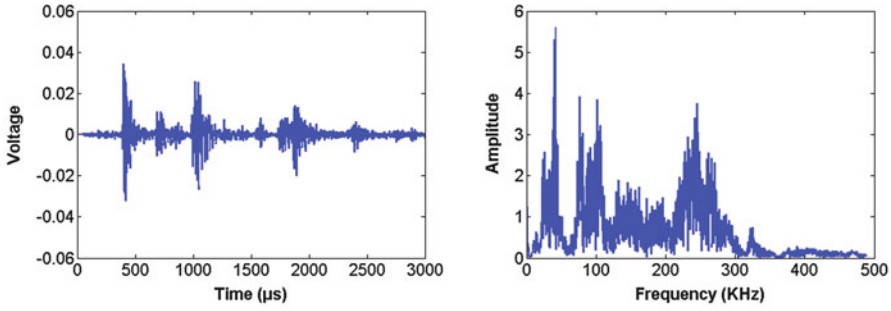

b) Several hits were detected for the duration of 3 ms as a single hit due to a high HDT

Fig. 4 Defining the signal by HDT (**a**) proper setup of HDT (a single hit defined by HDT) and (**b**) when HDT is set too long (several hits were detected for the duration of 3 ms as a single hit due to a high HDT)

2.4 Maximum Duration

For a hit-based monitoring technique, it is undesirable for hits to be based on the maximum duration (Fig. 5). This can occur when the rock is close to its peak load, and unstable fracturing begins. In this case, emissions can be produced at a rate exceeding that set by the HLT and maximum duration, at which point the hit duration parameter becomes unrepresentative of the true hit rate. Given that a minimum mask time is required between hit registrations for most hit-based systems, it is then recommended in these scenarios to increase the maximum duration to the largest possible value such that the minimum amount of data loss occurs. The data can then be post-processed with a higher or a floating threshold to transform it into a useable format.

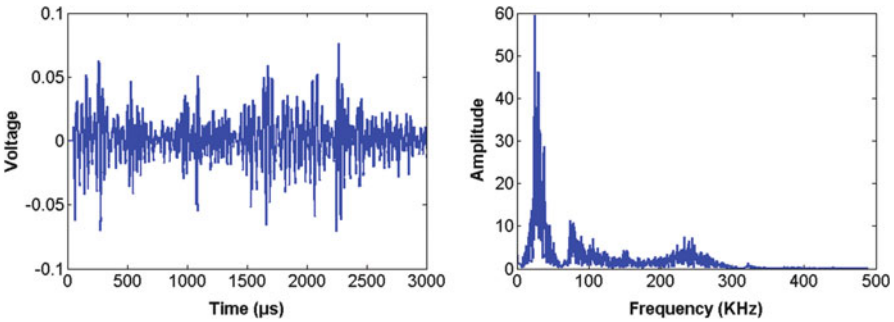

Fig. 5 Waveform and spectral density plot of a superimposed hit that has been defined by maximum duration

2.5 *Hit Lockout Time (HLT)*

The hit lockout time (HLT) is the parameter defined as the wait time after acquisition of a signal. The general use case of this is to prevent reflected or long duration signals from being considered as a fresh signal. However, an excessively long HLT time can prevent the capture of next rapidly occurring emissions. In rock, given that the quality factor Q tends to be much lower than for metals [3], reflections tend to decrease in energy rapidly while signals tend to be short in duration and so small HLT values are recommended. Short HLT values are also recommended given that rupture in rock can cause a large number of hits within a short time period, as seen in Fig. 6. Data loss due to HLT can be calculated from:

Data loss = (Max duration)/(Max duration + HLT), if the signal is defined by Max duration.

2.6 *Sampling Rate*

The sampling rate controls the accuracy of the timestamp of any data since the error is equivalent to time between recordings. Time can be converted to distance since the wave velocities are generally known, for example to achieve an accuracy of 1 mm in a medium with $v = 4000$ m/s, a time accuracy of $4000/0.001 = 4$ MHz is required. However, note that this constitutes only the theoretical accuracy of localization, whereas in experiments typically larger errors stem from issues such as inaccuracy in arrival time picking, mismeasurement of sensor locations, and anisotropy in velocity model.

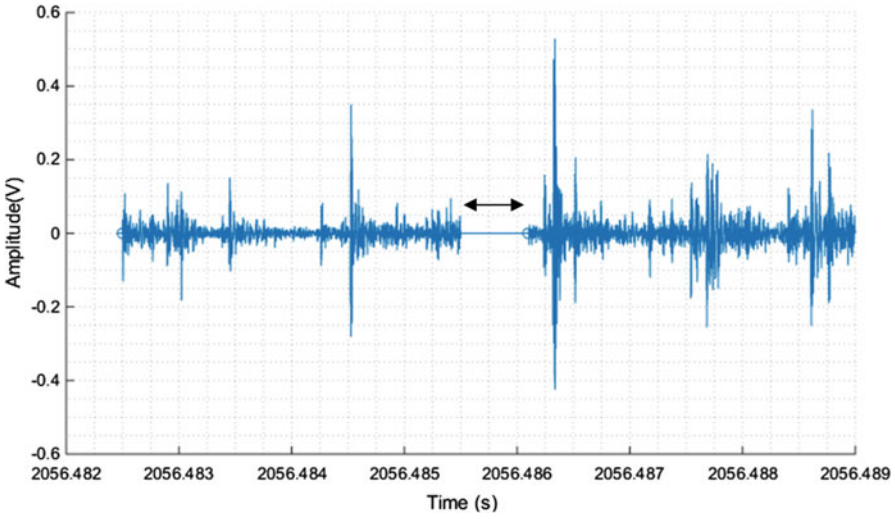

Fig. 6 Data loss due to HLT

3 System Saturation Close to the Failure: Case Study from Hydraulic Fracturing Tests on Granite

The described method employs PCI-2 data acquisition cards from Mistras Group. These cards are specified to have a sampling rate up to 40 MHz at 18 bit resolution. The cards are designed with a hit-based architecture, in that the card requires time to re-arm after every acoustic hit. This effect is also known as the mask time. The cards have continuous streaming capability, but only 10 MHz can be streamed over all channels whereas 5 MHz on eight channels is required in our experiments. The details of the experimental setup have been presented in [4–6].

The AE system was used in hydraulic fracturing experiments done at MIT, where it was noted that two classes of problems with the AE system occur close to the time of fracturing. These two cases are illustrated in Figs. 7 and 8, and the AE setup parameters used in these tests are given in Table 1.

Synchronizing the analog and digital systems in the acquisition makes it possible for the acquisition card to consistently trigger, particularly around the time of fracturing. This however requires a significant usage of computational resources since large volumes of data are received in this period, and it was noted that data acquisition was bottlenecked by the computer accessing the acquisition cards. This is illustrated in Fig. 7 where no data are gathered in the 4 s prior to fracture. It can then be concluded that a relatively fast CPU and hard drive are required for an AE system. These requirements were satisfied when the PCI-2 acquisition system was upgraded to a computer with an Intel i7-4790k CPU, 16 GB of DDR3 RAM, and a 5400 rpm WD hard drive.

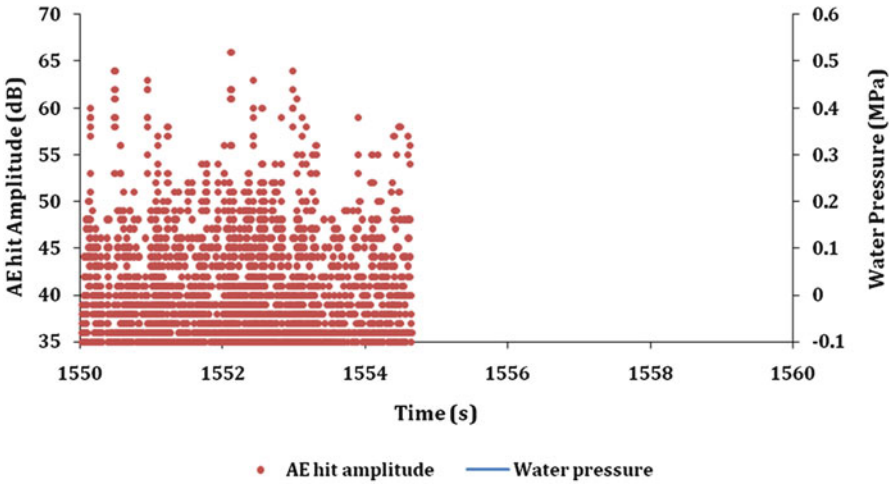

Fig. 7 System saturation due to high AE hits rate close to the rock fracture—Specimen 1

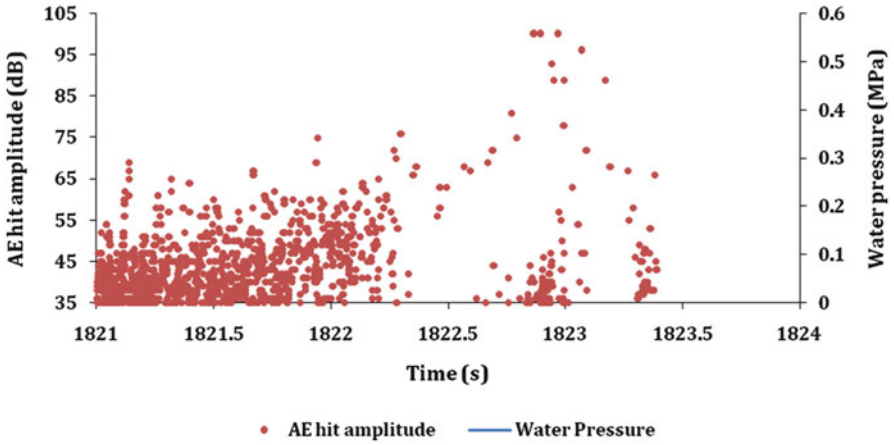

Fig. 8 Data loss due to large duration or continuous AE hits around rock fracture—Specimen 2

In Fig. 8, the number of hits decreases near to the drop in pressure, and it was noted that the time between hits was exactly 100 ms when this occurred. This phenomenon can be explained by the acquisition card architecture. The system operates on an analog basis, in that parametric information such as duration, amplitude, and energy are recorded without digitally logging the voltages of the waveform trace. The analog-digital converter that produces voltage recording is only activated when the analog side is activated, but the end conditions differ between the analog and digital systems. The analog system has a flexible condition that ends the hit when the voltage does not exceed the threshold for a specified hit

Table 1 AE parameters for experiments shown in Figs. 7 and 8

Sampling rate	40 MHz
Number of sensors	8
Preamplification	40
Maximum duration	100 ms
File length	15 k
Waveform time length	384 μs
Pre-trigger	50 μs
PDT	200 μs
HDT	800 μs
HLT	2 μs
Threshold type	Fixed
Threshold	35 dB

definition time (HDT), or when the maximum duration is reached if the HDT condition is not met for a long period of time. On the other hand, the digital system is static in that it saves for a specified amount of time only. It was observed that over the course of an experiment the HDT controls acquisition for most of the test, while the maximum duration parameter controls acquisition close to failure. This is seen in Fig. 8, where the maximum duration was set to 100 ms and the length of digital trace to 0.384 ms, resulting in significant data loss close to failure. To avoid this problem, in subsequent tests the length of digital traces was set to match the maximum duration. The AEwin software used with the PCI-2 cards limits digital traces to 15,360 samples, which corresponds to 3.072 ms at a sampling rate of 5 MHz. Consequently, 3 ms is used as the maximum duration parameter such that minimal data are lost during acquisition.

Currently the majority of a logged waveform contains voltage data; however, as seen in Fig. 9, there is a small segment at the beginning and end of each signal that contains zeros.

The reason for this is that the analog waveform only saves 3 ms exactly, while the length of the digital logging corresponds to 3.072 ms. The total time of the beginning and end zeros corresponds to this difference of 72 μs. The time of zeros at the beginning also corresponds to the amount of pre-trigger time, and suggests that no data can be recorded in the period of time where the AE card is re-arming. As a result, increasing the pre-trigger during the time of data saturation will not yield additional data as the voltages will be zero. It also suggests that the pre-trigger should not be set to more than 72 μs as the length of useful data will then be less than 3 ms and more data will be lost. It was also found that some gaps in acquisition occur when the pre-trigger is set too low to a value of 25 μs, and so the previously used value of 50 μs will continue to be used.

The second issue pertains to the time in between recorded waves, as shown in Fig. 6.

This time appears to be related to the programming of the data acquisition card, in that time is required between recordings for "re-arming." It appears that this time is unstable if the hit length time (HLT) is short, as shown in Fig. 10.

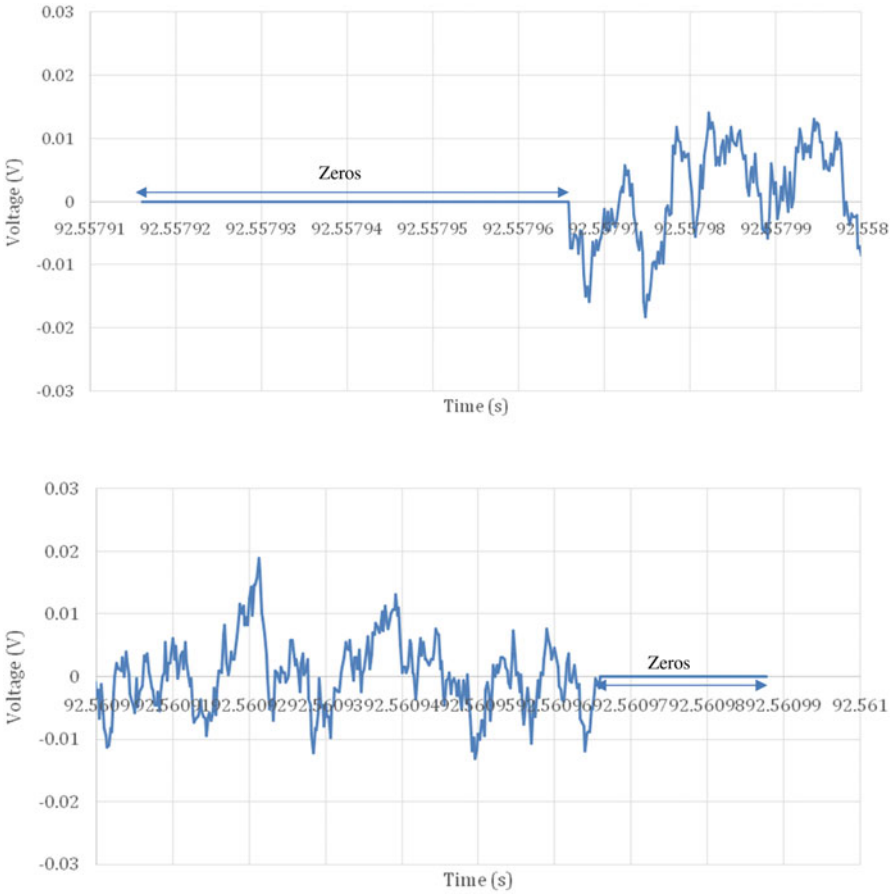

Fig. 9 Small segment at the beginning and end of each signal that contains zeros

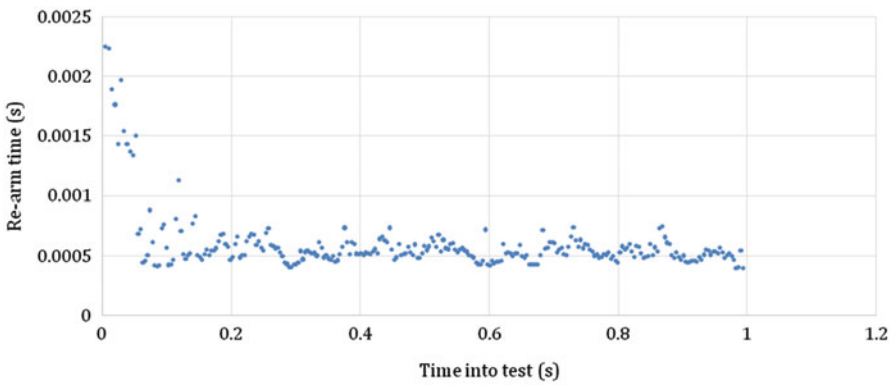

Fig. 10 System re-arm time at HLT = 350 μs

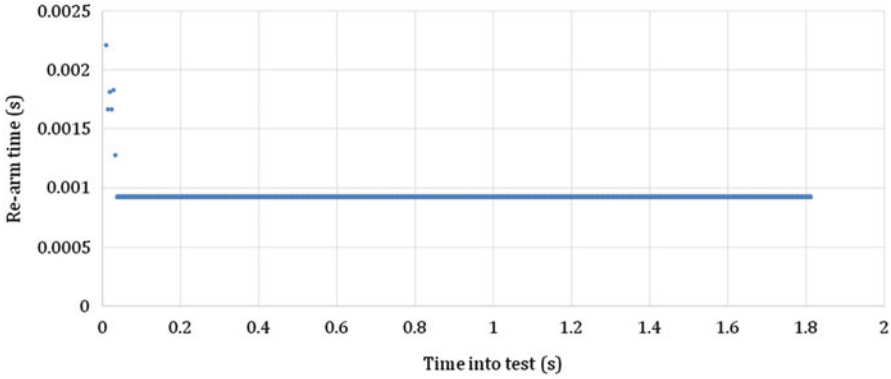

Fig. 11 System re-arm time at HLT = 1000 μs

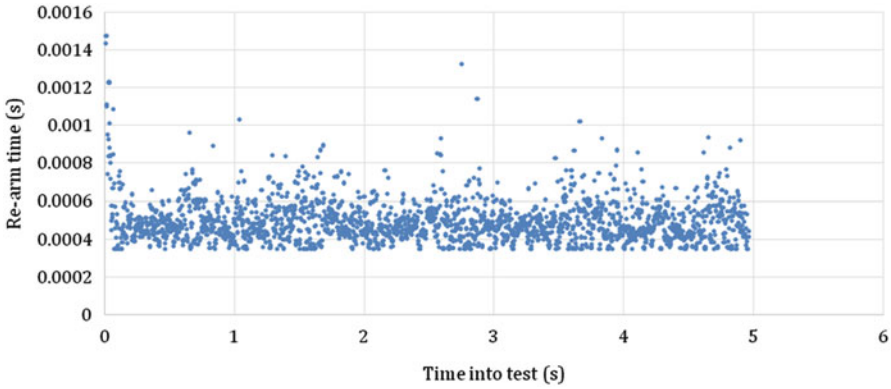

Fig. 12 System re-arm time at HLT = 350 μs and 2 ms segments

The re-arm time is initially high, and then fluctuates between 400 and 800 μs, averaging around 570 μs. This would correspond to a downtime of 570/(3072 + 570) = 15.7%. If the HLT is increased, the system reaches a state of stability around HLT = 1000 μs, as shown in Fig. 11.

However, to reach this state of stability the HLT was increased beyond the re-arm time of an unstable HLT, and the average time between hits is 928 μs, as opposed to 570 μs before. Since the unstable re-arm time is not a significant issue, it is more desirable to operate at a low but unstable HLT as less data are lost.

Another possibility is to use shorter save segments, since it is unknown if the re-arm time scales with the amount of data saved. Currently saved segments are 3 ms long. An HLT of 350 μs was used with 2 ms data saves, as shown in Fig. 12.

It appears that the re-arm time decreases slightly to an average value of 492 μs. However, the scaling is less than linear, i.e., it does not scale by 2/3, and so it is more desirable to collect in 3 ms segments. Some occurrences of the case of system/

Table 2 The modified AE settings used the rest of the tests

Sampling rate	5 MHz
Number of sensors	8
Preamplification	20 dB
Maximum duration	3 ms
File length	15 k
Time/waveform	3 ms
Pre-trigger	50 μs
PDT	200 μs
HDT	800 μs
HLT	350 μs
Threshold type	Fixed
Threshold	37 dB

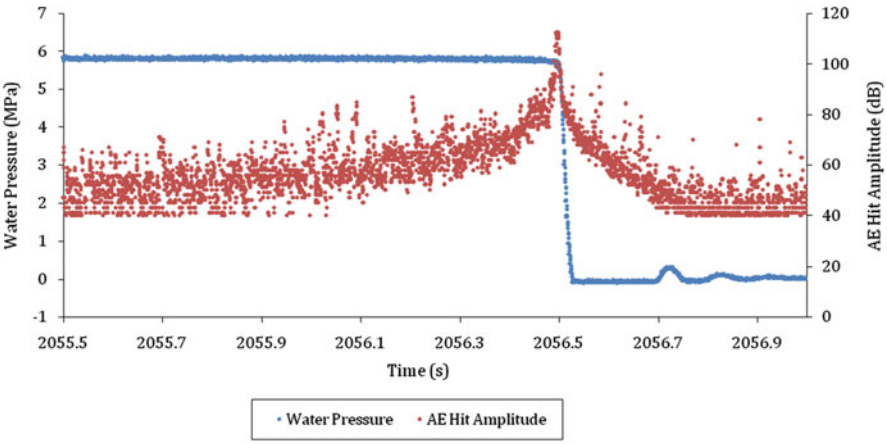

Fig. 13 Modification of the CPU and the AE data setup reduces the effects seen in Figs. 7 and 8

card overload was also noted using 2 ms segments and so 3 ms segments are also recommended for reliability.

As a result of the above analyses, it appears that the system is capped at 84% uptime for a sampling rate of 5 MHz. This can be achieved by the three following parameters while ensuring that as few parametrics as possible are collected.

1. 30 μs < Pre-trigger < 72 μs
2. HLT < 400 μs
3. 3 ms data segments sampled at 5 MHz

The full list of settings is shown in Table 2. Figure 13 shows the test results of a granite specimen tested with the modified setup in Table 2. No saturation occurred for the new setup.

4 Conclusions

The two common DAQ setups are continuous-based streaming and hit-based streaming. In the continuous streaming method, the system registers indiscriminately and therefore consumes significant memory space. As a result, the analysis can become more difficult due to large volumes of data. Various algorithms can then be used in post-processing to separate the data file into discrete hits.

Since rock fractures produce signals in bursts, the hit-based method is commonly used. In hit-based method, the DAQ system calculates the AE parameters of each hit and stores them. If necessary, it can also save the waveform (mostly a portion of it but not the whole). The main limitation of such a system is the hit-based architecture, which is a significant asset during burst type emissions but prevents continuous monitoring during periods of high activity. This is due to the acquisition card needing to re-arm after every hit, resulting in small blanks between hits.

Close to the failure point where macro-cracks initiate, propagate, and coalesce, the event rate in the rock is high and the DAQ cards became overloaded due to being triggered constantly thus the system may go to saturation. Upgrading the CPU of the system and modifying the acquisition setup largely solved this problem.

Observations using the synthetic continuous signal showed that given a sampling rate of 5 MHz, the re-arm time of the acquisition card is approximately 570 μs in between 3000 μs digital traces, which corresponds to $\frac{570\,\mu s}{570\,\mu s+3000\,\mu s} = 15\%$ downtime. It appears this re-arm time is a limitation of the acquisition card, and as a result cannot be further reduced by improving the computer.

Alternatively, it is possible to avoid this situation by increasing the threshold, using a floating threshold or lowering the loading rate such that failure occurs more slowly. It should be noted that even using a floating threshold may cause loss of potentially useful lower amplitude signals since the floating threshold tends to be implemented with some lag.

References

1. H.R. Hardy Jr., *Acoustic emission/microseismic activity* (Balkema Publishers, Lisse, 2003)
2. E. Eberhardt, D. Stead, B. Stimpson, R.S. Read, Identifying crack initiation and propagation thresholds in brittle rocks. Can. Geotech. J. **35**(2), 222–233 (1998)
3. F. Birch, Velocity and attenuation from resonant vibrations of spheres of rock, glass, and steel. J. Geophys. Res. **80**, 756–764 (1975)
4. B. Goncalves da Silva, B. Li, Z. Moradian, J. Germaine, H.H. Einstein, *Development of a test setup capable of producing hydraulic fracturing in the laboratory with image and acoustic emission monitoring* (ARMA Symposium, San Francisco, 2015)
5. B.Q. Li, Z. Moradian, B. Goncalves da Silva, J. Germaine, *Observations of acoustic emissions in a hydraulically loaded granite specimen* (ARMA Symposium, San Francisco, 2015)
6. Z. Moradian, H.H. Einstein, G. Ballivy, Detection of cracking levels in brittle rocks by parametric analysis of the acoustic emission signals. Rock Mech. Rock Eng. J **49**, 785–800 (2016)

Acoustic Emission Monitoring of Brittle Fatigue Crack Growth in Railway Steel

Zhiyuan Han, Guoshan Xie, Hongyun Luo, Mayorkinos Papaelias, and Claire Davis

Abstract Rail networks are gradually getting busier with rolling stock traveling at higher speeds and carrying heavier axle loads than ever before. In order to consider the further application of acoustic emission (AE) for railway damage monitoring, the fatigue and AE characteristics during the fatigue crack growth (FCG) process in a rail steel were investigated in this study. For better recognition and prediction fatigue damage of rail steel, the relationship between the micromechanism and the characteristics of AE signals were studied. The FCG experiments were carried out, and the AE signals emitted from FCG process were studied by AE parameters and Fast Fourier Transformed (FFT) spectra analysis. The AE results were also compared with the fracture surfaces. The results show that the AE technique is capable of acquiring and identifying brittle fracture events during FCG of rail steel.

1 Introduction

Rail networks are gradually getting busier with rolling stock traveling at higher speeds and carrying heavier axle loads than ever before. These operating conditions frequently lead to wear and fatigue damage under cyclic loading and generate various types of rail defects, such as head check, split head, bolt-hole crack, and transverse crack defects [1]. Further growth of these defects will finally cause the service failure of rail if they remain undetected. Therefore, inspection and assessment of the growth of these defects in service is critical in making maintenance decisions and ensuring the smooth operation of the rail network.

Z. Han (✉) • G. Xie
Pressure Vessel Department, China Special Equipment Inspection and Research Institute, Beijing, China
e-mail: hzy19851227@163.com

H. Luo
Key Laboratory of Aerospace Advanced Materials and Performance, Ministry of Education, School of Materials Science and Engineering, Beihang University, Beijing, China

M. Papaelias • C. Davis
School of Metallurgy and Materials, University of Birmingham, Birmingham, UK

G. Shen et al. (eds.), *Advances in Acoustic Emission Technology*, Springer Proceedings in Physics 179, DOI 10.1007/978-3-319-29052-2_32

Acoustic emission (AE) is widely used as a structural health monitoring technique for detecting fracture processes and damage evolution in steel structures. The continuous monitoring of fatigue crack growth (FCG) processes is one of the most important applications of AE, which is difficult to achieve by any other nondestructive evaluation techniques. Previous studies considering AE characteristics during the FCG process have showed that AE was capable of detecting FCG even at a FCG rate of 2.5×10^{-8} m/cycle [2]. The relationship between AE parameters, such as count and energy, and the stress intensity factor range has also been well established in a variety of steels to predict fatigue life and crack length [3–6]. These results suggest that the AE technique can be used as a potential quantitative method for FCG monitoring and damage evaluation in rail steels.

However, it is noteworthy that railway steel has a microstructure that is mainly composed of pearlite, which is very different in terms of fatigue and AE behavior from the ferrite steels investigated in most previous studies. Though Papaelias et al. [7], Bassim et al. [8], and Thakkar et al. [9] have reported some important AE features recorded during the development of damage in rail steel, the AE characteristics and relationship between AE signals and fracture events during FCG of rail steel have not been extensively studied yet. Thus this study is an attempt to reveal the AE characteristics related to the damage mechanisms during the FCG process in a pearlitic rail steel to order to consider the further application of AE for railway damage monitoring.

2 Experimental Details

2.1 Materials and Specimens

Standard single edge notched specimens were extracted from 260 grade rail steel (0.7 C and 1.0 Mn in wt%) with dimensions 120 × 20 × 10 mm. As can be seen in Fig. 1, the specimens were extracted from the web plane and in the longitudinal orientation of the rail steel. The nominal mechanical properties of the 260 grade rail steel are given in Table 1.

2.2 Test Instrument and Procedure

Three point bending fatigue tests were carried out on a Dartec 50 kN servo-hydraulic universal test machine at ambient temperature (300 K). Three specimens were pre-cracked to initial crack lengths of 9.5 mm, 10 mm, and 10.8 mm respectively. All specimens were tested under sinusoidal cyclic loading at a frequency of 1 Hz and load ratio of 0.1. The peak load was 3.5 kN for all specimens. The fatigue crack length was measured by electrical potential difference (EPD) method which

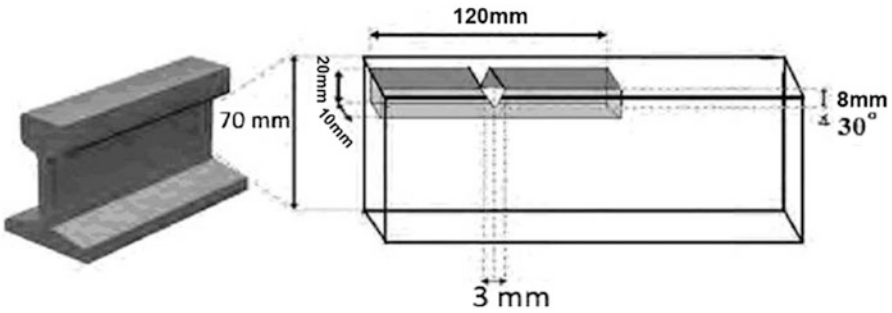

Fig. 1 Details of four point bending specimen

Table 1 Typical mechanical properties of 260 grade rail steel

Minimum tensile strength	Yield strength	Minimum elongation at rupture	Brinell
≥1.040 MPa	≥608 MPa	9%	320–360 HB

was set at initial notch. The crack length data and the stress intensity factor range ΔK were calculated after the tests. After the fatigue tests, the fracture surfaces were observed using a JEOL scanning electron microscope.

2.3 Acoustic Emission Monitoring

AE signals generated during the fatigue tests were recorded and analyzed by using a DiSP with an AEwin v2.19 acoustic emission system (Physical Acoustic Corporation, USA). Two Pico wideband piezoelectric transducers with a bandwidth range between 150 and 750 kHz were used to pick up these AE signals. The sensors were coupled to the surface of the sample using grease and held in place using strong adhesive tape. The AE sensors were mounted approximately 20 mm away from the center of the sample, one on either side of the cracked region. This position was also used to make a linear source location of the AE signals. A preamplifier with 40 dB gain and a compatible filter (150–750 kHz), which has been proved to be sensitive to crack signals [4, 5], were used to capture the AE signals; the sampling rate of AE system is 2 MSPS. The AE amplitude and duration thresholds during recording were set as 40 dB and 50 μs respectively to minimize the number of mechanical noise-related hits being recorded during tests. The linear AE source location was also used to make sure that the obtained signals were generated from the crack area.

3 Results and Discussion

3.1 FCG and AE Characteristics

The plots of fatigue crack length versus fatigue cycle number with corresponding AE amplitude are shown in Fig. 2a–c for specimens A–C respectively. Due to the different initial crack lengths, the total fatigue life was different between the different specimens. However, all these specimens show a sudden rupture at a crack length of approximately 13 mm as can be seen in Fig. 2. The corresponding AE amplitude results in Fig. 2 show that numerous AE events are generated during the FCG process. The amplitude of most of the AE events recorded ranges between 40 and 60 dB, and there is a significant increase in number of these events as the crack length increased. However, the most interesting phenomenon is the appearance of high amplitude (>70 dB) events in all specimens, some of which even reached 99 dB, which is the upper limit of the recording system, as seen at the top of the figures. Such high amplitude events are rarely reported in previous studies concerned with ferritic steels [10–12], suggesting that a different AE source mechanism exists in pearlitic rail steel during the FCG process, which will be discussed in the following sections.

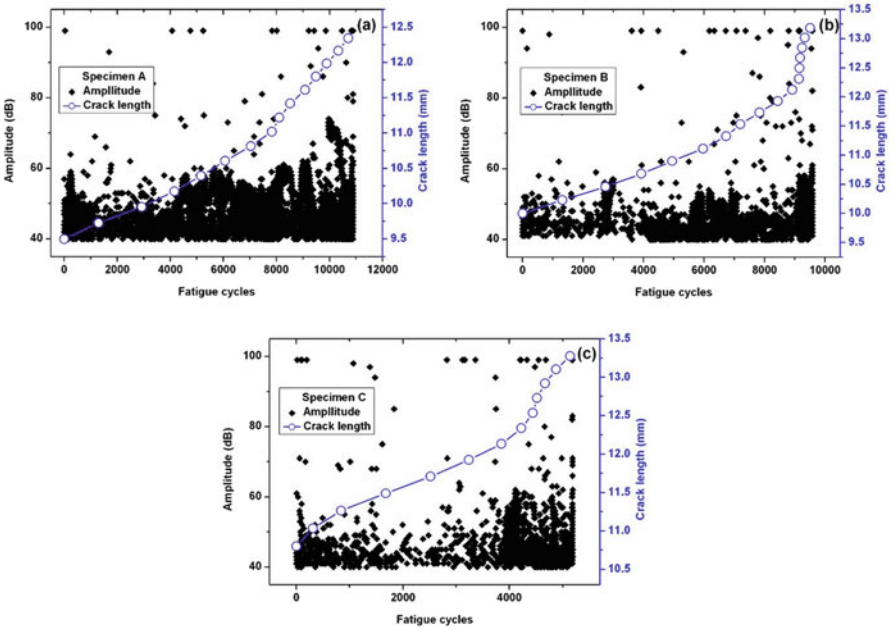

Fig. 2 Fatigue crack length versus fatigue numbers with corresponding AE amplitude for (**a**) Specimen A, (**b**) Specimen B, (**c**) Specimen C

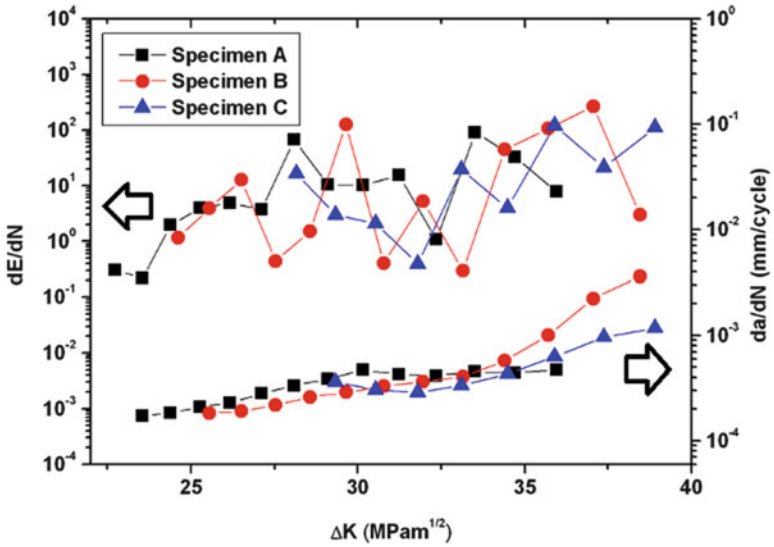

Fig. 3 FCG rates and AE count rates for different specimens

AE energy and energy rate is used for quantitative analysis of the AE data. Figure 3 shows the FCG rates (*da*/*dN*) and AE energy rates (*dE*/*dN*) versus stress intensity factor ranges ΔK on double logarithmic axes. It can be seen that the *da*/*dN* obeyed the Paris law for all specimens and show good consistency [13]:

$$\frac{da}{dN} = C\Delta K^m, \quad \text{or}: \quad \log\left(\frac{da}{dN}\right) = \log\ C + m\log\ \Delta K \tag{1}$$

where C and m are constants for a particular material, and their fitting values are summarized in Table 2, which are consistent with that in [1]. On the other hand, the *dE*/*dN* exhibit a similar general trend as *da*/*dN* (i.e., increasing value with stress intensity factor). The well-established relationship between *dE*/*dN* and ΔK can be described as [6, 14]:

$$\frac{dE}{dN} = B\Delta K^p, \quad \text{or}: \quad \log\left(\frac{dE}{dN}\right) = \log\ B + p\log\ \Delta K \tag{2}$$

It should be noted that although the trend of energy rates for three specimens basically obeyed (2) and showed a certain similarity in fitting parameters, the data fluctuation is significantly large even in one specimen. It can be clearly seen in Fig. 3 that *dE*/*dN* can exceed 100 even at lower ΔK level, which is nearly two orders of magnitude higher than that at some higher ΔK level. It implies the sudden increase of AE energy during FCG, and indicates that the relation between *dE*/*dN*

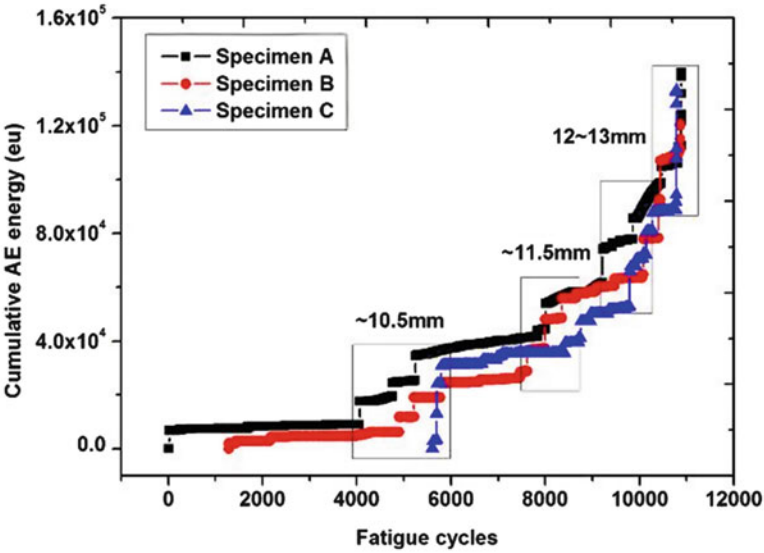

Fig. 4 Cumulative AE energy versus fatigue cycles

and ΔK ((2)) may not be as suitable for fatigue life predication in rail steel as in ferrite steels [6, 15, 16] due to its high instability.

The cumulative AE energy during FCG is given in Fig. 4. For better comparison, the fatigue cycles for specimens B and C are re-calculated to keep the same fatigue life as specimen A due to their similar FCG rates and final crack lengths. As can be seen in Fig. 4, the three specimens show a high consistency in cumulative AE energy throughout the FCG process. It is noteworthy that the increase of cumulative AE energy shows an intermittent characteristic. A sudden increase of AE energy with a few extremely high energy events can be observed around some certain fatigue cycles for all specimens as marked by boxes in Fig. 4; the corresponding crack lengths are also indicated in the figure. Further investigation revealed that these high energy events (>2000) are from the high amplitude (>90 dB) events observed in Fig. 2 and are also responsible for the high dE/dN during FCG in Fig. 3.

3.2 AE Source Mechanism and Brittle Fracture During FCG

The amplitude distribution ranging from 40 to 60 dB corresponding to the large number of low amplitude AE events observed during the FCG process in Fig. 2 is very similar to that seen in previous studies. The AE source for these events can be attributed to plastic deformation in the plastic zone around the crack tip or to ductile crack extension events [12]. To further understand these high energy and amplitude events, the fracture surface of the specimens was examined and is shown

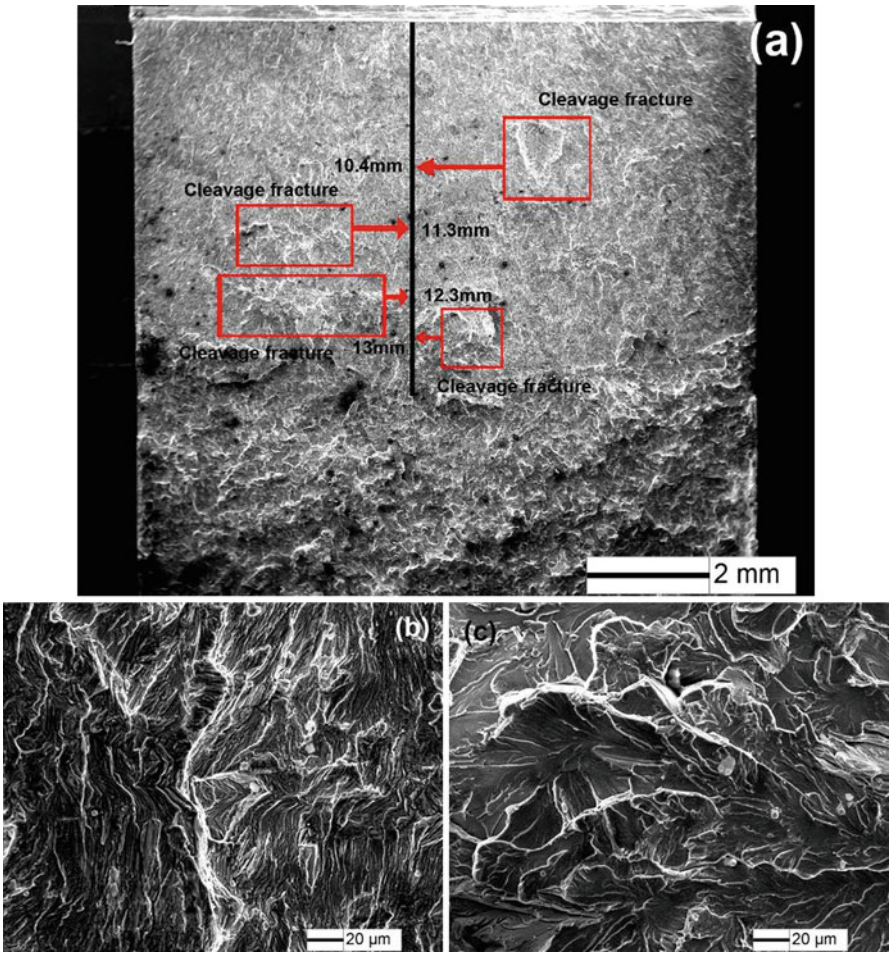

Fig. 5 Scanning electron micrographs of fracture surfaces: (**a**) low magnification images, (**b**) high magnification of flat surface, (**c**) high magnification of cleavage fracture

in Fig. 5. Figure 5a shows a low magnification image of the fracture surface for macro-observation. Most parts of the flat surface are characterized by transgranular fracture as shown in Fig. 5b with some ductile characteristics, which is in agreement with the result in Ref. [1]. In addition, some typical cleavage fracture facets with river patterns are also distributed on the fracture surface as marked in Fig. 5a by boxes and shown in Fig. 5c. The crack lengths corresponding to when these brittle fractures occurred were approximated on the fracture surface and given in Fig. 5a. Coincidentally, the crack lengths for these cleavage fractures match very well with those determined for the high amplitude and energy AE events as indicated in Fig. 4. This suggests that the AE source mechanism for the high amplitude and energy AE events can be attributed to brittle cleavage fracture during

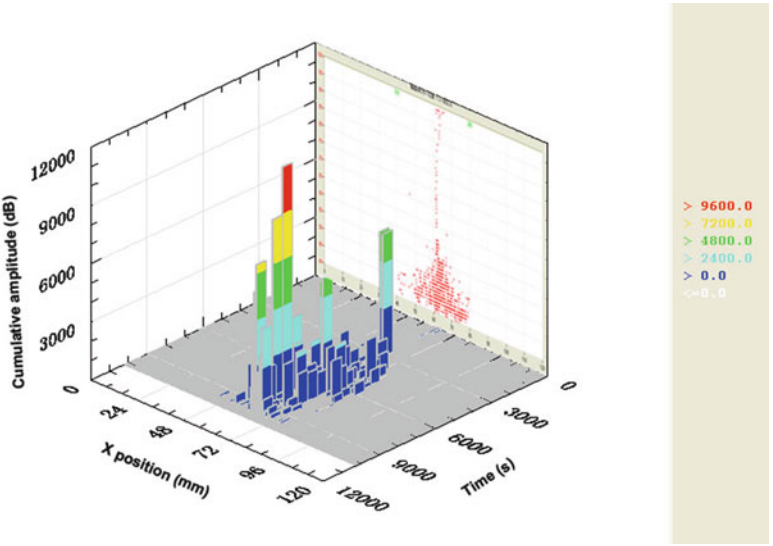

Fig. 6 AE source location result where the crack position is located at 60 mm in the X-position axis

FCG of rail steel. This explanation is reasonable because brittle fracture generally releases much higher energy and results in much higher AE activity as compared to ductile fracture [17]. The AE source location result, as shown in Fig. 6, also indicates that all of these high amplitude events are generated exactly from the middle of the specimen, suggesting they are crack propagation events rather than noise from other sources.

3.3 Identification of Brittle Fracture Events by AE During FCG

It has been discussed above that the high amplitude and energy AE events are related to the brittle cleavage fracture events during FCG. Identification of these events is of great important for AE monitoring of fatigue damage in rail steel. Though the high amplitude and energy distribution can be used to identify these events, other characteristics such as frequency spectra and multiparametric analysis are still needed to distinguish these brittle fracture events from other sources signals, particularly if AE monitoring of rail in service is desired.

The typical waveforms and Fast Fourier Transformed (FFT) spectra for the high amplitude and low amplitude events during FCG are shown in Figs. 7a, b, c, d respectively. The burst type waveform can be observed for both signals in Fig. 7a, c, which is usually the fingerprint for crack propagation events. The FFT spectra for these two types of signals in Fig. 7b, d show that they all have a peak frequency at

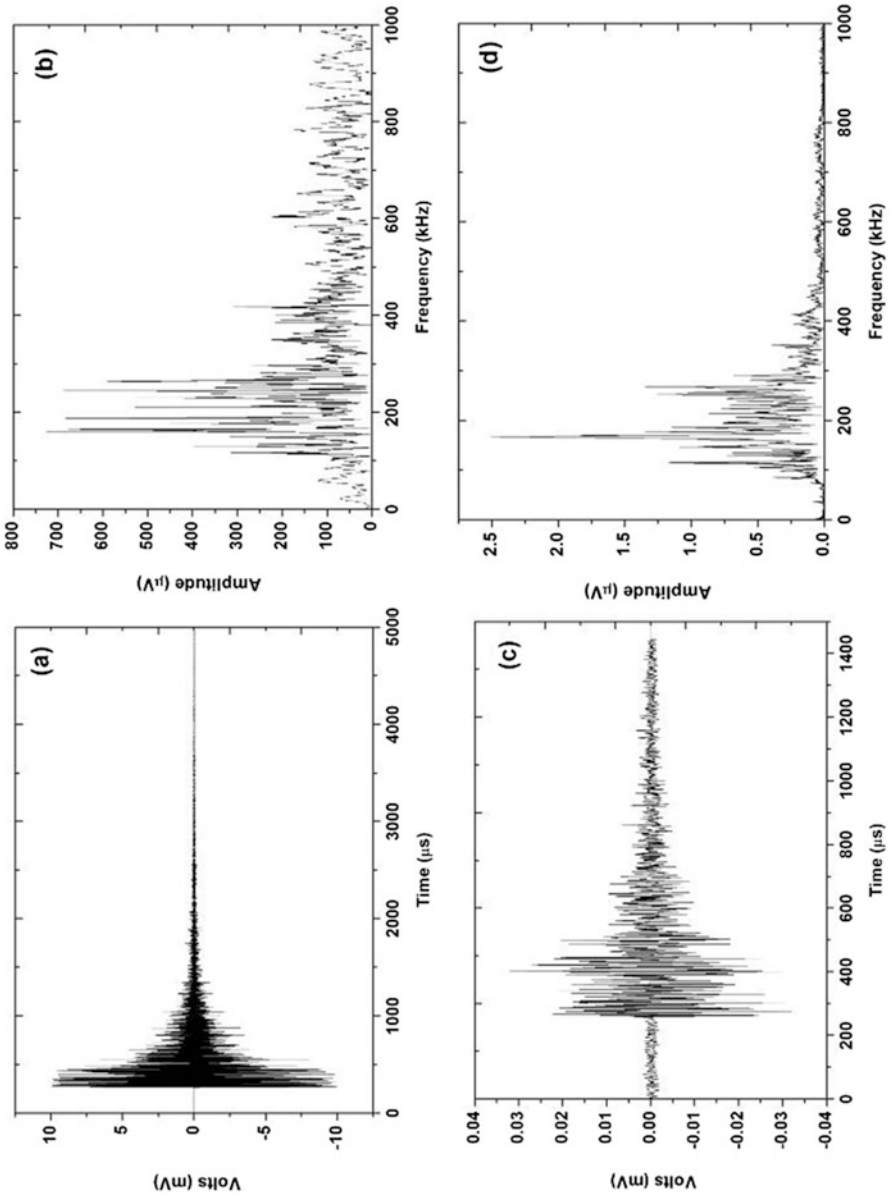

Fig. 7 Typical waveforms and FFT spectra for (**a**, **b**) high amplitude events, and (**c**, **d**) low amplitude events

around 150 kHz. However, compared to the low amplitude events, the high amplitude events also exhibit much higher amplitude at frequencies around 250 kHz and above 400 kHz. The high frequency components in high amplitude events can be attributed to the fast energy release of brittle fracture. Khamedi et al.

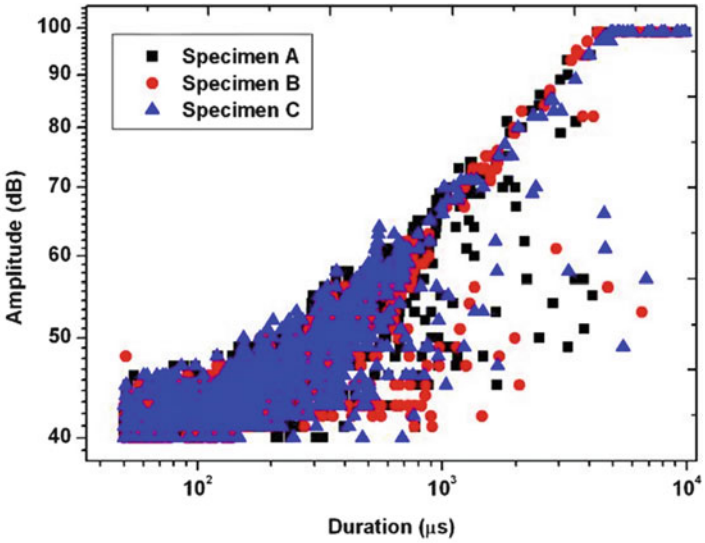

Fig. 8 Relationship between AE amplitude and duration

studied the AE spectra during the fracture process of dual phase steels, and suggested that the components in the frequency ranges of 125–250 and 500–625 kHz could be attributed to ferrite deformation and martensite phase fracture [18], which is in agreement with the present study except that for rail steels it will be pearlite fracture.

A multiparametric analysis of AE amplitude and duration was performed and the typical results are shown in Fig. 8. It can be seen that most high amplitude AE events in the range beyond about 65 dB amplitude and below 99 dB are concentrated at long duration, and showing a linear relationship between amplitude and duration on logarithmic axes. The slope of the linear fitting of this correlation is about 0.23. The results are highly repeatable in all three specimens, thus suggesting the relationship is reliable for identifying the high amplitude events and predication of the extremely high amplitude (99 dB) brittle fracture events during FCG. It should be noted that the amplitude—duration relationship of the low amplitude events and some scatter in the events distributed below 70 dB causes deviation in this linearity, and that this is similar to the results of a ductile steel in Ref. [11], which suggests they are plastic events rather than brittle fracture events during FCG.

4 Conclusions

The fatigue and AE characteristics during the FCG process in a rail steel were investigated in this study. The results show that the AE technique is capable of acquiring and identifying brittle fracture events during FCG of rail steel. The results obtained from the present study can be summarized as follows:

1. The brittle fracture occurred during FCG of rail steel could be directly related to the high amplitude (>70 dB) and high energy (>2000) AE events, which also leads to high dE/dN even at lower ΔK level. The relation between dE/dN and ΔK may be not suitable for fatigue life predication in rail steel, even though it is used for ferrite steels, due to its high variability.
2. The AE energy and fractography results showed that brittle fracture occurred intermittently during FCG for all specimens. It indicates that brittle fracture may be induced by accumulated fatigue damage and can be quantitative characterized by AE energy.
3. The brittle fracture AE events exhibited characteristic spectrum with high frequency components and specific amplitude–duration relationship, which can be used to identify these events from other sources.

References

1. H.A. Aglan, Z.Y. Liu, M.F. Hassan, M. Fateh, Fatigue crack growth behavior of rail steel under mode I and mixed mode loadings. J. Mater. Process Tech. **151**, 268–274 (2004)
2. D.O. Harris, H.L. Dunegan, *Continuous Monitoring of Fatigue-Crack Growth by Acoustic-Emission Techniques, Experimental Mechanics*, Third SESA International Congress on Experimental Mechanics, May 13–18, 1973 (Los Angeles, CA, 1973), pp. 71–81
3. A. Berkovits, D. Fan, Study of fatigue crack characteristic by acoustic emission. Eng. Fract. Mech. **51**, 401–416 (1995)
4. T.M. Roberts, M. Talebzadeh, Acoustic emission monitoring of fatigue crack propagation. J. Constr. Steel Res. **59**, 695–712 (2003)
5. T.M. Roberts, M. Talebzadeh, Fatigue life prediction based on crack propagation and acoustic emission count rates. J. Constr. Steel Res. **59**, 679–694 (2003)
6. J. Yu, P. Ziehl, B. Zárate, J. Caicedo, Prediction of fatigue crack growth in steel bridge components using acoustic emission. J. Constr. Steel Res. **67**, 1254–1260 (2011)
7. M. Papaelias, C. Roberts, C.L. Davis, A review on non-destructive evaluation of rails: state-of-the-art and future development. J. Rail Rapid Transit. **222**, 367–383 (2013)
8. M.N. Bassim, S.S.T. Lawrence, C.D. Liu, Detection of the onset of fatigue crack growth in rail steels using acoustic emission. Eng. Fract. Mech. **41**, 207–214 (1994)
9. N.A. Thakkar, J.A. Steel, R.L. Reuben, Rail–wheel interaction monitoring using acoustic emission: a laboratory study of normal rolling signals with natural rail defects. Mech. Syst. Signal Pr. **24**, 256–266 (2010)
10. Z.F. Wang, Z. Zhu, W. Ke, Behavior of acoustic emission for low-strength structural steel during fatigue and corrosion fatigue. Metall. Trans. B **22**, 2677–2680 (1991)
11. H.L. Chen, J.H. Choi, Acoustic emission study of fatigue cracks in materials used for AVLB. J. Nondestruct. Eval. **33**, 133–151 (2004)
12. Z. Han, H. Luo, Y. Zhang, J. Cao, Effects of micro-structure on fatigue crack propagation and acoustic emission behaviors in a micro-alloyed steel. Mater. Sci. Eng. A **559**, 534–542 (2013)
13. S. Suresh, *Fatigue of materials* (Cambridge University Press, Cambridge, 1991)
14. E.T. Ng, G. Qi, Material fatigue behavior characterization using the wavelet-based AE technique – a case study of acrylic bone cement. Eng. Fract. Mech. **68**, 1477–1492 (2001)
15. J. Yu, P. Ziehl, Stable and unstable fatigue prediction for A572 structural steel using acoustic emission. J. Constr. Steel Res. **77**, 173–179 (2012)

16. M. Rabiei, M. Modarres, Quantitative methods for structural health management using in situ acoustic emission monitoring. Int. J. Fatigue **49**, 81–89 (2013)
17. O.N. Romaniv, K.I. Kirillov, Y.V. Zima, G.N. Nikiforchin, Relationship of acoustic emission to the kinetics and micromechanism of fatigue failure of high-strength steel with a martensitic structure. Mekh. Mater. **23**, 51–55 (1987)
18. R. Khamedi, A. Fallahi, A.R. Oskouei, Effect of martensite phase volume fraction on acoustic emission signals using wavelet packet analysis during tensile loading of dual phase steels. Mater. Des. **31**, 2752–2759 (2010)

Experimental Research on Acoustic Emission Monitoring of Dynamic Corrosion on a Simulated Tank Floor

Ying Zhang, Chengzhi Li, Wei Li, Feng Qiu, and Yongtao Zhao

Abstract In this work, an acoustic emission monitoring experiment of a tank floor plate was conducted in a laboratory simulation of practical production conditions. In addition to analysis of the corrosion mechanism, emission signals were collected in experiments using acoustic emission signal parameter analysis, and the acoustic emission characteristics of the tank floor corrosion process were obtained under different working conditions. Thus this chapter provides a basis for acoustic emission testing and evaluation in the field, with improved reliability.

1 Introduction

Among the various types of storage tank corrosion, corrosion on the tank floor is both the most common and the most serious. As this corrosion occurs because the lower surface is in contact with the foundation, it is typically not present on the upper surface. Thus the maintenance and detection of tank floor corrosion is especially difficult [1, 2]. Traditional detection methods, which require the tank to be shut down and replaced or the tank bottom cleaned, or involve a point-by-point scan and inspection, are time-consuming and carry a high cost of manpower and detection expense. In contrast, the recently developed acoustic emission method is an online, highly efficient, economical, and internationally recognized detection technique for large-scale atmospheric metal storage tank floors. Earlier tank floor corrosion experiments using acoustic emission characteristics were able

Y. Zhang (✉) • C. Li • W. Li • F. Qiu
College of Mechanical Science and Engineering, Northeast Petroleum University, Daqing 163318, China
e-mail: aezy163@163.com

Y. Zhao
Security Environmental Protection Technology Research Institute China Petroleum Group, Beijing 100102, China
e-mail: zhaoyongtao@petrochina.com.cn

G. Shen et al. (eds.), *Advances in Acoustic Emission Technology*, Springer Proceedings in Physics 179, DOI 10.1007/978-3-319-29052-2_33

to monitor only static corrosion, making it difficult to reflect the true state of tank floor corrosion [3]. In actual production processes, however, tanks will experience different operating conditions, such as cleaning, feeding, and discharging. These conditions all affect the state of corrosion on the tank floor, for which the corresponding acoustic emission signals are not yet well known [4, 5]. Therefore, in this work, changes in operating conditions caused by cleaning, oil feeding/discharging, and liquid level changes in the tank in actual production processes were simulated to mimic changes in the field, and acoustic emission monitoring was performed on our tanks in different settings (idle tank, used tank, tank floor stirring, partial destruction of corrosion products on the tank floor) under laboratory conditions. Using the idle tank emission signal as a reference value, we conducted a comparison analysis of the other three acoustic emission signals. Therefore, through the analysis of acoustic emission signal characteristics under the four operating conditions, this work explores how changes in operating conditions influence corrosion of the tank floor.

2 Experimental Study

2.1 Tank Floor Corrosion Acoustic Emission Detection System

The storage tank simulation is shown in Fig. 1. The experiment uses a third-generation all-digital SAMOS system (Physical Acoustics Corporation, USA), an R3α sensor, a 2/4/6 preamplifier with 1–1200 kHz filter range and 35 dB gain, and vacuum grease as couplant. The simulated storage tank material is Q235 carbon structural steel with dimensions of $\varphi 600 \times 700 \times 4$ mm. The rust in the tank bottom is removed with sandpaper, and the inner and outer walls of the tank are evenly coated with anti-corrosion paint. Based on the material and the structure size, we chose acoustic emission system parameter settings as shown in Table 1.

2.2 Experimental Program

Under laboratory conditions, acoustic emission monitoring tests are conducted for four storage tank simulations, with tanks numbered from 1 to 4. The test data were monitored 6 h every day for 29 days. The sensor arrangement is shown in Fig. 2. Three sensors are arranged around 60 mm of the tank bottom wall so that the sound transmitting signal can be effectively received by the sensor. Storage tank 1 (sensor numbers 1, 2, 3), storage tank 3 (sensor numbers 7, 8, 9), and storage tank 4 (sensor numbers 7, 8, 9) are new, while storage tank 2 (sensor numbers 4, 5, 6) has been used and has undergone rust cleaning. The medium in the tank is clean water, and

Fig. 1 Simulated tank

Table 1 Parameter settings for the acoustic emission system

Threshold (dB)	Sampling rate (K/s)	PDT (μs)	HDT (μs)	HLT (μs)
35	1024	300	600	600

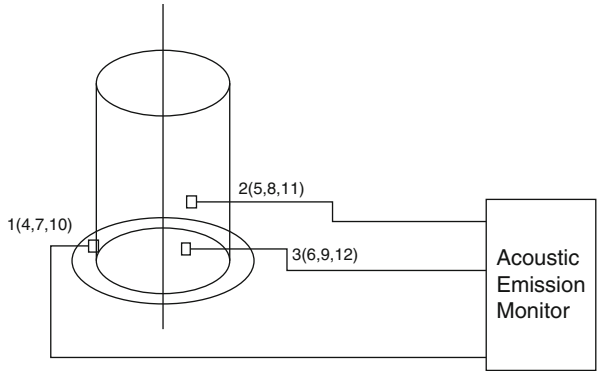

Fig. 2 Schematic of the sensor arrangement

the liquid level is 60%. All the acoustic emission monitoring experiments are performed after the medium is stable. In the first set of experiments, the acoustic emission signals of storage tanks 1 and 2 are monitored to analyze the effect of the tank cleaning treatment on the corrosion of the bottom plate. The second group of experiments entails monitoring the acoustic emission signals of storage tank 3 to analyze the impact of a disturbance to operations on the medium in the tank after the acoustic emission signal appears to be in a steady state. In the third set of

experiments, the acoustic emissions of storage tank 4 are monitored for the purpose of analyzing the effects of local scouring with injected liquid after a change to the original operating conditions from local damage to the storage tank bottom.

3 Analysis of Experimental Results

3.1 Statistical Analysis of Corrosion Signal of Bottom Plate Under Different Operating Conditions

As shown in Fig. 3, among the four storage tanks, sensors 3, 4, 7, and 11 receive slightly higher clashing figures than the other channels of the respective tanks, indicating that there are many acoustic emission signals near them. Therefore, we select the data of these four sensors for the experimental analysis.

Table 2 presents the total parameter ranges over 29 days (6 h/day) of monitoring the received acoustic emission signals. From the amplitude statistics we can see that the signal amplitude of sensor 6 is significantly higher than that of sensor 1, and the signal amplitudes of sensors 7 and 11 are slightly higher than that of sensor 1. From the range of the storage tank energy we can see that the highest signal energy values for sensors 1 and 11 are obviously lower than the maximum for sensor 6, while the energy of sensor 7 is slightly lower than that of sensor 1. This implies that the corrosion activity on the bottom plate of tank 2 is much greater than that of tank 1, and the corrosion activity for tanks 3 and 4 is slightly higher than for tank 1, which is in a static operating condition.

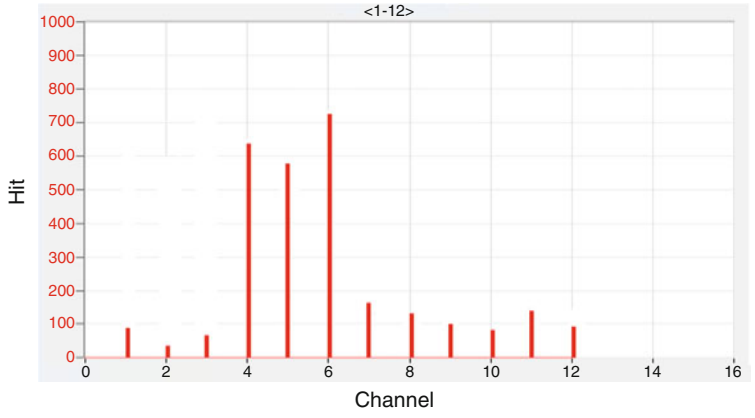

Fig. 3 Hit-channel chart

Table 2 The range of AE signal parameters in different working conditions

Tank no.	Working conditions	Sensor no.	Range (dB)	Impact count	Energy
1	Static state	1	35–45	9–98	1–827
2	Use history	6	35–84	73–730	1–596
3	Disturbance to the floor	7	35–56	6–150	1–817
4	Damage to the bottom plate	11	35–67	16–172	1–652

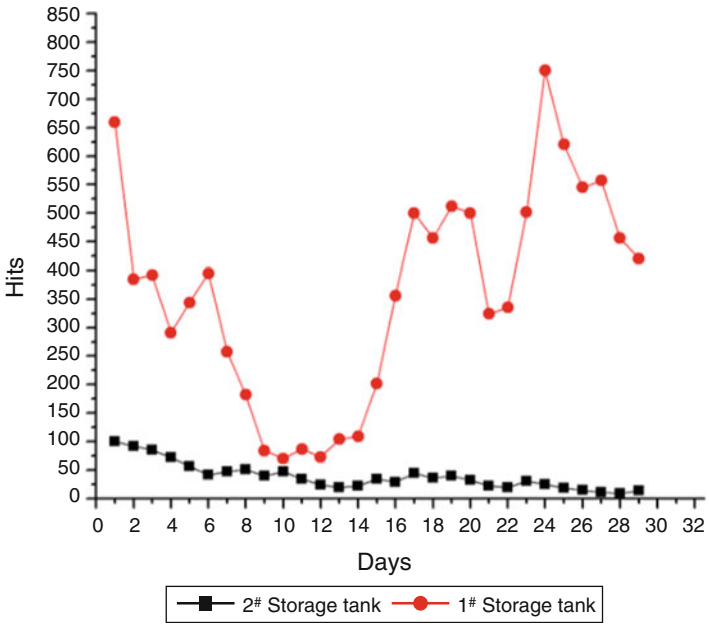

Fig. 4 Corrosion process diagram for floors of tanks 1 and 2

3.2 Analysis of the Corrosion Process in Different Working Conditions

3.2.1 Corrosion Acoustic Emission Characteristics of New Storage Tanks vs. Cleaned Storage Tanks

The first set of experiments is shown in Fig. 4, with comparative analysis of the effect of tank cleaning on the corrosion of the bottom plate. As the picture shows, the impact number is greater in tanks 1 and 2 in the initial corrosion stage, but the initial corrosion of tank 2 is more obvious than that of tank 1. As the corrosion process continues, the impact number of the bottom plate of tank 1 gradually stabilizes, while the impact number of tank 2 shows an increasing trend. According to the corrosion mechanism of metal materials, the impact number is greater in the initial corrosion period because the substrate has no corrosive products to protect

the corrosion reaction. However, after a period of corrosion, the corrosion products on the surface of the substrate have a protective effect on the substrate, so the corrosion rate decreases. Tank 2 has suffered corrosion in the past, and some residual corrosion products remain even after cleaning of the surface. The substrate surface is not smooth, so local corrosion forms easily. The combination of the formation of corrosion products and the poor matrix enable peeling and acceleration of corrosion. However, the surface of tank 1 is complete, and the newly formed corrosion products are closely related to the matrix, which protects the matrix, so corrosion tends to be flat.

3.2.2 Comparison of Acoustic Emission Characteristics Between the Static Stage and post- Perturbation

The second set of tests is shown in Fig. 5. These are the experience drawings of acoustic emission signals for simulation tests of the disturbance condition. From the picture we can see that tank 3 in a static state receives a large number of impacts in the early stage of corrosion and tends to flatten as time passes. After the perturbation, the impact number is obviously increased, and then it moderates with time. This is due to the loosening of corrosion products on the tank bottom after the disturbance, and the second contact of the corrosion solution with the metal forms a certain degree of secondary corrosion, but the magnitude is modest and the effect is small, and the new corrosion product is quickly formed, leaving the corrosion in a relatively stable state.

3.2.3 Comparison of Acoustic Emission Characteristics of the Tank Bottom Plate Before and After Damage

The third set of tests is shown in Fig. 6. These are the experience drawings of acoustic emission signals for the damage condition of local corrosion products. From the diagram we can see that the acoustic emission hit number increases significantly after local corrosion damage to the bottom plate of tank 4, and the process of higher hit numbers continues for a long period and then gradually flattens out. This is because the corrosion products caused by local damage are loosened after the long period of immersion in water, and the matrix is then again exposed to the corrosive medium, which accelerates the local/regional corrosion process, with an increase in hit numbers. New corrosion products are generated and cover the base plate over time; the corrosion process flattens out again, and the acoustic emission signal stabilizes.

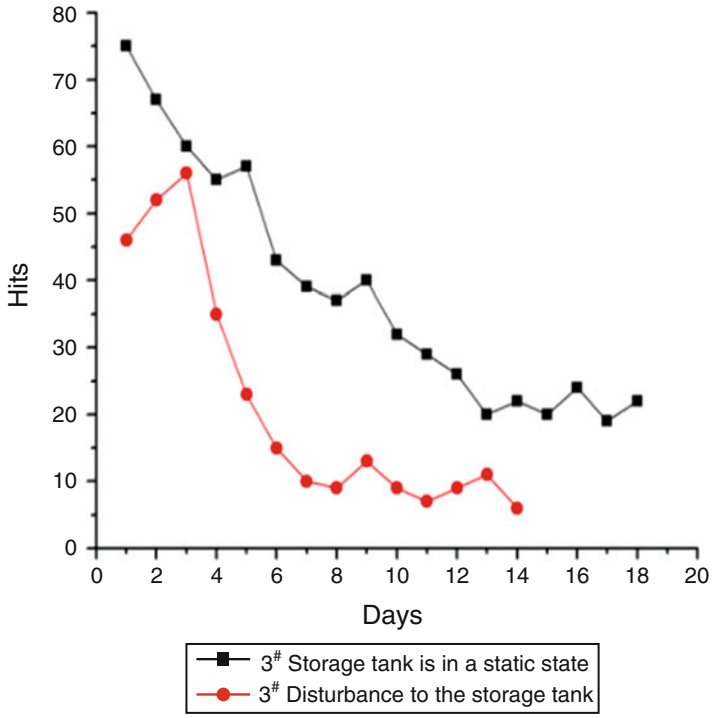

Fig. 5 Corrosion process diagram for tank 3 before and after change in working condition of tank floor plate

3.3 Amplitude Analysis

Samples were collected from the four tanks every 6 h during monitoring over 29 days. The test results show that the acoustic emission signal rarely decreases in the limited transmission range because of the small volume of the test tank. Signals emitted by the acoustic source are thus effectively received by the sensors. Stable corrosion signals can be divided into two parts: one with a range of 40–55 dB, low signal amplitude, and continuous signal as the base for corrosion; and the other with a range of 55–80 dB, high signal amplitude, and discrete distribution, indicated the respective loosening, rupture, and stripping processes of the corrosion layer.

The first set of tests is shown in Figs. 7 and 8, with a comparative analysis of the influence of tank treatment on bottom plate corrosion. The representative early and stable corrosion stages of tanks 1 and 2 are chosen for amplitude comparison. The experiment compares the amplitude parameters of the corrosion on the first and 29th days to distinguish the influence of two kinds of working conditions on storage tank floor corrosion. From the experience drawing of the first day, it is easy to observe that the signal amplitude for both tanks is low and the signals are

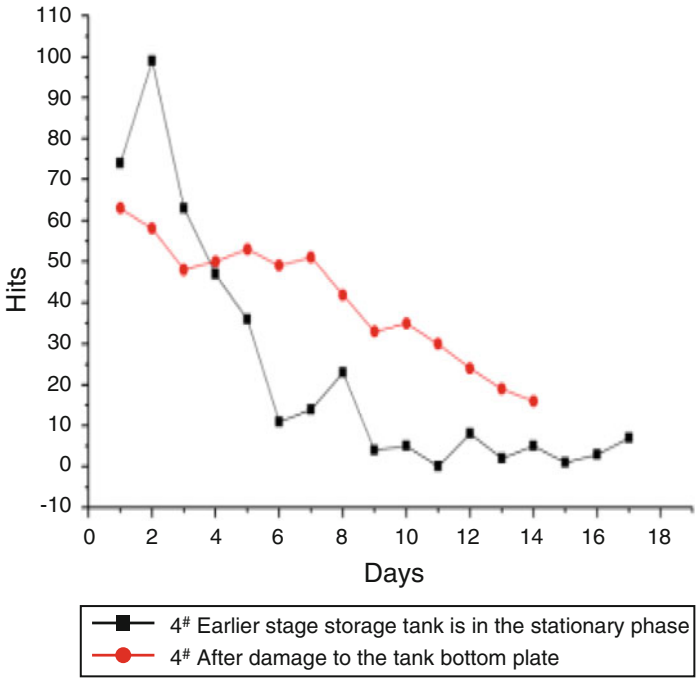

Fig. 6 Corrosion process diagram for tank 4 before and after change in working condition of tank floor plate

continuous; however, the increase in the corrosion signal in the initial stage in tank 2 is greater than that of tank 1, which reveals that at the beginning of the corrosion process, the corrosion activity is higher in tank 2 than tank 1. Monitoring on the 29th day shows that after a long period of corrosion, the signal amplitude of tank 2 is significantly increased, and some of the signals are distributed in the region of 55–80 dB, indicating that a severe corrosion reaction occurs in the base plate. However, there are few acoustic emission signals in 1 tank 1, which implies that the corrosion flattens out.

The second set of experiments is shown in Fig. 9. Here, the magnitude of the change in tank 3 is compared across three stages: the first phase is the first day of the stationary state (initial corrosion); the second stage is the 14th day, at the static stage before the disturbance of the base (stable corrosion period); the third phase is the 16th still day after resumption of the disturbance. The amplitude history across stages indicates that tank 3 has more low-amplitude signals at the beginning of the corrosion process, primarily basic corrosion signals. Over time, the signal decreases and corrosion is mitigated. The signal is increased after the disturbance, and signal amplitude also increases. Some of the signals are distributed in the region of 55–80 dB, which indicates that the disturbance loosens the corrosion product to a certain degree, and the peeling accelerates the corrosion of the bottom plate.

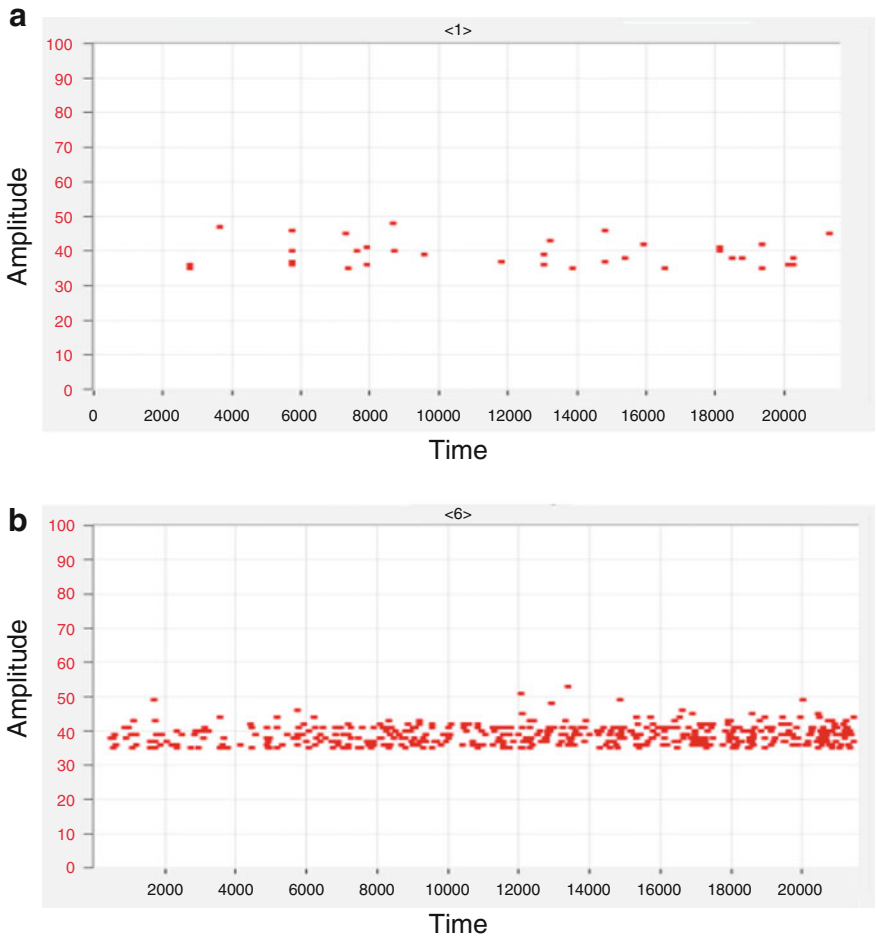

Fig. 7 (**a**) The first day of storage tank 1 monitoring. (**b**) The first day of storage tank 2 monitoring

The third test group is shown in Fig. 10. Here, the magnitude of the signals in tank 3 is compared across three stages: the first phase comprises the first day of the stationary state (initial corrosion); the second stage is the 14th day, representing the static stage before the disturbance to the base (stable corrosion period); and the third phase is the 16th still day after the resumption of the disturbance. The history of the three amplitude demonstrates that from the initial to the stable corrosion stage, the amplitudes diminish and signals decrease. When the corrosion reaches a stable period, associated with the static stage, disturbance is applied to part of the base, and we find that signal amplitude increases and is distributed mainly in the region of 55–80 dB. This indicates that regional damage to the bottom plate ruptures the passive coating, and the separation of the corrosion layer results in the exposure of regional metal, which in turn undergoes further erosion.

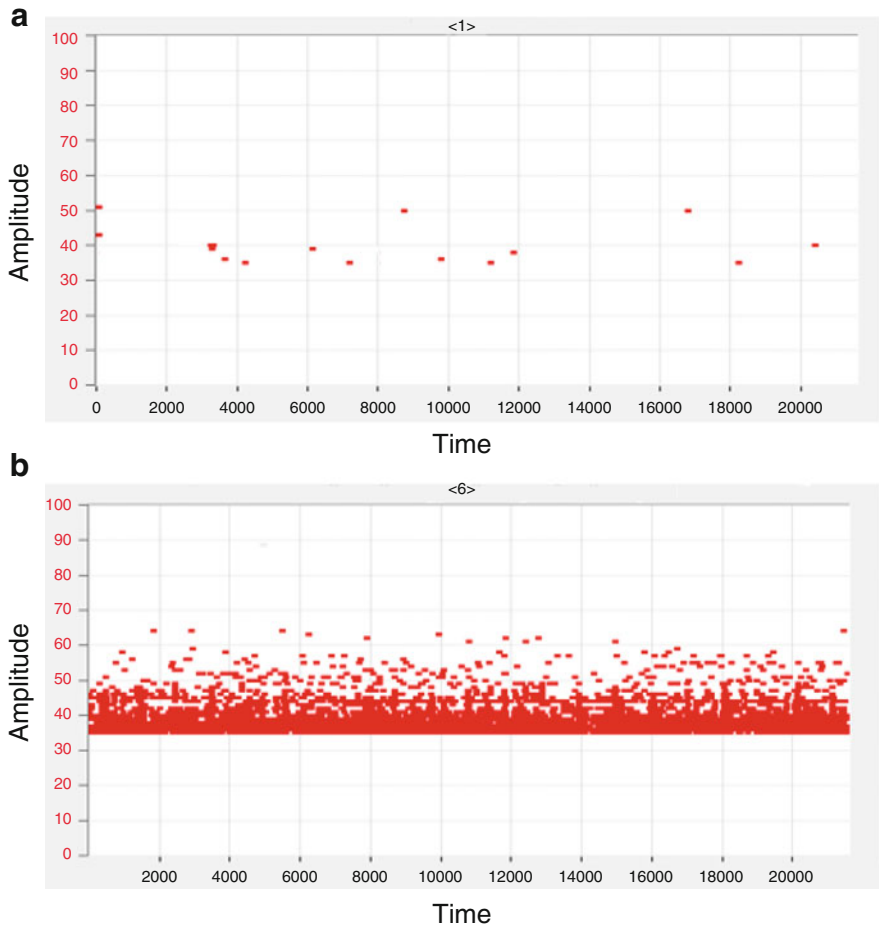

Fig. 8 (**a**) The 29th day of storage tank 1 monitoring. (**b**) The 29th day of storage tank 1 monitoring

3.4 Correlation Analysis

The corrosion signal amplitude and energy-related characteristics of the three test groups are then analyzed. From the signal energy association graph, we can see that a stable corrosion signal is divided into two amplitude categories: class A, comprising 35–45 dB, and class B, comprising 45–65 dB. In Fig. 11, the energy–amplitude correlation diagram for the first day of the first group shows that tanks 1 and 2 are at the initial stage of corrosion, with corrosion signals concentrated primarily in the class A range of 35–45 dB. A portion of the signal energy in storage tank 1 is higher than that in tank 2, but the storage tank 2 signal energy is obviously greater than the tank 1 signal energy. The Class A signal amplitude is relatively

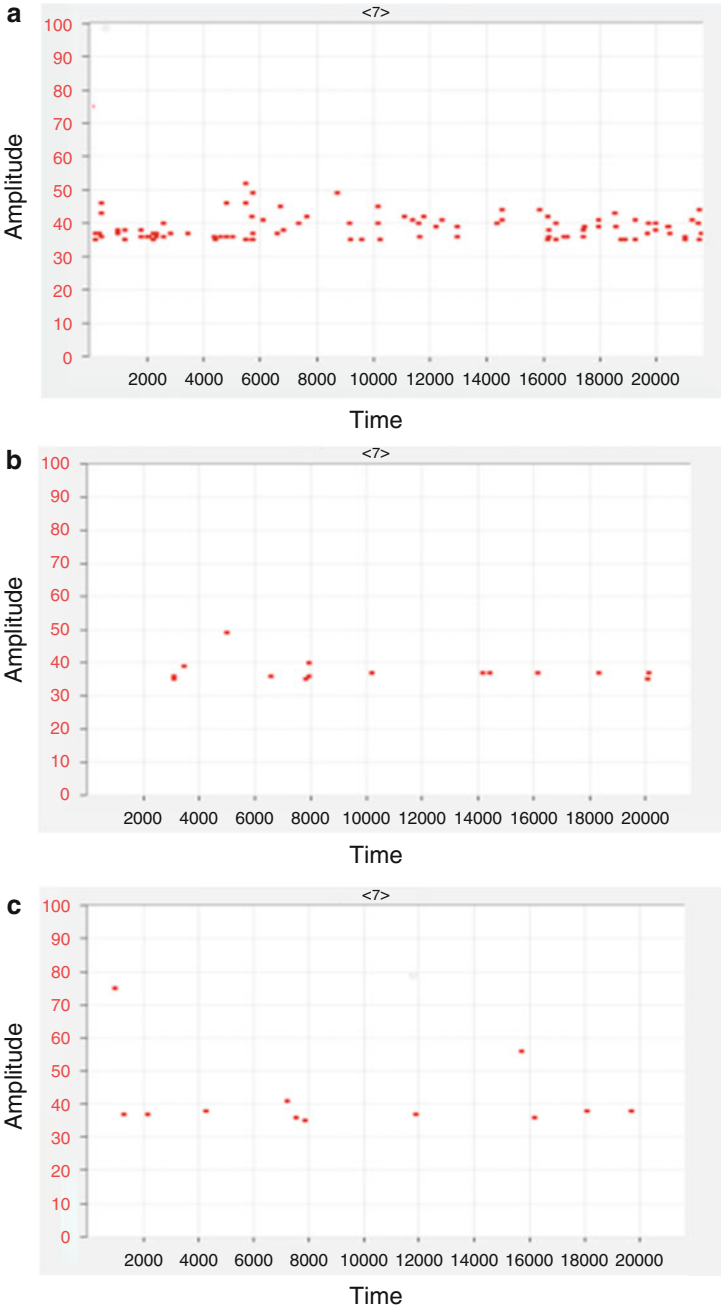

Fig. 9 Corrosion process diagram for tank 3 before and after change in working conditions. (**a**) Initial stage of stationary phase. (**b**) Stable period of stationary phase corrosion. (**c**) The corrosion process after disturbance

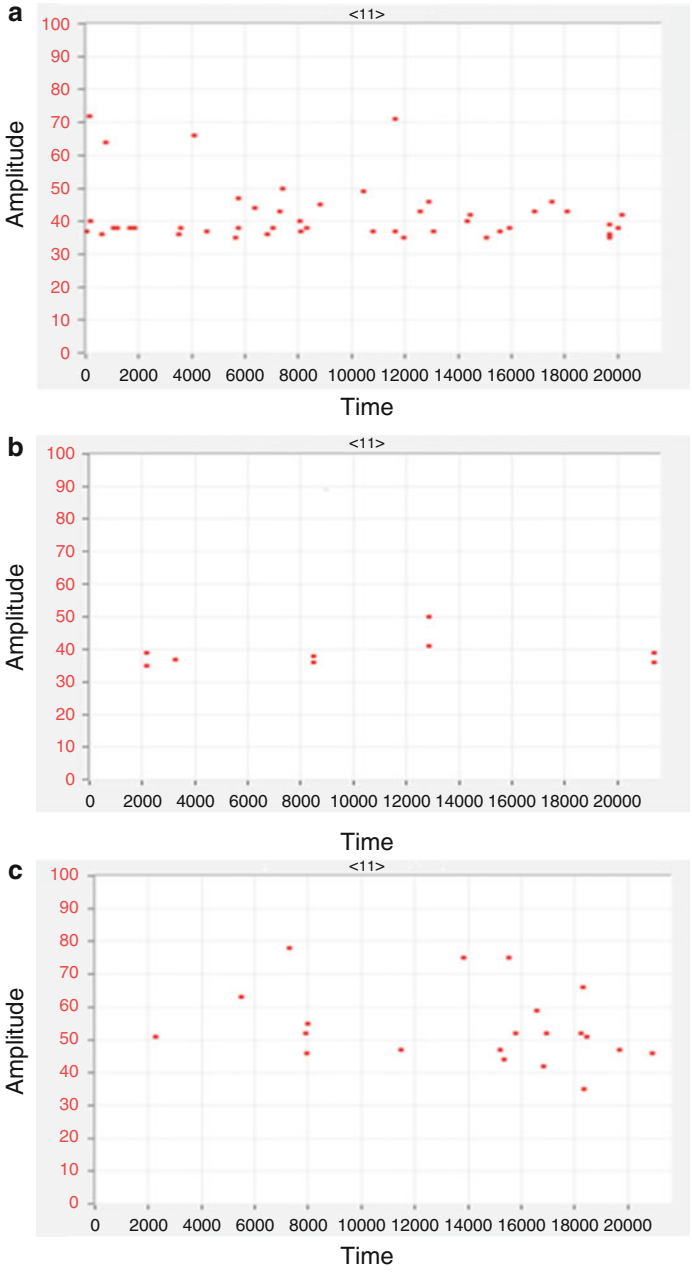

Fig. 10 Corrosion process diagram for tank 4 before and after change in working conditions. (**a**) Initial stage of stationary phase corrosion. (**b**) Stable period of stationary phase corrosion. (**c**) Plate corrosion process after local failure

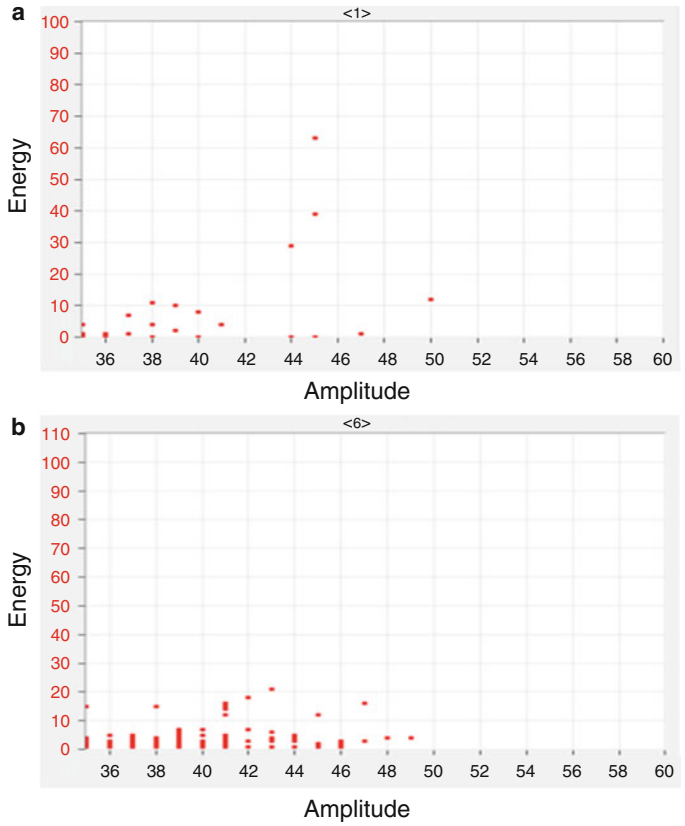

Fig. 11 (**a**) Energy–amplitude correlation diagram for storage tank 1 monitoring on the first day. (**b**) Energy–amplitude correlation diagram for storage tank 2 monitoring on the first day

small and distributed in a low-amplitude range, but its energy is higher, as the class A signals correspond to the base of stable corrosion. This stage comprises the process of corrosion, including the electrochemical reaction, the accumulation of corrosion products, and liquid infiltration of the corrosion layer. The entire process is relatively stable, with no dramatic signal changes. In Fig. 12, the energy–amplitude correlation diagram for the 29th day illustrates that after a longer period of storage tank corrosion, the energy and amplitude of tank 2 signals exhibit an arc distribution. With increased amplitude, the corrosion signal energy also increases. In addition to the lower-energy class A signals, a large number of higher-energy class B signals are distributed, mainly in the high-amplitude region corresponding to the loosening of the corrosion product, the bubble burst, and other corrosion signal energy release processes, although the total number of these signals is far less than that in the low-amplitude signal region. In addition, very few acoustic emission signals are present in tank 1. The low signal energy and high amplitude indicate that

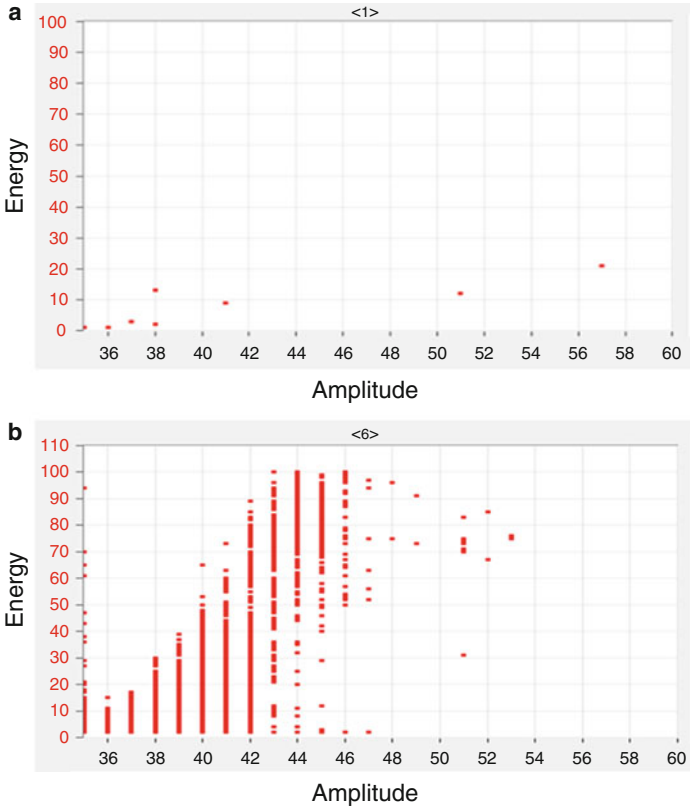

Fig. 12 (**a**) Energy–amplitude correlation diagram for storage tank 1 monitoring on the 29th day. (**b**) Energy–amplitude correlation diagram for storage tank 2 monitoring on the 29th day

the corrosion is stable, and the corrosion signal is stronger and more active in tank 2 than tank 1.

The second group of experiments is shown in Fig. 13. The energy–amplitude correlation diagram shows a comparison of the three stages of the three storage tanks: the first stage, first day at rest (early corrosion); the second stage, 14th day at rest (corrosion stability period) prior to the disturbance of the base plate; and the third stage, 16th day after disturbance recovery. The diagram reveals that the energy count of the initial corrosion period is greater than that of the corrosion stability period, but the amplitude is lower. In addition, the energy of the storage tank is increased after the tank disturbance, and the amplitude is higher than that of the stationary phase, although still distributed mainly in the A region. The degree of change is limited, primarily because the disturbance only loosens the corrosion product, and peeling does not occur. Thus, the disturbance will affect the bottom plate corrosion, but the change will be small and the effect limited.

The third group of experiments is shown in Fig. 14, and the energy–amplitude correlation diagram for the three stages of storage tank 4 are compared and

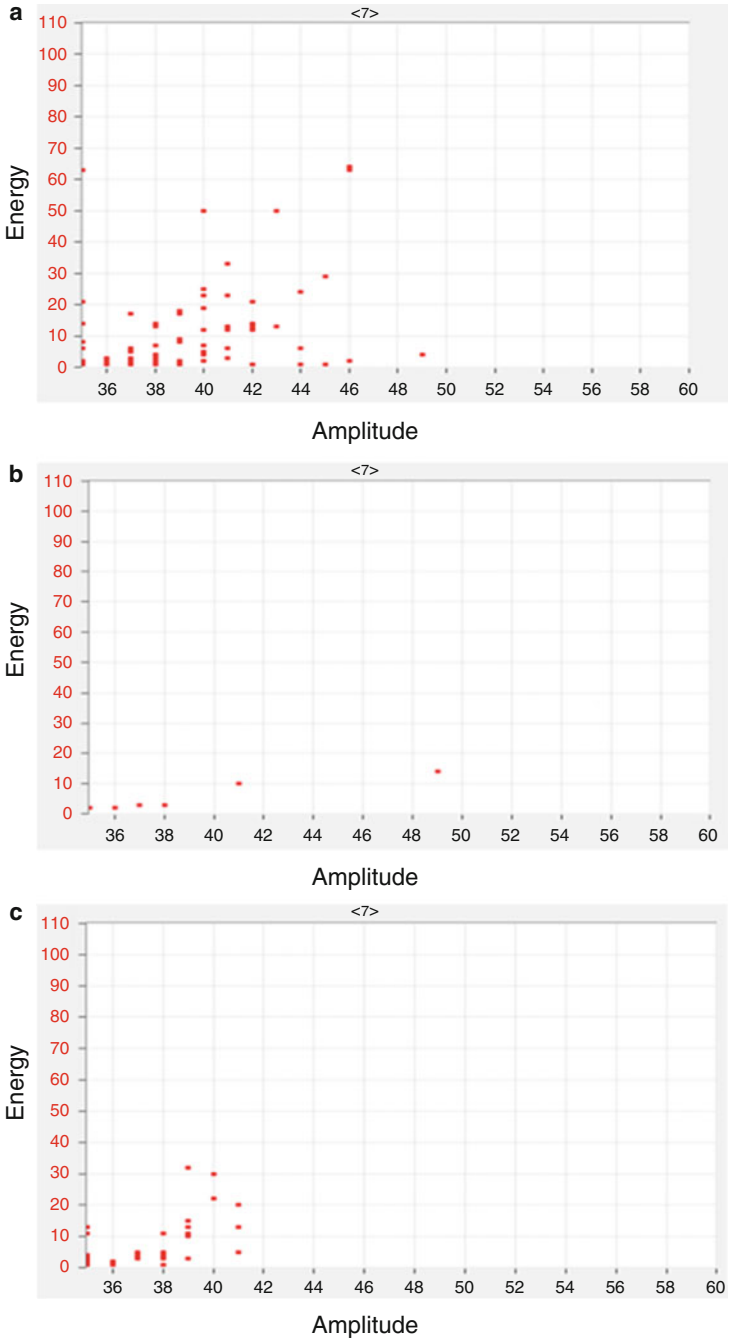

Fig. 13 Energy–amplitude correlation diagram for storage tank 3 before and after change in working conditions. (**a**) Initial corrosion period of the stationary phase. (**b**) Stable corrosion period of the stationary phase. (**c**) Corrosion process after the disturbance

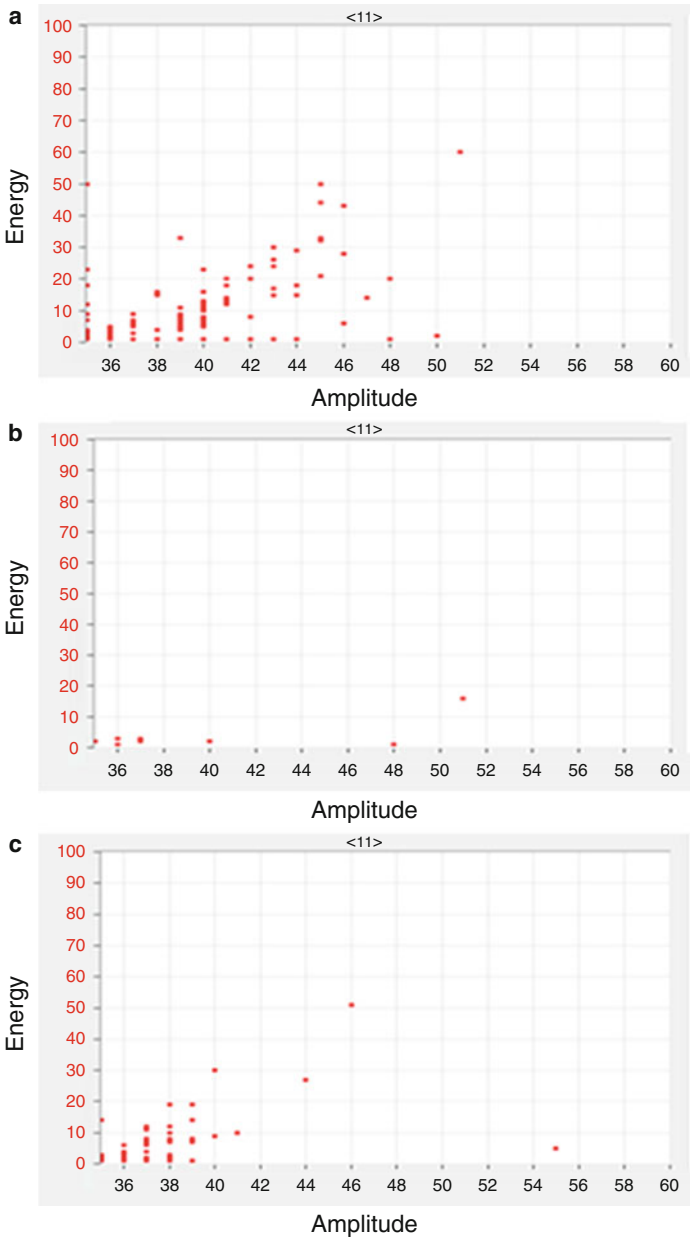

Fig. 14 Energy–amplitude correlation diagram of storage tank 4 before and after changes in working conditions. (**a**) Initial corrosion period of the stationary phase. (**b**) Stable corrosion period of the stationary phase. (**c**) Corrosion process of the tank bottom plate after local damage

analyzed, as follows: first stage, first day at rest (early corrosion); second stage, 14th day at rest (corrosion stability period) prior to local damage to the base plate; third stage: 16th day after recovery from the damage. The diagram shows that after the local damage to the base plate, the total energy clearly increases, the amplitude is increased, and a portion of the signal is distributed in the B region. This is mainly because the local damage to the base plate causes the oxide film to rupture and the corrosion product to peel off, and the body is exposed to the medium, leading to corrosion. This explains why the damage to the bottom plate results in a greater degree of change in the impact of the medium on corrosion of the base plate.

4 Conclusions

1. Under different working conditions, the bottom plate can exhibit different acoustic emission phenomena (different acoustic emission signal characteristics) corresponding to the corrosion state of the tank bottom. Through acoustic emission monitoring, we can better understand the influence of the change in working conditions on bottom plate corrosion.
2. Compared with new storage tanks, the medium in old storage tanks causes more severe bottom plate corrosion. The bottom plate of a tank with a history of use shows a U-type distribution as time increased. The energy and amplitude association diagram shows that corrosion acoustic emission signals have an arc distribution: with increasing time, the impact number of the new tank decreases exponentially, with fewer signals and more sporadic distribution in association with energy and amplitude.
3. The influence of the medium on bottom plate corrosion is altered by the disturbance to the storage tank, but the magnitude of the change is not large and has little influence on the corrosion process. As the energy is gradually reduced, the amplitude increases. After the disturbance, the impact number increases, but as the monitoring duration increases, the impact number is reduced, and the energy is higher than in the static state.
4. Local damage to the bottom plate will accelerate corrosion. After the local corrosion products of tank bottom plates are destroyed, the impact number is obviously higher than that of a static state, with significantly higher energy and amplitude. As monitoring time increases, the impact number shows an exponential decline. However, the acoustic emission signal is reduced at a slower rate than at rest.

Acknowledgements The authors would like to thank the China National Petroleum Corporation Science and Technology Development Project (No. 2014D-460203) and the Northeast Petroleum University Innovation Foundation for Postgraduate (No. YJSCX2014-024NEPU) for their financial support.

References

1. Z. Yanbing, G. Jianping, et al., Tank corrosion acoustic emission test for a long period of time. J. Nondestr. Test. **30**(2), 32–36 (2013)
2. A.V. Sokolkin, I.Y. Ledev, Prospects of applications of acoustic emission methods to testing bottoms of tanks for oil and oil derivatives. Russ. J. Nondestr. Test. **38**(2), 113–115 (2012)
3. M. Fregonese, H. Idrissi, H. Mazille, L. Renaud, Y. Cetre, Initiation and propagation steps in pitting corrosion of austenitic stainless steels: monitoring by acoustic emission. Corros. Sci. **43** (4), 627–541 (2001)
4. P. Sosoon, K. Shigeo, K. Kenji, et al., AE source and relation between AE activity and rate of corrosion of oil tank bottom plate on acidic soil. Mater. Trans. **46**(11), 2490–2496 (2012)
5. E.P. Serrano, M.A. Pabio, Application of the wavelet transform to acoustic emission signal processing. IEEE Trans. Process. **44**(5), 1270–1275 (2013)

Part VII
Miscellaneous

Study on the Influence Rule of Residual Stress on Ultrasonic Wave Propagation

Chunguang Xu, Wentao Song, Jianfeng Song, Hongyu Qian, and Hanming Zhang

Abstract Residual stress has significant impacts on the performance of the mechanical components, especially on its strength, fatigue life, corrosion resistance, and dimensional stability. In this chapter, based on acoustoelasticity theory, the ultrasonic linear detection method of residual stress and the nonlinear detection method are analyzed in theory. In the study of ultrasonic linear detection method, the time of longitudinal wave propagation along the stress direction and shear wave with a propagation direction perpendicular to the stress direction and a polarization direction parallel to the stress direction are used to characterize the stress value. In the study of ultrasonic nonlinear detection method, ultrasonic nonlinear coefficient of second order and third order is used to characterize the stress. To build experimental systems to contrast the detection results of linear method and nonlinear method, it shows that the two methods have good agreement. At last, the linear and nonlinear method are applied to field detection of residual stress, and achieved good results.

1 Introduction

The engineering properties of materials and structural components, notably fatigue life, distortion, dimensional stability, corrosion resistance, and brittle fracture, can be considerably influenced by residual stresses [1]. Such effects usually bring to considerable expenditure in repairs and restoration of parts, equipment, and structures. Accordingly, residual stress analysis is a compulsory stage in the design of parts and structural elements and in the estimation of their reliability under real service conditions [2].

Determination of the stress state, as well as its magnitude and its depth, which extends inside the material, has been traditionally done by diffraction techniques such as X-ray or synchrotron radiation [3–5]. More recently, a nondestructive method which shows promise for subsurface stress measurement uses acoustic transducer as an ultrasonic strain gauge [6, 7].

C. Xu (✉) • W. Song • J. Song • H. Qian • H. Zhang
School of Mechanical Engineering, Beijing Institute of Technology, Beijing 100081, China
e-mail: xucg@bit.edu.cn

G. Shen et al. (eds.), *Advances in Acoustic Emission Technology*, Springer Proceedings in Physics 179, DOI 10.1007/978-3-319-29052-2_34

This chapter analyzes the ultrasonic linear detection method of residual stress and the nonlinear detection method theoretically, based on the theory of acoustoelasticity. Through the establishment of the experimental system, the detection results of two methods are compared, and they are basically identical.

2 Principle of Residual Stress Testing Method

2.1 Ultrasonic Linear Detection Principle

Acoustoelasticity theory is one of the main bases for ultrasonic stress testing. Acoustoelasticity theory is based on the finite deformation of continuum mechanics to study the relationship between the elastic solid stress state and the macroscopic elastic wave velocity.

Based on the four basic assumptions of acoustoelasticity, the elastic wave formula (acoustoelasticity formula) in stress medium under initial coordinates can be obtained [8–10] using the following equation:

$$\frac{\partial}{\partial \mathbf{X_J}}\left[\left(\delta_{IK}\mathbf{t}^{i}_{\mathrm{JL}} + \mathbf{C_{IJKL}}\right)\frac{\partial \mathbf{u_K}}{\partial \mathbf{X_L}}\right] = \rho^{i}\frac{\partial^2 \mathbf{u_I}}{\partial t^2} \tag{1}$$

where δ_{IK} is Kronecker delta function; ρ^i is the density of the solid in the loading condition; $\mathbf{u_I}$ and $\mathbf{u_K}$ are the dynamic displacements; X_J and X_L are the particle position vectors; $\mathbf{C_{IJKL}}$ is the equivalent stiffness, which depends on the material constant and the initial displacement field; and $\mathbf{t}^{i}_{JL}$ is the Cauchy stress shown in the initial coordinates under the solid loading state.

In the case of homogeneous deformation, (1) can be simplified as follows:

$$\left(\mathbf{C}_{IJKL} + \delta_{IK}\mathbf{t}^{i}_{JL}\right)\frac{\partial^2 \mathbf{u}_K}{\partial \mathbf{X}_J \partial \mathbf{X}_L} = \rho^{i}\frac{\partial^2 \mathbf{u}_I}{\partial t^2} \tag{2}$$

When the solid is isotropic, (2) can be analytically expressed [11]: For the longitudinal wave propagating along the stress direction:

$$\rho_0 V^2_{111} = \lambda + 2\mu + \frac{\sigma}{3\lambda + 2\mu}\left[\frac{\lambda + \mu}{\mu}(4\lambda + 10\mu + 4m) + \lambda + 2l\right] \tag{3}$$

For the shear wave with a propagation direction perpendicular to the stress direction and a polarization direction parallel to the stress direction [12]:

$$\rho_0 V_{133}^2 = \mu + \frac{\sigma}{3\lambda + 2\mu}\left[\frac{\lambda n}{4\mu} + \lambda + 2\mu + m\right] \tag{4}$$

In (3 and 4), λ and μ are the Lame constants; l, m, n are the Murnaghan constants; ρ_0 is the density of the solid before deformation; and σ is the stress applied in one direction (tensile stress is positive and compressive stress is negative).

2.2 Ultrasonic Nonlinear Detection Principle

The existence of stress is closely related to the nonlinear effect of ultrasonic after its transmission through the material, which shows the increase and change of the high-frequency harmonic component of ultrasonic wave.

Using the perturbation method to solve (2), it can be gained [13]:

$$u(x,t) = A_1 \sin(kx - \omega t) - \frac{\beta}{8}A_1^2 k^2 x \cos 2(kx - \omega t) - \frac{\delta}{48}A_1^3 k^3 x[\cos 3(kx - \omega t) + 3\cos(kx - \omega t)] \tag{5}$$

In the formula, ω denotes circular frequency, and k is wave number. The amplitudes of the second and the third formulas in (5) are set to A_2 and A_3 (i.e., the amplitude of the second and the third harmonic of the ultrasonic receiving signal), respectively, and then the following formula is obtained:

$$\beta = \frac{8A_2}{k^2 x A_1^2} \tag{6}$$

$$\delta = \frac{48A_3}{k^3 x A_1^3} \tag{7}$$

By (6) and (7), when the transducer frequency and propagation distance are fixed, the second-order nonlinear coefficient β and the third-order nonlinear δ are directly proportional to A_2/A_1^2 and A_3/A_1^3, respectively. In the process of detection, the relative nonlinear coefficients of the second order and third order are defined, respectively, as:

$$\beta' = \frac{A_2}{A_1^2} = \frac{k^2}{8}\beta x \tag{8}$$

$$\delta' = \frac{A_3}{A_1^3} = \frac{k^3}{48}\delta x \tag{9}$$

Based on the dislocation model, the relationship between the second-order and the third-order nonlinear coefficient and the residual stress can be obtained, respectively [14]:

$$\beta' = -\frac{E_3}{E_2} + \frac{16\pi^2\Omega\Lambda_{dp}h^3R^2(1-\nu)^2E_2^2}{G^2b} + \frac{384\pi^3\Omega\Lambda_{dp}h^4R^3(1-\nu)^3E_2^2}{G^3b^2}\sigma \tag{10}$$

$$\delta' = \frac{384\pi^3\Omega\Lambda_{dp}h^4R^3(1-\nu)^3E_2^3}{G^3b^2} - \frac{5376\pi^4h^5\Omega\Lambda_{dp}R^4(1-\upsilon)^4E_2^3}{G^4b^3}\sigma \tag{11}$$

In the formula, E_2 and E_3 represent the second-order and third-order elastic constants of metal materials; Λ_{dp} is the unipolar dislocation density; L denotes the dislocation chord length; R is the conversion coefficient between shear stress and normal stress; G is the shear modulus; b is the Burgers vector; Ω is the conversion coefficient between shear strain and normal strain.

In the case of the incident ultrasonic amplitude A_1 is large, the second harmonic amplitude A_2 and third harmonic amplitude A_3 caused by the nonlinearity of medium will be large enough. Therefore, the ultrasonic signal of a single frequency can be used to penetrate the specimen with residual stress. After the ultrasonic signal is acquired, through the measurement of A_2, A_3, and the fundamental amplitude A_1, the residual stress values of different ultrasonic nonlinear behaviors can be obtained by formulas (10) and (11).

3 Establishment of Test System

3.1 Ultrasonic Linear Detection System

Based on the principle of ultrasonic linear detection system of residual stress, a linear detection system is established, as shown in Fig. 1. Using one-sending-one-receiving work pattern, the basic hardware of the system consists of industrial control computer, ultrasonic receiving and sending card, data acquisition card, temperature transducer, ultrasonic transducer, and temperature sensor. In order to weaken the guided wave effect and improve the resolution of the stress field, the ultrasonic transducer with a center frequency of 5 MHz and a size of 0.25 in is used.

Temperature variation will cause ultrasonic wave speed change and then cause stress measurement error. To assure the measurement accuracy, the measurement error deduced by temperature variation should be corrected. To implement the compensation of the relationship between temperature and ultrasonic transit time between transducers, the experimental results are presented in Fig. 2.

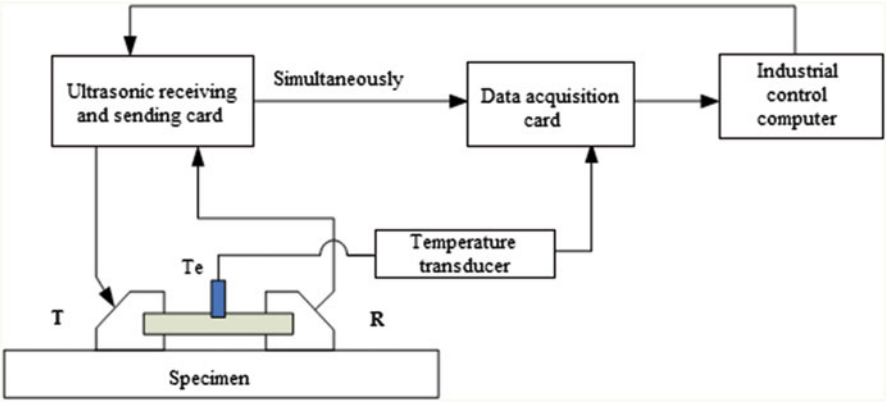

Fig. 1 Principle diagram of ultrasonic linear detection system of residual stress

Fig. 2 The curve of temperature and transit time difference

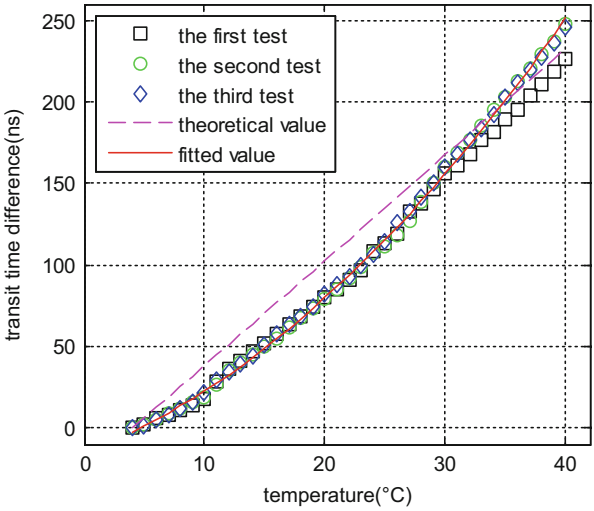

3.2 Ultrasonic Nonlinear Detection System

The principle diagram of nonlinear ultrasonic detection system is shown in Fig. 3. The system mainly includes the sine-wave generator, digital oscilloscope, amplifier, excited receiving surface wave transducer, and computer.

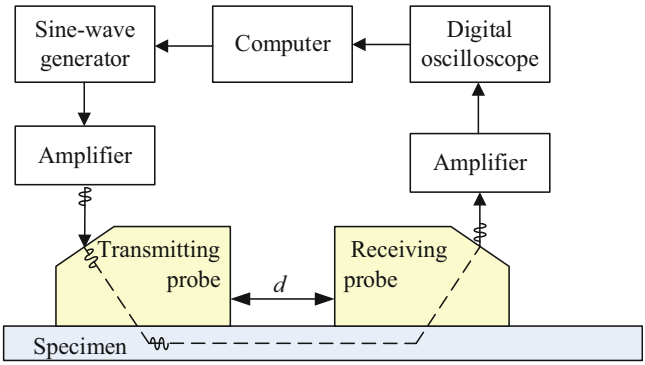

Fig. 3 Nonlinear ultrasonic testing system

Table 1 Chemical composition of 45 steel

Composition	Si	Mn	P	S	Cr	Ni	Cu	Fe
Contents (%)	0.20	0.60	0.04	0.03	0.20	0.20	0.18	The rest

The experimental system is excited by the sine-wave generator to generate the excitation signal, then surface wave transducer with center frequency of 5 MHz is driven, and acoustic signal is generated in the specimen. In order to get better harmonic amplitude of the received signal, the signal is received by the transducer with a center frequency of 10 MHz and the FFT transform of the received waveform is used to measure the fundamental amplitude of A_1 and higher harmonic amplitudes A_2 and A_3. Study on the second-order relative nonlinear coefficient β and tensile stress σ is taken.

3.3 Experimental Materials and Processes

3.3.1 Sample Material Properties and Specimen Preparation

45 steel is a high-quality carbon structural steel, one of the most commonly used steel. Its chemical composition is shown in Table 1.

The density of 45 steel is 7850 kg/m^3, elastic modulus E is 210 GPa, and Poisson's ratio μ is 0.269. The yield limit of 45 steel obtained by standard tensile test is 355 MPa, the strength limit is 490 MPa, the hardness is 60.4 HRB, the surface wave velocity is 3000 m/s, and the longitudinal wave velocity is 5900 m/s.

3.3.2 Stress Loading

In the experiment, in order to observe the effect of tensile stress on the nonlinear phenomenon of ultrasonic better, to stop loading for 20 s every 20 MPa, the stress loading range of 45 steel is 0 ~ 400 MPa. Using the system to record the waveform of the received signal, the loading experimental field and tensile stress-time curve are shown in Figs. 4 and 5.

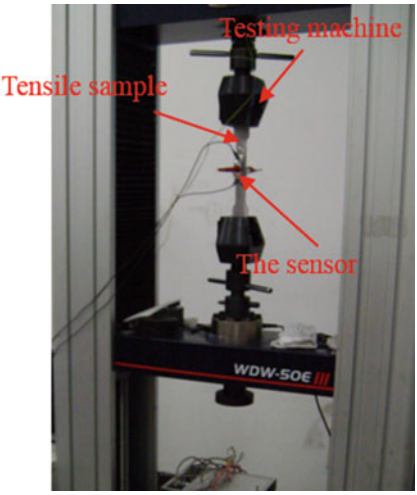

Fig. 4 Setup of stress loading

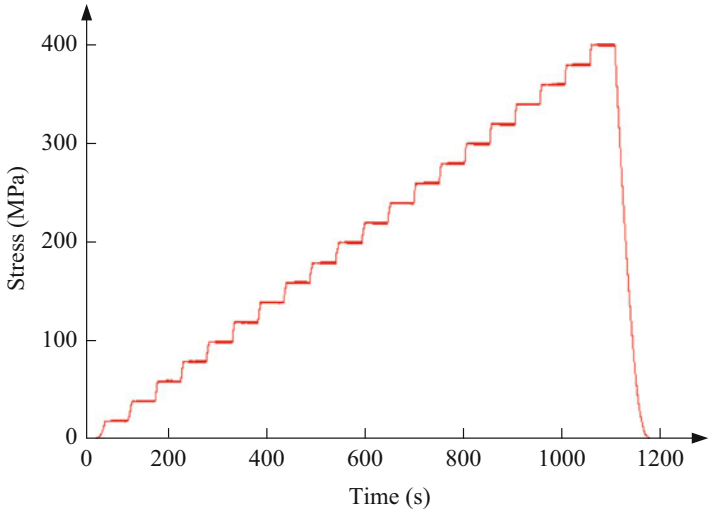

Fig. 5 Tensile stress-time curve

4 Results

4.1 Experimental Results of Ultrasonic Linear Detection Method

Figure 6a, b shows the relationship between the change of the sound time Δt and the output tensile stress of the stretching device $\Delta\sigma$. The measured points are not less than 10, the number of repeated stretching is not less than five times, the average value of the data is linear fitting, and the reciprocal of linear slope is namely the stress coefficient K.

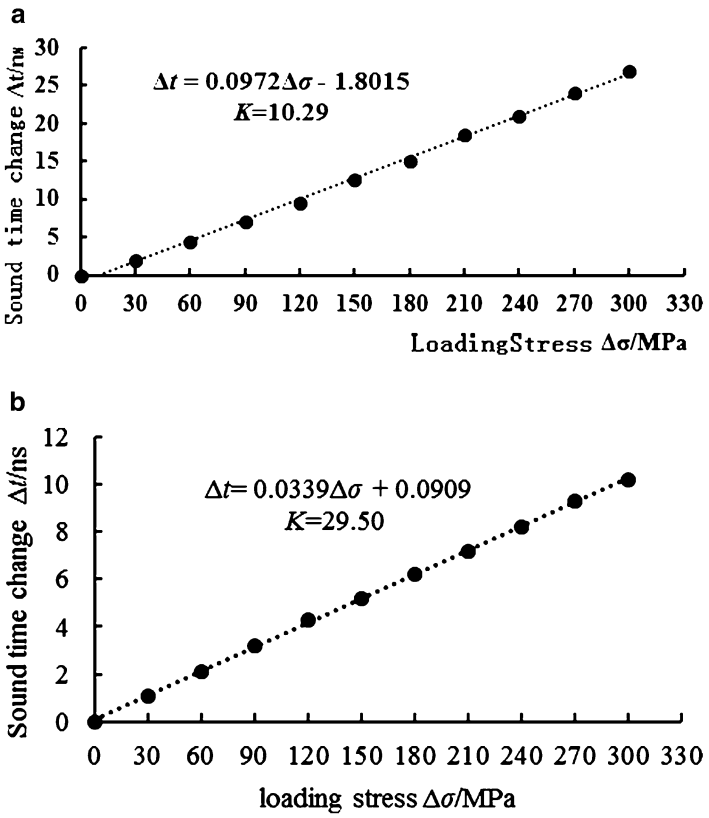

Fig. 6 The relationship between the time and the tensile stress. (**a**) The relationship between the time and the tensile stress of the longitudinal wave propagating along the stress direction and (**b**) the relationship between the time and the tensile stress of the shear wave with a propagation direction perpendicular to the stress direction and a polarization direction parallel to the stress direction

For the longitudinal wave propagating along the stress direction:

$$\Delta t = 0.0972\Delta\sigma - 1.8015 \tag{12}$$

For the shear wave with a propagation direction perpendicular to the stress direction and a polarization direction parallel to the stress direction:

$$\Delta t = 0.0339\Delta\sigma + 0.0909 \tag{13}$$

Thus, as for the plastic material in the elastic range, the stress state of the current along the wave propagation direction can be characterized by the stress coefficient K of the material measured in the experiment.

4.2 Experimental Results of Ultrasonic Nonlinear Detection Method

The relationship between the ultrasonic relative nonlinear coefficient and tensile stress in the tensile test of 45 steel is shown in Fig. 7a, b. When the tensile stress is less than 300 MPa (about 84.5% of yield limit), the second-order relative nonlinear coefficient β and tensile stress are approximately linear relationship; when the tensile stress is more than 300 MPa, the second-order nonlinear coefficient β with the tensile stress increased changes rapidly.

The relationship between the third-order relative nonlinear coefficient δ' and tensile stress σ is consistent with the one between the second-order nonlinear coefficient and tensile stress.

To fit the experimental curve, the fitting curve of the relative nonlinear coefficient and tensile stress is obtained, and fitting curve of the second-order nonlinear coefficient β' and tensile stress σ is shown below:

$$\beta' = 5 \times 10^{-6}\sigma^2 + 0.0008\sigma + 0.154 \tag{14}$$

Fitting curve of the third-order nonlinear coefficient and tensile stress σ is shown below:

$$\delta' = 1 \times 10^{-5}\sigma^2 + 0.0007\sigma + 0.0045 \tag{15}$$

By formulas (14) and (15), the relative second-order nonlinear coefficient β' and third-order nonlinear coefficient δ' obtained by measurement, namely, can be used to characterize the stress state.

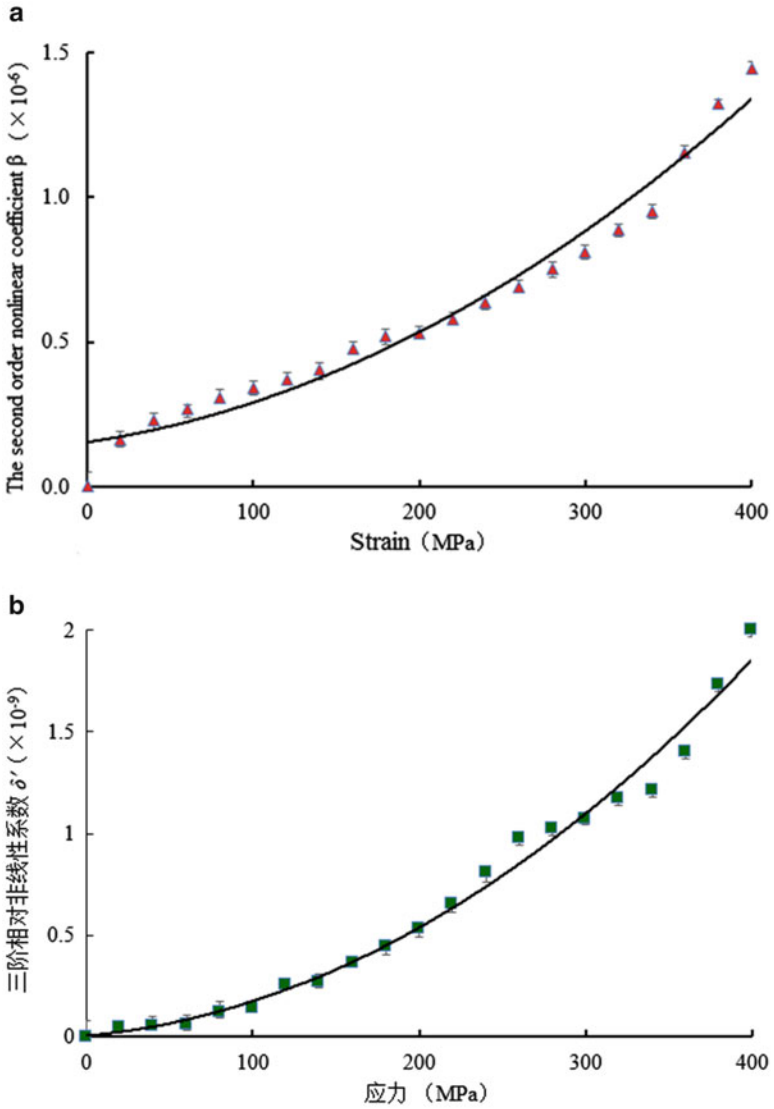

Fig. 7 The relationship between ultrasonic nonlinear coefficient and tensile stress. (**a**) The relationship between ultrasonic second-order relative nonlinear coefficient and tensile stress and (**b**) the relationship between ultrasonic third-order relative nonlinear coefficient and tensile stress

5 Application

5.1 Application of Linear Ultrasonic Contact Detection Method

5.1.1 Welding Stress Detection in Pipelines

The material of pipeline is X70 steel and welding procedure is manual arc welding. We tested residual stress around straight weld joint in a section of pipeline. The results are shown in Fig. 8. In order to verify the accuracy of the test results, a hydrostatic test has been carried out. From Fig. 9, it is observed that the blasting area is consistent with the dangerous area evaluated by ultrasonic wave method.

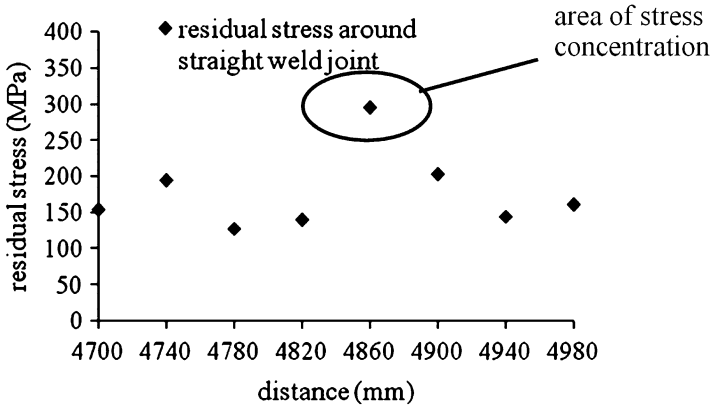

Fig. 8 Distribution curve of residual stress

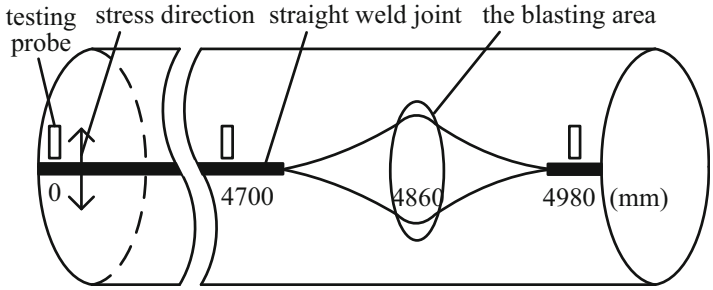

Fig. 9 Hydrostatic experimental verification

Fig. 10 Experimental setup

5.1.2 Gear Residual Stress Testing

We evaluated the residual stresses in the gear tooth root using an ultrasonic measurement method, Fig. 10. The gear tooth root was divided into six equal sections in the axial direction. Each regional stress value was measured twice. The results are shown in Fig. 11a. The measurement results of 23 teeth are shown in Fig. 11b.

5.2 Application of Nonlinear Ultrasonic Noncontact Detection Method

Using robots, scanning was carried out on the welded aluminum plate through water coupling as shown in Fig. 12. Based on nonlinear method the result of second-order nonlinear coefficient of aluminum plate is shown in Fig. 13. This method is a rapid, noncontact, and nondestructive testing technology.

In addition, we also carried out application research on residual stress testing of high-pressure pipe, vehicle driving shaft, vehicle shell weld joint, aviation turbine disk, blade of aviation engine, aluminum alloy plates, high-speed railway track, component with coating layer, glass and ceramics, circuit board, gear tooth root, bearing, thin pipe or tube, fiber composites, and so on. The states of residual stress distribution in those mechanical components we tested match with the actual results. Up to now, there already have been more than 20 corporations in China using the ultrasonic detector to nondestructive testing residual stress.

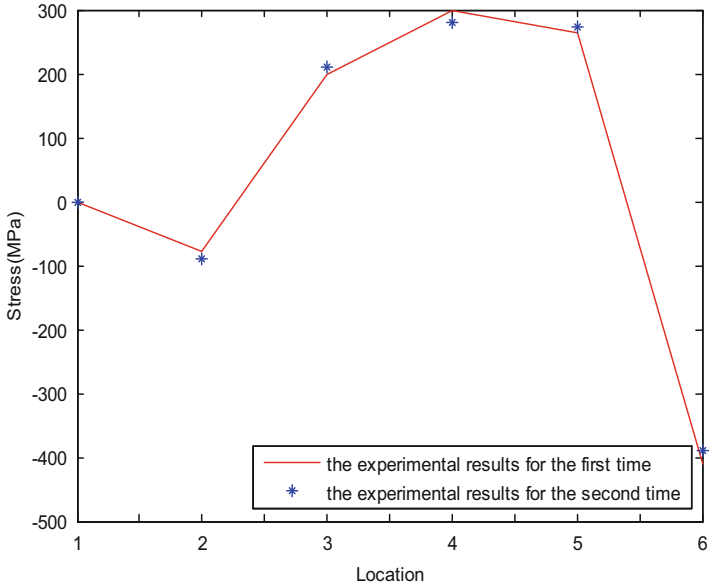

(a)

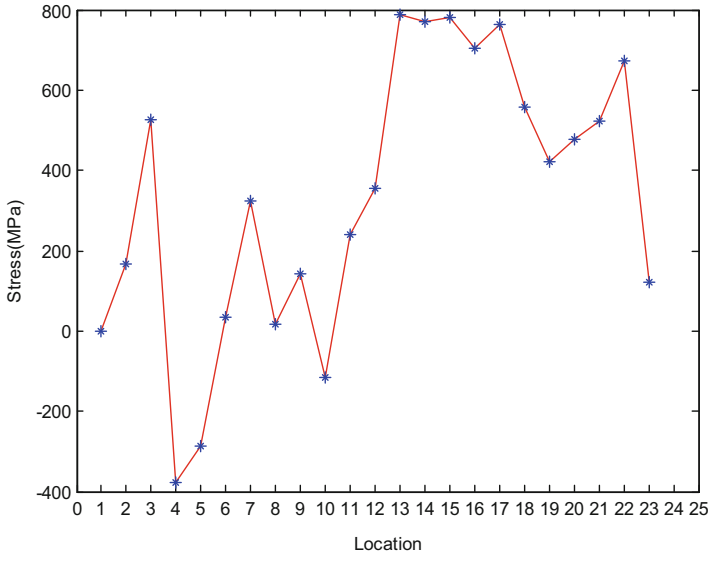

(b)

Fig. 11 Gear residual stress distribution. (**a**) Axial direction of the gear stress distribution in the tooth root and (**b**) teeth root stress distribution in 23 tooth gear

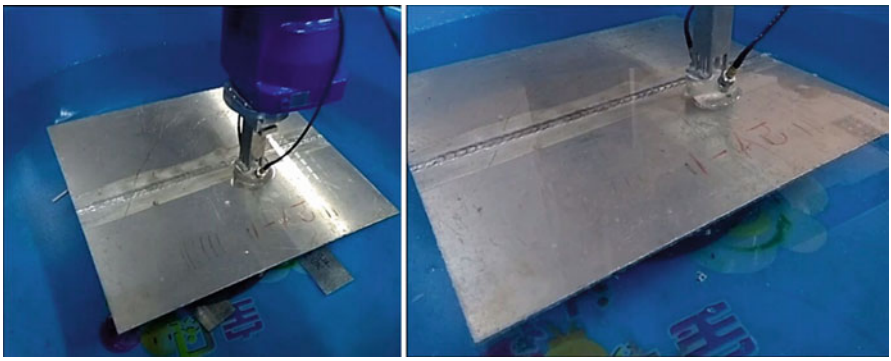

Fig. 12 Experimental setup

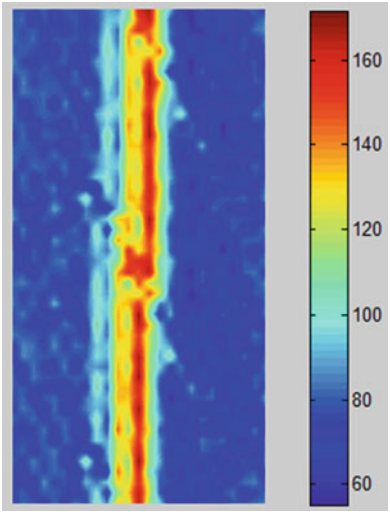

Fig. 13 Second-order nonlinear coefficient distribution

6 Conclusion

1. Based on the theory of acoustoelasticity, the linear ultrasonic testing method and the ultrasonic nonlinear detection method are analyzed, respectively, in theory. The linear relationship between stress and ultrasonic longitudinal and shear propagating velocity are obtained. Furthermore, the relational expression between stress and the second and third nonlinear ultrasonic coefficient is also obtained.
2. By setting up an experimental system, to compare the results of linear and nonlinear residual stress detection, it shows that the two methods can effectively measure the residual stress, and the detection results are in good agreement.

References

1. G.E. Totten, M. Howes, T. Inoue, *Handbook of Residual Stress and Deformation of Steel* (ASM International Publishers, Materials Park, OH, 2002), pp. 417–444
2. J.L. Jacomino, J.S. Burgos, A.C. Cruz, et al., Use of explosives in the reduction of residual stresses in the heated zone of welded joints. Weld. Int. **24**, 920–925 (2010)
3. N.S. Rossini, M. Dassisti, K.Y. Benyounis, et al., Methods of measuring residual stresses in components. Mater. Des. **35**, 572–588 (2012)
4. J. Epp, T. Hirsch, Residual stress state characterization of machined components by X-ray diffraction and multiparameter micromagnetic methods. Exp. Mech. **50**, 195–204 (2010)
5. Q. Wang, K. Ozaki, H. Ishikawa, et al., Indentation method to measure the residual stress induced by ion implantation. Nucl. Instrum. Methods Phys. Res. B **242**, 88–92 (2006)
6. J. Yashar, A.N. Mehdi, et al., Residual stress evaluation in dissimilar welded joints using finite element simulation and the LCR ultrasonic wave. Russ. J. Nondestr. Test. **48**, 541–552 (2012)
7. W.T. Song, Q.X. Pan, C.G. Xu, et al., in *Benchmark of Residual Stress for Ultrasonic Nondestructive Testing*, 2013 Far East Forum on Nondestructive Evaluation/Testing: New Technology, & Application (2013), pp. 73–76
8. H. Miao, D.W. Zuo, M. Wang, et al., Numerical calculation and experimental research on residual stresses in precipitation-hardening layer of NAK80 steel for shot peening. Chin. J. Mech. Eng. (Engl. Ed.) **24**(3), 439–445 (2011)
9. P.J. Withers, Mapping residual and internal stress in materials by neutron diffraction. C. R. Phys. **8**(8), 806–820 (2007)
10. S. Desvaus, M. Duquennoy, J. Gualandri, et al., Evaluation of residual stress profiles using the Barkhausen noise effect to verify high performance aerospace bearings. Nondestr. Test. Eval. **20**(1), 9–24 (2005)
11. K.Y. Jhang, H.H. Quan, J. Ha, et al., Estimation of clamping force in high-tension bolts through ultrasonic velocity measurement. Ultrasonics **44**, e1339–e1342 (2006)
12. J.L. Rose, *Ultrasonic Waves in Solid Media* (Cambridge University Press, Cambridge, 1999)
13. J.-Y. Kim, J. Qu, L.J. Jacobs, J.W. Littles, M.F. Savage, Acoustic nonlinearity parameter due to microplasticity. J. Nondestr. Eval. **25**(1), 29–37 (2006)
14. M. Liu, G. Tang, L.J. Jacobs, et al., Measuring acoustic nonlinearity by collinear mixing waves. Rev. Prog. Quant. Nondestr. Eval. **30**, 322–329 (2011)

Author Index

G. Shen et al. (eds.), *Advances in Acoustic Emission Technology*, Springer Proceedings in Physics 179, DOI 10.1007/978-3-319-29052-2

Subject Index

G. Shen et al. (eds.), *Advances in Acoustic Emission Technology*, Springer Proceedings in Physics 179, DOI 10.1007/978-3-319-29052-2